UNIVERSITÀ
DEGLI STUDI
DI PADOVA

Sede Amministrativa: Università degli Studi di Padova

Dipartimento di Scienze Chimiche

Scuola di Dottorato di Ricerca in Scienza e Ingegneria dei Materiali

XXIV ciclo

New hybrid inorganic-organic proton conducting membranes for PEMFC: synthesis, properties and conduction mechanisms

Direttore della Scuola: Ch.mo Prof. Gaetano Granozzi

Supervisore: Ch.mo Prof. Vito Di Noto

Dottorando: Matteo Piga

Acknowledgements

Several people helped me to complete this thesis and deserve to be mentioned and thanked.

My scientific supervisor Professor Vito Di Noto, for giving me the opportunity to research and for taking into account my proposals and work. With his help, for me these years resulted not only in a scientific maturation but also in a human growth.

I want to thank all friends and colleagues of Prof. Di Noto's research group: Federico, Enrico, Gwen, Sandra, Claudio, Keti, Andrea, Giuseppe, Shun, Reese, Matteo and Francesco. Thank you very much for the good time spent together.

Heartfelt thanks goes to my family. To my parents, Franco and Cinzia, and to my brother Luigi. Thank you for having never doubted about my ability to conclude this research activity and, in the case of my brother, thanks also for your fundamental "logistic" contribution.

A special thank goes to Elisa. Thank you for your support and unconditional trust. Your presence has been crucial to the achievement of this purpose.

Matteo Piga

Abstract

Electrochemical devices for the conversion of chemical energy into electrical power, such as proton exchange membrane fuel cells (PEMFCs), are of intense interest to industry and the scientific community because of their high energy conversion efficiency, low environmental impact, and the possibility for use in a wide variety of applications from portable electronic devices to light-duty electric vehicles. At the core of the fuel cell is a PEM that allows the transport of hydrogen ions, evolved at the anode, to the cathode where oxygen is reduced to water. Todays prevalent PEMs feature perfluorinated main chains functionalized with perfluoroether side chains terminated with acidic -SO_3H groups. These materials (DupontTM Nafion®, Asashi Aciplex®, Dow®, and Flemion®) generally are characterized by a high chemical, thermal and mechanical stability; they also exhibit good proton conductivity at high levels of hydration. The hydration requirements limit the widespread commercial use of conventional PEMs, which have inadequate proton conductivity at temperatures above 90°C and at low values of relative humidity. Fuel cells capable of operating above 120°C at low levels of hydration would: obviate the need of bulky and expensive water management modules, simplify thermal management; and reduce the impact of catalyst poisons such as carbon monoxide. In an effort to overcome the limitations of conventional PEMs, this work reports the synthesis and characterization of new proton conducting membrane alternatives to classic fluorinated polymers for application in PEMFCs. The materials were synthesized according to two distinct strategies: 1) dope a Nafion membrane in order to improve its thermo-mechanical properties and proton conductivity or extend its operating conditions to temperatures above 100°C and an anhydrous environment; 2) synthesize and characterize proton exchange membranes based on polybenzimidazole and polysulfone as an alternative to perfluorinated polymers.

The first point regarded the study of two different systems obtained by doping a Nafion membrane with the [$(ZrO_2)(Ta_2O_5)_{0.119}$] inorganic “core-shell” nanofiller or with two different

proton conducting ionic liquids, triethylammonium methanesulfonate and triethylammonium perfluorobutanesulfonate. The study of new PEMs alternative to fluorinated polymers has been developed considering polybenzimidazole and sulfonated poly(p-phenylenesulfone) membranes whose properties have been modulated by the addition of phosphoric acid and an hybrid filler or poly(1-oxotrimethylene) and silica, respectively. All the proposed materials were extensively characterized in terms of their thermal, mechanical, structural and electrical properties in order to highlight the interactions between the different components present within the membranes. These interactions govern the membranes macroscopic properties that need to be improved in order to optimize and predict the behavior of these materials under operating conditions in fuel cells.

Abstract (Italiano)

Celle a combustibile basate su membrane a scambio protonico (PEMFCs) sono dispositivi elettrochimici per la conversione di energia chimica in energia elettrica. Le PEMFCs suscitano notevole interesse sia nel mondo industriale che accademico a causa della loro elevata efficienza di conversione, basso impatto ambientale e vasta gamma di utilizzo che spazia dall'elettronica portatile fino all'autotrazione.

All'interno della cella a combustibile si trova la membrana a scambio protonico (PEM), che consente il trasferimento di protoni dall'anodo al catodo.

Attualmente le membrane polimeriche a scambio protonico maggiormente utilizzate sono costituite da polimeri fluorurati funzionalizzati con gruppi polieterei terminanti con gruppi acidi (tipicamente -SO_3H). Questi materiali (DupontTM Nafion®, Asashi Aciplex®, Dow®, and Flemion®) generalmente presentano elevata stabilità chimica, termica e meccanica ma tuttavia mostrano valori di conducibilità sufficienti per il loro impiego in cella a combustibile solo per elevati livelli di idratazione. La scarsa conducibilità protonica dei polimeri perfluorurati per temperature maggiori di 90°C e bassi livelli di idratazione limita fortemente il loro utilizzo su larga scala.

Celle a combustibile che operano a temperature superiori a 120°C e bassi livelli di idratazione non necessitano dell'introduzione di sistemi di umidificazione e raffreddamento, riducendo il costo e semplificando la realizzazione ed ingegnerizzazione del dispositivo finale. Inoltre, l'aumento di temperatura riduce l'avvelenamento del catalizzatore da contaminanti esterni come ad esempio il monossido di carbonio.

Al fine di superare le limitazioni delle PEMs convenzionali, questo lavoro di tesi riporta la sintesi e la caratterizzazione di nuove membrane polimeriche a conducibilità protonica alternative ai classici polimeri fluorurati per applicazioni in celle a combustibile.

I materiali sono stati sintetizzati seguendo due diverse strategie: 1) drogare una membrane di Nafion al fine di aumentare il suo intervallo di stabilità termico e meccanico e la sua conducibilità protonica così da estenderne le condizioni operative di utilizzo a temperature maggiori di 90°C e per bassi o nulli livelli di idratazione; 2) sintetizzare e caratterizzare PEMs basate su polibenzimidazolo e polisulfone come materiali alternativi ai classici polimeri fluorurati.

Il primo punto ha riguardato lo studio di due diversi sistemi ottenuti drogando una membrana di Nafion con il filler inorganico [$(ZrO_2)(Ta_2O_5)_{0.119}$] oppure con due diversi liquidi ionici a conducibilità protonica, il trietilammonio-metansolfonato ed il trietilammonio-perfluorobutansolfonato.

Lo studio di nuove membrane alternative ai polimeri fluorurati è stato sviluppato considerando membrane di polibenzimidazolo (PBI) e polisulfone solfonato ($sPSO_2$) le cui proprietà sono state modulate dall'aggiunta di acido fosforico e di un filler ibrido a base di silice funzionalizzata (nel caso del PBI) o di poliossotrimetilene e silice (per le membrane a base di $sPSO_2$).

Al fine di delucidare le interazioni esistenti tra i diversi componenti presenti all'interno delle membrane, tutti i materiali sono stati ampiamente caratterizzati dal punto di vista delle loro proprietà termiche, meccaniche, strutturali ed elettriche. Queste interazioni governano le proprietà macroscopiche delle membrane che necessitano di essere migliorate al fine di ottimizzare e prevedere il comportamento di questi materiali in condizioni di esercizio in celle a combustibile.

Table of contents

Chapter I

Proton Exchange Membrane Fuel Cell

1.1. Perspectives on hydrogen energy

The events of recent years have made the availability of inexpensive and accessible energy a world-wide concern. Since the turn of the 21st century, crude oil prices have experienced between a two and a seven-fold increase [1] resulting in increased attention directed towards alternative and renewable energy sources. One avenue of research is focused on the production, storage and consumption of energy derived from hydrogen, i.e., the development of a "hydrogen-based economy".

In a hydrogen-based economy, fuel cells are used for the conversion of chemical energy stored in the fuel to electrical energy. Fuel cells provide several advantages over conventional methods of energy conversion, particularly the internal combustion engine, such as: a) increased energy conversion efficiency, which may exceed 60% (part a of Figure 1.1); b) reduced oil consumption – fuel cell electric vehicles can result in more than a 95% reduction in oil usage as compared to conventional internal combustion engine vehicles (Figure 1.1 part b); c) increased fuel flexibility – fuel cells can use clean energy sources such as biofuels, methanol, etc, or hydrogen produced from renewable or conventional energy sources; and d) reduced CO_2 and pollutant emissions –

for combined heat and power systems fuel cells can achieve a 35-50% or higher reduction in CO_2 emissions, depending on the fuel, and a 90% reduction of pollutant emissions (Figure 1.1 part c) [2,3].

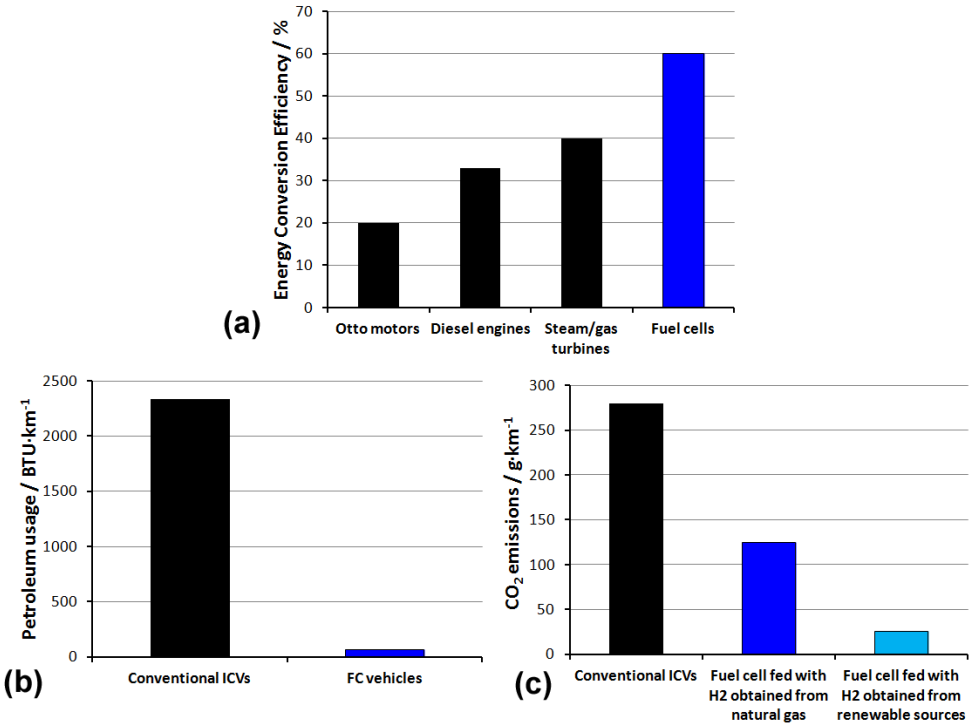

Figure 1.1 Comparison between conventional thermal engines and fuel cells in terms of: a) energy conversion efficiency [2]; (b) petroleum usage [3,4]; and (c) overall CO_2 emissions [3,4].

To properly consider emission reductions, the entire energy cycle must be considered and not only the end-use application. This means that for fuel cells the wells-to-wheels emissions, i.e. emissions resulting from both hydrogen production and conversion, should be analysed. In mid-sized vehicles powered with internal combustion engines running on gasoline, 280 grams of CO_2 are emitted per kilometre of travel. In comparison, only 125 grams of CO_2 are emitted by a fuel cell electric vehicle where the hydrogen fuel was produced from natural gas. This number can be reduced to about 25 grams when the hydrogen fuel is produced from a clean renewable energy source [3,4].

There are several different types of fuel cells that can be implemented depending on the end-use application, i.e. stationary, transportation or portable power, which include solid oxide, alkaline,

direct methanol, proton exchange membrane, phosphoric acid and molten carbonate fuel cells. The various families of fuel cells may be distinguished by the functional materials they adopt, particularly in terms of the electrolyte and the electrocatalyst materials, and by their operating temperature, which ranges from room temperature (e.g. in portable polymer electrolyte fuel cells fed with liquid fuels) up to 1000°C (e.g. in solid oxide fuel cells) [5].

This thesis reports the synthesis and characterization of new proton conducting polymer electrolytes for use in proton exchange membrane fuel cells (PEMFCs). The following sections of this chapter describe the components and the main characteristics of PEMFCs, particularly with regard to the proton exchange membrane (PEM).

1.2. Proton Exchange Membrane Fuel Cell (PEMFC)

1.2.1 PEMFC: past, present and future

PEMFCs were first invented at General Electric in 1959. While PEMFCs were tested as part of the NASA Gemini program in preparation for lunar missions, ultimately alkaline fuel cells replaced PEMFCs on the Apollo missions [6]. The PEMFCs used by NASA for the Gemini missions contained styrene sulfonic acid-based electrolyte membranes. However, these membranes suffered from a lack of durability and mechanical strength [7].

Proton exchange membrane fuel cells are electrochemical devices for the conversion of chemical into electrical energy and heat. PEMFCs are based on a proton-exchange membrane sandwiched between two porous electrodes covered by suitable electrocatalysts, which generally consist of nanoparticles of platinum-group metals supported on active carbons with a large surface area. PEMFCs are advantageous because they are compact, lightweight and have high power densities with high current densities as compared to some of the other families of fuel cells [8]. PEMFCs have already been integrated into niche markets in some sectors. Fuel cell integration has been possible in these markets because the lifetime cost and/or the disadvantages of the competing

technologies make the initial cost acceptable [9]. These markets include specialty applications such as forklifts and stationary, auxiliary and portable power units [3,9]. In addition, fuel cells are also being used for transportation to power some buses, boats, trains and scooters [8]. In 2008, Boeing announced that it had made the first fuel cell powered flight [10].

The United States Department of Energy (US DOE) has projected that the fuel cell market could reach maturity in the next 10 to 20 years, at which time revenues could total between 43 and 139 billion US dollars (USD) per year in the stationary, transportation and portable power sectors combined. The transportation market has the potential to contribute the largest portion of this revenue, with a projected 18–97 billion USD per year. Current market trends have shown a 36% increase in the fuel cell megawatts shipped between 2008 and 2010. These increases have occurred primarily in Japan, Korea and the United States. Research and development trends have also shown significant increases in the number of fuel cell patents issued in the past two years, up from a relatively constant trend of between 500 and 600 patents per year to almost 1000 in 2010, which corresponds to a greater than 57% increase [11].These numbers are almost three times higher than the number of patents in the next highest clean energy field, i.e. solar [11].The vast majority of patents granted are from US and Japan, followed by Germany and South Korea[3].

Despite promising gains in research, development, and implementation of fuel cells, there are still several important technological, economic and institutional barriers that must be overcome before the widespread commercialization of fuel cells can occur. The most significant technological barriers are cost, durability and fuel storage, in the case of systems running on hydrogen. For stationary applications, fuel cell costs must be reduced to 750 US dollars (USD) per kW and the power plant must be able to function for 40,000 hr. For transportation applications, the cost must be reduced to 30 USD per kW and the system must have a durability of at least 5,000 hr with cycling[3]. At the present time, the cost of a fuel cell for transportation

applications is 51 USD per kW, which represents a 30% decrease since 2008 and an 80% decrease since 2002 [3]. The consumer cost of hydrogen fuel "at the pump" must be reduced to 2 to 4 USD per gallon of gasoline equivalent (approximately one kg of hydrogen is equivalent to one gallon of gasoline by energy content) and vehicles should desirably have a storage capacity that provides a range greater than 480 km without compromising space and performance [3]. In addition to these technological hurdles, there is a need for the development and implementation of safety codes and standards and of infrastructure for fuel cell production, hydrogen storage and delivery. Finally, there must be public awareness and acceptance of these new technologies. If these obstacles are not overcome, the widespread commercialization of fuel cells will not be possible [3].

1.2.2 PEMFC: operating principle

A PEMFC is a multilayer system consisting essentially of two electrodes where the electrochemical reactions occur and an electrolyte, i.e. the proton exchange membrane, as shown in Figure 1.2. The PEM is squeezed between the two porous, electrically conductive electrodes and has to be impermeable to reagents and show proton, but no electronic conductivity. The electrodes are typically made of carbon cloth or carbon fiber paper. The reagents consist of an oxidant (air or pure O_2) and a fuel (H_2, ethanol, methanol), which reach the electrodes through two separate circuits and vary as function of the type of the device. At the interface between the porous electrode and the polymer membrane there is a layer with catalyst particles. For PEMFCs fed with hydrogen, the most common catalyst for both the oxygen reduction and hydrogen oxidation reactions is platinum supported on carbon powders (Vulcan XC72R) with a high mesoporous area (>75 m^2g^{-1}). In order to minimize the cell potential losses due to the rate of proton transport and reactant gas permeation into the depth of the electrocatalyst layer, this layer

should be made reasonably thin. At the same time, the metal active surface area should be maximized, for which the Pt particles should be as small as possible.

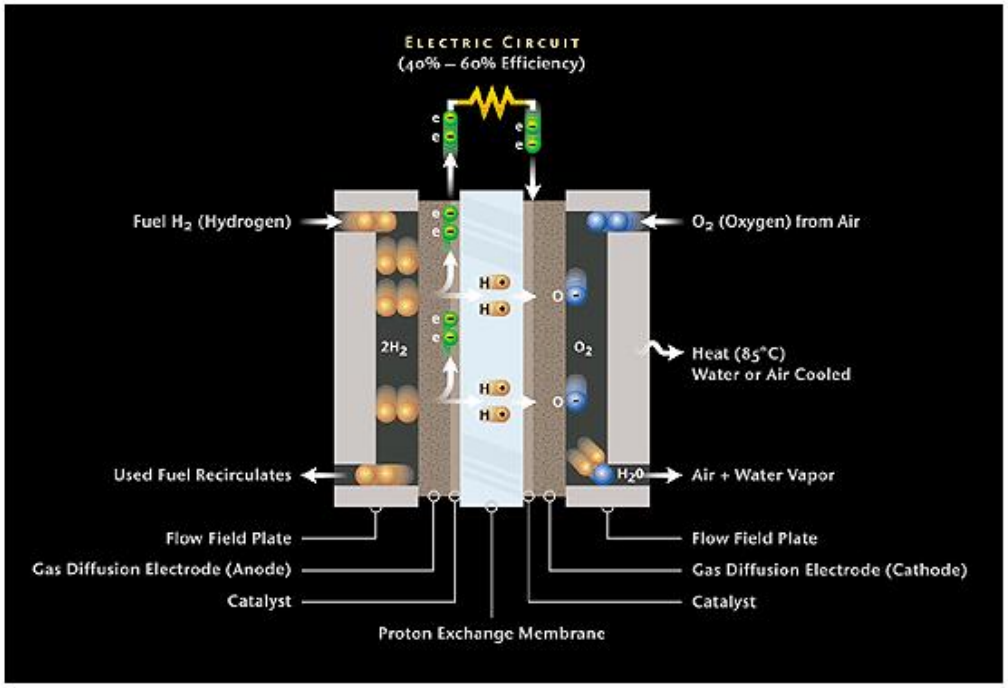

Figure 1.2 Scheme of a PEMFC.

Electrochemical reactions occur at the surface of the catalyst at the interface between the electrodes and the membrane. Hydrogen, which is fed on one side of the membrane, splits into its primary constituents – protons and electrons. Each hydrogen atom consists of one electron and one proton. Protons travel through the membrane, while the electrons travel through electrically conductive electrodes, the current collectors, and the outside circuit where they perform useful work and return to the other side of the membrane. At the catalyst sites between the membrane and the second electrode the electrons meet the protons that passed through the membrane and oxygen that is fed on that side of the membrane. Water is created in the electrochemical reaction, and is then pushed out of the cell with an excess flow of oxygen. The net result of these simultaneous reactions is a current of electrons through an external circuit. The electrode on the hydrogen side is negative and called the anode, while the electrode in

contact with oxygen is positive and called the cathode. The electrochemical reactions in a fuel cell happen simultaneously on both sides of the membrane – the anode and the cathode. The basic fuel cell reactions are:

At the anode: $$H_2 \rightarrow 2H^+ + 2e^- \quad (1.1)$$

At the cathode: $$\frac{1}{2}O_2 + 2H^+ + 2e^- \rightarrow H_2O \quad (1.2)$$

Overall: $$H_2 + \frac{1}{2}O_2 \rightarrow H_2O \quad (1.3)$$

The maximum amount of electrical energy generated in a fuel cell corresponds to the Gibbs free energy, ΔG, of the above reaction:

$$W_{el} = -\Delta G \quad (1.4)$$

The theoretical potential of a fuel cell, E, is then:

$$E = \frac{-\Delta G}{nF} \quad (1.5)$$

where n is the number of electrons involved in the reaction (n = 2) and F is the Faraday's constant. Since ΔG, n and F are all known, the theoretical hydrogen/oxygen fuel cell potential can also be calculated. At 25°C and atmospheric pressure, E = 1.23 V.

Assuming that all of the Gibbs free energy can be converted into electrical energy, the maximum possible (theoretical) efficiency of a fuel cell is a ratio between the Gibbs free energy and hydrogen higher heating value, ΔH:

$$\eta = \frac{\Delta G}{\Delta H} = \frac{237.34}{286.02} = 83\% \quad (1.6)$$

The theoretical (reversible) cell potential is a function of operating temperature and pressure:

$$E_{T,P} = -\left(\frac{\Delta H}{nF} - \frac{T\Delta S}{nF}\right) + \frac{RT}{nF} ln\left[\frac{a_{H_2} a_{O_2}^{0.5}}{a_{H_2O}}\right] \quad (1.7)$$

where *a* stands for activity (the ratio between the partial pressures of reactants (H_2 and O_2) or product (H_2O) and the atmospheric pressure (for liquid water product $a_{H_2O} = 1$)).

Actual cell potentials are always smaller than the theoretical ones due to irreversible losses. Voltage losses in an operational fuel cell are caused by several factors such as:

- kinetics of the electrochemical reactions (activation polarization);
- internal electrical and ionic resistance;
- mass transport limitations of the reactants to reach the reaction sites;
- internal (stray) currents;
- crossover of reactants.

A polarization curve, i.e. the voltage-current diagram is the most important characteristic of a fuel cell and its performance. It depends on numerous factors such as catalyst loading, membrane thickness and state of hydration, catalyst layer structure, flow field design, operating conditions (temperature, pressure, humidity, flow rates and concentration of the reactant gases), and uniformity of local conditions over the entire active area. Typically, a fuel cell operating at atmospheric pressure should generate more than 0.6 A/cm^2 at 0.6 V, and more than 1 A/cm^2 at 0.6 V when operated at pressures of (300 kPa or higher).

Each type of fuel cell operates at an optimal temperature, which is mainly dependent on the characteristics of the polymer membrane. The PEMFC typical operating temperature is between 60 and 80°C, in order to avoid membrane dehydration and thus the collapse of the PEM proton conductivity. The necessity to maintain the membrane in fully hydrated conditions and the operating temperature around 80°C involves the introduction of humidification and cooling systems into the fuel cell, which complicates the implementation and increases the costs of the final device.

1.3. Proton Exchange Membranes (PEMs)

1.3.1 Nafion

A material can make a good proton-conducting fuel cell membrane if it meets the following criteria: 1) good chemical and electrochemical stability within the operating cell; 2) mechanical strength and stability under operating conditions; 3) chemical properties of the membrane components are compatible with the bonding requirements of the membrane electrode assembly; 4) extremely low permeability to reactant species; 5) high water mobility to maintain uniform the electrolyte content and prevent localized drying; 6) high proton conductivity to support high currents with a minimal resistance loss and negligible electronic conductivity; and 7) a low production cost which is compatible with application [12,13].

The first significant step in the PEMs research and development occurred in 1966 with Dupont™'s production of Nafion®.[1] Nafion® exhibited significantly improved properties including doubling the specific conductivity and a four-fold increase in the lifetime [7]. These properties allowed Nafion® to quickly replace other membranes and made it the industry standard. A number of other companies, including Dow, Asahi Chemical, 3M and Solvay-Solexis, have since developed membranes based on the structure of Nafion®, i.e. ®, Aciplex®, the membrane originally manufactured by Dow®, Aquivion® and the membrane manufactured by 3M.

Nafion (chemical structure reported in Figure 1.3) consists of a polytetrafluoroethylene (PTFE) backbone endowed with perfluoroether side chains terminated with a sulfonic acid group [14].

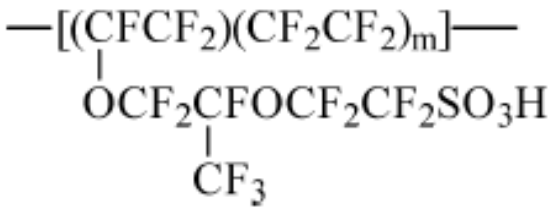

Figure 1.3 Chemical structure of Nafion. The index m depends on the equivalent weight of the polymer.

[1] The DuPont Oval Logo, DuPont™, The miracles of science™ and all products denoted as Dupont™ and Nafion® are trademarks or registered trademarks of DuPont or its affiliates.

The presence of the PTFE-like backbone is responsible for the high thermal and mechanical stability of Nafion, while the sulfonic acid groups are responsible for the membrane's proton conductivity. In fully hydrated conditions the proton conductivity of Nafion reaches values up to 0.1 S/cm [3]. The equivalent weight (EW) of Nafion is defined as the grams of dry Nafion per moles of sulfonic acid groups [14]. EW is an average value in the sense that the comonomer sequence distribution gives a distribution in the parameter *m* of Figure 1.3. *m* determines the number of CF_2 groups present between two comonomer units. The relationship between EW and *m* is given by $EW = 100m + 446$, where 100 and 446 are the molecular weights of one tetrafluoroethylene unit and the comonomer in the acid form, respectively [14]. As example, equivalent weights of 1100 and 1000 g/mol result in the presence of 14 and 11 CF_2 units between two side chains, respectively. The equivalent weight is related to the proton exchange capacity (PEC) by the equation: $PEC = 1000/EW$ [14].

Two different groups of structural models have been proposed for Nafion [14]. The first group of models is based on a materials structure in which ionic clusters of 3 – 5 nm diameter are interconnected in a three-dimensional structure through channels with a diameter of 1 – 1.5 nm (Figure 1.4). The acid terminated side chains of the PTFE backbone extend into the cages, giving rise to an inverted micelle structure where the water molecules are clustered, as shown in Figure 1.4.

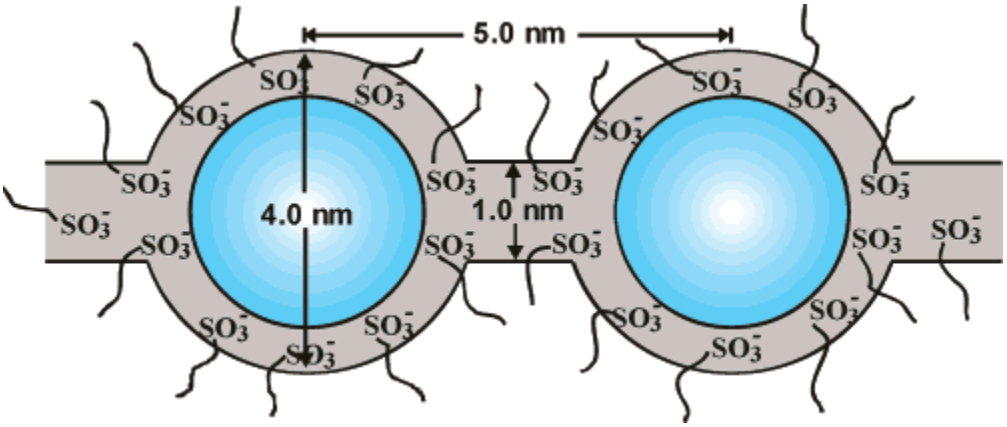

Figure 1.4 Structural model based on ionic clusters (adapted from [14]) for hydrated Nafion.

It was proposed that the average ionic cluster contains approximately 70 acid sites and 1000 water molecules, and that these clusters are dispersed in a hydrophobic polytetrafluoroethylene matrix with a cluster center-to-center periodicity ranging from 5 to 7 nm [14].

The second group of models describes Nafion as a semi-crystalline system in which fluorocarbon crystallites, ionic hydrophilic clusters and amorphous hydrophobic regions coexist and create irregularly shaped water aggregates with many interconnections [14]. In one of the most famous and accepted model, proposed by Rubatat et al. [15], a fraction of the Nafion PTFE chains aggregates to form semi-crystalline hydrophobic domains, where bundles of polytetrafluoroethylene chains are immersed in a continuous ionic matrix. The bundles of fluorocarbon chains have a diameter of about 4nm and a length greater than 80nm (Figure 1.5).

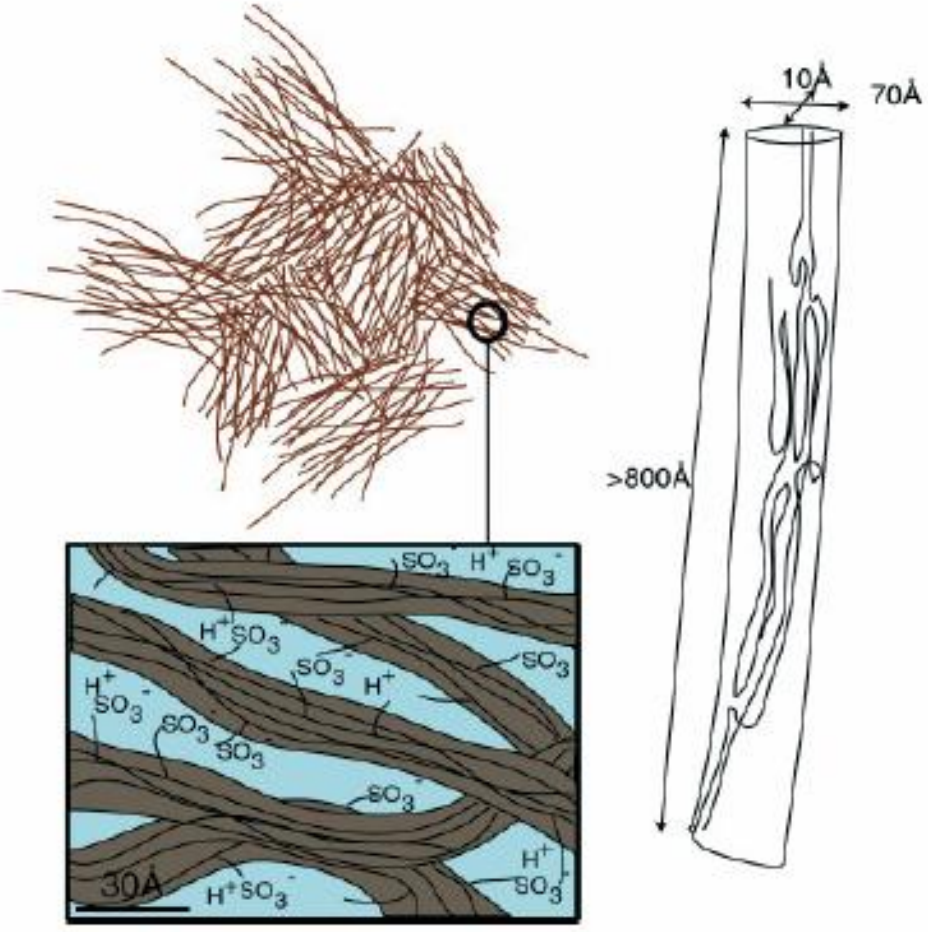

Figure 1.5 Structural model based on bundles of PTFE chains (adapted from [15]) for hydrated Nafion.

Chen and Rohr studied the chain dynamics on Nafion117® by ^{19}F and ^{19}F-^{13}C solid state NMR at 295K. The measures indicated that the conformational order of the backbone chains of Nafion resembles the helix of poly(tetrafluoroethylene) (PTFE) [16]. Furthermore the authors suggest that the persistence length of PTFE chains is 2-5 nm and thus the backbone helices must be quite stiff [16]. According to this interpretations, it follows that the semicrystalline regions in Nafion consists of PTFE-like fluorocarbone backbone chains with helical symmetry.

Today, perfluorinated membranes and Nafion in particular remain the reference material to which all new membranes are compared. Despite the prevalence of Nafion in fuel cell research, there are some serious drawbacks to its use. Most notably, Nafion suffers from insufficient conductivity at temperatures above 90°C and at low levels of hydration, and is very costly. In addition, the environmental impact of the synthesis, usage and disposal of perfluorinated membranes is not insignificant [17,18]. These problems have resulted in significant research on alternatives to the original Nafion. In an effort to benchmark and focus current research activities, the US DOE has set targets for proton exchange membranes. Some of these targets, which are shown in Table 1.1, have been achieved by the current state-of-the-art membranes, but there is still some significant work to be done.

Table 1.1. US Department of Energy PEMFC Membrane Targets [3].

Characteristic	**Units**	**2011 (status)**	**2017 (target)**	**Nafion®* NRE211**
Area specific resistance at:				
Max operating T & 40 – 80 kPa of P_{water}	ohm cm^2	0.023 (40 kPa) 0.012 (80 kPa)	0.02	0.186
-20 °C	ohm cm^2	0.1	0.2	0.179
Operating temperature	°C	< 120	≤ 120	120
Cost	$ m^{-2}		20	
Durability				
Mechanical	Cycles w/<10 sccm crossover	>20000	20000	5000
Chemical	hours	>2300	500	
Maximum oxygen crossover	mA cm^{-2}	< 1	2	2.7
Maximum hydrogen crossover	mA cm^{-2}	< 1.8	2	2.2

*Du Pont™ Nafion® NRE211 has a thickness of 25.4μm and a total acid capacity of 0.92meq/g.

New membranes should have a low area specific resistance (0.02 ohm cm^2) at the targeted operating conditions: high temperature (≤ 120°C) and low relative humidity (40 to 80 kPa P_{water}) [3]. Under these conditions, Nafion®'s specific resistance is one order of magnitude too high. However, other membranes have been reported to have a specific resistance that is close to this goal. The low-temperature conductivity is also an important target for the cold start operations. Operation at 120°C would simplify and reduce the size of thermal and water management systems in the fuel cell power plant, improve the electrode reaction kinetics and increase the catalysts' tolerance to CO poisoning [19-21]. Cost is another significant target. Currently between 18 to 45% of the cost of a fuel cell stack, depending on the production volume, arises from membranes. In order to reach the 2017 goal of 30 USD per kW it is estimated that membrane costs must be reduced to 20 USD/m^2 [3]. To reach these targets, significant effort has been focused on membranes for fuel cells, particularly membranes that function well in hot and dry conditions [9]. There have been several different research approaches that have been implemented to devise acceptable membranes, which include: i) morphological control via polymer structure to provide separation between the conductive and non-conductive domains (Figure 1.6); ii) morphological control by the introduction of a composite that provides good phase separation; iii) introduction of hydrophilic fillers and dopants which allow water to be maintained even at high temperatures; and iv) methods to provide a non-aqueous conduction mechanism by the use of proton conductors other than water [9].

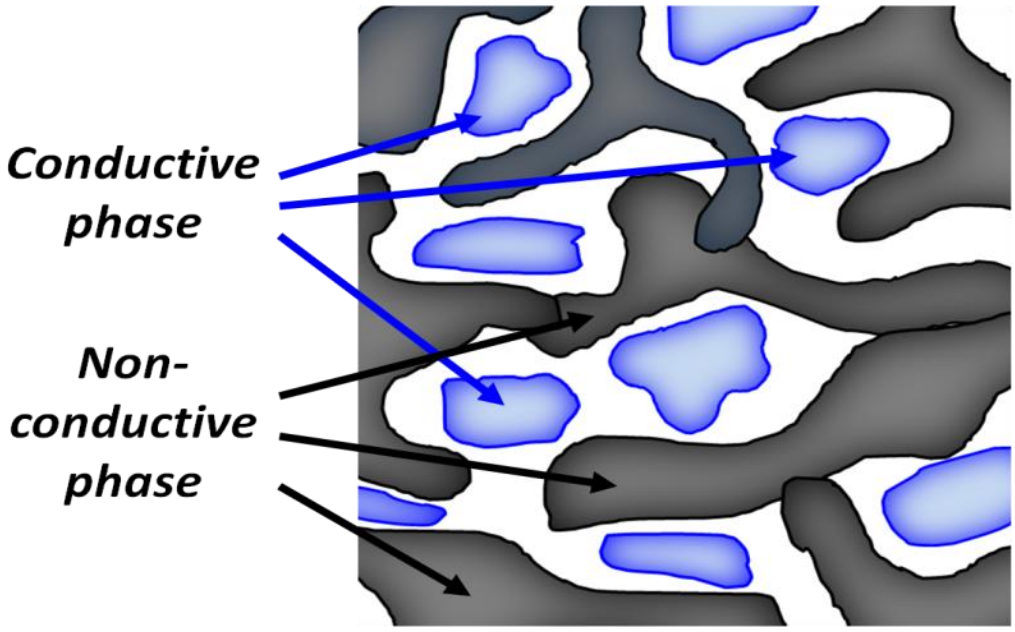

Figure 1.6 Typical phase-separated nanostructure of a generic polymer electrolyte for application in PEMFCs.

1.3.2 Research avenues on PEMs

The research into development of novel membranes has been directed toward four main categories of materials: fluorinated, hydrocarbon, aromatic, and hybrid membranes (Figure 1.7).

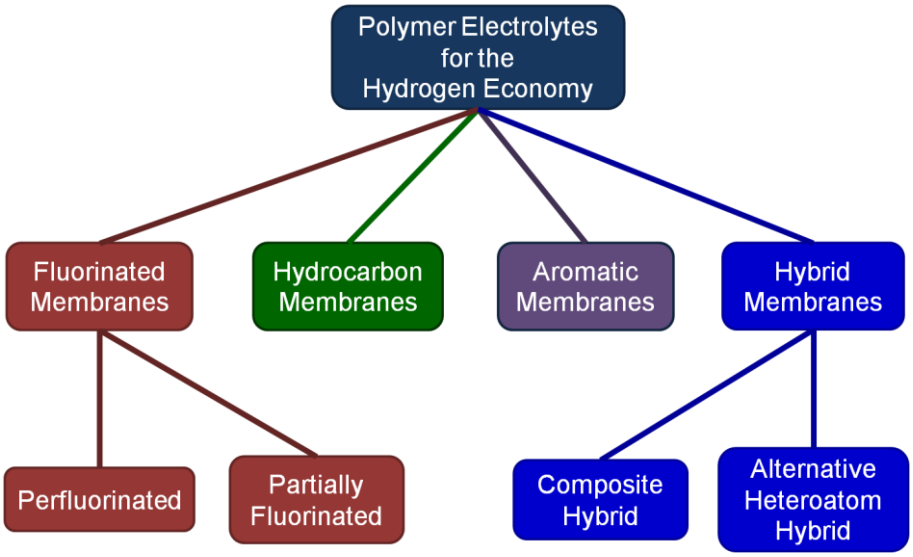

Figure 1.7 Families of proton exchange membranes.

These categories are divided primarily by the nature of the main polymer chain. In general, the main chain directs the morphology and some physical, thermal, and mechanical properties, while

the side group provides the functionality. Examples of some common polymer matrices containing perfluorinated, hydrocarbon, and aromatic main chains are shown in Figure 1.8.

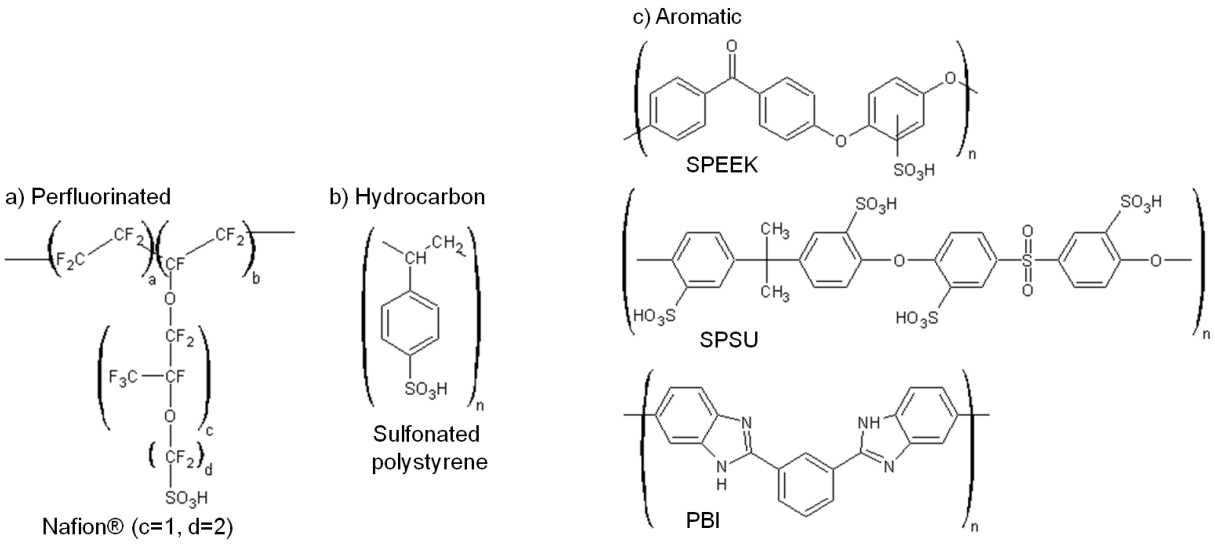

Figure 1.8 Some proton exchange membranes containing perfluorinated, hydrocarbon and aromatic main chains.

Many of the polymers investigated contain sulfonic acid groups either in the pendant side chains or as substituents along the backbone [22]. The strongly acidic nature of the sulfonic group provides proton-coordination sites to facilitate proton mobility through the membrane [22]. The choice of membrane in a functioning fuel cell will depend on the choice of fuel, operating conditions, and the end-use application [8].

I. Fluorinated membranes.

i. Perfluorinated membranes: These materials are probably the most recognized membranes for fuel cell applications. Despite its disadvantages, Nafion® is still the membrane of reference for fuel cell applications (see section 1.3.1). Nafion® is one of several commercially available perfluorosulfonic acid (PFSA) membranes, including Flemion®, Aciplex®, the membrane originally manufactured by Dow®, Aquivion® and the membrane manufactured by 3M. There are other perfluorinated materials that have been examined including perfluorocarboxylic acid [7,17], perfluorosulfonylimides [17,18], the Ballard Advanced Materials (e.g. BAM 3G) [23], and perfluorinated bis (sulfonylimide) acid (PFIA) membranes

[24. The BAM 3G membrane is a styrene-based membrane made from a family of sulfonated copolymers incorporating α,*β*,*β*-trifluorostyrene and substituted α,*β*,*β*-trifluorostyrene comonomers [8,23]. PFIA membranes represent a new class of materials containing multiple acidic sites. On the basis of early reports, these materials are close to meeting the 2015 US DOE targets for proton exchange membranes [24].

ii. Partially fluorinated membranes: This class of membranes contain a partially fluorinated main chain such as poly(vinylidene fluoride) (PVDF) [7]. Partially fluorinated membranes have been characterized as having good mechanical properties but are more prone to degradation than PFSAs [7].

II. Hydrocarbon Membranes.

This class of membranes contains polymers with aliphatic-type main chains. The aliphatic main chains can be generally divided into two groups: 1) polymers with polyethylene-like backbones, such as polystyrene, polyvinyl alcohol, poly acrylamide, polyvinylpyrrolidone, polyvinyl pyridine, and polyvinylimidazole; and 2) polymers with heteroatom-containing backbones, such as polyethylene oxide, polyethylenimine (linear and branched), polysilamine and nylon [19]. Polymers with polyethylene-like backbones contain their proton-conducting functionalities in the side chain. The membranes are generally more susceptible to chemical and thermal degradation than either the fluorinated or aromatic membranes [7,25]. One widely used method to improve the proton conductivity of these types of polymers has been to impregnate the polymer matrix with a strong acid such as phosphoric or sulfuric acid [19,26,27]. Many of these polymers have a somewhat basic nature, which results in dissociation of the dopant acids. It is the presence of these ionic species that is responsible for improved conductivity in both hydrated and dehydrated conditions. For the polymers listed above, phosphoric acid doping has ranged between 0 and 3 moles of phosphoric acid per repeat unit to give conductivities between 10^{-9} and 10^{-2} Scm^{-1} [19]. In these systems, the conductivity is a function of acid concentration and the lowest values occur

at the concentration where protonation of the acid is at a maximum [26]. Also, there are significant durability concerns with this class of material given the relative ease of oxidizing aliphatic moieties.

III. Aromatic Membranes.

This group of membranes likely includes the most significant contributions to research in alternative membranes, i.e. membranes not based on Nafion®. As the name suggests, these membranes contain main chains that consist of aromatic rings. One of the suspected downfalls of hydrocarbon membranes was that they are susceptible to radical oxidation [8]. Therefore, the aromatic membranes were an interesting research avenue because the aromatic CH bond is stronger than the aliphatic CH bond, therefore making it less susceptible to radical oxidative degradation [8]. Some of the most well-known membranes in this class of materials are based on polyetherether ketone (PEEK), polysulfone (PSU), polybenzimidazole (PBI), polyimides (PI) and polyphenylene sulfide. Many polymers in this class can be considered thermoplastics, so it unsurprising that they are thermally stable even at very high temperature [7,17,26]. Sulfonation of these polymers with concentrated sulfuric acid or other methods yields sulfonated polymers such as SPEEK, SPSU, SPBI and SPI. While sulfonation provides conductive functionalities, it can also alter the stability of the materials [17,19,28]. These sulfonated systems undergo desulfonation at temperatures above 200°C [26]. Although the main functionalities have been retained, significant synthetic attention has been focused on modifying the polymer structure of aromatic membranes to improve the properties [19,21]. Poly[2,2'-(*m*-phenylene)-5,5'-bibenzimidazole] has been commercially available from the Celanese corporation as Celazole® since 1983 and BASF produces a polybenzimidazole-based membrane (CELTEC-V) [19,29].

IV. Hybrid Membranes.

i. Composite Hybrid Membranes: For many of the materials described above, membranes produced from the pristine polymers are characterized by some physical properties that make

them unsuitable for application in a functioning fuel cell. However, there has been significant research into improving these membranes by embedding a filler or dopant into the membrane. The physical properties of these hybrid materials are not the simple sum of the individual contributions, but are dependent on the original properties and the interactions occurring at the interface between the system components.

There are many different types of additives that have been incorporated into the membranes matrix such as inorganic, modified-inorganic, proton conductive filler, ionic liquids, heteropolyacids, and carbon nanotubes.

a. Inorganic fillers: Inorganic solids, such as silica, zirconia, titania, other metal oxides, and zirconium phosphate to name a few, have been widely used as a filler in many different types of polymer matrices [30]. The incorporation of these insoluble solids is intended to improve the membrane characteristics. In general, a stronger interaction along the interface between the host matrix and the filler particles results in a greater modification of the original properties of the membrane [31]. The use of micro- and nanoparticles increases the surface area of the filler, which increases the interface interaction and maximizes the modification of the properties [19,31]. A wide variety of metal oxides have been incorporated into hybrid membranes to determine which solids produce the best materials [32,33]. The incorporation of inorganic fillers has resulted in membranes that show slightly lower conductivities than Nafion® at high relative humidities, but higher conductivities at high temperatures and low relative humidities [34]. In addition to the use of pure inorganic solids, "core-shell" and organic functionalized-inorganic fillers have also been studied [35-40].

b. Heteropolyacids (HPA): The incorporation of HPAs such as phosphotungstic acid, silicotungstic acid and phosphomolybdic acid has resulted in high proton conductivities in high hydration conditions [41]. However, membranes based on these materials can suffer from acid leaching [31,34]. One recent innovation to prevent leaching has been to immobilize the HPA by

incorporating the acid moieties directly into the membrane matrix. These membranes are produced by polymerizing the HPA with various hydrocarbon, aromatic or partially fluorinated linkers [9,42,43].

c. Ionic liquids: Ionic liquids (ILs) are salts that are in the liquid state at or close to ambient temperatures. The incorporation of ILs into membranes provides an interesting alternative to water to improve membrane conductivities, particularly when proton conducting ILs are used. Proton conducting ILs (PCILs) are similar to traditional ionic liquids, but the ionic components are formed when a proton is transferred during the reaction of a Brønsted acid with a Brønsted base [44,45]. In the most interesting PCILs the transfer of the proton is very energetic and, therefore, the original acid is not regenerated before the organic components decompose upon heating [45]. This results in a mobile proton and makes PCILs of interest for improving membrane conductivities in anhydrous conditions at high temperatures [8].

d. Carbon Nanotubes (CNTs): Single-walled and multi-walled CNTs have been studied as an anisotropic filler. However, their biggest downfall is that the incorporation of too large an amount of CNTs increases the risk of a short-circuit within the cell due to the inherent electronic conductivity of the filler. To reduce the probability of short-circuit, only small amounts of CNTs are used, which results in little improvement of the conductivity and the cell performance [8]. One possible solution is to functionalize the surface of multi-walled CNTs, which results in a non-electrically conductive protective surface [8]. Functionalizing the CNTs with sulfonic acid groups has the additional benefit of increasing the ionic exchange capacity [45]. Functionalizing CNTs with Nafion® improves the compatibility with a Nafion® host matrix and results in an increase in the conductivity as compared to pristine Nafion® [46].

e. Non-conductive polymers: Non-conductive materials such as PVDF impregnated with highly conductive ionomers or inorganic particles have been studied as an alternative to the use of ionomers such as Nafion®. The morphology of these types of materials mimics that of

Nafion®. The organic polymer constitutes the non-conductive domains like the hydrophobic domains of Nafion®, while the ionomer or inorganic solid makes up the conductive domains [8,31]. For these materials to be conductive, the conductive particles must aggregate to form percolation pathways [8,31]. Examples of such materials include PVDF, or blends and copolymers based on PVDF impregnated with metal oxides, alkoxysilanes, sulfated silica, or acid-containing ceramics [8].

ii. Alternative Heteroatom Hybrid Membranes: Alternatives to traditional organic-based polymers are included in this subclass of membranes. These include silicone and polyphosphazene-based polymers. Both of these materials have very low glass transition temperatures and can be modified to contain many different types of functionalities [17]. The properties of polyphosphazene materials are largely dependent on the choice of side groups. For example, phosphazene materials with aryloxy substituents are characterized by a high thermal, chemical and mechanical stability, while the presence of the aryl groups makes phosphazene materials hydrophobic [47,48]. These side group substituents are often functionalized with other moieties, i.e. sulfonic, phosphonic acid or sulfonylimide moieties, to allow good ionic conductivity. A variety of polyphosphazene materials have shown conductivities on the order of 10^{-2} Scm^{-1} [48].

In addition to the materials that fall into the classes given above, there has also been significant research into copolymers and polymer blends. These systems contain different components from one or more class in an attempt to tailor the physical and chemical properties of the membranes. In this way the membrane can maximize the advantages of each individual component and downplay the disadvantages. For example, some research has shown that block copolymers have the ability to maintain significant water content even as high as 200°C [9]. This is not possible for either block component alone.

1.3.3 Proton conduction in PEM

In order to a reach conductivity high enough for fuel cell application (>10^{-3}S/cm) the proton conduction in PEM is generally assisted by the presence of a solvent (generally water). The proton transfer phenomena follow two principal mechanisms [49,50]. The first type of proton migration, called a *vehicular mechanism*, involves the translational dynamics of protons belonging to bigger molecular species. In this mechanism, the proton diffuses through the medium together with a "vehicle" (for example, with H_2O as H_3O^+). The counter diffusion of unprotonated vehicles (H_2O) allows the net transport of protons. The observed conductivity, therefore, is directly dependent on the rate of vehicle diffusion. The other proton transfer phenomenon, i.e. the *Grotthuss mechanism*, involves the transfer of protons from one vehicle to the other via hydrogen bonds (proton hopping). Simultaneous reorganization of the proton environment, due to the reorientation of individual species or even more extended ensembles, leads to the formation of an uninterrupted pathway for proton migration. This reorganization usually involves the reorientation of solvent dipoles (for example H_2O), which is an inherent part of establishing the proton diffusion pathway. The rates of proton transfer and reorganization of proton's environment affect directly this mechanism.

The proton conductivity of the PEM increases with temperature due to an increase in the protons' mobility. Polymer electrolytes below the glass transition temperature, typically exhibit temperature-dependent conductivities that follow an Arrhenius form. Arrhenius behavior is represented mathematically by the equation:

$$\sigma = \sigma_0 e^{-\frac{E_a}{RT}} \tag{1.8}$$

where σ is the proton conductivity, σ_o the exponential prefactor, E_a is the activation energy for conduction, R the gas constant and T is the temperature (Kelvin). If an electrolyte obeys Arrhenius behavior, then a graph of the logarithm of the conductivity versus reciprocal

temperature produces a linear relationship (Figure 1.9) and the activation energy can be extracted from the slope of the line. Arrhenius behavior has a statistical mechanical interpretation that says the mechanism of ion transport is a thermally activated process and E_a is the energy barrier that must be overcome for conduction to occur. Furthermore, Arrhenius behavior suggests that the dynamics of the protons are independent from the dynamics of the polymer matrix. The latter does not participate in the proton conduction mechanism.

In glass-forming materials, at temperature near and above the glass transition temperature the temperature dependence of the conductivity deviates from Arrhenius behavior (see Figure 1.9) and is fitted by the empirical Voegel-Tamman-Fulcher equation [51-53].

$$\sigma = AT^{-\frac{1}{2}} e^{-\frac{E_{VTF}}{R(T-T_0)}} \tag{1.9}$$

E_{VTF} is the pseudo-activation energy and A and T_0 are constants. A brief description and derivation of the VTF equation is given in Appendix A.

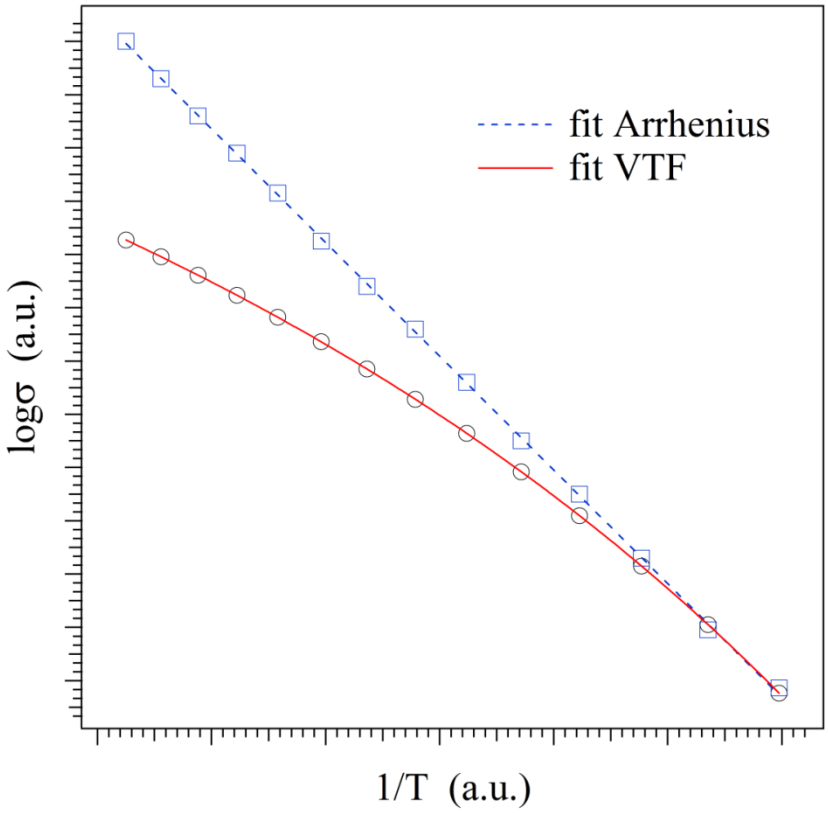

Figure 1.9 Simulation of Arrhenius and VTF behavior of the logarithm of the conductivity as a function of the inverse temperature.

The presence of the VTF behavior indicates that the proton conduction mechanism is affected by the dynamics of the polymer matrix [49]. In this condition the polymer matrix plays a fundamental role in regulating the charge transfer process and thus the performance of the entire final device. The pseudo-activation energy associated with the VTF trend is on the order of kJ/mol and is generally lower than $E_{a,Arrhenius}$ [54-56], while T_0 is a parameter related to the glass transition temperature of the polymer host matrix.

1.4. Aim of the work

As reported in the previous sections, conventional PEMs have inadequate proton conductivity at temperatures above 90°C and at low values of relative humidity, which limit their widespread commercial use. Fuel cells capable of operating above 120°C at low levels of hydration would: (a) obviate the need of bulky and expensive water management modules; b) simplify thermal management and reduce the impact of catalyst poisons such as carbon monoxide. In an effort to overcome the limitations of conventional PEMs, the aim of this work is the synthesis and characterization of new proton conducting membranes for application in PEMFC. The materials were synthesized according to two distinct strategies:

1. dope a Nafion membrane in order to improve its thermo-mechanical properties and proton conductivity or extend its operating conditions to temperatures above 100°C and an anhydrous environment (research carried out during the first and second year of PhD activity);
2. synthesize and characterize proton exchange membranes based on polybenzimidazole and polysulfone as an alternative to Nafion (third year of PhD activity).

The first point focused on the study of two different systems obtained by doping a Nafion membrane with an inorganic $[(ZrO_2)(Ta_2O_5)_{0.119}]$ “core-shell” nanofiller

(Nafion/[$(ZrO_2)\cdot(Ta_2O_5)_{0.119}$]$\Psi_{ZrO_2}$ membranes) or with two different proton conducting ionic liquids, triethylammonium methanesulfonate and triethylammonium perfluorobutanesulfonate (NTMS and NTPFBu membranes), respectively. The membranes synthesis and characterization and the discussion of the obtained experimental results are reported in Chapters 3 and 4 for Nafion/[$(ZrO_2)\cdot(Ta_2O_5)_{0.119}$]$\Psi_{ZrO_2}$ and NTMS and NTPFBu membranes, respectively.

The investigation of Nafion-alternative PEMs was carried out considering: a) poly-2,2'-(2,6-pyridine)-5,5'-bibenzimidazole membrane (PBI5N) containing a suitable hybrid inorganic-organic filler and doped with phosphoric acid and b) sulfonated poly(p-phenylenesulfone) membranes ($sPSO_2$) mixed with poly(1-oxotrimethylene) and SiO_2. The materials reported above are the objects of Chapters 5 and 6.

To describe the proposed materials and the obtained experimental results, Chapters 3-6 follow a general form which includes the presence of a brief introduction justifying the choice of the different materials, an experimental section that reports the synthesis and the adopted experimental methods and conditions, and sections reporting the discussion and interpretation of the data and some conclusions.

The membranes characterization presented in this work follows a general approach which involved the study of the materials' thermal, mechanical, electrical and structural properties determined from different measurement techniques (TG, DCS, DMA, BES, FT.IR, etc.). By correlating these results, it is possible to highlight the interactions between the different components present within the membranes. A brief description of the instruments used for the materials characterization is reported in Chapter 2 while the general conclusions of the work and a comparison between the different membranes are reported in Chapter 7.

1.5. References

1. US Energy Information Administration, Petroleum and Other Liquids, http://www.eia.gov/dnav/pet/hist/LeafHandler.ashx?n=PET&s=WTOTWORLD&f=W, accessed on August 28, **2011**.
2. Vielstich W.; *Ideal and effective efficiencies of cell reactions and comparison to Carnot cycles*. In: W. Vielstich; AL, H. A. Gasteiger; editor, *Handbook of Fuel Cells – Fundamentals, technology and applications*. Vol 1. Chichester: John Wiley & Sons; **2003**, p. 26.
3. Satyapal S.; Hydrogen and Fuel Cell Activities. 5th International Conference on Polymer Batteries & Fuel Cells, Argonne, Illinois: US Department of Energy: Energy Efficiency & Renewable Energy; **2011**.
4. Nguyen, T.; Ward, J.; Well-to-Wheels Greenhouse Gas Emissions and Petroleum Use for Mid-Size Light-Duty Vehicles: US Department of Energy: Offices of Vehicle Technologies & Fuel Cell Technologies, **2010**.
5. Hamnett, A.; *Introduction to fuel-cell types*, In: W. Vielstich, AL, H. A. Gasteiger, editor, *Handbook of Fuel Cells – Fundamentals, technology and applications*. Vol 1. Chichester: John Wiley & Sons; **2003**, p. 36.
6. Sandstede, G.; Cairns, E.J.; Bagotsky, V.S.; Wiesener, K.; *History of low-temperature fuel cells*, In: W. Vielstich, AL, H. A. Gasteiger editor, *Handbook of Fuel Cells – Fundamentals, technology and applications*. Vol 1. John Wiley & Sons, Chichester; **2003**, p. 145.
7. Smitha, B.; Sridhar, S.; Khan, A.A.; *J. Membr. Sci*. **2005**; 259, 10.
8. Laberty-Robert, C.; Valle, K.; Pereira, F.; Sanchez, C.; *Chem. Soc. Rev*. **2011**; 40, 961.
9. Epping, M.K.; Kopasz, J.P.; The U.S. DOEs High Temperature Membrane Effort. Fuel Cells **2009**; 9, 356.

10. Boeing Successfully Flies Fuel Cell-Powered Airplane, Boeing, http://www.boeing.com/news/releases/2008/q2/080403a_nr.html, accessed on August 28, **2011**.
11. Clean Energy Patent Growth Index, Cleantech Group, Heslin Rothenberg Farley & Mesiti P.C., http://cepgi.typepad.com/heslin_rothenberg_farley_/, accessed on August 28, **2011**.
12. Doyle, M.; Rajendran, G.; *Perfluorinated membranes*, In: W. Vielstich, AL, H. A. Gasteiger, editor, *Handbook of Fuel Cells – Fundamentals, technology and applications*. Vol 3. Chichester: John Wiley & Sons; **2003**, p. 351.
13. Grot, W.; *Fluorinated ionomers*. Norwich, NY: William Andrew **2008**.
14. Mauritz, K. A.; Moore R. B.; *Chem. Rev.* **2004**; 104, 4535.
15. Rubatat, L.; Rollet, A. L.; Gebel, G.; Diat, O., *Macromolecules* **2002**, 3, 4050.
16. Chen, Q.; Schmidt-Rohr, S.; *Macromol. Chem. Phys*., **2007,** 208, 2189.
17. Iojoiu, C.; Chabert, F.; Marechal, M.; Kissi, N.E.; Guindet, J.; Sanchez, J-Y; *J. Power Sources* **2006**, 153, 198.
18. Sanchez, J-Y; Alloin, F.; Iojoiu, C.; *J. Fluorine Chem*. **2006,** 127, 1471.
19. Asensio, J.A.; Sanchez, E.M.; Gomez-Romero, P.; *Chem. Soc. Rev*. **2010,** 39, 3210.
20. Li, Q.; He, R.; Jensen ,J.O.; Bjerrum, N.J.; *Chem. Mater*. **2003,** 15, 4896.
21. Bose, S.; Kuila, T.; Nguyen T.X.H.; Kim, N.H.; Lau K-t; Lee, J.H.; *Prog. Polym. Sci.* **2011,** 36, 813.
22. Ahmad, H.; Kamarudin, S.K.; Hasran, U.A.; Daud, W.R.W.; *Int. J. Hydrogen Energy* **2010,** 35, 2160.
23. Hickner, M.A.; Ghassemi, H.; Kim, Y.S.; Einsla, B.R.; McGrath, J.E; *Chem. Rev*. **2004**, 104, 4587.
24. Hamrock, S.; Membranes and MEAs for Dry, Hot Operating Conditions: 2010 Annual Progress Report: DOE Hydrogen Program; **2011**.

25. Souzy, R.; Ameduri, B.; Boutevin, B.; Gebel, G.; Capron, P.; *Solid State Ionics* **2005**; 176, 2839.

26. Lee, J.S.; Quan, N.D.; Hwang, J.M.; Lee, S.D.; Kim, H.; Lee, H. et al., *J. Ind. Eng. Chem.* **2006**; 12, 175.

27. Rikukawa, M.; Sanui, K.; *Prog. Polym. Sci*. **2000**; 25, 1463.

28. Akbarian-Feizi, L.; Mehdipour-Ataei, S.; Yeganeh, H.; *Int. J. Hydrogen Energy* **2010**; 35, 9385.

29. Gubler, L.; Kramer, D.; Belack, J.; Unsal, O.; Schmidt, T.,J.; Scherer, G.G.; Celtec, V.; *J. Electrochem. Soc.* **2007**; 154, B981.

30. Herring, A.M.; *Polymer Reviews* **2006**; 46, 245.

31. Alberti, G.; Casciola, M.; *Annu. Rev. Mater. Res.* **2003**; 33, 129.

32. Di Noto, V.; Gliubizzi, R.; Negro, E; Vittadello, M.; Pace, G; *Electrochim Acta* **2007**; 53, 1618.

33. Di Noto, V.; Lavina, S.; Negro, E.; Vittadello, M.; Conti, F.; Piga, M. et al., *J Power Sources* **2009**; 187, 57.

34. Sahu, A.K.; Pitchumani, S.; Sridhar, P.; Shukla, A.K.; *Bull. Mater. Sci*. **2009**; 32, 285.

35. Di Noto, V.; Piga, M.; Lavina, S.; Negro, E.; Yoshida, K.; Ito, R.; Furukawa, T.; *Electrochim. Acta* **2010**; 55, 1431.

36. Di Noto, V.; Piga, M.; Piga, L.; Polizzi, S.; Negro, E.; *J. Power Sources*, **2008,** 178, 561.

37. Di Noto, V.; Boaretto, N.; Negro, E.; Giffin G.A.; Lavina, S.; Polizzi, S.; *Int. J. Hydrogen Energy* **2011**;doi:10.1016/j.ijhydene.2011.07.132.

38. Di Noto, V.; Boaretto, N.; Negro, E.; Stallworth, P.E.; Lavina, S.; Giffin, G.A.; Greenbaum, S. G.; *Int. J. Hydrogen Energy* **2011**; doi:10.1016/j.ijhydene.2011.07.135.

39. Fernandez-Carretero, F.J.; Compan, V.; Riande, E.; *J. Power Sources* **2007**; 173, 68.

40. Navarra, M.A.; Croce, F.; Scrosati, B.; *J. Mater. Chem*. **2007**; 17, 3210.

41. Meng, F.; Aieta, N.V.; Dec, S.F.; Horan, J.L.; Williamson, D.; Frey, M.H. et al. *Electrochim. Acta* **2007**; 53, 1373.

42. Horan, J.L.; Genupur, A.; Ren, H.; Sikora, B.J.; Kuo, M.C.; Meng, F. et al., ChemSusChem **2009**; 2, 226.

43. Herring, A.M.; Horan, J.L.; Kuo, M-C.; Ziegler, Z.C.; Zhang F, Perdue, A.S. et al., *Novel Approaches to Immobilized Heteropoly Acid (HPA) Systems for High Temperature, Low Relative Humidity Polymer-Type Membranes: 2010 Annual Progress Report*: DOE Hydrogen Program; **2011**.

44. Greaves, T.L.; Drummond, C.J.; *Chem. Rev*. **2008**; 108, 206.

45. Angell, C.A.; Xu, W.; Yoshizawa, M.; Hayashi, A.; Belieres, J-P.; Lucas, P. et al., *Physical Chemistry of Ionic Liquids, Inorganic, Organic, Protic and Aprotic*, In: Ohno, H, editor, E*lectrochemical Aspects of Ionic Liquids*. 1st ed. Vol Hoboken, NJ: Wiley-Interscience; **2005**, p. 5-23.

46. Thiam, H.S.; Daud, W.R.W.; Kamarudin, S.K.; Mohammad, A.B.; Kadhum, A.A.H.; Loh, K.S. et al., *Int. J. Hydrogen Energy* **2011**; 36, 3187.

47. Allcock, H.R.; *Solid State Mater. Sci.* **2007**; 10, 231.

48. Allcock, H.R.; Wood, R.M.; *J. Polym. Sci., Part B: Polym. Phys*. **2006**; 44, 2358.

49. Premchand, Y. D.; Di Vona, M. L.; Knauth, P.; *Proton-Conducting Nanocomposites and Hybrid Polymers*, in: Knauth, P.; Schoonman, J.; editors, *Nanocomposites: ionic conducting materials and structural spectroscopies*, Springer, **2007**, p. 77.

50. Peckham, T.J.; Yang, Y.; Holdcroft, S.; *Proton Exchange Membranes* in: Wilkinson, D. P.; Zhang, J.; Hui, R.; Fergus, J.; Li, X.; editors, *Proton Exchange Membrane Fuel Cells: Materials Properties and Performance*, CRC Press Taylor&Francis Group, **2010**, p. 107.

51. Ratner, M.; in *Polymer Electrolytes Reviews*; MacCallum, J. R.; Vincent, C. A., eds.; Elsevier: London, **1987**.

52. Ediger, M. D.; Angell, C. A.; Nagel, S. R.; *J. Phys. Chem.,* **1996** , 100, 13200.

53. Ratner, M. A.; Shriver, D. F.; *Chemical Reviews*, **1988**, 88, 109.

54. Di Noto, V.; Negro, E.; Sanchez, J. Y.; Iojoiu, C., *J. Am. Chem. Soc.* **2010,** *132*, 2183.

55. Giffin, G. A.; Piga, M.; Lavina, S.; Navarra, M. A.; D'Epifanio, A.; Scrosati, B.; Di Noto, V.; *J. Power Sources*, **2012**, 198, 66.

56. Di Noto, V.; Piga, M.; Giffin, G. A.; Pace, G.; *J. Membr. Sci.*, **2012**, 390, 58**.**

Chapter II

Instruments and methods

2.1. Introduction

In the present work, the materials are characterized by a common protocol that allows the study of their: a) *thermal* properties using thermogravimetric (TG) and calorimetric (DSC) analysis; b) *mechanical* and *structural* properties analyzed by dynamic mechanical analysis (DMA) and infrared spectroscopy (FT-IR), respectively; c) electrical properties by broadband electric spectroscopy (BES) measurements.

The use of different measurement techniques, conducted over a wide temperature range, allows the identification and assignment of the phase transitions and the molecular relaxations that occur within the investigated materials in a unique way. In addition, the use of a common set of measurements allows the comparison of the properties of the different materials (as reported in Chapter 7 of this work).

This chapter outlines the main characteristics of the instruments used for the study of the proposed materials. In the case of standard measuring techniques (TG, DSC, FT-IR), commonly used in the characterization of materials, the specifications of the instruments will be simply reported. The instrumentation associated with less common techniques such as DMA and BES

will be described in detail in this chapter. Any other equipment (for example SEM, TEM, planetary ball mill, etc.) and the exact experimental conditions (ramp and temperature range, treatment of samples, etc..) adopted for the study of the different materials are reported in the different chapters present in this thesis.

Finally, this chapter describes the equipment assembled in this laboratory to perform the fuel cell tests (conducted on the systems described in Chapter 3) and the electrical measurements carried out at different relative humidity conditions on the membranes reported in Chapter 6.

2.2. Thermal analysis [1-4]

2.2.1 Thermogravimetry

Thermogravimetric analysis (TGA) measures the amount and rate of change in the weight of a material as a function of temperature or time in a controlled atmosphere. Measurements are used primarily to determine the composition of materials and to predict their thermal stability at temperatures up to 1000°C. The technique can characterize materials that exhibit weight loss or gain due to decomposition, oxidation, or dehydration.

For all the investigated materials the thermogravimetric analyses were carried out with a high resolution TGA 2950 (TA Instruments) thermobalance (Figure 2.1), with a resolution of 1 μg.

Figure 2.1 TGA 2950 (TA Instruments) thermobalance.

The heating rate varied from 50 to 0.001°C·min^{-1} depending on the first derivative of the weight loss. In this way, it was possible to optimize the measurement time and increase the resolution in the detection of thermal decompositions of small entities.

The measurements were conducted in the temperature range from room temperature to 900°C, with a N_2 flux of 100cm^3/min, using open platinum pans loaded with ca. 5-7mg of each sample.

2.2.2 Differential scanning calorimetry

The differential scanning calorimetry (DSC) determines the temperature and heat flow associated with material transitions as a function of time and temperature. It also provides quantitative and qualitative data on endothermic (heat absorption) and exothermic (heat evolution) processes of materials during physical transitions that are caused by phase changes, melting, oxidation, and other heat-related changes. In this work DSC analyses were performed using a mDSC 2920 (TA Instruments). The mDSC 2920 has two major parts: the 2920 CE instrument, which contains the system electronics, and the sample cell, which contains its own thermocouples (temperature sensor) for monitoring differential heat flow and temperature. The instrument measures differential heat flow of the sample and a reference. The sample and the reference are placed in aluminum pans that sit on raised platforms on a constantan disk, and heat is transferred through the disk up into the sample and reference. The differential heat flow is monitored by thermocouple wires welded to the disk. The mDSC 2920 can be operated below ambient temperatures using the Liquid Nitrogen Cooling Accessory (LNCA). The LNCA provides automatic and continuous programmed sample cooling within the range of –150°C to 725°C when used with the DSC heat exchanger installed on the DSC Cell. Heaters vaporize the liquid nitrogen in the LNCA tank. The cool gas is forced up and mixed with liquid nitrogen. The gas/liquid mix is delivered to the heat exchanger to cool the cell.

For all the materials, the measurements were made under a helium flux of 30 cm^3/min by loading about 6mg of sample inside a hermetically sealed aluminum pan.

The specifications of mDSC 2920 are listed below in Table 2.1.

Table 2.1 mDSC 2920 specifications.

Temperature range	Room temperature to 725°C range (inert atmosphere above 600C) as supplied; to –150°C with the LNCA.
Cooling rate	Dependent on accessory used and temperature range
Sample size	0.5 to 100 mg (nominal)
Sample volume	10 mm^3 in hermetic pans
Sample pans	Various open or hermetically sealed
Purge gases Recommended	air, argon, helium, nitrogen, or oxygen
Typical flow	25–50 mL/min rate
Cell volume	2 cm^3
Temperature repeatability	+0.1°C
Differential thermocouples	CHROMEL®*-constantan (Type E)
Sample thermocouple	CHROMEL-ALUMEL®* (Type K)
Calorimetric sensitivity	0.2 µW (rms)
Calorimetric precision	1% (based on metal samples)

2.3. Infrared spectroscopy [5]

Infrared spectra in the medium infrared region (4000 to 400 cm^{-1}) were collected using a FT-IR Nicolet Nexus spectrometer. The source is a Globar lamp, consisting of a silicon carbide candle heated to a temperature between 1300 K and 1500 K. The beamsplitter for the mid-infrared is KBr. The detector is a triglycine sulfate (TGS) piroelectric material. The absence of water in the measuring chamber is ensured by a circulating dry air system, consisting of filters in which dehydration occurs initially through a pre-condensation process in compressed atmosphere and then on a column of silica gel. The CO_2 is removed by zeolitic materials.

In this work, the infrared spectra of the polymeric membranes were collected in the ATR (*Attenuated Total Reflection*) mode using a Perkin-Elmer Frustrated Multiple Internal

Reflections accessory 186-0174. In the ATR technique, the sample is in contact with a crystal with high refractive index (Figure 2.2). The radiation passes through the crystal and reaches the sample. If the angle of incidence is greater than the critical angle θ, equal to the ratio between the refractive indices of the crystal and the sample, the radiation incident on the sample is reflected within the crystal (total reflection). However, the radiation penetrates the surface of the sample for a few microns (0.5 - 5 μm depending on the type of crystal and the angle of incidence). The evanescent wave (the infrared radiation penetrating the surface of the sample) is then attenuated or altered by the sample.

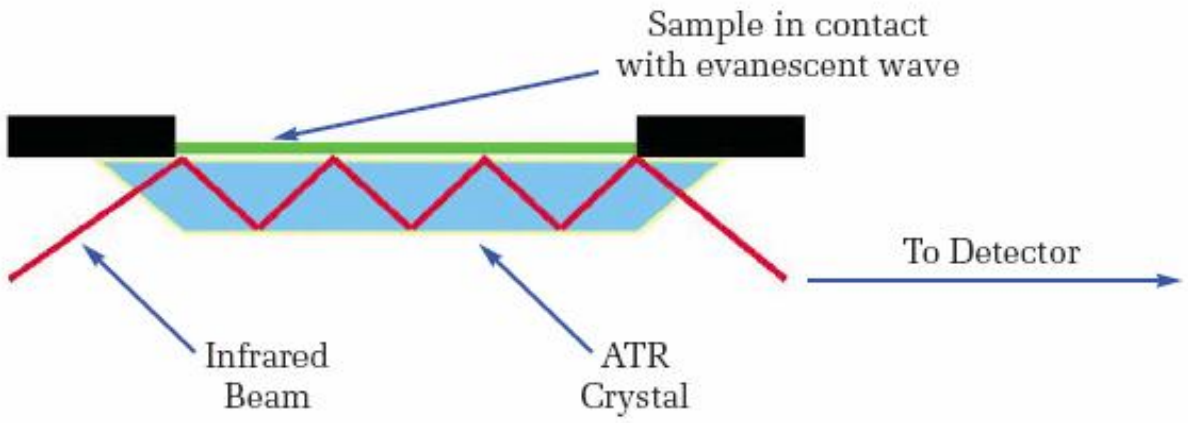

Figure 2.2 ATR mode. The radiation incident to the sample is reflected within the crystal The evanescent wave (the infrared radiation penetrating the surface of the sample) is then attenuated or altered by the sample.

The infrared beam exits on the opposite side of the crystal and is collected by the detector of the spectrometer (Figure 2.2). It is possible to obtain the infrared spectrum of the polymer film by the difference between the evanescent waves in the presence and absence (by placing a sheet of brass in contact with the crystal) of the sample.

In this work the polymeric membranes were squeezed between the surface of a prismatic germanium crystal of 18(height)×51(width)×2(thickness)mm^3. 50% ca. of the crystal surface was covered by the membrane. An incident light angle of 45°C with 25 total internal reflections was adopted.

2.4. Dynamic mechanical analysis [6,7]

Dynamic mechanical analysis (DMA) measures the viscoelastic properties of materials using either transient or dynamic oscillatory tests. The most common test is the dynamic oscillatory test, where a sinusoidal stress (or strain) is applied to the material and a resultant sinusoidal strain (or stress) is measured. Also measured is the phase difference, δ, between the two sine waves. The phase lag will be 0° for purely elastic materials and 90° for purely viscous materials. However, viscoelastic materials (e.g. polymers) will exhibit an intermediate phase difference with 0°<δ<90°.

For a viscoelastic material the application of a sinusoidal deformation ε gives rise to an oscillating stress σ shifted by an angle δ with respect to the applied deformation (Figure 2.3):

$$\varepsilon = \varepsilon_0 sin\omega t \tag{2.1}$$

$$\sigma = \sigma_0 sin(\omega t + \delta) = \sigma_0 sin\omega t cos\delta + \sigma_0 cos\omega t sin\delta \tag{2.2}$$

where ω is the angular frequency and δ the phase angle.

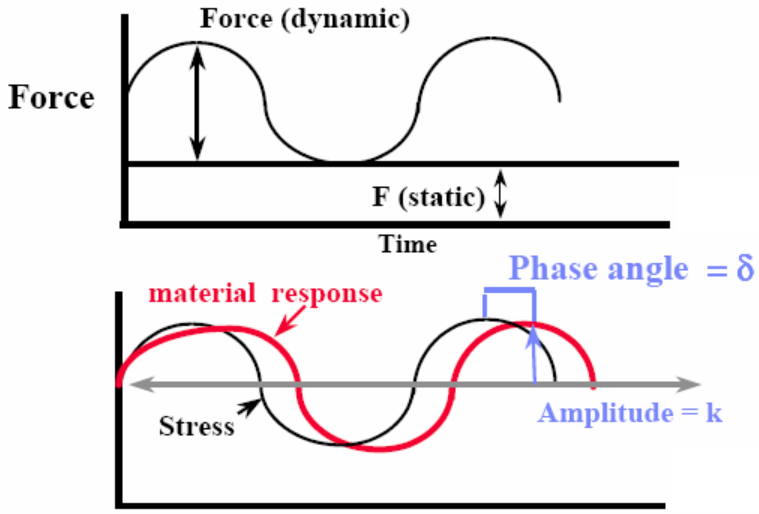

Figure 2.3 Mechanical response of a viscoelastic material subjected to a dynamic sinusoidal force. k is the strain amplitude and δ is the phase angle between the stress and the strain.

Equation 2.2 shows that the stress σ can be divided into two parts: the first, with an amplitude of $\sigma_0 cos\delta$ is in phase with the deformation, while the second, with an amplitude of $\sigma_0 sin\delta$ is out of phase by 90°. Thus the stress-strain relationship can be defined by a quantity G' in phase with the strain and G" out of phase by 90 °:

$$\sigma = \varepsilon_0 G^{'} sin\omega t + \varepsilon_0 G^{''} cos\omega t \tag{2.3}$$

with

$$G^{'} = \frac{\sigma_0}{\varepsilon_0} cos\delta \quad ; \quad G^{''} = \frac{\sigma_0}{\varepsilon_0} sin\delta \tag{2.4}$$

G' and G" define the complex modulus G^*.

$$G^* = \frac{\sigma_0}{\varepsilon_0} exp(i\delta) = \frac{\sigma_0}{\varepsilon_0}(cos\delta + isin\delta) = G^{'} + iG'' \tag{2.5}$$

G' and G" are related by the elastic energy *E* stored by the sample and the loss of energy Δ*E* dissipated during each cycle, respectively. The values of *E* and Δ*E* can be calculated by integrating σ between one quarter cycle (where the maximum elastic energy is accumulated in the sample) and a complete cycle (obtaining the energy dissipated during the cycle), respectively.

$$\Delta E = \oint \sigma d\varepsilon = \int_0^{\frac{2\pi}{\omega}} \sigma \frac{d\varepsilon}{dt} dt = \omega\varepsilon_0^2 \int_0^{\frac{2\pi}{\omega}} (G^{'} sin\omega t cos\omega t + G^{''} cos^2\omega t) = \pi G^{''} \varepsilon_0^2 \tag{2.6}$$

$$E = \oint \sigma d\varepsilon = \int_0^{\frac{\pi}{2\omega}} \sigma \frac{d\varepsilon}{dt} dt = \omega\varepsilon_0^2 \int_0^{\frac{\pi}{2\omega}} (G^{'} sin\omega t cos\omega t + G^{''} cos^2\omega t) = \frac{1}{2} G' \varepsilon_0^2 \tag{2.7}$$

The DMA measurement provides values of the elastic (*E'*) and loss modulus (*E''*) associated with the complex Young's modulus *E* = E' + iE''*. The relationship between E* and G* is provided by the generalized Hooke's law:

$$G^* = \frac{E^*}{2(1+\nu)} \tag{2.8}$$

where ν is the Poisson ratio.

2.4.1 Mechanical relaxations in polymers

The mechanical behavior of polymers varies with temperature: generally at low temperatures the materials behave like a glassy solid, where a small deformation of the material is associated with the application of very high tensile forces. At high temperatures, the elastic modulus shows very low values, and the materials behave like a viscous fluid. The two mechanical ranges are usually separated by a temperature region in which the mechanical behavior of the polymers is typically viscoelastic. In this region it is possible to distinguish different mechanical relaxations caused by molecular relaxations within the polymer and associated to a decrease in the materials elastic modulus. Conventionally the mechanical relaxations are labelled α, β, γ, δ in order of decreasing temperature.

Starting from the lowest temperature, the first detected mechanical relaxations (δ,γ modes) are molecular rearrangements associated with local relaxations of individual chemical groups. These transitions have the lowest activation energy and lead to limited changes in the elastic modulus. As the temperature increases the mechanical relaxations due to the fluctuation of the side chains or to due to the limited movement of the main chains (β relaxations) occur. The highest temperature mechanical relaxation (α mode) is related to the glass transition temperature T_g of the material and involves the segmental motion of the main chains of the polymer matrix.

The mechanical relaxations are assigned by coupling the DMA spectra with differential scanning calorimetry (DSC) and broadband electric spectroscopy (BES) measurements.

All the mechanical events involve a variation of the mechanical response (in terms of the elastic and loss modulus) of the materials and are easily detected by analyzing the temperature dependence of the $\tan\delta = E''/E'$ profiles. $\tan\delta$ is proportional to the ratio between the energy dissipated and stored by the material during the deformation cycle (Equations 2.6 and 2.7).

2.4.2 Instrument

The mechanical analyses were performed using a DMA Q800 (TA Instruments). The dynamic mechanical measurements can be carried out in various ways, e.g. by applying compression, tension, bending or twisting forces, depending mainly on the type of sample under investigation. It is possible to vary the experimental mode with the same instrument, simply by changing the holder terminals (see Figure 2.4). According to Figure 2.4, the sample can be subjected to four different modes of deformation.

Dual/Single Cantilever (part a of Figure 2.4): In this mode, the sample is clamped at both ends and either flexed in the middle (dual cantilever) or at one end (single cantilever). Cantilever bending is a good general-purpose mode for evaluating thermoplastics and highly damped materials (e.g., elastomers). Dual cantilever mode is ideal for studying the cure of supported thermosets.

Shear Sandwich (part b of Figure 2.4): In this mode, two equal-size pieces of the same material are sheared between a fixed and moveable plate. This mode is ideal for gels, adhesives, high viscosity resins, and other highly damped materials.

Tension (part c of Figure 2.4). In this mode, the sample is placed in tension between a fixed and moveable clamp. In oscillation experiments, the instruments use a variety of methods for applying a static load to prevent buckling and unnecessary creep. The clamps are suitable for both films and fibers.

Compression (part d of Figure 2.4). In this mode, the sample is placed on a fixed flat surface and an oscillating plate applies force. Compression is suitable for low to moderate modulus materials (e.g., foams and elastomers). This mode can also be used to make measurements of expansion or contraction, and tack testing for adhesives.

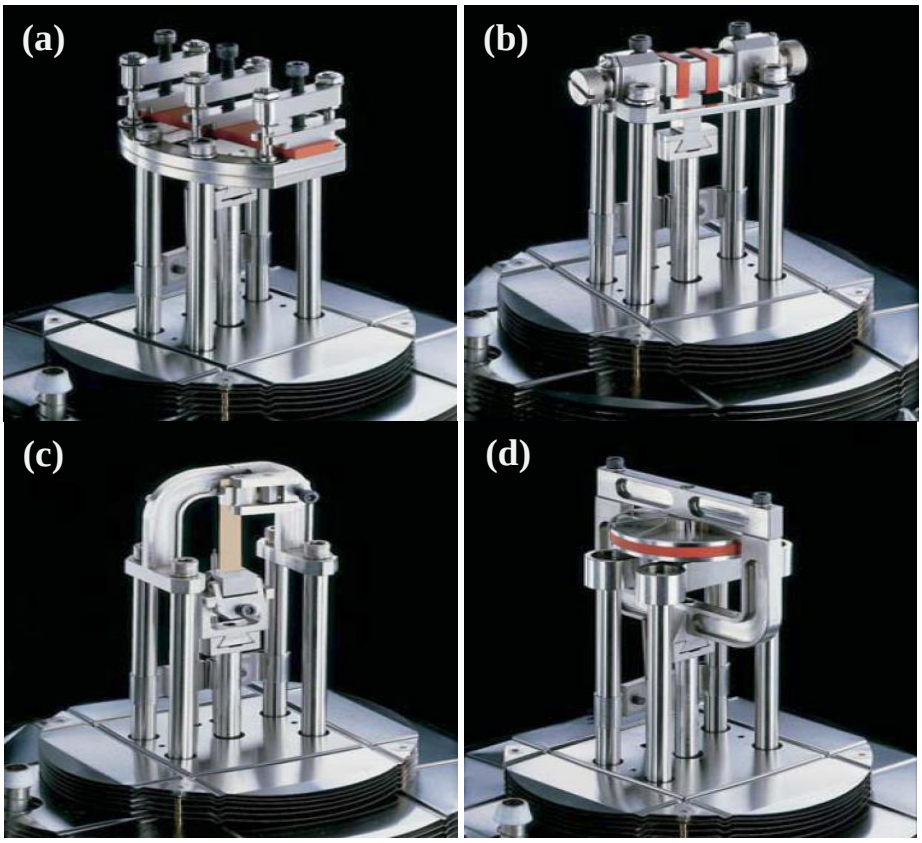

Figure 2.4 Terminals supplied to the DMA Q800: a) Dual Contilever; b) "Shear Sandwich"; c) Tension clamp; d) Compression clamp.

The experimental spectra can be obtained in terms of the storage modulus (E'), the loss modulus (E'') and tanδ = E'/E' as function of the frequency of the mechanical perturbation and temperature. Measurements are usually carried out by fixing the frequency and varying the temperature. DMA Q800 specifications are reported below in Table 2.2.

Table 2.2 DMA Q800 specifications.

Force range:	0.0001 - 18 N
Force resolution:	0.00001 N
Strain resolution:	1 nm
Range of Elastic Modulus:	10^3 - $3x10^{12}$ Pa
Modulus Precision	±1%
Frequecy range:	0.01 to 200 Hz
Strain range:	± 0.5 to 10 μm
Temperature range:	-150 – 600°C

The instrument, schematically shown in Figure 2.5, consists of a motor, an air bearing slide, an optical sensor, the tension clamp and a furnace.

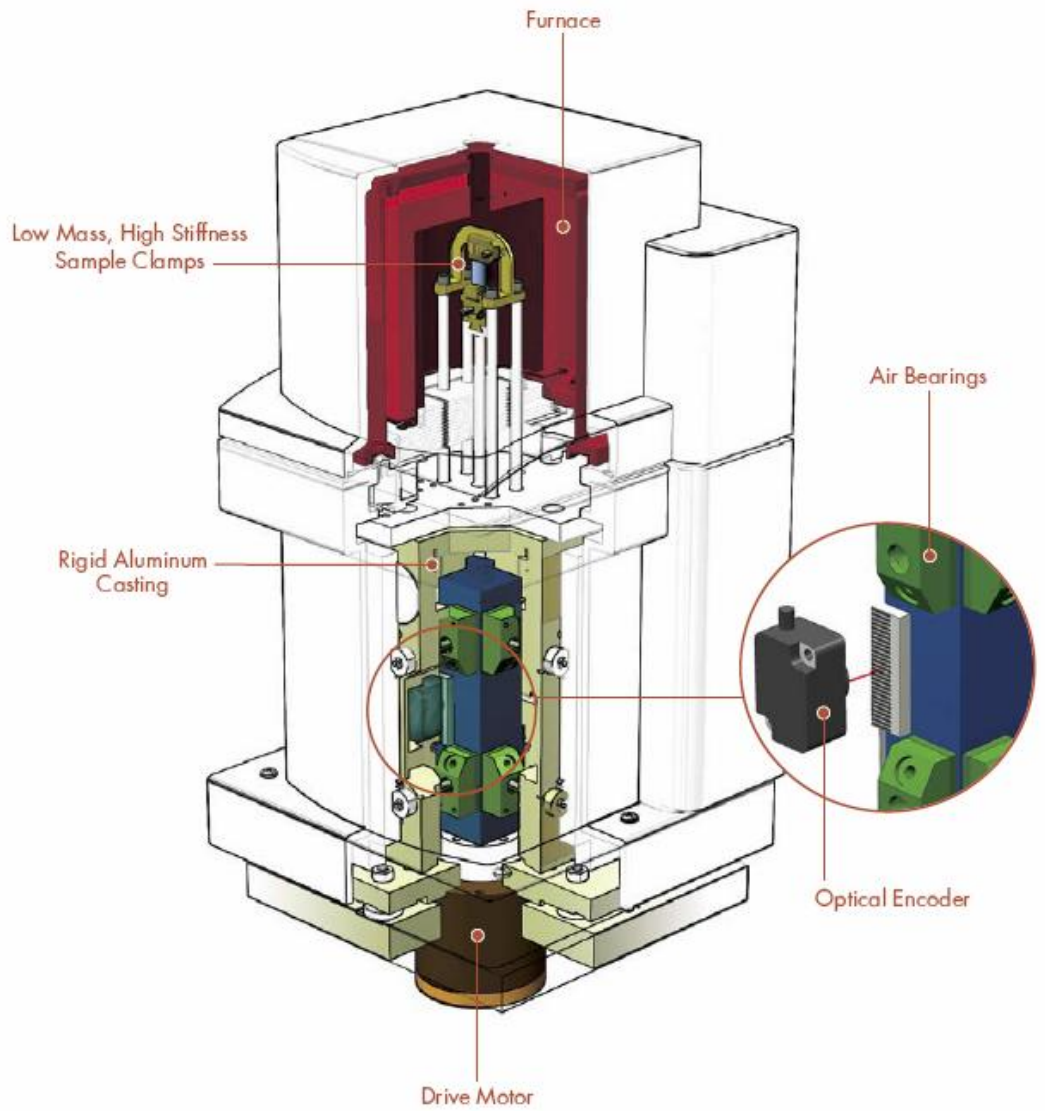

Figure 2.5 Main components of the dynamic mechanical analyzer.

The drive motor provides the oscillatory or static force required. The motor is thermostated to eliminate heat build-up even when using large oscillation amplitudes and high deformation forces. The non-contact drive motor transmits force directly to a rectangular air bearing slide. The slide is guided by eight porous carbon air bearings grouped into two sets of four near the top and bottom of the slide. Pressurized air or nitrogen flows to the bearings forming a frictionless surface that permits the slide to "float." A linear optical encoder, based on diffraction patterns of

light through gratings (one moveable and one stationary) is used to measure displacement on the Q800 DMA with a resolution of 1 nm. The sample holder is encapsulated in a self-closing furnace and connected to a liquid nitrogen cooling system. The whole structure is mounted on an thermostated aluminum frame. The Gas Cooling Accessory (GCA) extends the operating range of the Q800 to -150 °C. The GCA uses cold nitrogen gas generated from controlled evaporation of liquid nitrogen. Automated filling of the GCA tank can be programmed to occur after the scan is complete. The GCA will provide ballistic or controlled cooling rates over the entire operating range of the Q800 DMA (-150-600 °C). In general, the maximum cooling rate is a function of the installed clamp and the thermal characteristics of the sample.

2.4.3 Methods

For all the investigated membranes, the DMA measurements were performed using the tension clamp (part d of Figure 2.4). Temperature spectra were measured by subjecting a rectangular film sample of ca. 25(height)×7(width)×t(thickness) mm^3 to an oscillatory sinusoidal tensile deformation at a constant frequency of 1Hz, with an amplitude and a preload force of 4μm and 0.05N, respectively. The membranes mechanical response was analyzed in terms of E', E'' and tanδ as function of temperature. The measured temperature range varies for different samples and is reported within each of the chapters. The sampling rate and the equilibration time in isothermal conditions are 0.25 $°C^{-1}$and 2 minutes, respectively.

2.5. Broadband electric spectroscopy [8-10]

Broadband Electric Spectroscopy involves the interaction between matter and electromagnetic radiation in a wide frequency range between 10^{-7} and 10^{12} Hz. In the frequency range (10^{-2} – 10^{7} Hz) investigated in the electric measurements presented in this work, the interaction of electromagnetic radiation with matter involves phenomena associated with macroscopic

polarization phenomena due to: a) the orientation of dipoles present within the material (molecular relaxations); b) the motion of free charges (in the case of ionic conductors).

In general to analyze electric spectra, an overview is made of the spectra in various representations to determine the types of events present, and then the data are fit using an empirical equation (a description of the empirical equation is reported in Appendix B) to determine the values of conductivities, dielectric strengths and relaxation times associated with the electric relaxations.

In dielectric polymers, molecular relaxations arising from local or collective fluctuations of molecular dipole moments are typically revealed with BES. The events present at the lowest temperatures are those associated with the shortest relaxation times and the highest frequencies. The electric spectra of conductive polymers show the coexistence of molecular (dielectric) and mesoscopic phenomena, which are generally associated with very different values of permittivity. Mesoscopic behavior, which is related to collective charge motion, exhibits strong electric responses, while molecular relaxations are associated with lower permittivity values that are generally less than 100.

The electric measurement consists of the application of an oscillating voltage to the electrodes of the cell and in the measurement of the output current (Figure 2.6).

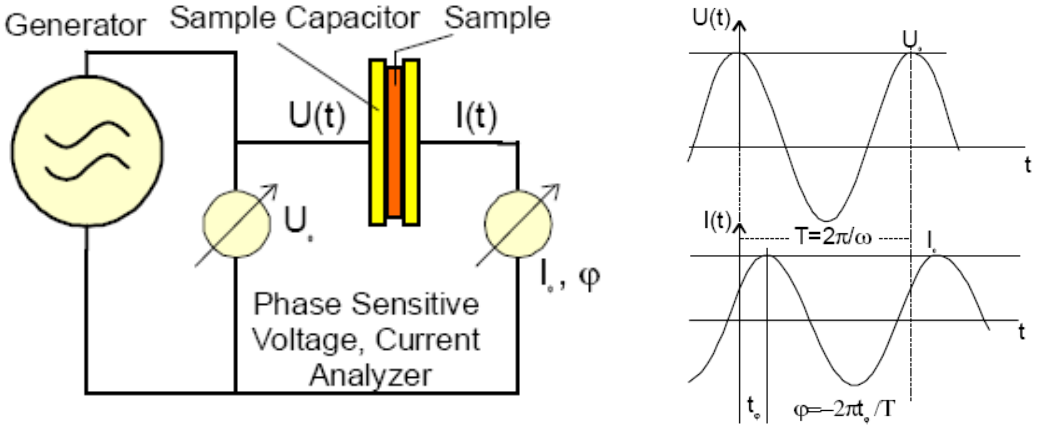

Figure 2.6 Principle of electric measurement. a) The sample is placed between two electrodes under a potential U(t); b) the output current I(t) is out of phase by an angle φ with respect to the applied voltage.

The output current I(t) is out of phase with respect to the voltage by an angle φ .

$$I(t) = I_0 cos(\omega t + \varphi) \tag{2.9}$$

The measurement is repeated for various values of ω in a frequency range from μHz to MHz. The analyzer measures the current I(t) and then the values of I*(ω) are calculated through a Fourier transform:

$$I^*(\omega) = \frac{2}{nT}\int_0^{nT} I(t)\, exp(i\omega t)dt = I^{'} + i\, I^{''} \tag{2.10}$$

The complex impedance Z*(ω) is obtained by dividing the applied voltage by I*(ω). The complex conductivity σ*(ω) is calculated by the expression:

$$\sigma^* = \sigma^{'} - i\sigma^{''} = \frac{1}{Z^*(\omega)}\frac{d}{A} \tag{2.11}$$

where A is the area of the electrode and d is the spacing. The relationship between the complex permittivity ε*(ω) and σ*(ω) is:

$$\varepsilon^*(\omega) = \varepsilon^{'}(\omega) + \, i\varepsilon^{''}(\omega) = \frac{\sigma^*(\omega)}{i\omega\varepsilon_0} \tag{2.12}$$

Thus, with a single measurement it is possible to represent the electric response of the material in terms of the real and imaginary component of the permittivity, the conductivity, impedance etc.. The most suitable spectral representation depends on the material's characteristics.

2.5.1 Dielectric relaxations in polymers

Conventionally, macromolecular systems such as polymers that present dielectric relaxations are studied in two steps. In the first step, the temperature spectra of tanδ at a constant frequency are analyzed to assign the relaxation modes. In the second step, the temperature and frequency profiles of complex conductivity or permittivity spectra are studied. The temperature spectra are

assigned by coupling the dielectric spectra with differential scanning calorimetry and dynamic mechanical measurements.

Permittivity/temperature spectra are obtained by plotting, as a function of temperature, the real and the imaginary components of permittivity (ε', ε'') or alternatively the tanδ = ε"/ε' profiles measured at a constant frequency. The highest temperature process is always *n* with the remaining peaks being labelled α, β, γ, δ in order of decreasing temperature. In the frequency spectra the above described relaxation modes are detected in the order n, α, β, γ and δ as the frequency increases.

The normal mode (*n*-relaxation) is related to both the geometry and the dynamics of the macromolecule. Theory predicts that the contribution of the n-relaxation process is proportional to the fluctuation of the end-to-end vector of a polymer chain. The relaxation parameters of this mode, i.e. the dielectric strength and relaxation time, depend on the molecular weight of the macromolecule.

The α-relaxation is related to the glass transition (T_g) of the material so this mode is referred to as the "dynamic glass transition". The α-mode is attributed to the diffusion of conformational changes along the macromolecular chain, i.e. the segmental motion of chain.

The β-relaxation originates in localized fluctuations of the dipole vector associated with parts of the main chain or with the rotational fluctuations of side groups or partial side groups of a macromolecule.

γ and δ modes are associated with fast local fluctuations of the molecular components of macromolecules.

2.5.2 Instrument

The BES measurements were collected in the 10 mHz - 10MHz frequency range using a Alpha-A analyzer coupled with a temperature control system, consisting of a cryostat operating with a

N_2 gas jet heating and cooling system (Figure 2.7). The temperature range varies for the investigated materials and is reported within the different chapters present in this thesis.

Figure 2.7 BES measuring system including the analyzer, temperature control system, the cryostat and sample holder cell, vacuum pump (hidden) and electronic data management.

The operating conditions for the Alpha-A analyzer are listed below in Table 2.3.

Table 2.3 Alpha A analyzer specifications.

Frequency range	3 μHz - 40 MHz
Frequency resolution	10^{-4}
Maximum sample resistance	10^{14} Ω
Capacity range	10^{-15} – 10^{0} F

The analyzer measures the complex impedance ($Z^*(\omega)$) or capacitance ($C^*(\omega)$) of the sample over a wide frequency range and then calculates the complex permittivity and conductivity $\varepsilon^*(\omega)$ and $\sigma^*(\omega)$. A software is used to control the electrical experimental parameters and for the collection, storage and display of the imaginary and real components of the $Z^*(\omega)$, $\sigma^*(\omega)$ and $\varepsilon^*(\omega)$ profiles.

The temperature control system, shown in Figure 2.8 is essential to: a) the correct temperature control of the sample, in order to ensure that the sample temperature does not exceed the set point temperature (especially near phase transition temperatures) to avoid damage or undermine the analyzed sample; b) reduce the measuring time, because the time of sample conditioning, for frequencies lower than 0.1 Hz, occupies most of the measurement time. For all the electric measurements carried out in this work, the temperature fluctuations are less than 0.2°C.

The temperature control system consists of a cryostat, a gas heating module, and a microprocessor controller (Figure 2.8).

The microprocessor controller has four independent loops that control the sample and gas temperature (gas heater), the temperature of liquid nitrogen and the pressure in the dewar. Inside the dewar, the evaporator heats the liquid nitrogen until the desired pressure and the cold gas flows under the effect of pressure up to the heating module. The connection line between the dewar and heating module is isolated by an external vacuum chamber. The gas inside the module is heated to the set point temperature and finally reaches the cryostat (thermally isolated by an external vacuum chamber), where the sample is mounted (Figure 2.8).

The temperature of the sample is stable with an error of 0.01°C. The lower temperature limit is equal to -160°C, provided there is adequate pressure applied on the nitrogen liquid. The pressure in the dewar is directly controlled by the microprocessor, and varies from 30 to 100mbar according to the set point temperature. The upper temperature limit is 450°C.

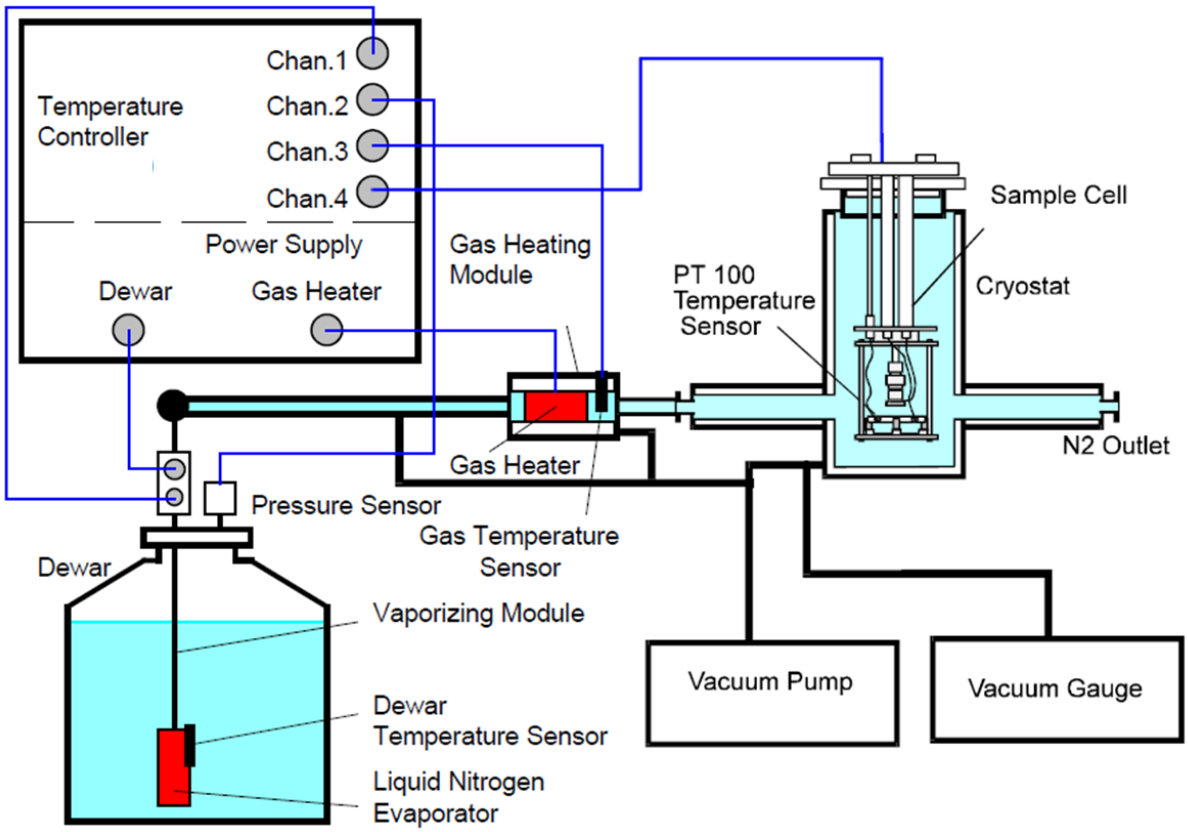

Figure 2.8 Scheme of the temperature control system including the cryostat (containing the sample cell), dewar, gas heating module and microprocessor controller.

2.5.3 Methods

The electrical measurements were performed by placing the samples between two gold circular electrodes with a diameter of 20.1 mm. The cell constant was determined from the area of the electrodes and their distance d. For polymer membranes, d is equal to the thickness of the samples (measured with a digital micrometer). In the case of measurements performed on liquid samples (like the ionic liquids reported in Chapter 4) the distance d was obtained by interposing two optical fibers with a thickness of 200μm between the electrodes.

All of the samples were placed between the electrodes within a sealed cell consisting of two teflon bodies which are bound together through two external brass rings. The cell is shown in Figure 2.9. Electric contact with the external gold electrodes through the teflon cell body is secured by two steel cylinders, coaxial and in contact with the gold electrodes (Figure 2.9). The

system allows the insulation of the sample from the external environment in order to prevent: a) sample dehydration during the measurement (for samples measured in wet conditions); b) the absorption of water from the external environment (for samples measured in dry conditions).

For wet samples, the free volume of the cell was partially filled with 100μL of bidistilled water in order to avoid sample drying during measurements at T>90°C. No corrections for thermal expansion of the cell were carried out. The absence of water loss during measurements was checked by weighing the closed cell before and after the measurements.

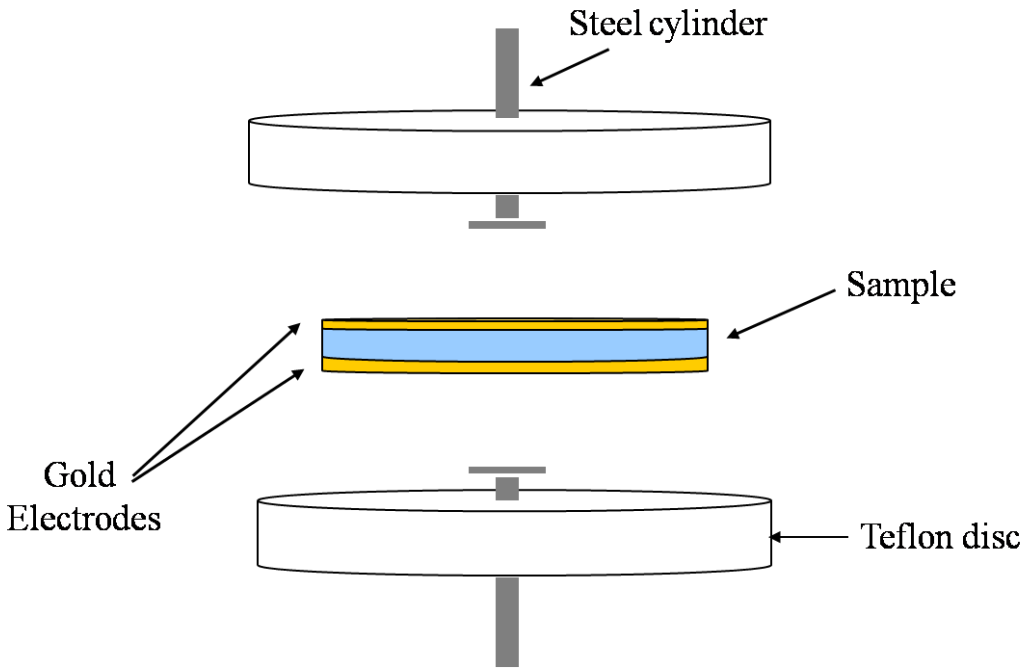

Figure 2.9 Cell for electric measurements

2.6. Broadband electric spectroscopy at different dew point temperature [11]

The electric spectra at different relative humidity were collected using a home-made BES spectrometer which was patented [11].

The system allows the collection of electric measurements of solid samples in presence of inert or reacting gases at various pressures, cell temperatures and dew point (R.H.%) temperatures. Figure 2.10 shows a block diagram of the instrument.

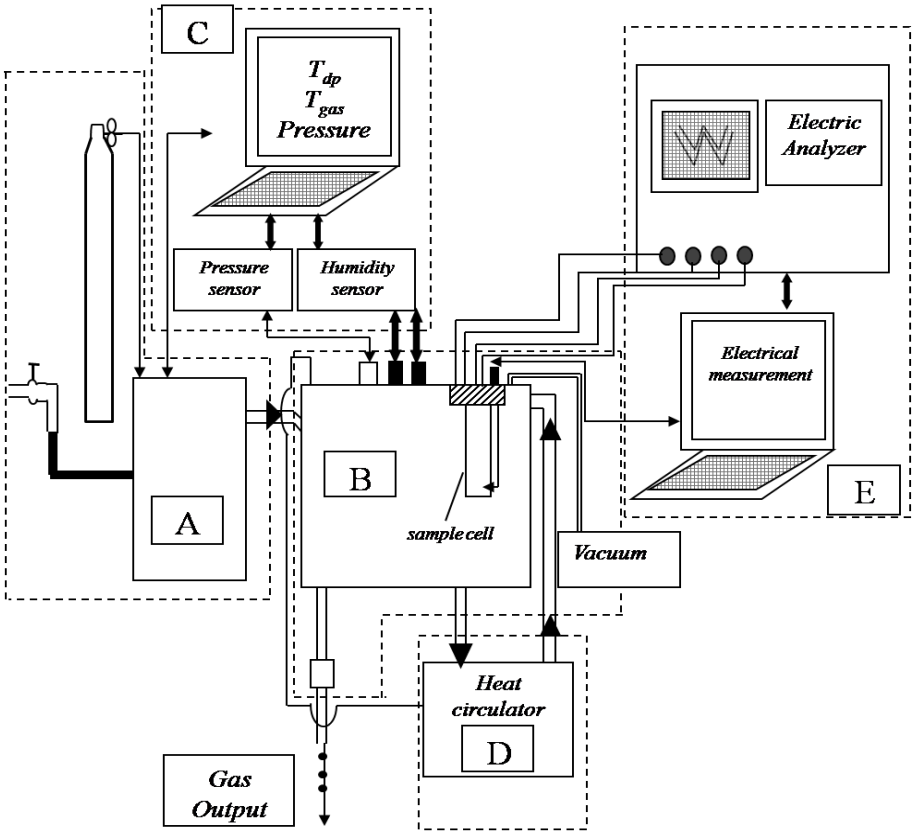

Figure 2.10 Block diagram of the temperature, pressure and relative humidity controlled instrument for electric measurements. Block A – humidification system. Block B – measurement cell. Block C – pressure, temperature and relative humidity control sensors. Block D – heat circulator. Block E - broadband electric spectrometer (BES)

Block A is the humidity generator (*Dew Point Humidifier System, 5SLPM 750/2200W DPH* from Arbin Instruments) capable of humidifying a gas to a dew point up to 99°C and heating the gas output up to 140°C. The maximum gas flow is 1 sL/min.

This device allows the desired relative humidity value to be obtained for each dew point temperature, T_{dp}, by setting the gas output temperature, T_{gas}, with $T_{dp} \leq T_{gas}$. The instrument can use any carrier gas, such as air, N_2, Ar, He etc. In this work nitrogen was used because it is stable, chemically inert and inexpensive. The temperature of the gas (T_{gas}) and of the dew point (T_{dp}) were controlled with two FDC 9300 controllers (*Futuredesign controls*) equipped with a display that shows both the set point and the value measured by the sensor. The temperatures T_{dp} and T_{gas} of gas exiting the humidifier are regulated with a precision of ±0.1°C.

The B block illustrates the measuring cell. The cell is composed of three concentric stainless steel cylindrical chambers. The internal chamber (Chamber 1) contains the sample holder and the temperature, dew point and pressure sensors. A duct crosses the middle chamber (Chamber 2) to carry the cell's heating fluid. The heating fluid enters the coil from the duct in the bottom of the cell and exits from duct on the top. The external chamber (Chamber 3) is connected to a vacuum pump (10^{-6} bar, *803 CIT Alcatel High Vacuum Technology)* that guarantees thermal isolation from the external environment. The humidified gas enters the internal chamber (Chamber 1) and comes in contact with the sample to maintain a fixed value of relative humidity. It then exits from the gas output situated on the bottom of the measurement cell. The thermal stability of the cell is guaranteed by the heating fluid that circulates in the middle chamber and by the vacuum created in the external chamber. The temperature, pressure and relative humidity sensors are situated near the sample to increase the accuracy in the determination of these parameters.

The sample, with a known diameter and thickness, is clamped between two porous electrodes (made of sintered stainless steel powder and covered with a layer of platinum) and placed within a capacitor in the lower part of the cell. The sample temperature is measured with a PT100 thermocouple situated near the material. Four BNC connectors are located on the top of the sample for the electric measurement.

The C block includes the electronics for control of the sensors to measurement the pressure and the dew point and gas temperature (T_{dp} and T_{gas}) inside the cell.

The cell is heated from room temperature to 140°C with a silicon oil heat circulator (Julabo E06, Block D). This system is flexible and allows for consistent heating and cooling cycles. Block E contains the Agilent 4294A impedance analyser. This instrument can measure the electrical properties of materials with impedance values between 0.003 and 5×10^{8} Ω over the frequency range from 40 to 15×10^{6}Hz with a resolution of $\tan\delta < 10^{-3}$. The *Novocontrol WinDETA* software is used for the data management of the electric measurements.

The values of electrical parameters (permittivity, conductivity, impedance etc.) can be expressed as a function of the cell and dew point temperature. In particular in the present work the electric measurements were performed at constant cell temperature (90°C), varying the dew point temperature and thus the relative humidity inside the measuring cell.

2.7. Facility for fuel cell tests

The facility used for testing the membrane in single fuel cell is reported in Figure 2.11.

Figure 2.11 Facility for single fuel cell tests.

The system shown in Figure 2.11 allows the investigation of the polarization curve characteristics of the membrane electrode assembly (MEA), while feeding the anode of the fuel cell with both hydrogen or alcohol, and air or pure oxygen can be used as oxidant at the cathode. The measurement conditions (temperature, pressure, reagents flows and humidification levels etc.) are controlled by software. The general structure of the system is characterized by the presence different interconnected subsystems, listed below:

- *Module for gas processing*: consists of pressure regulators, solenoid valves, control valves, pressure gauges and flow meters (Mass Flow Controllers, MFCS).
- *Module for cooling water treatment*: including heat exchangers and water pumps.
- *Module for humidification of gases*: including humidifiers and water pumps.
- *Alcohol supply module*: consists of a tank and a group of pumps and heat exchangers.
- *Power Module*: provides the current to systems.
- *Electronic Control Module*: computers and interfaces connected to the system.

The measuring cell, containing the membrane-electrode assembly shown in Figure 2.12, consists of two graphite bipolar plates that distribute the reagents within the cell and at the same time act as current collectors.

Figure 2.12 Graphite bipolar plates.

In the present work, single fuel cell tests were performed on the materials described in Chapter 3, using hydrogen and pure oxygen as fuel and oxidant, respectively, at constant cell temperature (80°C) and varying relative humidities of the reactant gases.

2.8. References

1. Skoog, D., A.; Leary, J., J.; *Principles of Instrumental Analysis*, IV Ed. , Saunders College Publishing, Orlando (1992)
2. Baxter, R., A.; *Thermal Analysis*, R.F. Schwenker and Garn Eds., New York, Academic Press, 1969
3. *SDT Simultaneous DSC-TGA 2960 Instrument Manuals*, TA Instruments
4. *DSC 2920 Instrument Manual*, TA Instruments
5. *FT-IR 5SXC, Instrument Manual,* Nicolet
6. Ward, I. M.; Sweeney, J.; *The Mechanical Properties of Solid Polymers* – 2nd edition, John Wiley & Sons, Ltd, Chichester, 2004
7. *DMA Q800 Instrument Manual*, TA Instruments
8. Schonhals, A., Kremer, F.; eds., *Broadband Dielectric Spectroscopy*, Springer, Berlin, **2003**.
9. Di Noto, V.; Giffin, G.A.; Vezzù, K.; Piga, M.; Lavina, S.; *Broadband Dielectric Spectroscopy: A Powerful Tool for the Determination of Charge Transfer Mechanisms in Ion Conductors*, in: P. Knauth, M.L.D. Vona (Eds.) *Solid State Proton Conductors: Properties and Applications in Fuel Cells*, Wiley, Chichester, **2012**.
10. *Alpha-A impedance analyzer Instrument Manual*, Novocontrol
11. Di Noto, V.; Piga, M.; Lavina, S.; Negro, E.; Pace, G.; "Cella per misurare spettri elettrici di materiali in condizioni controllate di pressione, temperatura e temperatura di Dew Point (DPT)", Italian patent application PD2009A000041 filed on March 10th, **2009.**

Chapter III

New hybrid inorganic-organic proton conducting membranes based on Nafion and $[(ZrO_2)(Ta_2O_5)_{0.119}]$ core shell nanofiller

3.1. Introduction

One of the most interesting routes in the preparation of promising electrolytes for application in fuel cells consists of the synthesis of organic-inorganic composite membranes based on Nafion® and inorganic micrometer to nanometer size fillers [1-8]. Thus, Nafion® membranes doped with: (a) heteropolyacids, such as phosphotungstic acid (PTA), allowed the design of fuel cells with high performance at lower relative humidity (RH) and elevated temperature (ca. 120°C); (b) hygroscopic oxides, such as SiO_2, TiO_2, ZrO_2, Al_2O_3 and others, were proposed with the aim of increasing the water uptake of the membranes and decreasing the humidification requirements of the PEMFCs [1–8]. The effects of the silica concentration in [Nafion/$(SiO_2)_x$] nanocomposite membranes with $0 \leq x \leq 15$ wt% have been studied demonstrating the presence of four different water species domains embedded in the bulk membranes. The inorganic filler affects the dynamic relaxations of Nafion® and thus, the material conductivity [9]. In addition, it was

shown that the formation of dynamic $SiO_2\cdots HSO_3–$ crosslinks in the hydrophilic polar clusters influences the chain dynamics of the hydrophobic fluorocarbon domains of the host material. Further investigations were performed on the [Nafion/$(M_xO_y)_n$] membranes with M = Ti, Zr, Hf, Ta and W where n = 5 wt% [10,11]. It was demonstrated by vibrational spectroscopy that fluorocarbon domains of the [Nafion/$(M_xO_y)_n$] materials consist mostly of chains with a 15_7 helical conformation and a smaller amount of 10_3 helices [10,11]. The concentration of 10_3 helical chains varies within the range 9 – 16% and depends on the type of metal oxide used in the preparation of the composite membrane. Along the IV group of the periodic table, the concentration of 10_3 helical chains increases in the order Ti<Zr<Hf and it decreases in the order Hf>Ta>W along the VI period. Furthermore, it was revealed that [10,11]: a) the amount of each of the four water domains detected in the bulk membranes depends on the acidity of M_xO_y oxocluster; b) the mechanical, thermal and dynamic characteristics of Nafion® host polymer depend on the concentration of dynamic $RSO_3H\cdots M_xO_y\cdots HSO_3R$ cross-links in bulk material, which are responsible for the good thermal, mechanical and electrical stability of the materials; c) in [Nafion/$(M_xO_y)_n$] materials, the concentration and strength of $RSO_3H\cdots M_xO_y\cdots HSO_3R$ cross-links occurring inside polar hydrophilic cages of the membranes increase along the IV group and decrease along the VI period of the periodic table. Of the [Nafion/$(M_xO_y)_n$] membranes, [Nafion/$(HfO_2)_n$] exhibits the best physicochemical properties owing to strong acid-base interactions that take place in ion aggregate domains between HfO_2 and the sulfonic acid groups of host polymer matrix [10,11,12]. This is due to the acidic characteristic of HfO_2, which is the lowest among the investigated oxoclusters of the IV groups [10,11,12].

Recently, it was reported that a reduction of the water uptake and an increase in both the mechanical properties and the proton conductivity, with respect to pristine Nafion and [Nafion/$(M_xO_y)_n$] membranes, is obtained in [Nafion/$(M_1O_x)(M_2O_y)_n$] membranes [13,14]. In such systems, Nafion is doped with different concentrations (from 3 to 15wt%) of an inorganic

[$(M_1O_x)(M_2O_y)$] "core-shell" nanofiller. The nanofiller is prepared by milling together two oxides with different Mohs index and acidity in presence of a solvent. In this way, nanometric particles consisting of a "core" of the harder oxide (M_1O_x) covered by a thin layer of the softer oxide (M_2O_y) were obtained [13,14].

By studying the properties of [Nafion/$(ZrO_2)(HfO_2)_{0.25}$] and [Nafion/$(SiO_2)(HfO_2)_{0.28}$] membranes [15,16], with n = 5,10 and 15wt%, Di Noto et al. reveal that the best thermal, mechanical and electrical properties and performance in fuel cell are obtained for the membranes containing the filler with the higher basic character, [$(ZrO_2)(HfO_2)$]. Nevertheless, the [Nafion/$(ZrO_2)(HfO_2)_n$] materials present an increased water uptake with respect to [Nafion/$(ZrO_2)(SiO_2)_n$] membranes and pristine Nafion due to the basicity of the filler [15,16].

In an effort to extend that work and elucidate the effect of the nanofiller on the membrane's structure and thermal, mechanical and electrical properties, the research activity conducted during the first years of PhD research activity involves the synthesis and the characterization of new proton conducting membranes based on Nafion and [$(ZrO_2)(Ta_2O_5)_{0.119}$] oxide core-shell nanofiller. The nanofiller is prepared with the intent of combining the improvements obtained from the core-shell nanofillers with the intrinsic characteristics of the individual oxides in order to: a) maintain strong $RSO_3H\cdot\cdot[(M_1O_x)(M_2O_y)]\cdot\cdot HSO_3R$ interactions; and b) reduce the water uptake of the membranes. For this reason, among the oxoclusters of the IV group and VI period previously investigated [9-16], ZrO_2 and Ta_2O_5, which present different in Mohs index and an overall reduced basicity with respect to [$(ZrO_2)(HfO_2)$] filler, were selected.

The aim of this work is to obtain Nafion-based hybrid membranes where the proton conduction occurs through appropriate percolation pathways formed at the interfaces between an inorganic nanofiller and the polymer matrix. Such a pathway allows the membranes to maintain high proton conductivity values for low levels of membrane hydration. By integrating the information obtained from a variety of independent techniques such as DMA, MDSC and BES, it is possible

to highlight that the filler stabilizes the hydrophobic and hydrophilic domains of the membranes through the formation of R-SO_3H···[(ZrO_2)(Ta_2O_5)]···HO_3S-R bridges. These cross-linking interactions contribute to the development of a hybrid three-dimensional network that binds the fluorocarbon chains of Nafion and regulates the long-range charge transfer mechanism. In particular, proton conduction in the hybrid membranes occurs at the interface between the nanofiller and the polar domains of Nafion and is mediated by the dynamics of the fluorocarbon chains of the host polymer matrix.

3.2. Experimental

3.2.1 Reagents

Nafion® with a proton exchange capacity of 0.80 meq·g^{-1} (5 wt% perfluorosulfonic acid PTFE copolymer solution, Alfa Aesar, ACS grade) and M_xO_y nanometric oxoclusters (Aldrich, ACS grade), where M is Zr or Ta, were used as received. ZrO_2 had an average particle size less than 100 nm, a density of 5.89 g/mL and a Mohs hardness of 8.5, while Ta_2O_5 had an average particle size less than 5 μm, a density of 8.20 g/mL and a Mohs hardness of 7 [17]. Solvents were purchased from Aldrich and used as received. Bidistilled water was used in all procedures.

3.2.2 Nanofiller preparation

The procedure followed for the preparation of the nanofiller is shown in Scheme 3.1. 12mL of a dimethylformamide (DMF) suspension containing 1.5 g of ZrO_2 (70wt%) and 0.643 g of Ta_2O_5 (30 wt%) was milled for 5 h at 500 rpm in a tungsten carbide grinding jar using a planetary ball mill (RETSCH PM 100). The mixture was transferred into a 100mL volumetric flask and diluted with DMF and treated in an ultrasonic bath for 1 h. Thus a solution of [(ZrO_2)·(Ta_2O_5)$_{0.119}$] "core–shell" nanoparticles (dispersion A), with a molar ratio between Ta_2O_5 and ZrO_2 of 0.119 was obtained.

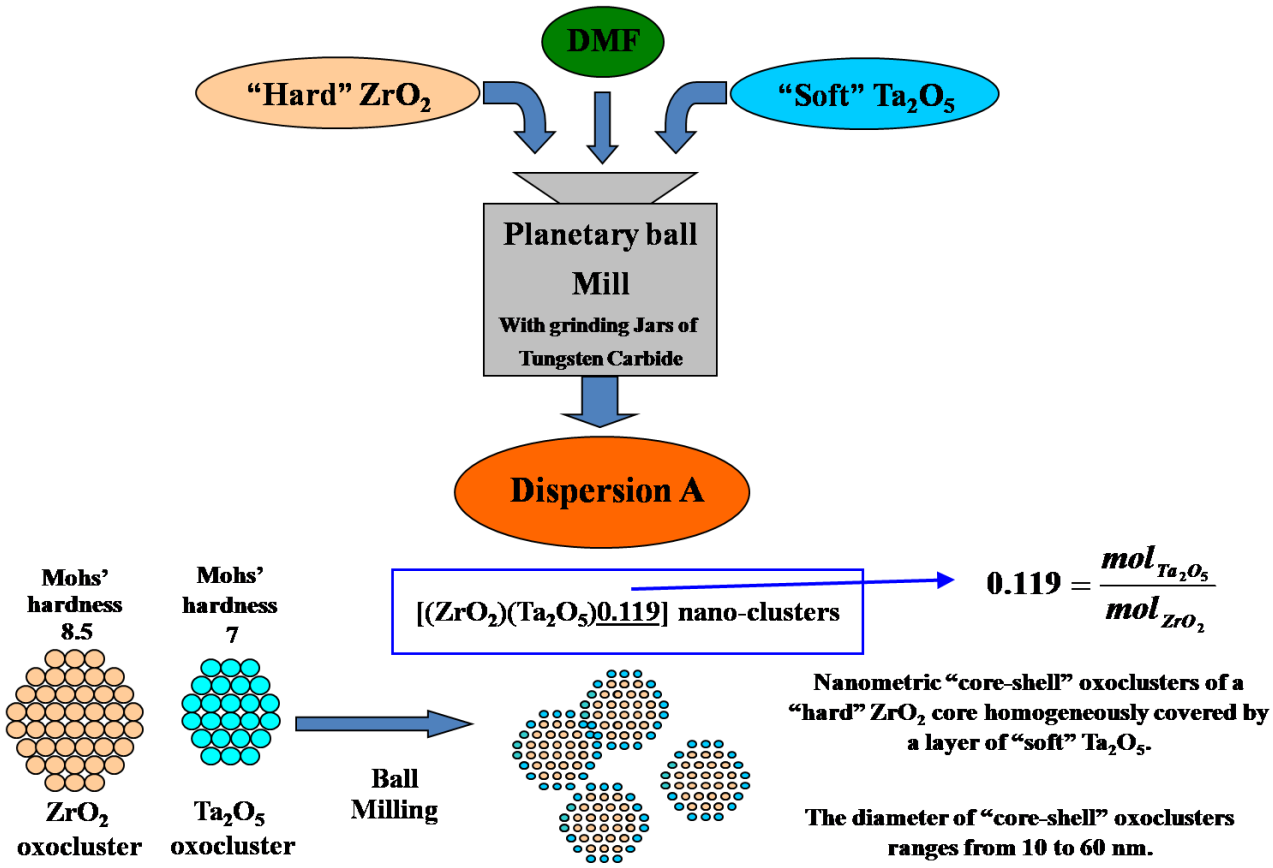

Scheme 3.1 Synthesis of the $[(ZrO_2)(Ta_2O_5)_{0.119}]$ "core-shell" nanofiller.

After the milling process, nanoparticles composed of a core of ZrO_2 covered by a thin layer of Ta_2O_5 are obtained. This reaction occurred thanks to the difference in Mohs hardness of the used nanopowders, 8.5 and 7 for ZrO_2 and Ta_2O_5, respectively; and to the different acid–base characteristics of the ZrO_2 and Ta_2O_5 materials. Part a) of Figure 3.1 shows the SEM of the ZrO_2 powder before the milling process, while parts b and c of Figure 3.1 report the TEM images of the $[(ZrO_2)\cdot(Ta_2O_5)_{0.119}]$ nanofiller at two different magnifications.

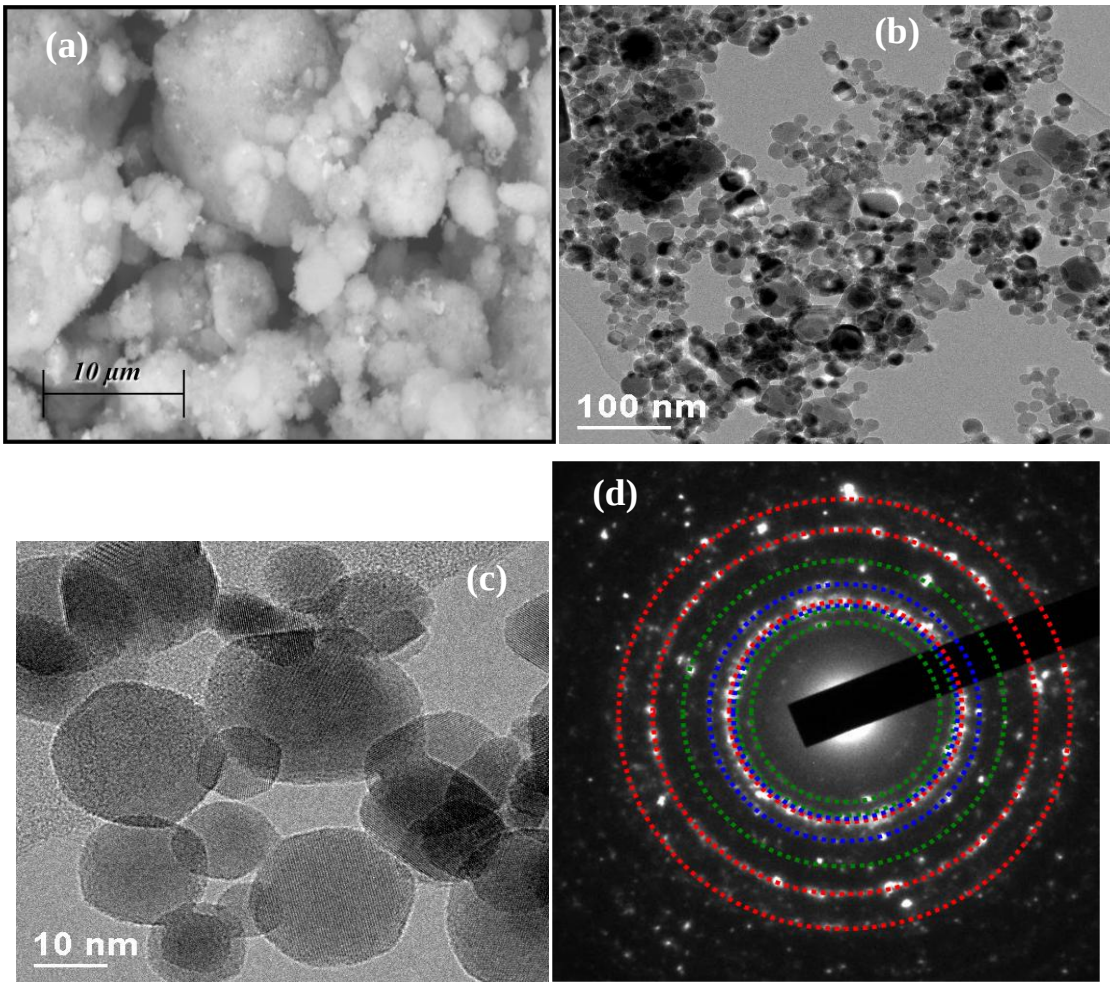

Figure 3.1 (a) SEM micrograph of pristine ZrO_2 powders. (b) and (c) TEM image of the $[(ZrO_2)\cdot(Ta_2O_5)_{0.119}]$ nanoparticles. (d) electron diffraction pattern of the $[(ZrO_2)\cdot(Ta_2O_5)_{0.119}]$ nanofiller.

Results indicated that: 1) the milling process strongly reduces the diameter of the particles, going from micro- to nanometric sizes (part a and b of Figure 3.1); 2) after the milling process, the diameter of the particles ranges from 10 to 50nm (Figure 3.1 part b); 3) the absence of two distinct phases (Figure 3.1 part c). The formation of the "core-shell" structure between ZrO_2 (core) and Ta_2O_5 (shell) is supported by inspecting the analysis of the electron diffraction pattern reported in part d of Figure 3.1. Three phases are revealed: t-ZrO_2, m-ZrO_2 and trace amounts of m-Ta_2O_5. Furthermore X-ray fluorescence (data not shown) did not show evidence of any grains containing only Ta_2O_5. Taken together, these results reveal that: 1) the nanoparticles contain both ZrO_2 and Ta_2O_5; b) most of Ta_2O_5 is chemically bonded to the surface of the ZrO_2 "core" nanoparticles, forming a "shell" with an isomorphic structure. Similar results are recently

obtained by Di Noto et al. for [$(ZrO_2)(HfO_2)_{0.25}$] core shell nanofiller [15,16]. In that work the authors defined, on the basis of the interactions between the oxides forming the "core" and the "shell" of the nanoparticles, two class of "core-shell" nanofillers: A and B type. In A type core-shell, a "core" with a higher Mohs index or with a higher crystallinity is chemically covered by a "shell" of a softer material characterized by a lower Mohs hardness. A chemical-bonding interaction occurs between the shell and the core oxides when the two materials have compatible crystal structures and chemical behaviour. In the B type "core-shell", a simple adhesion of the soft phase, characterized by a low Mohs hardness or less crystalline nanoparticles, onto the surface of the nanoparticles with a high Mohs hardness is expected. Physical "core-shell" nanoparticles occur when the two materials forming the "core-shell" have very different and incompatible crystal structures. In this situation, the soft and hard phases are clearly distinguishable [15,16]. Thus, considering the obtained experimental results and according to the work of Di Noto et al. [15,16], it is possible to define the [$(ZrO_2)\cdot(Ta_2O_5)_{0.119}$] as a A-type core shell nanofiller.

3.2.3 Membranes preparation

Nanocomposite membranes with the formula {Nafion/[$(ZrO_2)\cdot(Ta_2O_5)_{0.119}$]$\Psi_{ZrO_2}$}, where Ψ_{ZrO_2} = mol_{ZrO_2}/mol_{SO_3H} is in the range 0 – 1.937, were prepared using the following general solvent casting procedure (Scheme 3.2). Nafion (0.45 g) suspended in a water/alcohol mixture was cast in a beaker and heated at 80°C for 40 min to remove the low-boiling solvents. The resulting brittle film was dissolved in DMF and mixed with an appropriate amount of nanofiller dispersion A (Scheme 3.2) [13,14].

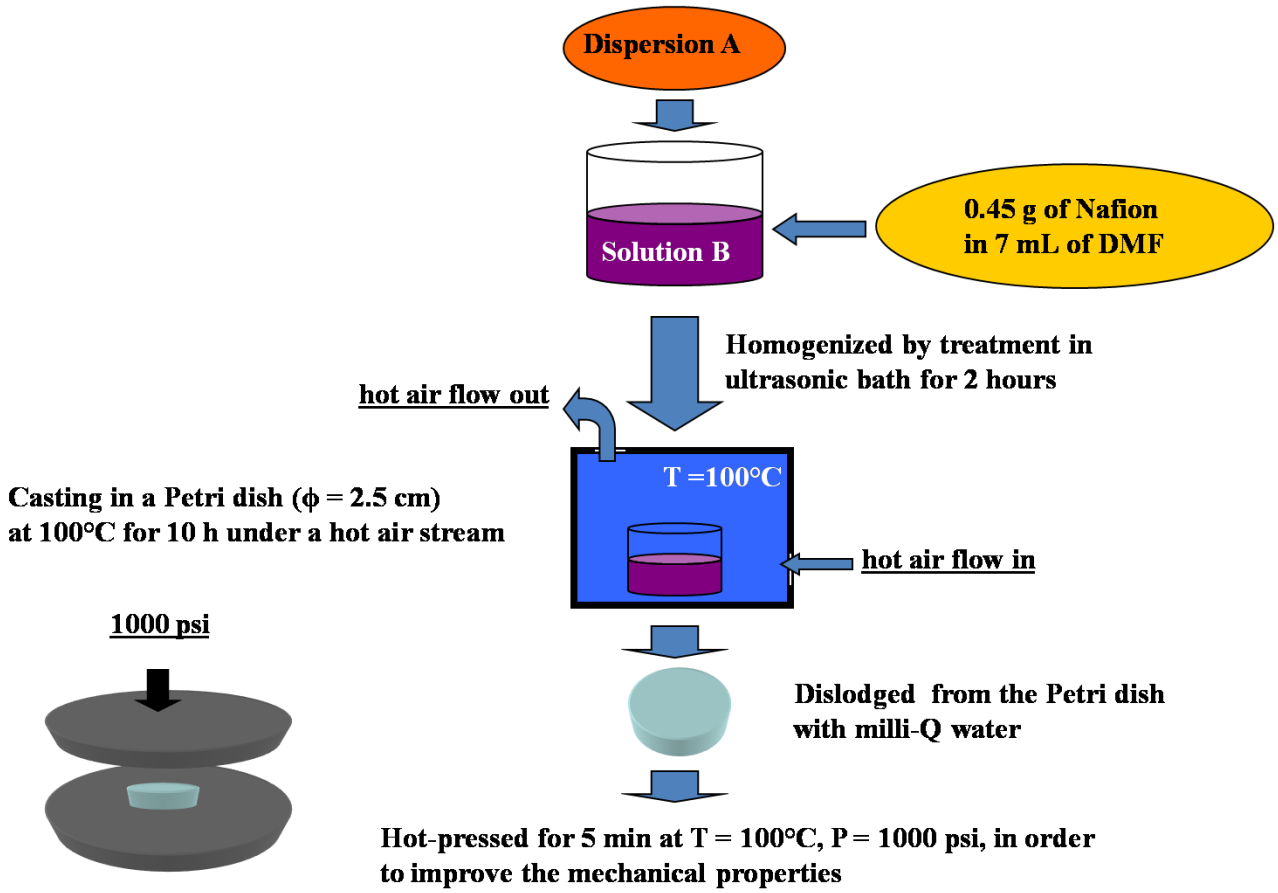

Scheme 3.2 Preparation by solvent casting of the {Nafion/$[(ZrO_2)\cdot(Ta_2O_5)_{0.119}]\Psi_{ZrO_2}$}nanocomposite membranes.

The mixture was homogenized in ultrasonic bath for 2 h and was then recast on a Petri dish at 100 °C for 10 h under a hot air stream. The resulting membranes were: (a) dislodged from the Petri dish by a treatment with hot milli-Q water (T ≈ 60°C) for 30 min; (b) dried under air at room temperature for 1 h; (c) treated in oven for 4 h at 130°C; and (d) hot-pressed at T = 100°C and p ≈ 68 bar for 5 min. The thickness of the films was between 200 and 280 μm. All of the hybrid membranes had a smooth, glossy side and an opaque side. The opaque side was the side in contact with the Petri dish during the solvent casting process. The composition and molar ratios of the {Nafion/$[(ZrO_2)\cdot(Ta_2O_5)_{0.119}]\Psi_{ZrO_2}$} membranes are summarized in Table 3.1.

Table 3.1 Reagent composition and molar ratios for {Nafion/[$(ZrO_2)\cdot(Ta_2O_5)_{0.119}$]$\Psi_{ZrO_2}$}membranes.

Reagents				***Molar ratios***			
ZrO_2 /(g)	Ta_2O_5 /(g)	Nafion / (g)	$wt\%_{ZrO_2}$ [a]	Ψ_{ZrO_2} [b]	$\Psi_{Ta_2O_5}$ [c]	Ψ [d]	φ [e] / (meq/g)
-	-	0.45	0	0	0	0	0.800
0.0141	0.0060	0.45	3	0.318	0.038	0.356	0.775
0.0242	0.0103	0.45	5	0.546	0.065	0.611	0.758
0.0465	0.0198	0.45	9	1.047	0.125	1.172	0.724
0.0587	0.0251	0.45	11	1.324	0.158	1.482	0.707
0.0718	0.0307	0.45	13	1.619	0.193	1.812	0.690
0.0859	0.0367	0.45	15	1.937	0.231	2.167	0.674

[a] $wt\% = m_{ZrO_2} / m_{composite}$ [b] $\Psi_{ZrO_2} = mol_{ZrO_2} / mol_{-SO_3H}$ [c] $\Psi_{Ta_2O_5} = mol_{Ta_2O_5} / mol_{-SO_3H}$

[d] $\Psi = (mol_{ZrO_2} + mol_{Ta_2O_5}) / mol_{-SO_3H}$ [e] $\varphi = (meq_{Nafion} + meq_{ZrO_2} + meq_{Ta_2O_5}) / m_{composite}$

3.2.4 Membranes purification and activation

The purification and activation of the hybrid membranes were carried out by a series of treatments at 80°C as described elsewhere [9,14]. Each of the membranes was soaked in bidistilled water, a 3 wt% solution of H_2O_2 and a 1M H_2SO_4 solution for 1h. Following this series of treatments, the membranes were purified by three washing steps of 1 h in bidistilled water. Finally, the films were hydrated in an autoclave at RH=100%, T = 135°C and p = 3.3 bar. This hydrated state was considered the "reference zero point" (RZP) of the membranes thermal history. The membranes were stored in milli-Q water at room temperature inside PET bags.

3.2.5 Stoichiometry and proton exchange capacity (PEC)

The proton exchange capacity of the precursor materials and membranes was determined by titration of a heterogeneous water solution of the sample with 5mM NaOH, using phenolphthalein as an indicator as described elsewhere [10-16]. The heterogeneous water solution of the sample was obtained by soaking the material into a NaCl 1M water solution for

12 h. These analyses allowed the determination of the stoichiometry parameters Ψ_{ZrO_2}, $\Psi_{Ta_2O_5}$, and Ψ which correspond to the molar ratio mol_{ZrO_2}/mol_{SO_3H}, $mol_{Ta_2O_5}/mol_{SO_3H}$ and $(mol_{ZrO_2} + mol_{Ta_2O_5})/mol_{SO_3H}$ (Table 3.1), respectively. The total exchange capacity of the nanocomposite membranes is $\varphi = (meq_{Nafion} + meq_{ZrO_2} + meq_{Ta_2O_5})/m_{composite}$, where $m_{composite}$ is the weight in grams of the materials (see Table 3.1).

3.2.6 Instruments and methods

The morphology of the nanofiller was examined by transmission electron microscopy (TEM) and electron diffraction (ED), performed using a Jeol 3010 apparatus operated at 300 kV with a high-resolution pole piece (0.17 nm point-to-point resolution) and equipped with a Gatan slow-scan 794 CCD camera. Energy-dispersive X-ray spectroscopy (EDX) was carried out using an Oxford Instrument EDS detector (Mod. 6636). The sample powders were suspended in isopropanol and a 5μL drop of this suspension was deposited on a holey carbon film supported on 3mm copper grid for TEM investigation.

The TG profiles were collected in the 20<T<800°C temperature range. Dynamic Mechanical analyses were performed in the -10 to 200 °C temperature range at a rate of 4 °C/min. MDSC measurements were made with a heating rate of 3 °C/min in the -50 < *T* < 350°C temperature range.

FT-IR-ATR spectra of the membranes were collected in ATR mode at a resolution of 4 cm^{-1} by averaging 1000 scans. Electrical measurements were performed in the frequency range between 10 mHz and 10 MHz and from 5 to 155°C, collecting spectra every 10°C. The fuel cell tests were performed using the system described in Chapter 2.

3.2.7 Water uptake (W.U.) and membrane reference conditions (RC)

The water uptake (W.U.) of nanocomposite films in RZP conditions was determined as reported elsewhere [10,13,14,18], by using the isothermal mass elimination, TG profiles vs. time, of materials and Equations 3.1 and 3.2.

$$W.U. = \frac{wt(t) - wt_{dry}}{wt_{dry}} \tag{3.1}$$

$$\lambda(t) = \left[\frac{wt(t) - wt_{dry}}{wt_{dry}\, MW_{H_2O}\, \frac{meq}{g}\,(1 - \%wt_{ox})}\right] \tag{3.2}$$

λ(t) is the number of moles of water per equivalent of acid groups, *wt(t)* and wt_{dry} are the weight of the membrane at time t and in dry condition, respectively. MW_{H_2O} is the molecular weight of water; meq/g is the proton exchange capacity of Nafion and $\%wt_{ox}$ is the weight percentage of $[(ZrO_2)\cdot(Ta_2O_5)_{0.119}]$ nanoparticles. W.U. measurements were conducted in isothermal conditions, heating the samples at 30°C for 90 min and then at 120°C for 50 minutes. The profiles of λ(t) as function of time are shown for pristine Nafion and the hybrid membranes in Figure 3.2. For all the investigated materials, the water elimination occurs in two steps, each characterized by a time-independent plateau. The first and the second plateau are reached after t = 60 and 120 min, respectively. W.U. was determined with Equation 3.1, by adding the amount of H_2O eliminated from the membrane isothermally at 30°C to that eliminated after heating the membrane at 120°C. The residual amount of water per sulfonate group present within the membranes after 60min of water elimination is defined as $\lambda_{RC} = \lambda(t = 60min) - \lambda(t = 120min)$. The membranes water content at λ_{RC} (after t = 60 min of water elimination at room temperature) was assumed to be the "dry reference condition" (DRC).

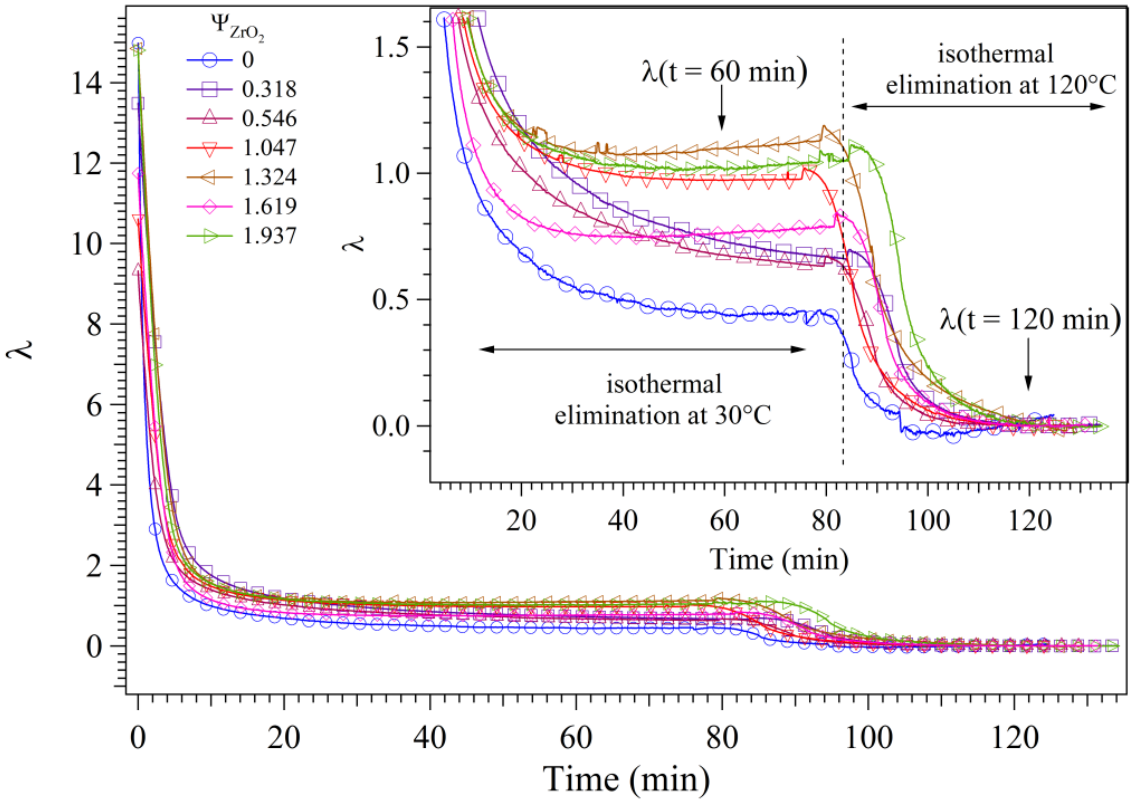

Figure 3.2 Dependence of λ vs. time for the of {Nafion/[$(ZrO_2)\cdot(Ta_2O_5)_{0.119}$]$\Psi_{ZrO_2}$} membranes with $0 \leq \Psi_{ZrO_2} \leq 1.937$.

It should be highlighted that the membranes at DRC status are (a) very easy to obtain and manipulate and (b) are representative of all the interactions present in multiphasic hybrid Nafion membranes. To obtain information about the properties of the Nafion/[$(ZrO_2)\cdot(Ta_2O_5)_{0.119}$]$\Psi_{ZrO_2}$} membranes with $0 \leq \Psi_{ZrO_2} \leq 1.937$ in a reproducible condition, the TG, MDSC, DMA and FT-IR ATR analyses were conducted on samples at DRC conditions. To avoid misunderstandings between the RZP, defined in section 3.2.4 and the DRC conditions, the first indicates the reference state for wet membranes after the preparation and activation procedure, while DRC is the reference state chosen, after the preparation and activation procedure, for the thermo-mechanical and infrared investigations of the materials. Thus, electric measurement, due to the necessity of measured membranes proton conductivity, were conducted in the wet materials at RZP condition.

3.2.8 Fabrication of membrane-electrode assemblies (MEAs)

MEAs were prepared with a catalyst-coated substrate (CCS) procedure as described elsewhere [19]. The platinum loading on both the anodic and the cathodic electrocatalyst layers was 0.4 $mg \cdot cm^{-1}$. The Nafion/C ratio was 0.6 [20]. The electrocatalytic layers were deposited on GDS1120 carbon paper obtained from Ballard Power Systems. The resulting gas diffusion electrodes (GDEs) were hot-pressed onto the membranes according to a protocol detailed elsewhere [21].

3.2.9 Tests in a single-cell configuration

Single fuel cell tests were carried out using a 5 cm^2 single cell with a two-channel serpentine flow field for both the anodic and the cathodic sides, and fed with pure hydrogen as the fuel and pure oxygen as the oxidant. The temperature of the cell and reagent streams were kept constant at 85°C. The hydrogen flow rate was 800 $ml \cdot min^{-1}$. Oxygen flow rates were set at 1700 and 500 $ml \cdot min^{-1}$, respectively. Polarization curves were collected with fully-humidified reagent streams at a back pressure of 1 bar. Subsequently, the activity of the water vapour (a_{H_2O}) of both reagent streams was lowered to 0.75 and the polarization curves were measured after the system reached stability. Finally, polarization curves were determined with both reagent streams having the same a_{H_2O} of 0.50, 0.25, 0.12 or 0.05. All the measurements with reagent streams characterized by $a_{H_2O} < 1$ were collected at a back pressure of 1 bar. The polarization curves were not corrected for internal resistance losses.

3.3. Results and discussion

3.3.1 Water uptake and thermal analysis

The profile of λ and W.U. calculated with Equations 3.1 and 3.2 are shown in part a of Figure 3.3 as function of the nanofiller concentration. The nanofiller concentration is expressed by the

parameter Ψ_{ZrO_2} defined above in section 3.2.5. It is possible to observe that: (a) the water uptake of pristine Nafion is about 25 wt% and this value is consistent with the literature [13,14,22]; (b) the W.U. values of {Nafion/[$(ZrO_2)\cdot(Ta_2O_5)_{0.119}$]$\Psi_{ZrO_2}$} membranes are lower than that of pristine Nafion and depend on Ψ_{ZrO_2}. The latter result suggests an increase of the density of dynamic nanofiller-Nafion cross-links in the hybrid membranes, which corresponds to a decrease of the membrane swelling ability and thus to a reduction of the amount of water absorbed by the membranes.

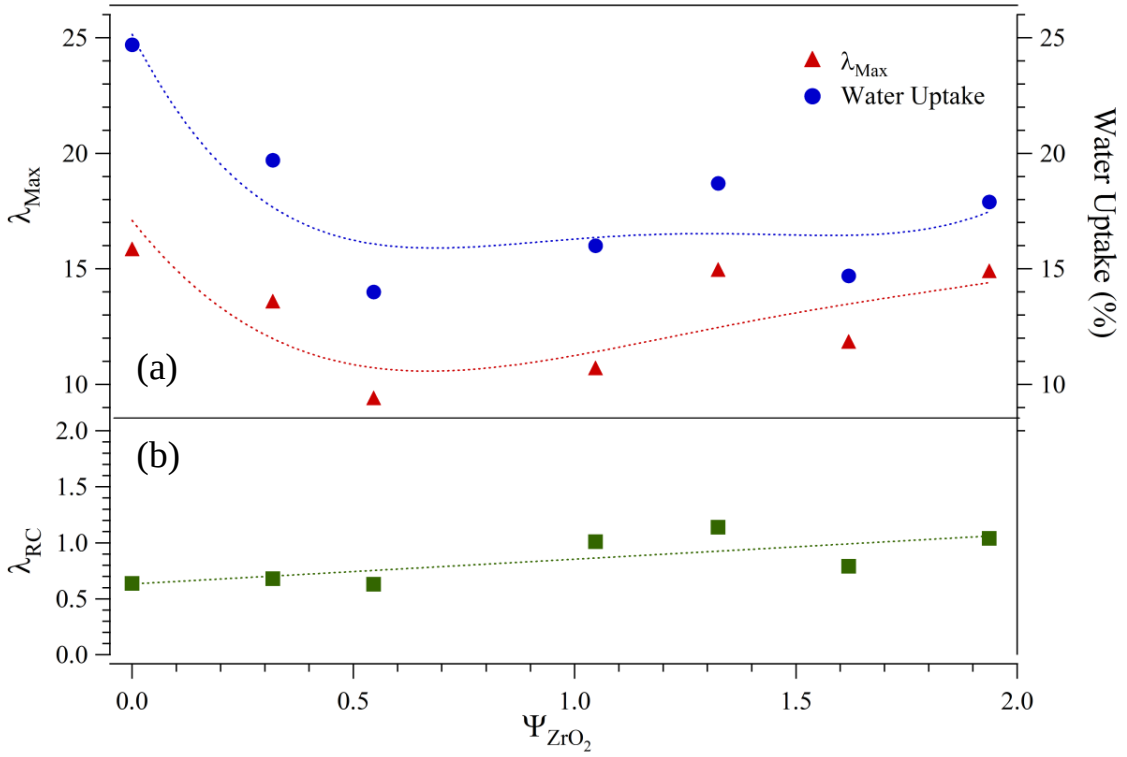

Figure 3.3 Dependence on Ψ_{ZrO_2} of: (a) W.U and λ_{Max} ; (b) $\lambda_{RC} = \lambda(t=60min) - \lambda(t=120min)$. The dashed lines are a guide for the eye.

The profiles of W.U. and λ_{Max} shown in Figure 3.3 indicate that: a) in the $0 \leq \Psi_{ZrO_2} \leq 1.047$ range a minimum of W.U. is revealed, which indicates that the density and strength of dynamic $RSO_3H\cdots[(ZrO_2)(Ta_2O_5)_{0.119}]\cdots HSO_3R$ cross-links between the nanofiller and Nafion's acid groups are higher at lower $[(ZrO_2)(Ta_2O_5)_{0.119}]$ concentrations; b) in the $1.047 \leq \Psi_{ZrO_2} \leq 1.937$ range the nanofiller-polymer interactions become stronger, and the WU is almost independent of

Ψ_{ZrO_2}. The residual water (λ_{RC}) is reported in part b of Figure 3.3. λ_{RC} is between 0.6 and 1 and slightly increases with the nanofiller concentration, according to the hygroscopic character of the filler. This latter result is very important because it indicates that the presence of the inorganic nanofiller increases the concentration of water molecules directly solvating the sulfonic acid groups (interfacial water). As will be discussed later in detail and supported by the electric measurements and the fuel cell test, the increased amount of interfacial water allows the hybrid membranes, with respect to reference Nafion, to maintain good proton conductivity even when a low water content is present in the bulk membranes and thus to work efficiently in fuel cell at low relative humidity conditions.

The TG profiles of {Nafion/[$(ZrO_2)\cdot(Ta_2O_5)_{0.119}$]$\Psi_{ZrO_2}$} materials with $1.047 \leq \Psi_{ZrO_2} \leq 1.937$ are reported in Figure 3.4.

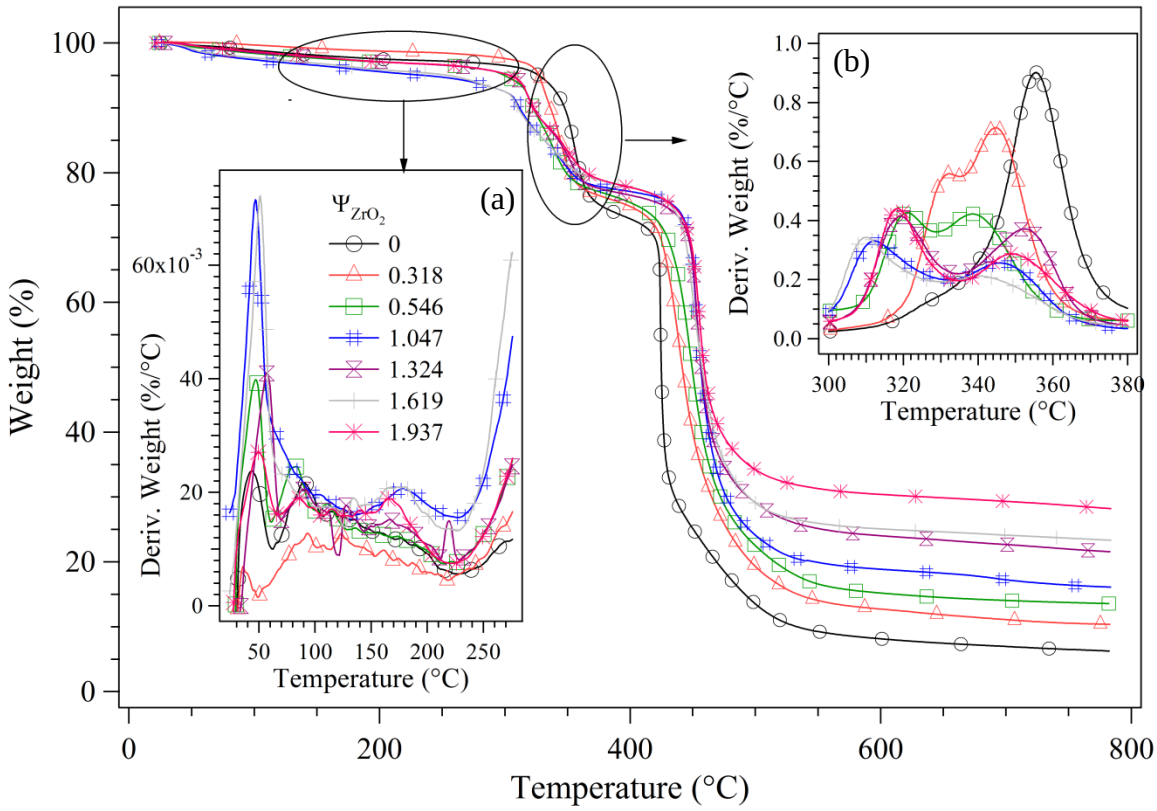

Figure 3.4 TG measurements of {Nafion/[$(ZrO_2)\cdot(Ta_2O_5)_{0.119}$]$\Psi_{ZrO_2}$} membranes with $0 \leq \Psi_{ZrO_2} \leq 1.937$. Insets show the dependence of the derivative of TG profiles on temperature in regions: (a) 30-270°C; and (b) 300 – 380°C.

The TG curves show that the composite membranes are thermally stable up to ca. 160°C and thus can be used in fuel cell at temperature higher than 100°C. For all the investigated materials the TG profiles reveal the presence of four thermal decompositions, which are assigned as follows [9-16]. In the 30–130°C range, the mass elimination corresponds to traces of water (<4%wt) present within the materials. The analysis of TG derivative curves shown in the inset a of Figure 3.4 indicates that, in agreement with previous studies [12-15], the mass loss in the 130–250°C region is associated with the degradation of $–SO_3H$ groups. It should be noticed that, with respect to pristine Nafion, a slight thermal stabilization of the $–SO_3H$ groups in {Nafion/$[(ZrO_2)\cdot(Ta_2O_5)_{0.119}]\Psi_{ZrO_2}$} membranes is observed. The weight loss observed in the 300–380°C region is associated with the thermal degradation of the polyether side chains [10-15].

The fourth mass elimination, detected in the 400–500°C range, is due to the decomposition of the fluorocarbon chains of the polymer matrix [9-15]. At T>600°C, the mass residue is related to the amount of the inorganic moiety present in bulk membranes and shows a trend which is in accordance with the nanofiller concentrations reported in Table 3.1. TG measurements revealed that a partial thermal stabilization of Nafion host polymer occurs. Indeed, the presence of the inorganic nanofiller in the {Nafion/$[(ZrO_2)\cdot(Ta_2O_5)_{0.119}]\Psi_{ZrO_2}$} materials reduces the thermal stability of the polyether chains and increases the thermal stability of the sulfonic acid groups and PTFE-like backbone chains.

For the investigated membranes the MDSC scan, reported in Figure 3.5, reveals the presence of four overlapping endothermic peaks: I, II, III, and IV. The temperatures of peak positions, reported in Table 3.2, depend on the nanofiller concentration and were determined by fitting the MDSC experimental curves with a Gaussian function (Figure 3.5) [9,11,14].

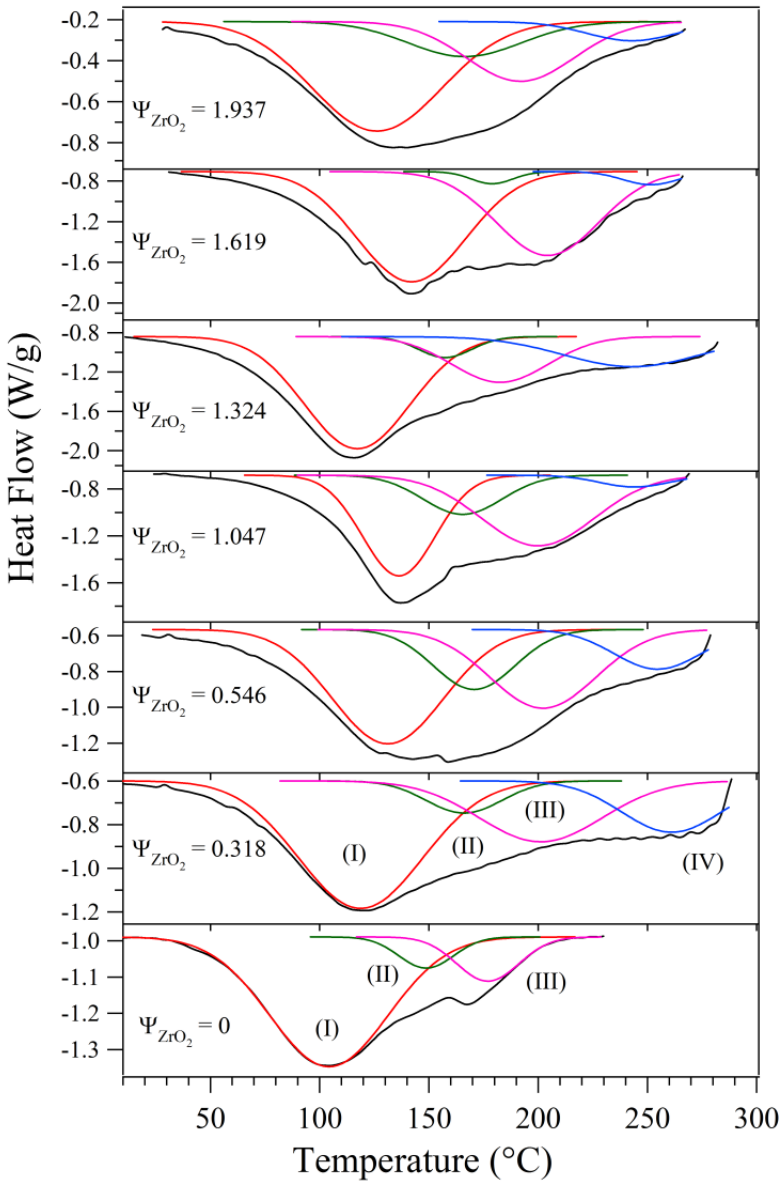

Figure 3.5 MDSC measurements of {Nafion/[$(ZrO_2)\cdot(Ta_2O_5)_{0.119}$]$\Psi_{ZrO_2}$} membranes with $0 \leq \Psi_{ZrO_2} \leq 1.937$. Decomposition by Gaussian functions of the MDSC curves in the 40 – 280°C temperature region is shown. I, II, III and IV indicate the detected endothermic peaks.

Peak I is assigned to the melting of small and imperfect fluorocarbon nanocrystalline domains of Nafion [14,23]. A similar peak is also present for other PEMs, like sulfonated polyether ether ketone [24,25] and arises from the coexistence of a polymer matrix, with a partial order of crystallinity, and polar domains. The presence of the hydrogen-bonding interactions between the acid groups in the polar domains reduces the size of the ordered microdomains of the polymer matrix, generating the nanocrystalline domains. Furthermore, as revealed by TG and W.U

analysis, the membranes in DRC condition contain 3-4 wt% of water. The melting temperature of Peak I, reported in Table 3.2 are higher for the hybrid membranes with respect to pristine Nafion, which indicates that hydrophobic nanodomains are stabilized owing to the density of dipolar nanofiller–Nafion cross-links present in hydrophilic regions. Thus, I is a thermal event diagnostic of the type and intensity of side groups-environment interactions within the Nafion host polymer. Peak II (140–220°C) is assigned to the endothermic degradation of acid $–SO_3H$ groups in accordance with the thermogravimetric measurements discussed above [14,23].

Table 3.2 MDSC transition temperatures of $\{Nafion/[(ZrO_2)\cdot(Ta_2O_5)_{0.119}]\Psi_{ZrO_2}\}$ membranes with $0 \leq \Psi_{ZrO_2} \leq 1.937$.

Ψ_{ZrO_2}	Peak I (°C)	Peak II (°C)	Peak III (°C)	Peak IV (°C)
0	104	149	177	-
0.318	119	166	201	261
0.546	131	171	202	255
1.047	136	165	200	244
1.324	117	157	182	243
1.619	142	179	204	251
1.937	126	166	192	243

Table 3.2 indicates that the $RSO_3H\cdots[(ZrO_2)(Ta_2O_5)_{0.119}]$ interactions thermally stabilize the $–SO_3H$ groups, in accordance with the increased decomposition temperature of the acid groups in the hybrid membranes as revealed by TG analysis. Peaks III and IV, detected in the 170–205°C and 240–270°C temperature ranges, respectively (see Figure 3.5 and Table 3.2), are attributed to two different types of melting transitions of the hydrophobic fluorocarbon microcrystalline regions of Nafion [14]. III corresponds to the PTFE domains with a larger size, while IV is assigned to the domains stabilized by the interactions of the Nafion nanoparticles with the environment. The melting temperatures in Table 3.2 indicates that the $RSO_3H\cdots[(ZrO_2)(Ta_2O_5)_{0.119}]$ interactions stabilize the PTFE domains of Nafion, thus increasing their melting temperatures. Taken together, this thermal analysis suggests that in the

{Nafion/[$(ZrO_2)\cdot(Ta_2O_5)_{0.119}$]$\Psi_{ZrO_2}$} nanocomposite membranes, the nafion-nanofiller interactions give rise to a slight increase in the thermal stability of the $-SO_3H$ groups, and an increase in the thermal stability of endothermic events occurring in the hydrophobic domains of Nafion.

3.3.2 Dynamic mechanical analysis

The influence of the Nafion-nanofiller interactions on the mechanical properties of membranes was investigated by analyzing the temperature spectra of the storage modulus (E'), loss modulus (E'') and tanδ = E''/E'. The logarithmic values of the storage modulus E' and the loss modulus E'' as function of temperature are shown in part a) and b) of Figure 3.6, respectively, for the {Nafion/[$(ZrO_2)\cdot(Ta_2O_5)_{0.119}$]$\Psi_{ZrO_2}$} nanocomposite membranes.

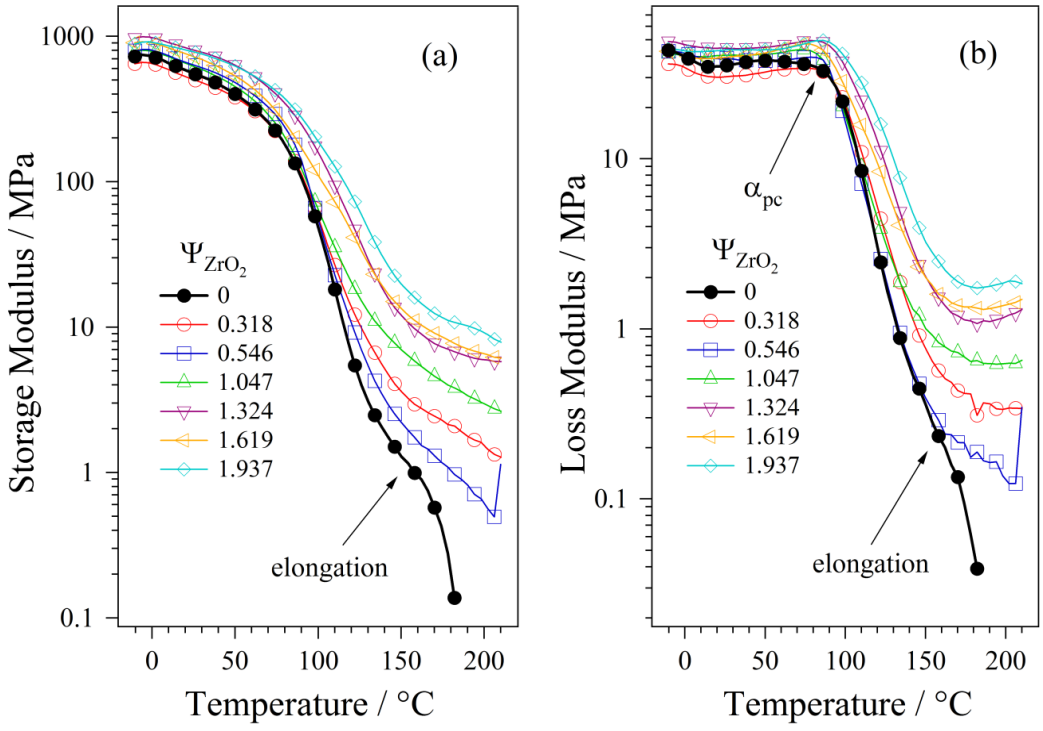

Figure 3.6 Temperature spectra of the storage (a) and loss (b) modulus of {Nafion/[$(ZrO_2)\cdot(Ta_2O_5)_{0.119}$]$\Psi_{ZrO_2}$} membranes with $0 \leq \Psi_{ZrO_2} \leq 1.937$.

A mechanical relaxation event, attributed to the α_{pc}-relaxation of the Nafion host polymer, was detected at ca. 120°C in the profiles of the loss modulus. This mechanical relaxation mode is

assigned to the long-range motion of both the backbone and the side chains which results when a weakening of electrostatic interactions within the ionic aggregates occurs [10-16]. The "pc" subscript of α_{pc} indicates that this mechanical mode, unlike the α-mechanical relaxation associated with the segmental motion of the perfluorinated backbone (see below), involves the dynamics of both the hydrophobic and hydrophilic domains of nN117.

The temperature dependence of E' and E'' reveals that at T>160°C an irreversible elongation of the film was observed for Nafion reference. A remarkable result is that for Ψ_{ZrO_2}>0.318 this event is not observed. Indeed, the {Nafion/[$(ZrO_2)\cdot(Ta_2O_5)_{0.119}$]$\Psi_{ZrO_2}$} membranes with Ψ_{ZrO_2} > 0.318 exhibit a storage modulus which remains higher than 1MPa up to 200°C (Figure 3.6). The values of E' for pristine Nafion and the hybrid membranes, at 26 and 50°C, are shown as function of Ψ_{ZrO_2} in Figure 3.7. E' increases with Ψ_{ZrO_2}. This behavior is opposite of that observed for water uptake of {Nafion/[$(ZrO_2)\cdot(Ta_2O_5)_{0.119}$]$\Psi_{ZrO_2}$} membranes.

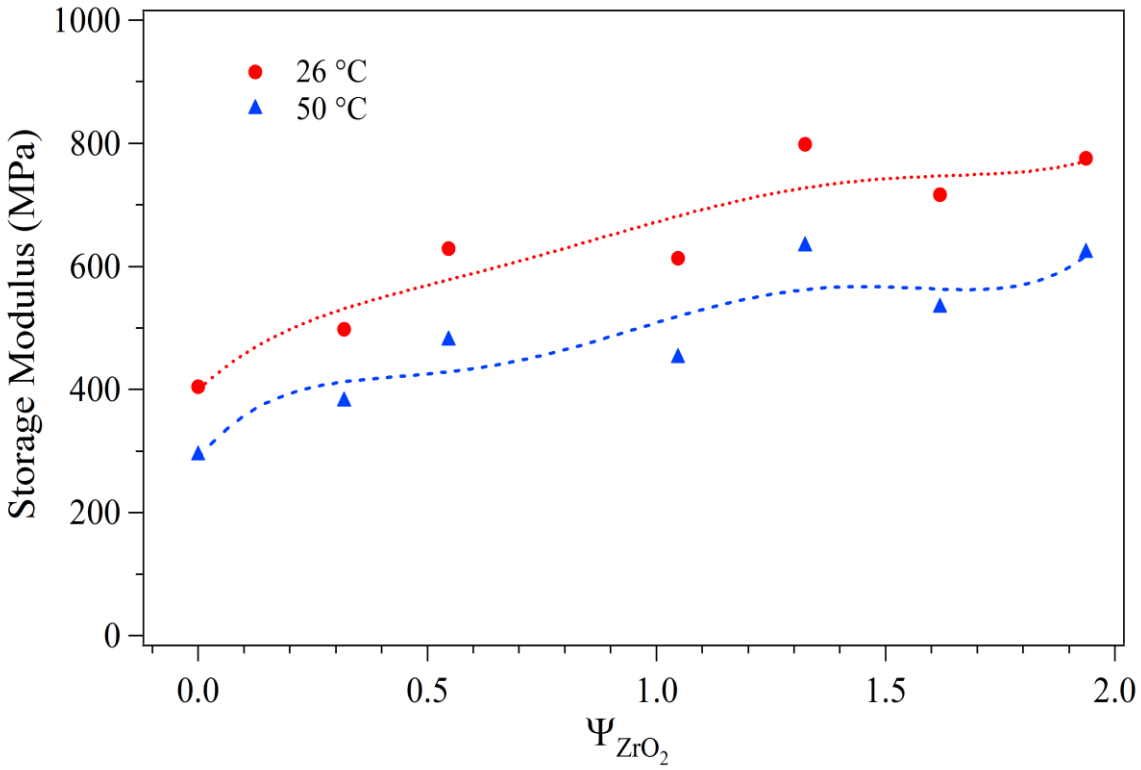

Figure 2.7 Storage modulus as function of Ψ_{ZrO_2} of the nanocomposite membranes measured at 26°C (circle) and 50°C (triangle). The dashed lines are a guide for the eye.

The density *n* of the interchain cross-links in a polymer network is proportional to the elastic modulus E' [9,14,26].

$$E' = gnkT + E_{en} \quad (3.3)$$

k is the Boltzmann's constant, *T* the thermodynamic temperature, E_{en} the contribution of polymer entanglements to *E*', and *g* is a constant value ranging from 0.6 to 1. The increase of E' with Ψ_{ZrO_2} allows the conclusion that the density of R– $RSO_3H\cdots[(ZrO_2)(Ta_2O_5)_{0.119}]$ crosslinks (*n*) is responsible for: (a) a significant improvement of the mechanical properties of $\{Nafion/[(ZrO_2)\cdot(Ta_2O_5)_{0.119}]\Psi_{ZrO_2}\}$ membranes with increasing Ψ_{ZrO_2}, with respect to pristine Nafion; (b) the modulation of the water uptake of hybrid materials. As expected, increasing *n* decreases the W.U., thus demonstrating that when R–SO_3H side groups are involved in the $RSO_3H\cdots[(ZrO_2)(Ta_2O_5)_{0.119}]$ interactions, a lower amount of water is required to solvate the acid side groups of Nafion. The tanδ = E''/E' profiles reported in part a) of Figure 3.8, allowed the presence of four mechanical relaxation events, α_{pc}, α_{pc}', α and α' to be revealed [14]. According to the E'' profiles of Figure 3.6, the α_{pc}, and α_{pc}' modes, measured at T>100°C, are assigned to the long-range motions of both the backbone and the side chains facilitated by the weakening of electrostatic interactions within the ionic aggregates [14,23]. In particular the α_{pc}' and α_{pc} relaxations correspond to hydrophobic PTFE-like domains stabilized and not stabilized by the Nafion-nanofiller interactions, respectively [14].

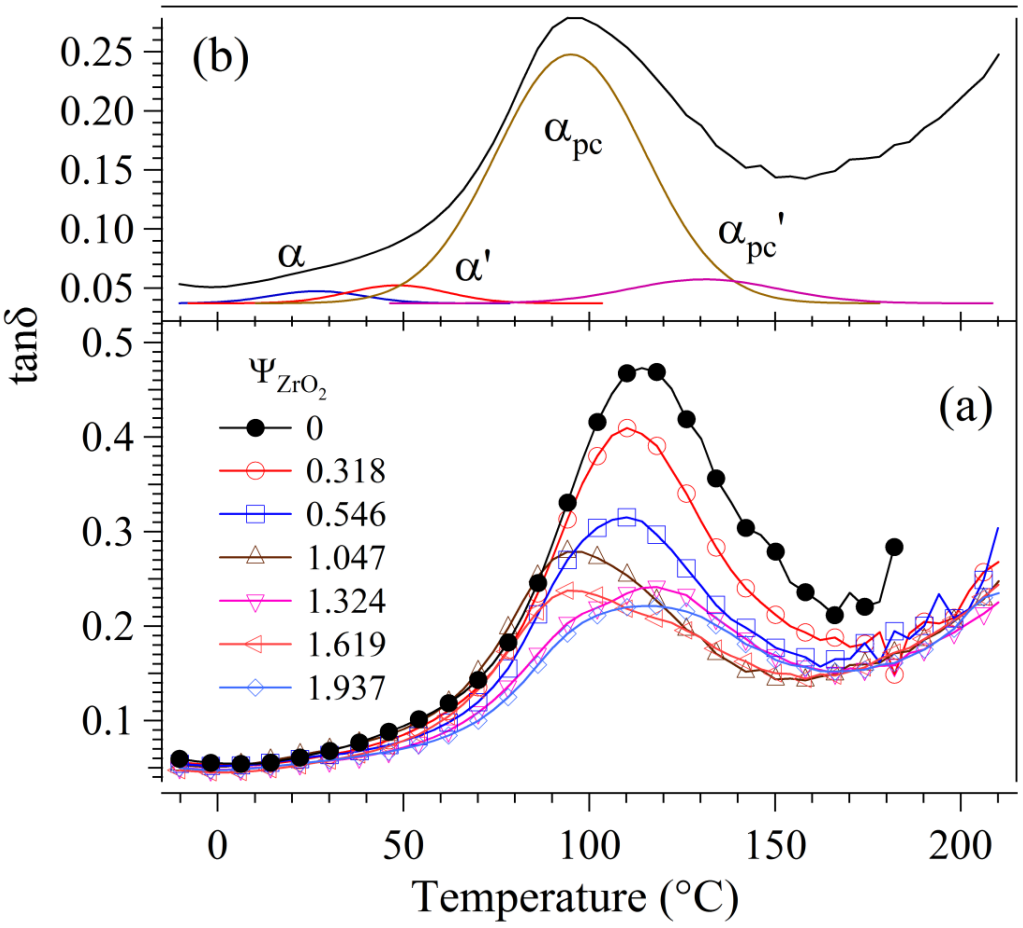

Figure 3.8 (a) tanδ vs. temperature of {Nafion/[$(ZrO_2)\cdot(Ta_2O_5)_{0.119}$]$\Psi_{ZrO_2}$} membranes with $0 \leq \Psi_{ZrO_2} \leq 1.937$. (b) Typical fit of α_{pc} , α_{pc}', α and α' relaxation modes.

α and α' relaxation events, measured around 40 and 65°C, are attributed to the $13_6 \rightarrow 15_7$ and to the order-disorder conformational transitions occurring in hydrophobic PTFE-like domains of Nafion, respectively [13,14]. The latter assignments are based on the works of Zerbi et al. [27,28] and E.S. Clark [29], who reported the presence of two transitions at 19°C and 30°C for PTFE, associated with a conformational transition between the 13_6 to 15_7 helical geometry of the PTFE chains and a transition due to the partial destruction of the crystalline order along the chains, respectively [27,28]. According to the chemical structure of Nafion, which consists of PTFE-like backbone chains, the α and α' mechanical transitions are associated with the dynamics of the PTFE chains. The dynamic mechanical transition temperatures $T_{\alpha_{pc}}$, $T_{\alpha_{pc}'}$, T_{α} and $T_{\alpha'}$ of the α_{pc}, α_{pc}', α and α' relaxations, respectively, are reported below in Figure 3.9 as

function of Ψ_{ZrO_2}. The mechanical transition temperatures were determined by fitting the tanδ profiles with Gaussian functions [14], as shown in part b of Figure 3.8.

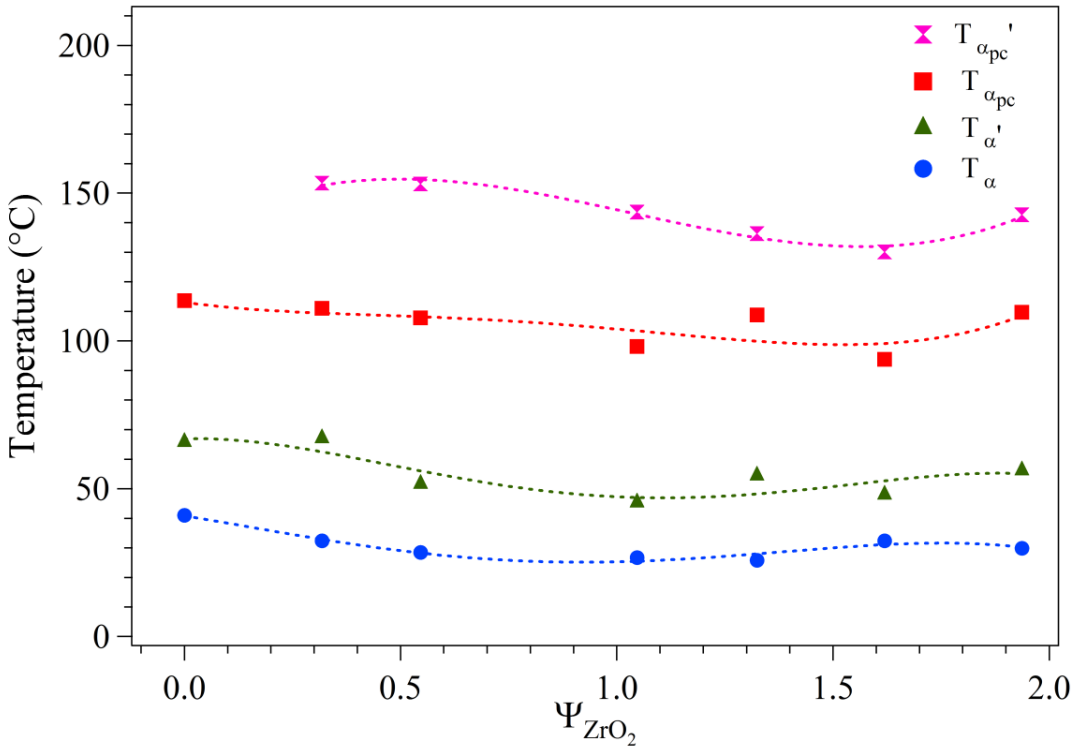

Figure 3.9 Dependence of the dynamic mechanical transition temperatures on Ψ_{ZrO_2} of {Nafion/[$(ZrO_2)\cdot(Ta_2O_5)_{0.119}$]$\Psi_{ZrO_2}$} membranes. The dashed lines are guide for the eye.

It should be observed that, with respect to the dependence of water uptake on Ψ_{ZrO_2}, $T_{\alpha_{pc}'}$ presents an opposite behavior. Indeed, a lower water uptake implies an increases of the density of the $RSO_3H\cdots[(ZrO_2)(Ta_2O_5)_{0.119}]$ interactions, thus increasing the $T_{\alpha pc'}$ transition temperature of the PTFE-like domains stabilized by the Nafion–nanofiller interactions. In hybrid membranes the T_α values are lower with respect to pristine Nafion, which demonstrate that the strength of $RSO_3H\cdots[(ZrO_2)(Ta_2O_5)_{0.119}]$ interactions in polar ionic aggregate domains trigger the fluorocarbon chains present in hydrophobic domains to assume the most stable 15_7 helical conformation geometry. $T_{\alpha'}$, as function of the nanofiller concentration, exhibits a behavior similar to the water uptake, which suggests that the order-disorder transition depends on the

$RSO_3H\cdots[(ZrO_2)(Ta_2O_5)_{0.119}]$ interactions. This will be confirmed by FT-IR ATR spectroscopy measurements.

Taken together, DMA results are in accordance with the DSC analyses and reveal that the values and the strength of $RSO_3H\cdots[(ZrO_2)(Ta_2O_5)_{0.119}]$ interactions that occur inside polar hydrophilic domains of membranes, improve the mechanical stability of both hydrophobic and hydrophilic domains of the materials. Thus, it can be hypothesized that the $[(ZrO_2)(Ta_2O_5)_{0.119}]$ "core–shell" oxocluster acts: (a) to promote a conformational transitions toward the most stable helical geometries of fluorocarbon chains of Nafion; and (b) to restrict the main chain mobility events in both the side chain aggregates and in hydrophobic fluorocarbon domains of Nafion component.

3.3.3 Vibrational spectroscopy studies

Informations on the secondary structure of Nafion in the $\{Nafion/[(ZrO_2)\cdot(Ta_2O_5)_{0.119}]\Psi_{ZrO_2}\}$ membranes and on the interactions taking place between the components of nanocomposite membranes were obtained by performing a FT-IR ATR characterization of materials. The structural and compositional asymmetry of the materials was investigated by collecting the FT-IR ATR spectra of both side A, the top of the film, and side B, the bottom side of the membrane after the casting procedure, which are shown in parts a and b of Figure 3.10, respectively. A preliminary comparison of the profiles revealed that (a) the same peaks are detected on A and B sides of membranes; and (b) significant differences in the band shape and intensity are observed when some of vibrational modes from the A and B sides are compared.

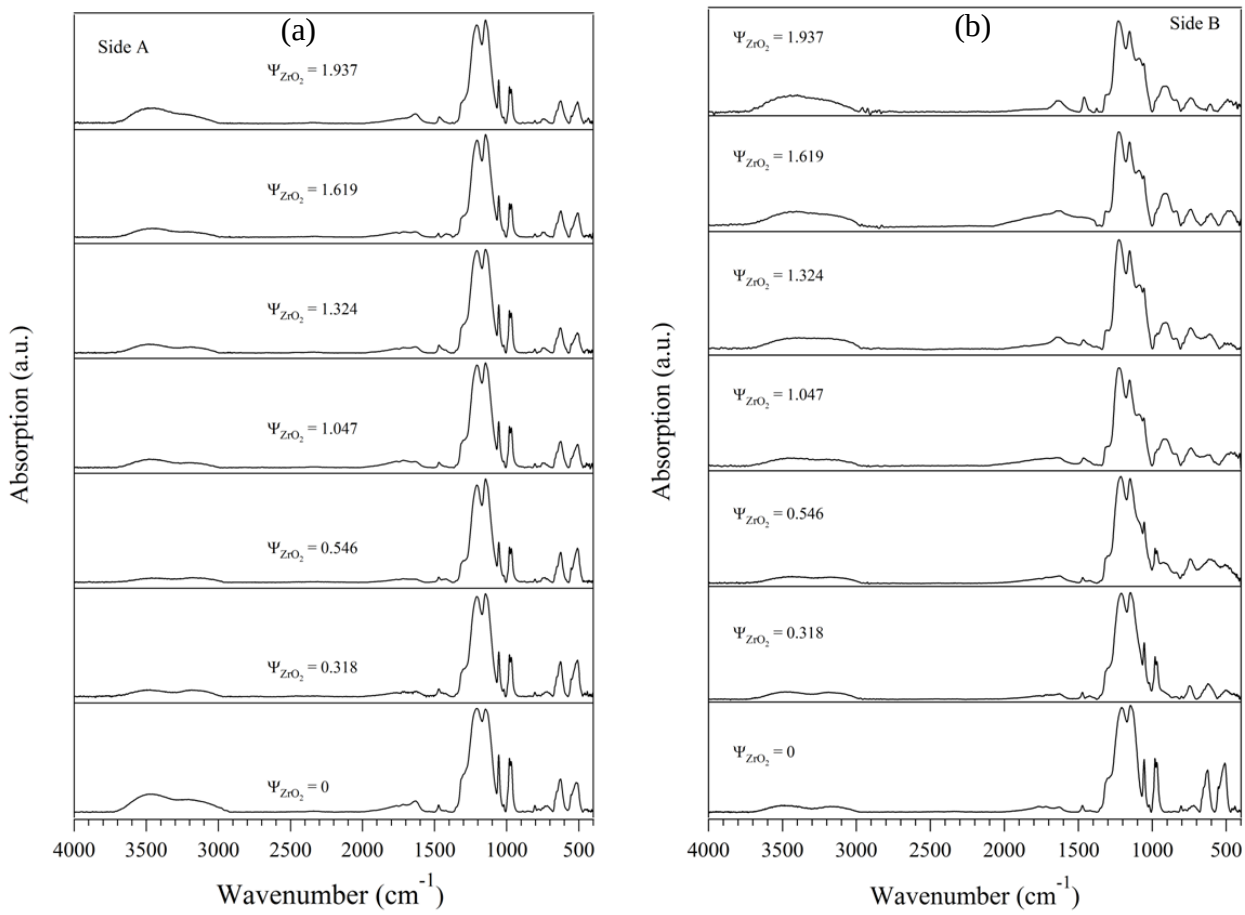

Figure 3.10 Vibrational spectra of side A (a) and B (b) of {Nafion/[$(ZrO_2)\cdot(Ta_2O_5)_{0.119}$]$\Psi_{ZrO_2}$} membranes with $0 \leq \Psi_{ZrO_2} \leq 1.937$. A is the top surface of the membrane after solvent casting process, while B is the bottom side.

For all the investigated membranes, the FT-IR ATR spectra show different spectral features, which are directly correlated with the vibrational modes of [12-14,27-30]: (a) the backbone fluorocarbon chain conformations in hydrophobic domains of Nafion (CF region 1000–1300 cm^{-1}); (b) the Nafion side chains (940–1000cm^{-1}); (c) the $–SO_3H$ acid groups (1530 and 1230cm^{-1}) and (d) the types of water domains embedded in bulk nanocomposites. The correlative attribution of the main vibrational peaks detected in FT-IR ATR spectra of {Nafion/[$(ZrO_2)\cdot(Ta_2O_5)_{0.119}$]$\Psi_{ZrO_2}$} nanocomposite membranes is summarized in Table 3.3.

Table 3.3 FT-IR ATR assignments [a] of {Nafion/[$(ZrO_2)\cdot(Ta_2O_5)_{0.119}$]$\Psi_{ZrO_2}$} membranes with $0 \leq \Psi_{ZrO_2} \leq 1.937$.

Ψ_{ZrO_2}								
0	**0.318**	**0.546**	**1.047**	**1.321**	**1.619**	**1.937**	**Band assigments[b]**	**Ref.**
509(m)	509(m)	507(w)	509(w)	509(m)	509(w)	509(vw)	15_7+10_3: ν_s[CF_2(17)]; δ[FCF(68)]	[13,14,30]
627(m)	627(m)	627(w)	627(w)	627(w)	627(w)	625(vw)	10_3 : ν[CF]; δ[CCF]; ν[CC]	[13,14,30]
969(m)	969(m)	969(m)	969(m)	969(m)	969(m)	969(m)	15_7: ν_s[C-O-C]	[13,14]
983(w)	983(w)	983(w)	983(w)	983(w)	983(w)	983(w)	15_7:ν_{as}[C-O-C]	[13,14]
993(w)	993(w)	993(w)	993(w)	993(w)	993(w)	993(w)	15_7 +10_3 : ν[CF_2]; δ[CCF]; ν[CO];	[13,14]
1055(w)	1055(w)	1055(w)	1055(w)	1055(w)	1055(w)	1055(w)	10_3 : ν_s[CF_2]; δ[FCF]	[14]
1132(m)	1132(m)	1132(w)	1132(m)	1132(w)	1132(w)	1132(w)	10_3 : ν_s[CF_2]; δ[FCF]	[13,14,30]
1148(m)	1148(m)	1148(s)	1148(m)	1148(s)	1148(s)	1148(m)	15_7 : ν_s[CF_2(82)]; δ[FCF(21)]	[13,14,30]
1196(vw)	1196(vw)	1196(vw)	1196(vw)	1196(vw)	1196(vw)	1196(vw)	10_3 : ν_s[CF_2]	[13,14,30]
1212(s)	1212(s)	1212(s)	1212(s)	1212(s)	1212(s)	1212(s)	15_7 : ν_{as}[CF_2(112)]	[13,14,30]
1241(w)	1241(w)	1241(w)	1241(w)	1241(w)	1241(w)	1241(w)	15_7 : ν_{as}[CF_2(112)]	[13,14,30]
1245(vw)	1245(vw)	1245(vw)	1245(vw)	1245(vw)	1245(vw)	1245(vw)	10_3 : ν_{as}[CF_2]	[13,14,30]
1310(w)	1314(w)	1316(w)	1316(w)	1316(w)	1316(w)	1316(w)	10_3 : ν [CC]	[13,14,30]
1422(w)	1422(w)	1420(w)	1422(w)	1420(w)	1422(w)	1421(w)	10_3 : A_s	[14,30]
1445(w)	1443(w)	1441(w)	1445(w)	1444(w)	1443(w)	1445(w)	10_3 : A_a	[14,30]
1472(w)	1472(w)	1471w)	1472(w)	1473(w)	1470(w)	1472(w)	15_7 : Acid group interacting with the environment	[14,30]

[a)] Relative intensities of observed bands are reported in parentheses: vs, very strong; s, strong; m, medium; w, weak; vw, very weak; b, broad; sh, shoulder;
[b)] ν, stretching; δ, bending; ω, wagging; t, twisting; r, rocking; as, antisymmetric mode; s, symmetric mode.

An in depth study of the CF region, between 1000 and 1300cm^{-1} revealed that at room temperature the hydrophobic PTFE domains of the Nafion component consist of a blend of fluorocarbon chains with 15_7 and 10_3 helical conformation geometries [10,13,14,27-30].

In 1973, Zerbi et al. in two fundamental works reported a theoretical and experimental investigations on the vibrational normal modes of poly-tetrafluoroethylene (PTFE) [27,28]. The authors, while studying the molecular dynamics of a single infinite and perfect PTFE chain, predicted the existence of four different conformation geometries: 2_1 (D_{2h}), 15_7 ($D_{14\pi/15}$), 10_3 ($D_{6\pi/10}$) and 4_1 (D_4). By comparing the theoretical predictions with the experimental data on the infrared spectrum of PTFE, Zerbi revealed: a) that the ordered domains present within PTFE mainly consist of a mixture of helical chains with 2_1 and 15_7 geometries; b) the existence of segmental chains with 10_3 and 4_1 conformations [27,28].

Di Noto analyzed the molecular dynamics on Nafion with DFT calculations, starting from the four different chains conformation proposed by Zerbi. Results indicate that, in Nafion only the 15_7 and 10_3 helical conformations remain due to the introduction of the side chains [30]. Thus, the vibrational modes in the CF region, between 1000 and 1300cm^{-1} for both pristine Nafion and the hybrid membranes are associated with the fluorocarbon chains with 15_7 and 10_3 helical conformation geometries. The semiquantitative analysis of the fraction ρ_{10_3} and ρ_{15_7} (with ρ_{15_7} = 1 - ρ_{10_3}) of each type of fluorocarbon chain composing the hydrophobic PTFE domains of Nafion host polymer, was determined as described elsewhere [10,12-14] by using the formula $\rho_{10_3} = A_{as,10_3}(1245)/[\ A_{as,10_3}(1245) + A_{as,15_7}(1212)]$. $A_{as,10_3}(1245)$ and $A_{as,15_7}(1212)$ are the band areas of the CF_2 antisymmetric stretching vibrations of 10_3 and 15_7 fluorocarbon helical chains at 1245 and 1212cm^{-1}, respectively. The band areas were determined by decomposing the CF spectral region with Gaussian functions [10,12-14], as shown in Figure 3.11. For all the investigated materials, the following conditions were imposed while performing this decomposition: a) the band assignments of the Nafion membrane obtained by DFT calculations as initial boundary conditions [30]; b) the intensity ratio of the peak at 1212 cm^{-1} with respect to the peak at 1241cm^{-1} was 1.39 [12-14]. This ratio is expected to be roughly conserved, since the

bands at 1212 and 1241cm^{-1} correspond to the A_2 antisymmetric stretching CF_2 of the helix 15_7 of Nafion [30]. This latter choice was fundamental in order to derive a semi-quantitative evaluation of the small band around 1245cm^{-1}.

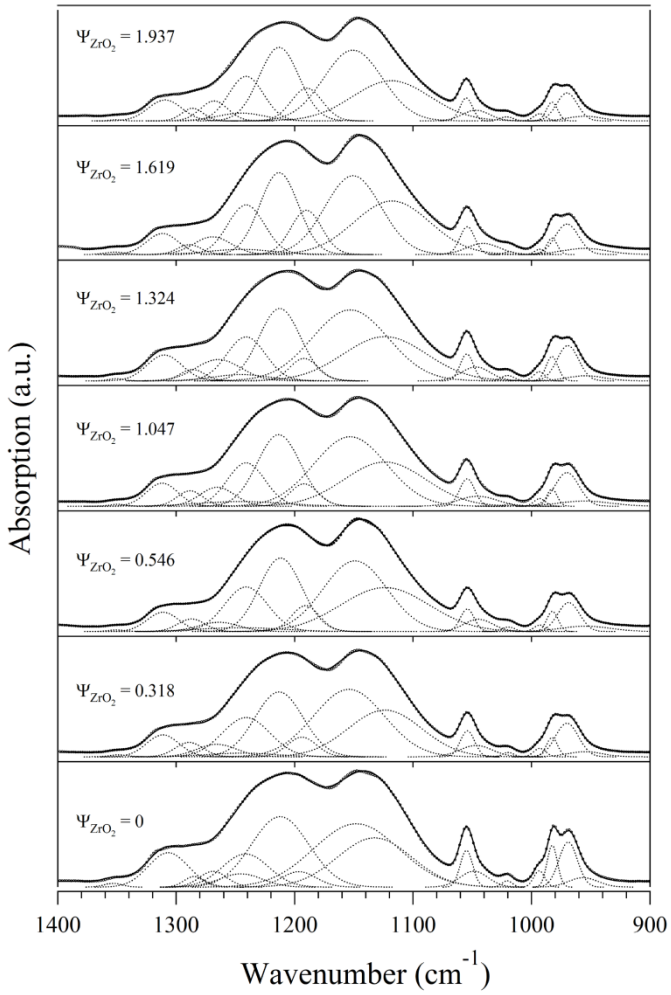

Figure 3.11 Decomposition by Gaussian functions of the FT-IR ATR spectra of side A of {Nafion/[$(ZrO_2)\cdot(Ta_2O_5)_{0.119}$]$\Psi_{ZrO_2}$} membranes with $0 \leq \Psi_{ZrO_2} \leq 1.937$. A is the upside surface of the membrane after solvent casting process.

The dependence of ρ_{10_3} on Ψ_{ZrO_2} is reported in Figure 3.12. The results revealed that: (a) the fraction of the 10_3 helical conformation ranges from 6% to 14%; (b) the fluorocarbon chains with 15_7 geometry prevail; (c) ρ_{10_3} vs. Ψ_{ZrO_2} shows a profile similar to that of water uptake. This information suggests that the W.U. parameter is correlated to the 10_3-15_7 conformational transition of fluorocarbon chains composing hydrophobic PTFE-like domains of Nafion. In particular, a lower water uptake results in a lower fraction of fluorocarbon chains with the 10_3

helical conformation. Zerbi suggested that the amorphous portion of the PTFE materials consists of the 10_3 helical fluorocarbon chain phase [12,27,28]. According to this interpretation, for the investigated materials the presence of strong $RSO_3H\cdots[(ZrO_2)(Ta_2O_5)_{0.119}]$ interactions, which reduces the membranes' swelling and water uptake, increases ρ_{15_7} and thus reduces the temperature of the order-disorder transition Tα'(due to a reduced number of hydrophobic fluorocarbon domains involved in the transition), in accordance with the DMA results discussed in section 3.4.2.

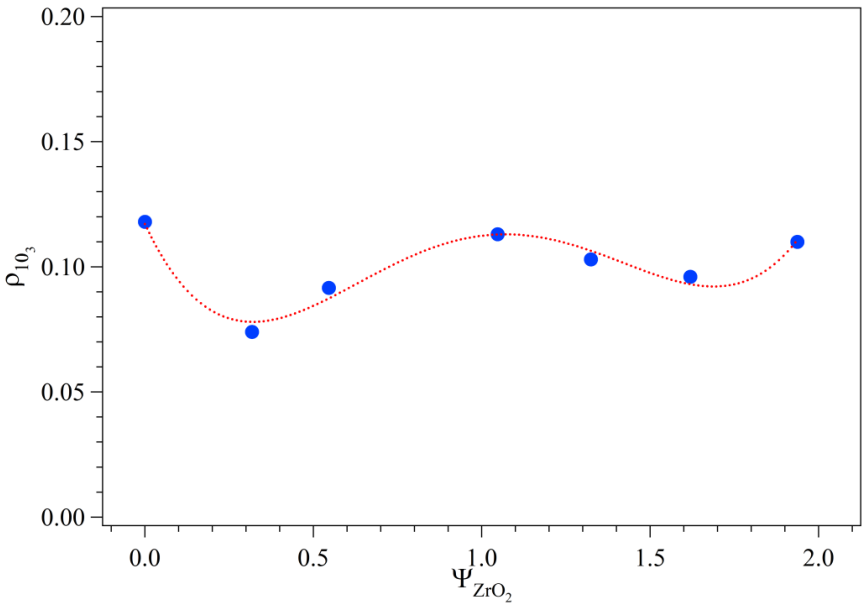

Figure 3.12 Dependence of ρ_{10_3} on Ψ_{ZrO_2} for $\{Nafion/[(ZrO_2)\cdot(Ta_2O_5)_{0.119}]\Psi_{ZrO_2}\}$ membranes with $0\leq\Psi_{ZrO_2}\leq1.937$. ρ_{10_3} is the fraction of fluorocarbon chains with 10_3 helical conformation. The dashed line is a guide for the eye.

The detailed analysis of the compositional asymmetry of the $\{Nafion/[(ZrO_2)\cdot(Ta_2O_5)_{0.119}]\Psi_{ZrO_2}\}$ was performed by analyzing the FT-IR ATR difference spectra determined by using the spectra of Figure 3.10 that were normalized to the peak at 980 cm^{-1}[14]. Figure 3.13 reports the difference spectra obtained by subtracting the FT-IR ATR spectrum of side A from that of side B. The results indicated that the intensity of peaks in the CF region, which correspond to the 15_7 fluorocarbon chains (see Table 3.3), is higher on side B with respect to side A. In addition, as Ψ_{ZrO_2} rises, the concentration of 15_7 fluorocarbon chains on side B increases. The same results

are reported in literature for a similar system, consisting of a Nafion membrane doped with different amounts of $[(ZrO_2)(SiO_2)_{0.67}]$ "core shell" nanofiller [13]. The study of the difference spectra allowed the conclusion that the morphologies of Nafion matrix, consisting of PTFE-nanodomains, are significantly influenced by the conformational transition $10_3 \rightarrow 15_7$ of fluorocarbon backbone chains. This conformational transition is stimulated by the density and strength of $RSO_3H\cdots[(ZrO_2)(Ta_2O_5)_{0.119}]$ crosslinks. The materials with a higher density of Nafion-filler crosslinks are characterized by a lower fraction of chains with 10_3 helical conformation in PTFE domains. These phenomena cause the supramolecular networked material which is composing the B side of membranes after the solvent casting process.

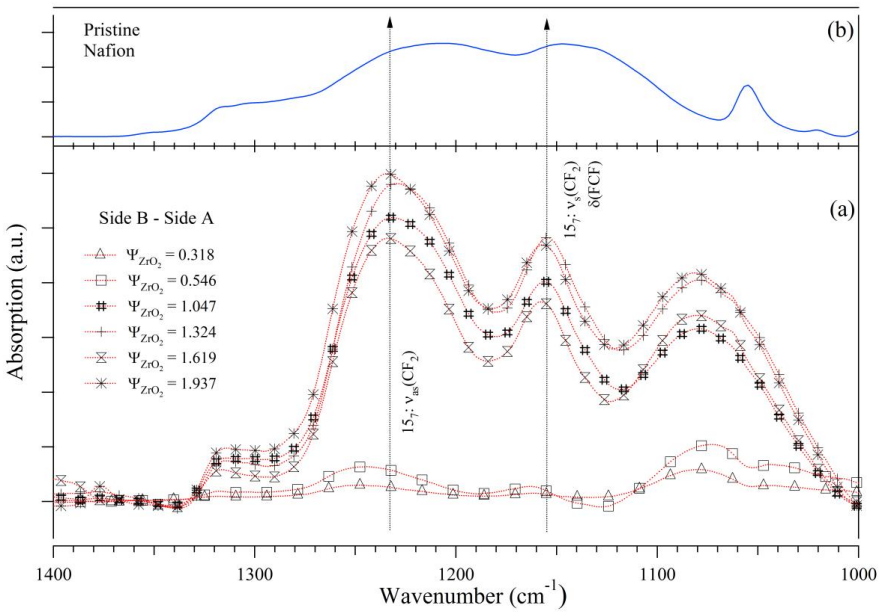

Figure 3.13 (a) Difference spectra of for $\{Nafion/[(ZrO_2)\cdot(Ta_2O_5)_{0.119}]\Psi_{ZrO_2}\}$ membranes with $0.318 \leq \Psi_{ZrO_2} \leq 1.937$. Each spectrum is the result of the subtraction of the FT-IR ATR spectrum of side A from that of side B shown in Figure 3.10. (b) FT-IR ATR spectrum of reference Nafion.

Further information on the type of interactions occurring between Nafion side groups and $[(ZrO_2)(Ta_2O_5)_{0.119}]$ oxoclusters was obtained by comparing the acid spectral region (for the Nafion-rich Side A) of the nanocomposite membranes reported in part a of Figure 3.14 with that of dry, $\lambda = 3$ and Na^+-neutralized Nafion, shown in part b of Figure 3.14. The nanofiller does not neutralize the $R–SO_3H$ side groups of 15_7 fluorocarbon backbone chains. The peak at $1470cm^{-1}$,

which corresponds to the $-SO_3H$ vibrational mode of 15_7 fluorocarbon backbone chains (Table 3.3), is present in $\{Nafion/[(ZrO_2)\cdot(Ta_2O_5)_{0.119}]\Psi_{ZrO_2}\}$ and dry Nafion while it is absent in $\lambda = 3$ (where the proton is dissociated due to the presence of 3 water molecules solvating the sulfonic acid groups) and Na^+-neutralized Nafion. Furthermore, the peak between 1400 and 1450cm^{-1}, attributed to the $-SO_3H$ vibrational modes of 10_3 fluorocarbon chains (Table 3.3), decreases in intensity as Ψ_{ZrO_2} is raised, thus confirming that the concentration of 10_3 chains in PTFE-like domains of Nafion decreases as the nanofiller concentration rises. In summary, the analysis of the acid spectral region permitted to affirm that Nafion-nanofiller interactions occur owing to strong dipolar interactions of the type $RSO_3H\cdots[(ZrO_2)(Ta_2O_5)_{0.119}]$.

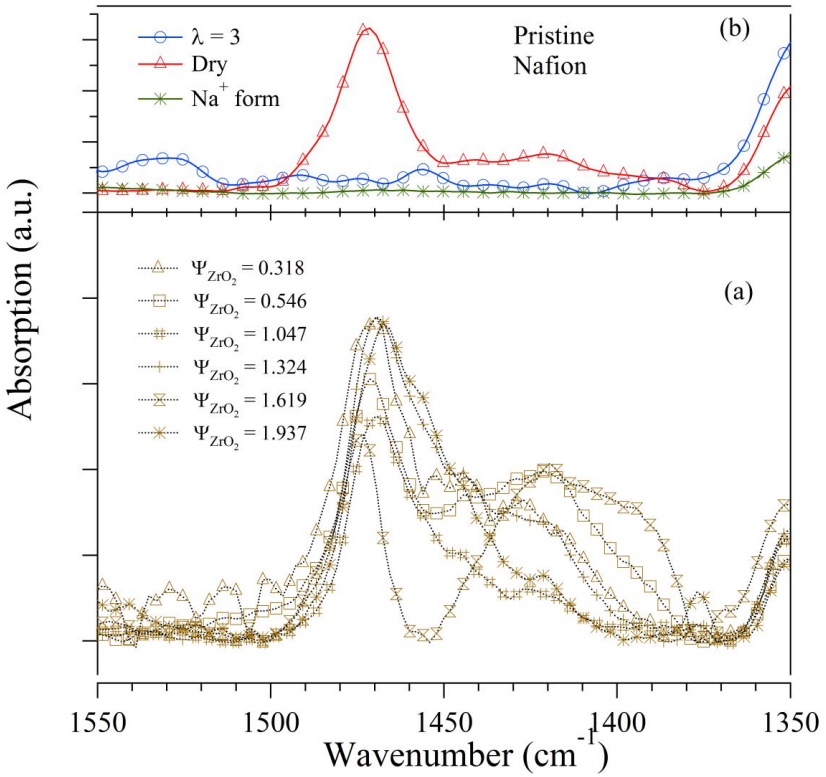

Figure 3.14 FT-IR ATR absorption spectra from 1350 to 1550cm^{-1} of: a) side A of $\{Nafion/[(ZrO_2)\cdot(Ta_2O_5)_{0.119}]\Psi_{ZrO_2}\}$ membranes with $0.318 \leq \Psi_{ZrO_2} \leq 1.937$; b) dry, $\lambda = 3$ and Na^+-neutralized Nafion.

The water bending vibrations in the region 1590–1770 cm^{-1} are diagnostic for the study of the various water domains present in the $\{Nafion/[(ZrO_2)\cdot(Ta_2O_5)_{0.119}]\Psi_{ZrO_2}\}$ membranes [10,12,13,14]. Semiquantitative analyses, carried out by decomposing the water bending region

with Gaussian functions as shown in part (a) of Figure 3.15, distinguished six overlapped peaks named as I, I', II, II', III and IV [13,14]. I, peaking at 1769cm^{-1}, is associated with the bending of water molecules solvating hydronium ions directly interacting with the R–SO_3^- anion groups ($\delta([H_3O^+\cdots SO_3^-]\cdot(H_2O)_n)$). I', measured at 1780cm^{-1}, is associated with the $\delta(([(ZrO_2)\cdot(Ta_2O_5)_{0.119}]\cdots H_3O^+\cdots SO_3^-)\cdot(H_2O)_n)$ bending vibration, corresponding to water molecules solvating the $([(ZrO_2)\cdot(Ta_2O_5)_{0.119}]\cdots H_3O^+\cdots SO_3^-)$ cross-links. II, detected at 1680cm^{-1}, is attributed to modes of water molecules hydrating hydronium ions ($[H_3O^+\cdots(H_2O)_n]$). II', peaking at 1719cm^{-1}, is assigned to the $\delta([ZrO_2)\cdot(Ta_2O_5)_{0.119}H]^+\cdots SO_3^-)\cdot(H_2O)_n)$ bending mode of water molecules solvating the $([(ZrO_2)\cdot(Ta_2O_5)_{0.119}H]^+\cdots SO_3^-)$ cation–anion interacting bridges. III, revealed at 1632cm^{-1}, is attributed to bulk water $[(H_2O)_n]$, not associated with H_3O^+. Peak IV, measured at 1559cm^{-1}, is attributed to $\delta([(ZrO_2)\cdot(Ta_2O_5)_{0.119}]\cdots(H_2O)_n)$, the bending vibrational modes of water molecules forming the primary solvation shell of the metal oxoclusters.

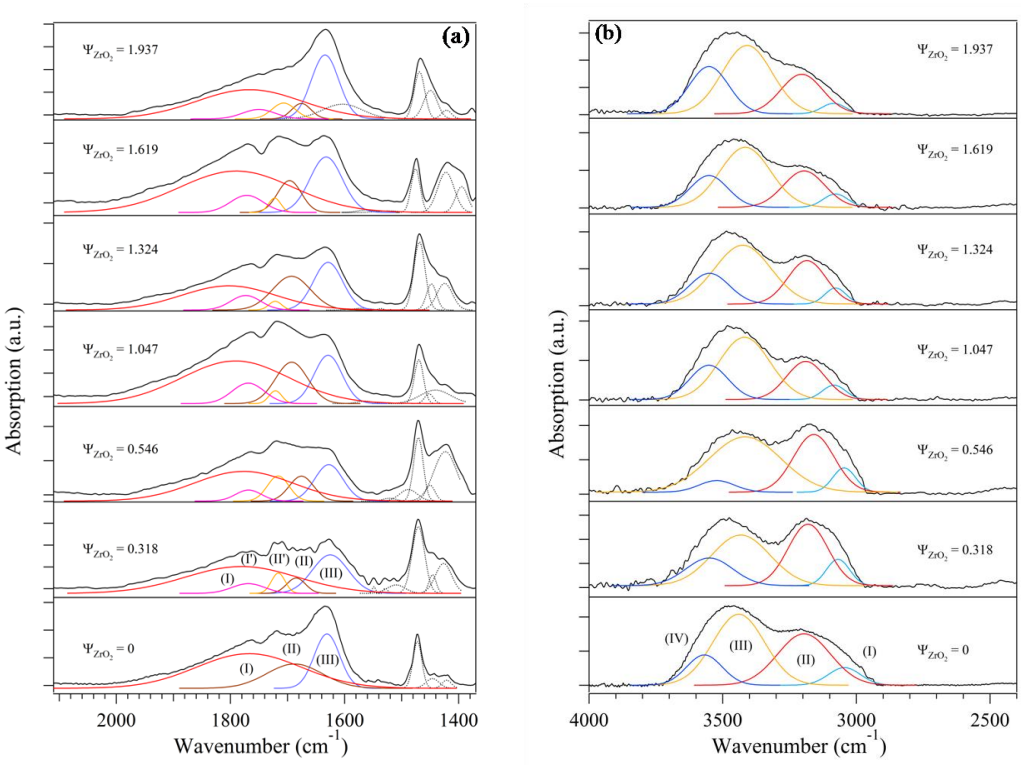

Figure 3.15 Decomposition with Gaussian function of the FT-IR ATR spectral range from 1400 to 2100 cm^{-1} (a) and from 2500 to 4000 cm^{-1} of side A of $\{Nafion/[(ZrO_2)\cdot(Ta_2O_5)_{0.119}]\Psi_{ZrO_2}\}$ membranes with $0\leq\Psi_{ZrO_2}\leq1.937$.

From the area of the fitting peaks reported in part a of Figure 3.15 is possible to calculate the fraction f_i, with i = I, I', II, II'and III, of each type of structurally different H_2O domains by the expression [12-14]:

$$f_i = \frac{A_i}{\sum_{i=1}^{n} A_i} \tag{3.4}$$

where A_i is the band area of peak ith and n is the number of bands considered. Part a of Figure 3.16 reports the dependence of f_i on Ψ_{ZrO_2}. Results indicate that: (a) water is involved almost totally in the solvation of the $[H_3O^+\cdots SO_3^-]\cdot(H_2O)_n$) bridges (I) and as bulk water $[(H_2O)_n]$ (III); (b) the fraction of water solvating the hydronium ion clusters $[H_3O^+\cdots(H_2O)_n]$ (II) and the $[H_3O^+\cdots SO_3^-]\cdot(H_2O)_n$) bridges (I) vs. Ψ_{ZrO_2} exhibits behavior similar to that of ρ and WU; (c) the fraction of the bulk water $[(H_2O)_n]$ (III) is lower for hybrid membranes (20 - 30%) with respect to pristine Nafion (50%) in accordance with W.U. measurements.

Further informations on the structure of water domains embedded in bulk nanocomposite membranes were obtained by carrying out semi-quantitative investigations by decomposition with Gaussian functions on the water stretching region from 4000 to 2400cm^{-1} shown in part b) of Figure 3.15. In the water stretching region, three peaks, I, II and III, diagnostic of water hydrogen bonding networks are revealed. III, peaking at 3448cm^{-1}, is ascribed to the symmetric stretching mode of water molecules not involved in hydrogen bonding structures (isolated bulk water). The corresponding antisymmetric stretching vibration (Peak IV) is found at 3564cm^{-1}. Peak II, detected at 3155cm^{-1}, is assigned to domains of water molecules forming hydrogen bonding network structures in bulk membranes. I, measured at 3070cm^{-1}, is attributed to the antisymmetric OH stretching vibrations of H_3O^+. Part b) of Figure 3.16 shows the dependence of the fraction h_i on Ψ_{ZrO_2}, which is determined with Equation 3.4 (with n = 3), by considering the area of the fitting peaks reported in part b of Figure 3.15. h_i provides a semiquantitative measure of the different distribution of water molecules in hydrogen bonding network domains [13,14].

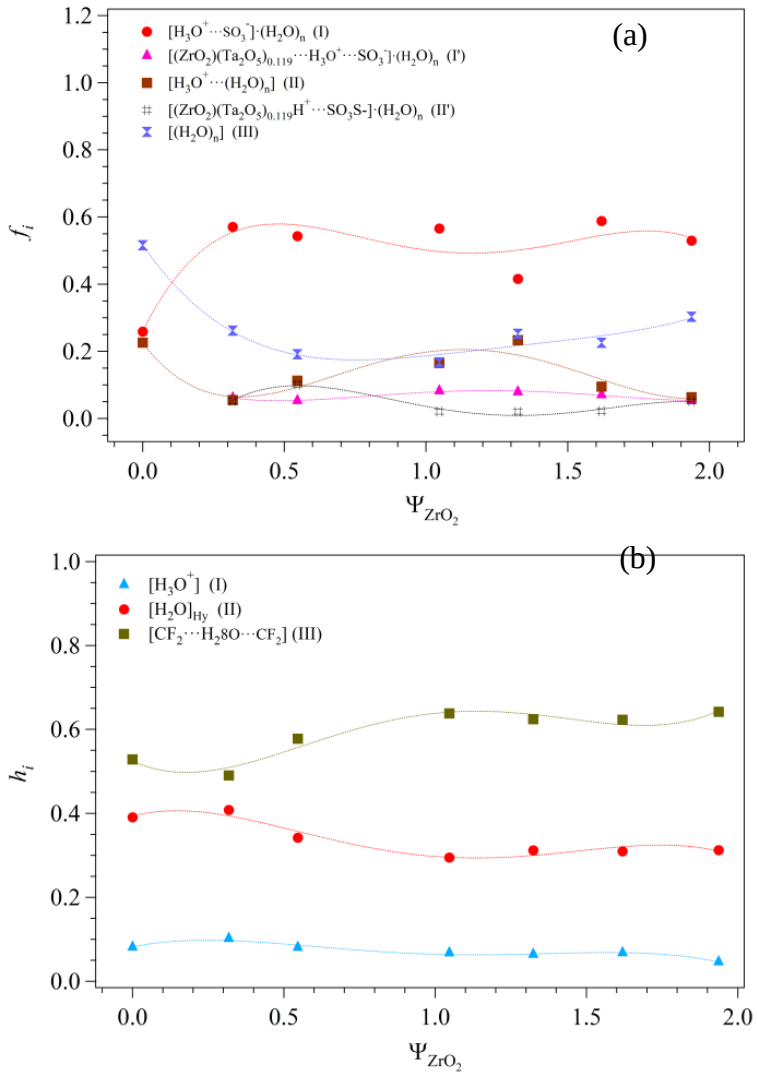

Figure 3.16 f_i (a) and h_i (b) vs. Ψ_{ZrO_2} for {Nafion/$[(ZrO_2)\cdot(Ta_2O_5)_{0.119}]\Psi_{ZrO_2}$} membranes with $0\leq\Psi_{ZrO_2}\leq1.937$. The lines are a guide for the eye.

The results indicate that: a) the fraction of water interacting with hydronium ions in bulk materials is lower than 10%; (b) the amount of water forming domains by hydrogen bonding structures $[H_2O]_{hy}$, is 40% and decreases with increasing Ψ_{ZrO_2}; and (c) the "matrix isolated" water molecules, i.e., not involved in hydrogen bonding interactions, increases with the nanofiller concentration. The latter result suggest that a higher concentration of water in the hybrid membranes is present at the interfaces between hydrophobic and hydrophilic domains due to the presence of the inorganic nanofiller. Taken together, the vibrational investigations revealed that the density and the strength of $RSO_3H\cdots([(ZrO_2)\cdot(Ta_2O_3)_{0.119}]$ interactions are

crucial parameters in organizing the water molecules of the detected water domains into hydrophilic polar ionic aggregate regions of hybrid membranes and in modulating the ratio of 10_3 - 15_7 fluorocarbon chains in hydrophobic PTFE-like domains.

3.3.4 Broadband electric spectroscopy

The electrical properties of the {Nafion/[$(ZrO_2)\cdot(Ta_2O_5)_{0.119}$]$\Psi_{ZrO_2}$} membranes in RZP (see section 3.2.4) condition are investigated by broadband electric spectroscopy (BES). As an example, the profiles of the imaginary component of the permittivity ε" and the real part of the conductivity σ' for pristine Nafion and the hybrid membrane with Ψ_{ZrO_2} = 1.619 are reported as function of temperature and frequency in parts a and b of Figure 3.17, respectively.

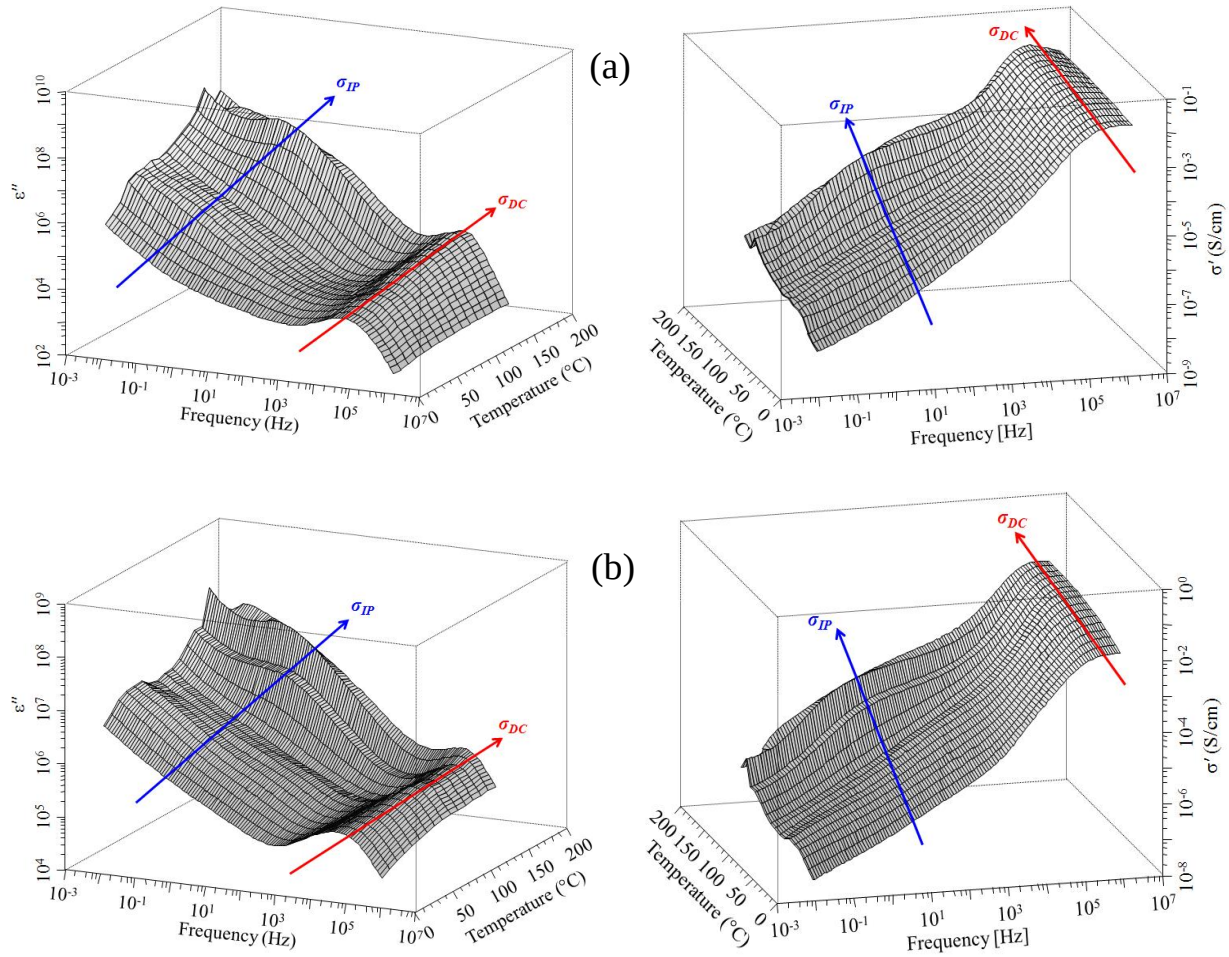

Figure 3.27 3D plot of the imaginary component of the permittivity and the real component of the conductivity as a function of temperature and frequency for {Nafion/[$(ZrO_2)\cdot(Ta_2O_5)_{0.119}$]$\Psi_{ZrO_2}$} membranes with Ψ_{ZrO_2}:a) 0; b) 1.619.

The spectra of ε" show: 1) a peak at frequencies greater than 10^5 Hz, which shifts to higher frequencies with increasing temperature and corresponds to a rapid increase of σ' followed by a plateau; and 2) a second event at frequencies less than 10^3 Hz that increases with increasing temperature and is identified by increasing values of ε" with decreasing frequency, which corresponds to the appearance of a second plateau in σ' profiles.

The σ' values taken from the high-frequency plateau correspond to the "bulk" conductivity, σ_{DC}, of the materials [13,14,31]. The presence of the intense peak in ε" and the corresponding decrease of σ' is due to the electrode polarization (EP) phenomenon which is caused by the measuring electrodes that block the charge carriers at the interface between the electrodes and the polymeric membranes [16,24,32-34]. The electrical event present at medium frequencies is due to interfacial polarization (IP) associated with the conductivity σ_{IP}. The presence of secondary conductivity contributions at high temperatures are typically observed in ionic conductors consisting of two or more phases having different dielectric constants [24,32-34] and results from the accumulation of charge at the interfaces between domains with different permittivities. In the case of Nafion membranes, the conductivity σ_{IP} arises from the coexistence of domains with low permittivity (ε'~2.2) [35] consisting of the PTFE-like matrix and polar conducting domains with higher permittivity containing acid groups and water molecules [36]. The appearance of electric relaxations associated with the bulk (σ_{DC}) and interfacial (σ_{IP}) conductivities are easily observable in the tanδ = ε"/ε' profiles shown in parts a, b of Figure 3.18 for the reference Nafion and the hybrid membrane with Ψ_{ZrO_2} = 1.619, respectively.

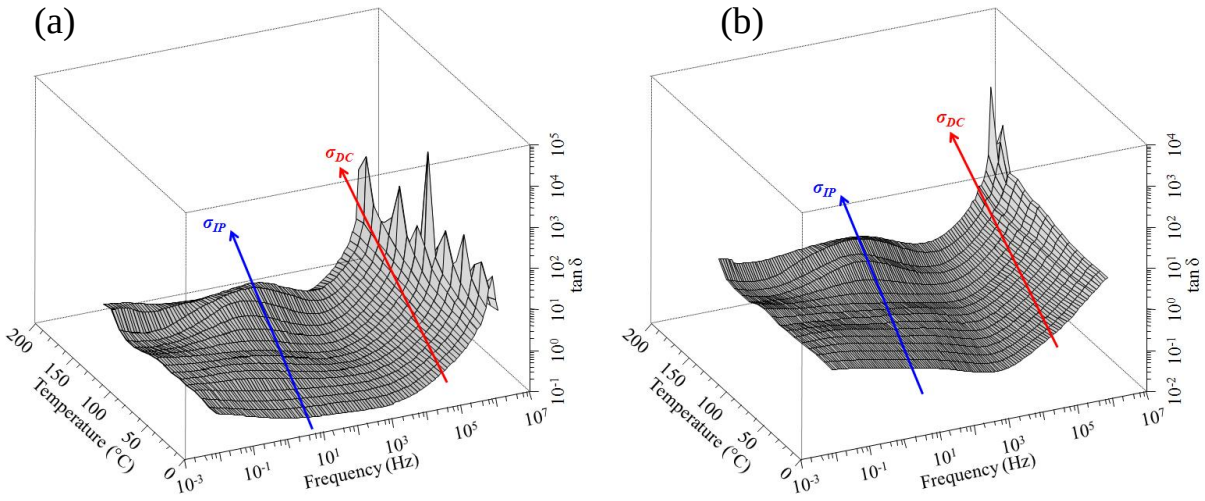

Figure 3.18 3D plot of the imaginary component of tanδ as a function of temperature and frequency for {Nafion/[$(ZrO_2)\cdot(Ta_2O_5)_{0.119}$]$\Psi_{ZrO_2}$} membranes with Ψ_{ZrO_2}:a) 0; b) 1.619.

The tanδ profiles clearly show the presence of two peaks that shift to higher frequencies with increasing temperature. As in the σ' and ε" spectra, the first peak at frequencies lower than 10^3 Hz is due to the interfacial conductivity σ_{IP}, while the second more intense event is associated to the "bulk" conductivity σ_{DC}.

As mentioned above, at high frequency (>10^4Hz), the electrical response of the materials arises from the long-range proton conductivity (σ_{DC}) and the presence of the blocking measuring electrodes. Profiles of σ'(ω) exhibiting the combination of electrode polarization and bulk conductivity are typically present in polymer electrolytes [16,24,32-34] and can be simulated with equivalent circuits, i.e. combining resistors and capacitors together in series and parallel [26,31]. The "bulk" conductivity and the electrode polarization can be modelled with a resistor and two capacitors in series as shown in Figure 3.19.

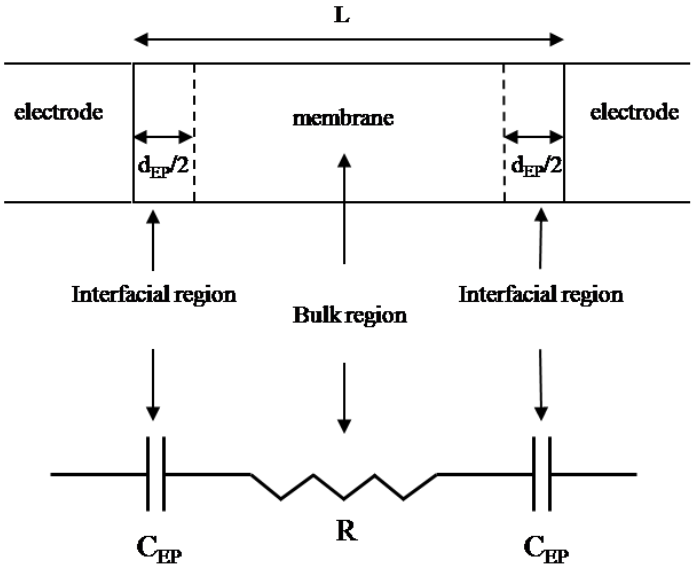

Figure 3.19 Equivalent circuit used to model the electrode polarization phenomenon in $\{Nafion/[(ZrO_2)\cdot(Ta_2O_5)_{0.119}]\Psi_{ZrO_2}\}$ membranes with $0\leq\Psi_{ZrO_2}\leq1.937$. C_{EP} and R indicate a capacity and a resistor used to simulate the electrical properties of the membrane.

The resistor R simulates the "bulk" conductivity, while the capacitors C_{EP} simulate the electrode polarization phenomenon. Given that $d_{EP}/2$ is the thickness of each interfacial region near the electrodes and L is the total sample length, for $L >> d_{EP}$ it is possible to obtain the total complex permittivity ε* and the relaxation time τ_{EP} associated with the EP with the following expressions [24].

$$\varepsilon^* = \frac{\sigma_{DC}}{i\omega\varepsilon_0}\frac{(i\omega\tau_{EP})}{[1+(i\omega\tau_{EP})]} + \varepsilon_\infty \tag{3.5}$$

$$\tau_{EP} = \frac{\varepsilon_0\varepsilon_{EP}}{\sigma_{DC}}\left(\frac{L}{d_{EP}}\right) \tag{3.6}$$

In Equations 3.5 and 3.6, σ_{DC} is the bulk conductivity and ε_{EP} is the complex permittivity of the interfacial region. ε_0 and $\varepsilon\infty$ are the vacuum permittivity and the electronic contribution to the permittivity of the material, respectively. Typically d_{EP} is on the order of nanometers [37] while the thickness L for these materials is about 200μm, so the condition $L >> d_{EP}$ is satisfied. Equation 3.6 indicates that τ_{EP} increases with the sample thickness L and decreases with increasing charge carrier concentration and mobility. For $\{Nafion/[(ZrO_2)\cdot(Ta_2O_5)_{0.119}]\Psi_{ZrO_2}\}$

membranes, Equation 3.6 can be used to analyze the relaxation time $\tau_{EP}=1/f_{EP}$ and the conductivity σ_{DC}, which is read directly from the high frequency peak position in the ε" spectra (part a of Figure 3.17) and the conductivity plateau in the σ' spectra (part b of Figure 3.17), respectively. Table 3.4 reports the values of $\tau_{EP,}$ and σ_{DC} at different temperatures for hybrid membranes with Ψ_{ZrO_2}= 0.546, 1.047 and 1.937.

Table 3.4 Values of σ_{DC} and $\tau_{EP,}$ at different temperatures for hybrid membranes with Ψ_{ZrO_2}= 0.546, 1.047 and 1.937.

Ψ_{ZrO_2}	T = 25°C		T = 45°C		T = 65°C		T = 105°C	
	σ_{DC} (S/cm)	τ_{EP} (s)	σ_{DC} (S/cm)	τ_{EP} (s)	σ_{DC} (S/cm)	τ_{EP} (s)	σ_{DC} (S/cm)	τ_{EP} (s)
0.546	0.024	$2.23\cdot10^{-5}$	0.030	$1.88\cdot10^{-5}$	0.036	$1.69\cdot10^{-5}$	0.045	$1.70\cdot10^{-5}$
1.047	0.034	$9.61\cdot10^{-6}$	0.044	$9.07\cdot10^{-6}$	0.055	$8.62\cdot10^{-6}$	0.075	$8.77\cdot10^{-6}$
1.937	0.025	$1.17\cdot10^{-5}$	0.033	$1.03\cdot10^{-5}$	0.040	$9.84\cdot10^{-6}$	0.058	$8.93\cdot10^{-6}$

According to Equation 3.6, considering that the electrodes' area and the sample's length L are constant and assuming that d_{EP} is almost constant for all the membranes and around 1nm [36], an increase in the σ_{DC} conductivity should lead to a reduction of τ_{EP}. This is confirmed for the investigated samples by considering the values of σ_{DC} and τ_{EP} reported in Table 3.4. In the temperature range between 5 and 85°C, increasing σ_{DC} corresponds to a decrease in τ_{EP} . At temperatures higher than 85°C, both the conductivity and the relaxation time increase. From Equation 3.5 this is possible if there is an increase in the permittivity ε_{EP} of the interfacial region. As will be discussed below and according to the DMA analysis (section 3.4.2), the variation of ε_{EP} is associated with the presence of the α_{pc} relaxation at T>85°C, that involves a weakening of the interactions between the Nafion polar domains that give rise to a change in the proton conduction mechanisms of the membranes.

As previously described, the interfacial conductivity σ_{IP} is the product of charge accumulation at the interfaces between the hydrophobic and hydrophilic domains present inside {Nafion/$[(ZrO_2)\cdot(Ta_2O_5)_{0.119}]\Psi_{ZrO_2}$} membranes. As a result, the conductivity can no longer be

modelled with the simple resistor shown in Figure 3.19 but also must be related to capacitive phenomena owing to structural heterogeneity in the membranes.

To determine the values of the conductivity and the relaxation times associated with the various polarization phenomena, the experimental profiles are analyzed with the Equation 3.7 [16,24,33,34].

$$\varepsilon^* = \sum_{k=1}^{2} \frac{\sigma_k}{i\omega\varepsilon_0} \frac{(i\omega\tau_k)^{\gamma_k}}{[1+(i\omega\tau_k)^{\gamma_k}]} + \varepsilon_\infty \qquad (3.7)$$

This equation accounts for the electrode (k=1) and interfacial (k=2) polarization phenomena. σ_k and τ_k are the conductivity and relaxation time associated with the k^{th} polarization, while γ_k is a shape parameter that describes the broadness and asymmetry of the k^{th} peak. An exhaustive discussion of Equation 3.7 is present in ref. [38] and is partially reported in Appendix B. In ref. [38], the authors demonstrate that, starting from a different equivalent circuit and using some approximations applicable for the PEMs even the interfacial conductivity can be described with an equation similar to Equation 3.6, but with a different expression for the relaxation time. Combining the expressions for the EP and IP phenomena is possible to obtain Equation 3.7. Equation 3.7 is used to simultaneously fit the spectra of ε', ε", σ' and σ" based on the relationship between the complex conductivity and the complex permittivity, $\sigma^*=i\omega\varepsilon_0\varepsilon^*$. An example of the fitting results, in which the experimental curves of ε'' and σ' are decomposed into the EP (related to σ_{DC} and f_{EP}) and IP (associated to σ_{IP} and f_{IP}) components, is reported in Figure 3.20 for pristine Nafion (part a) and the hybrid membrane with Ψ_{ZrO_2} = 0.318 (part b).

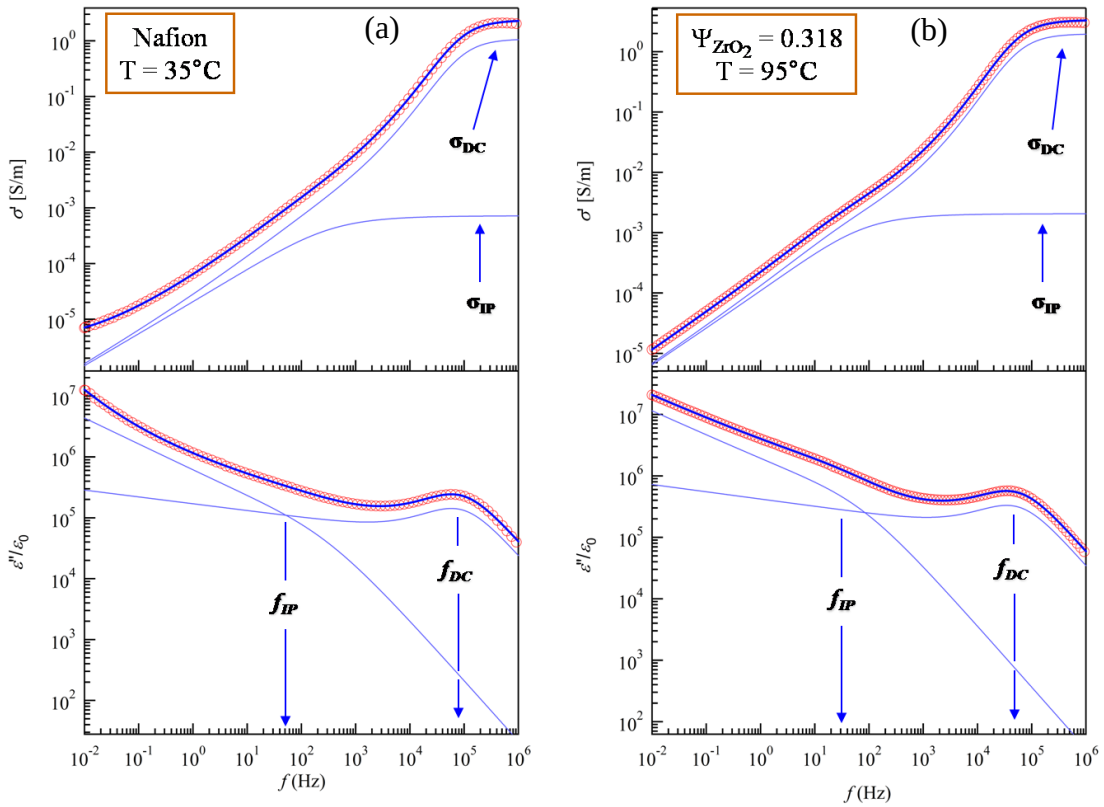

Figure 3.20 Fitting of ε'' and σ' for (a) pristine Nafion and (b) {Nafion/[$(ZrO_2)\cdot(Ta_2O_5)_{0.119}$]$\Psi_{ZrO_2}$} membrane with Ψ_{ZrO_2}= 0.318. σ_{DC} , f_{EP} and σ_{IP} , f_{IP} are the conductivity and the relaxation frequencies related to the electrode and interfacial polarizations, respectively.

The logarithmic values of the conductivities σ_{DC} and σ_{IP}, obtained by fitting the experimental data with Equation 3.7, are reported as a function of reciprocal temperature for the {Nafion/[$(ZrO_2)\cdot(Ta_2O_5)_{0.119}$]$\Psi_{ZrO_2}$} membranes with $0 \leq \Psi_{ZrO_2} \leq 1.937$ in Figure 3.21. The temperature dependence of $\log\sigma_{DC}$ and $\log\sigma_{IP}$ can be divided into two different temperature regions, I (T < 75°C) and II (T > 75°C). Except for the membrane with Ψ_{ZrO_2} = 0.318, the values of the bulk conductivity σ_{DC} for the hybrid membranes in regions I and II are higher than those of pristine Nafion. In particular, the highest value of conductivity is observed for the nanocomposite membrane with Ψ_{ZrO_2} = 1.324. This latter material exhibits σ_{DC} values of 7.5×10^{-2} and 7.7×10^{-2} Scm^{-1} at 115 and 135°C, respectively. Table 3.5 summarizes the σ_{DC} and σ_{IP} conductivities at 115°C and the Stability Range of Conductivity (SRC) [9,12,14] of {Nafion/[$(ZrO_2)\cdot(Ta_2O_5)_{0.119}$]$\Psi_{ZrO_2}$} membranes. SRC is defined as the temperature range that

fulfils the condition $\partial(\log \sigma_{DC})/\partial(1/T) < 0$ [9,12]. The best materials in terms of σ_{DC} conductivity and SRC parameter, are those having Ψ_{ZrO_2} = 1.047 and 1.324.

Table 3.5 Values of σ_{DC} and σ_{IP} at 115°C and SRC. In the table the activation energies $E_{a,\sigma i}$ associated with the conductivities σ_{DC} and σ_{IP} for the {Nafion/[$(ZrO_2)\cdot(Ta_2O_5)_{0.119}$]$\Psi_{ZrO_2}$} membranes with 0 ≤$\Psi_{ZrO_2}$ ≤ 1.937 are also reported.

				Region I		***Region II***	
Ψ_{ZrO2}	σ_{DC} (Scm^{-1})	σ_{IP} (Scm^{-1})	***SRC (°C)***	$E_{a,\sigma DC}$ ***(kJ/mol)***	$E_{a,\sigma IP}$ ***(kJ/mol)***	$E_{a,\sigma DC}$ ***(kJ/mol)***	$E_{a,\sigma IP}$ ***(kJ/mol)***
0	$3.3\cdot10^{-2}$	$4.3\cdot10^{-4}$	5<T<105	1.6 ± 0.1	2.1± 0.2	0.22 ± 0.02	0.09± 0.02
0.318	$3.6\cdot10^{-2}$	$1.8\cdot10^{-4}$	5<T<135	2.7 ± 0.1	3.9± 0.2	0.92 ± 0.02	1.05 ± 0.1
0.546	$4.6\cdot10^{-2}$	$1.7\cdot10^{-4}$	5<T<135	2.0 ± 0.1	1.0± 0.2	0.51 ± 0.02	0.34 ± 0.04
1.047	$7.0\cdot10^{-2}$	$1.5\cdot10^{-4}$	5<T<155	2.3 ± 0.1	0.4± 0.2	0.33 ± 0.02	0.36 ± 0.04
1.324	$7.5\cdot10^{-2}$	$7.2\cdot10^{-4}$	5<T<145	2.2 ± 0.2	5.1± 0.2	0.21 ± 0.02	1.40 ± 0.05
1.619	$5.7\cdot10^{-2}$	$7.9\cdot10^{-5}$	5<T<145	2.8 ± 0.1	4.3± 0.2	0.50 ± 0.02	0.71 ± 0.04
1.937	$5.6\cdot10^{-2}$	$1.1\cdot10^{-4}$	5<T<155	2.3 ± 0.1	4.1± 0.2	0.36 ± 0.02	0.51 ± 0.04

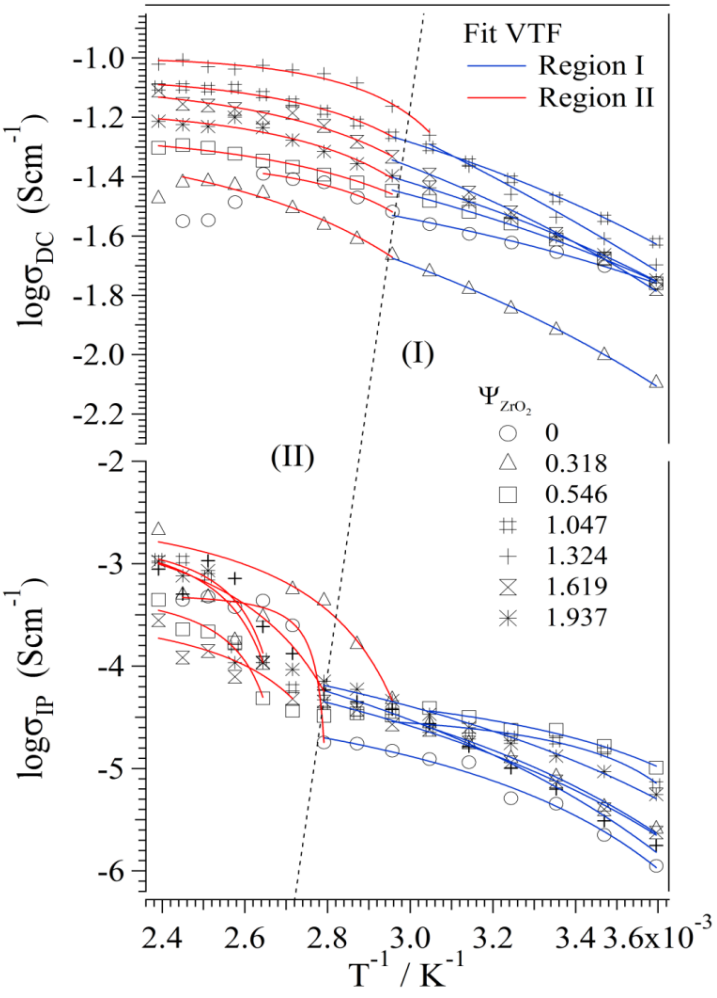

Figure 3.21 Log plot of bulk (σ_{DC}) and interfacial (σ_{IP}) conductivities as a function of T^{-1} for {Nafion/[$(ZrO_2)\cdot(Ta_2O_5)_{0.119}$]$\Psi_{ZrO_2}$} membranes with 0 ≤$\Psi_{ZrO_2}$ ≤ 1.937. I and II indicate different temperature regions where the data are fitted with VTF (solid line)

In regions I and II the dependence of σ_{DC} and σ_{IP} vs. 1/T shows the typical Vogel–Tamman–Fulcher (VTF) behavior [9,13,14,31,33,34], thus indicating that segmental motion of the polymer host is a crucial factor in the modulation of the charge transfer mechanisms.

The interfacial conductivity σ_{IP}, reported as function of the inverse temperature in Figure 3.21, is 2-3 orders of magnitude lower than σ_{DC} and is higher (in region I) for the hybrid membranes with respect to pristine Nafion. This evidence indicates that: a) the $[(ZrO_2)(Ta_2O_5)_{0.119}]$ inorganic nanofiller enhances the protons accumulation at the interfaces between hydrophobic and hydrophilic domains; and b) the protons are delocalized at the Nafion-nanofiller interfaces

The presence of two different temperature regions for conduction is the reason for the decoupling between σ_{DC} and τ_{EP} at T>85°C discussed above (see Table 3.4). According to the DMA analysis, around 80°C all the materials undergo the α_{pc} mechanical transition. Due to the origin of this transition, that implies a weakening of the dipolar interactions and an increase in the motion of both the primary and secondary structure of Nafion, is reasonable to hypothesize that this relaxation alters the structure of the membrane, and thus also the interfacial layer between the membrane and the blocking electrodes, in particular increasing its permittivity ε_{EP}. This interpretation is also in accordance with the DSC results, that showed the presence of a broad endothermic peak around 100°C (with an onset temperature around 70°C) for all the materials mainly due to the melting of the semi-crystalline PTFE-like nanodomains of Nafion. It is also possible to hypothesize that at T>80°C there is an increase in the amorphous fraction of the membranes, that give rise to a more homogeneous distribution of the hydrophilic domains within the hydrophobic polymer matrix. This structural reorganization increases the polar character of the membrane and thus its dielectric permittivity.

In region I and II the pseudo activation energies E_{a,σ_i} associated with the long range and interfacial proton conduction mechanism can be obtained by fitting the values of σ_{DC} and σ_{IP} reported in Figure 3.21 with the VTF equation [31].

$$\sigma_i = AT^{-\frac{1}{2}} e^{-\frac{E_{VTF,\sigma_i}}{R(T-T_0)}} \quad (3.8)$$

A brief description and derivation of the VTF equation is given in Appendix A. The fit curves are shown in Figure 3.21 and the pseudo-activation energies $E_{a,\sigma_{DC}}$ and $E_{a,\sigma_{IP}}$ for regions I and II are given in Table 3.5 and shown as function of the nanofiller concentration Ψ_{ZrO_2} in Figure 3.22.

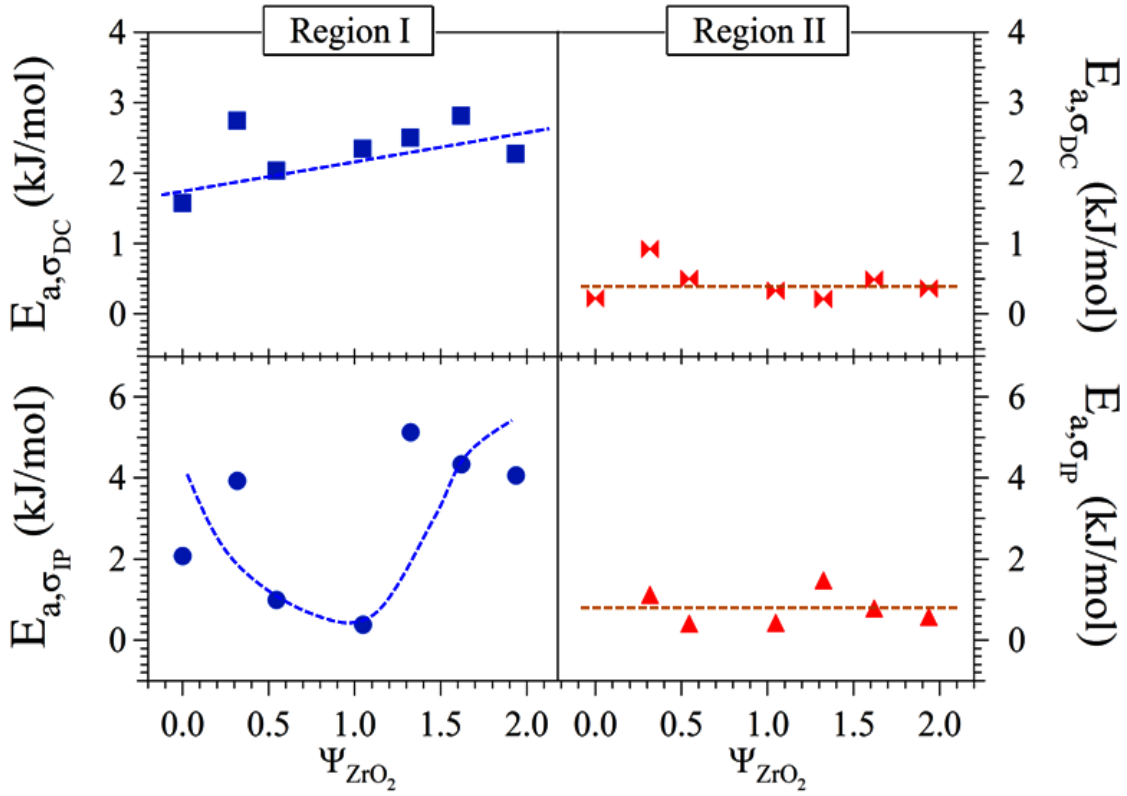

Figure 3.22 Dependence of the activation energies $E_{a,\sigma_{DC}}$ and $E_{a,\sigma_{IP}}$ on Ψ_{ZrO_2} for $\{Nafion/[(ZrO_2)\cdot(Ta_2O_5)_{0.119}]\Psi_{ZrO_2}\}$ membranes with $0 \leq \Psi_{ZrO_2} \leq 1.937$. The dashed lines are a guide for the eye.

The pseudo-activation energies for conduction in region II are lower than those determined in region I. Furthermore, in region I the activation energies $E_{a,\sigma_{DC}}$ for the hybrid membranes are higher than that of pristine Nafion and increase with Ψ_{ZrO_2}. This evidence confirm that in region I the segmental motion of the fluorocarbon backbone chains in the PTFE-like domains of Nafion is strongly influenced and hindered by the density and the strength of $RSO_3H\cdots[(ZrO_2)(Ta_2O_5)_{0.119}]$ cross-links.

In region I, the interfacial conductivity $E_{a,\sigma_{IP}}$ vs Ψ_{ZrO_2} has a minimum at $\Psi_{ZrO_2} \approx 1$, indicating that: a) in the $0 < \Psi_{ZrO_2} < 1.2$ range the density of cross-links facilitate the proton migration at the Nafion-filler interfaces; b) at $\Psi_{ZrO_2} > 1.2$, the filler-filler interactions inhibit the interfacial proton exchange processes.

In region II, $E_{a,\sigma_{DC}}$ and $E_{a,\sigma_{IP}}$ are similar and independent of Ψ_{ZrO_2}. The coupling between the relaxation events of the hydrophilic and the hydrophobic domains (segmental motion) of the Nafion host matrix, due to the α_{pc} transition (see section 3.3.2), is reflected in the coupling between the interfacial and "long-range" proton conduction mechanisms.

It is possible to determine the proton diffusion coefficient D^{H+} and therefore the mean distance of proton hopping <r> associated with the bulk conductivity using the Nernst-Einstein (Equation 3.9) and the Einstein-Smoluchowski (Equation 3.10) equations [24,36,39]:

$$D_{H^+} = \frac{\sigma_{DC} RT}{n_{H^+} F^2} \tag{3.9}$$

$$\langle r \rangle = \sqrt{6 D_{H^+} \tau_{EP}} = \sqrt{\frac{6\, \sigma_{DC} \tau_{EP} RT}{n_{H^+} F^2}} \tag{3.10}$$

where n_{H+} is the charge carrier concentration, R is the universal gas constant, T is the temperature in Kelvin and F is the Faraday constant. The charge carrier concentration n_{H+} is obtained from the values of PEC (see Table 3.1) and the density of Nafion, equal to 1.77 g/cm^3 [40]. <r> values calculated with the Equation 3.10 are shown in Figure 3.23. The values of <r> range from 40 to 100nm, increase with temperature and are higher in the hybrid membranes than pristine Nafion. These factors indicate that the presence of the $[(ZrO_2)(Ta_2O_5)_{0.119}]$ nanofiller facilitates the long-range proton transfer, which occurs via a Grotthus-like mechanism between water molecules and acid groups and is mediated by the dynamics of the polymer host matrix. The relatively high values of <r> are due to the inclusion of the "bulk" conductivity in Equation 3.10. Consequently, <r> is reported as a mean value of the proton migration distance inside polar

hydrophilic domains (intra-cluster migration) and between different ionic clusters (inter-cluster migration). The results seem to be in accordance with the Nafion structural model proposed by Gebel [41] on the basis of SAXS and SANS studies. The authors claim that Nafion consists of ”bundles” of fluorocarbon chains with a diameter of about 4nm, a length greater than 100 nm and surrounded by the electrolyte solution. According to this interpretation, and assuming that the “inter-cluster migration” process is the “rate-determining step” for the conduction, it is reasonable to hypothesize that long-range charge migrations occurs when a proton is exchanged between the various hydrophilic domains of Nafion. The hydrophobic domains of Nafion, which are present between the polar clusters, consist of bundles of fluorocarbon chains which are cross-linked together through R-SO_3H···[(ZrO_2)(Ta_2O_5)]···HSO_3-R bridges or by R-SO_3H···HSO_3R interacting side groups.

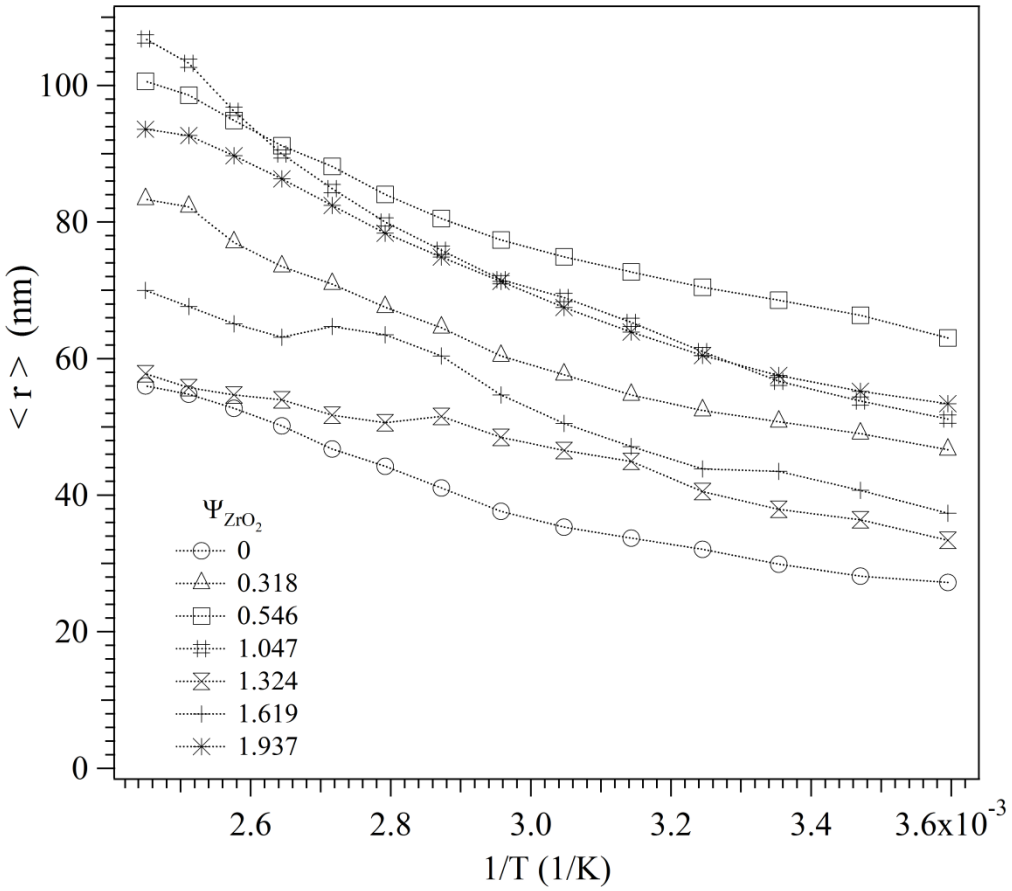

Figure 3.23 Mean free path of proton hopping <r> as a function of reciprocal temperature for {Nafion/[(ZrO_2)·(Ta_2O_5)$_{0.119}$]Ψ_{ZrO_2}} membranes with $0 \leq \Psi_{ZrO_2} \leq 1.937$.

In summary, BES spectroscopy revealed the presence of two polarization phenomena in all the investigated materials associated with the "bulk" (σ_{DC}) and the interfacial (σ_{IP}) conductivities. In hybrid materials, σ_{DC} and σ_{IP} are higher with respect pristine Nafion, which indicates that the inorganic nanofiller enhances the proton conduction mechanism. In order to test the hybrid membranes under operative conditions, the next section reports the fuel cell test conducted using as PEMs pristine Nafion and the hybrid membrane with Ψ_{ZrO_2} = 1.047 that showed the best performance in terms of σ_{DC} and SRC.

3.3.5 Fuel cell test

Parts a and b of Figure 3.24 show the envelopes of the polarization curves determined for the reference Nafion and the hybrid membrane with Ψ_{ZrO_2} = 1.047, respectively, as a function of the water vapour activity in the reagent streams.

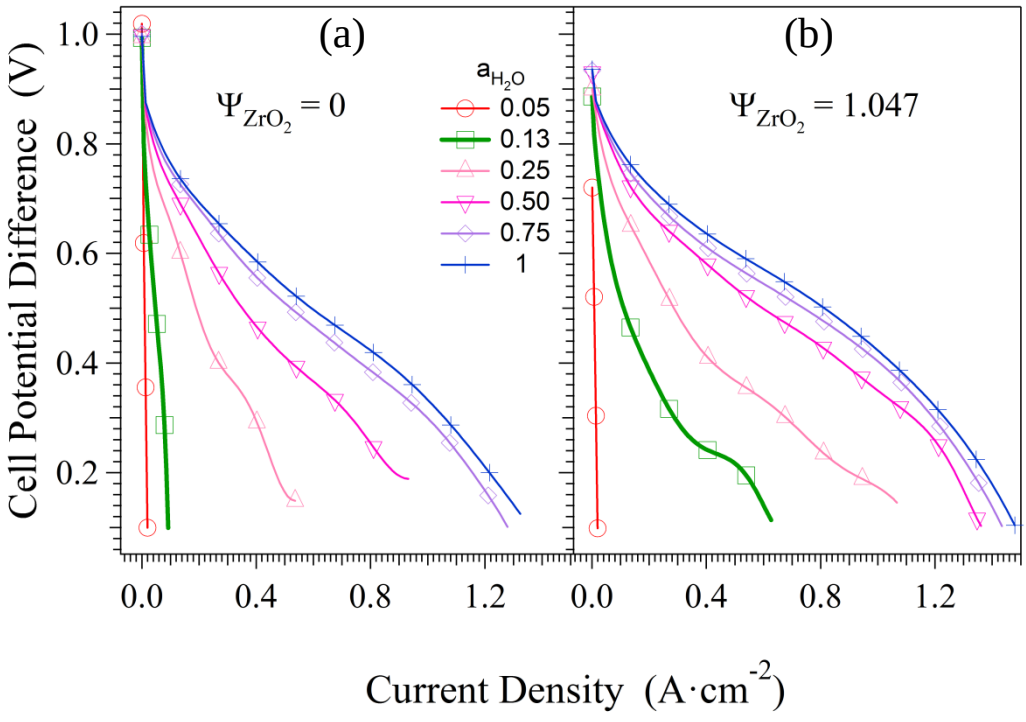

Figure 3.24 Envelope of the polarization curves of the MEA assembled with Nafion (a) and the hybrid membrane (b) as a function of a_{H_2O} in the reagent streams. The oxidant is pure oxygen and the back pressure is 1 bar.

Using fully-humidified reagent streams (a_{H_2O}=1) the two membranes are characterized by polarization curves with a very similar S-shape. This shape originates from: (a) a sharp drop at the highest cell potentials, which essentially arises from the limited effectiveness of the cathode electrode due to the sluggishness of the oxygen reduction reaction; (b) a linear section at intermediate cell potentials, where the slope depends mainly on the various ohmic losses; and (c) a further drop at the lowest cell potentials due to mass transport limitations [15,42,43]. The initial potential drop of the MEA containing the {Nafion/[(ZrO_2)/Ta_2O_5)$_{0.119}$]$_{1.047}$} hybrid membrane is very similar to the Nafion reference membrane, indicating that the initial portion of the polarization curve is controlled mainly by the electrode processes, particularly the oxygen reduction reaction [42,43,44]. It is well-known that the slope of the I-V polarization curve of a MEA is a first approximation of its overall ohmic resistance, assuming that the cell potential: (a) is low enough to disregard contributions arising from electrode kinetics; and (b) no losses due to mass transport issues are observed [42,43,44]. In general, these conditions are satisfied by the linear section of the polarization curve located at intermediate cell potentials. According to the experimental procedure: (a) all the MEAs mount gas-diffusion electrodes (GDEs) prepared with the same porous materials; (b) all the GDEs bear electrocatalytic layers sharing the same formulation and using the same functional materials (ionomer and electrocatalysts); and (c) all the MEAs are assembled according to the same protocol. Since the MEAs containing the reference Nafion and the {Nafion/[(ZrO_2)/Ta_2O_5)$_{0.119}$]$_{1.047}$} hybrid membrane mount the same electrodes, the linear portion of the polarization curve is essentially coincident as the ohmic contribution associated with the membranes proton conductivity. The slopes of the linear section of the polarization curve of the {Nafion/[(ZrO_2)/Ta_2O_5)$_{0.119}$]$_{1.047}$} membranes is similar to the reference Nafion. In addition, the thickness of the two membranes are comparable (ca. 120 μm). Thus, it can be concluded that: a) according to the BES results in fully hydrated condition, the proton conductivity of the hybrid membrane is similar to that of pristine Nafion; b) wet

conditions are not crucial in order to investigate the effect of the inorganic nanofiller on the fuel cell performance of the materials.

Changing the humidification degree (a_{H_2O}) of the reaction streams (Figure 3.24) reveals: a) that the overall performance of the membranes decreases as the a_{H_2O} in the reagent streams decreases due to a decrease of the membranes proton conductivity; and b) several differences between the polarization curves of Nafion and {Nafion/[$(ZrO_2)/Ta_2O_5)_{0.119}]_{1.047}$} appear.

Parts a (Nafion membrane) and b (hybrid membrane) of Figure 3.25 report the power curves derived from the polarization curves shown in Figure 3.24.

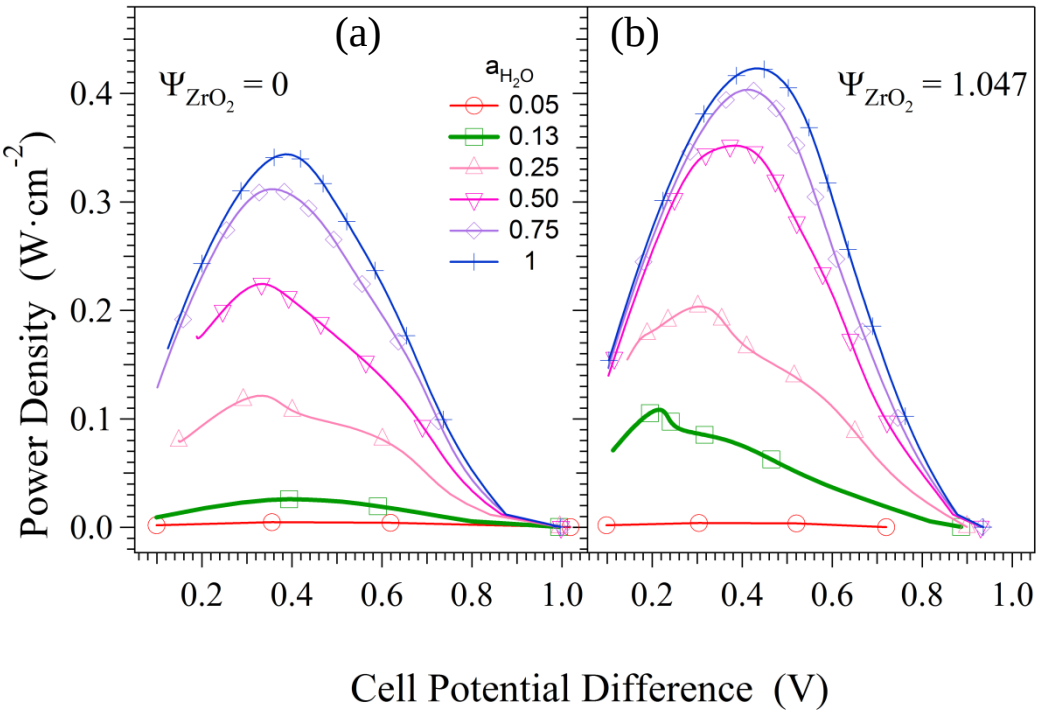

Figure 3.25 Envelope of the power curves of the MEA assembled with Nafion (a) and the hybrid membrane (b) as a function of a_{H_2O} in the reagent streams. The oxidant is pure oxygen and the back pressure is 1 bar.

The power density curves show a maximum between 0.3 and 0.5V. In general, this maximum is located at potentials (current densities) which are: (a) high enough (low enough) to disregard the contributions arising from mass transport issues; and (b) low enough (high enough) to consider the electrode losses constant [15]. These conditions are usually satisfied in the linear section of

the polarization curve of a MEA, exactly where the ohmic contribution of the proton-conducting membrane plays the most important discriminating role.

One way to gauge the overall performance of a MEA is to consider the maximum power density it can yield, reported as function of the water activity of the reagent streams in Figure 3.26.

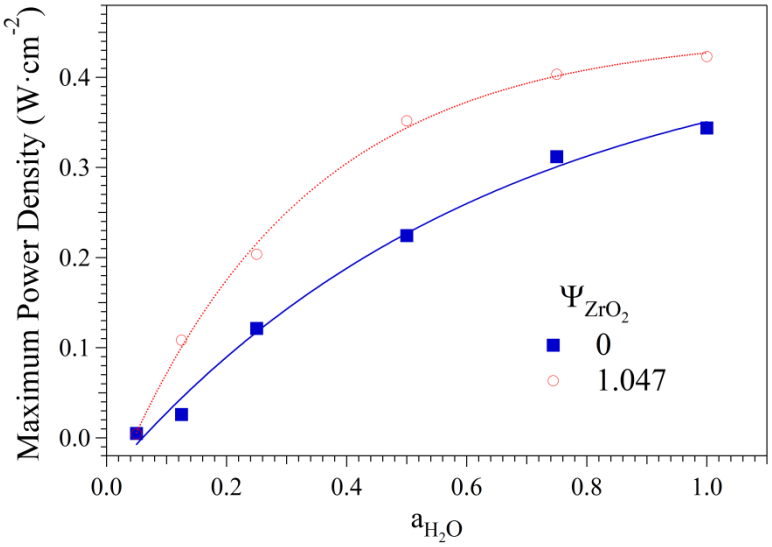

Figure 3.26 Dependence of the maxima of power curves on a_{H_2O} of MEAs assembled with Nafion (Ψ_{ZrO_2} = 0) and the hybrid membrane with Ψ_{ZrO_2} = 1.047.

The maximum power density performance of MEAs increases steadily with a_{H_2O} and is higher for the hybrid membrane with respect to pristine Nafion. In particular, the largest improvement in performance is observed for $0.2 < a_{H_2O} < 0.8$. The better performance of the hybrid membranes with respect to pristine Nafion is due to the higher conductivity of the doped membrane at low water content. According with the previous results, this effect is ascribed to the presence of the inorganic "core-shell" nanofiller, that interacts with the polymer matrix forming $SO_3H\cdots[(ZrO_2)(Ta_2O_5)_{0.119}]$ cross-links that delocalize the proton on the nanofiller surface.

3.4. Conclusions

According to the aim of the research activity, this chapter reports the synthesis and characterization of six hybrid inorganic-organic proton conducting membranes of formula

{Nafion/[$(ZrO_2)\cdot(Ta_2O_5)_{0.119}$]$\Psi_{ZrO_2}$}, with Ψ_{ZrO_2} ranging from 0.318 to 1.937. The research activity was conducted during the first year of the doctoral stage. The basic idea was to dope a Nafion membrane with an inorganic "core-shell" nanofiller in order to improve its thermo-mechanical properties and proton conductivity and extend its operating conditions to temperatures above 100°C and to low levels of membrane hydration. Membranes were prepared following a two-step protocol. First, the "core–shell" nanofiller [$(ZrO_2)(Ta_2O_5)_{0.119}$] was prepared by reacting ZrO_2 and Ta_2O_5 nanopowders by a ball milling process. Second, six hybrid {Nafion/[$(ZrO_2)\cdot(Ta_2O_5)_{0.119}$]$\Psi_{ZrO_2}$} nanocomposite membranes were obtained by a solvent casting procedure,. Water uptake values of the hybrid materials were lower than that of pristine Nafion. The proposed materials are thermally stable up to 170°C, as indicated by TG analyses. MDSC investigations reveal the presence of four endothermic transitions in the 50–300°C temperature range. TG and MDSC studies demonstrate that the presence of $RSO_3H\cdots[(ZrO_2)(Ta_2O_5)_{0.119}]$ cross-links increase the thermal stability of the $-SO_3H$ groups and the temperature of thermal relaxation events occurring in hydrophobic domains of Nafion. DMA analysis reveals four mechanical relaxation events: α, α', α_{pc} and α_{pc}'. DMA results indicated that the concentration and the strength of the $RSO_3H\cdots[(ZrO_2)(Ta_2O_5)_{0.119}]$ interactions in bulk {Nafion/[$(ZrO_2)\cdot(Ta_2O_5)_{0.119}$]$\Psi_{ZrO_2}$} nanocomposite membranes improve the mechanical stability of both hydrophobic and hydrophilic domains of materials. FT-IR ATR studies reveal that the hydrophobic PTFE-like domains of Nafion in {Nafion/[$(ZrO_2)\cdot(Ta_2O_5)_{0.119}$]$\Psi_{ZrO_2}$} membranes consist of a blend of fluorocarbon chains with 15_7 and 10_3 helical conformation. The concentration of 10_3 helical chains ranges from 6% to 14% and presents an S-shape behavior similar to that of W.U as function of Ψ_{ZrO_2}. Detailed analyses, carried out in the stretching and bending regions of FT-IR ATR spectra, reveal six different species of water domains in bulk nanocomposite membranes. Furthermore, it was demonstrated that the fraction of water: (a)

solvating hydronium ions is lower than 10%; (b) aggregated into hydrogen bonding cluster domains, $[H_2O]_{hy}$, is 40%; and (c) embedded in the materials as "matrix isolated" water molecules is ≈55%. The electric response of membranes was studied by broadband dielectric spectroscopy in the 10^{-2}Hz–10MHz and 5–155°C ranges. An analysis and comparison of the membranes electrical properties reveal the presence of two electric relaxations associated with the material's interfacial (σ_{IP}) and bulk proton conductivity (σ_{DC}). Fitting the experimental profiles of ε* and σ* produced the conductivity values associated to each conduction mechanism. σ_{DC} is 2-3 orders of magnitude higher than σ_{IP} and between 5 and 155°C shows VTF behaviour as function of temperature, which indicates that the long-range conductivity is closely related to the segmental motion of the Nafion host matrix. The conductivity studies suggest that the concentration and the strength of $RSO_3H\cdots[(ZrO_2)(Ta_2O_5)_{0.119}]$ cross-links significantly affect the conductivity and the stability range of conductivity of the hybrid membranes. Interestingly, wet $\{Nafion/[(ZrO_2)\cdot(Ta_2O_5)_{0.119}]\Psi_{ZrO_2}\}$ with Ψ_{ZrO_2} = 1.047 exhibits a conductivity of 7.0×10^{-2} Scm^{-1} at 115°C, and a SRC of 5<T<155°C. In the same conditions, Nafion shows a conductivity of 3.3×10^{-2} Scm^{-1} and SRC of 5<T<105°C. Finally, the fuel cell tests, conducted on the reference Nafion and the hybrid membrane with Ψ_{ZrO_2} = 1.047 reveal that the performance of the MEA containing the hybrid membrane, specifically the power density, is better than that of the MEA containing pristine Nafion particularly at low values of relative humidity.

All these results allow the classification of these new materials as very promising proton conducting systems for application in PEMFCs operating at temperatures higher than 90°C.

Taken together, all results indicate that the $[(ZrO_2)\cdot(Ta_2O_5)_{0.119}]$ nanofiller stabilizes both the hydrophobic and the hydrophilic domains of materials, owing to the formation of R-$SO_3H\cdots[(ZrO_2)(Ta_2O_5)_{0.119}]\cdots HSO_3$-R bridges which interconnect the bundles of fluorocarbon chains in a 3D hybrid polymeric network and reduces the size of the PTFE-like domains, as

shown in part a and b of Figure 3.27. As a result, the hybrid membranes show a reduction in swelling and an increases in mechanical properties with respect to pristine Nafion.

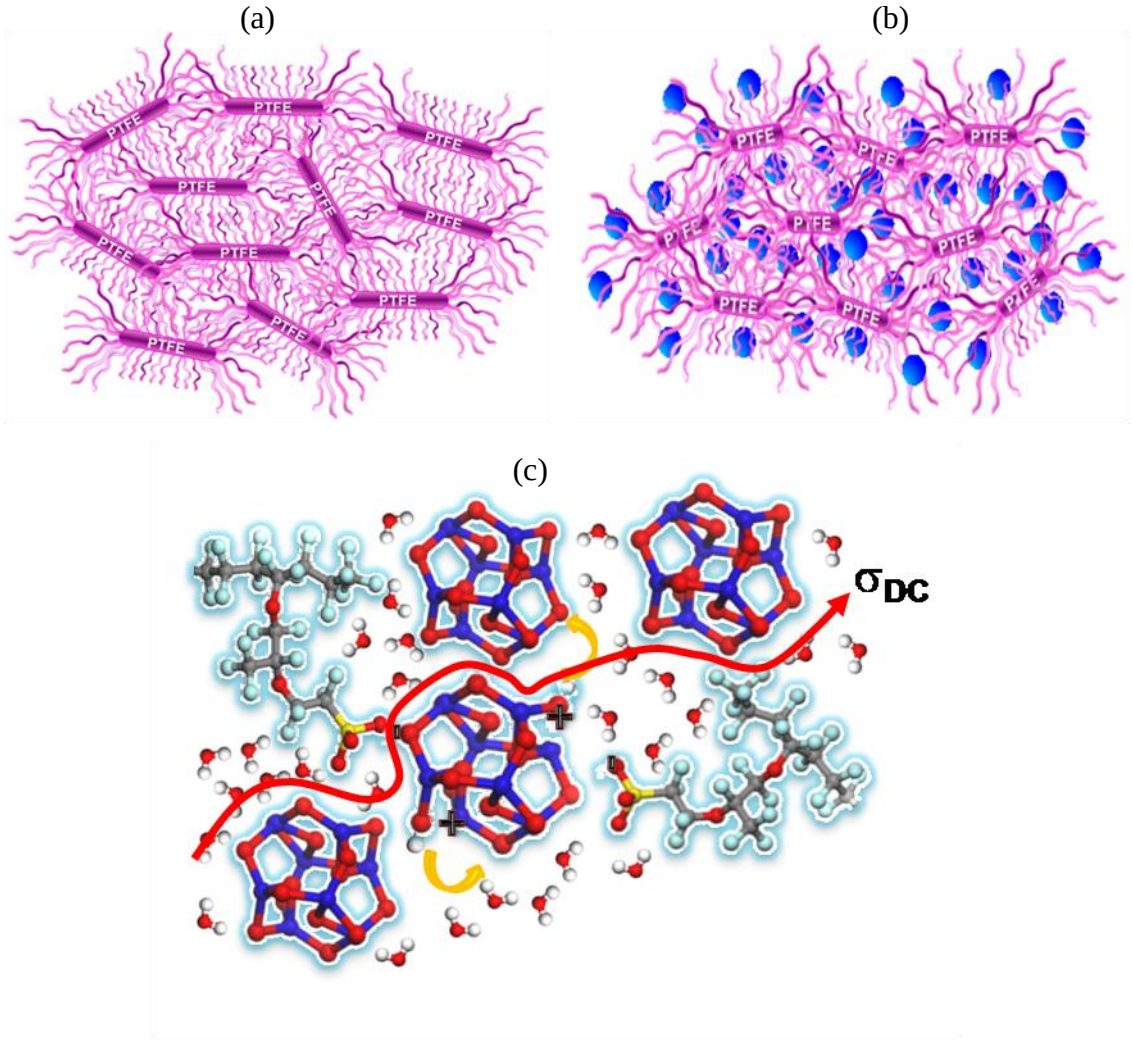

Figure 3.27 Hypothesis of membrane structure for pristine Nafion (a) and hybrid membranes (b). (c). Proton conduction mechanism proposed for the {Nafion/[$(ZrO_2)\cdot(Ta_2O_5)_{0.119}$]$\Psi_{ZrO_2}$} nanocomposite membranes.

Furthermore, although a reduction in the water uptake, {Nafion/[$(ZrO_2)\cdot(Ta_2O_5)_{0.119}$]$\Psi_{ZrO_2}$} membranes present, with respect to pristine Nafion, higher values of both the bulk and the interfacial conductivity. These results suggest that the proton conduction occurs at the interfaces between the nafion polar domains and the nanofiller, as shown in part c of Figure 3.27. The presence of proton percolation pathways at the Nafion-nanofiller interfaces reduces the amount of water necessary to maintain good proton conduction.

Despite the improvement of the performance as compared to pristine Nafion, the {Nafion/[$(ZrO_2)\cdot(Ta_2O_5)_{0.119}$]$\Psi_{ZrO_2}$} membranes still need to be in contact with partially humidified reactants to be used in PEMFC, thus complicating the development and management of the final device. In order to overcome this limitation and obtain Nafion-based membranes which can operate under completely anhydrous conditions, the research activity carried out during the second year of the doctoral stage focused on the synthesis and the study of new proton conducting membranes based on Nafion doped with two different proton conducting ionic liquids. The discussion of these experimental results is the subject of the next chapter.

3.4. References

1. Mauritz, K. A.; *Mat. Sci. Eng. C-Bio. S.*; **1998**, 6, 121.
2. Alberti, G.; Casciola, M.; *Annu. Rev. Mater. Res.*, **2003,** 33,129.
3. Neergat M.; Friedrich, K.A.; Stimming, U.; in: Vielstich, W.; Lamm, A.; Gasteiger, H.A. (Eds.); *Handbook of Fuel Cells—Fundamentals, Technology and Applications*, Vol.4, John Wiley & Sons, Hoboken, New Jersey, **2003**, pp.856.
4. Nakao, M.; Yoshitake, M.; in: Vielstich, W.; Lamm, A.; Gasteiger, H.A. (Eds.); *Handbook of Fuel Cells—Fundamentals, Technology and Applications*, Vol.3, John Wiley & Sons, Hoboken, New Jersey, **2003**, pp. 412.
5. Thampan, T.M.; Jalani, N.H.; Choi, P.; Datta, R.; *J. Electrochem. Soc*., **2005**, 152, A316.
6. Jalani, N.H.; Dunn, K.; Datta, R.; *Electrochim. Acta*, **2005**, 51, 553.
7. Aparicio, M.; Klein, L.C.; *J. Electrochem. Soc*. 152, **2005**, A493.
8. Satterfield, M.B.; Majsztrik, P.W.; Ota, H.; Benziger, J.B.; Bocarsly, A.B.; *J. Polym. Sci. Pol. Phys.* 44, **2006**, 2327.
9. Di Noto, V.; Gliubizzi, R.; Negro, E.; Pace, G.; *J. Phys. Chem. B*, **2006**, 110, 24972.

10. Di Noto, V.; Gliubizzi, R.; Negro, E.; Vittadello, M.; Pace, G.; *Electrochim. Acta*, **2007**, 53, 1618.

11. Di Noto, V.; Lavina, S.; Negro, E.; Vittadello, M.; Conti, F.; Piga, M.; Pace, G.; *J. Power Sources*, **2009**, 187, 57.

12. Vittadello, M.; Negro, E.; Lavina, S.; Pace, G.; Safari, A.; Di Noto, V.; *J. Phys. Chem. B*, **2008**, 112, 16590.

13. Di Noto, V.; Piga, M.; Piga, L.; Polizzi, S.; Negro, E., J. *Power Sources* **2008**, 178 (2), 561-574.

14. Di Noto, V.; Piga, M.; Lavina, S.; Negro, E.; Yoshida, K.; Ito, R.; Furukawa, T., *Electrochim. Acta* **2010**, 55 (4), 1431.

15. Di Noto, V.; Boaretto, N.; Negro, E.; Giffin G.A.; Lavina, S.; Polizzi, S.; *Int. J. Hydrogen Energy* **2011**; doi:10.1016/j.ijhydene.2011.07.132.

16. Di Noto, V.; Boaretto, N.; Negro, E.; Stallworth, P.E.; Lavina, S.; Giffin, G.A.; Greenbaum, S. G.; *Int. J. Hydrogen Energy* **2011**; doi:10.1016/j.ijhydene.2011.07.135.

17. http://en.wikipedia.org/wiki/Cubic_zirconia. Information retrieved on December 15th, 2011; http://hitopmould.en.makepolo.com/productshow/5645272.html. Information retrieved on December 15th, 2011.

18. Zawodzinski, T. A.; Derouin, C.; Radzinski, S.; Sherman, R. J.; Smith, V. T.; Springer, T. E.; Gottesfeld, S.; *J. Electrochem. Soc*. **1993**, 140, 1041.

19. Di Noto V.; Negro, E.; *Fuel Cells*, **2010**, 10, 234.

20. Kocha S.S.; Principles of MEA preparation. In: Vielstich W., Lamm A., Gasteiger H.A., (Eds). *Handbook of fuel cells: Fundamentals, Technology and Applications*, Wiley, Chichester; **2003**, 538.

21. Gasteiger H. A.; Kocha S. S.; Sompalli B.; Wagner FT; *Appl. Catal. B,* **2005**; 56, 9.

22. Doyle, M.; Rajendran, G.; In: Vielstich W., Lamm A., Gasteiger H.A., (Eds). *Handbook of fuel cells: Fundamentals, Technology and Applications*, Wiley, Chichester; **2003**, p. 351.

23. Page, K. A.; Cable, K. M.; Moore, R. B.; *Macromolecules* **2005**, 38, 6472.

24. Di Noto, V.; Piga, M.; Giffin, G. A.; Pace, G.; *J. Membr. Sci.*, **2012**, 390, 58**.**

25. Carbone, A.; Pedicini, R.; Portale, G.; Longo, A.; D'Ilario, L.; Passalacqua, E.; *J. Power Sources*, **2006**, 163, 18.

26. Di Noto, V.; *J. Phys. Chem. B*, **2000**, 104, 10116.

27. Zerbi, G.; Sacchi, M.; *Macromolecules*, **1973**, 6, 692.

28. Masetti, G.; Cabassi, F.; Morelli, G.; Zerbi, G.; M.; *Macromolecules*, **1973**, 6, 700.

29. Clark, E.S., *Polymer*, **1999**, 40, 4659.

30 Di Noto V. et al., Assignments by DFT calculations, paper in preparation.

31. Di Noto, V.; *J. Phys. Chem. B*, **2002**, 106, 11139.

32. Schonhals, A.; Kremer, F. eds.; *Broadband Dielectric Spectroscopy*, Springer, Berlin, **2003**.

33. Di Noto, V.; Negro, E.; Sanchez, J.Y.; Iojoiu, C.; *J. Am. Chem. Soc*., **2010**, 132, 2183.

34. Giffin, G.A.; Piga, M.; Lavina, S.; Navarra, M.A.; D'Epifanio, A.; Scrosati, B.; Di Noto, V.; *J. Power Sources,* **2012,** 198, 66.

35. Lu, Z.; Polizos, G.; Macdonald D. D.; Manias E., *J. Electrochem. Soc.*, **2008**, 155, B163.

36. Kreuer, K.D.; *J. Membr. Sci.*, **2001**, 185, 29.

37. Serghei, A.; Tress, M.; Sangoro, J.R.; Kremer, F.; *Phys. Rev. B: Condens. Matter*, **2009**, 80, 184301.

38. Di Noto, V.; Giffin, G.A.; Vezzù, K.; Piga, M.; Lavina, S.. *Broadband Dielectric Spectroscopy: A Powerful Tool for the Determination of Charge Transfer Mechanisms in Ion Conductors*, in: Knauth, P.; Di Vona, M.L. (Eds.). *Solid State Proton Conductors: Properties and Applications in Fuel Cells*, Wiley, Chichester, **2012**.

39. Atkins, P.; de Paula, J., *Physical Chemistry*. 8th ed.; Oxford University Press: Oxford, **2006**.

40. Oberbroeckling, K. J.; Dunwoody, D. C.; Minteer, S. D.; Leddy, J.; *Anal. Chem.* **2002**, 74, 4794.

41. Rubatat, L.; Rollet, A. L.; Gebel, G.; Diat, O., *Macromolecules* **2002**, 3, 4050.

42. Srinivasan, S.; *Fuel Cells - From Fundamentals to Applications*. New York: Springer Science; **2006**.

43. O'Hayre, R.; Cha, S. W.; Colella, W.; Prinz, F. B., *Fuel Cell Fundamentals*. New York: John Wiley & Sons; **2006**.

44. Spiegel, C. S.; *Designing and Building Fuel Cells*. New York: McGraw-Hill; **2007**.

Chapter IV

Proton conducting membranes based on neutralized Nafion 117®, Triethylammonium methanesulfonate and Triethylammonium perfluorobutanesulfonate

4.1. Introduction

In an effort to overcome the limitations of conventional PEMs, innovative PEMs based on polymeric membranes doped with proton-conducting ionic liquids (PCILs) have been recently developed [1-3]. PCILs are a category of ionic liquids (IL) and are synthesized by directly reacting a Bronsted acid with a Bronsted base [4]. The distinguishing feature of PCILs, versus ILs, is the transfer of protons between proton-donor and proton-acceptor sites, which can subsequently be used in the formation of hydrogen bonds [4]. PCILs have highly mobile protons and are thus ideal candidates for fuel cell electrolyte components that can function at medium temperatures, between 100°C and 150°C, and possibly in anhydrous conditions [5-8].

In PEM/PCIL system, the basic idea is to replace water present within the membrane and necessary for the proton conduction with a PCIL. Thus, due to the thermal stability and proton conductivity of PCIL, is possible to increase the membrane's operating condition in fuel cell at temperature higher than 100°C and anhydrous condition. Recently, Di Noto *et al.* [7] reported that PEMs based on Dupont™ Nafion 117® [9] neutralized with triethylamine (TEA) and doped with the PCIL triethylammonium trifluoromethanesulfonate (TEA-TF) are characterized by an increased stability range of conductivity and show higher conductivity values (7.3×10^{-3} $S\cdot cm^{-1}$) at 145°C versus the standard Nafion 117® [7]. Thus PCIL-doped membranes are ideal electrolytes for medium-temperature fuel cells. The research conducted during the 2nd year of PhD activity extends that work with the preparation and the study of two new membranes based on Nafion 117 neutralized with TEA and doped with either of two PCILs (i.e. triethylammonium methanesulfonate (TMS) and triethylammonium perfluorobutanesulfonate (TPFBu)). This work is a fundamental study of: 1) the structural modulation of Nafion due to the incorporation of an IL dopant into the host matrix and 2) the effect of PCIL anion exchange on the structural reorganization and the properties of the system, specifically the conductivity. The thermal and mechanical properties of these materials are studied by thermogravimetric analyses, differential scanning calorimetry and dynamic-mechanical analysis, while the structure and the interactions between the membrane components are investigated by Fourier transform infrared spectroscopy. Finally, the effect of the PCILs incorporation on the electrical properties of the membranes, in terms of dielectric relaxations and proton conduction mechanism is investigated by Broadband Electric Spectroscopy.

4.2. Experimental

4.2.1 Synthesis of TMS and TPFBu proton-conducting ionic liquids

Methanesulfonic (MS) and perfluorobutanesulfonic (PFBu) acids (Aldrich) were used as received. Triethylamine (TEA) and the other organic solvents used in the synthesis of the ionic liquids were distilled before use. The ILs were synthesized by the reaction of the organic acid with triethylamine as according to the procedure previously reported by Martinez [8]. Briefly, a solution of the organic acid (10 mL of organic acid in 100 mL of water) was cooled in an ice-bath, stirred for 10 minutes, and then neutralized with triethylamine to a pH = 8. The excess water and triethylamine were removed by evaporation under vacuum and by freeze-drying, respectively, yielding the ionic liquids triethylammonium methanesulfonate (TMS) and triethylammonium perfluorobutanesulfonate (TPFBu). The purification of TMS was carried out by dissolving the ionic liquid in methanol, filtering the solution through an active carbon column and finally evaporating the excess methanol. The purification of TPFBu was obtained by the recrystallization of the ionic liquid in a 50/50 (v/v) solution of acetonitrile and diethyl ether. The ionic liquids were dried (48 h) at 130°C under vacuum. The chemical structures of TMS and TPFBu are shown in Figure 4.1.

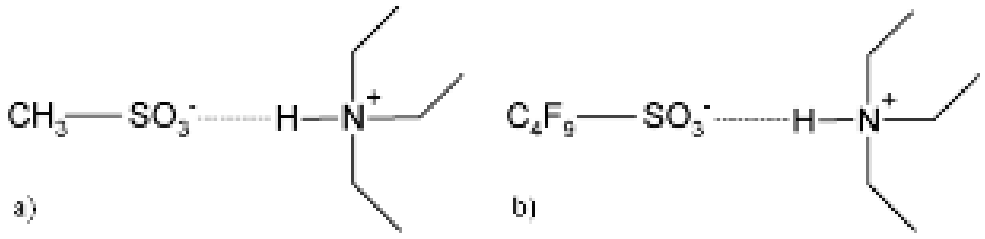

Figure 4.1 Chemical structure of PCILs: (a) triethylammonium methanesulfonate (TMS) and (b) triethylammonium perfluorobutanesulfonate (TPFBu).

4.2.2 Membranes preparation

Doped-membranes were prepared following the procedure of Martinez et al. [8], reported in Scheme 4.1. Nafion 117® [9] (N117) was immersed in 2M HNO_3 and refluxed for 2h. The membrane was subsequently neutralized by immersion in a 50/50 (v/v) solution of ethanol and 4M $TEA_{(aq)}$ for 48 h at ambient temperature, yielding the neutralized Nafion (nN117). The

nN117 was finally washed with distilled water, dried at 130°C for 48 h under vacuum and moved into a dry box. All further preparation and manipulation of the samples and the ionic liquids were carried out within the dry box. The membrane was doped with the ionic liquid by immersion into either TMS or TPFBu, for 48 h at 80°C to yield NTMS and NTPFBu, respectively. The NTMS and NTPFBu were stored for one week inside a dry box in argon.

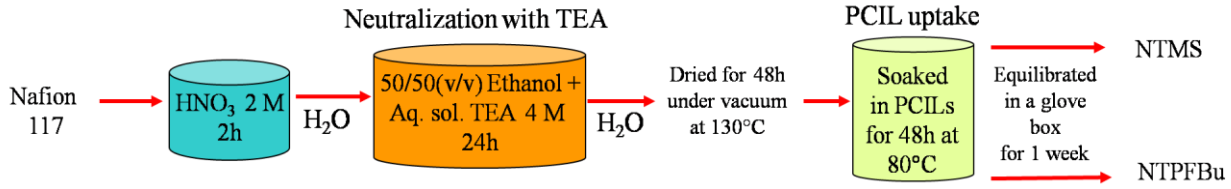

Scheme 4.1 Experimental procedure for the neutralization with TEA and the doping with PCILs of Nafion117®.

The uptake of ionic liquid (%PCIL) was calculated using Equation 4.1:

$$\%\ PCIL = \frac{w_{wet} - w_0}{w_0} \cdot 100 \qquad (4.1)$$

where w_0 and w_{wet} are the membrane mass before and after the absorption of ionic liquid, respectively. The uptake of TMS by NTMS is 25 wt%, while that of TPFBu by NTPFBu is 40 wt%.

4.2.3 Instruments and Methods

TG profiles were collected from 20 to 800°C. The heating rate was varied from 50 to 0.001°C·min^{-1}, depending on the first derivative of the weight loss. Differential Scanning Calorimetry (DSC) analyses were carried out in the temperature range from -100 to 200°C for TMS and TPFBu and between -100 and 350°C for the polymeric membranes. Dynamic-Mechanical spectra (DMA) for NTMS and NTPFBu were collected every 5°C from -100 to 200°C. FT-IR spectra of the pristine ionic liquids were obtained in transmission placing the samples between KBr pellets. The infrared spectra of the doped membranes were obtained in attenuated total reflectance (ATR) mode (Chapter 2). For all the investigated materials the FT-IR

spectra were collected by a signal averaging of 500 scans. BES measurements were performed over the frequency range from 10^{-2} to 10^{7} Hz and from -100 to 150 °C in 10°C intervals with accuracy better than ± 0.1 °C. To avoid exposure of the samples to ambient humidity, the samples and electrodes were loaded into a home-made teflon cell (Chapter 2) inside a dry box.

4.3. Results and discussion

4.3.1 Thermogravimetric analysis

TG profiles are recorded for the ionic liquids, TMS and TPFBu, and for the PCIL-doped membranes, NTMS and NTPFBu to explore: 1) the temperature region where the materials are thermally stable; and 2) the effect of the IL-nN117 and the IL-IL interactions on the thermal degradation of the doped membranes. The TG profiles are shown in Figure 4.2 along with the TG results of nN117 obtained from the literature [7]. The insets (I), (II) and (III) of Figure 4.2 show the derivative dw%/dT from 25 to 160°C, from 150 to 350°C, and from 350 to 600°C respectively.

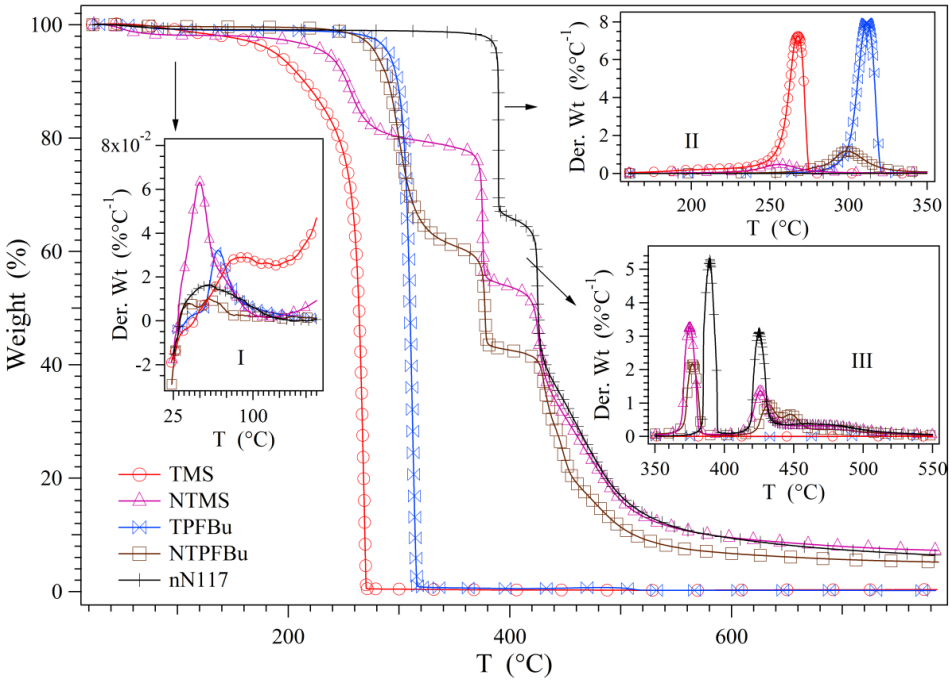

Figure 4.2 TG profiles of TMS, TPFBu, NTMS, NTPFBu and nN117. The insets show the derivative dw%/dT in the temperature range: (I) 30 – 160°C, (II) 150 – 350°C, (III) 350 – 600°C. The TG curve of nN117 is taken from the literature [7].

Three different thermal degradation processes, divided into regions I, II, and III, were identified. The elimination of traces of water occurs in region I between 20 and 150°C. It is expected that the level of hydration of the doped membranes is negligible as compared to pristine Nafion because the hydrophilic domains are filled with the ILs. Therefore, the water content of the membranes depends on the water uptake of the ILs. The weight loss due to water at 150°C is about 2.3 wt%, 2 wt%, 1 wt% and 0.5 wt% for samples TMS, NTMS, TPFBu and NTPFBu respectively. These data suggest that: (a) the ionic liquid TPFBu includes about half as much water as TMS due to its higher hydrophobicity, which arises from the presence of the C_4F_9 group; (b) the water content of the NTMS and NTPFBu membranes is less than their respective ILs and follows the behaviour of their respective pristine PCIL, i.e., the water content of NTPFBu (0.5%) is lower than that of NTMS (1%). Overall, the doped membranes are more hydrophobic due to the presence of the ILs.

The mass elimination detected in region II, between 200 and 350°C (Figure 4.2 (II)) is due to the thermal degradation of the ionic liquid, according to the following: (1) the TG profiles of pristine MST and TPFBu reveal a weight loss of approximately 100% in this temperature range; and (2) the absence of a mass reduction event in this temperature range for nN117. The ionic liquid content of the NTMS and NTPFBu membranes can be estimated using the weight change from 170 to 350 °C. The uptake of ionic liquid is determined to be 20 and 39 wt% for NTMS and NTPFBu, respectively. These values are in agreement with the results determined during the synthesis of the doped membranes as reported in the experimental section, which are equal to 25 and 40 wt% for NTMS and NTPFBu, respectively. Using the uptake values, the molecular weight of ionic liquid, 198 and 402 $g \cdot mol^{-1}$ for TMS and TPFBu, respectively, and a nN117 side group concentration of $0.83 \cdot 10^{-3}$ $mol \cdot g^{-1}$, the ratio (φ) between the moles of PCIL and the moles of sulfonate groups in the polymeric matrix can be determined. The values of φ for NTMS and

NTPFBu are 2.02 and 2.00, respectively, indicating that the uptake of ionic liquid per moles of sulfonate group of nN117 is the same in both the PCIL-doped membranes.

Using the derivative dw%/dT shown in inset II of Figure 4.2, the initial thermal degradation temperature, $T_{d,ons}$, and the maximum thermal degradation temperature, $T_{d,max}$, are determined as shown in Figure 4.3.

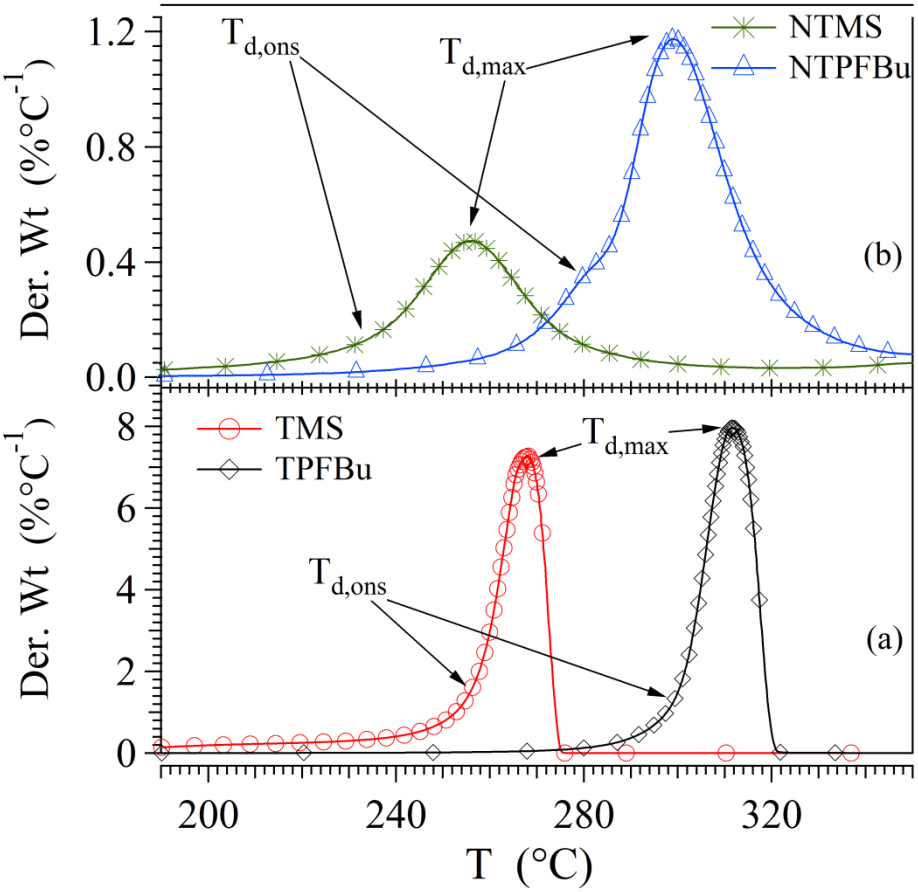

Figure 4.3 Behaviour of dw%/dT in the thermal range 210 – 350°C for: (a) TMS and TPFBu; (b) NTMS and NTPFBu.

The values of $T_{d,ons}$ and $T_{d,max}$, reported in Table 4.1, show that the TMS decomposition temperature is lower than that of TPFBu even when the ionic liquids are embedded in bulk polymer membranes. The increased $T_{d,ons}$ and $T_{d,max}$ for TPFBu are explained by the increased acid dissociation constants of pristine organic acids (perfluorobutanesulfonic acid (PFBuH), pKa= -13.2 and methanesulfonic acid (MSH), pKa = -2) used in the preparation of the ionic

liquids [8]. Indeed, the increased thermal stability of TPFBu versus TMS indicates that the anion (conjugated base) of PFBuH is a weaker base than the anion of MSH. Therefore, the anion-cation interaction should be more important in TMS than in TPFBu. However, as PFBuH is more acidic than MSH acid, the equilibrium AH + TEA $\rightleftharpoons$ A^- + $TEAH^+$ should be shifted further to the right with PFBuH than with MSH, resulting in a delay of the weight loss to higher temperature.

The $T_{d,ons}$ and $T_{d,max}$ of the ionic liquids are reduced by approximately 20 and 12°C, respectively, when they are incorporated into the nN117 membrane (ΔT of Table 4.1). The reduction of the thermal stability of the ionic liquids incorporated into the membrane is explained by the diminished strength of the interactions between the ions as compared to the pristine ionic liquids, probably due to the formation of electrostatically interacting confined nanodomains within the bulk nN117. The presence of the IL in very small domains results in a large surface area that is available for interaction with the membrane. As a result, there are significant IL-membrane interactions that lead to a decrease of the ion-ion interactions in the PCILs. Consistent with prior studies [10-12] and with the TG profile of nN117 [7], the weight reductions corresponding to region III, between 350 and 600 °C, are assigned to polymer matrix decomposition. The peaks between 350 and 400°C correspond to the decomposition of the polyether side chain, while the peaks between 400 and 550°C are associated with the degradation of the main fluorocarbon backbone chain. The decomposition of the polyether side chains in the doped membranes occurs approximately 13°C lower than in nN117. This reduction in temperature is attributed to the plasticizing effect of the ionic liquid in the NTMS and NTPFBu membranes. The ionic liquid causes a weakening of the electrostatic interactions within the neutralized side groups of nN117, resulting in a reduction of thermal stability.

Table 4.1 Values of onset, $T_{d,ons,}$ and thermal degradation temperatures, $T_{d,max}$.

	TMS	NTMS	$\Delta T_{TMS/NTMS}$	TPFBu	NTPFBu	$\Delta T_{TPFBu/NTPFBu}$
$T_{d,ons}$ / °C	256	233	23	300	281	19
$T_{d,max}$ /°C	268	256	12	312	299	13

It could be hypothesized that the weakening of electrostatic interactions is due to the aggregation of IL cations and anions. These aggregates interact with the neutralized side groups of the host matrix. The phenomenon acts to weaken the $SO_3^-\cdots TEAH^+$ interactions as compared to the pristine nN117 by the formation of $SO_3^-\cdots TEAH^+\cdots$[aggregate] moieties via an extended hydrogen bonding network. Indeed, it is expected that the electrostatic interactions between the Nafion side groups are higher in nN117, where the $R\text{-}SO_3^-\cdots{}^+HTEA\cdots TEAH^+\cdots{}^-SO_3\text{-}R$ van der Waals interactions are present between ethyl-terminated side groups, than in the doped membranes, where the neutralized side groups are solvated and plasticized by PCIL forming $R\text{-}SO_3^-\cdots{}^+HTEA\cdots$[aggregate] $\cdots TEAH^+\cdots{}^-SO_3\text{-}R$ interactions.

The thermal decompositions attributed to the degradation of the main fluorocarbon backbone chain, shown in inset (III) of Figure 4.2, appear to be independent of the ionic liquid used. To summarize, TG measurements show that the polymeric membranes NTMS and NTPFBu: (a) are thermally stable up to temperatures of approximately 200°C; (b) include 20 and 39 wt% of TMS and TPFBu, respectively; (c) show three distinct thermal degradation processes; and (d) are characterized by a lower thermal stability than the ionic liquids they contain (Table 4.1).

4.3.2 DSC analysis

DSC analysis elucidates thermal transitions in the pristine ionic liquids and in the PCIL-doped membranes. The DSC profiles of the pristine ionic liquids, shown in Figure 4.4, exhibit a glass transition, T_{gIL}, between -30 and -15°C. By considering T_{gIL} as the midpoint between the onset

and the endpoint temperatures of the glass transition, values of -17 and -23°C are obtained for TMS and TPFBu, respectively. Endothermic peaks present at $T_{m1,TMS}$ = 38.4°C and $T_{m1,TPFBu}$ = 61.3°C are due to the melting of the ordered aggregates of ionic liquids [8].

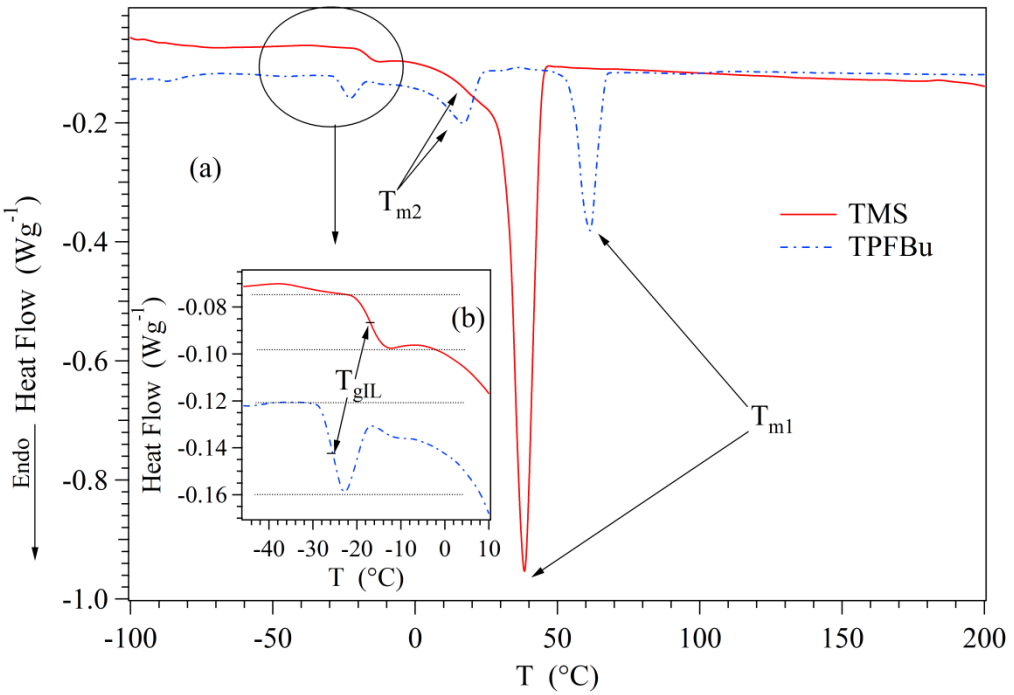

Figure 4.4 (a) DSC curves of TMS and TPFBu collected in the temperature range from -100 to 200°C. (b) Expansion of the DSC curves at the glass transition temperature, $T_{gIL} \approx$ -20°C.

According to Martinez et al. [8], the melting temperature T_{m1} depends on the properties of the pristine organic acids used in the synthesis, and increases with ionic liquid hydrophobicity. The DSC results of both ionic liquids show the presence of a second endothermic peak, T_{m2}, which is less intense and shifted to lower temperatures with respect to T_{m1}. For TMS, the second endothermic peak $T_{m2,TMS}$ is observed at approximately 20°C as a shoulder on the $T_{m1,TMS}$ peak, while for TPFBu, the peak $T_{m2,TPFBu}$ is well-resolved and centered at 17°C. The presence of T_{m2} suggests that at low temperatures the ionic liquid nanostructure consists of two distributions of ordered aggregates with different sizes, which on average melt at T_{m1} and T_{m2}. The DSC curve of the NTMS and NTPFBu samples, together with that of nN117 [7], are reported in Figure 4.5. All examined samples show a thermal transition in the range from -30 to -10°C. In the case of

nN117, this thermal event is associated with a conformational transition involving the polyether side groups of nN117 [2]. In the PCIL-doped membranes, the thermal events between -30 and -10°C are attributed to the superposition of two different phenomena: (1) the glass transition of the pristine ionic liquid as seen in Figure 4.4; and (2) the conformational transition of the polyether side groups in the nN117 polymeric matrix.

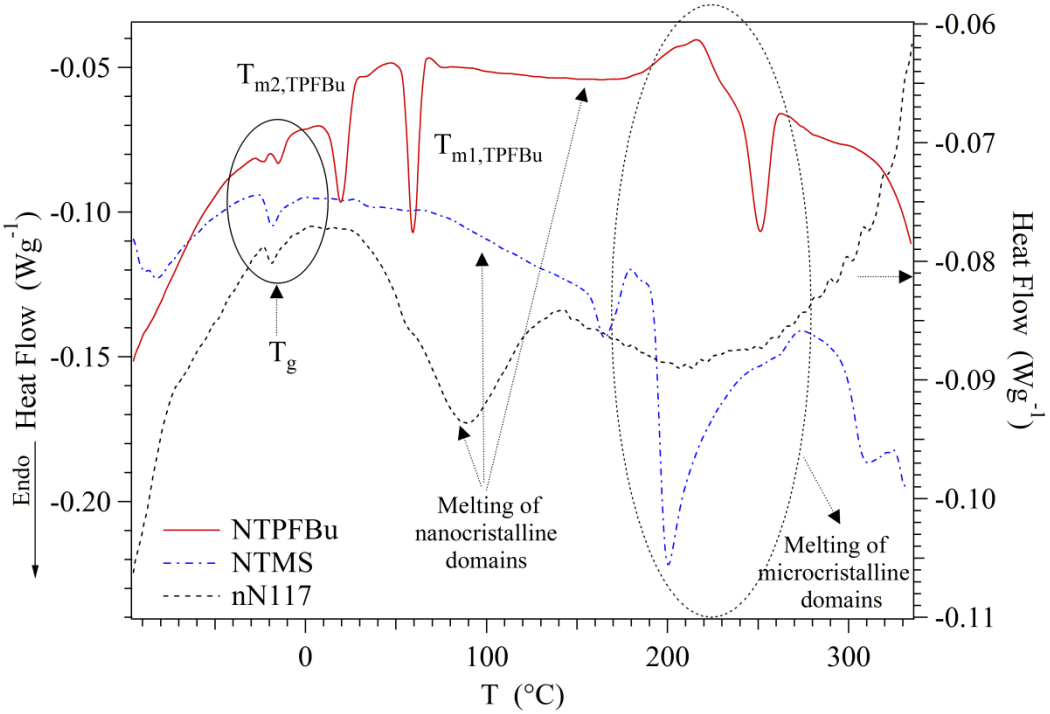

Figure 4.5 DSC curves of NTMS, NTPFBu and nN117 collected in the temperature range from -100 to 350 °C. The DSC curve of nN117 are shown for the sake of comparison and are taken from the literature [7].

By comparing the DSC curves in Figure 4.4 and Figure 4.5, it is observed that the first melting peak of the pristine ionic liquid in the NTMS membranes, $T_{m1,TMS}$, has vanished. In the NTPFBu membrane, both TPFBu melting peaks remain and can be located at $T_{m1,TPFBu}$ = 19.4°C and $T_{m2,TPFBu}$ = 59.3°C. The absence of the DSC melting peak $T_{m1,TMS}$ of NTMS suggests that even at low temperatures the ionic liquid TMS embedded inside the membrane is well dispersed forming nanodomains with very small sizes. The highly dispersed state of TMS likely results from interactions between TMS and the polymer matrix. These interactions significantly reduce the size of the ionic liquid nanoaggregates that are confined inside the polar domains of nN117

efficiently solvating the surface of its hydrophobic domains. The presence of partially-ordered TPFBu nanodomains inside the NTPFBu membrane suggests that TPFBu···$TEAH^+$···N117 interactions are weaker than TMS···$TEAH^+$···N117 interactions and, as a consequence, the size of nanodomains of TPFBu inside the membranes are larger than that of TMS. The enthalpy of fusion values $\Delta H_{f,Tm1}$ and $\Delta H_{f,Tm2}$ associated with the first and second melting peaks are shown in Table 4.2.

Table 4.2 Enthalpy of fusion $\Delta H_{f,i}$ for TMS, NTMS, TPFBu and NTPFBu.

$\Delta H_{f,i}$ / Jg^{-1}	TMS	NTMS	TPFBu	NTPFBu
$\Delta H_{f,Tm1}$	70.5	/	23.2	4.9
$\Delta H_{f,Tm2}$	22.1	/	12.7	3.9

The total enthalpy of fusion, $\Delta H_{f,tot} = \Delta H_{f,Tm1} + \Delta H_{f,Tm2}$, of the pristine ionic liquids are 92.6 $J \cdot g^{-1}$ (18.3 $kJ \cdot mol^{-1}$) and 35.9 $J \cdot g^{-1}$ (14.4 $kJ \cdot mol^{-1}$) for TMS and TPFBu, respectively. These values suggest that the exchange of the methanesulfonate anion in TMS with the perfluorobutylsulfonate anion in TPFBu reduces the lattice energy by about 20% . The total enthalpy of fusion for the PCIL inside NTPFBu is 8.8 $J \cdot g^{-1}$. Given that according to TG measurements, NTPFBu includes 39 wt% of TPFBu, the total enthalpy of fusion, $\Delta H_{f,tot}$, for TPFBu inside the nN117 can be estimated to be $\Delta H_{f,tot}$ = 8.8 $J \cdot g^{-1}$/39wt% = 22.5 $J \cdot g^{-1}$. This is 37% lower than the enthalpy of fusion of the pristine ionic liquid. The DSC analyses suggest that the confinement of the ionic liquid inside the polymer matrix yields effects that depend on the interactions between the two system components and on the nanostructuring of PCILs in bulk materials. For the NTMS membrane, confinement results in the presence of a completely dispersed ionic liquid TMS that is confined in very small amorphous nanoaggregates. For the NTPFBu membranes, the outcome of the confinement involves a reduction in crystallinity by approximately 37% with respect to that of the pristine ionic liquid.

The broad endothermic peaks between 100 and 180°C in the DSC curves of NTMS and NTPFBu (Figure 4.5) are due to the melting of the hydrophobic nanocrystalline domains of the nN117 that consist of fluorocarbon chains [11]. In the case of the nN117 membrane, the melting of the nanocrystalline hydrophobic domains is identified by a large peak that spans from 30 to 150°C [7] and occurs about 50 to 60°C lower than in the NTMS and NTPFBu membranes. Finally, at temperatures higher than 160°C, the endothermic peaks present in each of the DSC profiles of NTMS, NTPFBu and nN117 are due to the melting of microcrystalline hydrophobic domains of the nN117 membrane formed by fluorocarbon chains [7,10-12]. The enthalpies of fusion for the microcrystalline hydrophobic domains, ΔH_{mc}, are 31.5, 46.7 and 15.1 $J \cdot g^{-1}$ for nN117 [7], NTMS and NTPFBu, respectively. These values indicate that nN117 has a degree of microcrystallinity in the hydrophobic domains between that of NTPFBu and NTMS and that the degree of crystallinity of the NTPFBu polymeric matrix is 67% smaller than that of NTMS. The trend in the crystallinity degree of the hydrophobic perfluorinated microdomains of doped membranes is the opposite of that of the ionic liquids present within nN117. The polymer matrix in NTMS shows a higher degree of crystallinity than NTPFBu, while TMS is completely dispersed in the bulk material and TPFBu is partially crystallized. This behaviour can be explained by considering that the presence of a highly dispersed ionic liquid (e.g. TMS) inside the polar domains of the nN117 matrix allows the ionic liquid with a low steric hindrance and thus, with small nanoaggregates sizes to more efficiently plasticize the nN117 side chains which allows increased motion of host fluorocarbon polymeric matrix. As a result of these two effects, TMS acts as a very efficient plasticizing agent. In contrast, the presence of partially-ordered ionic liquid domains with larger sizes like those detected in pristine TPFBu inside nN117 hampers the possibility for long-range ordering of the fluorocarbon chains and limits the total degree of crystallinity of the host polymer because of its rigidity and formation of ordered nanostructures in the hydrophilic domains of the membranes. DSC measurements elucidate thermal transitions

in these materials, which reveal that a stronger PCIL-nN117 interaction (plasticization phenomenon) stimulates the organization of the nN117 fluorocarbons chains into a microcrystalline structure. Specifically, the DSC results show that: (a) the glass transition temperature of ionic liquids is about -20°C and both pristine ionic liquids undergo two melting processes, which occur at the temperatures of 20 and 38.4°C for TMS and 17 and 61.3°C for TPFBu, respectively; (b) the confinement of the ionic liquids inside the doped membrane reduces their degree of crystallinity (by 37% for TPFBu and by 100% for TMS); and (c) the degree of micro-crystallinity of the NTPFBu fluorocarbon chains is approximately 67% smaller than that of NTMS.

4.3.3 Dynamic mechanical studies

The effect of the PCIL-nN117 interactions on the mechanical properties and the structural relaxations of the doped membranes was investigated by measuring the temperature dependent spectra of the elastic modulus (E'), loss modulus (E'') and tanδ, shown in parts a, b and c of Figure 4.6, respectively. These profiles show a loss of mechanical properties in the doped membranes at temperatures greater than 140°C, while this does not occur until temperatures greater than 150°C for nN117. Above -80°C, the elastic modulus for the membranes containing the ionic liquids is clearly inferior to that of nN117. Values of E' for all three systems are reported for -50, 50 and 100°C in Table 4.3.

Table 4.3 Elastic modulus (E') of nN117, NTMS and NTPFBu measured at T = -50, 50 and 100°C.

	E' /MPa		
Membrane	**T / -50°C**	**T / 50°C**	**T / 100°C**
nN117	1248	326	13
NTPFBu	1061	60	0.7
NTMS	191	10	1.7

The reduction of the mechanical stability range of the doped membranes, in terms of the elastic modulus, is due to the plasticizing effect of the ionic liquids. This effect is enhanced with temperature due to the progressive increase of the fluidity and the solvation effect of the IL domains within the polymeric matrix. In the case of NTPFBu, the profiles of E' and E'' show an abrupt decrease at about 60°C which corresponds to the melting temperature T_{m1} of TPFBu revealed by the DSC measurements. The E' and E'' profiles of NTMS do not show a sharp decrease near the TMS melting temperature, but instead a monotonic decrease starting at approximately -80°C. This trend is consistent with the DSC data for NTMS which showed the absence of the TMS melting peak at approximately 38°C. These results confirm that TMS is completely dispersed at the interfaces between the hydrophobic and hydrophilic nanodomains of the doped membranes because of the formation of an efficient plasticizing solvation shell on the surface of hydrophobic and hydrophilic domains of nN117 host material.

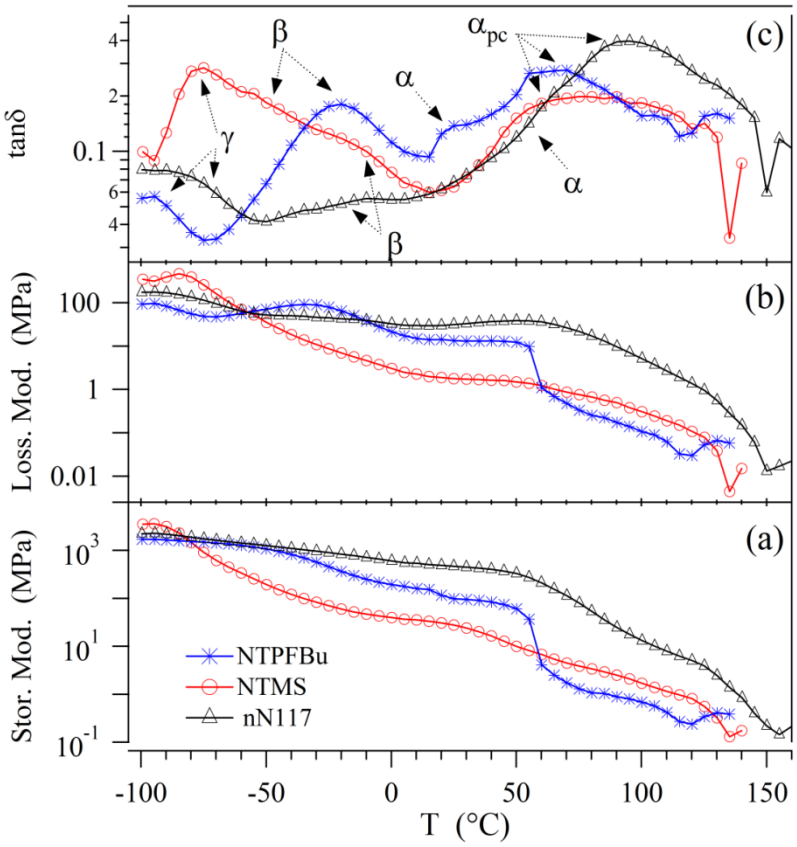

Figure 4.6 DMA profiles of NTMS, NTPFBu and nN117. The graphs show the behaviour of: a) the elastic modulus (E'); b) the loss modulus (E''); and c) tanδ with respect to the temperature.

By comparing the elastic modulus of the doped membranes both in Figure 4.6 a and Table 4.3, it is observed that from -80 to 60°C NTPFBu shows higher values of E' than NTMS. This difference in E' values is attributed to: (a) the difference in the dimensions of the nanodomains of the PCILs, which is a result of the molecular dimensions of the constituent anions (both PCILs include triethylammonium as the cation) and their interactions with the polymeric matrix; and (b) the difference in structural organization of the PCILs when they are present inside the interfaces between the hydrophobic-hydrophilic nanodomains of polymeric membranes. TPFBu nanoclusters are larger because they contain the perfluorobutanesulfonate anion, which has an extended perfluorinated chain unlike the much smaller methyl group in the methanesulfonate anion of TMS. Below 20°C, when both PCILs contained inside the polar domains of the polymer membrane are expected to be in the solid state, the steric hindrance of the nanodomains of TPFBu is greater than that of TMS, resulting in an increased elastic modulus for NTPFBu. Furthermore, below the PCILs melting point, TPFBu in NTPFBu is partially organized in an ordered nanostructure, while TMS is highly dispersed within the NTMS membranes. Consequently, the difference in the structural organization of the PCILs at the interfaces between hydrophobic and hydrophilic domains of the nN117 host material results in a reduction of the mechanical properties of NTMS as compared to NTPFBu.

Part c of Figure 4.6 shows the tanδ profiles of the PCIL-doped membranes and nN117. According to the DMA results reported in Chapter 3 for $\{Nafion/[(ZrO_2)\cdot(Ta_2O_5)_{0.119}]\Psi_{ZrO_2}\}$ membranes, the transition present at approximately 100°C is attributed to the α_{pc} mechanical relaxation related to the long-range movement of the fluorocarbon domains and side chains of Nafion [7,11,13,14]. When comparing the doped membranes to nN117, the α_{pc} peak shows a reduction in intensity and a shift to slightly lower temperatures with a maximum at approximately 70°C. This behavior has been reported in the literature for similar systems [13,

14]. The trend in the α_{pc} peak suggests that the energy dissipated in the long-range motion of both the nN117 primary and secondary structure during the α_{pc} transition is higher in nN117. This is due to the steric hindrance and weak Van der Waals interactions within the polar domains between the different $TEAH^+$-neutralized anionic side groups. In the doped membranes, the energy dissipated is very small since the polar side groups, which are neutralized by the $TEAH^+$ cation, are solvated and plasticized by the ionic liquid resulting in the reduction of the dipolar interactions within the hydrophilic domains of the membrane. The α_{pc} peak of the doped membranes is broader than in nN117 because of the superposition of PCIL melting in this temperature range.

The analysis of tanδ profiles for the temperatures from 0 to 50°C also reveals the presence of α–type relaxations associated with the mechanical energy dissipated by the segmental motion of the fluorocarbon backbone chain of nN117 [11, 13]. As seen above with the α_{pc} transition, in the doped membranes the α-type mechanical relaxation occurs at temperatures lower than that observed for nN117, which shows transitions at *ca.* T_α = 40°C and $T_{\alpha'}$ = 65°C (see Chapter 3). According to the DMA results reported in Chapter 3 for $\{Nafion/[(ZrO_2)\cdot(Ta_2O_5)_{0.119}]\Psi_{ZrO_2}\}$ membranes, α-type transitions occur due to conformational relaxation modes of the fluorocarbon backbone chains of PTFE domains, specifically a $13_6 \rightarrow 15_7$ conformational transition for α and an order-disorder conformational transition for α' [11, 13]. In the PCIL-doped membranes the α transition is found at ca. T_α = 30°C. The reduction of T_α for the NTMS and NTPFBu membranes, as compared to nN117, is attributable to the ionic liquid that solvates and plasticizes the $TEAH^+$-neutralized side group of nN117. The presence of the PCIL reduces the dipolar interactions inside the polar domains of host polymer resulting in a consequent mobility increase of the main fluorocarbon backbone chains. Between -50 and 0°C, the tanδ profiles show a β–secondary mechanical transition that is attributed, according to the DSC analysis, to the

conformational relaxation mode of the polyether side groups. These modes correspond to the fluctuations of the dipole moments associated with the polyether side-chain groups of nN117. The intensity of the β-transition peaks of NTMS and NTPFBu appears to be significantly larger than that of nN117. The presence of PCILs inside of the nN117 polymer matrix causes a reduction in the dipolar interaction crosslinks between the polyether side groups and consequently, increases the number density of nN117 side chains involved in the β-mechanical relaxations. Finally in the tanδ curve shown in Figure 4.6 part c for nN117, there is a mechanical relaxation present at approximately -80°C associated with a γ transition resulting from the relaxation mode associated with the local fluctuations of dipole moments of CF_2 moieties. These CF_2 moieties belong to the main fluorocarbon chains of the PTFE hydrophobic domains of nN117 [15,16]. The intensity and temperature maximum of the γ peak decrease according to the degree of microcrystallinity of the nN117 matrix in the order NTMS > nN117 > NTPFBu. This result indicates that increasing the degree of order in the fluorocarbon hydrophobic domains increases the density of CF_2 groups involved in the γ transition. DMA measurements reveal: (a) the membranes doped with PCILs present a thermal mechanical stability of about 140°C and inferior mechanical properties than nN117, in terms of the elastic modulus E'; (b) the elastic modulus of the doped membranes at lower temperatures depends on the degree of crystallinity and the dimension of embedded PCIL nanoaggregates; and c) there are four mechanical relaxations α_{pc}, α, β, and γ. The α_{pc} and α relaxations in the doped membranes shift to lower temperatures as compared to nN117. This shift is due to the plasticizing effect of the PCIL contained within the membranes. Finally, the γ transition depends on the microcrystallinity degree in hydrophobic domains of the polymeric matrix of nN117.

4.3.4 FT-IR studies

The TMS and NTMS infrared spectra are reported in parts (a) – (c) of Figure 4.7, while those for TPFBu and NTPFBu are in Figure 4.7 parts (d) – (f). Parts (a) and (d), (b) and (e), and (c) and (f) show the IR spectra divided into three spectral regions, 400 to 900 cm^{-1}, 900 to 1700 cm^{-1} and 2000 to 4000 cm^{-1}, respectively. These spectra are compared to the IR spectra of the nN117 found in the literature [7]. Evidence of water is visible in the FT-IR spectra of Figure 4.7c and 4.7f, consistent with TG results. The broad peak between 3700 cm^{-1} and 3200 cm^{-1} is due to vibrational modes arising from water OH stretching motions (see Chapter 3). The breadth of this very weak peak indicates the presence of water molecules with varying hydrogen-bond strengths that are likely present in a range of hydrogen-bonding environments. The intensity of ν(OH) stretching peaks confirms TG measurements, indicating that traces of water are present in investigated materials. The CH_3 and CH_2 antisymmetric and symmetric stretching modes are found between 3000 and 2600 cm^{-1}. The CH stretching modes cover a larger frequency range, in accordance with the spectra of compounds where the CH-containing moieties are located next to a nitrogen atom [17,18], particularly when the nitrogen atom is protonated. All of the examined samples, including the nN117 membrane, have a band at approximately 2500 cm^{-1}. This band is seen in the expanded spectra shown in Figure 4.8 and is associated with the $N\text{-}H^+$ stretching mode of the $TEAH^+$ cation [19,20].

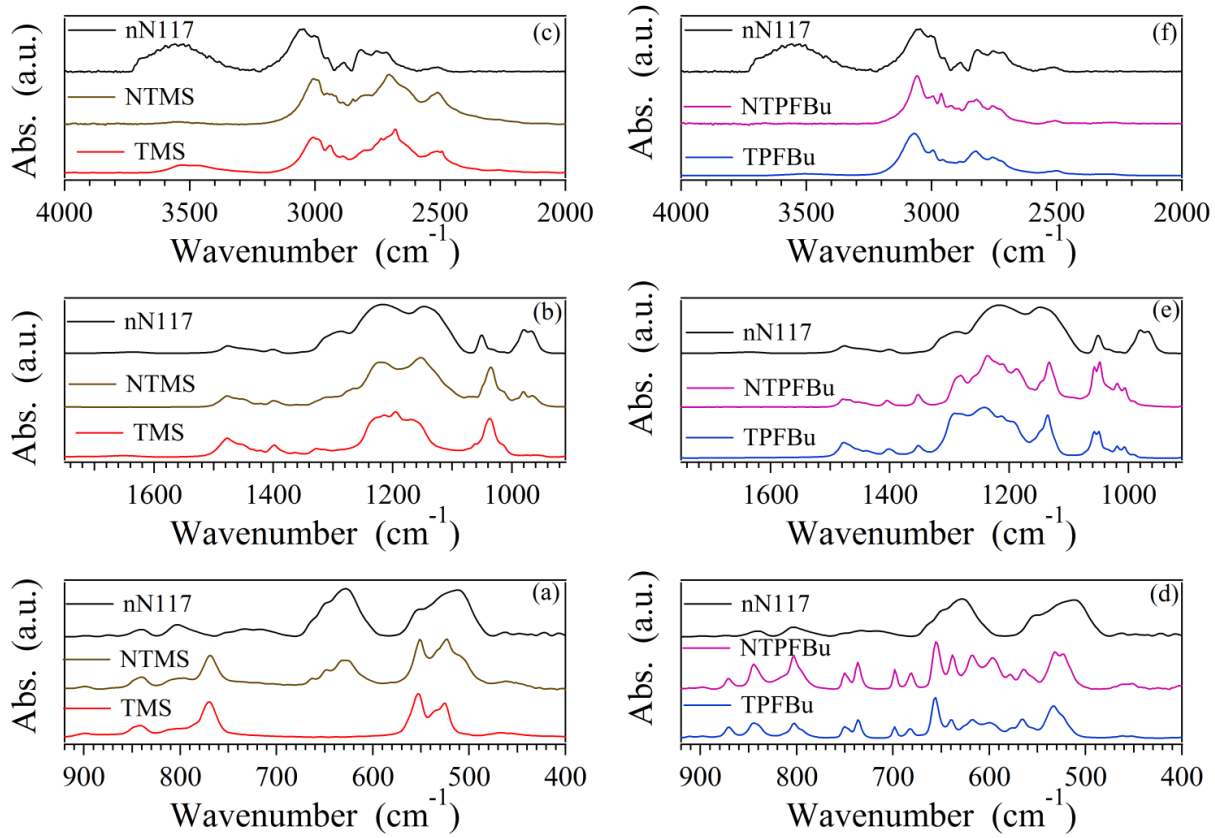

Figure 4.7 Infrared spectra of TMS, TPFBu, NTMS, NTPFBu and nN117. (a) and (d) show the spectral region from 900 to 400 cm^{-1}. (b) and (e) show the spectral region from 1700 to 900 cm^{-1}. (c) and (f) show the spectral region from 4000 to 2000 cm^{-1}. The spectrum of nN117 is taken from the literature [7].

Here, the N-H^+ stretching band contains two spectral features, one at higher frequencies, labelled I at ca. 2530 cm^{-1}, and another at lower frequencies, labelled II ranging between 2512 and 2501 cm^{-1}. There is an additional feature present in the TMS spectrum at 2491 cm^{-1}. The presence of two or three features in the N-H^+ stretching band indicates that the $TEAH^+$ cations are involved in hydrogen-bonding networks of varying strengths. I and II remain when the PCILs are incorporated into the doped membranes, but the peak at 2491 cm^{-1} in TMS is no longer visible in the spectrum. The population of $TEAH^+$ cations responsible for this peak experiences the strongest hydrogen bonds. It is possible that the loss of this cation population may be correlated to the loss of crystallinity when TMS is embedded in the nN117 membranes. Finally, there is a slight shift of feature I in the N-H^+ stretching band to higher frequency when the PCILs are present in the polymeric membrane. This phenomenon is consistent with a weakening of the

hydrogen-bond strength and a reduced interaction between anions and cations of the PCIL in the doped membrane.

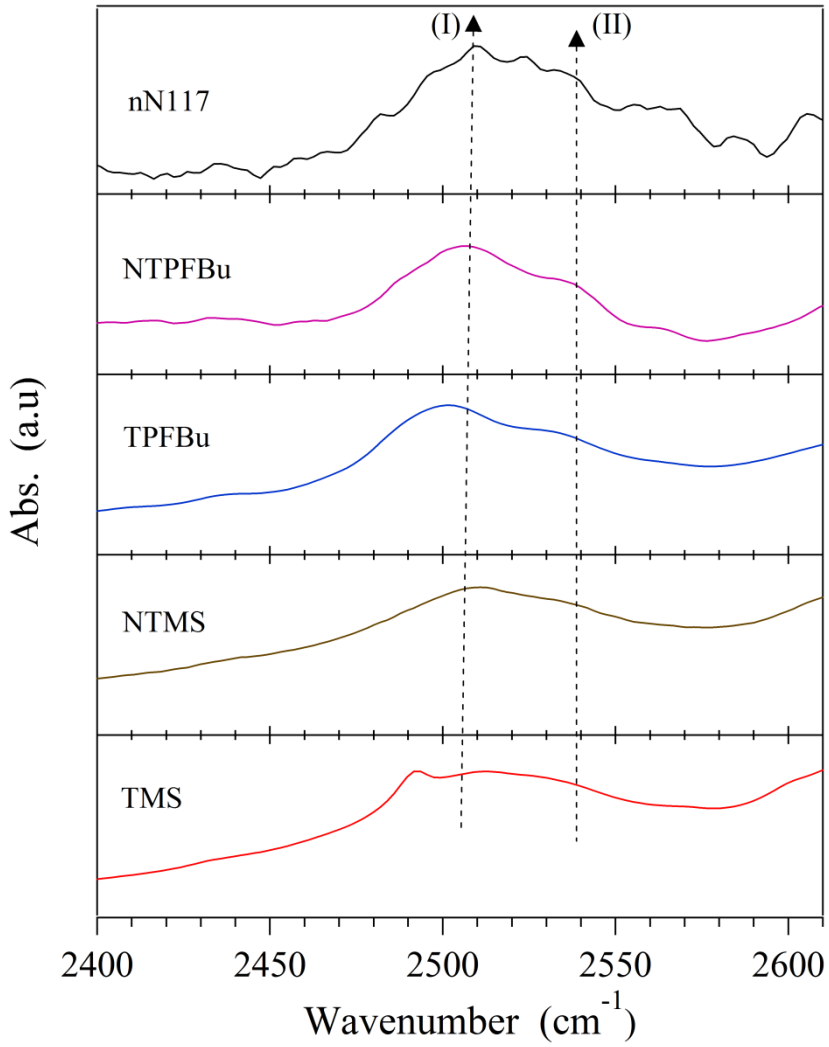

Figure 4.8 Infrared spectra in the spectral region from 2400 to 2610 cm^{-1}. The spectrum of nN117 is taken from the literature [7].

As described in the Chapter 3, the spectral region shown between 1380 and 1080 cm^{-1} (parts b and e of Figure 4.7) primarily contains modes associated with the CF_2 moieties of the nN117 membrane [11-13,21]. These modes are sensitive to the backbone conformation and contain contributions from CF_2 internal coordinates of both the 15_7 and 10_3 helices typical of Nafion [7,11]. Significant differences in the modes can be seen when comparing the bands of NTMS and NTPFBu. In NTMS, while there is evidence of the TMS peaks in the spectrum, the CF_2

band shape remains largely unchanged and still strongly resembles the spectrum of nN117. In contrast, the NTPFBu spectrum more strongly resembles the spectrum of TPFBu and only small contributions from the nN117 matrix can be seen. The IR data in this spectral region suggest that the presence of TPFBu in the nN117 membrane slightly influences the morphology of the hydrophobic domains of the membrane, maintaining primarily the features of both the pristine PCIL and the nN117 phases, while TMS has strong effect on the overall structure of the matrix. Indeed, the main spectral features of the TMS disappears and the profiles of CF regions of nN117 are significantly modified. These results are in agreement with the previously discussed DSC results. This trend also is revealed throughout the entire lower frequency region of the spectra. In general, while the NTMS spectrum can be described as the result of interactions between nN117 and the TMS component, the NTPFBu spectrum is clearly dominated by peaks associated with TPFBu. This trend can be seen also in the C-O-C stretching modes of the polyether side chain visible in the spectrum of nN117 at 980 cm^{-1} and 967 cm^{-1} [7, 11]. These ether modes are clearly present in both the nN117 and the NTMS spectra, but are not visible in the spectrum of NTPFBu. Results indicate that in CF region of: (a) NTPFBu, TPFBu forms PCIL nanodomains of larger size, which are segregated in the bulk membranes; (b) NTMS, TMS is completely dispersed in bulk material and forms a uniform solvation shell on the hydrophobic and hydrophilic domains of the host nN117 polymer owing to the strong nN117···TMS interactions. In detail, as a result of these latter interactions, in NTMS membrane no predominance of the TMS spectral profile is revealed in the CF region. This phenomenon is easily explained if we consider that the spectral features of fluorocarbon backbone hydrophobic domains, which are weaker in intensity in nN117 as compared to the bands of pristine PCILs, are diagnostic vibrational modes of the nN117···TMS interactions.

4.3.5 Broadband electric spectroscopy

For the pure ionic liquids TMS and TPFBu, the imaginary component of the permittivity (ε") and the real component of the conductivity (σ') as function of frequency at temperatures between -150 and 150°C are shown in Figures 4.9 and 4.10, respectively.

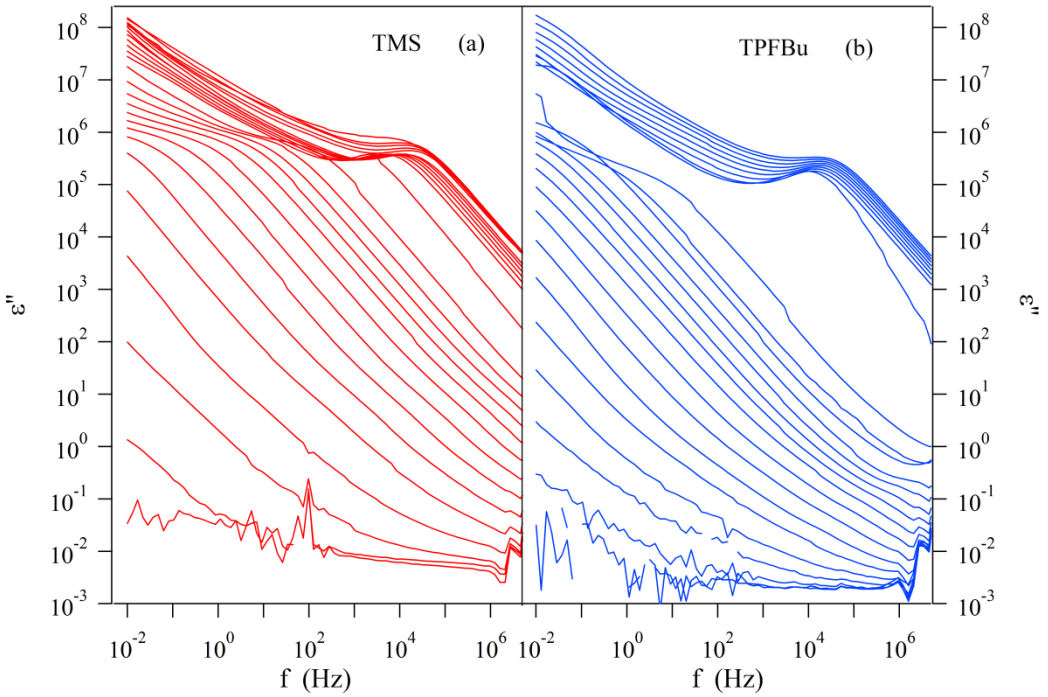

Figure 4.9 Profiles of ε" as a function of frequency at temperatures between -100 and 150°C for PCILs: a) TMS and b) TPFBu.

Several trends are evident in Figure 4.9. Melting of the ionic liquid increases ε" above 30°C for TMS and above 60°C for TPFBu. These data are consistent with DSC measurements. With increasing temperature a peak with values of ε" ranging from 10^5 to 10^6 appears and moves toward higher frequencies. Furthermore, this peak exhibits a large shift to higher frequency at the T_{m1} of the ionic liquids. At temperatures below 0°C and frequencies above 100 Hz the presence of a dielectric relaxation for both TMS and TPFBu is identified by an inflection point in ε". Finally, for lower frequencies and temperatures near and above the PCIL melting point, ε" increases with decreasing frequency.

The σ' spectra, reported in Figure 4.10, undergo a step increase of 2-3 orders of magnitude in conductivity at temperature above the ionic liquid melting temperature T_{m1}. This trend is more evident for TPFBu than TMS. The profiles of σ' show an inflection point, marking the beginning of a plateau that is correlated with the appearance of the intense peaks in the spectra of ε". This plateau indicates the "bulk" conductivity, σ_{DC}, of the ionic liquid [22,23].

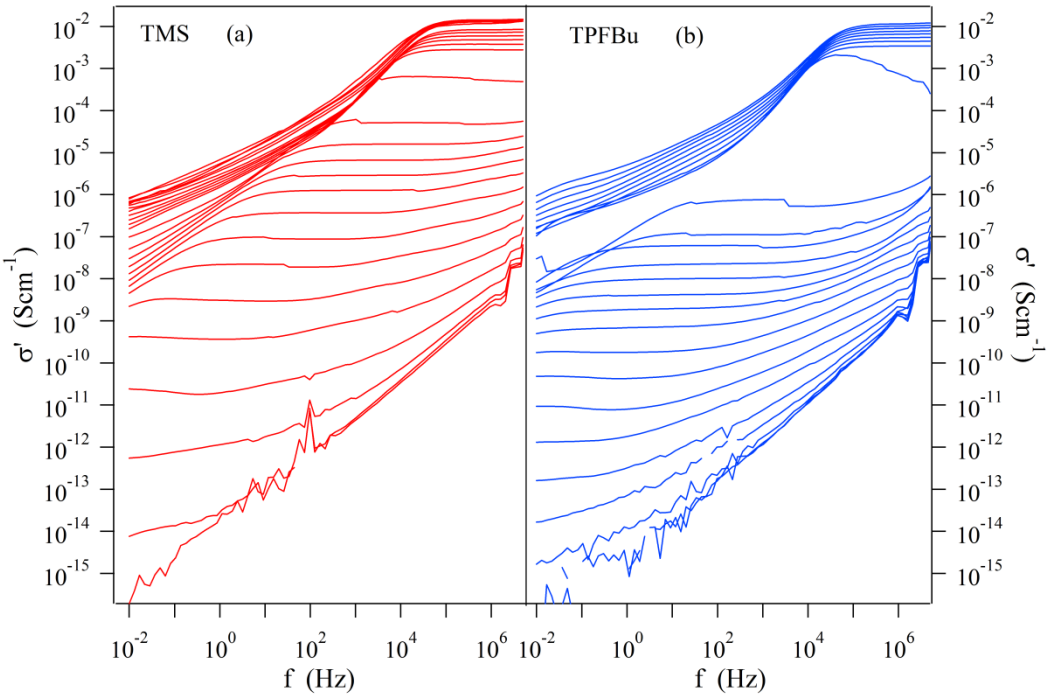

Figure 4.10 Profiles of σ' as a function of frequency at temperatures between -150 and 150°C for PCILs: a) TMS and b) TPFBu.

The presence of the intense peak in ε" and the corresponding decline in σ' indicates that this behaviour corresponds to the electrode polarization event, caused by the measurement electrodes, that block the charge carriers of the PCILs at the interface of the electrode and the electrolyte [24,25]. Profiles of σ', similar to those reported in Figure 4.10, were recently obtained for "imidazolium-based" ionic liquids and resulted from the combination of the bulk conductivity and the electrode polarization [26,27]. Comparing the profiles for the permittivity and the conductivity reported in Figures 4.9 and 4.10 show: a) the increase of σ' below T_{m1} and above 100 Hz due to the presence of a dielectric relaxation; and b) for low frequency and

temperatures close to or higher than T_{m1}, the increase in ε" suggests the presence of interfacial polarization phenomena.

As discussed in the previous section for the {Nafion/[$(ZrO_2)\cdot(Ta_2O_5)_{0.119}$]$\Psi_{ZrO_2}$} membranes (Chapter 3): a) the electrode polarization phenomenon results from the accumulation of charge at the electrode-material interfaces when blocking electrodes are used; b) interfacial polarization occurs in heterogeneous materials due to the accumulation of charge densities at the interfaces between two nanodomains with different dielectric constants and conductivities [24]. For TMS and TPFBu, this scenario could occur assuming the partial formation of nanoaggregates in a variety of morphologies induced by Van der Waals interactions between the alkyl chains in both the cationic and the anionic components of the PCILs. This hypothesis is consistent with the work of Di Noto *et al.* that suggests the ionic liquid triethylammonium trifluoromethanesulfonate (TEATF) confined in the nN117 membrane has a nanostructure in which the triflate anions organize into aggregates [7]. Martinez *et al.* have shown that the presence of the perfluorinated butane chain in TPFBu results in a reduction of the degree of dissociation, as compared to TEATF and TMS, and the possible formation of micellar-like structures [8]. The possibility of aggregation in "dialkyl-imidazolium-based" room temperature ionic liquids (RTILs) was reported by Turton et al. [28]. They found that data from both optical Kerr effect spectroscopy and BES suggested the formation of clusters due to interactions between the imidazolium rings or due to the coupling of the cation alkyl tails. Triolo *et al.* used x-ray diffraction to investigate alkylimidazolium-based RTILs to demonstrate the existence of nanosegregation induced by the presence of the alkyl chains [29,30]. Dyson *et al.* detected the formation of aggregates between 30 and 100°C with a predominance of cationic and anionic complexes such as C_2A^+, $C_3A_2^+$, CA_2^- and $C_2A_3^-$ for N-butylpyridinium tetrafluoroborate using Electrospray Ionization Mass Spectrometry (ESI-MS) [31]. The presence of aggregates in PCILs was discovered 30 years ago by Kholer et al. [32,33] during a study of the thermodynamic and physicochemical properties of

a mixture of acetic acid and triethylamine. They suggested the formation of a A_3B complex (A=acetic acid, B=triethylamine) occurred due to the attractive interactions between the polar molecule AB and an acetic acid dimer [32,33]. Conductometric measurements by Hojo *et al.* [34] showed the formation of aggregates containing ions of the type M_2X^+ (MX_2^-) and M_2X_2 for trialkylammonium salts in the presence of aprotic organic solvents. Using ESI-MS, Kennedy *et al.* found the following for PCILs based on dialkylammonium nitrates: a) ethyl, propyl and butylammonium nitrates formed stable $C_8A_7^+$ nanoaggregates (C=cation, A=anion) where the abundance and stability of these aggregates is independent of the length of the cation alkyl chain; b) anionic aggregates are equally dispersed in clusters of different dimensions; c) the dimensions of the cationic clusters are reduced with increasing order of the amine cations, i.e. from primary, secondary and tertiary amines, due to increased steric hindrance and fewer hydrogens available for the formation of hydrogen bonds; d) the formation of nanoaggregates increases in the presence of anions with higher charge densities, such as the nitrate ion, and decreases with increasing anionic dimension [35]. The literature consistently points out that the PCILs containing primary, secondary and tertiary alkylammonium cations form both ionic and neutral aggregates.

The spectra of ε" and σ' measured for NTMS and NTPFBu shown in Figures 4.11 and 4.12 are very similar to those of their respective PCILs, suggesting that the electric properties of the doped membranes are strongly influenced by the PCIL.

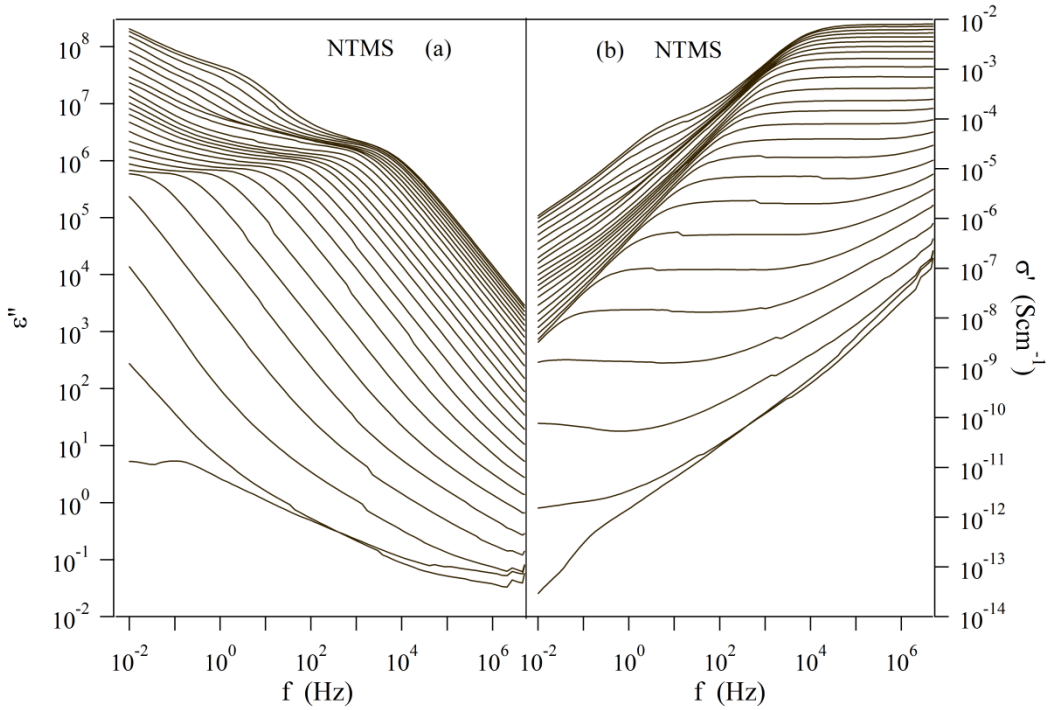

Figure 4.11 Profiles of a) ε" and b) σ' as a function of temperature for NTMS.

The profiles of ε" and σ' of the polymeric membranes reveal: a) the presence of an intense peak due to electrode polarization with values of ε" of the order of 10^6; this peak moves to higher frequency with increasing temperature and corresponds to the beginning of a plateau in σ' associated with the "bulk" conductivity σ_0 of the material; b) the absence of a sharp increase in ε" and σ' for NTMS at the melting point $T_{m1,TMS}$= 38.4°C; c) an increase in the values of ε" and σ' for NTPFBu at $T_{m1,TPFBu}$= 61.3°C; d) the presence of a dielectric relaxation at temperatures below the PCIL melting point and frequencies higher than 100 Hz; and e) an increase of ε" and a decrease of σ' with decreasing frequency for frequencies less than 1000 Hz and temperatures higher than 50°C that suggests the presence of interfacial polarization phenomena.

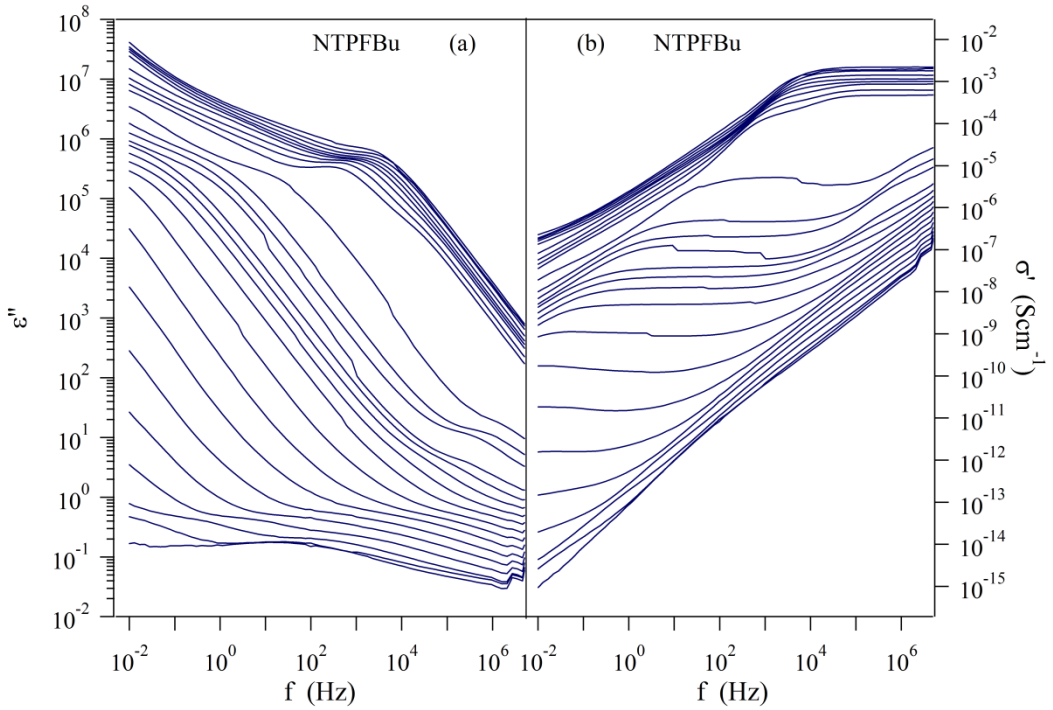

Figure 4.12 Profiles of a) ε" and b) σ' as a function of temperature for NTPFBu.

In the polymer membranes, the presence of interfacial polarizations is due to the accumulation of charge at interfaces between domains with different dielectric constants [7]. The doped membranes are characterized by the coexistence of hydrophobic domains with lower permittivity (≈2.2) consisting of the fluorocarbon chains of nN117 and hydrophilic polar domains with slightly higher permittivities consisting of the anionic groups of the nN117 side chains and the ionic liquids [36,37]. Rollet *et al.* report that hydrated Nafion 117® membranes neutralized with $N(CH_3)_4^+$ have segregated hydrophilic and hydrophobic nanodomains, where the interfaces consist of the negatively charged sulfonate groups and the $N(CH_3)_4^+$ cations [38]. These data suggest the existence of increased interfacial polarization phenomena [7,39]. In the ε" profiles of the PCILs and the doped membranes, dielectric relaxations can be seen at temperatures below the melting point of the PCILs. These dielectric relaxations can be easily observed by plotting the values of tan δ = ε"/ε' as a function of temperature at three reference frequencies: 20 Hz, 1

kHz and 10 kHz. These plots are shown in Figure 4.13 for the pure PCILs (parts a and d), the doped membranes (parts b and e) and the nN117 matrix (parts c and f) [7].

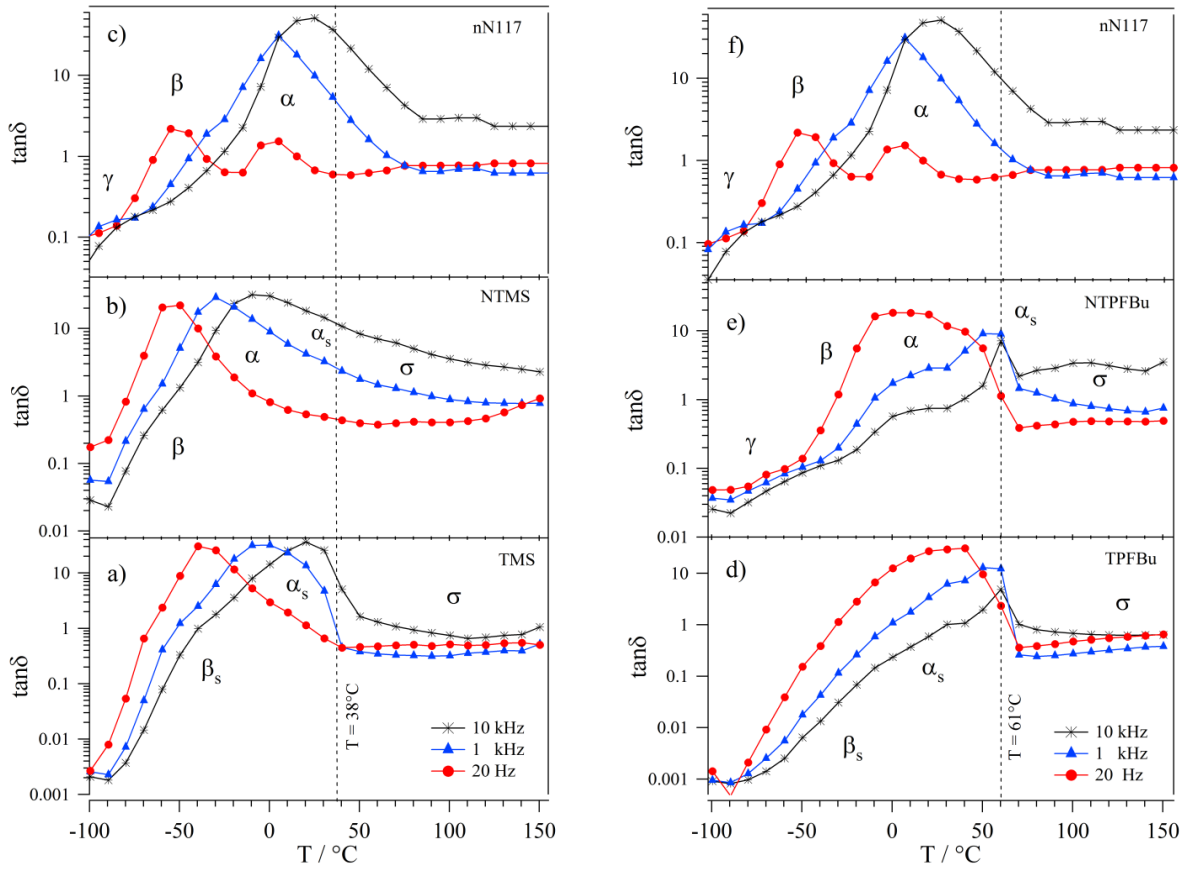

Figure 4.13 Profiles of tanδ as a function of temperature measured at 20 Hz, 1 kHz, and 10 kHz for: a) TMS, b) NTMS, d) TPFBu and e) NTPFBu. For the sake of comparison, parts c) and f) report the profiles of tanδ for nN117 presented by Di Noto *et al.*[4]

Below the melting point, the PCILs exhibit the presence of α_s and β_s relaxations that are associated with a solid state order-disorder transition linked to the glass transition temperature (T_g) and the local "bulk" relaxation modes of the PCILs, respectively [7]. The spectra of nN117 reveals typical α and β relaxations associated with a conformational transition involving the main fluorocarbon chains (α) and the polyether side groups (β) of the nN117 matrix and γ relaxations related to the local fluctuations of the CF_2 groups on the main fluorocarbon chain [7,40]. α_s and β_s are relaxations that are completely different from the α, β, and γ relaxations that occur in membranes. For NTMS and NTPFBu, the profiles of tan δ show the presence of

transitions associated with both the polymeric matrix and the PCILs. Below the PCIL melting points, in agreement with the DSC profiles (see section 4.3.2), there are peaks connected to β modes (T less than 0°C) and α modes (T between 0°C and the melting point). These peaks are associated with the relaxation of the nN117 matrix interacting with the ionic liquid. In agreement with the profiles of tan δ obtained from the DMA analysis (section 4.3.3), the tan δ spectra of the membranes (Figure 4.13) show the appearance of the electric α_{pc} transition at temperatures above approximately 70°C. As previously described, the α_{pc} transition derived from the long-range movement of the fluorocarbon chains and the side groups due to reduced electrostatic interactions between the dipolar domains [11,12]. In addition, for NTPFBu at temperatures below -50°C, there is a γ transition related to the short-range molecular fluctuations of the CF_2 groups belonging to main nN117 fluorocarbon chain [40].

For all the investigated materials, to determine the conductivity values and to investigate the relaxation times associated with the polarization phenomena and the dielectric relaxations, the experimental profiles of $\varepsilon^*(\omega)$ and $\sigma^*(\omega)$ are fit with Equation 4.2 [7,39-41] (see Appendix B).

$$\varepsilon^* = \sum_{k=0}^{2} \frac{\sigma_k}{i\omega\varepsilon_0} \frac{(i\omega\tau_k)^{\gamma_k}}{[1+(i\omega\tau_k)^{\gamma_k}]} + \sum_{j=1}^{2} \frac{\Delta\varepsilon_j}{\left[1+\left(i\omega\tau_j\right)^{\mu_j}\right]} + \varepsilon_\infty \qquad (4.2)$$

The relation between the complex electric permittivity $\varepsilon^*(\omega)$ and the complex electric conductivity $\sigma^*(\omega)$ is given by Equation 4.3.

$$\sigma^*(\omega) = i\omega\varepsilon_0\varepsilon^*(\omega) \qquad (4.3)$$

The first term of equation 4.2 accounts for the electrode (*k=0*) and interfacial (*k=1,2*) polarization phenomena. The variables σ_k and τ_k are the conductivity and relaxation time associated with the k^{th} polarization event, while γ_k is a shape parameter that describes the broadness and asymmetry of the k^{th} peak. The second term of equation 4.2 expresses the dielectric relaxation through a Cole-Cole type equation [42]. Specifically, $\omega = 2\pi f$ is the angular

frequency of the electric field, τ_j is the relaxation time of the j^{th} event of intensity $\Delta\varepsilon_j$, and μ_j is a shape parameter bound to the distribution of the relaxation times associated with the j^{th} event. Equation 4.2 is used to simultaneously fit the experimental spectra of tan δ, ε', ε", σ' and σ" which were determined from the permittivity spectra from Equation 4.3. The experimental data are fit using: a) one conductivity σ_0 and two dielectric relaxations, α and β at temperatures less than the melting point of the ionic liquids; and b) three conductivity terms σ_0, σ_1 and σ_2 at temperatures higher than the ILs melting point.

As example, the conductivity components determined by fitting the experimental data with Equation 4.2 are shown below in Figure 4.14 in the spectra of σ' at 120°C for TMS and TPFBu.

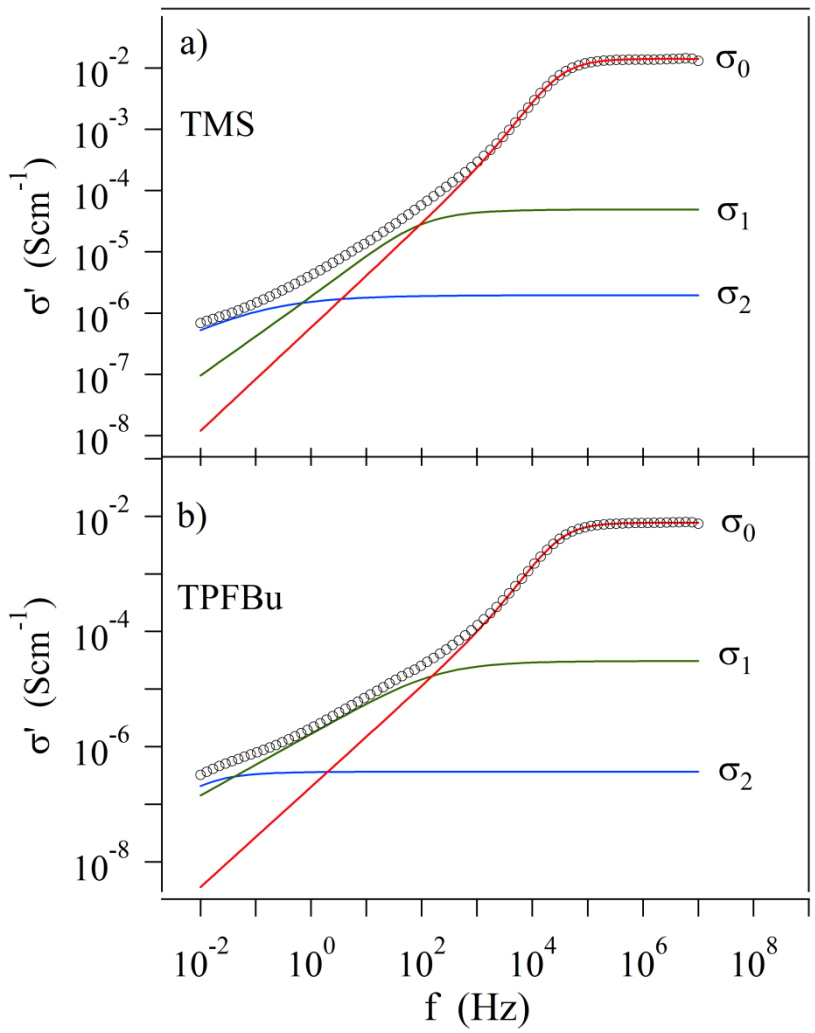

Figure 4.14 Spectra of σ' as a function of frequency measured at 120°C for TMS (a) and TPFBu (b). σ_0, σ_1 and σ_2 are the conductivities associated with polarization phenomena.

The values of the conductivities σ_0, σ_1, and σ_2 are reported as a function of reciprocal temperature for TMS and TPFBu in Figure 4.15. The values of σ_0 determined by the fit correspond to those read directly from the high frequency plateau of the σ' spectra [11,22,23]. In the solid PCILs ($T<T_{m1}$), proton conduction must occur via proton hopping between acid and base sites. The logarithm of σ_0 as a function of reciprocal temperature has a Vogel–Tammann–Fulcher (VTF) form [42]. Furthermore, at temperatures below the PCIL melting points, the $\sigma_{0\,TMS}$ values are about three orders of magnitude higher than those of σ_{0TPFBu}. The higher values of $\sigma_{0\,TMS}$ are attributed to the smaller size of the constituent PCIL anion: TPFBu forms larger nanoaggregates because the perfluorobutane group of TPFBu is larger than the TMS methyl group. This nanometric TPFBu morphology increases the median distance between the proton hopping sites and thus reduces the overall conductivity. At $T<T_{m1}$, the activation energy and the temperature T_0 obtained by fitting $\log(\sigma_0)$ vs. T^{-1} with VTF equation (Chapter 1 and Appendix A) are 16±1 kJ/mol and 124 K for TMS and 21±1 kJ/mol and 112 K for TPFBu.

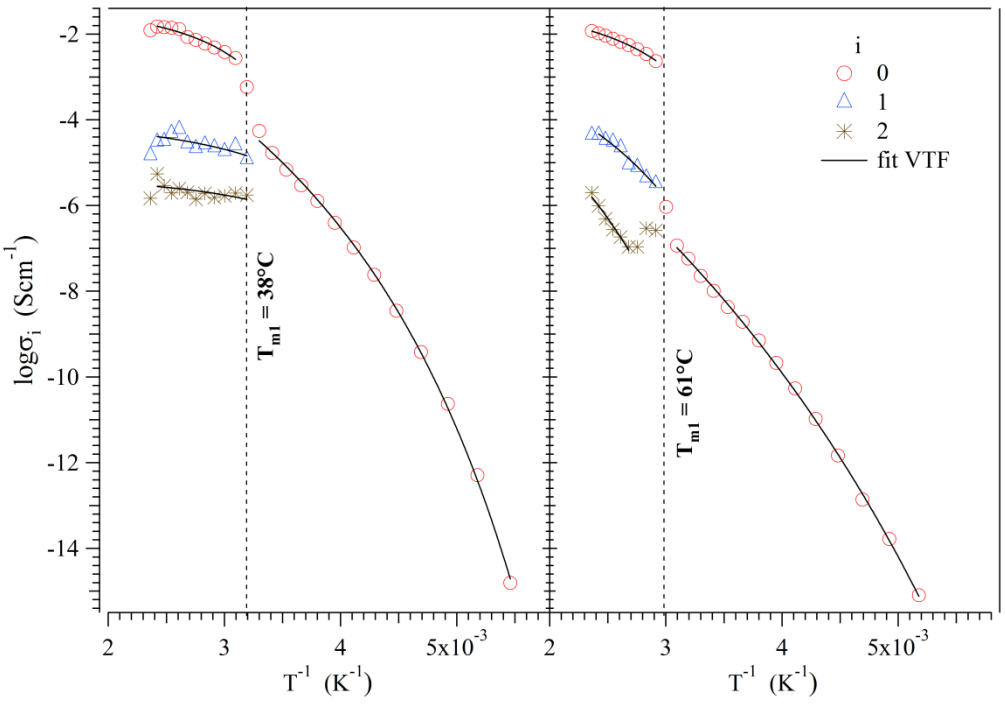

Figure 4.15 Log plot of conductivities σ_0, σ_1 and σ_2 as a function of reciprocal temperature for the PCILs: a) TMS and b) TPFBu. The dashed vertical line shows the melting point of the ionic liquid.

Above the PCIL melting points, the log(σ_0) vs. reciprocal temperature follows VTF-like behaviour and yields activation energies of 2.3±0.1 kJ/mol and 3.2±0.1 kJ/mol for TMS and TPFBu respectively. These values are in agreement with PCIL activation energies between 3.4 and 5.3 kJ/mol reported by Iojoiu *et al.* [43]. For TEATF, Di Noto *et al.* determined an activation energy for conduction of the "bulk" material of 1.37±0.04 kJ/mol above the melting point [7]. For TMS and TPFBu, the values of T_0 obtained from the VTF fit are 245 K and 241 K, respectively. These values are in agreement with the T_g values of these PCILs determined by DSC measurements. Above the T_{m1}, $\sigma_{0\ TMS}$ is larger than $\sigma_{0\ TPFBu}$ because of the higher viscosity of the fluorinated ionic liquid [8]. At 120°C, $\sigma_{0\ TMS}$ and $\sigma_{0\ TPFBu}$ are 0.0137 and 0.0076 Scm^{-1}, respectively. The σ_0 values enable calculation of diffusion coefficients for ions involved in the long-range conduction through the Nernst-Einstein equation [44].

$$D = \frac{\sigma_0 RT}{F^2 c} \tag{4.4}$$

In Equation 4.4, F is Faraday's constant, c is the molar concentration of the ionic liquid, T is degrees Kelvin and R is the universal gas constant. The diffusion coefficients from 100 to 150°C are found to be between 5×10^{-7} and 1×10^{-6} cm^2s^{-1} for TMS and between 5.3×10^{-7} and 1.3×10^{-6} cm^2s^{-1} for TPFBu.

Judeinstein *et al.* measured diffusion coefficients of several PCILs containing the $TEAH^+$ cation using pulse field gradient nuclear magnetic resonance (PFG-NMR); they obtained similar diffusion coefficient values for protons (D^+), anions (D^-) and triethylamine (D^{TEA}) [45]. Martinez *et al.* reported diffusion coefficients determined with PFG-NMR at 120°C of $D^+=2.71\times10^{-6}$ cm^2s^{-1}, $D^{TEA}= 2.67\times10^{-6}$ cm^2s^{-1} and $D^-=2.38\times10^{-6}$ cm^2s^{-1} for TMS and for TPFBu values of $D^+=1.14\times10^{-6}$ cm^2s^{-1}, $D^{TEA}=1.13\times10^{-6}$ cm^2s^{-1} and $D^-=8.43\times10^{-7}$ cm^2s^{-1} [8]. Almost identical values were found for all species in diethylmethylammonium trifluoromethanesulfonate $\approx 4\times10^{-6}$ cm^2s^{-1} at 120°C by Lee *et al.* [46]. The diffusion coefficients determined at 120°C with

Equation 4.4 are $D^{ch} = 9.1\times10^{-7}$ cm^2s^{-1} for TMS and $D^{ch} = 7.9\times10^{-7}$ cm^2s^{-1} for TPFBu and are of the same order of magnitude as the D^+, D^- and D^{TEA} values reported by Martinez et al. [8]. It is noteworthy that diffusion coefficients estimated from conductivity measurements are generally lower than those obtained from PFG-NMR because PFG-NMR examines local dynamics, while conductivity measures long-range migration [8,45]. In contrast, the self-diffusion coefficients of cations derived from conductivity measurements and PFG-NMR are very similar for an aqueous electrolyte solution containing the TEA cation [47]. In PCILs like those presented here the mesoscopic structure, which is based on the cations and anions aggregates, results in a differentiation between the long range charge migration and the local charge migration. The local charge migration detected by NMR is associated with the exchange of protons between different neighboring Lewis base sites, while the long range charge migration in bulk PCILs is directly related to the charge migration between aggregates and therefore depends on the mesoscopic morphology of the materials. However similar values for the diffusion coefficients obtained from BES measurements and PFG-NMR [8] indicate that the mobility of protons, anions and cations in the PCILs are comparable and that all three species participate in the mechanism of charge conduction. This suggests that proton conduction occurs through a vehicular-type mechanism where the proton is transported by the TEA cation ($D^+ \approx D^{TEA}$). However, this mechanism does not explain a diffusion coefficient for the anion that is almost the same as that for the proton and TEA, particularly in the case of TPFBu considering the difference in the molecular mass of the TEA cation (101 $gmol^{-1}$) and the perfluorobutanesulfonate anion (300 $gmol^{-1}$).

Martinez *et al.* have shown that TMS and TPFBu are partially dissociated by comparing the experimental conductivity (σ_{exp}) with those calculated from the diffusion coefficients D^+ and D^- (σ_{calc}). These authors estimate degrees of dissociation of 35% and 22% at 120°C for TMS and TPFBu [8], respectively, and ascribe the lower degree of dissociation for TPFBu to the partial

formation of ionic micellar-like aggregates. The literature results and the appearance of phenomena attributed to interfacial polarization in the electric spectra (Figure 4.15) suggest that ionic liquids exist as nanoaggregates composed of both ionic and neutral species. The presence of these nanoaggregates is due to the formation of hydrogen bonds between the polar heads of the PCIL constituent ions and Van der Waals interactions between the nonpolar groups of the PCIL cations and the anions. These nanoaggregates contain proton-acceptor ($-SO_3^-$, TEA) and proton-donor sites ($-SO_3H$, $TEAH^+$) that participate cooperatively and simultaneously in the mechanism of proton transport via short-range inter- and intra-cluster transfer according to the mechanism reported in Scheme 4.2. On a local scale, the mechanism of charge transfer shown in Scheme 4.2 is the result of proton hopping between the donor and acceptor sites of ionic and neutral nanoaggregates present inside the PCILs indicating a Grotthuss-like process. The transfer of protons involves a constant exchange of the ionic species ($-SO_3^-$, $TEAH^+$) and their respective neutral forms ($-SO_3H$, TEA), which is limited by the rate of proton exchange resulting in $D^+ \approx D^- \approx D^{TEA}$ in accordance with the results of Martinez *et al.* [8].

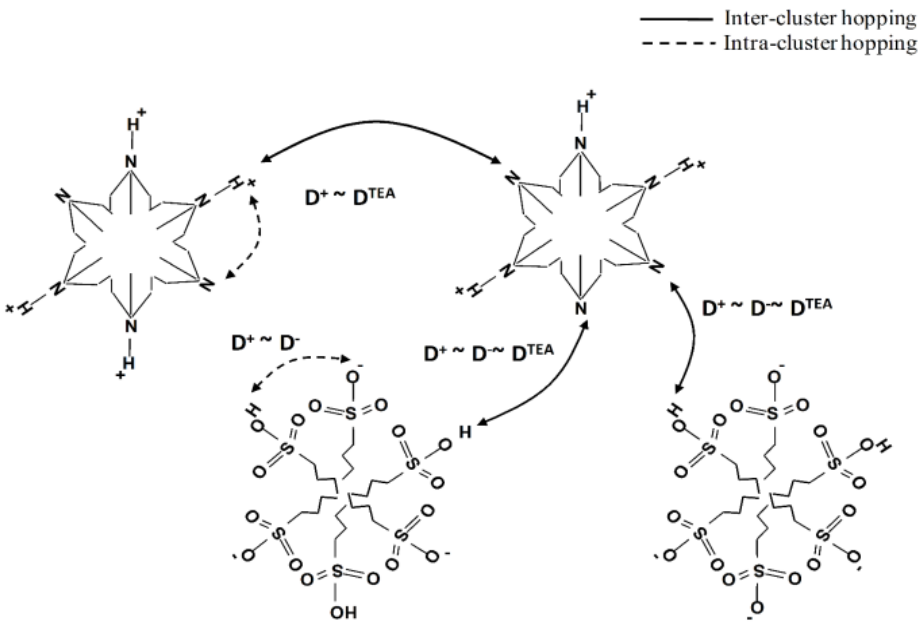

Scheme 4.2 Short-range mechanism of charge transfer due to proton hopping between the proton-donor and proton-acceptor sites of the ionic and neutral nanoaggregates present in the PCILs.

BES measurements reveal three different PCIL conductivities, σ_0, σ_1 and σ_2 that could contribute to the long-range mechanism of charge conduction. Consideration of the PCIL nano-morphologies described above suggests the existence of three contributions to the long-range mechanism of proton transfer:

1) *Cationic-Cationic "Homosite" Hopping (CCHH);* This processes describes proton transfer through cationic clusters (C^{m+}, C^{p+}) according to Reaction 4.5.

$$[(TEAH)_m^+(TEA)_n]^{m+} + \left[(TEAH)_p^+\,(TEA)_q\right]^{p+}$$
$$\leftrightarrow [(TEAH)_{m-1}^+(TEA)_{n+1}]^{(m-1)+} + \left[(TEAH)_{p+1}^+\,(TEA)_{q-1}\right]^{(p+1)+}$$
$$C^{m+} + C^{p+} \leftrightarrow C^{(m-1)+} + C^{(p+1)+} \tag{4.5}$$

2) *Cooperative Cationic-Cationic Anionic-Anionic "Homosite" Hopping (CoCC&AA):* This relaxation event describes a proton transfer process which occurs through a concerted mechanism between the cationic clusters (C^{m+}, C^{p+}) and between anionic clusters (A^{x-}, A^{z-}) according to Reactions 4.6 and 4.7 that occur simultaneously.

$$[(TEAH)_m^+(TEA)_n]^{m+} + \left[(TEAH)_p^+\,(TEA)_q\right]^{p+}$$
$$\leftrightarrow [(TEAH)_{m-1}^+(TEA)_{n+1}]^{(m-1)+} + \left[(TEAH)_{p+1}^+\,(TEA)_{q-1}\right]^{(p+1)+}$$
$$C^{m+} + C^{p+} \leftrightarrow C^{(m-1)+} + C^{(p+1)+} \tag{4.6}$$

$$\left[(A)_{x+1}^-\,(AH)_{y-1}\right]^{(x+1)-} + [(A)_z^-\,(AH)_w]^{z-} \leftrightarrow \left[(A)_x^-\,(AH)_y\right]^{x-} + [(A)_{z+1}^-\,(AH)_{w-1}]^{(z+1)-}$$
$$A^{(x+1)-} + A^{z-} \leftrightarrow A^{x-} + A^{(z+1)-} \tag{4.7}$$

3) *Cationic-Anionic "Heterosite" Hopping (CAEH):* In this case the relaxation phenomenon takes in account a proton transfer process that occurs directly between cationic (C^{n+}) and anionic clusters (A^{m-}) as in Reaction 4.8.

$$C^{(m+1)+} + A^{z-} \leftrightarrow C^{m+} + A^{(z-1)-} \quad (4.8)$$

Reactions 4.5 – 4.8 imply that two conditions must be satisfied for long-range proton conduction to occur: 1) the PCILs must be partially dissociated; this condition is satisfied according to the results of Martinez *et al.*[8]; and 2) reactions 4.5 – 4.8 must possess a significant degree of reversibility. For the sake of clarity, it is possible to represent the processes CCHH, CoCC&AA and CAEH through the structures shown in parts a, b, and c of Scheme 4.3, respectively. The CCHH mechanism involves the transfer of protons from a weak acid cluster C^{m+} ($TEAH^+$, pKa=10.8) to a weaker acid cluster, C^{p+} with m>p. In this case, the difference in Gibbs free energy between final and initial states is small so subsequent transfer events, which require that the reverse processes occur easily and frequently, allow an efficient long-range migration of charge. The CoCC&AA mechanism involves the transfer of protons through cationic clusters and the simultaneous transfer of protons between anionic clusters in the opposite direction. The CoCC&AA mechanism can be viewed as a long-range extension of the dynamics of local proton transfer.

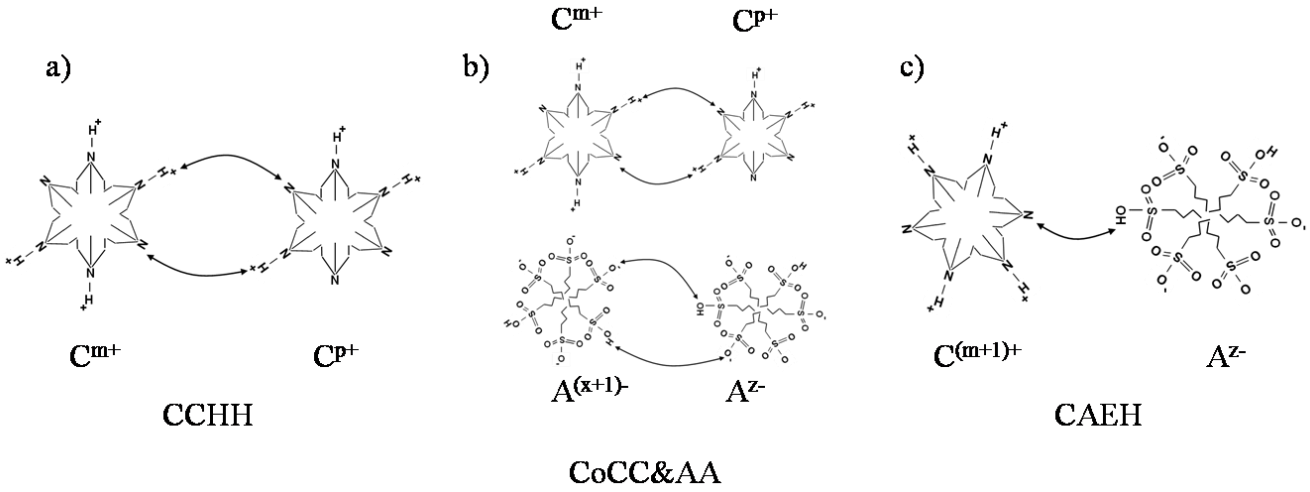

Scheme 4.3 Mechanism of long-range proton conduction: a) CCHH, b) CoCC&AA and c) CAEH.

The difference in free energy associated with proton transfer between anionic clusters is larger than the energy difference associated with the cationic clusters due to the presence of the strong

acid functionality R-SO_3H, where pKa=-2 for R=CH_3 and pKa=-13.2 for R=C_4F_9 [8]. This effect reduces the overall reversibility of the anionic exchange required for proton hopping and the conductivity values associated with the CoCC&AA mechanism as compared to the CCHH mechanism. The CAEH mechanism, that describes proton transfer between cationic and anionic nanoaggregates, strongly favors the passage of protons from strong acids to TEA. Due to the larger difference in free energy between the initial states (R-SO_3H, TEA) and the final states (R-SO_3^-, $TEAH^+$), reprotonation of the anion of a strong acid is less favorable. This significantly inhibits the overall process of conduction associated with this mechanism. In this scenario, a mechanism for charge transfer can be derived from the BES measured conductivities and relaxation times. The conductivity σ_0 and the corresponding relaxation time τ_0 are associated with the CCHH mechanism, where the protons are transferred by a hopping mechanism between cationic clusters. These events involve the highest values of conductivity and are associated to the smallest relaxation time indicating the highest proton mobility. The conductivity σ_1 (associated with τ_1) is associated with the CoCC&AA mechanism and involves proton exchange between cationic clusters, which must correspond to a simultaneous exchange of protons between anionic clusters. It is clear that this event occurs at a longer relaxation time and is less frequent than the CCHH process. Finally, the CAEH mechanism is ascribed to the lowest conductivity values σ_2 and the longest relaxation times because of the low probability associated with the mutual transfer of protons between cationic and anionic clusters.

From the profiles reported in Figure 4.15, conductivities σ_1 and σ_2 are between 10^{-7} and 10^{-4} S/cm and show VTF behaviour as a logarithmic function of reciprocal temperature. Activation energies for these conductivities are $E_{\sigma 1}$=2.0 ± 0.5 kJ/mol and $E_{\sigma 2}$=0.7 ± 0.3 kJ/mol for TMS and $E_{\sigma 1}$=7.9 ± 0.5 kJ/mol and $E_{\sigma 2}$=15 ± 1 kJ/mol for TPFBu. The activation energies associated with the conductivities σ_1 and σ_2 for TMS are not substantially different and are lower than those associated with TPFBu. This implies that the energy difference between the cationic and anionic

clusters of TMS is smaller than the same difference in TPFBu. Thus, exchange between these clusters is thermodynamically favourable for TMS. For TPFBu, $E_{\sigma 2}$ is equal to approximately $2E_{\sigma 1}$. The activation energy $E_{\sigma 2}$ associated with the CAEH mechanism is much higher than the other activation energies because it involves protonation by a weak acid, TEAH+, to form a superacid, PFBuH. In summary, pure TMS and TPFBu above the T_{m1} consists primarily of cationic and anionic nanoaggregates. The mechanism of proton conduction involves proton transport between these nanoclusters. The σ_0 conductivity can be described as proton hopping between the cationic nanoclusters, while conductivities σ_1 and σ_2 are associated with conduction involving both the cationic and anionic nanoaggregates.

Conductivities σ_0, σ_1 and σ_2 for NTMS and NTPFBu obtained by fitting the experimental data with Equation 4.2 are plotted versus reciprocal temperature in Figure 4.16.

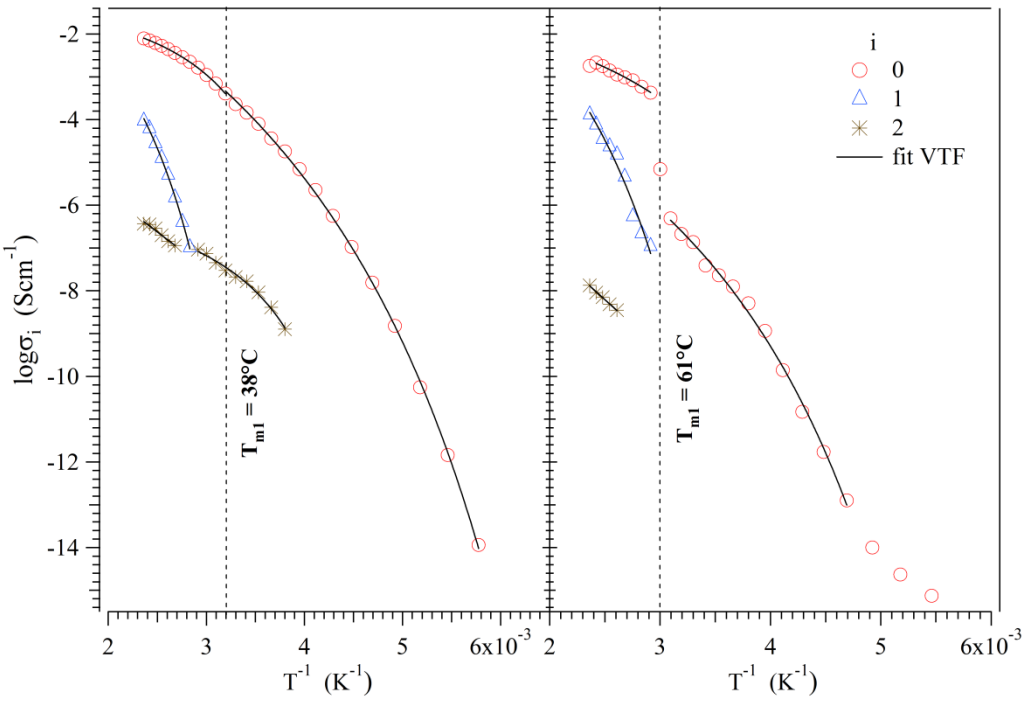

Figure 4.16 Log plot of conductivities σ_0, σ_1 and σ_2 as a function of reciprocal temperature for the doped membranes: a) NTMS and b) NTPFBu. The dashed vertical line shows the melting point of the ionic liquid.

NTPFBu shows a jump in conductivity σ_0 at the T_{m1} of TPFBu (61°C), while presenting VTF behaviour above and below the T_{m1}. In contrast, there is no discontinuity at the TMS melting

point (T_{m1} = 38°C) in the σ_0 conductivities of NTMS (according with the DSC and DMA results) and the data exhibit a VTF-type trend that is divisible into two regions: one above and one below the TMS T_{m1}. Between 70 and 150°C, where both ionic liquids are expected to be present in liquid nanodomains inside the polymeric membrane, the conductivity σ_0 of NTMS is larger than that of NTPFBu. At 120°C $\sigma_{0,NTMS}$= 0.0053 Scm^{-1} and $\sigma_{0,NTPFBu}$= 0.0014 Scm^{-1}. Conductivity depends on the concentration and mobility of free charge carriers. The membranes contain a similar number of moles of the PCILs per sulfonic acid group, as shown in the TG measurements, so the reduction of the NTPFBu conductivity as compared to NTMS is due to a lower mobility of the free charge carriers in the membrane. This reduced mobility results from: 1) the higher viscosity of TPFBu ionic liquid [8]; and 2) the presence of TPFBu nanoaggregates in the polymer membrane that are larger in dimension than those of TMS, probably due to perfluorobutane chains that tend to organize in a micellar-like structure [7]. The activation energies $E_{\sigma 0}$ are obtained by fitting the values of σ_0 with the VTF equation at temperatures above and below the PCIL T_{m1}. These $E_{\sigma 0}$ are reported for the membranes and their respective pure ionic liquids in Table 4.4. Also shown in Table 4.4 are the activation energies, E_{f0}, obtained from fitting the frequency values f_0 with a VTF equation [23,42] (data not shown) above and below the PCIL T_{m1}, where $f_0=1/(2\pi\tau_0)$ and τ_0 is the relaxation time associated with the conductivity σ_0.

Table 4.4 Values of the activation energy $E_{\sigma 0}$ and E_{f0} for TMS, TPFBu, NTMS and NTPFBu.

	LT ($T<T_{m1}$)		**HT ($T>T_{m1}$)**	
	$E_{\sigma 0}$ ($kJmol^{-1}$)[a]	***E_{f0} ($kJmol^{-1}$)[b]***	***$E_{\sigma 0}$ ($kJmol^{-1}$)[a]***	***E_{f0} ($kJmol^{-1}$)[b]***
TMS	16 ± 1	17 ± 1	2.3 ± 0.1	2.2 ± 0.5
NTMS	15 ± 1	13 ± 1	3.9 ± 0.1	3.8 ± 0.1
TPFBu	21 ± 1	18 ± 1	3.2 ± 0.1	1.9 ± 0.1
NTPFBu	15 ± 1	12 ± 1	2.6 ± 0.5	1.7± 0.3

a. Values determined by fitting data of Figures 4.15 and 4.16 with the VTF equation (see Chapter 1).
b. Values determined by fitting data (not shown) with the VTF equation (see Chapter 1).

The activation energies associated with the conductivity and the relaxation times τ_0 obtained for the doped membranes are similar to those obtained for the pure PCILs. This similarity indicates that: 1) the mechanism of long-range charge transfer in the doped mechanism is dependent on the dynamics of the polymer membrane and of the PCILs contained within; and 2) in both membranes, as in the pure PCILs, long-range conduction is due to the transfer of protons between PCIL cationic clusters present inside the polar domains of nN117. In the doped membrane, the sulfonate group is neutralized with TEA. Therefore, the chemical species involved in charge conduction are the same as for the pure PCILs (TEA, $TEAH^+$, $-SO_3H$, $-SO_3^-$). It is important to distinguish between two types of sulfonates: one belonging to the PCIL anion and one bound to the fluorocarbon chain of nN117. As the charged species are the same, the mechanisms of charge conduction described above (CCHH, CoCC&AA, and CAEH) for the pure PCILs can also explain conduction in the doped membrane. Conductivities σ_0, σ_1 and σ_2 can be associated respectively with mechanisms similar to CCHH, CoCC&AA, and CAEH as described for the pure PCILs.

The interfacial conductivities σ_1 and σ_2 appear at temperatures higher than 60°C. The values of σ_1 and σ_2 expressed as a function of reciprocal temperature are fit with the VTF equation (Figure 4.16). From the fitting equation, activation energies are obtained for both membranes: $E_{\sigma 1}$=15.2 ± 0.2 kJ/mol and $E_{\sigma 2}$=6.7 ± 0.5 kJ/mol for NTMS and $E_{\sigma 1}$=19.6 ± 1.2 kJ/mol and $E_{\sigma 2}$=9.5 ± 0.5 kJ/mol for NTPFBu. Considering the activation energies for σ_1 and σ_2, $E\sigma_1$ is approximately equal to $2E\sigma_2$. The activation energies indicate a lower energy barrier for the CAEH mechanism suggesting that this conduction process is facilitated by the host matrix more than the CoCC&AA mechanism. While the activation energies for σ_0 remain almost the same when the PCIL is embedded within the composite membrane, the activation energies $E_{\sigma 1}$ and $E_{\sigma 2}$ (TMS only) exhibit an increase with $E_{\sigma 2} > E_{\sigma 1}$. This behaviour is the opposite of that detected in the

pristine PCILs. This indicates that the distribution of the PCILs inside the nN117 host material is controlled by interactions with the matrix, which therefore reduces the ability of the PCIL anions to substantially participate in the conduction process. Furthermore, the difference between the $E_{\sigma 1}$ values for TMS is significantly larger than the same difference in TPFBu, which supports, according with the previous results, a stronger interaction with the nN117 matrix for the unfluorinated PCIL. The activation energy $E_{\sigma 2}$ for NTPFBu is lower than $E_{\sigma 2}$ for pristine TPFBu, suggesting that the CAEH is enhanced by the dynamics of the nN117 host matrix. The presence of VTF-like behaviour for conductivities is consistent with the DMA tanδ results. At temperatures above 60°C both samples exhibit a mechanical transition α_{pc} associated with a decrease in the long-range electrostatic interactions involving the entire nN117 structure (primary and secondary structure) [7,11,13,14]. In this context, it is plausible that the electric properties of the membrane, particularly the interfacial polarizations, are dependent on the system morphology and result in the transition at mid to high temperatures (60 – 150°C). From the molecular relaxations observed below the PCIL T_{m1}, the values of the relaxation time associated with the α and β transitions for the membranes and α_s and β_s for the PCILs at different temperatures can be determined by fitting the ε" spectra with the second term of Equation 4.2. The frequency data ($f_m = (2\pi\tau_m)^{-1}$ with m=α, β, α_s or β_s) as a function of reciprocal temperature are shown in Figure 4.17. For the PCILs and the doped membranes, fitting with Arrhenius (for β, β_s modes) and VTF (α, α_s rexations) equations for the $\log f_m$ yields the activation energies, E_m and T_0 as reported in Table 4.5. $E_{\alpha s}$ and $T_{0,\alpha s}$ are 20 kJ/mol and 115K for TMS and 16 kJ/mol and 106 K for TPFBu. These values are similar to the $E_{\sigma 0}$ and T_0 values determined from the VTF plots of conductivities at low temperature (Figure 4.15, Table 4.4), which indicates that the mechanism of long-range conduction occurs via the CCHH proton

exchange process, which in the membrane is mediated by the segmental motion of the nN117 chains and by the molecular dimensions of the ionic liquid moieties at lower temperatures.

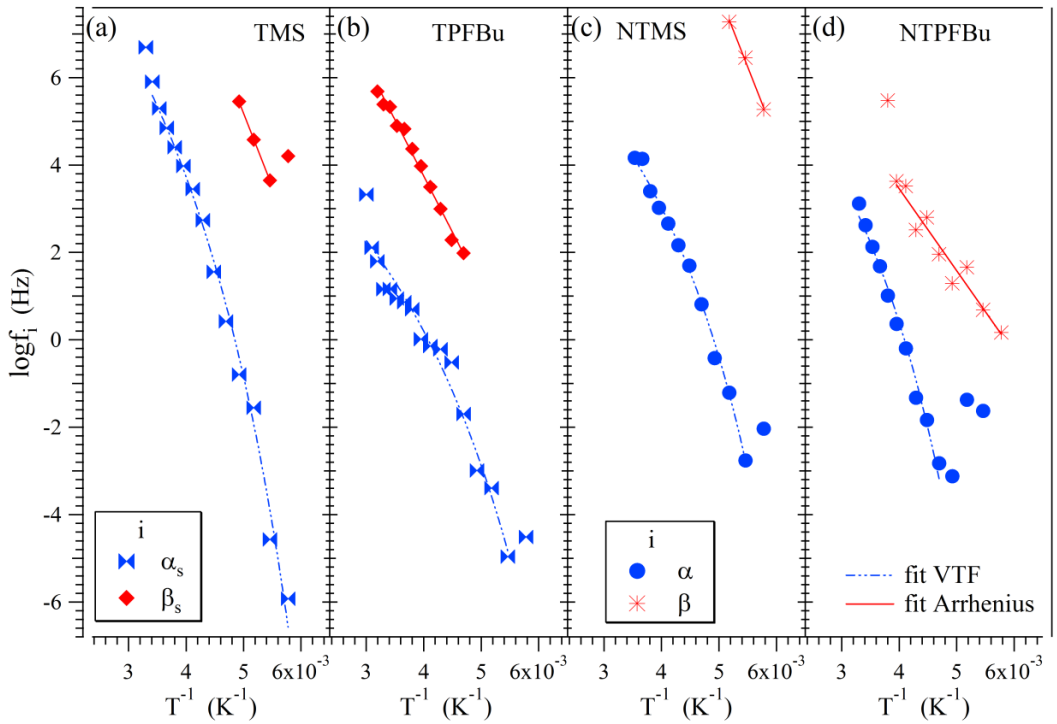

Figure 4.17. Profiles as a function of reciprocal temperature of: a), b) log $f_{\alpha s}$ and log $f_{\beta s}$ for TMS and TPFBu; c), d) log f_{α} and log f_{β} for NTMS and NTPFBu.

Table 4.5 Values of T_0 and the activation energy $E_{\beta s}$ and $E_{\alpha s}$ for TMS, TPFBu, and E_{β}, E_{α} for NTMS and NTPFBu.

	E_{β} or $E_{\beta s}$ (kJmol^{-1})*	***E_{α} or $E_{\alpha s}$ (kJmol^{-1})†***	***T_0 (K)†***
TMS	64 ± 1	20 ± 1	115 ± 10
NTMS	64 ± 5	14 ± 4	118 ± 13
TPFBu	49 ± 2	16 ± 2	106 ± 10
NTPFBu	36 ± 3	18 ± 3	131 ± 9

*Values determined by fitting data with the Arrhenius equation (see Chapter 1)
†Values determined by fitting data with the VTF equation (see Chapter 1).

A comparison of the activation energies, E_{β}, of the β transitions in the doped membranes sheds light on the interaction of the ionic liquid with the polymer matrix. As revealed by TG, DSC, DMA and FT-IR results, a stronger interaction exists between TMS and the polyether side chain

of the nN117 matrix than between TPFBu and the matrix. As discussed above, the β transition represents the relaxation of the polyether side chain interacting with the PCIL [40]. The activation energy E_β for NTMS is almost double that of NTPFBu. A higher activation energy indicates that more energy is required for the relaxation event to occur and therefore a stronger interaction. The implication of this interaction, according with the previous results, is a reduction in the size of the nanodomains of the ionic liquid TMS within the doped membrane NTMS as compared to TPFBu within NTPFBu.

Given that TG results revealed that the membranes contain similar amounts of PCIL per sulfonic group, domains of smaller size would necessarily imply that there is a larger number of PCIL clusters in NTMS and the distance between these clusters is smaller, as shown in Scheme 4.4. More nanodomains closer together would facilitate interaction with the host matrix and increase the density of the proton hopping processes between the domains, resulting in an increase in conductivity inside the hydrophilic domains. The greater conductivity in the NTMS membrane as compared to NTPFBu supports this interpretation. However, the total number of clusters and the ease of proton hopping in the polar local environment alone would not necessarily lead to increased long-range conductivity. The overall morphology of the polymer matrix also must be conducive to the long-range transport of protons: the effect of the PCIL on the overall polymer matrix is important. A stronger interaction of the PCIL with the nN117 side chain stimulates the organization of the nN117 fluorocarbon backbones into the microcrystalline domains. DSC results showed that the NTMS matrix had a 67% higher degree of microcrystallinity than the NTPFBu matrix. The higher crystallinity would increase the size of the ordered hydrophobic domains, which could result in a decreased interface between the hydrophobic and hydrophilic domains.

A smaller interface between the hydrophobic and hydrophilic domains increases the connectivity between ionic clusters within the hydrophilic domains and reduces the tortuosity of the channel-

like structure of the nN117 host matrix [48,49]. These phenomena promote the conduction process, which would result in an higher conductivity in NTMS when compared to NTPFBu, where the same degree of microcrystalline order is not present. The overall conduction process would have contributions from all three mechanisms and the total conductivity, σ_{total}, as shown in Equation 4.9 could be considered the sum of the three conductivities arising from the CCHH, CoCC&AA and CAEH conduction mechanisms (Scheme 4.3).

$$\sigma_{total} = \sum_{i=0}^{2} \sigma_i = \sigma_0 + \sigma_1 + \sigma_2 \tag{4.9}$$

For both NTMS and NTPFBu, σ_0 is at least two orders of magnitude higher than either σ_1 or σ_2, meaning that these two conductivities have a negligible contribution to the overall conductivity. Therefore, Equation 4.9 could be simplified to $\sigma_{total} = \sigma_0$ indicating that the long-range conduction process would be primarily due to the CCHH process.

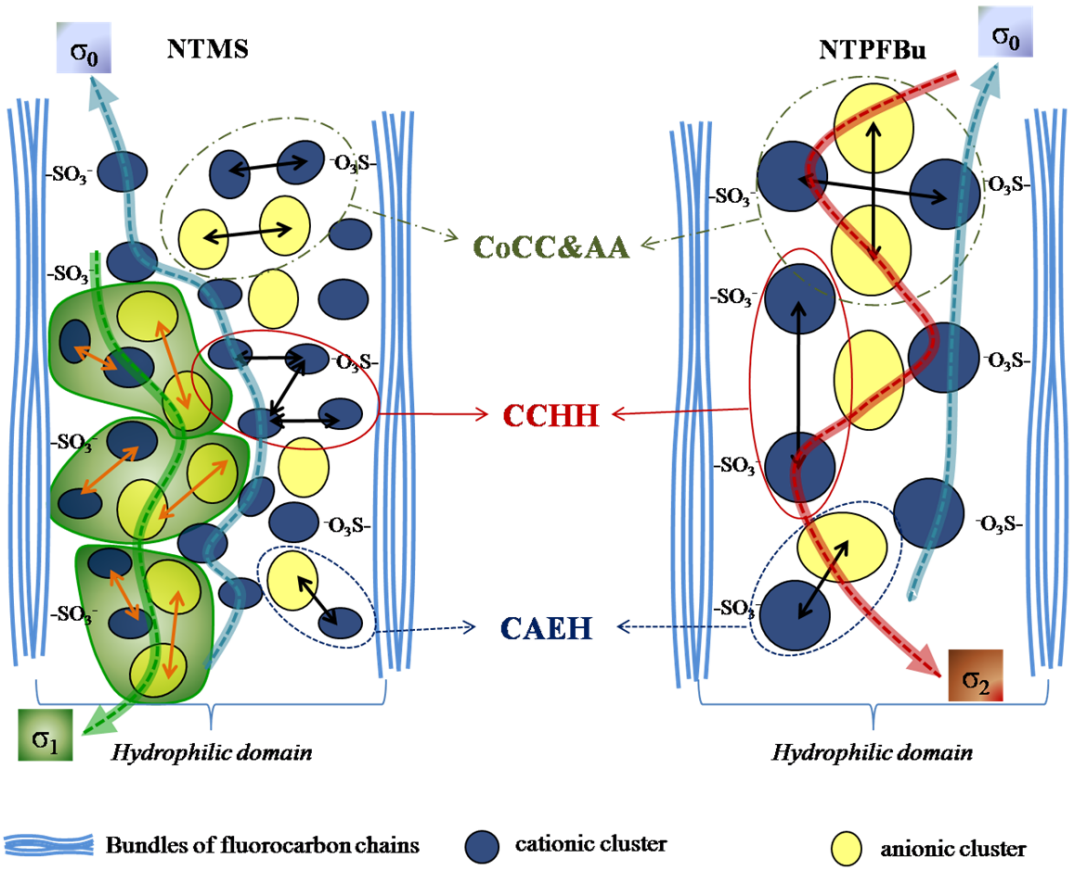

Scheme 4.4 Mechanisms of proton conduction CCHH, CoCC&AA and CAEH for the doped membranes NTMS and NTPFBu.

In Scheme 4.4, all the three conduction processes are shown for both membranes. However given the simplification of Equation 4.9, the long-range proton transfer largely occurs via proton exchange between cationic clusters that is mediated by the segmental motion which is associated with the dynamics of the fluorocarbon polymer host matrix.

4.4. Conclusions

The research activity conducted during the second year of PhD activity regards the synthesis and the study of two new PEMs based on nN117 doped with two ionic liquids, TMS and TPFBu. The membranes are obtained by a three-step protocol: (1) synthesis of the PCILs; (2) neutralization of N117 by TEA, yielding nN117; and (3) preparation of the PCIL-doped membranes by soaking nN117 in the PCILs. The materials are characterized with TG, DSC and FT-IR spectroscopy, while the mechanical and electrical properties of the NTMS and NTPFBu are analyzed by DMA and BES. The studies reveal that the anionic substitution of perfluorobutanesulfonate for methanesulfonate is reflected in varying thermal and structural properties of both the pristine ILs and the doped membranes due to increased steric hindrance, acidity, and hydrophobicity of the perfluorobutanesulfonate anion. The anion is responsible for different interactions between the PCIL and nN117. A stronger PCIL-nN117 interaction stimulates the organization of the fluorocarbon domains of the hosting nN117 in a microcrystalline structure and reduces the degree of crystallinity of the PCILs inside the membranes. The FT-IR studies provide evidence of the effect that ILs have on the structure of nN117 membrane components and confirm the significant difference between PCILs in their interactions with the host nN117 polymer. The presence of bands between 2450 cm^{-1} and 2560 cm^{-1} associated with the $N\text{-}H^{+}$ stretching modes indicates different hydrogen-bonding environments of the $TEAH^{+}$ cation. Shifts in this band are seen upon incorporation of the PCILs in the nN117 matrix signifying a change in the interaction between the anions and cations. NTMS shows vibrational bands typical of perfluorinated chains

contained inside the nN117 hydrophobic domains, while the NTPFBu spectrum is dominated by bands of the ionic liquid. The difference in the spectra in the CF_2 stretching region supports the DSC analysis that indicates a higher degree of crystallinity for NTMS. Structural differences between NTMS and NTPFBu also are reflected in the mechanical properties. Differences in storage modulus values are due to the dimensions of the nanodomains and the structural organization of the PCILs when they are present inside the polymeric membranes. Both doped membranes present a thermomechanical stability up to 140°C and the presence of four mechanical transitions. These transitions shift to lower temperatures in the doped membranes due to the plasticizing effect of the ionic liquid contained within. The ionic liquid solvates and plasticizes the nN117 side group reducing the cross-linking dipolar interactions inside the polar domains resulting in a mobility increase of the main fluorocarbon backbone chains. This phenomenon increases in the order NTPFBu < NTMS.

BES measurements of the electric properties of TMS, TPFBu and doped nN117 membranes elucidate the mechanism of charge conduction and the dielectric relaxations. For the pure PCILs above the melting temperature, the BES measurements show the presence of three interfacial polarizations associated with mechanisms of proton transfer that are dependent on the nanostructuring of the ionic liquids as molecular aggregates. For the doped membranes, the electric measurements show that the mechanism of long-range charge transfer is mediated by the dynamics of the fluorocarbon polymeric matrix and the nanostructure of the ionic liquids embedded inside the host nN117. In detail, BES measurements of the doped membranes also show the presence of three interfacial polarizations, which are dependent on the nanostructuring of the ionic liquid embedded within the polar domains of NTMS and NTPFBu membranes. This interpretation is in accordance with the structure of the doped membrane, which consists of amorphous, micro-crystalline and nano-crystalline domains of the fluorocarbon chains of nN117 and of the polar clusters containing the ionic liquids. These polar clusters are responsible for the

ionic conductivity of the material. For temperatures below the PCIL melting points, the BES measurements reveal the presence of two dielectric relaxations α and β that are associated with the dipolar relaxations involving the ionic liquids and the nN117 matrix. The increased activation energy of the β transition for NTMS indicates a stronger interaction between the side chain and the PCIL than in NTPFBu.

Taken together, all the obtained results suggest a composite membrane structure where the ionic liquids present within the nN117 hydrophilic channels are organized in cationic and anionic nanoaggregates. The size of these aggregates depend on the interaction between the PCIL and the nN117 matrix, resulting in smaller aggregates for TMS than TPFBu. In the composite membrane, the difference in composition is solely due to the selected PCIL anions, so the change in interaction is due to the anion. Stronger interactions lead to an increase in the nN117 matrix microcrystallinity. Together, these two effects result in higher conductivity in NTMS than NTPFBu. The conductivities measured at 130°C yield $\sigma_{TMS} = 1.4\times10^{-2}$S/cm, $\sigma_{TPFBu} = 9\times10^{-3}$S/cm, $\sigma_{NTMS} = 6.1\times10^{-3}$ S/cm and $\sigma_{NTPFBu} = 1.8\times10^{-3}$S/cm. In the membranes, the mechanism of long-range charge transfer occurs via a proton exchange process between cationic clusters, which is mediated by the segmental motion of the nN117 chains and the molecular dimensions of the ionic liquid aggregates.

This work leads to the conclusion that the conductivity of the system can be improved when the dopant stimulates the matrix to organize into percolation pathways for the migration of charge. In the NTMS and NTPFBu membranes, the PCILs present in the hydrophilic domains of the membrane create percolation pathways for the movement of protons. These percolation pathways provide “shortcuts” for the movement of protons through the membrane as compared to pristine N117 or nN117. Furthermore, the mechanical properties of NTMS and NTPFBu, which were reduced by the plasticizing effect of the PCILs, must be improved for the implementation of these membranes as PEMs in medium-temperature fuel cell. Despite a

necessity for improved mechanical properties, which are reduced by the plasticizing effect of the ionic liquids, the conductivities measured at temperatures above 100°C and the good thermal stability make NTMS and NTPFBu promising materials for PEMFCs operating at T>90°C.

4.5. References

1. Lee, S. Y.; Ogawa, A.; Kanno, M.; Nakamoto, H.; Yasuda, T.; Watanabe, M., *J. Am. Chem. Soc.* **2010,** *132*, 9764.
2. Lin, B.; Cheng, S.; Qiu, L.; Yan, F.; Shang, S.; Lu, J., *Chem. Mater.* **2010,** *22*, 1807.
3. Yan, F.; Yu, S.; Zhang, X.; Qiu, L.; Chu, F.; You, J.; Lu, J., *Chem. Mater.* **2009,** *21*, 1480.
4. Greaves, T. L.; Drummond, C. J., *Chem. Rev.* **2008,** *108*, 206.
5. Martinelli, A.; Matic, A.; Jacobsson, P.; Borjesson, L.; Fernicola, A.; Panero, S.; Scrosati, B.; Ohno, H., *J. Phys. Chem. B* **2007,** *111*, 12462.
6. Noda, A.; Susan, A. B.; Kudo, K.; Mitsushima, S.; Hayamizu, K.; Watanabe, M., *J. Phys. Chem. B* **2003,** *107*, 4024.
7. Di Noto, V.; Negro, E.; Sanchez, J. Y.; Iojoiu, C., *J. Am. Chem. Soc.* **2010,** *132*, 2183.
8. Martinez, M.; Molmeret, Y.; Cointeaux, L.; Iojoiu, C.; Lepretre, J. C.; El Kissi, N.; Judeinstein, P.; Sanchez, J. Y., *J. Power Sources* **2010,** *195*, 5829.
9. "The DuPont Oval Logo, DuPont™, The miracles of science™ and all products denoted with a ™ and ® are trademarks or registered trademarks of DuPont or its affiliates."
10. Di Noto, V.; Gliubizzi, R.; Negro, E.; Vittadello, M.; Pace, G., *Electrochim. Acta* **2007,** *53*, 1618.
11. Di Noto, V.; Piga, M.; Lavina, S.; Negro, E.; Yoshida, K.; Ito, R.; Furukawa, T., *Electrochim. Acta* **2010,** *55*, 1431.
12 Di Noto, V.; Piga, M.; Piga, L.; Polizzi, S.; Negro, E., *J. Power Sources* **2008,** *178*, 561.
13. Di Noto, V.; Gliubizzi, R.; Negro, E.; Pace, G., *J. Phys. Chem. B* **2006,** *110*, 24972.

14. Page, K. A.; Cable, K. M.; Moore, R. B., *Macromolecules* **2005,** *38*, 6472.

15. Hodge, I. M.; Eisenberg, A., *Macromolecules* **1978,** *11*, 289.

16. Yeo, S. C.; Eisenberg, A., *J. Appl. Polym. Sci.* **1977,** *21*, 875.

17. Lin-Vien, D.; Colthup, N. B.; Fateley, W. G.; Grasselli, J. G., *The Handbook of Infrared and Raman Characteristic Frequencies of Organic Molecules*. Academic Press, Inc.: New York, **1991**.

18. Socrates, G., *Infrared and Raman Characteristic Group Frequencies*. 3rd ed.; John Wiley & Sons: New York, **2001**.

19. DeTar, D. F.; Novak, R. W., *J. Am. Chem. Soc.* **1970,** *92*, 1361.

20. Giffin, G. A.; Boesch, S.; Bopege, D. N.; Powell, D. R.; Wheeler, R. A.; Frech, R., *J. Phys. Chem. B* **2009,** *113*, 15914.

21. Gruger, A.; Regis, A.; Schmatko, T.; Colomban, P., *Vib. Spectrosc* **2001,** *26*, 215.

22. Di Noto, V.; *J. Phys. Chem. B* **2002,** *106*, 11139.

23. Di Noto, V.; Vittadello, M.; Lavina, S.; Fauri, M.; Biscazzo, S., *J. Phys. Chem. B* **2001,** *105*, 4584.

24. Schonhals, A.; Kremer, F.; eds., *Broadband Dielectric Spectroscopy*. Springer: Berlin, **2003**.

25. Klein, R. J.; Zhang, S. H.; Dou, S.; Jones, B. H.; Colby, R. H.; Runt, J., *J. Chem. Phys.* **2006,** *124*, 144903.

26. Krause, C.; Sangoro, J. R.; Iacob, C.; Kremer, F., *J. Phys. Chem. B* **2010,** *114*, 382.

27. Serghei, A.; Tress, M.; Sangoro, J. R.; Kremer, F., *Phys. Rev. B: Condens. Matter* **2009,** *80*, 184301.

28. Turton, D. A.; Hunger, J.; Stoppa, A.; Hefter, G.; Thoman, A.; Walther, M.; Buchner, R.; Wynne, K., *J. Am. Chem. Soc.* **2009,** *131*, 11140.

29. Triolo, A.; Russina, O.; Bleif, H. J.; Di Cola, E., *J. Phys. Chem. B* **2007,** *111*, 4641.

30. Xiao, D.; Hines, L. G.; Li, S. F.; Bartsch, R. A.; Quitevis, E. L.; Russina, O.; Triolo, A., *J. Phys. Chem. B* **2009,** *113*, 6426.

31. Dyson, P. J.; Khalaila, I.; Luettgen, S.; McIndoe, J. S.; Zhao, D. B., *Chem. Commun.* **2004**, 2204.

32. Kohler, F.; Atrops, H.; Kalali, H.; Liebermann, E.; Wilhelm, E.; Ratkovics, F.; Salamon, T., *J. Phys. Chem.* **1981,** *85*, 2520.

33. Kohler, F.; Liebermann, E.; Miksch, G.; Kainz, C., *J. Phys. Chem.* **1972,** *76*, 2764.

34. Hojo, M.; Miyauchi, Y.; Imai, Y., *Bull. Chem. Soc. Jpn.* **1990,** *63*, 3288.

35. Kennedy, D. F.; Drummond, C. J., *J. Phys. Chem. B* **2009,** *113*, 5690.

36. Dura, J. A.; Murthi, V. S.; Hartman, M.; Satija, S. K.; Majkrzak, C. F., *Macromolecules* **2009,** *42*, 4769.

37. Rubatat, L.; Rollet, A. L.; Gebel, G.; Diat, O., *Macromolecules* **2002,** *35*, 4050.

38. Rollet, A.-L.; Diat, O.; Gebel, G., *J. Phys. Chem. B* **2002,** *106*, 3033.

39. Di Noto, V.; Lavina, S.; Negro, E.; Vittadello, M.; Conti, F.; Piga, M.; Pace, G., *J. Power Sources* **2009,** *187*, 57.

40. Giffin, G.A.; Piga, M.; Lavina, S.; Navarra, M.A.; D'Epifanio, A.; Scrosati, B.; Di Noto, V.; *J. Power Sources*, **2012**, 198, 66.

41. Di Noto, V.; Vittadello, M.; Greenbaum, S. G.; Suarez, S.; Kano, K.; Furukawa, T., *J. Phys. Chem. B* **2004,** *108* (49), 18832.

42. Vittadello, M.; Suarez, S.; Chung, S. H.; Fujimoto, K.; Di Noto, V.; Greenbaum, S. G.; Furukawa, T., *Electrochim. Acta* **2003**, 48 (14-16), 2227.

43. Iojoiu, C.; Judeinstein, P.; Sanchez, J. Y., *Electrochim. Acta*, **2007,** *53* (4), 1395.

44. Atkins, P.; de Paula, J., *Physical Chemistry*. 8th ed.; Oxford University Press: Oxford, **2006**.

45. Judeinstein, P.; Iojoiu, C.; Sanchez, J. Y.; Ancian, B., *J. Phys. Chem. B* **2008,** *112*, 3680.

46. Lee, S. Y.; Ogawa, A.; Kanno, M.; Nakamoto, H.; Yasuda, T.; Watanabe, M., *J. Am. Chem. Soc.* **2010,** *132*, 9764.

47. Hertz, H. G.; Lindman, B.; Siepe, V., *Ber. Bunsenges. Phys. Chem.* **1969,** *73*, 542.

48. Kreuer, K. D., *J. Membr. Sci.* **2001,** *185*, 29.

49. Wu, D.; Paddison, S. J.; Elliott, J. A., *Energ. Environ. Sci.* **2008,** *1*, 284.

Chapter V

Proton conducting membranes based on poly-2,2'(2,6-pyridine)-5,5'-bibenzimidazole, SiO_2-Im and H_3PO_4

5.1. Introduction

About 15 years ago Savinell et al. proposed polybenzimidazole (PBI) membranes doped with strong acid, such H_3PO_4 or H_2SO_4, as an alternative to Nafion PEMs [1,2]. PBI is a polymer containing a basic functionality that allows the uptake of acid that is responsible, and required, for the proton conduction. The electrical properties of various proton conducting polymer electrolytes containing acids such as H_2SO_4 and H_3PO_4 have been reviewed by Lassegues [3]. The polymers have been classified with respect to their basicity and according to the nature of the interaction between the acid and their basic acid solution. For weakly basic polymers such as polyethylene oxide, hydrogen bonding was proposed to explain the interaction between the acid and the polymer. For highly basic polymers such as polyethylene imine, protonation of the polymer was proposed. In PBI, the nitrogen of the imide group is likely to act as a strong proton acceptor [2,4].

For acid-doped PBI, some discrepancy exists among the conductivity values reported in the literature. Wang et al. [2] report a value of $2.3 \cdot 10^{-3}$ Scm^{-1} at 130°C, in a dry atmosphere, for a PBI film doped with 338 m/o of H_3PO_4. Fontanella et al. [5] report a value of $4.5 \cdot 10^{-5}$ Scm^{-1} for dry PBI doped with 600 m/o of H_3PO_4, at room temperature. Rikukawa et al. [6] have also measured the conductivity of PBI–$x$$H_3PO_4$ polymers and found a conductivity of 10^{-5} Scm^{-1} for high doping level (613 m/o), in the temperature range from 20 to 160°C.

However, despite the good proton conductivity values [2,4], the acid addition reduces the membrane's mechanical stability and leads to leaching problems at temperatures higher than 160°C[7]. Lobato et al. [8] have shown that the temperature (100-170°C) strongly influences the fuel cell performance of H_3PO_4-doped PBI membranes by different processes. In particular rising temperature: a) increases the membrane's conductivity and enhances the electrodic reactions; b) favors the electrolyte dehydration (by reducing the level of hydration of the membrane or, above 130-140°C by the self-dehydration of H_3PO_4). The authors revealed that the first process rapidly responds varying the temperature and determines the "short-term" behavior of the cell, whereas the response of the second process is more progressive and influences the cell performance in the "long-term" [8].

Quartarone et al. recently showed that by changing the number and/or the position of the nitrogen atoms in the PBI membranes improvements in both the conductivity and the acid retention can be obtained [9,10]. They reported that membranes based on poly-2,2'-(2,6-pyridine)-5,5'-bibenzimidazole (PBI5N, chemical structure reported in Figure 5.1) showed an increase of two orders of magnitude in the conductivity after washing in a water/methanol (1 M) solution, with respect to the commercially available poly-2,2'-m-phenylene-5,5'-bibenzimidazole (PBI4N). The same group also reported that preparation of composite membranes made from PBI4N and PBI5N doped with a SiO_2-based filler that is functionalized with imidazole to contain (SiO_2-Im, chemical structure shown in Figure 5.2) functional groups:

1) increases the permanent proton conductivity of the PBI4N composite membranes; 2) increases the thermal stability; and 3) allows a 20% increase in the maximum power density as compared to pristine PBI5N [7, 11-13].

In order to extend that study and elucidate the effect of the filler on the properties of PBI5N, the research activity conducted in the first part of the 3rd year of doctoral stage, reports a comparison between the thermal, mechanical and electrical properties of PBI5N, PBI5N doped with H_3PO_4 (named PBI5N/(H_3PO_4)) and PBI5N containing 10 wt% of SiO_2-Im filler and doped with H_3PO_4 (labelled PBI5N/(SiO_2-Im+H_3PO_4)). PBI-based materials are choose as Nafion-alternative membranes for application in high temperature fuel cell.

Infrared spectroscopy measurements supported with DMol3 quantum chemical calculations are used to assign the IR experimental spectrum of the membranes and to examine the nature of the phosphate. Electrical measurements, conducted on PBI5N, PBI5N/(H_3PO_4) and PBI5N/(SiO_2-Im+H_3PO_4), elucidate the proton conduction mechanisms and the modification on the electrical properties of the membranes due to the presence of H_3PO_4 and/or the SiO_2-Im filler, revealing that the presence of the filler reduces the activation energy associated with the proton conduction mechanism.

5.2. Experimental

5.2.1 Membranes preparation

The PBI5N powder was prepared according to Carollo et al.[9] via a monomer condensation process. Two monomers, 3,3',4,4'-biphenyltetramine (A) and 2,6-pyridinedicarboxylic acid (B), reported in Figure 5.1, were dissolved in polyphosphoric acid (PPA, 85% P_2O_5) and polymerized at 200°C under nitrogen atmosphere for 30 h. After the condensation reaction, the obtained PBI5N polymer were: 1) soaked in distilled water, in order to eliminate any residual of monomer

and PPA, and treated with a NaOH solution (10 wt%): 2) washed in boiling water, and finally dried under vacuum for 24 h.

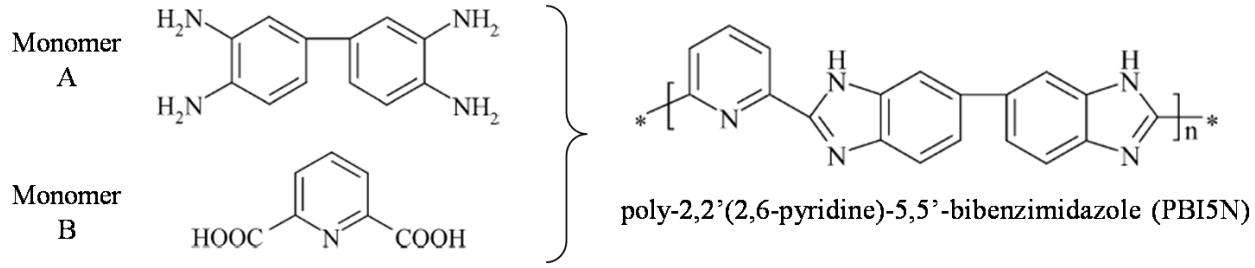

Figure 5.1 Chemical structure of 3',4,4'-biphenyltetramine (monomer A), 2,6-pyridinedicarboxylic acid (monomer B) and poly-2,2'-(2,6-pyridine)-5,5'-bibenzimidazole (PBI5N).

The polymer membrane was obtained by dissolving PBI5N powder (chemical structure reported in Figure 5.1) in dimethylacetamide (DMAc) and casting the solution at 80°C for 15h. The acid-doped PBI5N was obtained by immersion of PBI5N membrane in aqueous solution of phosphoric acid (85 wt.%, Prolabo) at room temperature for 72h, and then dried at 110°C for 24h.

The SiO_2-Im filler was prepared by a sol-gel technique as reported by Mustarelli et al.[11]. The imidazole-containing silica was synthesized by means of the standard basic hydrolysis/condensation process, starting from tetraethoxysilane (TEOS) and N-(3-triethoxysilylpropyl)-4,5-dihydroimidazole in a molar ratio 2:1 (Figure 5.2). The resulting bulky gel was dried at 100°C for 4 days. The SiO_2-Im filler has been characterized by Mustarelli et al. [11] and present an imidazole-groups concentration of 3.64 mmol/g, a surface area of 3.5m^2/g and a water content of 16wt%. As shown in Figure 5.2, the SiO_2-Im filler contains both the imidazole functionalized and the hydroxyl groups. The first, due to its high basic character (pKa~14[11]) and good chemical affinity with PBI5N [11] allows the SiO_2-Im: a) to interact strongly with the phosphoric acid; b) to be homogeneously distributed within the PBI5N membrane [11]. The hydroxyl groups present on the silica surface can interact with the basic functionalities of PBI5N forming hydrogen bonds. Thus, the SiO_2-Im filler can interact with both

H_3PO_4 and the polymer matrix. As discussed below, the presence of such interactions will lead to an improvement of the properties of PBI5N/(H_3PO_4+SiO_2-Im) with respect to PBI5N/(H_3PO_4).

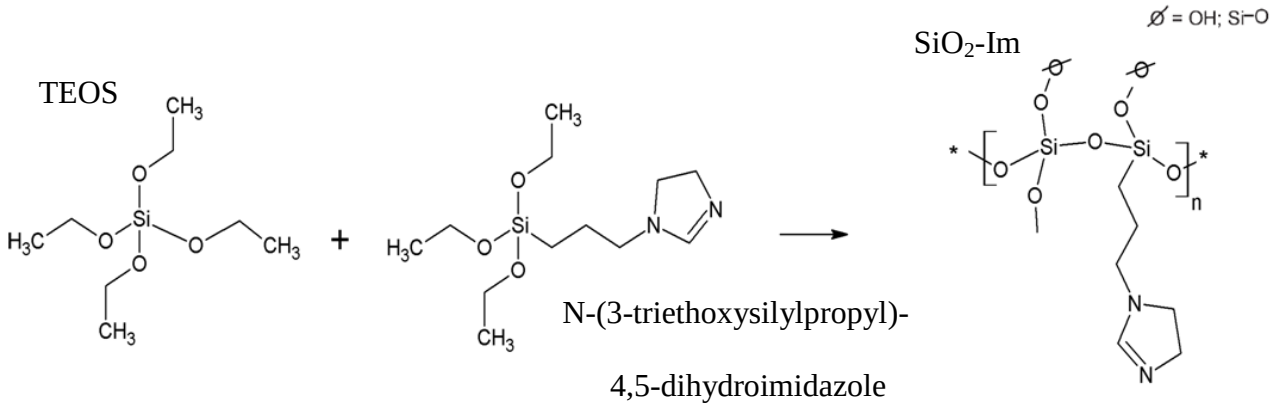

Figure 5.2 Synthesis of SiO_2-Im filler.

The PBI-composite membrane was prepared by the standard solvent casting technique. The pristine polymer was dissolved in dimethylacetamide at 100°C. Subsequently, 10 wt% of the SiO_2-Im filler was dispersed by sonication in the polymer solution, which was then cast to obtain a homogeneous film. The composite membrane was then activated with H_3PO_4 in the same conditions reported above for acid-doped PBI5N membrane.

For PBI5N/(H_3PO_4) and PBI5N/(H_3PO_4+SiO_2-Im), the acid uptake of H_3PO_4 (A.U.%) was calculated using Equation 5.1:

$$A.U.\% = \frac{w_{wet} - w_0}{w_0} \cdot 100 \qquad (5.1)$$

where w_{wet} and w_o are the weight of the membrane doped with H_3PO_4 and pristine, respectively. The uptake of phosphoric acid is 77 and 74wt% for PBI5N/(H_3PO_4) and PBI5N/(H_3PO_4+SiO_2-Im), respectively, corresponding to n = 7.4 and 7.3 moles of acid per monomer repeat unit.

5.2.2 Instruments and Methods

TG profiles were collected over the thermal range from 20 to 900°C. The heating rate (°C/min) was varied from 50 to 0.001°C/min, depending on the first derivative of the weight loss.

Differential Scanning Calorimeter (DSC) measurements were conducted in cyclic mode, using a heating rate of 6°C/min over a thermal range from -50 to 350°C. Dynamic-Mechanical Analyses (DMA) were collected by applying a sinusoidal deformation of amplitude 4 μm at 1 Hz in 5°C intervals over thermal range from -100 to 300°C. The FT-IR spectra of the membranes were obtained in ATR mode (see Chapter 2) while the spectrum of the H_3PO_4 solution was collected in transmission.

Broadband Electric Spectroscopy (BES) measurements were collected over the frequency range of 10^{-2} to 10^{7} Hz and in the thermal range between 5 and 135°C in 10°C intervals with an accuracy greater than ± 0.1°C. Samples were placed between two gold cylindrical electrodes.

5.3. DFT Calculations

Infrared spectra were calculated using density functional theory (DFT) methods implemented in an all-electron DFT code using the DMol3 program [14,15] as a part of the Materials Studio package (double numerical plus polarization basis set, gradient-corrected (GGA) BLYP functional). The polybenzimidazole PBI5N polymer was modelled using chains containing one, two and three repeat units. The internal modes were identified by animating the atomic motion of each calculated mode using features available in the DMol3 package.

5.4. Results and discussion

5.4.1 Thermal analysis

The TG curves of PBI5N, PBI5N/(H_3PO_4) and PBI5N/(SiO_2-Im+H_3PO_4) are shown in Figure 5.3 together with the derivative of the weight change (dW%/dT). Figure 5.3 also shows the thermal decomposition of an 85 wt% phosphoric acid solution.

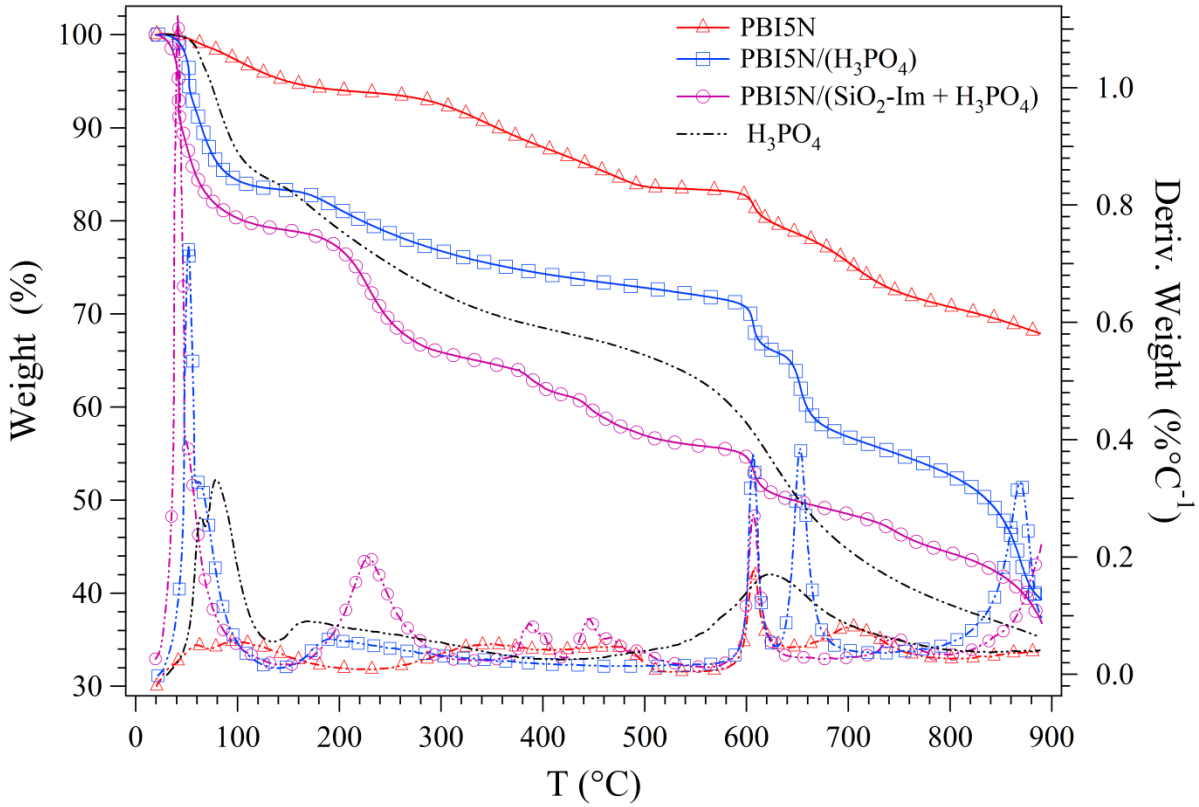

Figure 5.3 Weight loss (left axis) and derivative dw%/dT (right axis) in the temperature range from 20 to 900°C of PBI5N, PBI5N/(H_3PO_4) and PBI5N/(SiO_2-Im +H_3PO_4). The graph reports also the TG profile of the H_3PO_4 solution (85wt%).

Four mass losses are observed for all three membranes [16]. The first, in the temperature range between 20 and 120°C is due to the desorption of H_2O and CO_2. This process is present for all membranes and is higher in the samples treated with phosphoric acid (weight loss of 15 – 20 wt%) compared to the PBI5N membrane (~ 5 wt%). This difference is due to the presence of the H_3PO_4 solution, according to the TG profile of the acid solution which shows a mass loss of 15 wt% between 20 and 120°C. The second loss occurs between 120 and 320°C and is associated with the release of water during the formation of pyrophosphoric acid by the reaction: $2H_3PO_4 \rightarrow H_4P_2O_7 + H_2O$ [8,16]. This thermal event is absent in the TG profile of PBI5N. The weight loss associated with the release of water is 9, 14 and 15 wt% for PBI5N/(H_3PO_4), PBI5N/(SiO_2-Im+H_3PO_4) and H_3PO_4, respectively. Furthermore, the derivatives of the weight change reported in Fig. 5.3 show the temperature of the second loss peak maxima increase in the order H_3PO_4 <

PBI5N/(H_3PO_4) < PBI5N/(SiO_2-Im+H_3PO_4). These results indicate that the presence of the inorganic filler with basic character increases the thermal stability of phosphoric acid inside the PBI matrix, owing to the presence of SiO_2-Im···H_3PO_4 interactions. The third (300 – 550°C) and fourth (550 – 800°C) mass eliminations are associated with the thermal degradation of the PBI matrix [16]. According to literature, the main thermal decomposition products are CO, C_6H_6, CH_3CN and HCN [16]. In this temperature range, the derivative of weight change for the phosphoric acid shows a broad peak centered at about 630°C, due to the loss of water formed during the reaction: $H_4P_2O_7 \rightarrow 2HPO_3 + H_2O$ [16].

For all the three membranes, investigation of the thermal transitions was carried out by differential scanning calorimetry measurements. To ensure that the membranes had the same thermal history, the DSC measurements were conducted in a cycle mode. The samples were initially heated from 25 to 130°C (cycle 1), then cooled from 130 to -50°C (cycle 2) and finally heated from -50 to 350°C (cycle 3). The DSC curves collected during cycle 3 for PBI5N, PBI5N/(H_3PO_4) and PBI5N/(SiO_2-Im+H_3PO_4) are reported in Figure 5.4. The DSC curve of PBI5N shows the presence of two transitions: an event at about 210°C, associated to the glass transition temperature (T_g) of the material and an endothermic peak at ca. 250°C (Peak I in Figure 5.4) attributed to the melting of microcrystalline domains. This latter assignment is in accordance with the work of Carollo et al [9], which report by XRD measurement a semicrystalline order for pristine PBI5N.

For PBI/(H_3PO_4) peak I shifts towards higher temperatures and is significantly reduced in PBI5N/(SiO_2-Im+H_3PO_4), indicating that the presence of imidazolium-functionalized silica leads to a reduction of the degree of crystallinity of the PBI5N membrane. The presence of peak I in PBI/(H_3PO_4) is justified considering the experimental procedure adopted to impregnate the PBI5N membrane with H_3PO_4. Heat treatments were performed at temperatures below the melting of the crystalline domains. Thus, a partial order of crystallinity is expected to be present

even in the PBI5N/(H_3PO_4) membrane. In contrast, in the case of PBI5N/(SiO_2-Im+H_3PO_4) the filler is added before the solvent casting and thus the formation of the polymer membrane. During the solvent casting process the SiO_2-Im filler interacts with the polymer matrix blocking its tendency to organize into ordered structures.

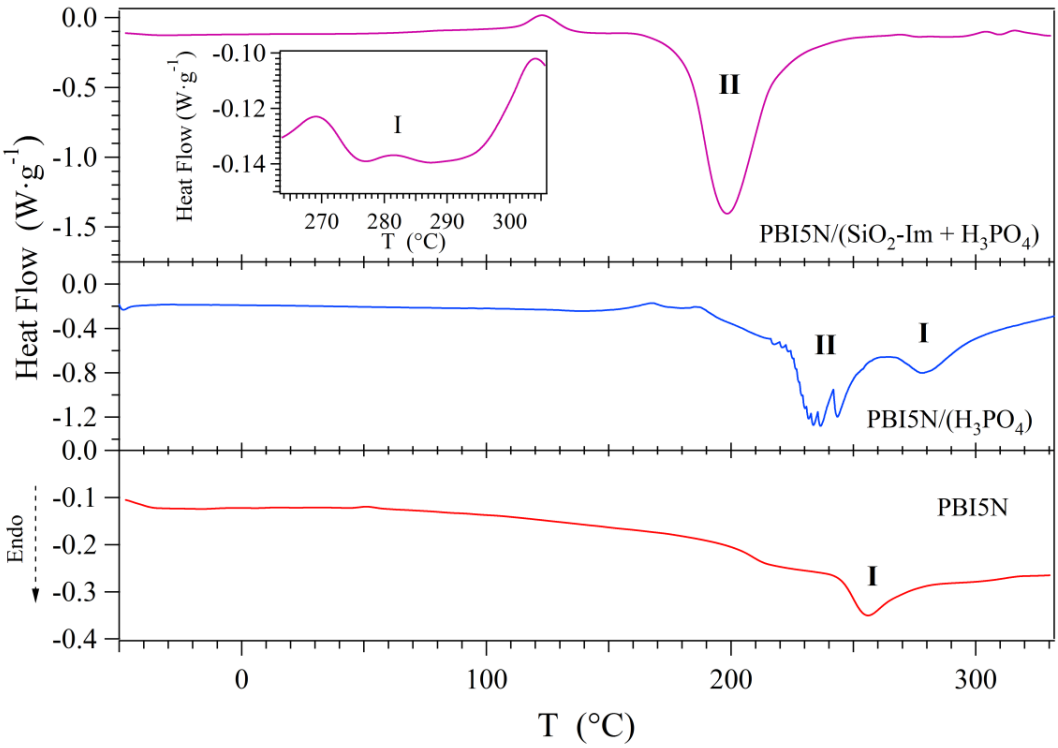

Figure 5.4 DSC curves of PBI5N, PBI5N/(H_3PO_4) and PBI5N/(SiO_2-Im +H_3PO_4) collected in the thermal range from -50 to 350 °C. The inset shows the expansion of the DSC curves from 260 to 305 °C for PBI5N/(SiO_2-Im+H_3PO_4).

Both the acid-doped membranes show the presence of an intense endothermic peak (peak II) between 200 and 250°C. This thermal event, which is absent in PBI5N, is associated with the elimination of water in the reaction: $2H_3PO_4 \rightarrow H_4P_2O_7 + 2H_2O$. This interpretation is supported by the enthalpies associated with peak II, which are 367 and 341 J/g for PBI5N/(SiO_2-Im+H_3PO_4) and PBI5N/(H_3PO_4), respectively. The enthalpy values are higher for the hybrid composite membrane, which according to the TG results releases a greater amount of water.

5.4.2 Dynamic mechanical studies

The spectra of the Storage Modulus (E'), the Loss Modulus (E'') and tanδ=E''/E' collected for the doped membranes and PBI5N in the temperature range between -100 and 300°C are reported in Figure 5.5. The addition of phosphoric acid leads to a reduction of the membranes' mechanical stability as is evident from the sharp decrease of E' for both the acid-doped membranes as compared to pristine PBI5N. The phosphoric acid, interacting with the PBI aromatic chains: a) creates hydrophilic domains within the membrane responsible for the proton conduction of the material and b) plasticizes the polymer matrix thus increasing the mobility of the PBI chains. At temperatures above 120°C, the values of E' for the hybrid membrane are significantly higher than those of the PBI5N membrane soaked in H_3PO_4. For example, at 200°C the storage modulus E' are 53.7 MPa and 2.65 MPa for PBI5N/(SiO_2-Im+H_3PO_4) and PBI5N/(H_3PO_4), respectively.

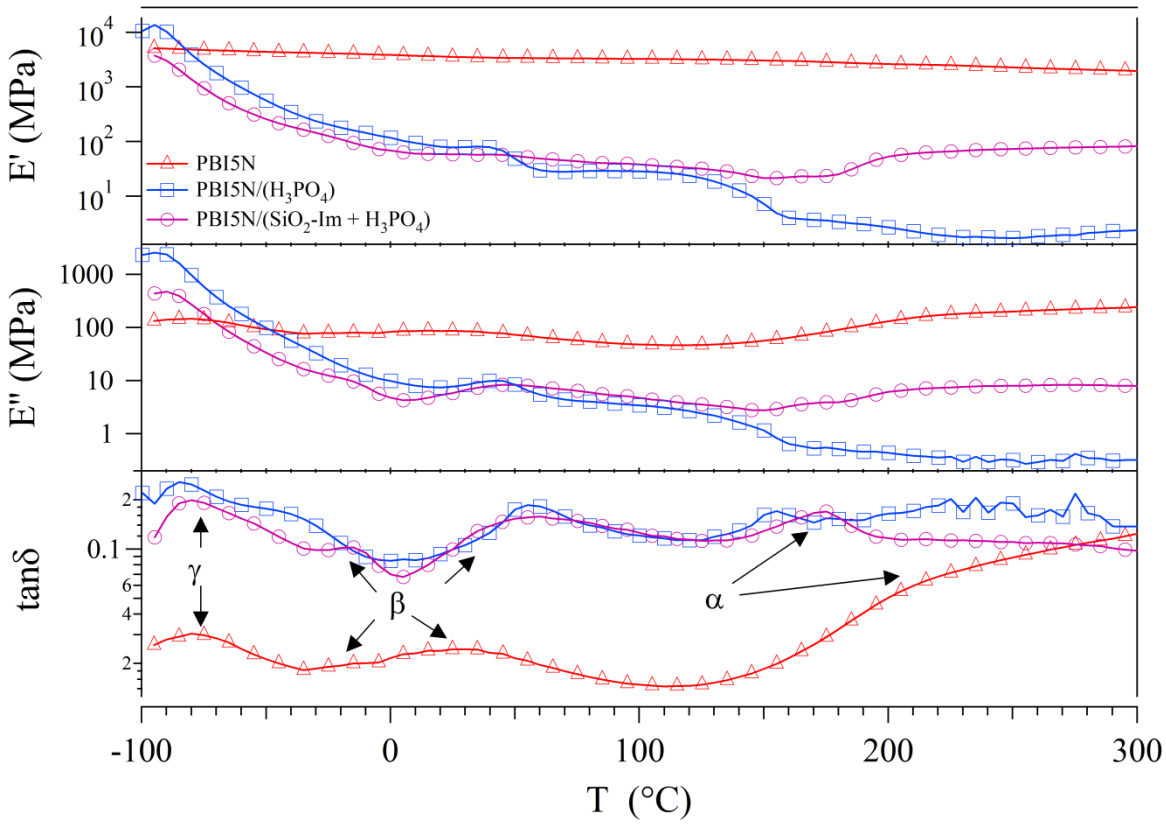

Figure 5.5 DMA profiles of PBI5N (triangle), PBI5N/(H_3PO_4) (square) and PBI5N/(SiO_2-Im+H_3PO_4) (circle). The graphs show the behaviour of the elastic modulus (E'), loss modulus (E'') and of tanδ with respect to the scanning temperature.

This difference in the mechanical properties of the acid-doped membranes is due to the presence of the SiO_2-Im filler, which interacts with both the orthophosphoric acid and the polymer matrix and increases the mechanical stability of the hybrid membrane, due to the formation of PBI5N···SiO_2-Im···H_3PO_4 interactions. In addition, for temperatures above 200°C, both the acid-doped membranes show a plateau in the elastic modulus. This behavior, in agreement with TG and DSC measurements, is due to the elimination of traces of water produced in the reaction $2H_3PO_4 \rightarrow H_4P_2O_7 + 2H_2O$. The tanδ profiles reported in Fig. 5.5 reveal the presence of three mechanical relaxation modes: γ, β and α. The γ relaxation between -100<T<-50°C is likely associated with local fluctuation of the aromatic rings occurring within asymmetric units of the polymer chain. β (-50<T<80°C) and α (120<T<220°C) transitions are caused by relaxation modes attributed to coupling of inter-chain dipole-dipole interactions and the segmental motion of polymer backbone chains, respectively. The nature of the β relaxation is discussed later in the section concerning the electrical studies.

In PBI5N the presence of the mechanical α transition around 200°C indicates that the glass transition temperature is significantly lower than that typically reported for PBI4N [4] (420°C), in agreement with the interpretation of the DSC results. Compared to PBI5N, the membranes soaked with H_3PO_4 show a shift of the β peak towards higher temperatures due to interactions between the polymer and the acid that increase the dipole-dipole inter-chain interactions. Furthermore, as compared to PBI5N/(H_3PO_4), the presence of the filler in the PBI5N/(SiO_2-Im+H_3PO_4) membrane causes the α peak to appear at higher temperatures as a result of the interactions between the SiO_2-Im filler and the polymer matrix that slightly reduce the mobility of the PBI5N aromatic chains.

5.4.3 FT-IR and DFT analysis

The IR spectrum of PBI4N has previously been assigned by a number of groups [4, 17-19]. The only structural difference between PBI4N and PBI5N is the presence of a pyridine unit in the PBI5N chain in the place of the phenyl group found in the PBI4N chain. Therefore, the differences in the vibrational spectra of PBI4N and PBI5N are small and should be found in modes attributed to the phenyl/pyridine groups. The infrared spectrum of PBI5N membrane can be found as a part of Figure 5.6 and the vibrational assignments are given in Table 5.1.

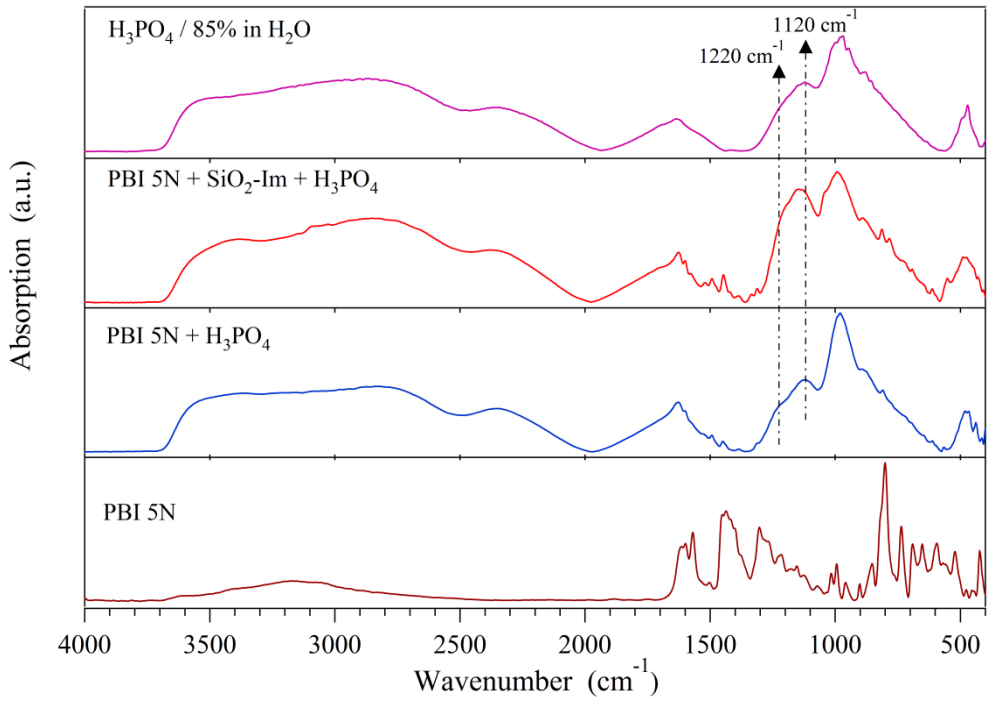

Figure 5.6 Infrared spectra from 4000 to 400 cm^{-1} for PBI5N, PBI5N/(H_3PO_4), PBI5N/(SiO_2-Im+H_3PO_4) and H_3PO_4 solution.

The vibrational assignments were made by comparing the previously published vibrational assignments of PBI4N [17,19], benzimidazole [20,21] and pyridine [22] and combining those with the DFT calculated modes determined with DMol3 [14,15]. The calculated modes were determined for chains with one, two and three repeat units of PBI5N. The dimer and trimer were examined to determine the validity of using one repeat unit to model the larger polymeric chain. The single repeat unit seems to provide a reasonably good model for the vibrations of PBI5N as

main differences between three models was found in the coupling between CH moieties in the in-plane and out-of-plane bending and stretching modes.

Table 5.1 Vibrational assignment of experimental PBI5N spectrum[a,b].

Wavenumber (cm^{-1})	Assignments[c]
1615, 1598	ν(C=C,C=N) bzim
1569	ν(C=C,C=N) py
1453	ν(ring) bzim
1435	ν(ring) py
1416	ν(ring) bzim & py
1400	ν(ring) bzim & py + δ_{ip}(NH)
1303	δ_{ip}(CH) bzim + δ_{ip}(NH) + ν(C–N)
1283	δ_{ip}(CH) bzim + δ_{ip}(NH) + ν(C–C) bzim phenyl
1266, 1228, 1216	δ_{ip}(CH) bzim + δ_{ip}(NH) + ν(C–C) bzim phenyl + ν(C–N)
1152	δ_{ip}(CH) py
1015	δ_{ip}(CH) bzim phenyl
994, 952	δ_{op}(CH) py
901, 850	δ_{op}(CH) bzim
799	bzim ring breathing
735	δ_{op}(CH) bzim & py
690	δ_{op}(ring) py + δ_{op}(CH) py
652	δ_{ip}(ring) bzim & py

[a] abbreviations: bzim = benzimidazole, py = pyridine, ν = stretch, δ = bend, ip = in plane, op = out of plane.

[b] Note: In the experimental spectrum, peaks attributed to the CH and NH stretching modes are not resolved and therefore not included in this table.

[c] The vibrational assignments were made correlatively on the basis of previously published PBI4N[17-19], benzimidazole[20, 21] and pyridine[22] spectra, which were then compared and confirmed with the DFT calculated modes determined with DMol3.[14, 15]

In the C=C and C=N stretching region (1650 – 1550cm^{-1}), the modes of the phenyl and benzimidazole moieties in PBI4N tend to be very close in frequency. In comparison, the pyridine C=C and C=N stretching modes (1569 cm^{-1}) in PBI5N occur at slightly lower frequencies than the same modes in benzimidazole (1615, 1598 cm^{-1}). The in-plane CH bending modes occur between 1500 and 1000 cm^{-1}. In the higher end of this frequency range, the NH in-plane bending modes tend to be coupled with the CH modes. Below 1000 cm^{-1}, the peaks can be attributed to

out-of-plane CH bending modes and in-plane and out-of-plane ring bending modes. Stretching modes of the NH (3450-3100 cm^{-1}) and CH (~ 3050 cm^{-1}) groups are typically found at high frequencies (greater than 2500 cm^{-1}) [7, 17-19] however, those modes are of unusually low intensity in the spectrum shown in Figure 5.6.

For the acid-doped membranes, the infrared spectra are dominated by phosphoric acid bands. Bands at approximately 3750 and 2350 cm^{-1} are attributed to the acid OH stretching modes [23]. Additionally, there are three strong bands in the lower frequency region of the spectrum (ca. 1120, 980 and 880 cm^{-1}). These bands are typical vibrational modes of the phosphate anion. The frequencies of these bands are similar in all three spectra. The lowest frequency band at ca. 880 cm^{-1} is attributed to the symmetric PO stretch of the $P(OH)_3$ moiety [4,7,23]. The other two bands, ca. 1120 and 980 cm^{-1}, are most likely associated with the $H_2PO_4^-$ anion, as the $P(OH)_2$ antisymmetric PO stretching mode and the PO_2 symmetric stretching motion, respectively [4,7,23]. Additionally, there is a high frequency shoulder ca. 1220 cm^{-1} which may contain contributions from the PO_2 antisymmetric stretching motion or the POH bending motion of H_3PO_4 [4,23]. These phosphate bands indicate the presence of both H_3PO_4 and $H_2PO_4^-$ species within the membranes. The presence of functionalized silica can be mostly easily detected by the difference spectra reported in Figure 5.7. The difference spectra are obtained by subtracting the spectrum of the phosphoric acid solution from the spectra of the PBI5N/(SiO_2-Im+H_3PO_4) membrane (curve II in Figure 5.7) and the PBI5N/(H_3PO_4) (curve I of Figure 5.7).

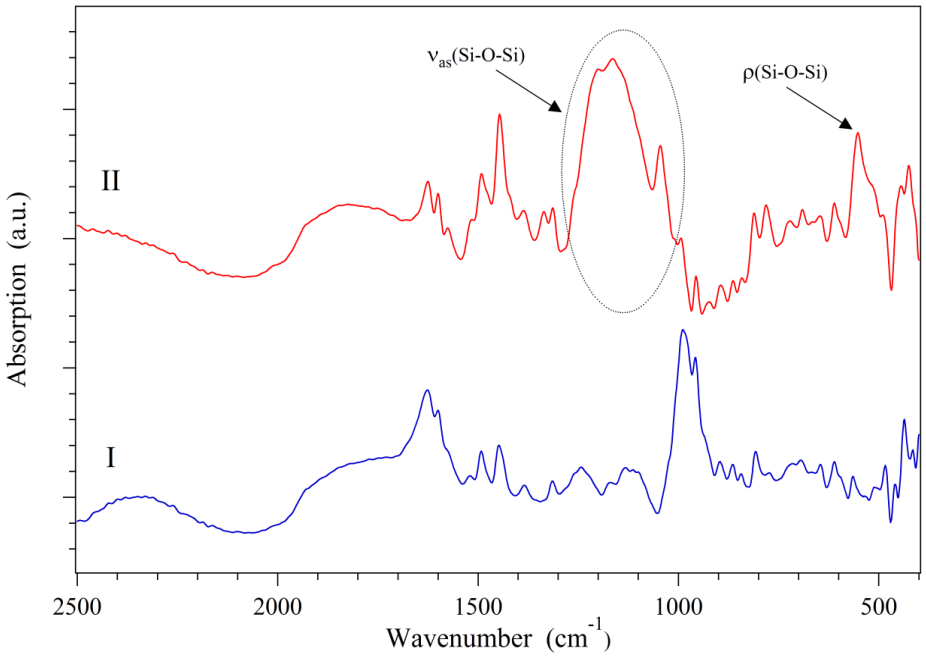

Figure 5.7 Difference spectra obtained subtracting the infrared spectrum of H_3PO_4 solution to PBI5N/(H_3PO_4) (curve I) and PBI5N/(SiO_2-Im+H_3PO_4) (curve II).

The spectra were normalized with the band centered at approximately 2350 cm^{-1} before subtraction. Spectral profile II shows the presence of absorption bands between 1300 and 1000 cm^{-1} and at ca. 550 cm^{-1}, associated to the asymmetric stretching and rocking modes of Si–O–Si group, respectively [24]. In PBI5N/(SiO_2-Im+H_3PO_4), comparing to H_3PO_4-doped PBI5N, the relative intensities of the peaks at 1130 and 1230 cm^{-1} increase when compared to the band at 990 cm^{-1} (see Fig. 5.6). Within PBI5N/(SiO_2-Im+H_3PO_4) membrane, this behavior could be associated with two phenomena: a) phosphoric acid in a less dissociated state than in the PBI5N/(H_3PO_4) [7] and/or b) the presence of the inorganic filler resulting in the superposition of the functionalized silica and phosphate peaks.

5.4.4 Broadband electric spectroscopy

For the investigated membranes, electrical measurements were performed in the frequency range from 10mHz to 10MHz for temperatures between 5 and 135°C. The spectra of the imaginary

component of permittivity ε'' and the real component of the conductivity σ' are shown as function of frequency at different temperatures in Figures 5.8 and 5.9, respectively.

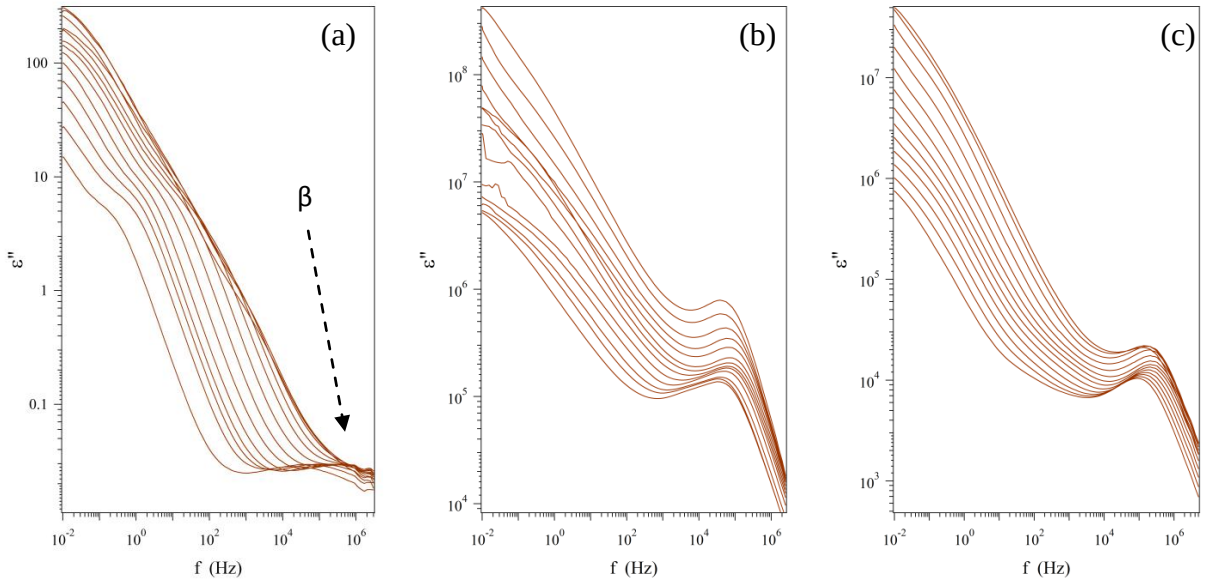

Figure 5.8 Profiles of ε'' as a function of frequency at temperatures between 5°C and 135°C for: (a) PBI5N; (b) PBI5N/(H_3PO_4); (c) PBI5N/(SiO_2-Im+H_3PO_4). β is the detected dielectric relaxation.

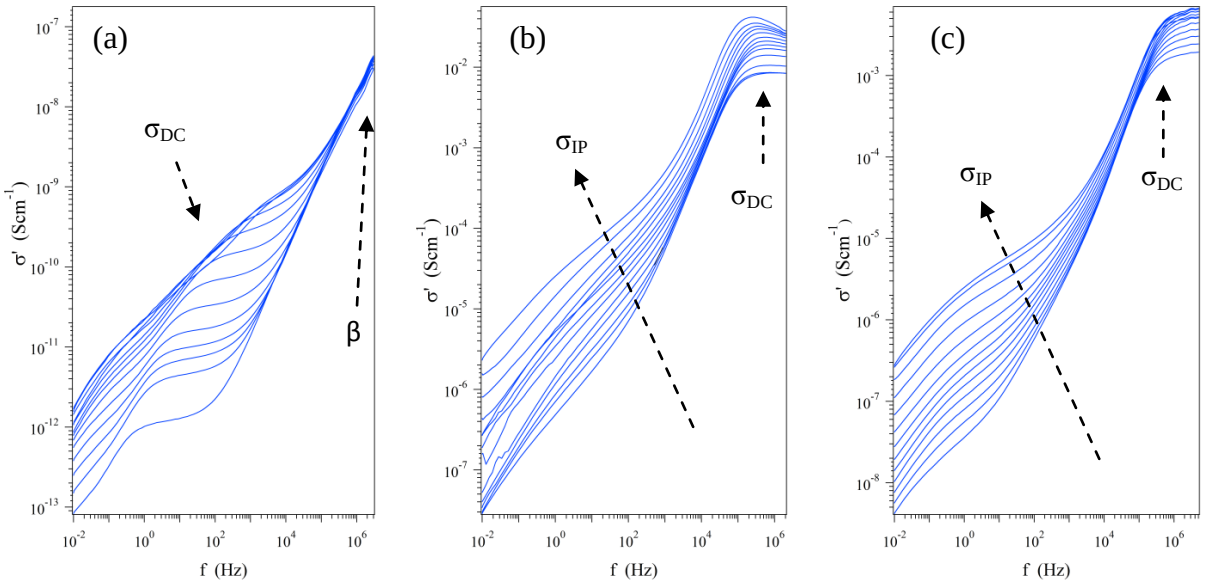

Figure 5.9 Profiles of σ' as a function of frequency at temperatures between 5°C and 135°C for: (a) PBI5N; (b) PBI5N/(H_3PO_4); (c) PBI5N/(SiO_2-Im+H_3PO_4). β is the dielectric relaxation and σ_{IP} and σ_{DC} are the interfacial and "bulk" conductivities, respectively.

From these spectra, it is evident that the addition of phosphoric acid leads to a substantial change in the electrical response of materials. For all samples, the values of ε'' increase with decreasing frequency and are 6 – 7 orders of magnitude greater in the membranes treated with H_3PO_4 than

in PBI5N. The profiles of σ' for the dry PBI5N membrane show values between 10^{-13} and 10^{-7} Scm^{-1} that increase by about 6 orders of magnitude after the treatment with H_3PO_4.

The ε" profile of PBI5N (Fig. 5.8 part a) at frequencies higher than 10^3Hz shows the presence of a broad peak, which shifts towards higher frequencies with increasing temperature. This peak is due to the β-electric relaxations, typically present in glassy systems for temperatures below the T_g [25, 26]. In the case of polymers of type B, where the dipole moments are rigidly attached to the main polymer chain, such as PVC or polycarbonates, β transitions are associated with changes in the dipole moments caused by local fluctuations in the main polymer chain [25, 26]. Since polybenzimidazole is a type-B polymer, it follows that in PBI5N the β relaxation modes arise from changes in the dipole moments induced by local motion of units within the polymer chain, as shown in Figure 5.10.

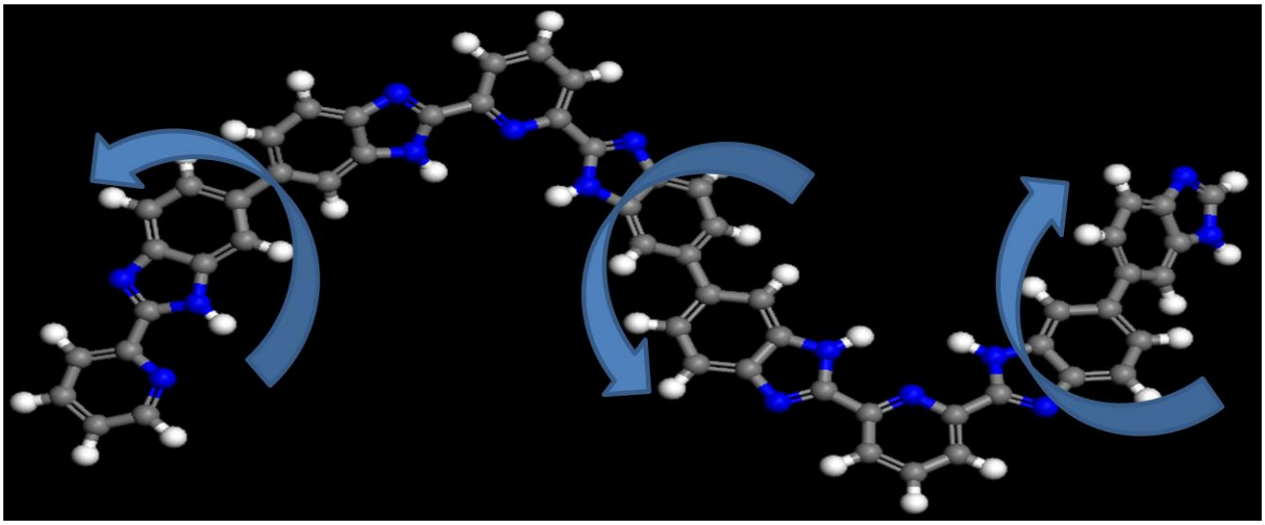

Figure 5.10 Origin of the β relaxation mode in PBI5N.

It should be noted that this mode is diagnostic of interactions between the PBI5N chains and the environment. For PBI5N between 0.1 and 10^3Hz, the ε'' profiles reported in part a of Figure 5.8 reveal the emergence of a peak that corresponds to a plateau in the conductivity spectra (Figure 5.9 part a). The σ' values taken at the plateau corresponds to membrane's bulk conductivity σ_{DC} [27], which increases with temperature from about 10^{-12} Scm^{-1} (5°C) to 10^{-9} Scm^{-1} (135°C).

These conductivity values: a) indicate that pristine PBI5N, in anhydrous conditions, behaves as a dielectric material; b) are in agreement with those found by Bouchet and Siebert, who reported for PBI4N a conductivity of 10^{-12} Scm^{-1} at 30°C and a conduction mechanism due to proton hopping between nitrogen atoms along the polymer chain [4]. As shown in part a of Fig. 5.8 for frequencies lower than 0.1Hz, the spectra of ε" increase with decreasing frequency. This response is due to the electrode polarization phenomenon (see Chapters 3 and 4), which involves the accumulation of charges at the interface between the measuring electrodes and the polymeric membrane [26]. Finally, the increases of σ' for frequencies higher than 10^3Hz is associated with the presence of the β relaxation. Detailed analysis of the PBI5N experimental data is conducted by fitting the permittivity profiles measured at different temperatures with Equation 5.2 [28-32] (see Appendix B).

$$\varepsilon^* = \frac{\sigma_{DC}}{i\omega\varepsilon_0}\frac{(i\omega\tau_{EP})^{\gamma}}{[1+(i\omega\tau_{EP})^{\gamma}]} + \frac{\Delta\varepsilon_{\beta}}{\left[1+\left(i\omega\tau_{\beta}\right)^{\mu_{\beta}}\right]} + \varepsilon_{\infty} \qquad (5.2)$$

The first term of Equation 5.2 simulates the electrode polarization, which is correlated to the bulk conductivity σ_{DC} of the material, with $0.5 < \gamma < 1$. The second term describes the molecular β relaxation using a Cole-Cole type equation [26]. $\omega = 2\pi f$ is the angular frequency of electric field and $\tau_\beta = 1/(2\pi f_\beta)$ is the relaxation time associated with the peak of intensity $\Delta\varepsilon_\beta$ and frequency position f_β. The parameter μ_β is a shape factor that controls the peak width and is related to the distribution of relaxation times associated with the dielectric relaxation. Finally, ε_∞ accounts for the electronic contribution to the permittivity of the material.

The resulting fit parameters $\Delta\varepsilon_\beta$ and μ_β are independent of temperature with values ranging between 0.2 – 0.27 and 0.26 – 0.4, respectively. For 5<T<65°C, the logarithmic values of f_β when plotted as a function of 1/T (part a of Figure 5.11) shows a VTF behavior (see Chapter 1 and Appendix A), with an activation energy E_β of 0.894 $kJmol^{-1}$. Such behavior suggests that the local and the segmental motion of the polymer chains are coupled together.

The logarithmic values of σ_{DC} and $f_{\sigma_{DC}}$ (with $f_{\sigma_{DC}} = 1/(2\pi\tau_{EP})$) plotted as function of the reciprocal temperature are shown in parts c) and b) of Figure 5.11, respectively. $Logf_{\sigma_{DC}}$ and $log\sigma_{DC}$ show similar trends and are divisible into two regions: VTF-type behaviour for 5<T<55°C (region I) and Arrhenius-type behavior between 55 and 115°C (region II).

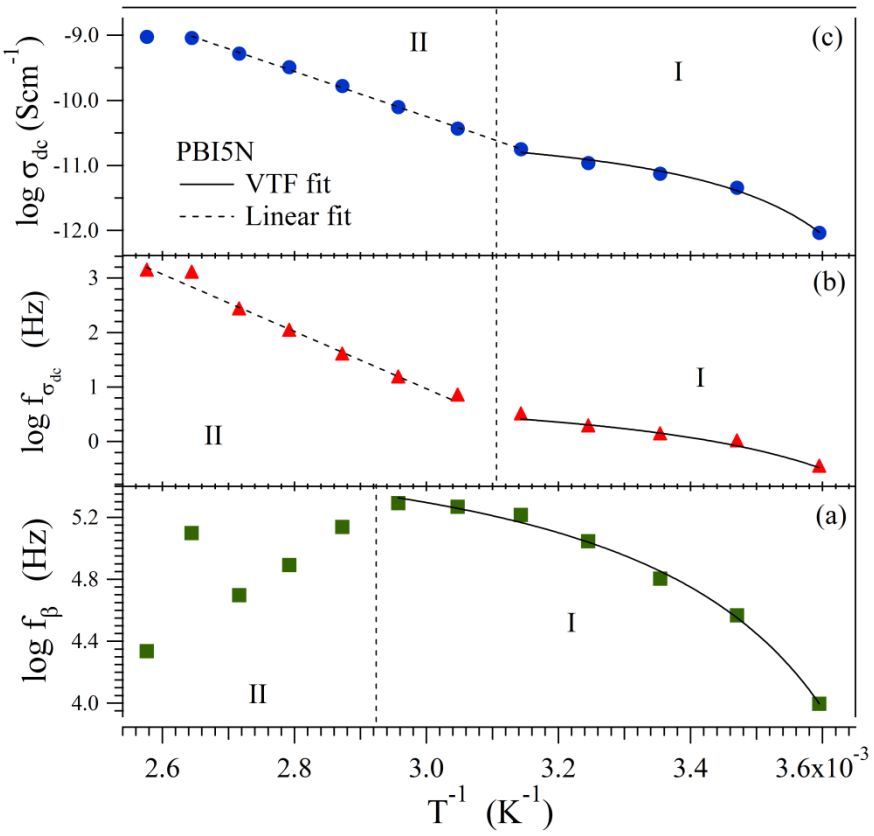

Figure 5.11 Log plot as a function of reciprocal temperature for PBI5N of: a) f_{β}; b) $f_{\sigma_{DC}}$; c) σ_{DC}.

For the temperature regions I and II the activation energies $E_{f\sigma_{DC}}$ and $E_{\sigma_{DC}}$ obtained by fitting the values of $logf_{\sigma_{DC}}$ and $log\sigma_{DC}$ with VTF and Arrhenius-type functions are reported in Table 5.2.

Table 5.2 Values of the activation energies E_{β}, $E_{f\sigma_{DC}}$ and $E_{\sigma_{DC}}$ for regions I and II for PBI5N.

	$E_{\beta}(kJmol^{-1})$	$E_{f\sigma_{DC}}(kJmol^{-1})$	$E_{\sigma_{DC}}(kJmol^{-1})$
Region I	0.894	0.862	0.645
Region II	/	99	66

For region I the values of $E_{f\sigma_{DC}}$ and $E_{\sigma_{DC}}$ are nearly coincident with E_{β}, indicating that the conduction mechanism, which occurs by "hopping" of the protons between the nitrogen atoms, is mediated by the local dipolar fluctuation and segmental motion of polymer chains. As the temperature increases (region II) the values of $logf_{\sigma_{DC}}$ and $log\sigma_{DC}$ follow an Arrhenius-type behavior with associated activation energies of $E_{f\sigma_{DC}}$=99 $kJmol^{-1}$ and $E_{\sigma_{DC}}$=66 $kJmol^{-1}$. These values are of the same order of magnitude as those found by Buchet and Siebert, who report for PBI doped with $0.2<x<3.5$ moles of acid per repeat unit of polymer an concentration-independent activation energy of about 77 kJ/mol [4]. The Arrhenius behavior indicates that for temperatures above 55 °C the motion of the protons is decoupled from that of the polymer chains.

As reported in Figures 5.8 and 5.9, for the acid-doped membranes, ε" values increased up to 6 orders of magnitude as compared to pristine PBI5N, while the spectra of σ' shows a plateau shifted to higher frequencies ($>10^5$Hz). The conductivity values taken at the plateau are between 10^{-2} and 10^{-3} Scm^{-1}, in agreement with those found by Bouchet and Siebert for PBI membranes doped with 1.45mol of H_3PO_4 per polymer repeat unit [4]. The high values of ε" and σ' indicate that for doped membranes the electrical response is entirely due to the motion of free charges. For the acid doped membranes, the permittivity and conductivity profiles reported in Figures 5.8 and 5.9 are similar to those found for the Nafion-based membranes reported in Chapters 3 and 4. Even for the acid-doped membranes, the electric profiles show the presence of the electrode ($f>10^5$Hz) and the interfacial ($f<10^3$Hz) polarizations. As described in Chapters 3 and 4, the electrode polarization is due to the accumulation of charges at the interfaces between the membrane and the measuring electrodes while the interfacial polarization is related to the accumulation of charges between domains with different permittivity [26,30-32]. For PBI5N/(H_3PO_4) and PBI5N/(SiO_2-Im+H_3PO_4), these domains are formed by phosphoric acid (hydrophilic domains) and PBI5N (hydrophobic domains).

Thus, the experimental profiles of ε" for PBI5N/(H_3PO_4) and PBI5N/(SiO_2-Im+H_3PO_4) are fitted considering the presence of multiple polarizations phenomena with Equation 5.3 [28-32] (see Appendix B).

$$\varepsilon^* = \sum_{k=1}^{2} \frac{\sigma_k}{i\omega\varepsilon_0} \frac{(i\omega\tau_k)^{\gamma_k}}{[1+(i\omega\tau_k)^{\gamma_k}]} + \varepsilon_\infty \tag{5.3}$$

The first term simulates: a) for k = 1 the electrode polarization related to the bulk conductivity σ_{DC}; b) for k = 2 the interfacial polarization event associated to the interfacial conductivity σ_{IP}. For the acid-doped membranes, the values of $\log\sigma_{DC}$, as a function of inverse temperature are shown in Figure 5.12, together with the bulk conductivity of PBI5N. For both doped membranes, the $\log\sigma_{DC}$ values are about six orders of magnitude greater than for PBI5N and show VTF behavior, as shown in inset b of Figure 5.12. The VTF behavior of $\log\sigma_{DC}$ is different from the Arrhenius behavior reported in previous works [4,10,33] but is in agreement with the study reported by Fontanella et al., where VTF behavior is observed for PBI doped with 6 mol of H_3PO_4 (similar doping level of the acid-doped membranes presented here) per repeat unit of PBI. This behavior is similar to that of a "true" polymer electrolyte in which the proton conduction mechanism is mediated by the segmental motion of the polymer chains [5]. The VTF behavior of $\log\sigma_{DC}$ plotted as a function of T^{-1} is in accordance with the DSC and DMA analysis that reveal: a) for PBI5N, a glass transition temperature below 200°C; b) for the acid-doped membranes, the presence of the α-mechanical transition induced by the segmental motion of the polymer chains.

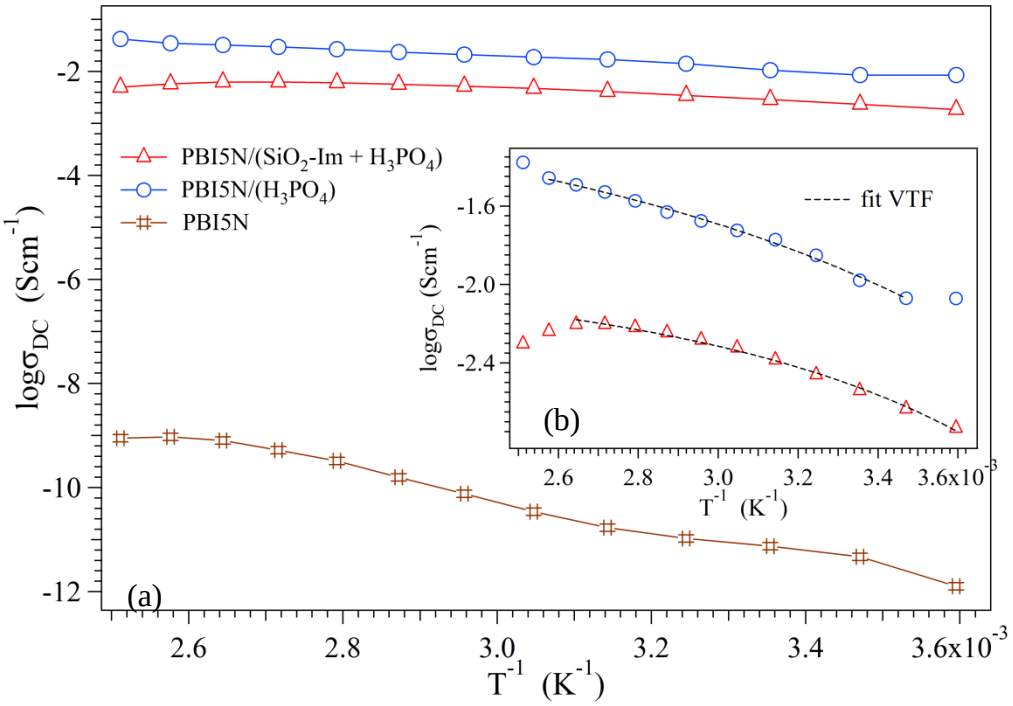

Figure 5.12 Log plot of the "bulk" conductivity σ_{DC} as a function of reciprocal temperature for: a) PBI5N, PBI5N/(H_3PO_4), PBI5N/(SiO_2-Im+H_3PO_4). The inset b shows the log of σ_{DC} as a function of 1/T for the acid-doped membranes.

The activation energy $E\sigma_{DC}$ associated to the bulk conductivity is 3.1 and 1.6 kJmol^{-1} for PBI5N/(H_3PO_4) and PBI5N/(SiO_2-Im+H_3PO_4), respectively. These values are of the same order of magnitude as the activation energy E_β related to β relaxation (0.894 kJmol^{-1}). In addition, as compared to PBI5N/(H_3PO_4), the lower activation energy for the hybrid membrane suggests that the presence of SiO_2-Im facilitates the proton conduction mechanism. For PBI5N/(SiO_2-Im+H_3PO_4) the conductivity values are lower than those of PBI5N/(H_3PO_4) (Fig. 5.12 inset b). This behavior, in accordance with vibrational spectroscopy results, could be due to the presence inside the hybrid membranes of phosphoric acid less dissociated than in the PBI5N/(H_3PO_4) membrane.

For the acid-doped membranes, the logarithmic values of the interfacial conductivity σ_{IP}, obtained by fitting the experimental data with Equation 5.3, are reported as a function of the inverse temperature in Figure 5.13.

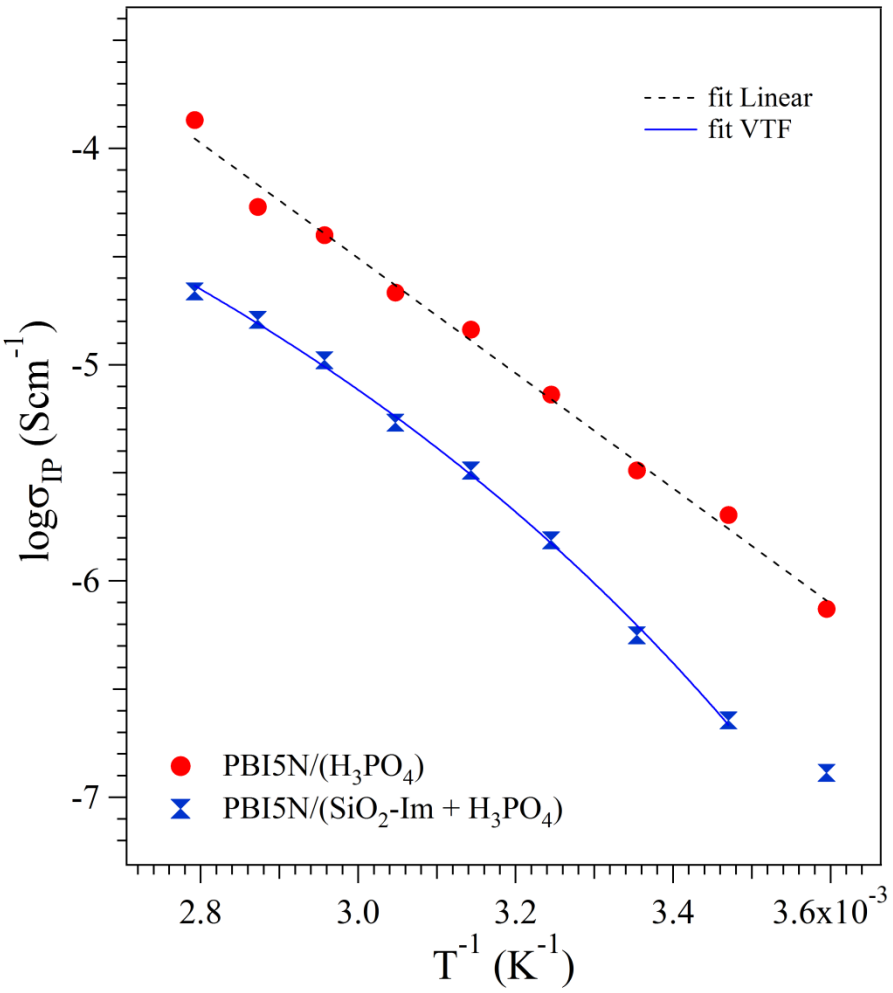

Figure 5.13 Log plot of σ_{IP} as a function of T^{-1} for PBI5N/(H_3PO_4) and PBI5N/(SiO_2-Im + H_3PO_4).

Logσ_{IP} vs. T^{-1} presents Arrhenius and VTF behavior for PBI/(H_3PO_4) and PBI/(SiO_2-Im+H_3PO_4), respectively. The presence of the filler, forming Im-SiO_2···PBI5N and SiO_2-Im···H_3PO_4 interactions, promotes the coupling between the dynamics of hydrophobic and hydrophilic domains present within the membranes. Thus, with respect to PBI5N/(H_3PO_4), in PBI5N/(SiO_2-Im+H_3PO_4) the proton conduction mechanism for the interfacial polarization is mediated by the segmental motion of the polymer matrix and shows a VTF-like temperature dependence. Furthermore, the interfacial conductivity is lower for PBI5N/(SiO_2-Im+H_3PO_4) with respect to PBI5N/(H_3PO_4), due to the presence inside the hybrid membranes of phosphoric acid less dissociated than in the PBI/(H_3PO_4) membrane. According to the BES results, it is possible

to hypothesize for the acid-doped membranes the proton conduction mechanisms reported in Figure 5.14.

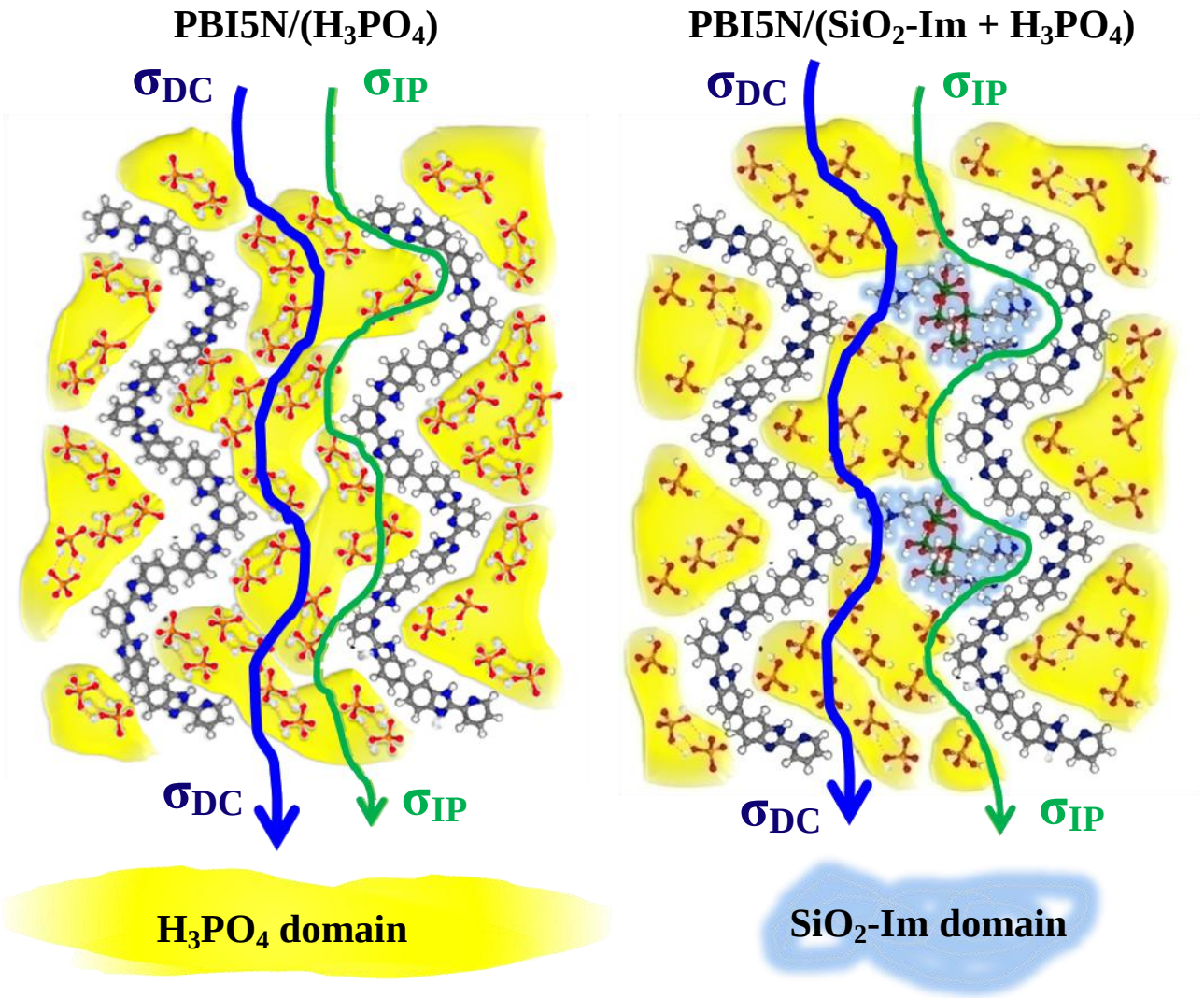

Figure 5.14 Proton conduction mechanism for PBI/(H_3PO_4) and PBI/(SiO_2-Im + H_3PO_4). σ_{DC} and σ_{IP} are the bulk and interfacial conductivity, respectively.

For both the acid-doped membranes the long-range σ_{DC} conductivity is due to proton hopping between the H_3PO_4 and water molecules present within the hydrophilic domains. This mechanism, due to the strong PBI···H_3PO_4 interactions, depends on the dynamic of the polymer matrix. In PBI5N/(SiO_2-Im+H_3PO_4), the SiO_2-Im filler facilitates the proton exchange processes between coordination sites and stabilizes the hydrophobic and hydrophilic domains of the membranes through the formation of PBI5N···SiO_2-Im and SiO_2-Im···H_3PO_4 interactions. These

interactions contribute to the development of a hybrid three-dimensional network that binds the aromatic chains of PBI5N and regulates the long-range and interfacial charge transfer mechanism. Proton conduction in the hybrid membranes occurs at the interface between the SiO_2-Im filler and the acid domains and is mediated by the dynamics of the fluorocarbon chains of the host polymer matrix.

5.5. Conclusions

This research activity, conducted during the first part of the 3rd year of doctoral stage, reports a detailed study of three PBI-based materials: polybenzimidazole (PBI5N), PBI5N impregnated with orthophosphoric acid (PBI5N/(H_3PO_4)) and PBI5N containing 10wt% of SiO_2-Im filler functionalized with imidazole groups and impregnated with orthophosphoric acid (PBI5N/(SiO_2-Im+H_3PO_4)). PBI-based materials are choose as Nafion-alternative membranes for application in high temperature fuel cell. The research are carried out in order to elucidate and understand the effect of the interactions between PBI5N , H_3PO_4 and the SiO_2-Im filler on the thermal, mechanical and electrical properties of the membranes.

The materials are characterized with TG, DSC and FT-IR spectroscopy, while their mechanical and electric properties are analyzed by DMA and BES studies. The thermogravimetric analyses showed: a) PBI5N is stable up to 300°C, while the acid-doped membranes present the thermal decomposition of H_3PO_4 in the temperature range from 120 to 320 °C; and b) the presence of the filler in bulk PBI5N increases the acid thermal stability within the membrane. The DSC measurements reveal that PBI5N has a glass transition temperature of 210°C and the presence of SiO_2-Im filler reduces the degree of crystallinity of the polymer membrane. The addition of phosphoric acid reduces the mechanical properties of doped membranes as compared to PBI5N, while the presence of the inorganic filler increases the mechanical stability of the hybrid membrane with respect to the acid-doped PBI5N. Furthermore, all of the membranes show the

presence of three mechanical transitions, γ, β and α, related to the dynamics of the polymer matrix.

The combination of DFT calculations and FT-IR allows assignment of the PBI5N spectrum. The C=C and C=N stretching modes of the pyridine unit in PBI5N tend to occur at lower frequencies that the phenyl modes in PBI4N. In the acid-doped membranes, the spectra indicate the presence of both H_3PO_4 and $H_2PO_4^-$ species within the membranes.

Electrical measurements show for the membrane PBI5N: a) the presence of a β-dielectric relaxation associated with fluctuations of the chain dipole moment induced by local motion of the polymer chains; and b) a proton conduction mechanism divisible into two different temperature regions: VTF for 5<T<55°C (region I) and Arrhenius for 55<T<115°C (region II). Acid-doped membranes present conductivity values of $10^{-2} – 10^{-3}$ Scm^{-1} and a VTF-type proton conduction mechanism, where proton hopping is coupled with the segmental motion of the polymer chain. This hypothesis is confirmed: 1) by the trend of $\log\sigma_{DC}$ as a function of 1/T that shows, in contrast to the dry PBI membrane, VTF behavior over the entire measured temperature range; and 2) by the presence of the α transition in the DMA tanδ profiles of wet membranes. In addition, the electric spectra of the acid-doped membranes reveal the presence of interfacial polarization phenomena due to the coexistence within the materials of hydrophobic and hydrophilic domains.

This work was conducted with the aim to improve the properties of PEMs for application in high-temperature fuel cells. In the PBI/(SiO_2-Im+H_3PO_4) membrane, a basic-functionalized filler allows increased acid uptake and to maintain a high conductivity due to the formation of percolation pathways at the interface between the polar and nonpolar domains. The optimal membrane for operation under these anhydrous conditions would result from the substitution or removal of water, while maintaining the thermal stability and the percolation pathways for good conductivity. Nanoscale and/or mesostructured fillers may be very useful to prepare PBI-based

membranes with better mechanical and transport properties. In particular, these materials can offer a valuable solution to the problem of acid leaching, which is chiefly relevant for thin membranes. A critical point to be addressed is the long-term stability of silica-based materials when they are in contact with phosphoric acid.

5.6. References

1. Wainright, J. S.; Wang, J. T.; Weng, D.; Savinell, R. F; Litt, M; *J. Electrochem. Soc.*, **1995**, 142, L121.
2. Wang, J. T.; Savinell, R. F.; Wainright, J.; Litt M.; Yu, H.; *Electrochim. Acta*, **1996**, 41, 193.
3. Lassègues, J. C.; in: Ph Colomban (Ed), *Proton conductors - Solids, membranes and gels – Materials and devices*, Cambridge University Press, **1992**, 311.
4. Bouchet R.; Siebert, E.; *Solid State Ionics*, **1999**, 118, 287.
5. Fontanella, J. J.; Wintersgill, M. C.; Wainright, J. S.; Savinell, R. F.; Litt, M.; *Electrochim. Acta*, **1998**, 43, 1289.
6. Rikukawa, M.; Morita, J.; Sanui, K.; Ogata, N.; *Proceedings of the Fifth International Symposium on Polymer Electrolytes*, Upsala, **1996**, 32.
7. Quartarone, E.; Magistris, A.; Mustarelli, P.; Grandi, S.; Carollo, A.; Zukowska, G. Z.; Garbarczyk, J. E.; Nowinski, J. L.; Gerbaldi C.; Bodoardo, S.; *Fuel Cells*, **2009**, 9, 349.
8. Lobato, J.; Canizares, P.; Rodrigo, M. A.; Linares, J. J.; *Electrochim. Acta*, **2007**, 52, 3910.
9. Carollo, A.; Quartarone, E.; Tomasi, C.; Mustarelli, P.; Belotti, F.; Magistris, A.; Maestroni, F.; Parachini, M.; Garlaschelli, L.; Righetti, P.P.; *J. Power Sources*, **2006**, 160, 175.
10. Quartarone, E.; Mustarelli, P.; Carollo, A.; Magistris, A.; Tomasi, C.; Garlaschelli, L.; Righetti, P.P.; *Mat. Res. Soc. Symp. Proc.*, **2007**, 972, 125.

11. Mustarelli, P.; Quartarone, E.; Grandi, S.; Carollo, A.; Magistris, A.; *Adv. Mater*., **2008**, 20, 1339.

12. Quartarone, E.; Mustarelli, P.; Carollo, A.; Grandi, S.; Magistris, A.; Gerbaldi, C.; *Fuel Cells*, **2009**, 9, 231.

13. Kurdakova, V.; Quartarone, E.; Mustarelli, P.; Magistris, A.; Caponetti, E.; Saladino, M. L.; *J. Power Sources*, **195**, 7765.

14. Delley, B.; *J. Chem. Phys*., **1990**, 92, 508.

15. Delley, B.; *J. Chem. Phys*., **2000**, 113, 7756.

16. Samms, S. R.; Wasmus S.; Savinell, R. F.; *J. Electrochem. Soc*., **1996**, 143, 1225.

17. Li, Q.; He, R.; Berg, R. W.; Hjuler, H. A.; Bjerrum, N. J.; *Solid State Ionics*, **2004**, 168, 177.

18. Musto, P.; Karasz, F. E.; MacKnight, W. J.; *Polymer*, **1989**, 30, 1012.

19. Musto, P.; Karasz, F. E.; MacKnight, W. J.; *Polymer*, **1993**, 34, 2934.

20. Infante-Castillo, R.; Rivera-Montalvo, L. A.; Hernandez-Rivera, S. P.; *J. Mol. Struct*., **2008**, 877, 10.

21. Morsy, M. A.; Al-Khaldi, M. A.; Suwaiyan, A.; *J. Phys. Chem. A*, **2002**, 106, 9196.

22. Urena, F. P.; Gomez, M. F.; Gonzalez, J. J. L.; Torres, E. M.; *Spectrochim. Acta, Part A*, **2003**, 59A, 2815.

23. Chapman, A. C.; Thrilwell, L. E.; *Spectrochim. Acta*, **1964**, 20, 937.

24. Di Noto, V.; Damioli, P.; Vittadello, M.; Dall'Igna, R.; Boella, F.; *Electrochim. Acta*, **2003**, 48, 2329.

25. Diaz-Calleja, R.; Riande, E.; *Mater. Sci. Eng., A*, **2004**, A370, 21.

26. Schonhals, A.; Kremer, F. eds.; *Broadband Dielectric Spectroscopy*, Springer, Berlin, **2003**.

27. Di Noto, V.; *J. Phys. Chem. B*, **2002**, 106, 11139.

28. Di Noto, V.; Lavina, S.; Negro, E.; Vittadello, M.; Conti, F.; Piga, M.; Pace, G.; *J. Power Sources*, **2009**, 187, 57.

29. Di Noto, V.; Vittadello, M.; Greenbaum, S. G.; Suarez, S.; Kano, K.; Furukawa, T.; *J. Phys. Chem. B*, **2004**, 108, 18832.

30. Di Noto, V.; Negro, E.; Sanchez, J. Y.; Iojoiu, C.; *J. Am. Chem. Soc*., **2010**, 132, 2183.

31. Giffin, G. A.; Piga, M.; Lavina, S.; Navarra, M. A.; D'Epifanio, A.; Scrosati, B.; Di Noto, V.; *J. Power Sources*, **2012,** 198, 66.

32. Di Noto, V.; Piga, M.; Giffin, G. A.; Pace, G.; *J. Membr. Sci.*, **2012**, 390, 58**.**

33. Pu, H.; Meyer, W. H.; Wegner, G.; *J. Polym. Sci., Part B: Polym. Phys.*, **2002**, 40, 663.

Chapter VI

Proton conducting membranes based on sulfonated poly(*p*-phenylenesulfone)/poly(1-oxotrimethylene)

6.1. Introduction

In order to overcome the drawbacks of perfluorinated ionomers (see Chapter 1), mainly associated with the fuel cell operating conditions limited to temperatures below 90°C and high levels of hydration of the membrane [1-6], a number of poly(arylene)-based ionomers such as sulfonated poly(ether ether ketone) or poly(ethersulfone) have been proposed [7-10]. These materials, present lower methanol crossover and improved mechanical characteristics at temperatures above 90°C as compared to the classical perfluorosulfonic acid polymers. In poly(arylene)-based ionomers, a reasonable ionic conductivity for practical applications in PEMFCs is obtained when a proton exchange capacity higher than two mequiv·g^{-1} is reached [11]. Nevertheless, under the hydration conditions typically adopted in PEMFCs, such a high proton exchange capacity leads to swelling and the loss of the membranes' mechanical properties. These effects result in decreased membrane performance in PEMFCs and in many

cases dissolution in water above 50°C [10]. Other poly(arylene) ionomers, such as sulfonated poly(p-phenylenesulfone), characterized by electron-deficient poly(arylene) chains and high ionic exchange capacity (IEC) were proposed [11-13]. The first property acts to increase the acidity and the thermal and thermo-oxidative stability of the materials, while the latter is a crucial parameter in improving the proton conductivity. The chemical structure of sulfonated poly(p-phenylenesulfone) (labelled $sPSO_2$) is reported in Figure 6.1.

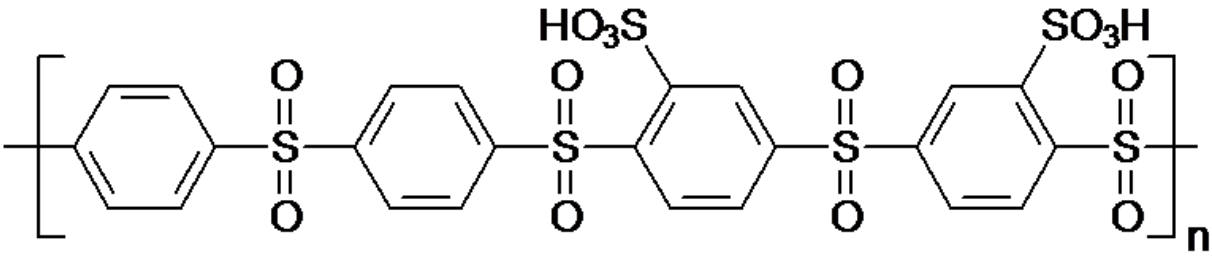

Figure 6.1 Chemical structure of sulfonated poly(p-phenylenesulfone).

In $sPSO_2$, the aromatic ring bearing the sulfonic acid group is connected to two sulfone linkages ($-SO_2-$) which are strongly electron withdrawing [12]. The reduced aromaticity of the ring significantly enhanced the hydrolytic stability of the sulfonic acid group, as reported in literature by Schuster et al. [12,13]. Thus, sulfonated poly(p-phenylenesulfone) presents lower solubility and swelling in water, and improved chemical stability [11-13] as compared to other sulfonated poly(arylene)s with similar IECs. These properties are nevertheless insufficient for practical application in PEMFCs operating at high temperatures.

In this study, nanocomposite proton-conducting membranes were prepared with the aim of stabilizing sulfonated poly(p-phenylenesulfone) ($sPSO_2$), in order to obtain new $sPSO_2$-based nanocomposite membranes with very low swelling and good electrical and mechanical properties at above 70°C. $sPSO_2$ has an equivalent weight (EW) of 360 $g \cdot equiv^{-1}$, which corresponds to a IEC of 2.77 $mequiv \cdot g^{-1}$ and a degree of sulfonation equal to 50% [11]. The high IEC is the reason for the large variation of the mechanical properties of $sPSO_2$ with relative humidity.

Under dry conditions $sPSO_2$ is very hard and brittle, but as the relative humidity increases, it starts to swell and loses its integrity at high water activities [11-13].

The materials were obtained by modulating the properties of $sPSO_2$ with poly(1-oxotrimethylene) (labelled PK, chemical structure reported in Figure 6.2).

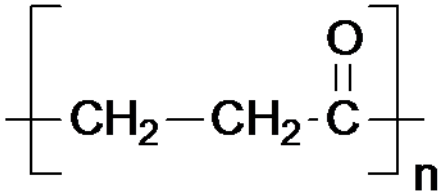

Figure 6.2 Chemical structure of poly(1-oxotrimethylene).

The PK copolymer was obtained by alternating CO-ethene copolymerization [14,15]. This strategy is very innovative and promising. It allows the enhancement of the thermal and mechanical properties of nano-composite $sPSO_2$ membranes, making them suitable for application in PEMFCs. PK is indeed a copolymer that is very stable both chemically and thermally [14,15]. Two series of membranes, A and B were prepared. Both types of membranes were obtained by a two-step process. For the A-type materials: 1) different copolymerization times for the reaction of CO with ethene in the presence of $sPSO_2$ was used to obtain a PK/$sPSO_2$ blend with 11, 28 and 33 wt% of PK; and 2) membranes were prepared by a solvent casting process from solutions containing the three different PK/$sPSO_2$ blends dissolved in dimethylacetamide (DMAc). For the B-type materials: 1) an inorganic-organic hybrid nanofiller [SiO_2/$(PK)_{0.65}$], where the weight fraction of PK equals 0.65, was synthesized by CO-ethene copolymerization in the presence of silica nanoparticles; 2) a solvent casting process was used to prepare membranes by dispersing 10, 20, 30 wt% of [SiO_2/$(PK)_{0.65}$] nanofiller in a $sPSO_2$/DMAc solution. TG measurements showed the high thermal stability (up to 280°C) of the membranes. The mechanical properties and the relaxation processes were investigated by dynamical mechanical analyses (DMA), revealing the presence of three mechanical transitions, α, β and γ.

The electrical properties were studied by broadband electric spectroscopy (BES). Electrical measurements were conducted for fully hydrated samples and at different values of relative humidity, in order to elucidate the effect of PK and the [SiO_2/$(PK)_{0.65}$] nanofiller on the proton conductivity of $sPSO_2$ as a function of the membranes' hydration state.

Results indicate that the presence of the hybrid nanofiller in B-type membranes reduces the water uptake and membrane swelling and increases the proton conductivity at low levels of membrane hydration as compared to pristine $sPSO_2$ and A-type materials.

6.2. Experimental

6.2.1 Synthesis of $sPSO_2$ powder

The $sPSO_2$ powder was synthesized according to Shuster et al. [12]. The reaction consists of a synthesis of poly(phenylene sulfide sulfone) (sPSS) bearing both an electron-donor and electron-acceptor group at each sulfonated aromatic ring which then allows the conversion of the donor group into an acceptor group, as reported in Scheme 6.1. This conversion is due oxidizing the sulfide to a sulfone functional group, corresponding to a conversion of a poly(phenylene sulfide sulfone) to a poly(phenylene sulfone). In details the procedure comprises the following steps: (1) polycondensation of disodium 3,3'-disulfonated 4,4'-difluorodiphenylsulfone with 4,4'-thiobisbenzenethiol to the corresponding sulfonated poly(phenylene sulfide sulfone) (sPSS) and (2) oxidation of the sulfonated poly(phenylene sulfide sulfone) to the corresponding sulfonated poly(phenylene sulfone) by using peroxide in acidic solution.

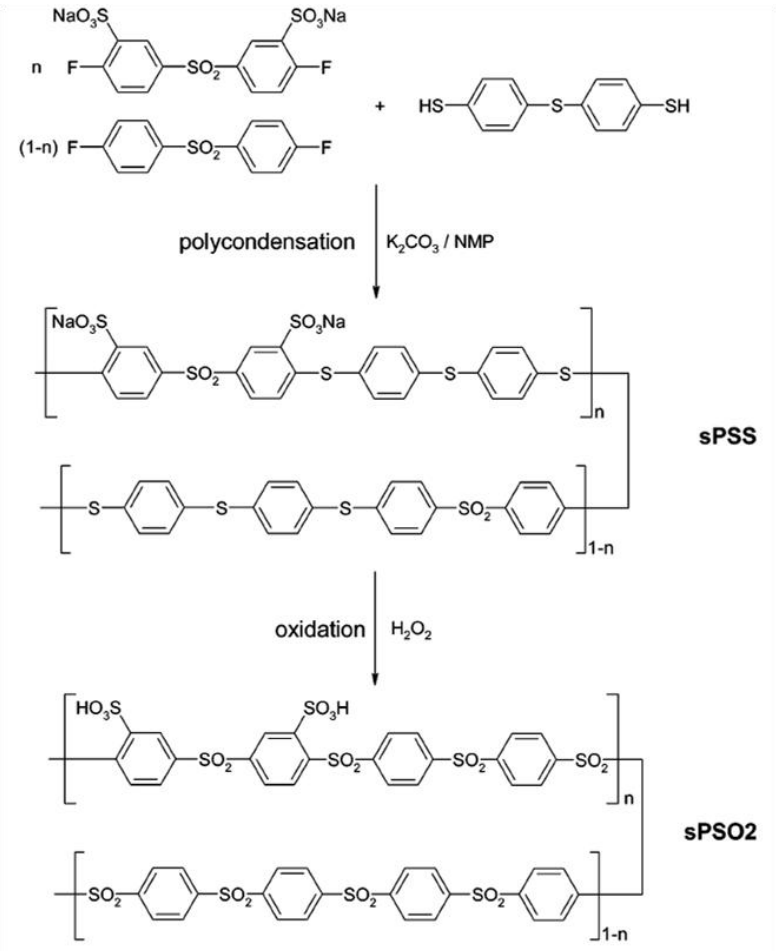

Scheme 6.1 Synthesis of sulfonated poly(p-phenylenesulfone).

The $sPSO_2$ powder has an equivalent weight of 360 g/equiv corresponding to a Proton Exchange Capacity of 2.77 mequiv/g.

6.2.2 Preparation of materials by CO/ethene copolymerization

$[SiO_2/(PK)_{0.65}]$, where the weight fraction (weight of polyketone/total weight) is 0.65, was prepared by CO-ethene copolymerization in the presence of porous silica following the procedure reported by Toniolo et al. [15,16] (Scheme 6.2). 8.8 mg (0.01 mmol) of $[Pd(TsO)(H_2O)(dppp)](TsO)\cdot H_2O$, 19 mg (0.1 mmol) of $TsOH\cdot H_2O$, 1.2 g of porous silica and 80 mL of MeOH were added to a glass bottle and placed in an autoclave (dppp = 1,3-bis(diphenylphosphino)propane; TsO = 4-methylbenzene sulfonate). The autoclave was flushed with CO, pressurised to 45 atm with CO/ethene (1:1 ratio) and heated at 85°C. The autoclave

was maintained at this temperature for 1 hour, and then cooled to room temperature and depressurized. The sample was constantly stirred during the reaction process. The resulting solid was collected by filtration, washed with MeOH and dried under vacuum, yielding 3.430 g of $[SiO_2/(PK)_{0.65}]$, where $0.65 = \chi_{PK} = (m_{Tot} - m_{SiO_2})/m_{Tot}$. A similar procedure was followed for the preparation of the fillers $[sPSO_2/(PK)_{0.11}]$, $[sPSO_2/(PK)_{0.28}]$ and $[sPSO_2/(PK)_{0.33}]$ used in the preparation of the A-type membranes, except that $sPSO_2$ was added in place of silica and the reaction times varied from 3 to 8 hours. In $[sPSO_2/(PK)_y]$, y = 0.11, 0.28 and 0.33 is the ratio between the weight of polyketone and the total weight of the composite material.

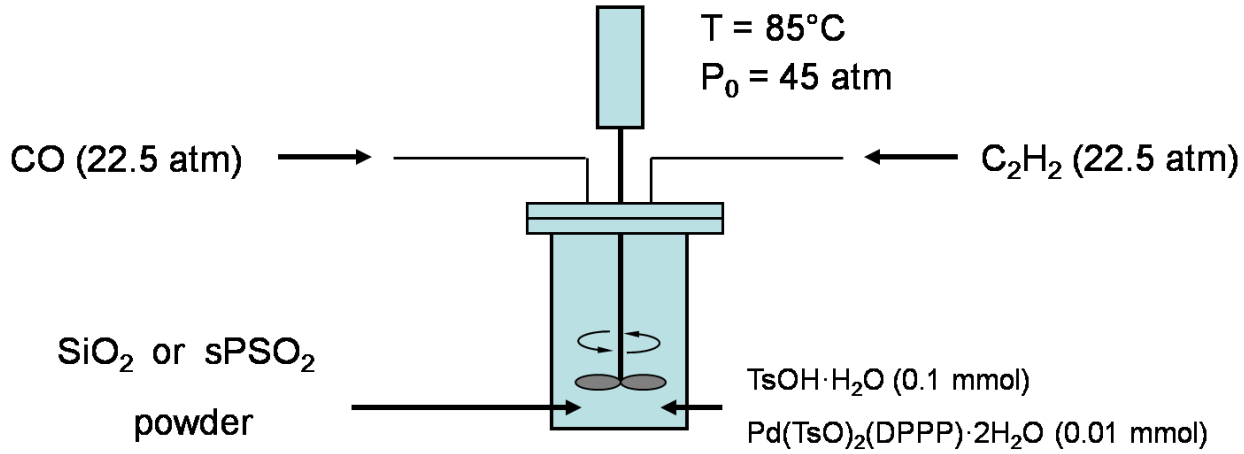

Scheme 6.2 Synthesis of $[SiO_2/(PK)_x]$ and $[sPSO_2/(PK)_y]$ fillers.

6.2.3 Membranes preparation

Pristine $sPSO_2$ membrane, used as reference material, was prepared by dissolving 500 mg of sulfonated poly(*p*-phenylenesulfone) in 7 mL of DMAc. The solution was recast onto a Petri dish and maintained at 80°C and under a dry air flow. The film was peeled from the Petri dish in 2-propanol and cured at 190°C for 15 h. The same procedure was followed for the preparation of A-type membranes, except that $[sPSO_2/(PK)_x]$, with x=11, 28 and 33 wt% was used instead of pristine $sPSO_2$. B-type membranes, having a composition of $[sPSO_2/(SiO_2)_y{\cdot}(PK)_z]$, where y and z are the respective weight fractions of SiO_2 and PK, were prepared by dissolving $sPSO_2$ in DMAc and by adding 10, 20 and 30 wt% of $[SiO_2/(PK)_{0.65}]$ filler to the solution. The dispersions

were homogenized by sonication and then recast onto a Petri dish as above. The resulting membranes are labelled [$sPSO_2/(SiO_2)_{0.035}(PK)_{0.065}$], [$sPSO_2/(SiO_2)_{0.069}(PK)_{0.131}$] and [$sPSO_2/(SiO_2)_{0.104}(PK)_{0.196}$] indicating membranes containing 10, 20 and 30 wt% of hybrid filler, respectively.

6.2.4 Instruments and methods

The proton exchange capacity (PEC) of the membranes was determined as follows. About 100 mg of each sample was dried for one week over P_2O_5, weighed in inert atmosphere, soaked in 100 mL of KCl 1 M and left stirring overnight. The solution was then titrated with 0.01 M KOH using a phenolphthalein indicator.

The water uptake (W.U.) and the number of water molecules per sulfonic acid group (λ) [17] were determined by TGA measurements, as described in Chapter 3, after soaking the samples in water at room temperature for one day. The initial (wt_0) and dry (wt_{dry}) weight of each sample was determined by registering the isothermal TGA desorption profile at 30°C and 120°C (see Chapter 3). The W.U. was determined using the following equation:

$$W.U. = \frac{wt_0 - wt_{dry}}{wt_{dry}} \tag{6.1}$$

λ depends on the W.U. and on the PEC as follows [18,19]:

$$\lambda = 1000\left[\frac{W.U.}{MW_{H_2O}PEC\chi_{sPSO_2}}\right] \tag{6.2}$$

where MW_{H_2O} is the molecular weight of water and χ_{sPSO_2} is the weight fraction of $sPSO_2$.

High-resolution transmission electron microscopy (HR-TEM) images were collected using a Jeol 3010 instrument operating at 300 kV with a high resolution pole piece (0.17 nm point-to-point resolution) and equipped with a Gatan slow-scan 794 CCD camera.

The infrared spectra of pristine PK, SiO_2 and $[SiO_2/(PK)_{0.65}]$ powders were collected using the spectrometer described in Chapter 2 equipped with a Smart Diffuse Reflectance Accessory (Thermo Scientific).

TG profiles were collected over the thermal range from 20 to 900°C. The heating rate (°C/min) was varied from 50 to 0.001°C/min. Dynamic mechanical analyses (DMA) were carried out in the range of temperature from -100 to 250°C at a rate of $4°C \cdot min^{-1}$. Before the measurements, each sample was dried at room temperature overnight.

The measurement of the complex conductivity spectra of wet samples was carried out in the frequency range from 10 mHz to 10 MHz and in the temperature range from 5 to 155°C. The measurements were performed in a closed home-made cell (see Chapter 2). The bulk conductivity of the samples, σ_{DC} was determined from the conductivity value extrapolated from the plateau of the $\sigma'(\omega)$ profiles at frequencies higher than 10^5 Hz, as described elsewhere [20] and in the previous sections of this work.

Electrical measurements at different relative humidity values were performed in the frequency range between 40 and 10^7 Hz using the system described in Chapter 2.

6.3. Results and discussion

6.3.1 Hybrid nanofiller characterization

The thermal stability of the $[SiO_2/(PK)_{0.65}]$ nanofiller was investigated by TG measurement. The TG profile of the hybrid filler is reported in Figure 6.3 together with the derivative of the weight change (dW%/dT). Figure 6.3 also shows the thermal decomposition of the PK powder. The $[SiO_2/(PK)_{0.65}]$ filler is stable up to 280°C, where starts the decomposition of PK and no thermal decomposition of the SiO_2 are revealed by the dW%/dT profile of $[SiO_2/(PK)_{0.65}]$. Furthermore, the first little weight elimination (1%wt) at T<100°C in $[SiO_2/(PK)_{0.65}]$ is due to water desorption, according to the hygroscopicity of SiO_2. From the

residues weight fractions at T = 800°C, equal to 28 and 46% for PK and [SiO_2/$(PK)_{0.65}$], respectively, and the thermal stability of SiO_2 in the investigated temperature range, it is possible to estimate the weight fraction of PK, equal to 0.62. This value is in good agreement with the value of 0.65 reported in section 6.2.2.

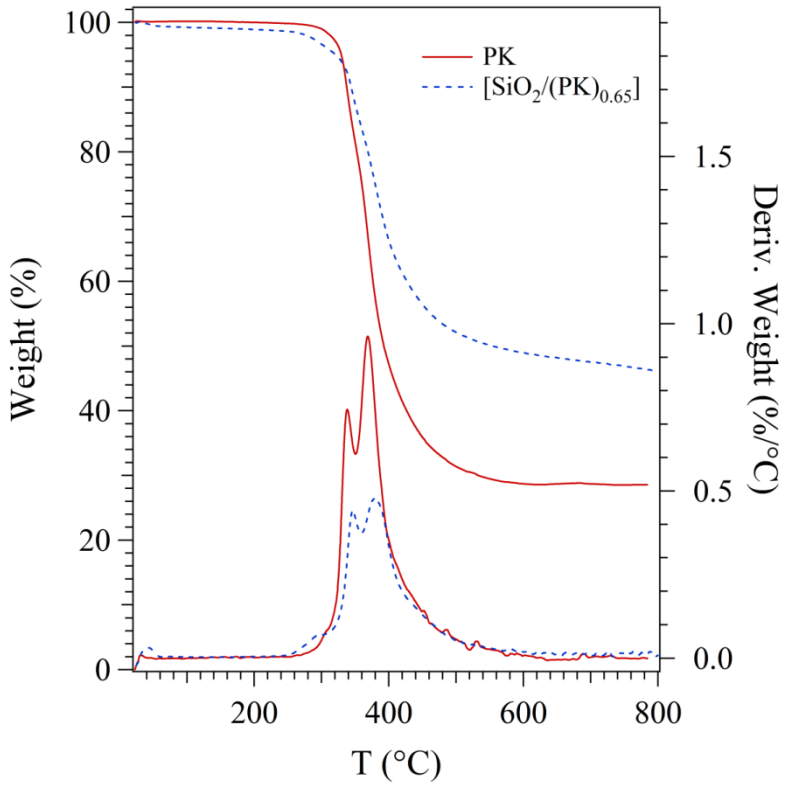

Figure 6.3 Weight loss (left axis) and derivative dw%/dT (right axis) in the temperature range from 20 to 800°C of PK and [SiO_2/$(PK)_{0.65}$].

The morphology of the hybrid nanofiller was determined by HR-TEM (Figure 6.4). The results lead to crucial insights into the growth mechanism of the PK nanofibres on the surface of SiO_2, which is schematically shown in part a of Figure 6.4. Parts b and c of Figure 6.4 reveal that PK horse-hair nanofibres are wrapped around a granular mass core of silica nanoparticles, while the analysis of Figure 6.4 d shows that the silica nanoparticles are about 20 nm in size.

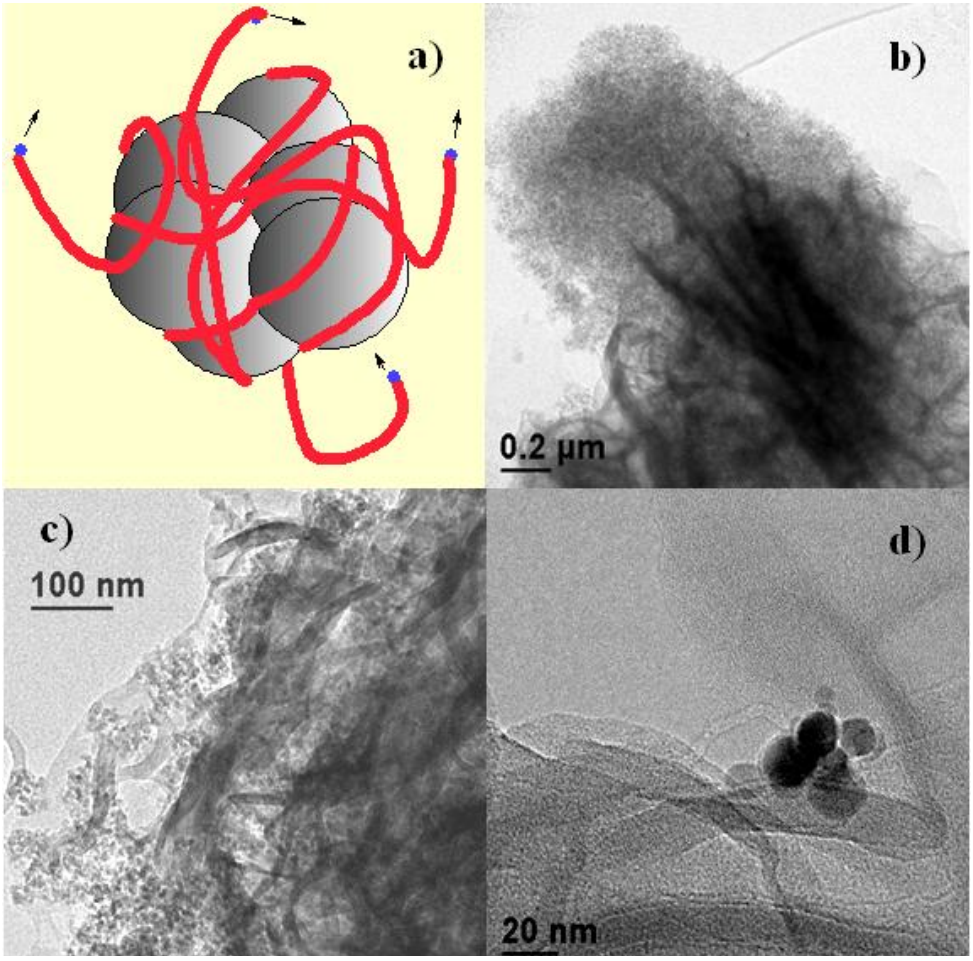

Figure 6.4 (a) Morphological hypothesis of the growth mechanism of PK on the surface of silica nanoparticle aggregates; (b) and (c) TEM images of the PK fibres wrapping the silica nanoparticle aggregates; (d) micrograph of primary silica nanoparticles wrapped with PK.

The infrared spectra of the SiO_2, $[SiO_2/(PK)_{0.65}]$ and PK powders are reported in Figure 6.5. The infrared spectrum of the $[SiO_2/(PK)_{0.65}]$ hybrid nanofiller is essentially the superposition of SiO_2 and PK spectra. Furthermore, the presence of the OH stretching modes of hydroxyl groups in the spectra of both pristine SiO_2 and $[SiO_2/(PK)_{0.65}]$ between 3800 and 3000cm^{-1} indicates that PK is coiled around the silica nanoparticles without forming chemical bonds with the OH groups present on the surface of the nanoparticles. Thus, the hydroxyl groups present on the surface of the silica nanoparticles can interact with the $sPSO_2$ polymer matrix. Such interactions, as will be discussed later are on the basis of the improvement of the properties of the B-type materials with respect to A-type membranes and pristine $sPSO_2$.

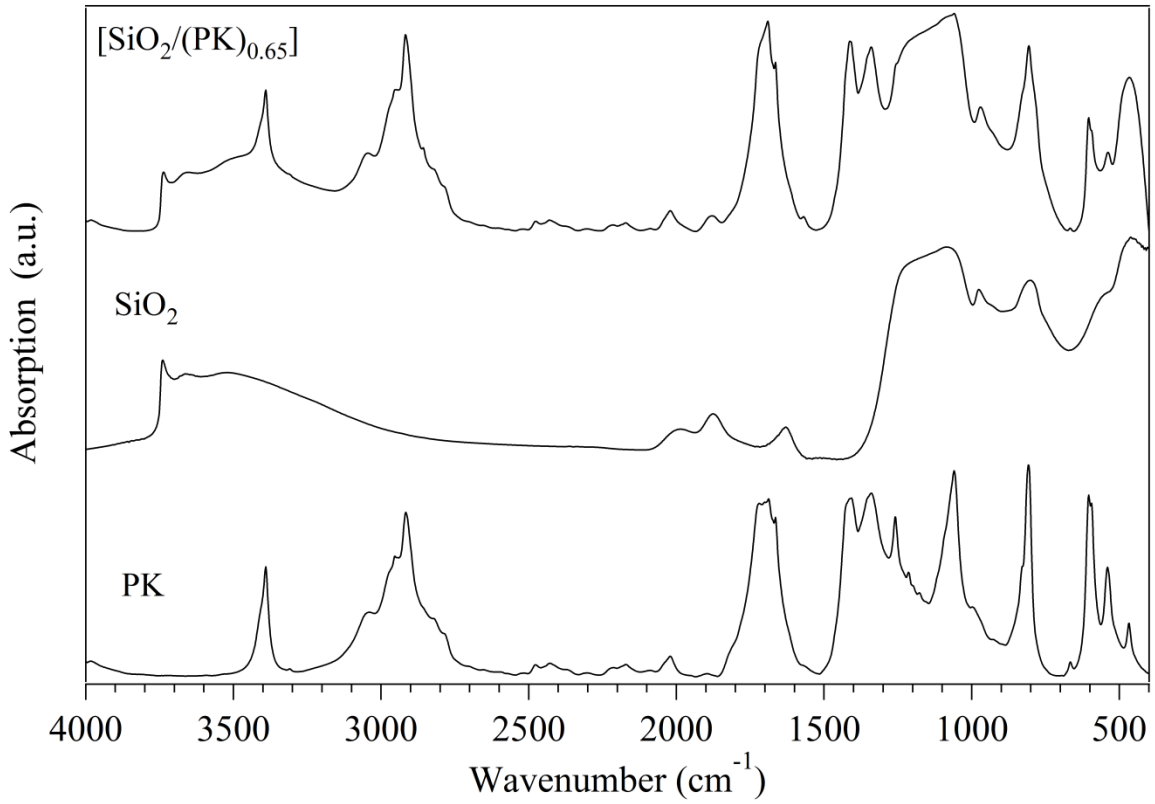

Figure 6.5 Infrared spectra of pristine PK, SiO_2 and the $[SiO_2/(PK)_{0.65}]$ hybrid nanofiller in the spectral region from 4000 to 400cm^{-1}.

6.3.2 Membranes characterization: water uptake, thermal stability and mechanical properties

The composition and select properties of the materials explored in this study are reported in Table 6.1. For the sake of completeness, the properties of the A- and B-type membranes are compared with those of pristine $sPSO_2$ reference membrane measured in the same conditions. The W.U. values are significantly different for each type of studied material (Table 6.1), while the number of water molecules per sulfonic acid groups (λ) is approximately the same for all membranes ranging between 7 and 11 except in the membranes with the highest amount of hybrid nanofiller (λ=15). The W.U. of the A and B-type membranes is close to half of that of pristine $sPSO_2$, with the lowest W.U. occurring in the $[sPSO_2/(PK)_{0.33}]$ membrane. This effect is ascribed to the dilution of the hydrophilic acid groups of $sPSO_2$ by PK nanofiller in bulk membranes that reduces the volume of the hydrophilic domains.

Table 6.1 Composition, Proton Exchange Capacity (PEC), Water Uptake (W.U.), Arrhenius and VTF pseudo-activation energies of $sPSO_2$, and A- and B-type membranes. λ is the ratio of water molecules per sulfonic acid group. I and II are the conductivity regions.

	Material	χ_{sPSO_2} [a]	f [b]	PEC (meq·g^{-1})	W.U. (%)[c]	λ[c]	S(%)[d]	E_a (kJ·mol^{-1})[e] I	E_a (kJ·mol^{-1})[e] II
	$sPSO_2$	1	0	2.44	50	11	109	17	0.6
A Type	$[sPSO_2/(PK)_{0.11}]$	0.89	0.12	2.17	24	7	20	9	1.5
	$[sPSO_2/(PK)_{0.28}]$	0.72	0.38	1.76	25	11	22	23	2.8
	$[sPSO_2/(PK)_{0.33}]$	0.67	0.49	1.63	17	9	21	12	3.2
B Type	$[sPSO_2/(SiO_2)_{0.035}(PK)_{0.065}]$	0.90	0.07	2.20	31	9	30	19	1.2
	$[sPSO_2/(SiO_2)_{0.069}(PK)_{0.131}]$	0.80	0.16	2.00	29	10	24	16	1.4
	$[sPSO_2/(SiO_2)_{0.104}(PK)_{0.196}]$	0.70	0.28	1.70	33	15	22	13	1.3

[a]weight fraction of poly(*p*-phenylene sulfone); [b] $f = \frac{wt_{PK}}{wt_{sPO_2}}$; [c]determined after soaking the sample one day in water at room temperature; [d]percentage of swelling as compared to the dry membrane with the same treatment; S(%) = $((L-L_0)/L_0)\cdot 100$, where L_0 and L are the thickness of the dry and wet membrane, respectively; [e]Activation energies are determined from fitting the conductivity profiles of wet samples with Arrhenius (region I) and VTF (region II) equations.

Even if the weight fraction of $sPSO_2$ in the A and B groups are similar (Table 6.1), the water uptake for B-type membranes is higher than those measured for the A-type membranes. This is due to the high nanoporosity of the hybrid $[SiO_2/(PK)_{0.65}]$ nanofiller that absorbs water molecules in the interstices between the surface of silica nanoparticles and the wrapping PK nanofibers. Specifically, in agreement with the swelling percentage, S(%), reported in Table 6.1, it is observed that: a) pristine polysulfone exhibits severe swelling even at room temperature and dissolves completely in boiling water; b) B-type membranes have a higher dimensional stability than $sPSO_2$ and only partially dissolve in boiling water; and c) A-type membranes exhibit no swelling at room temperature and are very stable even in boiling water. Recently Titvinidze et al. synthesized and studied a series of sulfonated poly(phenylene sulfone) membranes containing triphenylphosphine oxide moieties as constitutional units in the backbone, with PEC values (between 1.72 and 2.32 mequiv·g^{-1})

similar to those of the composite membranes here presented [22]. The authors reported water uptake values at 100% R.H. and room temperature between 40 and 50%, with values of λ between 19 and 28 [22]. In the investigated composite membranes, despite similar values of PEC, the presence of the PK nanofibres reduces membrane swelling and water uptake due to different membrane microstructure induced by the presence of PK nanofibres and the [SiO_2/$(PK)_{0.38}$] nanofiller.

Polysulfone-based materials [22] have previously shown that the through-plane swelling is larger than the in-plane swelling. However, in this work the measuring equipment was not sufficiently precise to accurately determine the in-plane swelling, so only the through-plane is reported. These experimental results indicate a decrease in permittivity and an improvement in mechanical stability of the nanocomposite membranes in polar environments such as water.

The TG profiles for $sPSO_2$, [$sPSO_2$/$(PK)_{0.28}$] and [$sPSO_2$/$(SiO_2)_{0.035}(PK)_{0.065}$] membranes are reported in Figure 6.6.

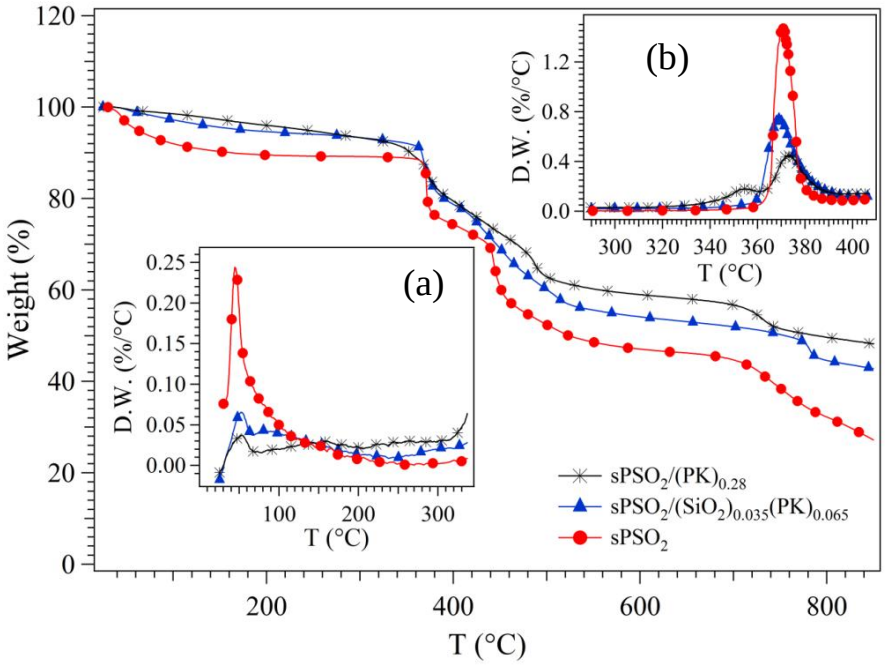

Figure 6.6 TG measurements of $sPSO_2$, [$sPSO_2$/$(PK)_{0.28}$] and [$sPSO_2$/$(SiO_2)_{0.035}(PK)_{0.065}$] membranes. Insets show the dependence of the derivative of TG profiles on temperature in regions: (a) 20-350°C; and (b) 290 – 410°C.

The membranes are thermally stable up to ca. 340°C, and thus up to 150°C higher than Nafion-based membranes (see Chapters 3 and 4), demonstrating the higher thermal stability of the polysulfone with respect to the classic fluorinated polymers. For all the investigated materials the TG curves and their derivatives as function of temperature reveal the presence of four thermal decompositions, assigned as follows [12,13]. In the range 30–130°C, the mass elimination corresponds to the desorption of traces of water. The water content within the membranes is 10, 6 and 4 wt% for $sPSO_2$, [$sPSO_2/(SiO_2)_{0.035}(PK)_{0.065}$] and [$sPSO_2/(PK)_{0.28}$]. The water content increases according with the fraction χ_{sPSO_2} of polysulfone present within the membranes (see Table 6.1). The second mass elimination, between 320 and 400°C is associated with the degradation of $–SO_3H$ groups [12,13]. For the membranes containing PK, according to the TG profiles of the fillers reported in Figure 6.3, the second mass elimination also contains a component due to thermal degradation of PK. TG derivative curves shown in the inset b of Figure 6.6 reveal that the presence of the fillers slightly changes the decomposition temperature of the acid groups. The weight losses observed at T>400°C are associated with the thermal degradation of the polysulfone matrix [12,13].

The mechanical properties of the dry materials were studied by DMA between -100 and 250°C at 1 Hz. The profiles of the Storage Modulus (E'), the Loss Modulus (E'') and tanδ are shown in parts a and b of Figure 6.7 for A- and B-type membranes, respectively.

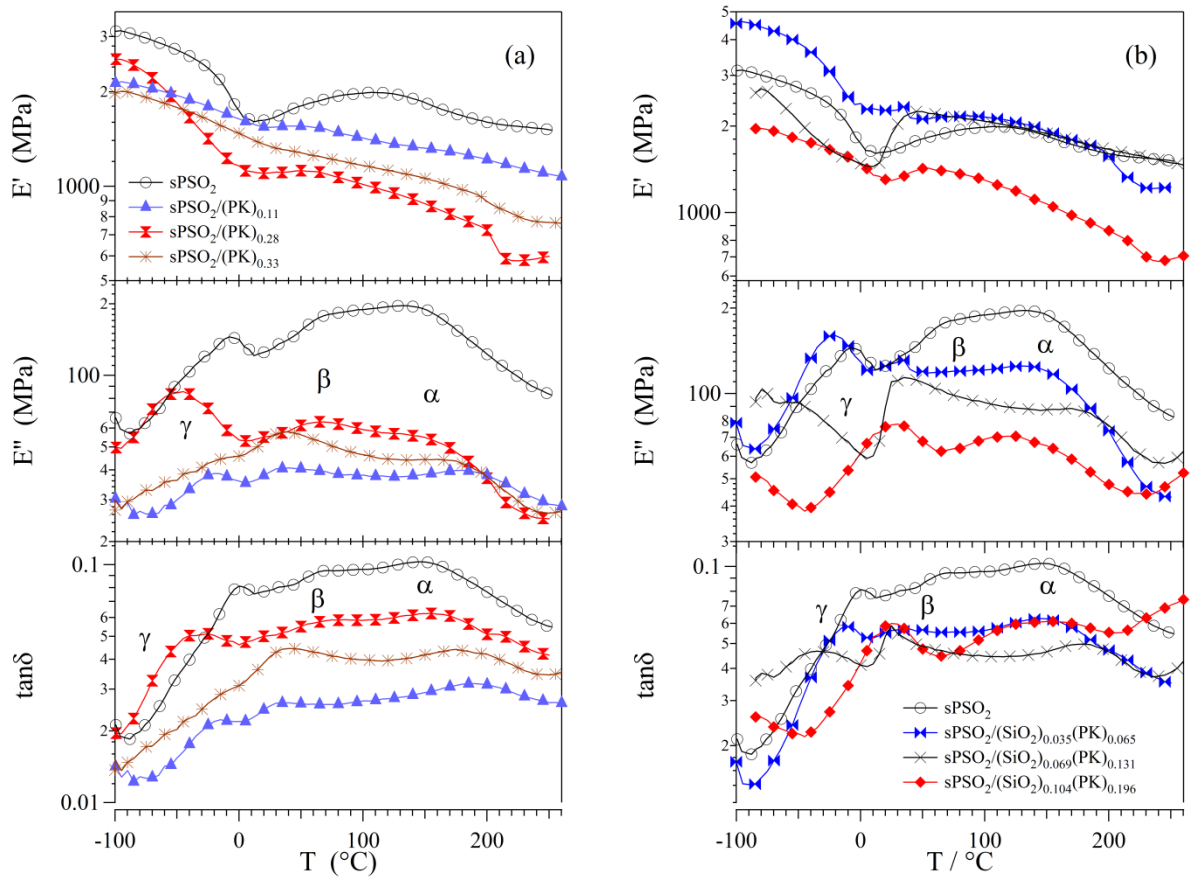

Figure 6.7 Profiles of the storage modulus (E'), loss modulus (E'') and tanδ = E''/E' versus temperature of the dry membranes, (a) $sPSO_2$ and A-type membranes and (b) $sPSO_2$ and B-type membranes.

It is observed that up to ca. 200°C, pristine dry $sPSO_2$ has a Storage Modulus (E') higher than 1700 MPa (Figure 6.7). The mechanical properties of poly(p-phenylenesulfone) are much better than those of pristine Nafion®, whose E' values decrease steadily above 100°C up to an irreversible elongation above 130°C [17-19,23,24]. As previously reported in Chapter 3 (Equation 3.3), the elastic modulus *E'* is proportional to the density *n* of the interchain crosslinks in a polymer network. The E' values of A-type membranes are lower than those of pristine $sPSO_2$ and the B-type materials, indicating that the density of hydrogen bonding cross-links in A-type membranes is lower than that in B-type. The difference in the mechanical properties of the A- and B-type membranes is due to the presence of the SiO_2 nanoparticles, which interact with the $sPSO_2$ acid groups to increase the mechanical stability of the hybrid membranes. In particular at temperatures above 100°C, the E' values of

membranes doped with 10 and 20 wt% of [SiO_2/$(PK)_{0.65}$] nanofiller are similar to that of pristine $sPSO_2$, with values of 1980, 2088 and 2003 MPa at 120°C for $sPSO_2$, [$sPSO_2$/$(SiO_2)_{0.035}(PK)_{0.065}$] and [$sPSO_2$/$(SiO_2)_{0.069}(PK)_{0.131}$], respectively. This indicates that at medium-high temperature, i.e. above 100°C, the strength of the hydrogen bonding interactions between sulfonic acid groups of $sPSO_2$ are similar to those between $sPSO_2$ and the silica hydroxyl groups. The major drawback of $sPSO_2$ is that its mechanical properties are strongly influenced by its hydration state [12,13]. To reveal the effect of hydration on the mechanical properties, the A- and B-type membranes, which showed the best mechanical properties in a dry state were measured in a wet state at room temperature (25°C). Wet $sPSO_2$ has an E' value of 16 MPa, while the E' values of [$sPSO_2$/$(PK)_{0.28}$] and [$sPSO_2$/$(SiO_2)_{0.035}(PK)_{0.065}$] are 100 and 48MPa, respectively. Both dry and wet [$sPSO_2$/$(SiO_2)_{0.035}(PK)_{0.065}$] have a slightly higher E' value than pristine $sPSO_2$ due to the formation of inter-chain hydrogen bonding cross-links between sulfonic acid, ketone and silica hydroxyl groups. Similar cross-linking interactions were described in literature [17-19,23,24] and in Chapter 3 of this work to improve the mechanical properties of hybrid Nafion-based membranes. For the wet materials, [$sPSO_2$/$(PK)_{0.65}$] has a higher E' than pristine $sPSO_2$ and [$sPSO_2$/$(SiO_2)_{0.035}(PK)_{0.065}$], which is in agreement with its lower W.U.

The temperature spectra of the loss modulus (E") and tanδ in Figure 6.7 reveal the presence of three thermo-mechanical relaxations for $sPSO_2$ centred at about -30, 50 and 100°C which were ascribed to the γ, β and α relaxations, respectively. The γ relaxation, which has the lowest energy barrier, is likely related to the local fluctuations of the aromatic rings of the $sPSO_2$ polymer chains. The β transition is associated with the relaxation modes of $sPSO_2$ side groups, which are involved in interchain dipole-dipole interactions between the sulfonic acid groups and the environment. The α relaxation is due to the segmental motion of $sPSO_2$ polymer backbone chains. The same three mechanical transitions are present for all the

composite membranes. As compared to pristine $sPSO_2$, the presence of PK in the A-type materials: a) shifts the α transition to higher temperatures indicating that the PK fibres reduce the mobility of the $sPSO_2$ chains; and b) slightly reduces the temperature of the β and γ transitions revealing that the presence of PK decreases the strength of the interchain dipolar interactions between sulfonic acid groups, which is in agreement with the E' values.

For the B-type membranes, the temperature of the mechanical transitions is modulated by the presence of the hybrid nanofiller due to its interactions with the $sPSO_2$ matrix. In particular, the γ transition temperature decreases with increasing hybrid nanofiller concentration. The β and α transition temperatures are changed only slightly as compared to pristine $sPSO_2$ indicating that: a) the strength of the interactions between acid side groups of $sPSO_2$ and hybrid nanofiller are on the same order of those of between the $sPSO_2$ acid groups; and b) the presence of $[SiO_2/(PK)_{0.65}]$ nanofiller increases the mobility of the $sPSO_2$ backbone chains as compared to that of the A-type materials. Taking together, the DMA results confirm that the strength of the dipole-dipole interactions between acid side groups of $sPSO_2$ and the environment in the dry composite membranes decreases in the order $sPSO_2$-$sPSO_2$ > $sPSO_2$-SiO_2-PK > $sPSO_2$-PK. Furthermore, it should be highlighted that in wet samples, the $sPSO_2$-PK interchain interactions are crucial in increasing the dimensional stability and mechanical properties of membranes due to their ability to reduce the hydrophilicity of the polar side chain groups in bulk materials.

6.3.3 Membranes proton conductivity

The real part of the conductivity (σ') as function of frequency and temperature is reported in part a, b and c of Figure 6.8 for $sPSO_2$, $[sPSO_2/(SiO_2)_{0.104}(PK)_{0.196}]$ and $[sPSO_2/(PK)_{0.33}]$, respectively. σ' profiles similar to those reported in Figure 6.8 are obtained for all the other investigated membranes.

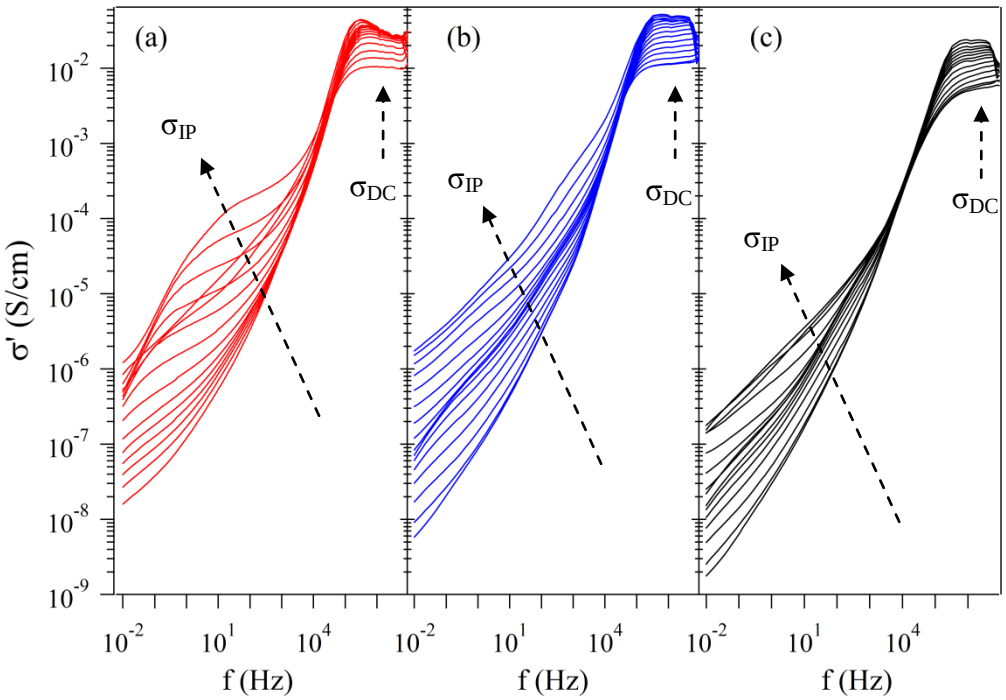

Figure 6.8 Profiles of σ' as a function of frequency at temperatures between 5°C and 155°C for: (a) $sPSO_2$; (b) $[sPSO_2/(SiO_2)_{0.104}(PK)_{0.196}]$ and $[sPSO_2/(PK)_{0.33}]$. σ_{IP} and σ_{DC} are the interfacial and "bulk" conductivities, respectively.

The conductivity profiles: a) increases with increasing frequency and temperature; b) reveal the presence of the interfacial (IP) and electrode (EP) polarization. As previously described in Chapters 3-5 for Nafion- and PBI- based membranes, the EP ($f>10^5$Hz), associated with the bulk conductivity σ_{DC}, arises from charge accumulation at the interfaces between the membrane and the measuring blocking electrodes while the IP, present at $f<10^4$Hz and related to the interfacial conductivity σ_{IP}, is due to the accumulation of charges between hydrophobic and hydrophilic domains present within the membrane. For the investigated materials, the hydrophilic domains consist of $sPSO_2$ acid groups and water molecules, while the hydrophobic domains are formed by PK and $sPSO_2$ backbone.

As revealed by the σ' profiles of Figure 6.8 the IP decreases in the order: $sPSO_2$ > $[sPSO_2/(SiO_2)_{0.104}(PK)_{0.196}]$ > $[sPSO_2/(PK)_{0.33}]$. According to W.U. results, this effect is ascribed to the dilution of the hydrophilic acid groups of $sPSO_2$ by PK nanofiller in bulk membranes that reduces the volume of the hydrophilic domains. The temperature dependence of the bulk conductivity σ_{DC} of the wet samples is shown in part a and part b of Figure 6.9

for the A- and B-type materials, respectively. Precise values of the bulk conductivity are determined by averaging the σ' values in the high frequency plateau of the conductivity spectra [18-20]. The conductivity of pristine Nafion is shown as a reference.

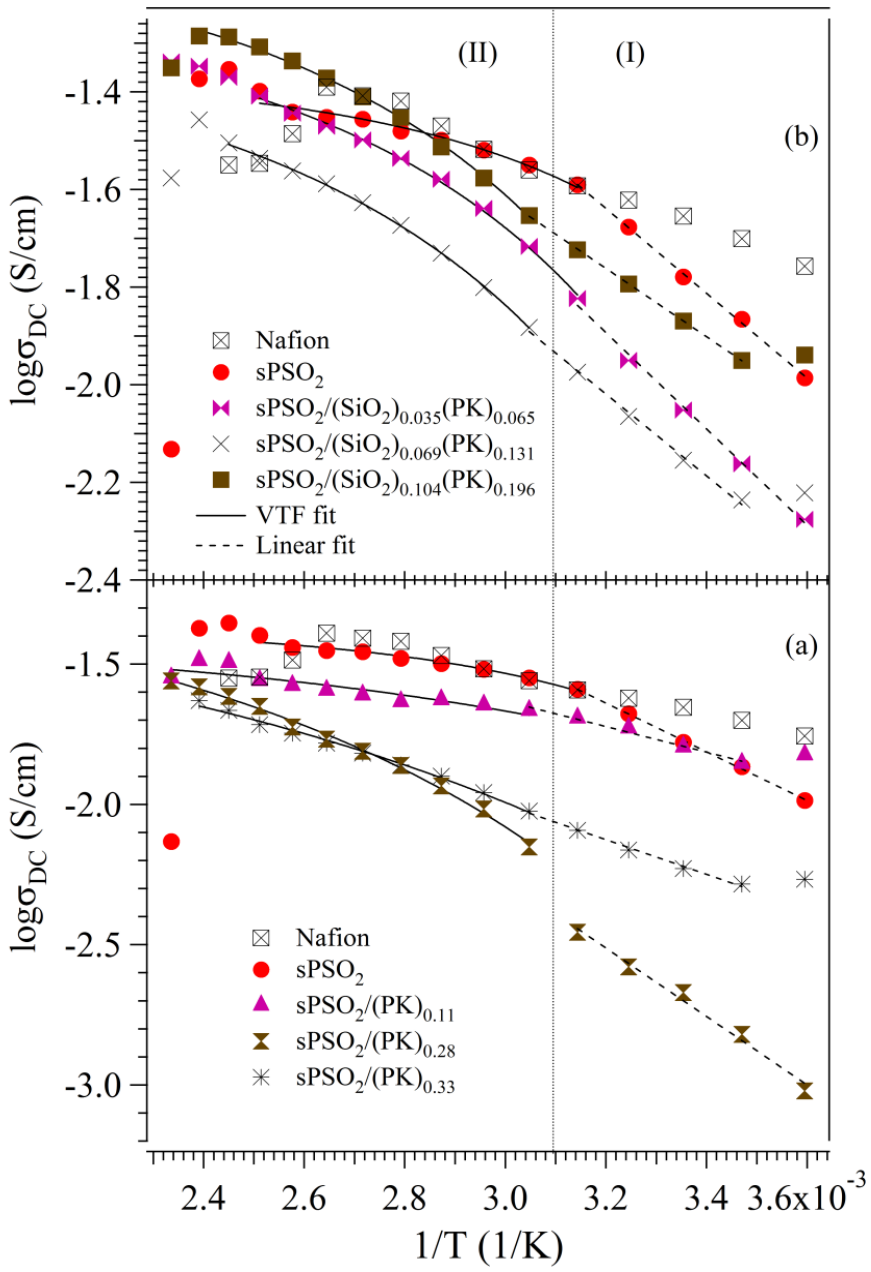

Figure 6.9 Plot of the bulk conductivity σ_{DC} vs. T^{-1}: a) $sPSO_2$ and A-type membranes; b) $sPSO_2$ and B-type membranes. I and II are the conductivity regions. The experimental data and the VTF and Arrhenius fit curves are indicated by markers and solid and dashed lines, respectively. σ_0 was extrapolated from the plateau of the conductivity spectra. The conductivity of Nafion is shown as a reference.

It should be observed that the conductivity of the membranes increases concurrently with the water uptake values. Thus, $sPSO_2$ presents the highest values, while the A-type membranes

present the lowest values.

Higher conductivity values for the B-type membranes than the A-type membranes result from the presence of the [SiO_2/$(PK)_{0.65}$] nanofiller at the interface between the hydrophobic and hydrophilic domains of the material that facilitates charge transfer between the acid groups of $sPSO_2$ and enhances the long range charge transfer between the $sPSO_2$ acid groups due to the formation of proton percolation pathways. This effect is confirmed by analyzing in detail the proton conductivities of the B-type membranes. Indeed, the highest conductivity values are revealed above 75°C for the membrane containing the highest amount of [SiO_2/$(PK)_{0.65}$] nanofiller. The curves in Figure 6.9 present two conductivity regions, I (below 50°C) and II (above 50°C), which are delimited by the temperature of the β mechanical relaxation event shown in Figure 6.7. The logarithm of σ_{DC} as function of reciprocal temperature shows an Arrhenius dependence in region I, while in region II the typical Vogel-Tamman-Fulcher (VTF) behaviour is seen [26-28]. Thus, the charge transfer process below 50°C is due to proton hopping between solvated acid side groups in the A-type materials and between the solvated acid side groups and the hydroxyl groups present on the surface of silica nanoparticles in B-type materials. Above 50°C the charge transfer process is modulated by the segmental motion of polymer chains in both A- and B-type materials. The activation energies (E_a) obtained by fitting the conductivities with Arrhenius (region I) and VTF (region II) equations [26-28] are reported in Table 6.1. The activation energies in region I: 1) decrease with increasing the hybrid nanofiller concentration for the B-type membranes, indicating that the [SiO_2/$(PK)_{0.65}$] nanofiller enhances the long-range proton hopping process; and 2) decrease with increasing membrane storage modulus E' for the A-type membranes (refer to part a of Figure 6.7) due to the presence of the PK fibres that dilute and confine the $sPSO_2$ chains. For the composite materials in region II, the E_a values are twice that of pristine $sPSO_2$ and greater for A-type materials than for B-type due to the

presence of the PK fibres that, according with DMA results, inhibit the $sPSO_2$ segmental motion. The congruence of the division between the conductivity regions and the DMA β transition signifies that charge transfer migration in the studied materials is directly correlated to the dynamics of the polymer host, which is significantly affected by the mechanical relaxation events of the membranes. Furthermore, in B-type membranes the pseudo-activation energies (Table 6.1) are influenced only slightly by the filler-$sPSO_2$ interactions. Finally, a remarkable phenomenon occurs above 100°C, where the conductivities of $sPSO_2$, $[sPSO_2/(SiO_2)_{0.035}(PK)_{0.065}]$ and $[sPSO_2/(SiO_2)_{0.104}(PK)_{0.196}]$ membranes are overlapped suggesting that B-type membranes are interesting materials for application in PEMFCs.

The dependence of the bulk conductivity σ_{DC} at 90°C as function of the relative humidity (R.H.%) is reported in Figure 6.10 for the A- (part a) and B-type membranes (part b) and compared to the $sPSO_2$ reference membrane. For all samples the conductivity increases monotonically with the relative humidity towards a plateau at R.H.≈100%. The effect of the hybrid nanofiller on the membranes' proton conductivity is evident for low values of relative humidity, less than 60%. At this condition, the proton conductivity of all B-type membranes is higher than that of pristine $sPSO_2$, while for A-type membranes this only occurs for the sample containing 11 wt% of PK. The hybrid nanofiller reduces the water content necessary for the long-range migration of the proton due to the formation of percolation pathways at the interfaces between the hydrophobic and hydrophilic domains present inside the material. These percolation pathways allow the B-type membranes to maintain good proton conductivity even at low water content. Furthermore, in agreement with the conductivity values measured when the materials are immersed in water (Figure 6.9), the highest conductivity value is obtained in the materials that exhibit the lowest β mechanical transition temperature, suggesting that the long range conductivity in these materials occurs due to a

facilitated side group relaxation, coupled with the segmental motion of the $sPSO_2$ backbone chains.

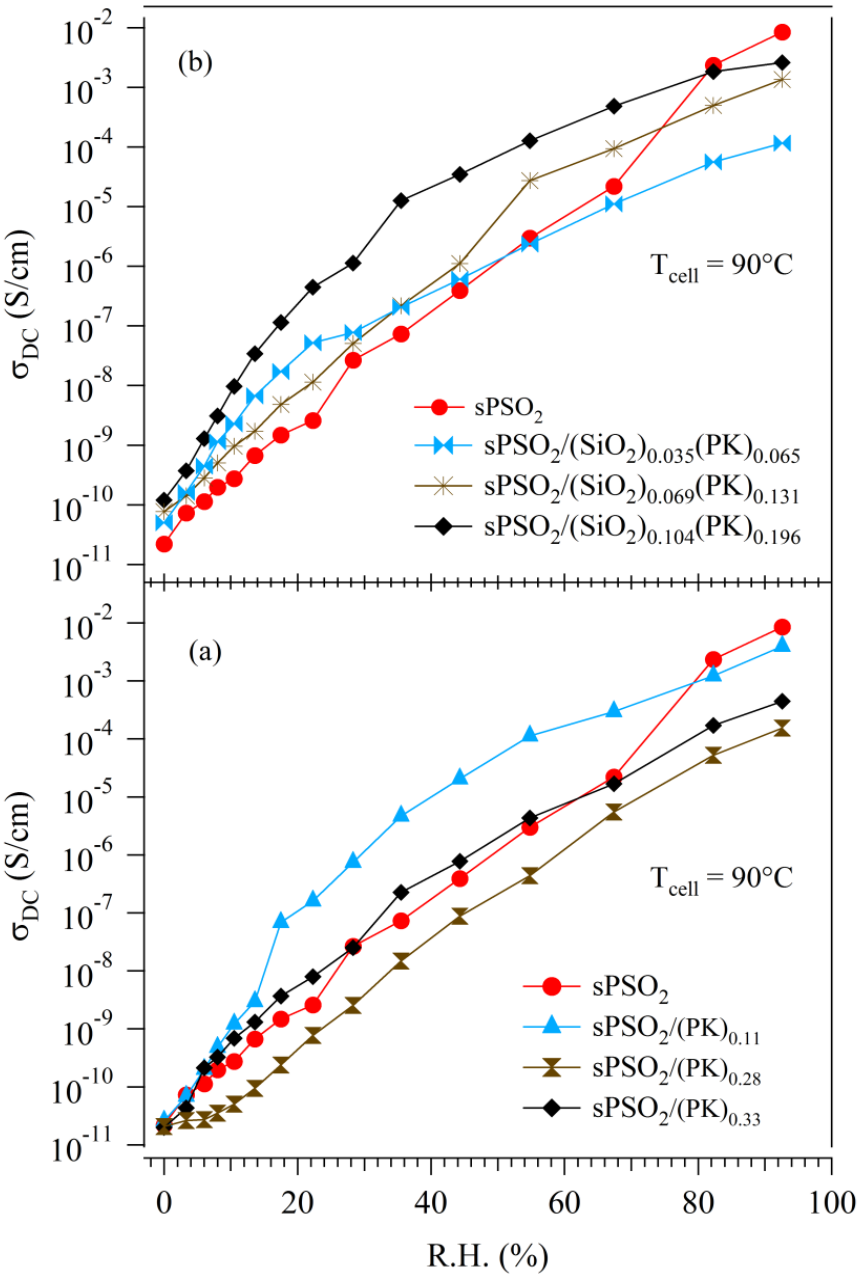

Figure 6.10 Plot of the bulk conductivity vs. relative humidity (R.H.) at 90°C: a) $sPSO_2$ and A-type membranes; b) $sPSO_2$ and B-type membranes. σ_{DC} was extrapolated from the plateau of the conductivity spectra.

Taken together, the experimental results reveal that in B-type materials the hybrid $[SiO_2/(PK)_{0.38}]$ nanofiller increases the proton conductivity as compared to the $[sPSO_2/(PK)_x]$ membranes by maintaining strong dipolar interactions and the segmental motion of $sPSO_2$

backbone. Therefore, it is possible to hypothesize membrane structures for the A- and B-type nanocomposite membranes as reported in parts a and b of Figure 6.11, respectively.

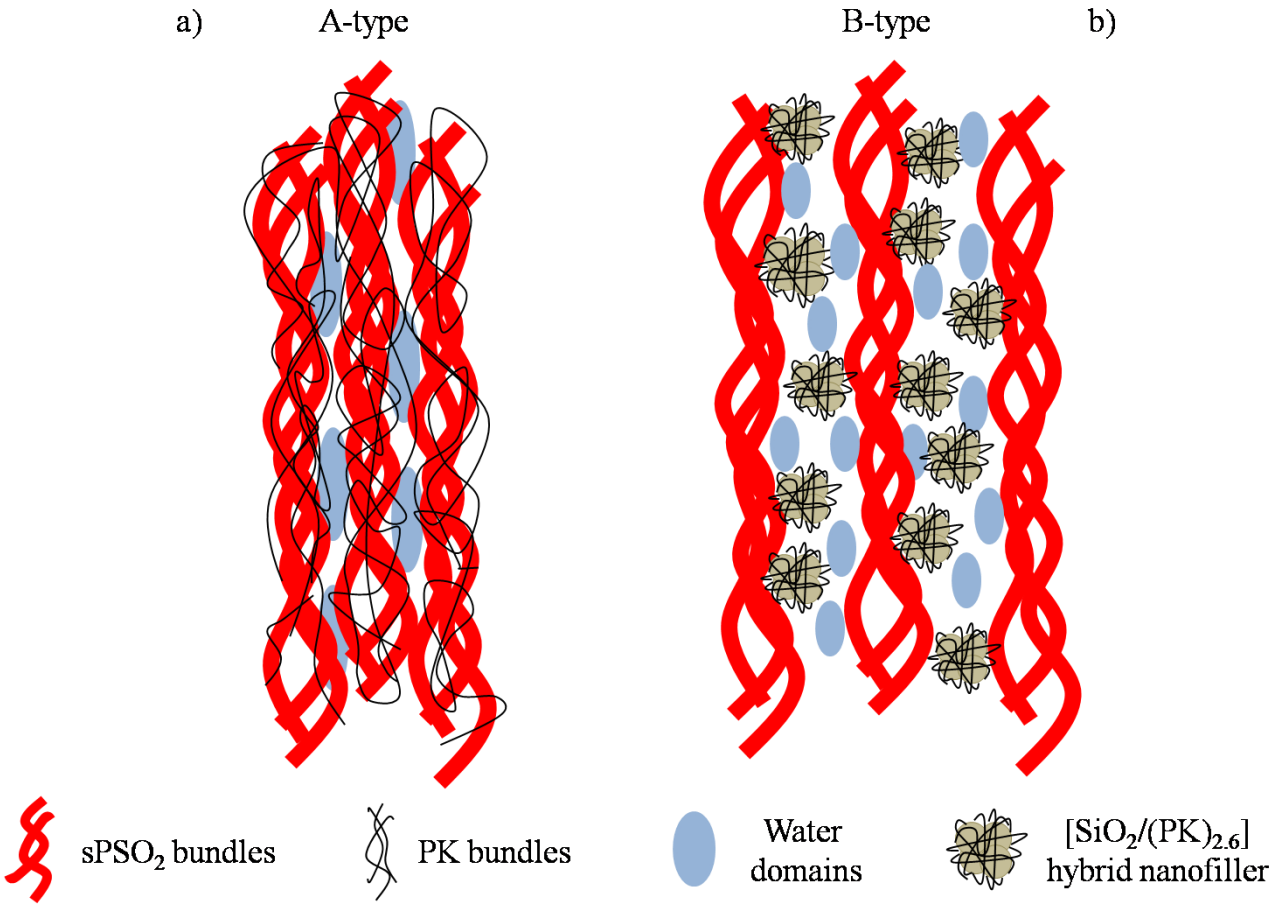

Figure 6.11 Schematic representation of membrane structure: a) A-type membranes; b) B-type membranes.

In A-type membranes, the PK fibers, coiled around the $sPSO_2$ chains, not only reduce membrane swelling and water uptake, but also reduce the proton conductivity, as compared to $sPSO_2$, by diluting the sulfonic acid groups and inhibiting the segmental motion of the $sPSO_2$ polymer chains. In B-type membranes, the hybrid nanofiller, consisting of silica nanoparticles wrapped with PK fibers, located at the interface between the hydrophobic and hydrophilic domains of $sPSO_2$ allows the material to maintain good mechanical properties and high proton conductivity values due to the formation of dipolar interactions between water, the hybrid nanofiller and the acids groups of $sPSO_2$ and due to the creation of percolation pathways at interface between the nanofiller and $sPSO_2$.

6.4. Conclusions

The research conducted during the second part of the 3rd year of PhD reports activity the synthesis and the characterization of nanocomposite proton exchange membranes based on poly(1-oxotrimethylene) (PK) and poly(p-phenylenesulfone) ($sPSO_2$). $sPSO_2$-based materials are choose as Nafion-alternative membranes for application in high temperature fuel cell. Two series (A and B) of membranes were prepared. A-type membranes, labelled [$sPSO_2/(PK)_x$], consist of a blend of $sPSO_2$ containing 11, 28 and 33 wt% of PK. B-type materials consist of nanoparticles of silica covered with PK, which are embedded in bulk poly(p-phenylenesulfone) material. The water uptake values of the A- and B-type membranes were half of that of pristine $sPSO_2$ and are higher for the membranes containing the hybrid nanofiller than for the [$sPSO_2/(PK)_x$] materials. Swelling tests reveal that the presence of PK and the [$SiO_2/(PK)_{0.65}$] nanofiller improve the mechanical stability of the composite membranes in a polar environment as compared to pristine $sPSO_2$.

Temperature dependent DMA studies conducted on dry samples showed that: a) the mechanical properties, in terms of the Storage Modulus E', of B-type materials are better than those of A-type membranes due to the presence of the hybrid nanofiller that increases the strength of the dipolar interactions between acid groups; and b) above 100°C the E' values for [$sPSO_2/(SiO_2)_{0.035}(PK)_{0.065}$] and [$sPSO_2/(SiO_2)_{0.069}(PK)_{0.131}$] are similar to those found for pristine $sPSO_2$. Furthermore, three mechanical transitions, α, β and γ, associated with segmental motion, side group relaxation and local fluctuation of $sPSO_2$ polymer chains were revealed, respectively, for all of the investigated materials.

Electric spectroscopy measurements performed on the fully hydrated materials and at different relative humidities reveal that the nanocomposite hybrid membranes show higher conductivity values than those of the [$sPSO_2/(PK)_x$] membranes. Furthermore, at 90°C and low R.H. all the membranes containing the hybrid nanofiller present conductivity values

higher than those of pristine $sPSO_2$. This phenomenon is due to the presence of the inorganic nanofiller located at the interface between the hydrophobic and hydrophilic domains of the material that facilitates the charge transfer between the acid groups of $sPSO_2$ and enhances the long range charge transfer between the $sPSO_2$ acid groups due to the formation of protons percolation pathways. Taken together, all these characteristics make B-type materials promising candidates for application in PEMFCs operating at temperatures higher than 100°C and low humidification conditions.

6.5. References

1. Gasteiger, H. A.; *Electrochemistry*, **2007**, 75, 103.
2. Kreuer, K. D.; *ChemPhysChem*, **2002**, 3, 771.
3. Kreuer, K. D.; *J. Membr. Sci*., **2001**, 185, 29.
4. Mauritz, K. A.; Moore, R. B., *Chem. Rev*., **2000**, 104, 4535.
5. Mathias, M.F.; Makharia, R.; Gasteiger, H. A.; Conley, J. J.; Fuller, T. J.; Gittleman, C. J.; Kocha, S. S.; Miller, D. P.; Mittelsteadt, C. K.; Xie, T.; Yan, S. G.; Yu, P. T.; *Electrochem. Soc. Interface*, **2005**, 14, 24.
6. Alberti, G.; Narducci, R.; Sganappa, M.; *J. Power Sources*, **2008**, 178, 575.
7. Harrison, W. L.; Hickner, M. A.; Kim, Y. S.; McGrath, J. E. ; *Fuel Cells*, **2005**, 5, 201.
8. Alberti, G.; Casciola, M.; Massinelli, L.; Baver, B.; *J. Membr. Sci*., **2001**, 185, 73.
9. Kreuer, K. D.; in *Handbook of Fuel Cells - Fundamentals, Technology and Applications*, Vielstich, W.; Lamm, A.; Gasteiger, H. A.; Eds. Wiley: Chichester, **2003**; Vol. 3, pp. 420.
10. Hickner, M. A.; Ghassemi, H.; Kim, Y. S.; Einsla, B. R.; McGrath, J. E.; *Chem. Rev*., **2004**, 104, 4587.
11. de Araujo, C. C.; Kreuer, K. D.; Schuster, M.; Portale, G.; Mendil-Jakani, H.; Gebel, G.; Maier, J.; *Phys. Chem. Chem. Phys*., **2009**, 11, 3305.

12. Schuster, M.; Kreuer, K. D.; Andersen, H. T.; Maier, J.; *Macromolecules*, **2007**, 40, 598.

13. Schuster, M.; de Araujo, C. C.; Atanasov, V.; Andersen, H. T.; Kreuer, K. D.; Maier, J.; *Macromolecules*, **2009**, 42, 3129.

14. Drent, E.; van Broekhoven, J. A. M.; Doyle, M. J.; *J. Organomet. Chem*., **1991**, 417, 235;

15. Cavinato, G.; Toniolo, L.; Vavasori, A.; *Top. Organomet. Chem*., **2006**, 18, 125.

16. Benetollo, F.; Bertani, R.; Bombieri, G.; Toniolo, L.; *Inorg. Chim. Acta*, **1995**, *233*, 5.

17. Vittadello, M.; Negro, E.; Lavina, S.; Pace, G.; Safari, A.; Di Noto, V.; *J. Phys. Chem. B*, **2008**, 112, 16590.

18. Di Noto, V.; Piga, M.; Piga, L.; Polizzi, S.; Negro, E.; *J. Power Sources*, **2008**, 178, 561.

19. Di Noto, V.; Piga, M.; Lavina, S.; Negro, E.; Yoshida, K.; Ito, R.; Furukawa, T.; *Electrochim. Acta*, **2010**, 55, 1431.

20. Di Noto, V.; *J. Phys. Chem. B*, **2002**, *106*, 11139.

21. Di Noto, V.; Lavina, S.; Wintersgill, M. C.; Fontanella, J. J.; *Phys. Chem. Chem. Phys*., **2010**, 12, 5993.

22. Titvinidze, G.; Kaltbeitzel, A.; Manhart, A.; Meyer, W. H.; *Fuel Cells*, **2010**, 10(3), 390.

23. Di Noto, V.; Gliubizzi, R.; Negro, E.; Pace, G.; *J. Phys. Chem. B*, **2006**, 110, 24972.

24. Di Noto, V.; Gliubizzi, R.; Negro, E.; Vittadello, M.; Pace, G.; *Electrochim. Acta*, **2007**, 53, 1618.

25. Di Noto, V.; *J. Phys. Chem. B*, **2000**, 104, 10116.

26. Vittadello, M.; Suarez, S.; Chung, S. H.; Fujimoto, K.; Di Noto, V.; Greenbaum, S. G.; Furukawa, T.; *Electrochim. Acta*, **2003**, 48, 2227.

27. Giffin, G. A.; Piga, M.; Lavina, S.; Navarra, M. A.; D'Epifanio, A.; Scrosati, B.; Di Noto, V.; *J. Power Sources*, **2012**, 198, 66.

28. Di Noto, V.; Piga, M.; Giffin, G. A.; Pace, G.; *J. Membr. Sci.*, **2012**, 390, 58**.**

Chapter VII

Conclusions

7.1. Brief summary of the research activity

The research activity conducted in the course of the three years of PhD activity focused on the synthesis and characterization of new proton conducting membranes alternatives to classic fluorinated polymers for application in Proton Exchange Membrane Fuel Cell. The materials were synthesized according two distinct strategies: 1) dope a Nafion membrane in order to improve its thermo-mechanical properties and proton conductivity or extend its operating conditions to temperatures above 100°C and an anhydrous environment (research carried out during the first and second year of PhD activity); 2) synthesize and characterize proton exchange membranes based on polybenzimidazole and polysulfone as an alternative to Nafion (third year of PhD activity).

The first strategy focused on the study of two different systems obtained by doping a Nafion membrane with the $[(ZrO_2)(Ta_2O_5)_{0.119}]$ inorganic "core-shell" nanofiller (Nafion/$[(ZrO_2)\cdot(Ta_2O_5)_{0.119}]\Psi_{ZrO_2}$ materials, results reported in Chapter 3) or with two different proton conducting ionic liquids, MST and PFBuT (NMST and NPFBuT membranes, results reported in Chapter 4), respectively.

In the Nafion/$[(ZrO_2)\cdot(Ta_2O_5)_{0.119}]\Psi_{ZrO_2}$ materials, the basic idea was to generate appropriate proton percolation pathways within the membranes formed at the interfaces between an inorganic nanofiller and the polymer matrix, which allow the membranes to maintain high proton conductivity values for low levels of membrane hydration. The results, reported in Chapter 3, show that the presence of the nanofiller reduces the water uptake and increases thermo-mechanical stability and the proton conductivity of hybrid membranes compared to reference Nafion, especially for low values of membrane hydration.

In the Nafion/PCIL system, the idea was to replace the water present within the membrane, which was responsible for the proton conduction, with a PCIL. Thus, it is possible to increase the membrane's operating conditions in fuel cells to temperatures higher than 100°C and anhydrous conditions due to the thermal stability and proton conductivity of PCILs. For the NTMS and NTPFBu membranes, the experimental results (reported in Chapter 4) highlighted that the PCILs present in the hydrophilic domains of the membrane create percolation pathways for the movement of protons. These percolation pathways provide "shortcuts" for the movement of protons through the membrane as compared to pristine N117 or nN117. These percolation pathways allow the membranes to reach conductivities of $\sigma_{NTMS} = 6.1\times10^{-3}$ S/cm and $\sigma_{NTPFBu} = 1.8\times10^{-3}$S/cm at 130°C and in a complete anhydrous environment. However, the mechanical properties of NTMS and NTPFBu, which were reduced by the plasticizing effect of the PCILs, must be improved for the implementation of these membranes as PEMs in medium-temperature fuel cells.

The study of new PEMs alternative to fluorinated polymers has been developed considering polybenzimidazole (PBI5N, results reported in Chapter 5) and polysulfone ($sPSO_2$, results described in Chapter 6) membranes, whose properties have been modulated by the addition of H_3PO_4/H_3PO_4+SiO_2- Im or PK/PK-SiO_2, respectively.

In PBI5N/(H_3PO_4) and PBI5N/(H_3PO_4+SiO_2-Im) materials, the uptake of the phosphoric acid is necessary to give to the material the proton conductivity, while the Im-SiO_2 filler was added in order to interact with both the PBI5N membrane and the phosphoric acid to improve the acid uptake and the mechanical properties of the composite membrane. The experimental results confirmed the initial hypotheses, showing that: a) the addition of phosphoric acid allows the membranes to reach conductivity values around 10^{-3}-10^{-2} S/cm; b) the presence of the Im-SiO_2 hybrid filler increases the elastic modulus and the thermal stability of the PBI5N/(H_3PO_4+SiO_2-Im) membrane.

In the [$sPSO_2$/$(PK)_x$] and [$sPSO_2$/$(SiO_2)_y$·$(PK)_z$] membranes the polyketone was added with the aim of reducing the high swelling and loss of mechanical properties of $sPSO_2$ membranes at high levels of hydration. In [$sPSO_2$/$(SiO_2)_y$·$(PK)_z$] the silica was added in order to facilitate the proton conduction mechanism and maintain good mechanical properties of membranes.

The experimental results showed that, with respect to pristine $sPSO_2$ the presence of: a) PK reduces the swelling (up to 70%) and the water uptake (up to 40%) of the composite membranes; and b) SiO_2 allows the [$sPSO_2$/$(SiO_2)_y$·$(PK)_z$] membranes to maintain proton conductivity values comparable (for fully hydrated membranes) or higher (at low membrane's hydration level) than those of pure $sPSO_2$.

7.2. Comparison between proton exchange membranes

The membranes characterization presented in this work follows a general approach which involved the study of the materials' thermal, mechanical, electrical and structural properties obtained from different measurement techniques (TG, DCS, DMA, BES, FT-IR, etc.). By correlating these results, it is possible to highlight the interactions between the different components present within the membranes. All the investigated materials consist of a combination of hydrophobic (formed by the polymer matrix) and hydrophilic (containing the

acid groups, water, ionic liquids or acid solution) domains, whose interactions can be modulated with the introduction of inorganic or hybrid nanofillers. The hydrophobic polymer matrix provides the material high thermal and mechanical stability, while the hydrophilic domains are responsible for the membrane's proton conductivity. The interactions between the different domains govern the membranes' macroscopic properties (thermal, mechanical, electrical) that need to be improved in order to optimize and predict the behavior of these materials under operating conditions in fuel cells.

To compare the properties of the different membranes, the values of the elastic modulus E', the proton conductivity σ_{DC} and the water uptake (W.U.) are given in Table 7.1 for the best membranes belonging to each of the four classes of materials. As a reference, the table also reports the values of E', σ_{DC} and W.U. obtained for pristine Nafion (see Chapter 3).

Table 7.1 Values of the water uptake (W.U.), the storage modulus (E') and the bulk proton conductivity (σ_{DC}) for the investigated membranes.

Material	**W.U. (%)**	**E' @ 115°C (MPa)**	**σ_{DC} @ 115°C (S/cm)**
Nafion	25	11	0.033
Nafion/$[(ZrO_2)\cdot(Ta_2O_5)_{0.119}]_{1.047}$	19	74	0.075
NTMS	/	1	0.0049
PBI5N/(SiO_2-Im +H_3PO_4)	/	34	0.0057
$[sPSO_2/(SiO_2)_{0.035}(PK)_{0.065}]$	31	2106	0.036
$[sPSO_2/(PK)_{0.11}]$	24	1387	0.026

All the materials show good proton conductivity (>$1\cdot10^{-3}$ S/cm), sufficient for their use as PEM in fuel cell. In particular, the proton conductivity at 115°C increases in the order:

NMST<PBI5N/(SiO_2+H_3PO_4-Im)<[$sPSO_2$/$(SiO_2)_{0.035}(PK)_{0.065}$]<Nafion/[$(ZrO_2)\cdot(Ta_2O_5)_{0.119}]_{1.047}$. The highest conductivity was obtained for the Nafion membrane doped with the inorganic [$(ZrO_2)(Ta_2O_5)_{0.119}$] "core-shell" nanofiller. This result suggests that the presence of nanometric filler with basic character results in the homogenous dispersion of the nanoparticles in the polymer matrix and in the formation of strong cross-link interactions between the nanofiller and the polar groups of the material.

However it should be noted that for the {Nafion/[$(ZrO_2)(Ta_2O_5)_{0.119}]\Psi_{ZrO_2}$}, [$sPSO_2$/$(PK)_{0.11}$] and [$sPSO_2/(SiO_2)_y\cdot(PK)_z$] materials, the conductivities were obtained under fully-hydrated membrane conditions. Thus, for a correct comparison of the membranes properties, it is necessary to compare the mechanical, thermal and electrical properties of Nafion/$[(ZrO_2)(Ta_2O_5)_{0.119}]_{1.047}$ with those of [$sPSO_2$/$(SiO_2)_{0.035}(PK)_{0.065}$] as they have been measured under the same level of hydration (wet for the conductivity and dry for DMA). Similarly, the properties of Nafion/PCIL membranes, measured in the absence of water must be compared with those of the PBI5N/(SiO_2+H_3PO_4) material.

Among the wet materials, although the [$sPSO_2/(SiO_2)_y(PK)_z$] and [$sPSO_2/(PK)_x$] membranes show water uptake up to 50% lower than pristine $sPSO_2$, the lowest values of W.U. are measured for the {Nafion/[$(ZrO_2)(Ta_2O_5)_{0.119}]\Psi_{ZrO_2}$}membranes. Furthermore, the mechanical properties (in dry condition) of $sPSO_2$–based membranes are better than those of the {Nafion/[$(ZrO_2)(Ta_2O_5)_{0.119}]\Psi_{ZrO_2}$} materials. These evidence are due to the higher PEC of the [$sPSO_2/(SiO_2)_y(PK)_z$] membranes (between 1.70 and 2.20 meq/g, see Chapter 6, Table 6.1) with respect to the {Nafion/[$(ZrO_2)(Ta_2O_5)_{0.119}]\Psi_{ZrO_2}$} materials (PEC between 0.67 and 0.78, see Chapter 3, Table 3.1), which implies: a) an increase in the hydrophilic character of the $sPSO_2$-based membranes; b) a higher density of hydrogen bonding interactions between the acid groups of $sPSO_2$ and the acid groups of $sPSO_2$ with SiO_2 with respect to the $RSO_3H\cdots HO_3SR$ and

$RSO_3H\cdots[(ZrO_2)(Ta_2O_5)_{0.119}]$ interactions presents in $\{Nafion/[(ZrO_2)(Ta_2O_5)_{0.119}]\Psi_{ZrO_2}\}$ membranes. Moreover, the $sPSO_2$-based membranes show a thermal stability (up to 280°C) about 100°C higher with respect to the Nafion-based material, where the thermal decomposition of the acid groups starts at temperature lower than 200°C (Chapter 3).

However, with respect to Nafion based materials, membranes containing polysulfone become hard and brittle with decreasing membrane hydration. This behavior significantly limits the use of $sPSO_2$-based materials in fuel cells in low-humidity conditions because a sudden reduction in the humidity of gaseous reactants can irreversibly damage the membrane electrode assembly.

Despite the good proton conductivity, membranes doped with protic solvents (H_3PO_4 or PCILs) show: a) thermal instability at medium-high temperatures (T> 150°C) due to decomposition of the ionic liquid (T>200°C) or the phosphoric acid (T>150°C); b) reduced mechanical properties as compared to Nafion membranes, due to the plasticizing effect of the solvents they contain.

As an example, the value of the storage modulus E' at 25°C for fully hydrated membranes is 131MPA for pristine Nafion (V. Di Noto, M. Piga, G. Pace, E. Negro, S. Lavina, *ECS Trans*., 16, 1183, 2008), 48MPa for $[sPSO_2/(SiO_2)_{0.035}(PK)_{0.065}]$ (Chapter 6) and 27 and 58 MPa for NMST and PBI5N/(SiO_2+H_3PO_4), respectively (Chapters 5 and 6).

In "wet" conditions and at room temperature, the values of E' for the composite membranes are 1/3 lower when compared to the pristine reference Nafion. This effect is due to the plasticizing effect of the solvents (H_3PO_4 and PCILs) present within the composite membranes, which leads to a reduction in the interactions between the sulfonic acid groups (for Nafion-based membranes) and an overall increased mobility of the main chains of the polymer matrices.

For all the reported materials, the study of the electrical properties showed the presence of two polarization phenomena: the electrode polarization, associated with the "bulk" σ_{DC} conductivity, and the interfacial polarization, related to the interfacial σ_{IP} conductivity. In particular, the

interfacial conductivity arises from the coexistence of hydrophobic and hydrophilic domains with different permittivity for all the investigated membranes.

The electrical measurements have shown that good conductivity values are obtained even for low or zero levels of hydration of the membranes. In the case of the {Nafion/[$(ZrO_2)(Ta_2O_5)_{0.119}$]Ψ_{ZrO_2}} and [$sPSO_2/(SiO_2)_y(PK)_z$] materials, it is important that the membrane absorbs the minimum amount of water required to solvated the sulfonic acid groups and thus dissociate the protons. At this point in the proton conduction mechanism, the filler plays a fundamental role by interacting with the sulfonic acid groups. The Nafion-nanofiller interaction, involves the delocalization of protons on the surface of the nanofiller to form percolation pathways at the interfaces between the polymer matrix and the filler nanoparticles. The presence percolation pathways acts to reduce the water content necessary for proton conduction, thus maintaining high values of conductivity for low levels of membrane hydration.

The fuel cell tests were performed only for the {Nafion/[$(ZrO_2)(Ta_2O_5)_{0.119}]_{1.047}$} membrane because: a) the aim of the activity research was the characterization and the study of new PEMs in order to assess their *potential* use and application in the device and not a detailed characterization of the *membrane electrode assembly* (MEA); b) the state-of-the-art procedure for the preparation of standard electrodes used for testing in fuel cell Nafion-based membranes is widely reported in the literature; and c) for the other proposed materials, the experimental procedure to be followed in the assembly of the MEA (composition of the electrodes, experimental protocol, etc.) is not known and would have required a considerable amount of time to be optimized.

However, for the commercial use of the proposed materials, a detailed analysis of their behavior in a fuel cell in different environmental conditions (temperature, pressure, nature and humidity of the reactants, testing time etc.) must be performed in order to highlight, for each material, the optimal operating conditions.

Another possibility to extend the membrane's operating conditions to temperature above 100°C and low humidity is to reduce or replace the water present within the membranes that is necessary for proton conduction, while maintaining the thermal stability and the percolation pathways. The presence of the solvent allows the membranes to maintain a high proton conductivity (~10^{-3}S/cm) at medium-high temperatures (~100-120°C), but decreases their mechanical properties due to the plasticizing effect of the solvent.

By combining the experimental results, it is possible to outline some strategies in order to overcome the limitations of the proposed materials.

1) In the case of [$sPSO_2/(SiO_2)_y(PK)_z$], the problems related to the brittleness and hardness of membranes can be solved by introducing a plasticizing agent within the membranes. For example, a suitable PCIL that is able to interact with both the hydrophobic and hydrophilic domains within the material could reduce the rigidity of the membranes, while maintaining good proton conductivity.

2) In order to improve the mechanical properties of Nafion/PCILs materials, a possible solution could be the use of a hybrid inorganic-organic Nafion membrane doped with a suitable "core-shell" nanofiller and then soaked in a protic ionic liquid as starting material.

In conclusion, this work demonstrated that doping PEMs with nanofillers that can interact with the different components present within the composite material is an ideal solution to improve the thermo-mechanical properties of polymeric membranes, while maintaining good proton conductivity.

Appendix A: Derivation of the VTF equation [1]

The Voegel-Tamman-Fulcher (VTF) equation is [2-5]:

$$\sigma = A_\sigma T^{-\frac{1}{2}} e^{-\frac{E_{VTF}}{k_B(T-T_0)}} \qquad (B.1)$$

where σ is the conductivity, E_{VTF} is the pseudo-activation energy for conduction, A_σ is a constant proportional to the charge carrier concentration, k_B is the Boltzmann constant, T is the absolute temperature (Kelvin) and T_0 is the ideal glass transition temperature (Kelvin). T_o is related to the real glass transition temperature of the material: $(T_g\text{-}55) \leq T_0 \leq (T_g\text{-}40)$. The VTF equation describes conductivity in polymers where the segmental motions regulates the ionic transport [2]. Historically, the VTF equation was developed independently to deal with the viscosity properties of supercooled liquids. It was written as an empirical relationship for the viscosity:

$$\eta = CT^{1/2} e^{\frac{B}{(T-T_0)}} \qquad (B.2)$$

where η is the material's viscosity, and C and B are temperature-independent constants. At any given temperature, non-Arrhenius relaxation processes can be characterized by an apparent activation energy $B = K[\partial(ln\mu)/\partial(1/T)] = E_{VTF}$.

By appling the Stokes-Einstein relation to polymer electrolytes, which is valid for the diffusive motion of spherical particles (the ions in this case) in a uniform medium (the polymer matrix), it is possible to relate the diffusion coefficient D to the material's viscosity η:

$$D = \frac{k_B T}{6\pi r_i \eta} \qquad (B.3)$$

where k_B is the Boltzmann's constant and r_i is the ionic radius of the spherical particles.

Combining Equations *B.2* and *B.3* gives:

$$D = \frac{C' k_B T^{\frac{1}{2}}}{6\pi r_i} e^{-\frac{E_{VTF}}{k_B (T - T_0)}} \qquad (B.4)$$

Taking into account the Nerst-Einstein equation:

$$\sigma = \frac{nq^2}{k_B T} D \qquad (B.5)$$

where σ is the conductivity and n and q are number density and the charge of the carriers. Substituting Equations *B.4* into *B.5* yields the VTF equation:

$$\sigma = \frac{C' T^{-\frac{1}{2}} nq^2}{6\pi r_i} e^{-\frac{E_{VTF}}{k_B (T - T_0)}} = A_\sigma T^{-\frac{1}{2}} e^{-\frac{E_{VTF}}{k_B (T - T_0)}} \qquad (B.6)$$

where

$$A_\sigma = \frac{C' nq^2}{6\pi r_i} \qquad (B.7)$$

The parameter A_σ depends on the density, charge and dimensions of the carriers.

References

1. Vittadello, M.; *"Synthesis, characterization and conductivity studies of lithium and magnesium ion-conducting hybrid inorganic-organic materials"* Ph.D. dissertation, University of Padova, **2003**.
2. Di Noto, V.; Negro, E.; Lavina, S.; Vittadello, M.; *Hybrid inorganic-organic polymer electrolytes*, in: Sequeira, C.; Santos, D.; (Eds.) *Polymer electrolytes: Fundamentals and applications,* Woodhead Publishing, **2010**.
3. Ratner, M.; in *Polymer Electrolytes Reviews*; MacCallum, J. R.; Vincent, C. A.; (Eds). Elsevier: London, **1987**.
4. Ediger, M. D.; Angell, C. A.; Nagel, S. R.; *J. Phys. Chem.,* **1996** , 100, 13200.
5. Ratner, M. A.; Shriver, D. F.; *Chemical Reviews*, **1988**, 88, 109.

Appendix B: BES general fit equation

B.1 General equation for the analysis in the frequency domain of σ(ω) and ε*(ω)*

In this work the BES spectra of the complex measured permittivity ε*(ω) are fitted using the general equation [1-8]:

$$\varepsilon_m^*(\omega) = \frac{\sigma_{EP}(i\omega\tau_{EP})^{\gamma_{EP}}}{i\omega[1+(i\omega\tau_{EP})^{\gamma_{EP}}]} + \sum_{i=1}^{n} \frac{\sigma_{IP}(i\omega\tau_{IP})^{\gamma_{IP}}}{i\omega[1+(i\omega\tau_{IP})^{\gamma_{IP}}]} + \sum_{k} \frac{\Delta\varepsilon_k}{[1+(i\omega\tau_k)^{a_k}]^{b_k}} + \varepsilon_\infty \qquad B.1$$

The complex conductivity σ*(ω) is obtained from Equation B.1 and the relationship between the complex permittivity and conductivity: $\sigma_m^*(\omega) = i\omega\varepsilon_m^*(\omega)$ [1].

The first and the second term of equation B.1 describe the electrode and interfacial polarization phenomena while the third term accounts for the dielectric relaxations. σ_{EP} and σ_{IP} are the electrode and interfacial conductivities, γ_{EP} and γ_{IP} are the exponential factors of the electrode and interfacial polarizations. Typically γ_{EP} and γ_{IP} range from 0.5 to 1. The relaxation times associated with the electrode, interfacial and dielectric relaxation modes are τ_{EP}, τ_{IP} and τ_k, respectively. Δε is the dielectric strength. The symmetric and asymmetric shape parameters of the k^{th} dielectric relaxation peaks, respectively, are a_k and b_k. Finally ε_∞ accounts for the electronic contribution to the permittivity of the material. The next sections describe the origin of the different terms of equation B.1

B.2 Electrode polarization (EP)

The electrode polarization occurs mainly in moderate to highly conductive samples and generally influences the dielectric properties at low frequencies. This effect originates in accumulation of charges at the sample/electrode interface and usually occurs when the measuring electrodes block or partially-block the charge carriers. Charge accumulation at the electrode leads to a separation of positive and negative charge density as shown in Figure B.1

where two parallel plates of area *A* are separated by a distance *L* [9,10]. The position inside the sample is described by the *z* coordinate which ranges from *z* = 0 to *z* = ± *L*/2. When a field is applied, free cations tend to accumulate near the negative electrode, leaving a positive charge density at the cathode and an uncompensated negative charge density at the anode ($\rho(z,t)$).

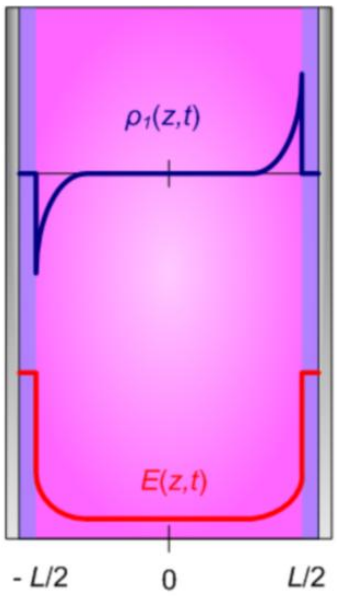

Figure B.1 Charge density (ρ(z,t)) and electric field (E(z,t)) profiles in a sample sandwiched between two electrodes.

For conducting materials, the electric response as a function of the frequencies of the EP event is well described by the equivalent circuit in Figure B.2, where the "bulk" conductivity of the material and the blocking electrodes can be modelled with a resistor and two capacitors in series, resulting in the complex conductivity [11-14]:

$$\sigma_{EP}^{*}(\omega) = \frac{1}{1/\sigma_{EP} + 1/i\omega\,\varepsilon_{el}^{*}(\omega)} \qquad B.2$$

σ_{EP} is the sample conductivity and ε^{*}_{el} the complex permittivity of the interfacial region. Using the complex function $\varepsilon_{el}^{*}(\omega) = \varepsilon_{EP}(i\omega)^{\gamma-1}$ [15], $\sigma_{EP}^{*}(\omega)$ becomes:

$$\sigma_{EP}^{*}(\omega) = \frac{\sigma_{EP}(i\omega\tau_{EP})^{\gamma_{EP}}}{1 + (i\omega\tau_{EP})^{\gamma_{EP}}} \qquad B.3$$

with $\tau_{EP} = \left(\frac{\varepsilon_{EP}\,L}{\sigma_{EP}\,2L_D}\right)^{\frac{1}{\gamma_{EP}}}$.

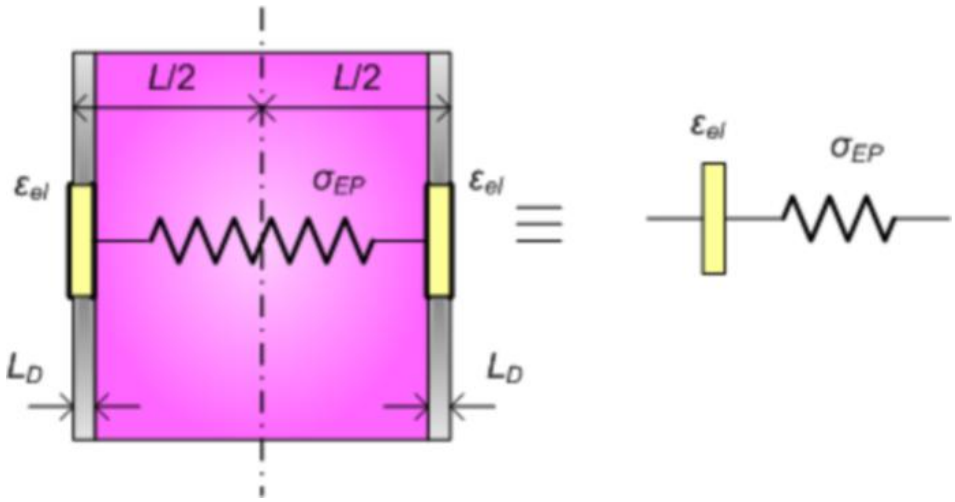

Figure B.2 Equivalent circuit of a sample sandwiched between two electrodes. L is the sample thickness, L_D is the Debye length, ε_{el} is the complex permittivity of the interfacial region and σ_{EP} is the sample conductivity.

Using the expression, $\varepsilon^*(\omega) = \sigma^*(\omega)/(i\omega)$, Equation B.3 is transformed into the permittivity profiles $\varepsilon^*_{EP}(\omega)$

$$\varepsilon^*_{EP}(\omega) = \frac{\sigma_{EP}(i\omega\tau_{EP})^{\gamma}}{i\omega[1 + (i\omega\tau_{EP})^{\gamma}]} \qquad B.4$$

This equation expresses the effect of σ_{EP} conductivity on ε^*_{EP} which originates in the electrode polarization phenomenon with a time constant τ_{EP}. The value of this last parameter depends on the thickness of the sample and on the σ_{EP} of the material. In particular:

- the time dependence of the electrode polarization is due to charging and discharging of the double layer (L_D);
- τ_{EP} depends on the conductivity of the sample, i.e. the EP phenomenon is shifted to higher frequencies as the conductivity of the sample increases;
- increasing the thickness of the sample shifts EP to lower frequencies;
- EP can be discriminated from the bulk relaxation of the sample by studying the effect of changing the electrode materials and the sample thickness on τ_{EP}.

B.3 Interfacial polarization (Maxwell/Wagner/Sillars polarization) [16-19]

In heterogeneous materials, a type of polarization occurs as a result of the accumulation of charge at the interface of two nanodomains that have different dielectric constants, ε_1 and ε_2, and conductivities, σ_1 and σ_2 where

$$\varepsilon_1\sigma_2 = \varepsilon_2\sigma_1 \quad \text{or} \quad \tau_1 = \frac{\varepsilon_1}{\sigma_1} = \tau_2 = \frac{\varepsilon_2}{\sigma_2} \qquad B.5$$

which represents an interfacial polarization (Figure B.3).

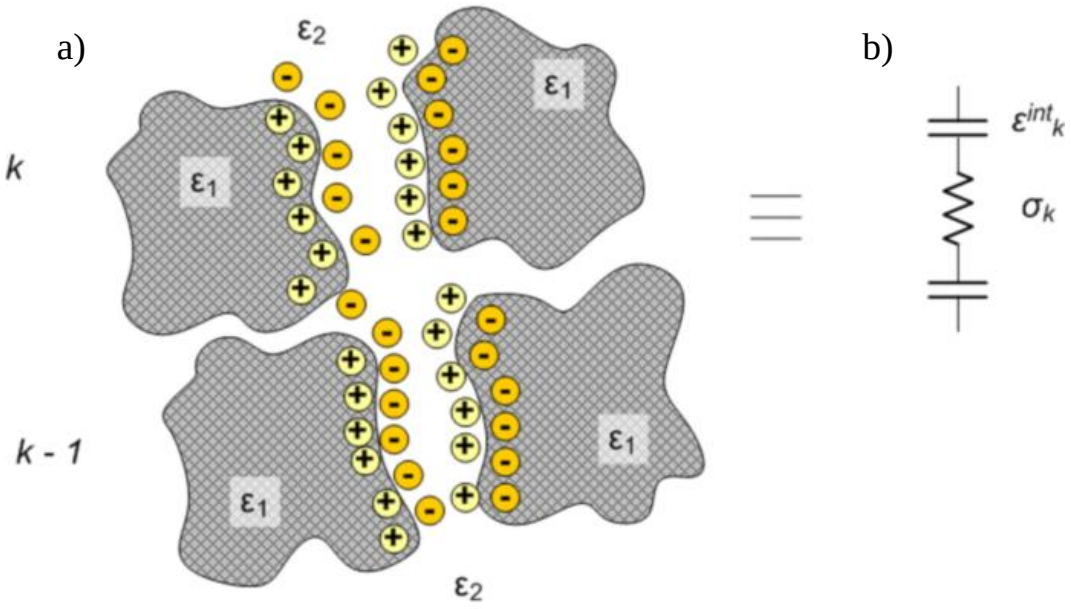

Figure B.3 a) The interfacial polarization that consists of the accumulation of virtual charges at the interface of two media having different dielectric constants, ε_1 and ε_2, and conductivities, σ_1 and σ_2; b) equivalent circuit describing the interfacial Maxwell/Wagner/Sillers polarization. ε_k^{int} is the permittivity associated with the capacitance between ε_1 and ε_2 nanodomains and σ_k is the conductivity associated with the charge exchange between k and k – 1 capacitor.

This accumulation of free charge is responsible for field distortion and the dielectric loss of energy, which causes a strong increase in the material's permittivity. The most simple model to describe an inhomogeneous structure is a double layer arrangement, where each layer is characterized by its permittivity ε_i, thickness d_i and its relative conductivity σ_i (Figure B.4).

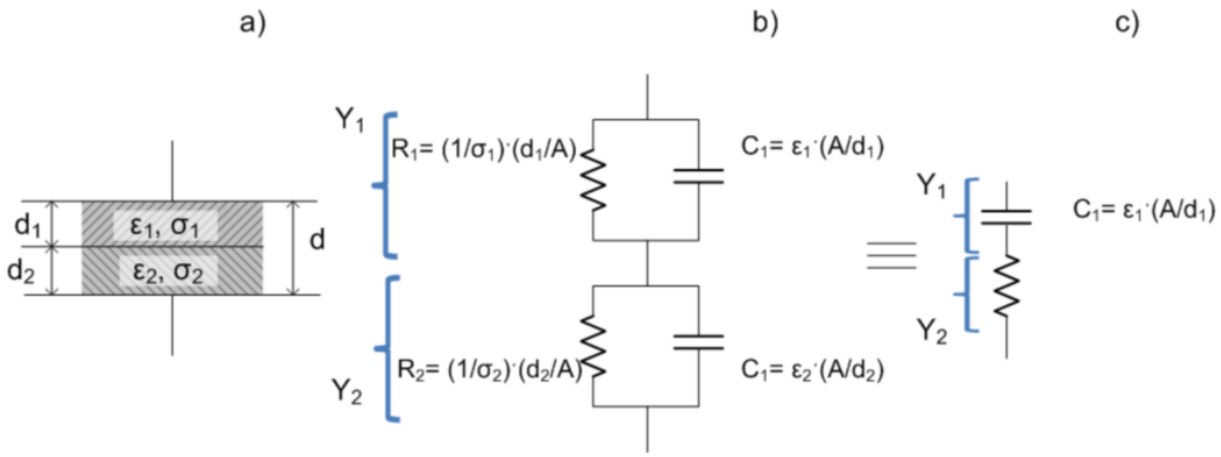

Figure B.4 a) The two layer model of interfacial polarization; b) Complete equivalent circuit of the system; c) equivalent circuit when $1/R_1 << C_1$ and $1/R_2 >> C_2$. Y_1 and Y_2 are the admittances of 1 and 2 parallel equivalent circuits.

The total admittance (Y) of the equivalent circuit shown in part b of Figure B.4 is given by:

$$Y_{IP} = \frac{Y_1 \cdot Y_2}{Y_1 + Y_2} \qquad B.6$$

where the admittances Y_1 and Y_2 are

$$Y_1 = \sigma_1 {}^{A}/_{d_1} + i\omega\varepsilon_0\varepsilon_1 {}^{A}/_{d_1} \text{ and } Y_2 = \sigma_2 {}^{A}/_{d_2} + i\omega\varepsilon_0\varepsilon_2 {}^{A}/_{d_2} \qquad B.7$$

If the first and second layer shown in part a of Figure B.4 are a dielectric and a good ionic conductor, respectively, it follows that:

$$\frac{1}{R_1} \ll C_1 \quad and \quad \sigma_1 \ll \varepsilon_0\varepsilon_1 \qquad B.8$$

$$\frac{1}{R_2} \gg C_2 \quad and \quad \sigma_2 \gg \varepsilon_0\varepsilon_2 \qquad B.9$$

and Eqns. B.7 are easily transformed into the Equations B.10.

$$Y_1 = i\omega\varepsilon_0\varepsilon_1 {}^{A}/_{d_1} \text{ and } Y_2 = \sigma_2 {}^{A}/_{d_2} \qquad B.10$$

On the basis of Eqns. B.10, Eqn. B.6 becomes:

$$Y^*_{IP}(\omega) = \frac{i\omega\varepsilon_0\varepsilon_1 {}^{A}/_{d_1} \cdot \sigma_2 {}^{A}/_{d_2}}{i\omega\varepsilon_0\varepsilon_1 {}^{A}/_{d_1} + \sigma_2 {}^{A}/_{d_2}} \qquad B.11$$

And the complex conductivity σ^*_{IP} of the system:

$$\sigma_{IP}^{*}(\omega) = \frac{(d_1 + d_2)}{A} Y_{IP}^{*} = \frac{(d_1 + d_2)}{d_1 \sigma_2} \frac{i\omega\varepsilon_0 \varepsilon_1^{*}}{1 + i\omega \left({\varepsilon_0 \varepsilon_1^{*} d_2} \Big/ {d_1 \sigma_2} \right)} \qquad B.12$$

It should be noted that Eqn. B.11 and Eqn. B.12 describe the equivalent circuit in Figure B.4c, which is very similar to that of the EP phenomenon shown in Fig. B.2 and quantified by Eqn. B.3.

Assuming that the complex function of ε^*_1 is given by [15]

$$\varepsilon_1^{*}(\omega) = \varepsilon_{IP} (i\omega)^{\gamma_{IP} - 1} \qquad B.13$$

Eqn. B.12 is transformed into:

$$\sigma_{IP}^{*}(\omega) = \frac{\sigma_{IP} \cdot (i\omega\tau_{IP})^{\gamma_{IP}}}{1 + (i\omega\tau_{IP})^{\gamma_{IP}}} \qquad B.14$$

with

$$\sigma_{IP} = \frac{(d_1 + d_2)}{d_2} \sigma_2 \text{ and } \tau_{IP} = \left(\frac{\varepsilon_0 \varepsilon_{IP} d_2}{d_1 \sigma_2} \right)^{\frac{1}{\gamma_{IP}}} \qquad B.15$$

In the permittivity representation, Equation B.15 becomes

$$\varepsilon_{IP}^{*}(\omega) = \frac{\sigma_{IP}}{i\omega} \frac{(i\omega\tau_{IP})^{\gamma_{IP}}}{1 + (i\omega\tau_{IP})^{\gamma_{IP}}} \qquad B.16$$

Eqns. B.14 and B.16 in the approximations described above express the effect of the conductivity (σ_2) on the electrical response, which results in the interfacial polarization (IP) of heterogeneous materials with time constant τ_{IP}. It should be observed that the two-layer capacitor leads to a single relaxation time (τ_{IP}) while *n* different layers are described by *n*-1 relaxation times. Eqn. B.15 shows that the relaxation time decreases as: a) the conductivity of the highest-conducting nanodomains increases; b) the thickness of the dielectric layer increases. In summary, interfacial polarization (IP) may be detected in materials having morphological inhomogeneities even when there is no orientational polarization of the polar inclusion or even if

the inclusions are not polar. In addition, when the nanodomains in bulk nanocomposite materials are far from electrical equilibrium (Eqn. B.17) [19],

$$\varepsilon_1\sigma_2 \neq \varepsilon_2\sigma_1 \qquad B.17$$

The accumulation of charge at interfaces requires the flow of charge though the different interfaces in order to re-equilibrate the Maxwell-Wagner conditions.

B.4 Dielectric Relaxation

Dielectric relaxation, which is commonly described as the dielectric dispersion (ε_0-ε_∞) or the dielectric loss, is the exponential decay of the polarization in a dielectric material when the external applied field is removed [19]. Dielectric relaxation is the cause of the anomalous dispersion that results in a decreasing dielectric constant with increasing frequency [20]. This phenomenon depends on the inner structural rearrangement of the molecules or macromolecules composing the dielectric material. The framework of phenomenological theory is described by [19,20]:

$$\frac{\varepsilon^*(\omega) - \varepsilon_\infty}{\varepsilon_0 - \varepsilon_\infty} = 1 - i\omega\mathcal{J}[\Phi(t)] \qquad B.18$$

where $\varepsilon^*(\omega)$ is the complex permittivity, $\varepsilon_0 - \varepsilon_\infty = \Delta\varepsilon$ is the total dielectric strength and $\mathcal{J}$ indicates a one-sided Fourier transform, i.e. a pure Laplace transform, and $\Phi(t)$ is a time-dependent macroscopic relaxation function. $\Phi(t)$ can be measured as the transient charge decay function following the steep withdrawal of a constant applied electric field from a sample or from the transient charge rise function ($1 - \Phi(t)$) when a steep electric field is applied to an unperturbed sample at $t = 0$.

For supramolecular materials, there are multiple dielectric relaxation regions with broad relaxation events. For a discrete distribution of relaxation processes, Eqn. B.18 yields [19]

$$\frac{\varepsilon^*(\omega)-\varepsilon_\infty}{\varepsilon_0-\varepsilon_\infty}=R(\omega)=\sum_j x_j R_j(\omega)=\sum_j x_j\left\{1-i\omega\mathcal{J}\left[\Phi_j(t)\right]\right\} \qquad B.19$$

where x_j is the fraction of total relaxation magnitude that is associated with the event j and $R_j(\omega)$ is its complex relaxation function in the frequency domain. $\Phi_j(t)$ is the real relaxation function of the j^{th} phenomenon in the t-domain and $\sum x_j = 1$. Assuming $\Phi_j(t)$ is a discrete relaxation time, it should be observed that

$$\phi_j(t)=\exp\left(-\frac{t}{\tau_j}\right) \qquad B.20$$

and $R_j(\omega)$ may be written as

$$R_j(\omega)=\frac{1}{1+i\omega\tau_j} \qquad B.21$$

When Eqn. B.21 is inserted into Eqn. B.19, the result is the well-known Debye single relaxation time equations for the real and imaginary components of permittivity [1,21,22],

$$\varepsilon'(\omega)=\varepsilon_\infty+\frac{\varepsilon_0-\varepsilon_\infty}{1+\omega^2\tau^2}=\varepsilon_\infty+\frac{\Delta\varepsilon}{1+\omega^2\tau^2} \quad \text{and} \quad \varepsilon''(\omega)=\frac{(\varepsilon_0-\varepsilon_\infty)\omega\tau}{1+\omega^2\tau^2}=\frac{\Delta\varepsilon\,\omega\tau}{1+\omega^2\tau^2} \qquad B.22$$

where $\Delta\varepsilon$ is the dielectric strength and τ is the relaxation time. The empirical expressions commonly used in the analysis of the experimental data (R_j) were obtained using suitable relaxation functions [1] whose results are summarized in Table B.1.

The most used empirical equations are the Debye, Cole-Cole and Cole-Davidson equations, which could be considered special approximations of the general Havriliak-Negami (HN) function [1]

$$R_j(\omega)=\frac{1}{\left[1+(i\omega\tau_j)^a\right]^b} \qquad B.23$$

where a and b are empirical constants ($0 \le a \le 1$, $0 \le b \le 1$). The Debye expression is obtained for a = b = 1, while the Cole-Cole or Cole-Davidson representations are obtained when b = 1 or a = 1, respectively. Therefore, the HN relaxation function (R_j) in Eqn. B.23 can be considered a

combination of the Cole-Cole and Cole-Davidson functions. The parameters a and b are associated with the symmetric and asymmetric broadening of complex dielectric functions. In general, peaks narrow with increasing temperature and broaden dramatically with macromolecular cross-linking or when the interaction of a particular relaxation mode with the environment increases.

Table B.1 Summary of dielectric relaxation model functions for the frequency domain

	Dielectric function	**Real part**	**Imaginary part**
Model function	$\frac{\varepsilon^*(\omega)-\varepsilon_\infty}{\Delta\varepsilon}$	$\frac{\varepsilon'(\omega)-\varepsilon_\infty}{\Delta\varepsilon}$	$\frac{\varepsilon''(\omega)}{\Delta\varepsilon}$
Debye	$\frac{1}{1+(i\omega\tau_D)}$	$\frac{1}{1+(i\omega\tau_D)^2}$	$\frac{\omega\tau_D}{1+(i\omega\tau_D)^2}$
Cole/Cole	$\frac{1}{1+(i\omega\tau_{CC})^{a_{CC}}}$ $0 < a_{CC} \le 1$	$1+(i\omega\tau_{CC})^{a_{CC}}\cos(a_{CC}\pi/2)r^{-1}(\omega)$ $r(\omega)=1+2(\omega\tau_{CC})^{a_{CC}}\cos(a_{CC}\pi/2)+(\omega\tau_{CC})^{2a_{CC}}$	$(\omega\tau_{CC})^{a_{CC}}\sin(a_{CC}\pi/2)r^{-1}(\omega)$
Cole/ Davidson	$\frac{1}{(1+i\omega\tau_{CD})^{b_{CD}}}$ $0 < b_{CD} \le 1$	$\cos(\Phi)^{b_{CD}} \quad \cos b_{CD}\Phi$ $\tan\Phi = \omega\tau_{CD}$	$\cos(\Phi)^{b_{CD}} \quad \sin b_{CD}\Phi$ $\tan\Phi = \omega\tau_{CD}$
Havriliak/ Negami	$\frac{1}{(1+(i\omega\tau_{HN})^{a_{HN}})^{b_{HN}}}$ $0 < a_{HN} \le 1$ $0 < a_{HN}b_{HN} \le 1$	$r(\omega)\cos[b_{HN}\psi(\omega)]$ $r(\omega)=\left[1+2(\omega\tau_{HN})^{a_{HN}}\cos\left(\frac{a_{HN}\pi}{2}\right)+(\omega\tau_{HN})^{2a_{HN}}\right]^{-b_{HN}/2}$ $\psi(\omega)=\arctan\left[\frac{\sin\left(\frac{a_{HN}\pi}{2}\right)}{(\omega\tau_{HN})^{-a_{HN}}+\cos\left(\frac{a_{HN}\pi}{2}\right)}\right]$	$r(\omega)\sin[b_{HN}\psi(\omega)]$

B.5 References

1. Di Noto, V.; Giffin, G.A.; Vezzù, K.; Piga, M.; Lavina, S.; *Broadband Dielectric Spectroscopy: A Powerful Tool for the Determination of Charge Transfer Mechanisms in Ion Conductors*, in: Knauth, P.; Di Vona, M.L. (Eds.). *Solid State Proton Conductors: Properties and Applications in Fuel Cells*, Wiley, Chichester, **2012**.
2. Vittadello, M.; Suarez, S.; Chung, S. H.; Fujimoto, K.; Di Noto, V.; Greenbaum, S. G.; Furukawa, T.; *Electrochim. Acta* **2003**, 48, 2227.
3. Di Noto, V.; Vittadello, M.; Greenbaum, S. G.; Suarez, S.; Kano, K.; Furukawa, T.; *J. Phys. Chem. B* **2004,** *108* , 18832.
4. Di Noto, V.; Gliubizzi, R.; Negro, E.; Pace, G.; *J. Phys. Chem. B*, **2006**, 110, 24972.
5. Di Noto, V.; Lavina, S.; Negro, E.; Vittadello, M.; Conti, F.; Piga, M.; Pace, G.; *J. Power Sources*, **2009**, 187, 57.
6. Di Noto, V.; Negro, E.; Sanchez, J. Y.; Iojoiu, C.; *J. Am. Chem. Soc.* **2010,** *132*, 2183.
7. Di Noto, V.; Boaretto, N.; Negro, E.; Stallworth, P.E.; Lavina, S.; Giffin, G.A.; Greenbaum, S. G.; *Int. J. Hydrogen Energy* **2011**; doi:10.1016/j.ijhydene.2011.07.135.
8. Giffin, G.A.; Piga, M.; Lavina, S.; Navarra, M.A.; D'Epifanio, A.; Scrosati, B.; Di Noto, V.; *J. Power Sources*, **2012**, 198, 66.
9. Coelho, R.; *Revue Phys. Appl.* **1983**, *18*, 137.
10. Coelho, R.; *J. Non-Cryst. Solids* **1991**, *131-133*, 1136.
11. Furukawa, T.; Imura, M.; Yuruzume, H.; *Jpn. J. Appl. Phys., Part 1* **1997**, *36*, 1119.
12. Kano, K.; Takahashi, Y.; Furukawa, T.; *Jpn. J. Appl. Phys., Part 1* **2001**, *40*, 3246.
13. Furukawa, T.; Yasuda, K.; Takahashi, Y.; *IEEE T. Dielect. El. In.* **2004**, *11*, 65.
14. Di Noto, V.; Piga, M.; Giffin, G. A.; Pace, G.; *J. Membr. Sci.*, **2012**, 390, 58**.**
15. Johnson, J. F.; Cole, R. H.; *J. Am. Chem. Soc.* **1951**, *73*, 4536.
16. Wagner, R. W.; *Arch. Electrotech.* **1914**, *2*, 371.

17. Sillars, R. W.; *J. Inst. Elect. Eng.* **1937**, *80*, 378.

18. Van Beek, L. K. H.; *Dielectric behavior of heterogeneous systems*. In *Progress in Dielectrics*; Birk, J. B., Hard, J., Eds.; Heywood Books: London, **1967**; Vol. 7; pp 71.

19. Ku, C. C.; Liepins, R.; *Electrical Properties of Polymers: Chemical Principles*; Carl Hanser Verlag: Munich, **1987**.

20. Runt, J. P.; Fitzgerald, J.J.; *Dielectric Spectroscopy of Polymeric Materials: Fundamentals and Applications*; American Chemical Society: Washington, D.C., **1997**.

21. McCrum, N. G.; Read, B. E.; Williams, G.; *Anelastic and Dielectric Effects in Polymeric Solids*; John Wiley and Sons, **1967**.

22. Debye, P.; *Polar Molecules*; Dover Publications, Inc.: New York, **1929**.

Appendix C: List of pubblications

1. Di Noto, V.; **Piga, M.**; Lavina, S.; Negro, E.; Pace, G.; "*Cella per misurare spettri elettrici di materiali in condizioni controllate di pressione, temperatura e temperatura di Dew Point (DPT)*", Italian patent application PD2009A000041 filed on March 10th, **2009.**

2. Di Noto, V.; **Piga, M**.; Giffin, G.A.; Quartarone, E.; Righetti, P.; Mustarelli, P.; Magistris, A.; Structure-property interplay of proton conducting membranes based on PBI5N, SiO_2-Im and H_3PO_4 for high temperature fuel cells. *Phys. Chem. Chem. Phys.*, **2011**, 13, 12146-12154.

3. Di Noto, V.; **Piga, M**.; Giffin, G.A.; Schuster, M.; Cavinato, G.; Toniolo, L.; Polizzi, S.; New Sulfonated Poly(p-phenylenesulfone)/Poly(1-oxotrimethylene) Nanocomposite Proton-Conducting Membranes for PEMFCs. *Chem. Mater.*, **2011**, 23, 4452-4458.

4. Di Noto, V.; **Piga, M**.; Giffin, G. A.; Pace, G.; Broadband Electric Spectroscopy of proton conducting SPEEK membranes. *J. Membr. Sci.*, **2012**, 390, 58-67**.**

5. Giffin, G.A.; **Piga, M**.; Lavina, S.; Navarra, M.A.; D'Epifanio, A.; Scrosati, B.; Di Noto, V.; Characterization of sulfated-zirconia/Nafion® composite membranes for proton exchange membrane fuel cells. *J. Power Sources*, **2012**, 198, 76-82.

6. Di Noto, V.; Giffin, G.A.; Vezzù, K.; **Piga, M.**; Lavina, S.. *Broadband Dielectric Spectroscopy: A Powerful Tool for the Determination of Charge Transfer Mechanisms in Ion Conductors*, in: Knauth, P.; Di Vona, M.L. (Eds.). *Solid State Proton Conductors: Properties and Applications in Fuel Cells*, Wiley, Chichester, **2012**.

7. Di Noto, V.; **Piga, M.;** Giffin, G.A.; Lavina, S.; Smotkin, E.S.; Sanchez, J-Y.; Iojoiu, C.; Influence of Anions on Proton-Conducting Membranes Based on Neutralized Nafion 117, Triethylammonium Methanesulfonate and Triethylammonium Perfluorobutanesulfonate. 1. Synthesis and Properties. *J. Phys. Chem. C*, **2011**, doi: 10.1021 / jp204241y.

8. Di Noto, V.; **Piga, M.;** Giffin, G.A.; Lavina, S.; Smotkin, E.S.; Sanchez, J-Y.; Iojoiu, C.; Influence of Anions on Proton-Conducting Membranes Based on Neutralized Nafion 117, Triethylammonium Methanesulfonate and Triethylammonium Perfluorobutanesulfonate. 2. Electrical Properties. *J. Phys. Chem. C*, **2011,** doi:10.1021 / jp204242q.

Appendix D: Proofs of papers extracted from the materials of the thesis

View Online / Journal Homepage / Table of Contents for this issue
Dynamic Article Links

PCCP

Cite this: *Phys. Chem. Chem. Phys.*, 2011, **13**, 12146–12154

www.rsc.org/pccp

PAPER

Structure–property interplay of proton conducting membranes based on PBI5N, SiO_2–Im and H_3PO_4 for high temperature fuel cells

Vito Di Noto,*[a] Matteo Piga,[a] Guinevere A. Giffin,[a] Eliana Quartarone,[b] Pierpaolo Righetti,[b] Piercarlo Mustarelli[b] and Aldo Magistris[b]

Received 24th March 2011, Accepted 19th April 2011
DOI: 10.1039/c1cp20902g

Published on 19 May 2011 on http://pubs.rsc.org | doi:10.1039/C1CP20902G
Downloaded by Universita di Padova on 22 December 2011

Polybenzimidazoles (PBIs) are among the polymers of choice to prepare membranes for high temperature polymer fuel cells. Poly-2,2′(2,6-pyridine)-5,5′-bibenzimidazole (PBI5N), doped with H_3PO_4, and acid-doped PBI5N containing 10 wt% of imidazole-functionalized silica membranes were studied with thermogravimetric analysis, differential scanning calorimetry, dynamic-mechanical analysis, infrared spectroscopy, and broadband electric spectroscopy to examine the structure–property relationships. Key results show that: (1) doped PBI5N membranes show thermal decomposition starting at 120 °C, while pristine PBI5N is stable up to 300 °C; (2) the presence of filler increases the acid uptake and decreases the crystallinity of PBI5N; (3) the addition of phosphoric acid reduces the mechanical properties of the membrane, while the addition of filler has the opposite effect; (4) acid-doped membranes have conductivity values on the order of 10^{-2}–10^{-3} S cm^{-1}; and (5) membranes exhibit a Vogel–Tamman–Fulcher (VTF) type proton conduction mechanism, where proton hopping is coupled with the segmental motion of the polymer chain. Infrared spectroscopy combined with DFT quantum mechanical calculations was used to assign the experimental spectrum of PBI5N.

1. Introduction

In the development of the Proton Exchange Membrane Fuel Cell (PEMFC) one of the main goals is to obtain devices that can operate at medium-high temperatures (100–200 °C) and under anhydrous conditions. The use of PEMFCs in these conditions: (1) increases the catalytic activity; (2) reduces the carbon monoxide poisoning of platinum-based catalysts; (3) facilitates the control of thermal management systems; and (4) eliminates the requirement of humidification.[1]

Currently, perfluorinated polymer electrolytes functionalized with acid groups are the most used PEMs for fuel cell applications.[1] These materials (Dupont™ Nafion®,[2] Asahi Aciplex®, Dow®, and Flemion®, and Aquivion®) generally have high chemical, thermal and mechanical stabilities, but exhibit good proton conductivities only if there is a high and constant water content inside the membrane.[1] This last requirement limits the commercial use of conventional proton exchange membranes (PEMs), which show low proton conduction at temperatures higher than 90 °C and low values of relative humidity.[3] The type of conduction, *i.e.* vehicular *vs.* Grotthus, and the morphological changes associated with conduction in perfluorinated PEMs have been explored by molecular dynamic simulations and other computational methods.[4–6] In an effort to overcome these limitations, PEMs based on polymeric membranes impregnated with proton conducting ionic liquids (PCILs) recently have been developed.[7–9] In these systems, the presence of PCILs allows the proton conduction and the possibility to increase the PEMFC operating temperature above 100 °C.

About 15 years ago Savinell *et al.* proposed polybenzimidazole (PBI) membranes doped with strong acids, such as H_3PO_4 or H_2SO_4, as an alternative to Nafion® PEMs.[10,11] PBI is a polymer containing a basic functionality that allows the uptake of acid, which is responsible, and required, for the proton conduction. However, despite the good proton conductivity values,[12] the acid addition reduces the membrane's mechanical stability and leads to leaching problems at temperatures higher than 160 °C.[13]

Quartarone *et al.* recently showed that by changing the number and/or the position of the nitrogen atoms in the PBI membranes improvements in both the conductivity and the acid retention can be obtained.[14,15] They reported that membranes based on poly-2,2′-(2,6-pyridine)-5,5′-bibenzimidazole (PBI5N) showed an increase of two orders of magnitude in the conductivity after washing in a water/methanol (1 M) solution, with respect to the commercially

[a] *Dipartimento di Scienze Chimiche, Università di Padova, Via Marzolo 1, I-35131 Padova (Pd), Italy. E-mail: vito.dinoto@unipd.it; Fax: +39 049 8275229; Tel: +39 049 8275229*
[b] *Dipartimento di Chimica, Università di Pavia, Via Taramelli 16, 27100 Pavia, Italy. E-mail: piercarlo.mustarelli@unipv.it; Tel: +39 0382 987205*

 This journal is © the Owner Societies 2011

Published on 19 May 2011 on http://pubs.rsc.org | doi:10.1039/C1CP20902G
Downloaded by Universita di Padova on 22 December 2011

available poly-2,2′-*m*-phenylene-5,5′-bibenzimidazole (PBI4N). The same group also reported that preparation of composite membranes made from PBI4N and PBI5N doped with a SiO_2-based filler that is functionalized with imidazole to contain (SiO_2–Im) functional groups: (1) increases the permanent proton conductivity of the PBI4N composite membranes; (2) increases the thermal stability; and (3) allows a 20% increase in the maximum power density as compared to pristine PBI5N.[13,16–18] In order to extend that study and elucidate the effect of the filler on the properties of PBI5N, this work reports a comparison between the thermal, mechanical and electrical properties of PBI5N, PBI5N doped with H_3PO_4 and PBI5N containing 10 wt% of SiO_2–Im filler and doped with H_3PO_4. IR spectroscopy supported with DMol3 quantum chemical calculations is used to assign the experimental spectrum and to examine the nature of the phosphate. Electrical measurements reveal that the presence of the filler reduces the activation energy associated with the proton conduction mechanism.

2. Experimental section

2.1 Membrane preparation

Pristine and acid-doped PBI5N. The polymer membrane was obtained by dissolving PBI5N powder, as prepared by Carollo *et al.*,[14] in dimethylacetamide and casting the solution at 80 °C for 15 h. Acid-doped PBI5N was obtained by immersion of the PBI5N membrane in an aqueous solution of phosphoric acid (85 wt%) at room temperature for 72 h, and then dried at 110 °C for 24 h.

PBI5N-composite membrane. The SiO_2–Im filler was prepared by a sol–gel technique as reported by Mustarelli *et al.*[16] The PBI-composite membrane was prepared by the standard solvent casting technique. The pristine polymer was dissolved in dimethylacetamide at 100 °C. Subsequently, 10 wt% of the filler was dispersed by sonication in the polymer solution, which was then cast to obtain a homogeneous film. The composite membrane was then activated with H_3PO_4 in the same conditions reported above for the acid-doped PBI5N membrane.

2.2 Instruments and methods

Thermogravimetric analyses (TG) were carried out using a high-resolution thermobalance TGA 2950 (TA Instruments) under a nitrogen flow at a rate of 100 cm^3 min^{-1}. The sensitivity of the instrument ranges from 0.1 to 2% per min and the resolution is 1 μg. TG profiles were collected over the thermal range from 20 to 900 °C. Approximately 6 mg of sample were loaded in an open platinum pan. The heating rate (°C min^{-1}) was varied from 50 to 0.001 °C min^{-1}, depending on the first derivative of the weight loss.

Differential Scanning Calorimetry (DSC) analyses were performed using a mDSC 2920 (TA instruments) equipped with a liquid nitrogen cooling system. Measurements were conducted in the cyclic mode, using a heating rate of 6 °C min^{-1} over a thermal range from −50 to 350 °C. The measurements were made by loading about 7 mg of sample inside a hermetically-sealed aluminium pan.

Dynamic-Mechanical Analyses (DMA) were made with a TA Instruments DMA Q800 equipped with a clamp specifically made for testing films in the tension mode. Spectra were collected by applying a sinusoidal deformation of amplitude 4 μm at 1 Hz in 5 °C intervals over a thermal range from −100 to 300 °C. A rectangular sample (20 × 30 × 5 mm^3) was subjected to a pre-loading force of 0.05 N. The viscoelastic behaviour of the samples was quantified in terms of elastic modulus (E'), loss modulus (E'') and loss factor (tanδ).

FT-IR spectra were collected using a Nicolet FT-IR Nexus spectrometer with a resolution of 4 cm^{-1}. The spectra of the membranes were obtained in ATR mode with a Perkin-Elmer Frustrated Multiple Internal Reflections 186-0174 accessory.

Broadband Electric Spectroscopy (BES) measurements were collected over the frequency range of 10^{-2} to 10^7 Hz using a Novocontrol Alpha analyzer. The electric spectra were measured in the thermal range between 5 and 135 °C in 10 °C intervals with an accuracy greater than ±0.1 °C. The temperature was controlled with a cryostat equipped with a gaseous nitrogen heating–cooling system. Samples were placed between two gold cylindrical electrodes.

3. Quantum mechanical calculations

Infrared spectra were calculated using density functional theory methods implemented in an all-electron DFT code using the DMol3 program[19,20] as a part of the Materials Studio package (double numerical plus polarization basis set, gradient-corrected (GGA) BLYP functional). The polybenzimidazole PBI5N polymer was modelled using chains containing one, two and three repeat units. The internal modes were identified by animating the atomic motion of each calculated mode using features available in the DMol3 package.

4. Results and discussion

4.1 Thermal analysis

The TG curves of PBI5N, PBI5N + H_3PO_4 and PBI5N/SiO_2–Im + H_3PO_4 are measured over the temperature range from 25 to 900 °C and are shown in Fig. 1 together with the derivative of the weight change (dw%/dT). Fig. 1 also shows the thermal decomposition of an 85 wt% phosphoric acid solution. Four mass losses are observed for all three membranes.[21] The first, in the temperature range between 20 and 100 °C is due to the desorption of H_2O and CO_2. This process is present for all membranes and is higher in the samples treated with phosphoric acid (weight loss of 15–20 wt%) compared to the PBI5N membrane (~5 wt%). This difference is due to the presence of the H_3PO_4 solution. The TG profile of the acid solution shows a mass loss of 15 wt% between 20 and 100 °C. The second loss occurs between 120 and 320 °C and is associated with the release of water during the formation of pyrophosphoric acid by the reaction: $2H_3PO_4 \rightarrow H_4P_2O_7 + H_2O$.[21] This thermal event is absent in the TG profile of PBI5N. The weight loss associated with the release of water is 9, 14 and 15 wt% for PBI5N + H_3PO_4, PBI5N/SiO_2–Im + H_3PO_4 and H_3PO_4, respectively.

Published on 19 May 2011 on http://pubs.rsc.org | doi:10.1039/C1CP20902G
Downloaded by Universita di Padova on 22 December 2011

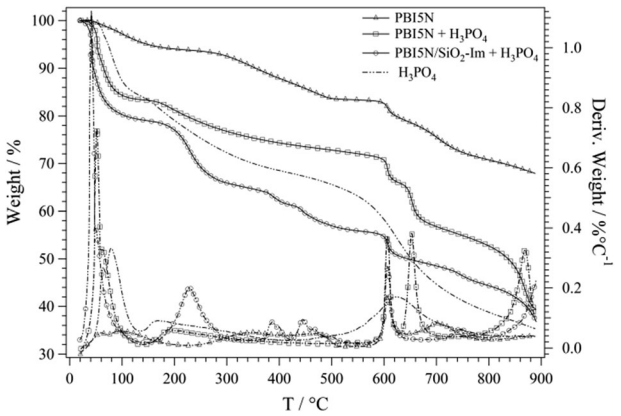

Fig. 1 Weight loss (left axis) and derivative dw%/dT (right axis) in the temperature range from 20 to 900 °C of PBI5N (triangle), PBI5N + H_3PO_4 (square) and PBI5N/SiO_2–Im + H_3PO_4 (circle). The graph reports also the TG profile of the H_3PO_4 solution (85 wt%).

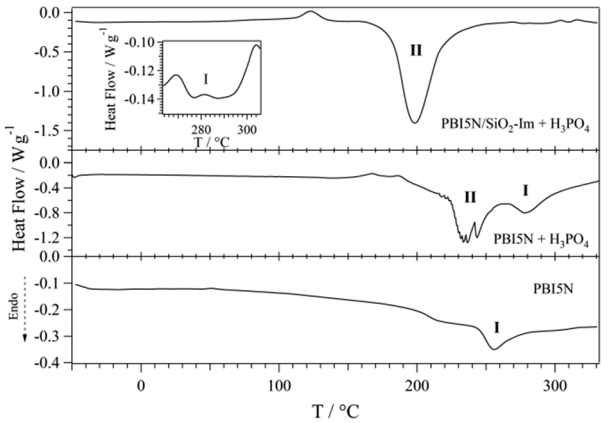

Fig. 2 DSC curves of PBI5N, PBI5N + H_3PO_4 and PBI5N/SiO_2–Im + H_3PO_4 collected in the thermal range from −50 to 350 °C. The inset shows the expansion of the DSC curves from 260 to 305 °C for PBI5N/SiO_2–Im + H_3PO_4.

Furthermore, the derivatives of the weight change reported in Fig. 1 show the temperature of the second loss peak maxima increases in the order H_3PO_4 < PBI5N + H_3PO_4 < PBI5N/SiO_2–Im + H_3PO_4. These results indicate that the presence of the inorganic filler with basic character increases the uptake and the thermal stability of phosphoric acid inside the PBI matrix, owing to the presence of SiO_2–Im···H_3PO_4 interactions.

The third (300–550 °C) and fourth (550–800 °C) losses are associated with the thermal degradation of the PBI matrix.[21] The main thermal decomposition products are CO, C_6H_6, CH_3CN and HCN.[21] In this temperature range, the phosphoric acid shows a broad peak centred at about 630 °C, due to the loss of water formed during the reaction: $H_4P_2O_7 \rightarrow 2HPO_3 + H_2O$.[21]

For all the three membranes, investigation of the thermal transitions was carried out by differential scanning calorimetry measurements. The samples were initially heated from 25 to 130 °C (cycle 1), then cooled from 130 to −50 °C (cycle 2) and finally heated from −50 to 350 °C (cycle 3). The DSC curves collected during cycle 3 for PBI5N, PBI5N + H_3PO_4 and PBI5N/SiO_2–Im + H_3PO_4 are reported in Fig. 2.

The DSC curve of PBI5N shows the presence of two transitions: an event at about 210 °C, associated with the glass transition temperature (T_g) of the material and an endothermic peak at *ca.* 250 °C (peak I in Fig. 2) attributed to the melting of microcrystalline domains. For PBI soaked with H_3PO_4, peak I shifts towards higher temperatures and is significantly reduced in the hybrid sample, indicating that the presence of imidazolium-functionalized silica leads to a reduction of the degree of crystallinity of the PBI membrane. Both the acid-doped membranes show the presence of an intense endothermic peak (peak II) between 200 and 250 °C. This thermal event, which is absent in PBI5N, is associated with the elimination of water in the reaction: $2H_3PO_4 \rightarrow H_4P_2O_7 + 2H_2O$. This interpretation is supported by the enthalpies associated with peak II, which are 367 and 341 J g^{-1} for PBI5N/SiO_2–Im + H_3PO_4 and PBI5N + H_3PO_4, respectively. The enthalpy values are higher for the hybrid composite membrane, which according to the TG results contains a greater amount of acid.

4.2 Dynamic mechanical studies

Fig. 3 reports the spectra of the storage modulus (E'), the loss modulus (E'') and tanδ = E''/E' collected for the doped membranes and PBI5N in the temperature range between −100 and 300 °C.

The addition of orthophosphoric acid leads to a reduction of the membrane's mechanical stability as is evident from the sharp decrease of E' for both the acid-doped membranes as compared to pristine PBI5N. At temperatures above 120 °C, the values of E' for the hybrid membrane are significantly higher than those of the PBI5N membrane soaked in H_3PO_4. For example, at 200 °C the storage moduli E' are 53.7 MPa and 2.65 MPa for PBI5N/SiO_2–Im + H_3PO_4 and PBI5N + H_3PO_4, respectively. This difference in the mechanical properties of the doped membranes is due to the presence of the SiO_2–Im filler, which interacts with both the ortho-phosphoric acid and the polymer matrix and increases the mechanical stability of the hybrid membrane. In addition, for temperatures above 200 °C, both the acid-doped membranes show a plateau in the elastic modulus. This behaviour, in

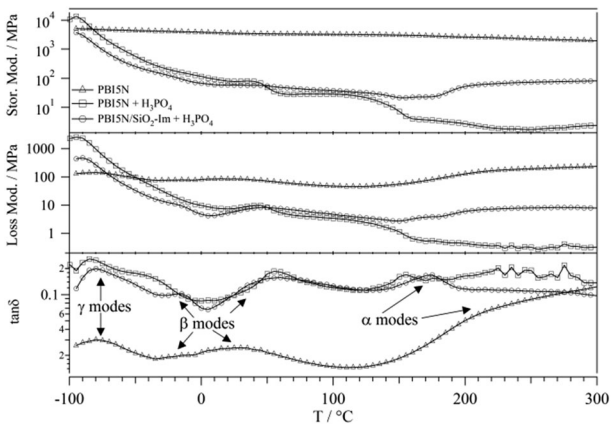

Fig. 3 DMA profiles of PBI5N (triangle), PBI5N + H_3PO_4 (square) and PBI5N/SiO_2–Im + H_3PO_4 (circle). The graphs show the behaviour of the elastic modulus (E'), loss modulus (E'') and of tanδ with respect to the scanning temperature.

 This journal is © the Owner Societies 2011

Published on 19 May 2011 on http://pubs.rsc.org | doi:10.1039/C1CP20902G
Downloaded by Universita di Padova on 22 December 2011

agreement with TG and DSC measurements, is due to the elimination of traces of water produced in the reaction $2H_3PO_4 \rightarrow H_4P_2O_7 + 2H_2O$.

The tanδ profiles reported in Fig. 3 reveal the presence of three mechanical relaxation modes: γ, β and α. The γ relaxation between $-100 < T < -50$ °C is likely associated with local fluctuation of the aromatic rings occurring within asymmetric units of the polymer chain. β ($-50 < T < 80$ °C) and α ($120 < T < 220$ °C) transitions are caused by relaxation modes attributed to coupling of inter-chain dipole–dipole interactions and the segmental motion of polymer backbone chains, respectively. The nature of the β relaxation is discussed later in the section concerning the electrical studies.

In PBI5N the presence of the mechanical α transition around 200 °C indicates that the glass transition temperature is significantly lower than that typically reported for PBI4N[12] (420 °C), in agreement with the interpretation of the DSC results.

Compared to PBI5N, the membranes soaked with H_3PO_4 show a shift of the β peak towards higher temperatures due to interactions between the polymer and the acid that increase the dipole–dipole inter-chain interactions. Furthermore, as compared to PBI5N + H_3PO_4, the presence of the filler in the hybrid membrane causes the α peak to appear at higher temperatures as a result of the interactions between the SiO_2–Im filler and the polymer matrix.

4.3 FT-IR and DFT analysis

The IR spectrum of PBI4N has previously been assigned by a number of groups.[12,22–24] The only structural difference between PBI4N and PBI5N is the presence of a pyridine unit in the PBI5N chain in the place of the phenyl group found in the PBI4N chain. Therefore, the differences in the vibrational spectra of PBI4N and PBI5N are small and should be found in modes attributed to the phenyl/pyridine groups. The infrared spectrum of the PBI5N membrane can be found as a part of Fig. 4 and the vibrational assignments are given in Table 1. The vibrational assignments were made by comparing the previously published vibrational assignments of PBI4N,[22,24] benzimidazole[25,26] and pyridine[27] and combining those with the DFT calculated modes determined with DMol3.[19,20] The calculated modes were determined for chains with one, two and three repeat units of PBI5N. The dimer and trimer were examined to determine the validity of using one repeat unit to model the larger polymeric chain. The single repeat unit seems to provide a reasonably good model for the vibrations of PBI5N as main differences between three models were found in the coupling between CH moieties in the in-plane and out-of-plane bending and stretching modes.

In the C=C and C=N stretching region (1650–1550 cm^{-1}), the modes of the phenyl and benzimidazole moieties in PBI4N tend to be very close in frequency. In comparison, the pyridine C=C and C=N stretching modes (1569 cm^{-1}) in PBI5N occur at slightly lower frequencies than the same modes in benzimidazole (1615, 1598 cm^{-1}). The in-plane CH bending modes occur between 1500 and 1000 cm^{-1}. In the higher end of this frequency range, the NH in-plane bending modes tend to be coupled with the CH modes. Below 1000 cm^{-1}, the peaks

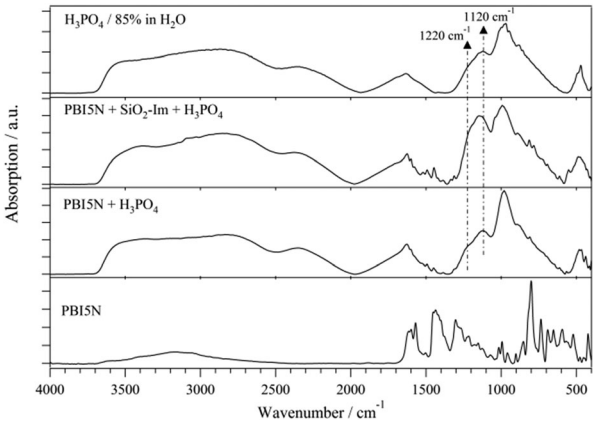

Fig. 4 Infrared spectra from 4000 to 400 cm^{-1} for PBI5N, PBI5N + H_3PO_4, PBI5N/SiO_2–Im + H_3PO_4 and H_3PO_4 solution.

Table 1 Vibrational assignments of the experimental PBI5N spectrum[a,b]

Wavenumber/cm^{-1}	Assignment[c]
1615, 1598	ν(C=C, C=N) bzim
1569	ν(C=C, C=N) py
1453	ν(ring) bzim
1435	ν(ring) py
1416	ν(ring) bzim & py
1400	ν(ring) bzim & py + δ_{ip}(NH)
1303	δ_{ip}(CH) bzim + δ_{ip}(NH) + ν(C–N)
1283	δ_{ip}(CH) bzim + δ_{ip}(NH) + ν(C–C) bzim phenyl
1266, 1228, 1216	δ_{ip}(CH) bzim + δ_{ip}(NH) + ν(C–C) bzim phenyl ν(C–N)
1152	δ_{ip}(CH) py
1015	δ_{ip}(CH) bzim phenyl
994, 952	δ_{op}(CH) py
901, 850	δ_{op}(CH) bzim
799	bzim ring breathing
735	δ_{op}(CH) bzim & py
690	δ_{op}(ring) py + δ_{op}(CH) py
652	δ_{ip}(ring) bzim & py

[a] Abbreviations: bzim = benzimidazole, py = pyridine, ν = stretch, δ = bend, ip = in plane, op = out of plane. [b] Note: in the experimental spectrum, peaks attributed to the CH and NH stretching modes are not resolved and therefore not included in this table. [c] The vibrational assignments were made correlatively on the basis of previously published PBI4N,[22,24] benzimidazole[25,26] and pyridine[27] spectra, which were then compared and confirmed with the DFT calculated modes determined with DMol3.[19,20]

can be attributed to out-of-plane CH bending modes and in-plane and out-of-plane ring bending modes. Stretching modes of the NH (3450–3100 cm^{-1}) and CH ($\sim$3050 cm^{-1}) groups are typically found at high frequencies (greater than 2500 cm^{-1}),[13,22–24] however, those modes are of unusually low intensity in the spectrum shown in Fig. 4.

For the acid-doped membranes, the infrared spectra are dominated by phosphoric acid bands. Bands at approximately 2750 and 2350 cm^{-1} are attributed to the acid OH stretching modes.[28] Additionally, there are three strong bands in the lower frequency region of the spectrum (*ca.* 1120, 980 and 880 cm^{-1}). These bands are typical vibrational modes of the phosphate anion. The frequencies of these bands are similar in all three spectra. The lowest frequency band at *ca.* 880 cm^{-1} is

Published on 19 May 2011 on http://pubs.rsc.org | doi:10.1039/C1CP20902G
Downloaded by Universita di Padova on 22 December 2011

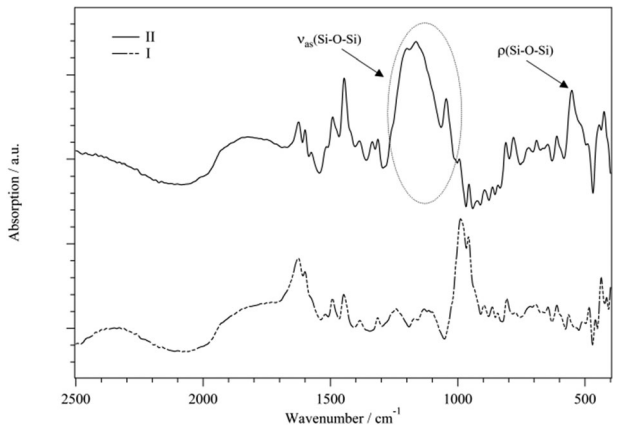

Fig. 5 Difference spectra obtained by subtracting the infrared spectrum of H_3PO_4 solution to PBI5N + H_3PO_4 (curve I) and PBI5N + SiO_2–Im + H_3PO_4 (curve II).

attributed to the symmetric PO stretch of the $P(OH)_3$ moiety.[12,13,28] The other two bands, *ca.* 1120 and 980 cm^{-1}, are most likely associated with the $H_2PO_4^-$ anion, as the $P(OH)_2$ antisymmetric PO stretching mode and the PO_2 symmetric stretching motion, respectively.[12,13,28] Additionally, there is a high frequency shoulder *ca.* 1220 cm^{-1} which may contain contributions from the PO_2 antisymmetric stretching motion or the POH bending motion of H_3PO_4.[12,28] These phosphate bands indicate the presence of both H_3PO_4 and $H_2PO_4^-$ species within the membranes.

The presence of functionalized silica can be mostly easily detected by the difference spectra reported in Fig. 5. Difference spectra are obtained by subtracting the spectrum of the phosphoric acid solution from the spectra of the hybrid doped-membrane (curve II in Fig. 5) and the acid-doped PBI5N (curve I of Fig. 5). The spectra were normalized with the band centred at approximately 2350 cm^{-1} before subtraction. Spectral profile II shows the presence of absorption bands between 1300 and 1000 cm^{-1} and at *ca.* 550 cm^{-1}, associated to the asymmetric bending and rocking modes of the Si–O–Si group, respectively.[29]

In the hybrid membrane when compared to acid-doped PBI5N, the relative intensities of the peaks at 1130 and 1230 cm^{-1} increase when compared to the band at 990 cm^{-1} (see Fig. 4). Within the PBI5N/SiO_2–Im + H_3PO_4 membrane, this behaviour could be associated with two phenomena: (a) phosphoric acid in a less dissociated state than in the PBI5N + H_3PO_4;[13] and/or (b) the presence of the inorganic filler resulting in the superposition of the functionalized silica and phosphate peaks.

4.4 Broadband electric spectroscopy studies

Electrical measurements were performed in the frequency range from 10 mHz to 10 MHz for temperatures between 5 and 135 °C. The spectra of the imaginary component of permittivity (ε'') and the real component of the conductivity (σ') as a function of frequency are shown at different temperatures in Fig. 6 and 7 respectively. From these spectra, it is evident that the addition of orthophosphoric acid leads to a substantial change in the electrical response of materials. For all samples, the values of ε'' increase with decreasing frequency and are 6–7 orders of magnitude greater in the membranes treated with H_3PO_4 than in PBI5N. The profiles of σ' for the dry PBI5N membrane show values between 10^{-13} and 10^{-7} S cm^{-1} that increase by about 6 orders of magnitude after the treatment with H_3PO_4.

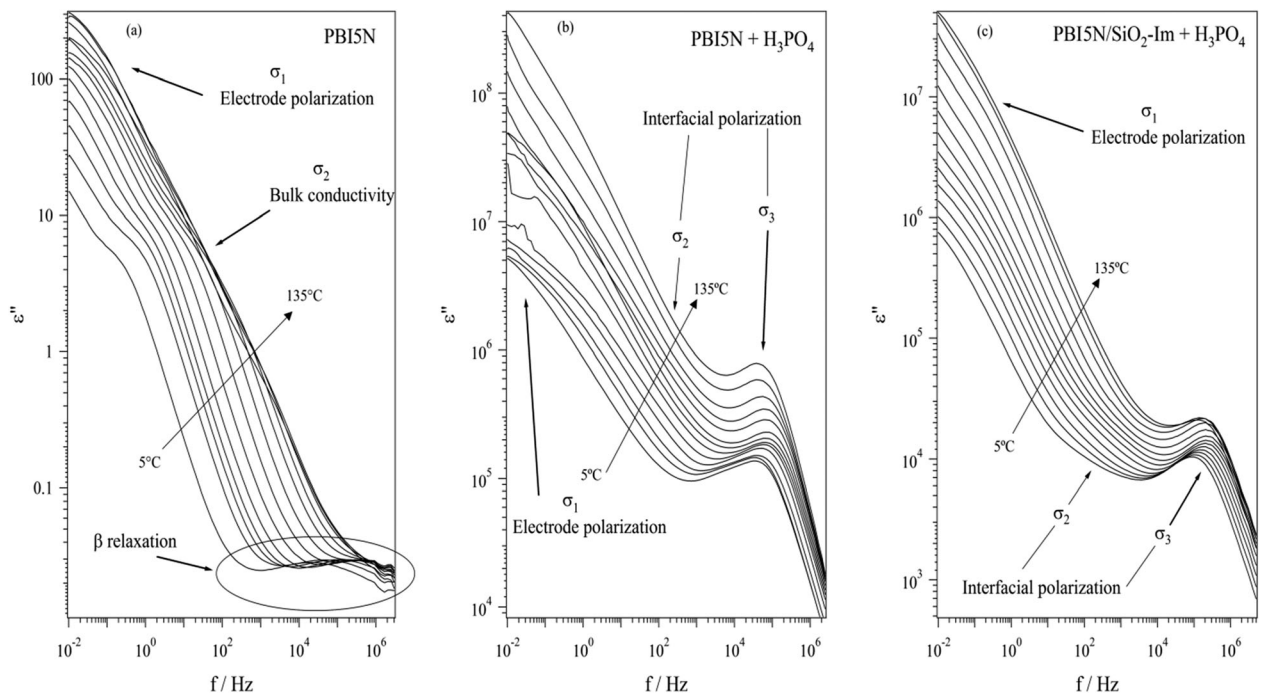

Fig. 6 Profiles of ε'' as a function of frequency at temperatures between 5 °C and 135 °C for (a) PBI5N; (b) PBI5N + H_3PO_4; (c) PBI5N/SiO_2–Im + H_3PO_4.

 This journal is © the Owner Societies 2011

Published on 19 May 2011 on http://pubs.rsc.org | doi:10.1039/C1CP20902G
Downloaded by Universita di Padova on 22 December 2011

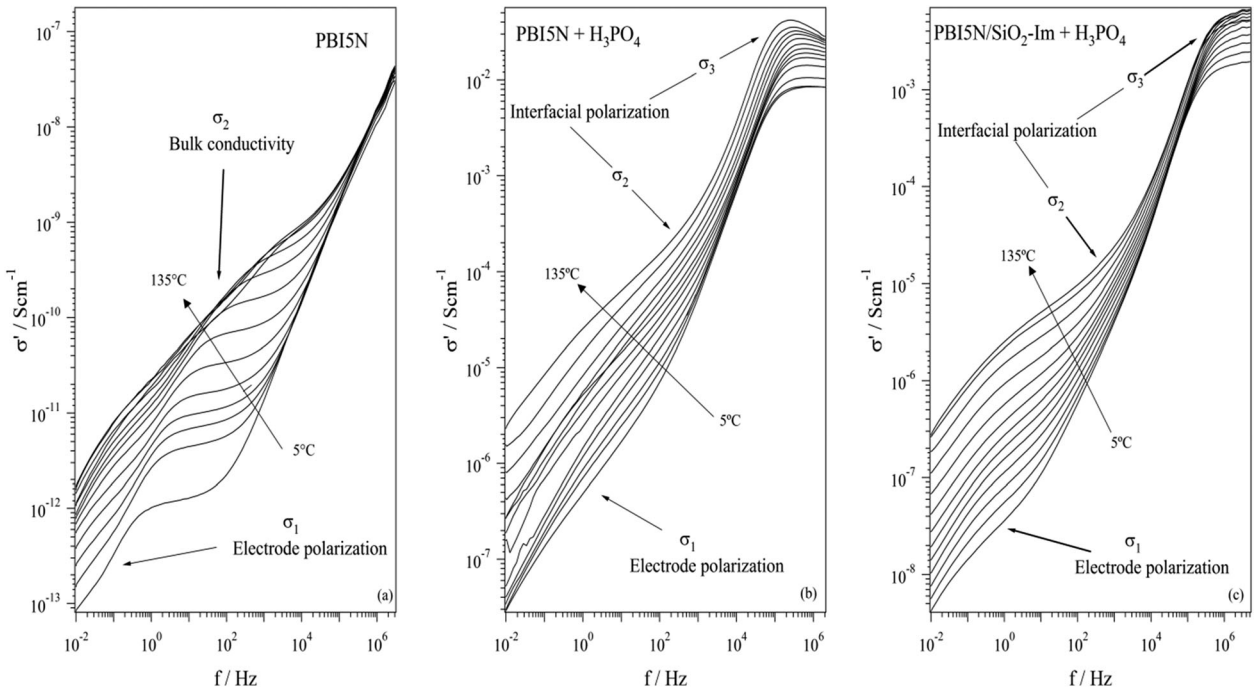

Fig. 7 Profiles of σ'' as a function of frequency at temperatures between 5 °C and 135 °C for (a) PBI5N; (b) PBI5N + H_3PO_4; (c) PBI5N/SiO_2–Im + H_3PO_4.

The ε'' profile of PBI5N (Fig. 6) at frequencies higher than 10^3 Hz shows the presence of a broad peak, which shifts towards higher frequencies with increasing temperature. This peak is due to the β-electric relaxations, typically present in glassy systems for temperatures below the T_g.[30,31] In the case of polymers of type B, where the dipole moments are rigidly attached to the main polymer chain, such as PVC or polycarbonates, β transitions are associated with changes in the dipole moments caused by local fluctuations in the main polymer chain.[30,31] Since polybenzimidazole is a type-B polymer, it follows that in PBI5N the β relaxation modes arise from changes in the dipole moments induced by local motion of units within the polymer chain. It should be noted that this mode is diagnostic of interactions between the PBI5N chains and the environment.

For PBI5N between 0.1 and 10^3 Hz, the ε'' profiles reported in Fig. 6a reveal the emergence of a peak that corresponds to a plateau in the conductivity spectra (Fig. 7a). The σ' values taken at the plateau correspond to membrane's bulk conductivity,[32] which increases with temperature from about 10^{-12} S cm^{-1} (5 °C) to 10^{-9} S cm^{-1} (155 °C). These conductivity values indicate that pristine PBI5N, in anhydrous conditions, behaves as a dielectric material. These conductivity values are in agreement with those found by Bouchet and Siebert, who reported for PBI4N a conductivity of 10^{-12} S cm^{-1} at 30 °C and a conduction mechanism due to proton hopping between nitrogen atoms along the polymer chain.[12] As shown in Fig. 6a for frequencies lower than 0.1 Hz, the spectra of ε'' increase with decreasing frequency. This response is due to electrode polarization phenomena, which involves the accumulation of charges at the interface between the measuring electrodes and the polymeric membrane.[31]

Detailed analysis of the PBI5N experimental data is conducted by fitting the permittivity profiles measured at different temperatures with eqn (1).[7,33,34]

$$\varepsilon^*(\omega) = \sum_{n=1}^{2} \frac{\sigma_n (i\omega\tau_n)^{\gamma_n}}{i\omega[1 + (i\omega\tau_n)^{\gamma_n}]} + \frac{\Delta\varepsilon_\beta}{[1 + (i\omega\tau_\beta)^{\mu_\beta}]} + \varepsilon_\infty \quad (1)$$

The first term of eqn (1) simulates the electrode polarization σ_1 ($n = 1$) and the interfacial polarization which is correlated to the bulk conductivity of the material σ_2 ($n = 2$), with $0.5 < \gamma_n < 1$. The second term describes the molecular β relaxation using a Cole–Cole type equation.[31] $\omega = 2\pi f$ is the angular frequency of electric field and $\tau_\beta = 1/(2\pi f_\beta)$ is the relaxation time associated with the peak of intensity, $\Delta\varepsilon_\beta$, and position, f_β. The parameter μ_β is a shape factor that controls the peak width and is related to the distribution of relaxation times associated with the dielectric relaxation. Finally, ε_∞ accounts for the electronic contribution to the permittivity of the material.

The resulting fit parameters $\Delta\varepsilon_\beta$ and μ_β are independent of temperature with values ranging between 0.2–0.27 and 0.26–0.4, respectively. For $5 < T < 65$ °C, the logarithmic values of f_β when plotted as a function of $1/T$ (Fig. 8 part (a)) show a VTF behaviour, with an activation energy E_β of 0.894 kJ mol^{-1}. Such behaviour suggests that the local motion of polymer chains is coupled with the segmental motion.

The logarithmic values of σ_2 and f_{σ_2} (with $f_{\sigma_2} = 1/(2\pi\tau_{\sigma_2})$) plotted as a function of the reciprocal temperature are shown in parts (c) and (b) of Fig. 8, respectively. log f_{σ_2} and log σ_2 show similar trends and are divisible into two regions: VTF-type behaviour for $5 < T < 55$ °C (region I) and Arrhenius-type behaviour between 55 and 115 °C (region II).

Published on 19 May 2011 on http://pubs.rsc.org | doi:10.1039/C1CP20902G
Downloaded by Universita di Padova on 22 December 2011

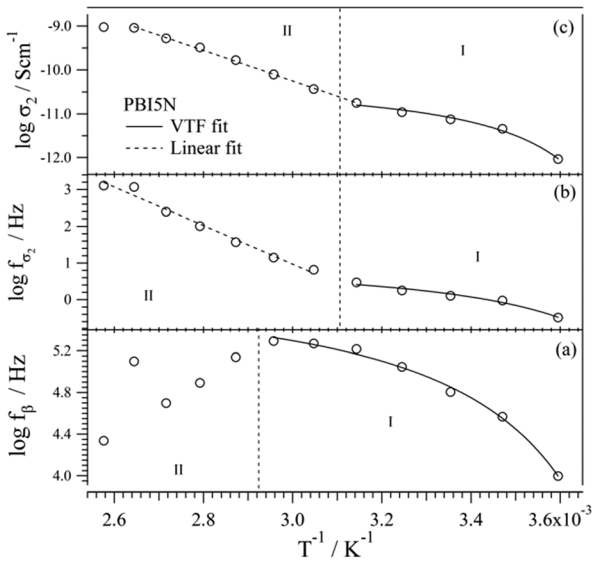

Fig. 8 log plot as a function of reciprocal temperature for PBI5N of: (a) f_β; (b) f_{σ_2}; (c) σ_2.

Table 2 Values of the activation energies E_β, $E_{f\sigma_2}$ and E_{σ_2} for regions I and II for PBI5N

	E_β/kJ mol^{-1}	$E_{f\sigma_2}$/kJ mol^{-1}	E_{σ_2}/kJ mol^{-1}
Region I	0.894	0.862	0.645
Region II	—	99	66

For the temperature regions I and II the activation energies $E_{f\sigma_2}$ and E_{σ_2} obtained by fitting the values of log f_{σ_2} and log σ_2 with VTF and Arrhenius-type functions are reported in Table 2.

For region I the values of $E_{f\sigma_2}$ and E_{σ_2} are nearly coincident with E_β, indicating that the conduction mechanism, which occurs by "hopping" of the protons between the nitrogen atoms, is mediated by the local dipolar fluctuation and segmental motion of polymer chains. As the temperature increases (region II) the values of log f_{σ_2} and log σ_2 follow an Arrhenius-type behaviour with associated activation energies of $E_{f\sigma_2}$ = 99 kJ mol^{-1} and E_{σ_2} = 66 kJ mol^{-1}. These values are of the same order of magnitude as those found by Bouchet and Siebert, who report for PBI doped with $0.2 < x < 3.5$ moles of acid per repeat unit of polymer a concentration-independent activation energy of about 77 kJ mol^{-1}.[12] The Arrhenius behaviour indicates that for temperatures above 55 °C the motion of the protons is decoupled from that of the polymer chains.

For the acid-doped membranes, ε'' values increased by up to 6 orders of magnitude as compared to pristine PBI5N, while the spectra of σ' show a plateau shifted to higher frequencies ($>10^5$ Hz). The conductivity values taken at the plateau are between 10^{-2} and 10^{-3} S cm^{-1}, in agreement with those found by Bouchet and Siebert for PBI membranes doped with 1.45 mol of H_3PO_4 per polymer repeat unit.[12] The high values of ε'' and σ' indicate that for doped membranes the electrical response is entirely due to the motion of free charges. Even for wet membranes at low frequencies, there is an increase of ε'' due to electrode polarization phenomena.

For PBI5N + H_3PO_4 and PBI5N/SiO_2–Im + H_3PO_4, the experimental profiles of ε'' are fitted considering the presence of multiple polarizations phenomena with eqn (2).[7,33,34]

$$\varepsilon^*(\omega) = \sum_{k=1}^{3} \frac{\sigma_k (i\omega\tau_k)^{\gamma_k}}{i\omega[1 + (i\omega\tau_k)^{\gamma_k}]} + \varepsilon_\infty \qquad (2)$$

The first term simulates: (a) for $k = 1$ the electrode polarization; (b) for $k = 2,3$ the interfacial polarizations or Maxwell–Wagner Polarization events, which typically are present in heterogeneous systems and are due to the accumulation of charges at the interfaces between domains with different permittivities.[31] In this case, these are domains of phosphoric acid and PBI5N.

For the acid-doped membranes, the values of log σ_3, as a function of inverse temperature, are shown in Fig. 9, together with the bulk conductivity of PBI5N (log σ_2). For both doped membranes, the log σ_3 values are about six orders of magnitude greater than the log σ_2 values and show VTF behaviour, as shown in inset (b) of Fig. 9.

The VTF behaviour of log σ_3 is different from the Arrhenius behaviour reported in previous works,[12,15,35] but is in agreement with the study reported by Fontanella *et al.*, where VTF behaviour is observed for PBI doped with 6 mol of H_3PO_4 (85% solution) per repeat unit of PBI. This behaviour is similar to that of a "true" polymer electrolyte in which the proton conduction mechanism is mediated by the segmental motion of the polymer chains.[36] The VTF behaviour of log σ_3 plotted as a function of T^{-1} is in accordance with the DSC and DMA analyses that reveal: (a) for PBI5N, a glass transition temperature below 200 °C; (b) for the acid-doped membranes, the presence of the α-mechanical transition induced by the segmental motion of the polymer chains.

The activation energy $E_{\sigma 3}$ associated with the bulk conductivity is 3.1 and 1.6 kJ mol^{-1} for PBI + H_3PO_4 and PBI/SiO_2–Im + H_3PO_4, respectively. These values are of the same order of magnitude as the activation energy E_β related to β relaxation (0.894 kJ mol^{-1}). In addition, as compared to PBI + H_3PO_4, the lower activation energy for the hybrid

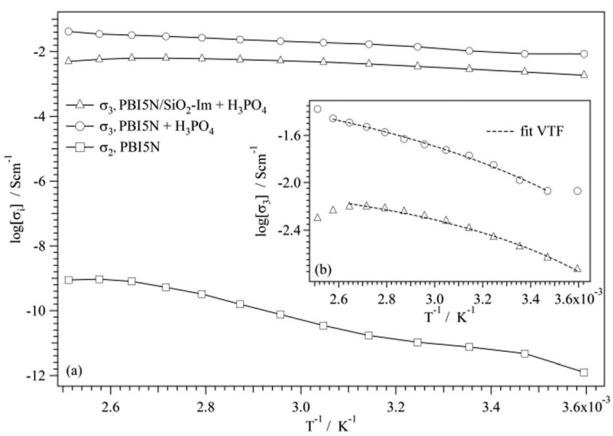

Fig. 9 log plot of conductivities as a function of reciprocal temperature for: (a) PBI5N, PBI5N + H_3PO_4, PBI5N/SiO_2–Im + H_3PO_4. The inset shows the log of σ_3 as a function of $1/T$ for the acid-doped membranes.

 This journal is © the Owner Societies 2011

Published on 19 May 2011 on http://pubs.rsc.org | doi:10.1039/C1CP20902G
Downloaded by Universita di Padova on 22 December 2011

membrane suggests that the presence of SiO_2–Im facilitates the proton conduction mechanism.

For PBI/SiO_2–Im + H_3PO_4 the conductivity values are lower than those of PBI + H_3PO_4 (Fig. 9, inset (b)). This behaviour, in accordance with vibrational spectroscopy results, could be due to the presence inside the hybrid membranes of phosphoric acid less dissociated than in the PBI + H_3PO_4 membrane.

In conclusion, electrical measurements show that for acid-doped membranes the proton conduction mechanism is favoured by the coupling of proton hopping with local β relaxation modes and segmental motion of the backbone polymer chains.

5. Conclusion

This paper reports a detailed study of three materials: polybenzimidazole (PBI5N), PBI5N impregnated with orthophosphoric acid (PBI5N + H_3PO_4) and PBI5N containing 10 wt% of SiO_2–Im filler functionalized with imidazole groups and impregnated with orthophosphoric acid (PBI5N/SiO_2–Im + H_3PO_4). The materials are characterized with TG, DSC and FT-IR spectroscopy, while their mechanical and electric properties are analyzed by DMA and BES studies.

The thermogravimetric analyses showed: (a) PBI5N is stable up to 300 °C, while the acid-doped membranes present the thermal decomposition of H_3PO_4 in the temperature range from 120 to 320 °C; and (b) the presence of the filler in bulk PBI5N increases the acid uptake of the membrane.

The DSC measurements reveal that PBI5N has a glass transition temperature of 210 °C and the presence of SiO_2–Im filler reduces the degree of crystallinity of the polymer membrane.

The addition of phosphoric acid reduces the mechanical properties of doped membranes as compared to PBI5N, while the presence of the inorganic filler increases the mechanical stability of the hybrid membrane with respect to the acid-doped PBI5N. Furthermore, all of the membranes show the presence of three mechanical transitions, α, β and γ, related to the dynamics of the polymer matrix.

The combination of DFT calculations and FT-IR allows assignment of the PBI5N spectrum. The C=C and C=N stretching modes of the pyridine unit in PBI5N tend to occur at lower frequencies than the phenyl modes in PBI4N. In the acid-doped membranes, the spectra indicate the presence of both H_3PO_4 and $H_2PO_4^-$ species within the membranes.

Electrical measurements show for the membrane PBI5N: (a) the presence of a β-dielectric relaxation associated with fluctuations of the chain dipole moment induced by local motion of the polymer chains; and (b) a proton conduction mechanism divisible into two different temperature regions: VTF for $5 < T < 55$ °C (region I) and Arrhenius for $55 < T < 115$ °C (region II).

Acid-doped membranes present conductivity values of 10^{-2}–10^{-3} S cm^{-1} and a VTF-type proton conduction mechanism, where proton hopping is coupled with the segmental motion of the polymer chain. This hypothesis is confirmed: (1) by the trend of log σ_{DC} as a function of $1/T$ that shows, in contrast to the dry PBI membrane, VTF behaviour over the entire measured temperature range; and (2) by the presence of the α transition in the DMA tanδ profiles of wet membranes.

This work demonstrates one approach to improve the properties of PEMs for application in high-temperature fuel cells. In the PBI/SiO_2–Im + H_3PO_4 membrane, a basic-functionalized filler allows increased acid uptake and allows the membrane to maintain a high conductivity due to the formation of percolation pathways at the interface between the polar and nonpolar domains. The optimal membrane for operation under these anhydrous conditions would result from the substitution or removal of water, while maintaining the thermal stability and the percolation pathways for good conductivity. Nanoscale and/or mesostructured fillers may be very useful to prepare PBI-based membranes with better mechanical and transport properties. In particular, these materials can offer a valuable solution to the problem of acid leaching, which is chiefly relevant for thin membranes. A critical point to be addressed is the long-term stability of silica-based materials when they are in contact with phosphoric acid. This will be the object of future investigations.

Acknowledgements

This research was funded by the Italian MURST project PRIN2008, entitled "Polymer electrolyte membrane fuel cells: synthesis and study in prototype cells of hybrid inorganic-organic membranes and electrode materials", and by the CARIPLO project "Nuove membrane micro- e nanocomposite a matrice polimerica per celle a combustibile".

Notes and references

1 J. S. Wainright, M. H. Litt and R. F. Savinell, in *Handbook of Fuel Cells: Fundamentals Technology and Applications*, ed. W. Vielstich, A. Lamm and H. A. Gasteiger, Wiley, West Sussex, 2003, vol. 3, pp. 436–446.
2 The DuPont Oval Logo, DuPont™, The miracles of science™ and all products denoted with a TM and ® are trademarks or registered trademarks of DuPont or its affiliates.
3 *Handbook of Fuel Cells: Fundamentals Technology and Applications*, ed. W. Vielstich, A. Lamm and H. A. Gasteiger, Wiley, West Sussex, 2003.
4 E. Allahyarov, P. L. Taylor and H. Lowen, *Phys. Rev. E: Stat., Nonlinear, Soft Matter Phys.*, 2010, **81**, 031805.
5 P. Commer, A. G. Cherstvy, E. Spohr and A. A. Kornyshev, *Fuel Cells*, 2002, **2**, 127–136.
6 S. Walbran and A. A. Kornyshev, *J. Chem. Phys.*, 2001, **114**, 10039–10048.
7 V. Di Noto, E. Negro, J. Y. Sanchez and C. Iojoiu, *J. Am. Chem. Soc.*, 2010, **132**, 2183–2195.
8 S. Y. Lee, A. Ogawa, M. Kanno, H. Nakamoto, T. Yasuda and M. Watanabe, *J. Am. Chem. Soc.*, 2010, **132**, 9764–9773.
9 V. Di Noto, M. Piga, G. A. Giffin, S. Lavina, E. S. Smotkin, J. Y. Sanchez and C. Iojoiu, *J. Phys. Chem. C*, submitted.
10 J. S. Wainright, J. T. Wang, D. Weng, R. F. Savinell and M. Litt, *J. Electrochem. Soc.*, 1995, **142**, L121–L123.
11 J. T. Wang, R. F. Savinell, J. Wainright, M. Litt and H. Yu, *Electrochim. Acta*, 1996, **41**, 193–197.
12 R. Bouchet and E. Siebert, *Solid State Ionics*, 1999, **118**, 287–299.
13 E. Quartarone, A. Magistris, P. Mustarelli, S. Grandi, A. Carollo, G. Z. Zukowska, J. E. Garbarczyk, J. L. Nowinski, C. Gerbaldi and S. Bodoardo, *Fuel Cells*, 2009, **9**, 349–355.
14 A. Carollo, E. Quartarone, C. Tomasi, P. Mustarelli, F. Belotti, A. Magistris, F. Maestroni, M. Parachini, L. Garlaschelli and P. P. Righetti, *J. Power Sources*, 2006, **160**, 175–180.

View Online

15 E. Quartarone, P. Mustarelli, A. Carollo, A. Magistris, C. Tomasi, L. Garlaschelli and P. P. Righetti, *Mater. Res. Soc. Symp. Proc.*, 2007, **972**, 125.
16 P. Mustarelli, E. Quartarone, S. Grandi, A. Carollo and A. Magistris, *Adv. Mater.*, 2008, **20**, 1339–1343.
17 E. Quartarone, P. Mustarelli, A. Carollo, S. Grandi, A. Magistris and C. Gerbaldi, *Fuel Cells*, 2009, **9**, 231–236.
18 V. Kurdakova, E. Quartarone, P. Mustarelli, A. Magistris, E. Caponetti and M. L. Saladino, *J. Power Sources*, 2010, **195**, 7765–7769.
19 B. Delley, *J. Chem. Phys.*, 1990, **92**, 508–517.
20 B. Delley, *J. Chem. Phys.*, 2000, **113**, 7756–7764.
21 S. R. Samms, S. Wasmus and R. F. Savinell, *J. Electrochem. Soc.*, 1996, **143**, 1225–1232.
22 Q. Li, R. He, R. W. Berg, H. A. Hjuler and N. J. Bjerrum, *Solid State Ionics*, 2004, **168**, 177–185.
23 P. Musto, F. E. Karasz and W. J. MacKnight, *Polymer*, 1989, **30**, 1012–1021.
24 P. Musto, F. E. Karasz and W. J. MacKnight, *Polymer*, 1993, **34**, 2934–2945.
25 R. Infante-Castillo, L. A. Rivera-Montalvo and S. P. Hernandez-Rivera, *J. Mol. Struct.*, 2008, **877**, 10–19.
26 M. A. Morsy, M. A. Al-Khaldi and A. Suwaiyan, *J. Phys. Chem. A*, 2002, **106**, 9196–9203.
27 F. P. Urena, M. F. Gomez, J. J. L. Gonzalez and E. M. Torres, *Spectrochim. Acta, Part A*, 2003, **59**, 2815–2839.
28 A. C. Chapman and L. E. Thrilwell, *Spectrochim. Acta*, 1964, **20**, 937–947.
29 V. Di Noto, P. Damioli, M. Vittadello, R. Dall'Igna and F. Boella, *Electrochim. Acta*, 2003, **48**, 2329–2342.
30 R. Diaz-Calleja and E. Riande, *Mater. Sci. Eng., A*, 2004, **370**, 21–33.
31 *Broadband Dielectric Spectroscopy*, ed. A. Schonhals and F. Kremer, Springer, Berlin, 2003.
32 V. Di Noto, *J. Phys. Chem. B*, 2002, **106**, 11139–11154.
33 V. Di Noto, S. Lavina, E. Negro, M. Vittadello, F. Conti, M. Piga and G. Pace, *J. Power Sources*, 2009, **187**, 57–66.
34 V. Di Noto, M. Vittadello, S. G. Greenbaum, S. Suarez, K. Kano and T. Furukawa, *J. Phys. Chem. B*, 2004, **108**, 18832–18844.
35 H. Pu, W. H. Meyer and G. Wegner, *J. Polym. Sci., Part B: Polym. Phys.*, 2002, **40**, 663–669.
36 J. J. Fontanella, M. C. Wintersgill, J. S. Wainright, R. F. Savinell and M. Litt, *Electrochim. Acta*, 1998, **43**, 1289–1294.

Published on 19 May 2011 on http://pubs.rsc.org | doi:10.1039/C1CP20902G
Downloaded by Universita di Padova on 22 December 2011

 This journal is © the Owner Societies 2011

CHEMISTRY OF MATERIALS

ARTICLE

pubs.acs.org/cm

New Sulfonated Poly(*p*-phenylenesulfone)/Poly(1-oxotrimethylene) Nanocomposite Proton-Conducting Membranes for PEMFCs

Vito Di Noto,*[,†] Matteo Piga,[†] Guinevere A. Giffin,[†] Michael Schuster,[‡] Gianni Cavinato,[†] Luigi Toniolo,[§] and Stefano Polizzi[∥]

[†]Department of Chemical Sciences, University of Padova, Via Marzolo 1, I-35131, Padova (PD), Italy

[‡]Fuma-Tech GmbH, Steinbeisstrasse 41-43, D-71665 Vaihingen/Enz, Germany

[§]Department of Chemistry, Università Ca' Foscari di Venezia, Dorsoduro, Calle Larga S. Marta 2137, 30123 Venezia, Italy

[∥]Department of Physical Chemistry, Università Ca' Foscari di Venezia, Via Torino 155/B, I-30123 Venezia-Mestre, Italy

ABSTRACT: Two series of membranes, A and B, were prepared by the following synthesis protocols. A-type membranes were obtained by a solvent casting process from solutions prepared by dissolving three different blends of poly(1-oxotrimethylene) (PK) and sulfonated poly(*p*-phenylenesulfone) ($sPSO_2$) in DMAc. B-type materials were prepared using a two-step process. First, an inorganic−organic hybrid nanofiller was synthesized by CO-ethene copolymerization in the presence of silica nanoparticles. From this synthesis, a hybrid nanofiller, $[SiO_2/(PK)_{0.65}]$, with 35 wt % of SiO_2 was obtained. Membranes were produced by a solvent casting process from solutions prepared by dispersing different amounts (10, 20, 30 wt %) of the $[SiO_2/(PK)_{0.65}]$ nanofiller in a $sPSO_2$/DMAc solution. As compared to pristine $sPSO_2$ and the A-type materials, the presence of the hybrid nanofiller in the B-type membranes reduces the water uptake and membranes' swelling and increases the proton conductivity at low membrane hydration levels.

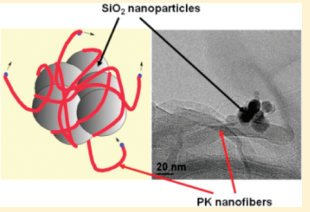

KEYWORDS: hybrid inorganic−organic membranes, polysulfone, polyketone, silica, proton exchange membrane fuel cell, dynamic mechanical analysis, proton conductivity

1. INTRODUCTION

One of the main targets in the academic and industrial research of proton exchange membrane fuel cells (PEMFCs) is the development of new proton-conducting membranes capable of operating at temperatures higher than 90 °C and at low relative humidity.[1,2] Despite their high cost perfluorinated ionomers, such as Dupont's Nafion, are the most widely studied and applied materials.[3,4] They function very well up to ca. 90 °C at high relative humidity.[5] However at temperatures greater than 90 °C, they are characterized by a poor performance owing to the membrane dehydration processes and the bulk thermo-mechanic transitions.[6]

A number of poly(arylene)-based ionomers such as sulfonated poly(ether ether ketone) or poly(ethersulfone) have been proposed,[7−10] which present lower methanol crossover and improved mechanical characteristics at temperatures above 90 °C as compared to the classical perfluorosulfonic acid polymers. In poly(arylene)-based ionomers, a reasonable ionic conductivity for practical applications in PEMFCs is obtained when a proton exchange capacity higher than two mequiv•g^{-1} is reached.[11] Nevertheless, under the hydration conditions typically adopted in PEMFCs, such a high proton exchange capacity leads to swelling and the loss of the membranes' mechanical properties. These effects result in decreased membrane performance in PEMFCs and in many cases dissolution in water above 50 °C.[10] Other poly(arylene) ionomers, such as sulfonated poly(*p*-phenylenesulfone), characterized by electron-deficient poly(arylene) chains and high ionic exchange capacity (IEC) were proposed.[11−13] The first property acts to increase the acidity and the thermal and thermo-oxidative stability of the materials, while the latter is a crucial parameter in improving the proton conductivity. Sulfonated poly(*p*-phenylenesulfone) presents lower solubility and swelling in water and improved chemical stability[11−13] as compared to other sulfonated poly(arylene)s with similar IECs. These properties are nevertheless insufficient for practical application in PEMFCs operating at high temperatures. In this study, nanocomposite proton-conducting membranes were prepared with the aim of stabilizing sulfonated poly(*p*-phenylenesulfone) ($sPSO_2$) with an equivalent weight (EW) of 360 g•equiv^{-1}. The low EW, which corresponds to a high IEC of 2.77 mequiv•g^{-1} and a degree of sulfonation equal to 50%, is the reason for the large variation in mechanical properties with relative humidity. Under dry conditions $sPSO_2$ is very hard and brittle, but as the relative humidity increases, it starts to swell and loses its integrity at high water activities.[11−13]

This work describes the preparation of new $sPSO_2$-based nanocomposite membranes with very low swelling and good electrical and mechanical properties above 70 °C. The materials were obtained by modulating the properties of $sPSO_2$ with poly(1-oxotrimethylene) (PK). The polyketone copolymer was obtained by alternating CO-ethene copolymerization.[14,15] This strategy is very innovative and promising. It allows the enhancement of the thermal and mechanical properties of

Received: May 26, 2011
Revised: September 13, 2011
Published: September 30, 2011

ACS Publications © 2011 American Chemical Society

dx.doi.org/10.1021/cm2014797 | *Chem. Mater.* 2011, 23, 4452–4458

nanocomposite $sPSO_2$ membranes, making them suitable for application in PEMFCs. PK is a copolymer that is very stable both chemically and thermally.[14,15] Two series of membranes, A and B, were prepared. Both types of membranes were obtained by a two-step process. For the A-type materials 1) different copolymerization times for the reaction of CO with ethene in the presence of $sPSO_2$ were used to obtain a PK/$sPSO_2$ blend with 11, 28, and 33 wt % of PK; and 2) membranes were prepared by a solvent casting process from solutions containing the three different PK/$sPSO_2$ blends dissolved in dimethylacetamide (DMAc). For the B-type materials 1) an inorganic−organic hybrid nanofiller $[SiO_2/(PK)_{0.65}]$, where the weight fraction of PK equals 0.65, was synthesized by CO-ethene copolymerization in the presence of silica nanoparticles; and 2) a solvent casting process was used to prepare membranes by dispersing 10, 20, 30 wt % of $[SiO_2/(PK)_{0.65}]$ nanofiller in a $sPSO_2$/DMAc solution. The mechanical properties and the relaxation processes were investigated by dynamical mechanical analyses (DMA), revealing the presence of three mechanical transitions, α, β, and γ. The electrical properties were studied by broadband electric spectroscopy (BES). Electrical measurements were conducted for fully hydrated samples and at different values of relative humidity, in order to elucidate the effect of the inorganic nanofiller on the proton conduction as a function of the membranes' hydration state.

Results indicate that the presence of the hybrid nanofiller in B-type membranes reduces the water uptake and membrane swelling and increases the proton conductivity at low levels of membrane hydration as compared to pristine $sPSO_2$ and A-type materials.

2. EXPERIMENTAL SECTION

2.1. Preparation of Materials by CO/Ethene Copolymerization. $[SiO_2/(PK)_{0.65}]$, where the weight fraction (weight of polyketone/total weight) is 0.65, was prepared by CO-ethene copolymerization in the presence of porous silica by the following procedure. 8.8 mg (0.01 mmol) of $[Pd(TsO)(H_2O)(dppp)](TsO)\cdot H_2O$,[16] 19 mg (0.1 mmol) of $TsOH\cdot H_2O$, ca. 1.3 g of porous silica, and 80 mL of MeOH were added to a glass bottle and placed in an autoclave (dppp = 1,3-bis(diphenylphosphino)propane; TsO = 4-methylbenzene sulfonate). The autoclave was flushed with CO, pressurized to 45 atm with CO/ethene (1:1 ratio), and heated at 85 °C. The autoclave was maintained at this temperature for 1 h and then cooled to room temperature and depressurized. The sample was constantly stirred during the reaction process. The resulting solid was collected by filtration, washed with MeOH, and dried under vacuum to yield 3.430 g of $[SiO_2/(PK)_{0.65}]$. A similar procedure was followed for the preparation of the fillers $[sPSO_2/(PK)_{0.11}]$, $[sPSO_2/(PK)_{0.28}]$ and $[sPSO_2/(PK)_{0.33}]$ used in the preparation of the A-type membranes, except that $sPSO_2$ was added in place of silica and the reaction times varied from 3 to 8 h.

2.2. Preparation of the Membranes. Pristine $sPSO_2$ membrane, used as reference material, was prepared by dissolving 500 mg of sulfonated poly(*p*-phenylenesulfone) (EW = 360 g·equiv^{-1}) in 7 mL of DMAc. The solution was recast onto a Petri dish and maintained at 80 °C and under a dry air flow. The film was peeled from the Petri dish in 2-propanol and cured at 190 °C for 15 h. The same procedure was followed for the preparation of A-type membranes, except that $[sPSO_2/(PK)_x]$, with x = 11, 28, and 33 wt % was used instead of pristine $sPSO_2$. B-type membranes, having a composition of $[sPSO_2/(SiO_2)_y\cdot(PK)_z]$, where y and z are the respective weight fractions of SiO_2 and PK, were prepared by dissolving $sPSO_2$ in DMAc and by adding 10, 20, and 30 wt % of $[SiO_2/(PK)_{0.65}]$ filler to the solution. The dispersions were homogenized by sonication and then recast onto a Petri dish as above. The resulting membranes are labeled $[sPSO_2/(SiO_2)_{0.035}(PK)_{0.065}]$, $[sPSO_2/(SiO_2)_{0.069}(PK)_{0.131}]$, and $[sPSO_2/(SiO_2)_{0.104}(PK)_{0.196}]$ indicating membranes containing 10, 20, and 30 wt % of hybrid filler, respectively.

2.3. Instruments and Methods. The proton exchange capacity was determined as follows. About 100 mg of each sample was dried for one week over P_2O_5, weighed in inert atmosphere, soaked in 100 mL of KCl 1 M, and left stirring overnight. The solution was then titrated with 0.01 M KOH using a phenolphthalein indicator.

The water uptake (W.U.) and the number of water molecules per sulfonic acid group (λ) were determined by TGA measurements as described elsewhere[17] after soaking the samples in water at room temperature for one day. The initial (wt_0) and dry (wt_{dry}) weight of each sample was determined by registering the isothermal TGA desorption profile at 30 °C. The W.U. was determined using the following equation

$$\text{W.U.} = \frac{wt_0 - wt_{dry}}{wt_{dry}} \quad (1)$$

λ depends on the W.U. and on the Ionic Exchange Capacity (IEC) as follows[18,19]

$$\lambda = 1000\left[\frac{\text{W.U.}}{MW_{H_2O}\text{IEC}\chi_{sPSO_2}}\right] \quad (2)$$

where MW_{H2O} is the molecular weight of water, and χ_{sPSO_2} is the weight fraction of $sPSO_2$.

High-resolution transmission electron microscopy (HR-TEM) images were collected using a Jeol 3010 instrument operating at 300 kV with a high resolution pole piece (0.17 nm point-to-point resolution) and equipped with a Gatan slow-scan 794 CCD camera.

The infrared spectra of pristine PK, SiO_2, and $[SiO_2/(PK)_{0.65}]$ powders were collected using a Nicolet FT-IR Nexus spectrometer equipped with a Smart Diffuse Reflectance Accessory (Thermo Scientific).

Dynamic mechanical analyses (DMA) were carried out with a DMA Q800 (TA Instruments) using the film/fiber tension clamp. Temperature spectra were measured by subjecting a rectangular sample to an oscillatory sinusoidal tensile deformation at 1 Hz with an amplitude of 4 μm and a preloading force of 0.05 N. Measurements were carried out in the range of temperature from −100 to 250 °C at a rate of 4 °C·min^{-1}. Before the measurements, each sample was dried at room temperature overnight. The mechanical response of the materials was analyzed in terms of elastic (E′), storage modulus (E″), and tan δ = E″/E′.

The measurement of the complex conductivity spectra of wet samples was carried out in the frequency range from 10 mHz to 10 MHz using a Novocontrol Alpha-A analyzer. The temperature range from 5 to 155 °C was explored using a homemade cryostat operated with a N_2 gas jet heating and cooling system. The measurements were performed in a closed homemade cell that allowed the water to be retained in the wet membrane in the explored temperature range. The geometric constant of the cell was determined by measuring the electrode−electrolyte contact surface and the distance between electrodes with a micrometer. The temperature was measured with accuracy greater than ±0.1 °C. Weighing the closed cell before and after the measurements ensured an absence of water loss. The complex impedance ($Z^*(\omega)$) was converted into complex conductivity ($\sigma^*(\omega) = \sigma'(\omega) + i\sigma''(\omega)$) using the equation

$$\sigma^*(\omega) = k\cdot[Z^*(\omega)]^{-1} \quad (3)$$

where k is the cell constant in cm^{-1}, and $\omega = 2\pi f$ (f is the frequency in Hz). The bulk conductivity of the samples, σ_0, was determined from the conductivity value extrapolated from the plateau of the $\sigma'(\omega)$ profiles at frequencies higher than 10^5 Hz, as described elsewhere.[20]

dx.doi.org/10.1021/cm2014797 |Chem. Mater. 2011, 23, 4452–4458

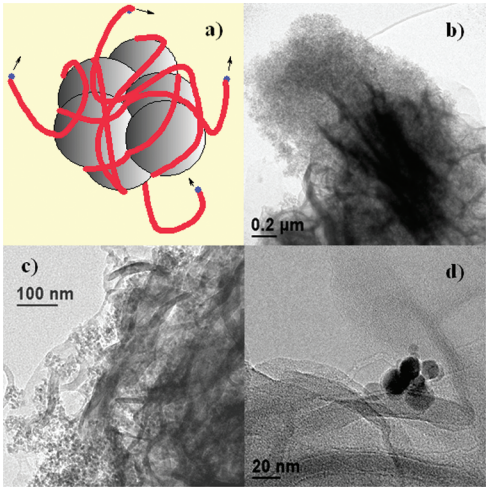

Figure 1. (a) Morphological hypothesis of the growth mechanism of PK on the surface of silica nanoparticle aggregates; (b) and (c) TEM images of the PK fibers wrapping the silica nanoparticle aggregates; (d) micrograph of primary silica nanoparticles wrapped with PK.

Electrical measurements at different relative humidity values were performed in the frequency range between 40 and 10^7 Hz using an Agilent 4294A Analyzer. The sample was placed between two steel porous electrodes inside a homemade chamber where the humidity is generated by an Arbin Instrument (USA) humidifier.[21] The relative humidity (R.H.), the Dew Point temperature (T_{DP}), and the temperature (T_C) inside the measuring chamber were controlled by an optical system (Optidew Remote, Michell Instruments) and a Pt100 sensor.[21]

3. RESULTS AND DISCUSSION

3.1. Hybrid Nanofiller Morphology. The morphology of the hybrid nanofiller was determined by HR-TEM (Figure 1). The results lead to crucial insights into the growth mechanism of the PK nanofibers on the surface of SiO_2, which are shown in Figure 1a. Figure 1b,c reveals that PK horse-hair nanofibers are wrapped around a granular mass core of silica nanoparticles, while the analysis of Figure 1d shows that the silica nanoparticles are about 20 nm in size.

The infrared spectra of SiO_2, $[SiO_2/(PK)_{0.65}]$ and the PK powders are reported in Figure 2. The infrared spectrum of the $[SiO_2/(PK)_{0.65}]$ hybrid nanofiller is essentially the superposition of SiO_2 and PK spectra. Furthermore, the presence of the OH stretching modes of hydroxyl groups in the spectra of both pristine SiO_2 and $[SiO_2/(PK)_{0.65}]$ between 3800 and 3000 cm^{-1} indicates that PK is coiled around the silica nanoparticles without forming chemical bonds with the OH groups present on the surface of the nanoparticles.

3.2. Water Uptake and Mechanical Properties. The composition and select properties of the materials explored in this study are reported in Table 1. For the sake of completeness, the properties of the A- and B-type membranes are compared with those of a pristine $sPSO_2$ reference membrane measured in the same conditions. The W.U. values are significantly different for each type of material studied (Table 1), while the number of water molecules per sulfonic acid groups (λ) is approximately the same for all membranes ranging between 7 and 11 except in the membranes with the highest amount of hybrid nanofiller (λ = 15). The W.U. of the A and B-type membranes is close to half of that of pristine $sPSO_2$, with the lowest W.U. occurring in the

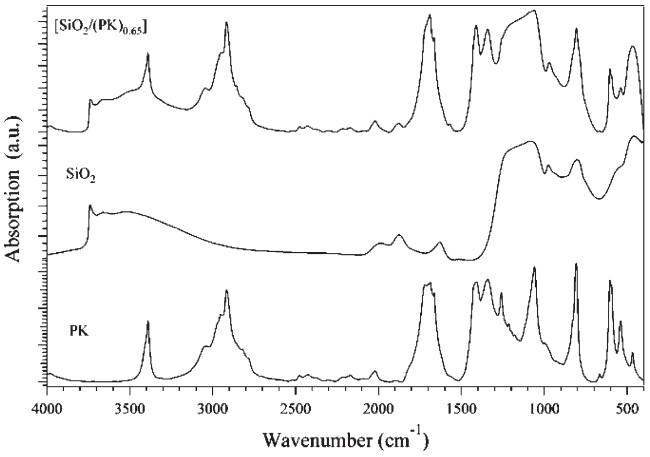

Figure 2. Infrared spectra of pristine PK, SiO_2 and the $[SiO_2/(PK)_{0.65}]$ hybrid nanofiller in the spectral region from 4000 to 400 cm^{-1}.

$[sPSO_2/(PK)_{0.33}]$ membrane. This effect is ascribed to the dilution of the hydrophilic acid groups of $sPSO_2$ by PK nanofiller in the bulk membranes that reduces the volume of the hydrophilic domains. Even if the weight fraction of $sPSO_2$ in the A and B groups is similar (Table 1), the water uptake for B-type membranes is higher than those measured for the A-type membranes. This is due to the high nanoporosity of the hybrid $[SiO_2/(PK)_{0.65}]$ nanofiller that absorbs water molecules in the interstices between the surface of silica nanoparticles and the wrapping PK nanofibers. Specifically, in agreement with the swelling percentage, S(%), reported in Table 1, it is observed that a) pristine polysulfone exhibits severe swelling even at room temperature and dissolves completely in boiling water; b) B-type membranes have a higher dimensional stability than $sPSO_2$ and only partially dissolve in boiling water; and c) A-type membranes exhibit no swelling at room temperature and are very stable even in boiling water. Polysulfone-based materials[22] have previously shown that the through-plane swelling is larger than the in-plane swelling. However, in this work the measuring equipment was not sufficiently precise to accurately determine the in-plane swelling, so only the through-plane is reported. These experimental results imply a decrease in permittivity and an improvement in mechanical stability of the nanocomposite membranes in polar environments such as water.

The mechanical properties of the dry materials were studied by DMA between −100 and 250 °C at 1 Hz. The profiles of the Storage Modulus (E′), the Loss Modulus (E″), and tan δ are shown in parts a) and b) of Figure 3 for A- and B-type membranes, respectively.

It is observed that up to ca. 200 °C, pristine dry $sPSO_2$ has a Storage Modulus (E′) higher than 1700 MPa (Figure 3). The mechanical properties of poly(*p*-phenylenesulfone) are much better than those of pristine Nafion, whose E′ values decrease steadily above 100 °C up to an irreversible elongation above 130 °C.[17−19,23,24] The E′ values of A-type membranes are lower than those of pristine $sPSO_2$ and the B-type materials, indicating that the density of hydrogen bonding cross-links in A-type membranes is lower than that in B-type. The difference in the mechanical properties of the A- and B-type membranes is due to the presence of the SiO_2 nanoparticles, which interact with the $sPSO_2$ acid groups to increase the mechanical stability of the hybrid membranes. In particular at temperatures above 100 °C,

dx.doi.org/10.1021/cm2014797 |*Chem. Mater.* 2011, 23, 4452–4458

Table 1. Composition, Ionic Exchange Capacity (IEC), Water Uptake (W.U.), Arrhenius and VTF Pseudo-Activation Energies of $sPSO_2$, and A- and B-Type Membranes[f]

	material	χ_{sPSO2}[a]	f[b]	IEC (meq·g^{-1})	W.U. (%)[c]	λ[c]	S(%)[d]	E_a (kJ·mol^{-1})[e] I	E_a (kJ·mol^{-1})[e] II
	$sPSO_2$	1	0	2.44	50	11	109	17	0.6
A Type	$[sPSO_2/(PK)_{0.11}]$	0.89	0.12	2.17	24	7	20	9	1.5
	$[sPSO_2/(PK)_{0.28}]$	0.72	0.38	1.76	25	11	22	23	2.8
	$[sPSO_2/(PK)_{0.33}]$	0.67	0.49	1.63	17	9	21	12	3.2
B Type	$[sPSO_2/(SiO_2)_{0.035}(PK)_{0.065}]$	0.90	0.07	2.20	31	9	30	19	1.2
	$[sPSO_2/(SiO_2)_{0.069}(PK)_{0.131}]$	0.80	0.16	2.00	29	10	24	16	1.4
	$[sPSO_2/(SiO_2)_{0.104}(PK)_{0.196}]$	0.70	0.28	1.70	33	15	22	13	1.3

[a] Weight fraction of poly(*p*-phenylene sulfone). [b] $f = (wt_{PK})/(wt_{sPSO_2})$. [c] Determined after soaking the sample one day in water at room temperature. [d] Percentage of swelling as compared to the dry membrane with the same treatment; $S(\%) = ((L\text{-}L_0)/L_0)\cdot 100$, where L_0 and L are the thickness of the dry and wet membrane, respectively. [e] Activation energies are determined from fitting the conductivity profiles of wet samples with Arrhenius (region I) and VTF (region II) equations. [f] λ is the ratio of water molecules per sulfonic acid group. I and II are the conductivity regions.

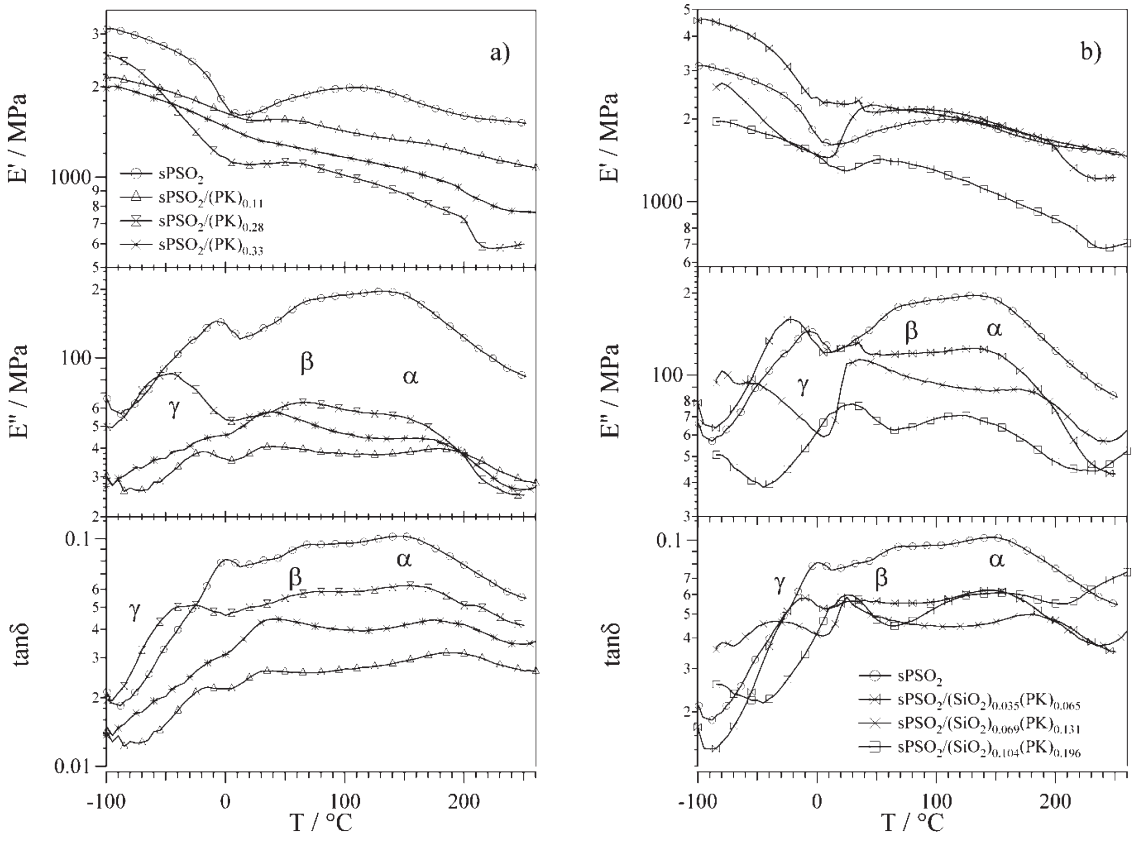

Figure 3. Profiles of the storage modulus (E′), loss modulus (E″), and tan δ = E″/E′ versus temperature of the dry membranes: a) $sPSO_2$ and A-type membranes and (b) $sPSO_2$ and B-type membranes.

the E′ values of membranes doped with 10 and 20 wt % of $[SiO_2/(PK)_{0.65}]$ nanofiller are similar to that of pristine $sPSO_2$, with values of 1980, 2088, and 2003 MPa at 120 °C for $sPSO_2$, $[sPSO_2/(SiO_2)_{0.035}(PK)_{0.065}]$ and $[sPSO_2/(SiO_2)_{0.069}(PK)_{0.131}]$, respectively. This indicates that at medium-high temperature, i.e. above 100 °C, the strength of the hydrogen bonding interactions between sulfonic acid groups of $sPSO_2$ are similar to those between $sPSO_2$ and the silica hydroxyl groups. The major drawback of $sPSO_2$ is that its mechanical properties are strongly influenced by its hydration state.[12,13] To reveal the effect of hydration on the mechanical properties, the A- and B-type membranes, which showed the best mechanical properties in a dry state were measured in a wet state at room temperature. Wet $sPSO_2$ has an E′ value of 16 MPa, while the E′ values of $[sPSO_2/(PK)_{0.28}]$ and $[sPSO_2/(SiO_2)_{0.035}(PK)_{0.065}]$ are 100 and 48 MPa, respectively (data not shown). Both dry and wet $[sPSO_2/(SiO_2)_{0.035}(PK)_{0.065}]$ have a slightly higher E′ value than pristine $sPSO_2$ due to the formation of interchain hydrogen bonding cross-links between sulfonic acid, ketone, and silica hydroxyl groups. Similar cross-linking interactions were

dx.doi.org/10.1021/cm2014797 |*Chem. Mater.* 2011, 23, 4452–4458

described elsewhere[17−19,23,24] to improve the mechanical properties of hybrid Nafion-based membranes. For the wet materials, $[sPSO_2/(PK)_{0.65}]$ has a higher E′ than pristine $sPSO_2$ and $[sPSO_2/(SiO_2)_{0.035}(PK)_{0.065}]$, which is in agreement with its lower W.U.

The temperature spectra of the loss modulus (E″) and tan δ in Figure 3 reveal the presence of three thermo-mechanical relaxations for $sPSO_2$ centered at about −30, 50, and 100 °C which were ascribed to the γ, β, and α relaxations, respectively. The γ relaxation, which has the lowest energy barrier, is likely related to the local fluctuations of the aromatic rings of the $sPSO_2$ polymer chains. The β transition is associated with the relaxation modes of $sPSO_2$ side groups, which are involved in interchain dipole−dipole interactions between the sulfonic acid groups and the environment. The α relaxation is due to the segmental motion of $sPSO_2$ polymer backbone chains. The same three mechanical transitions are present for all the composite membranes. As compared to pristine $sPSO_2$, the presence of PK in the A-type materials a) shifts the α transition to higher temperatures indicating that the PK fibers reduce the mobility of the $sPSO_2$ chains and b) slightly reduces the temperature of the β and γ transitions revealing that the presence of PK decreases the strength of the interchain dipolar interactions between sulfonic acid groups, which is in agreement with the E′ values.

For the B-type membranes, the temperature of the mechanical transitions is modulated by the presence of the hybrid nanofiller due to its interactions with the $sPSO_2$ matrix. In particular, the γ transition temperature decreases with increasing hybrid nanofiller concentration. The β and α transition temperatures are changed only slightly as compared to pristine $sPSO_2$ indicating that a) the strength of the interactions between acid side groups of $sPSO_2$ and hybrid nanofiller are on the same order of those of between the $sPSO_2$ acid groups and b) the presence of $[SiO_2/(PK)_{0.65}]$ nanofiller increases the mobility of the $sPSO_2$ backbone chains as compared to that of the A-type materials. Taken together, the DMA results confirm that strength of the strong dipole−dipole interactions between acid side groups of $sPSO_2$ and the environment in the dry composite membranes decreases in the order $sPSO_2$-$sPSO_2$ > $sPSO_2$-SiO_2-PK > $sPSO_2$-PK. Furthermore, it should be highlighted that in wet samples, the $sPSO_2$-PK interchain interactions are crucial in increasing the dimensional stability and mechanical properties of membranes due to their ability to reduce the hydrophilicity of the polar side chain groups in bulk materials.

3.3. Proton Conductivity. The temperature dependence of the ionic conductivity of the wet samples is shown in Figure 4 part a) for the A-type materials and part b) for the B-type materials. The conductivity of pristine Nafion is shown as a reference.[19] It should be observed that the conductivity of the membranes increases concurrently with the water uptake values. Thus, $sPSO_2$ presents the highest values, while the A-type membranes present the lowest values. Higher conductivity values for the B-type membranes than the A-type membranes result from the presence of the $[SiO_2/(PK)_{0.65}]$ nanofiller at the interface between the hydrophobic and hydrophilic domains of the material that facilitates charge transfer between the acid groups of $sPSO_2$ and enhances the long-range charge transfer between the $sPSO_2$ acid groups due to the formation of proton percolation pathways. This effect is confirmed by analyzing the conductivities of the B-type membranes in detail. Indeed, the highest conductivity values are revealed above 75 °C for the membrane containing the highest amount of $[SiO_2/(PK)_{0.65}]$

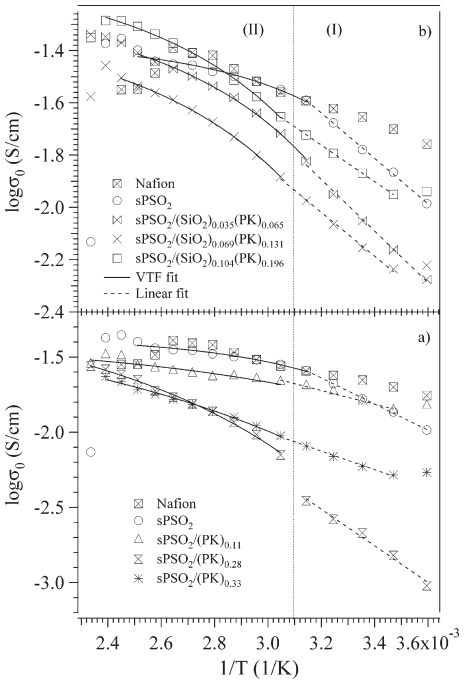

Figure 4. Plot of the bulk conductivity vs T^{-1}: a) $sPSO_2$ and A-type membranes and b) $sPSO_2$ and B-type membranes. I and II are the conductivity regions. The experimental data and the VTF and Arrhenius fit curves are indicated by markers and solid and dashed lines, respectively. σ_0 was extrapolated from the plateau of the conductivity spectra.

nanofiller. The curves in Figure 4 present two conductivity regions, I (below 50 °C) and II (above 50 °C), which are delimited by the temperature of the β mechanical relaxation event shown in Figure 3. The logarithm of σ_{dc} as a function of reciprocal temperature shows an Arrhenius dependence in region I, while in region II the typical Vogel−Tamman−Fulcher (VTF) behavior is seen.[25] Thus, the charge transfer process below 50 °C is due to proton hopping between solvated acid side groups in the A-type materials and between the solvated acid side groups and the hydroxyl groups present on the surface of silica nanoparticles in B-type materials. Above 50 °C the charge transfer process is modulated by the segmental motion of polymer chains in both A- and B-type materials. The activation energies (E_a) obtained by fitting the conductivities with Arrhenius (region I) and VTF (region II) equations[25] are reported in Table 1.

The activation energies in region I 1) decrease with increasing the hybrid nanofiller concentration for the B-type membranes, indicating that the $[SiO_2/(PK)_{0.65}]$ nanofiller enhances the long-range proton hopping process, and 2) decrease with increasing membrane storage modulus E′ for the A-type membranes (refer to part a of Figure 3) due to the presence of the PK fibers that dilute and confine the $sPSO_2$ chains. For the composite materials in region II, the E_a values are twice that of pristine $sPSO_2$ and greater for A-type materials than for B-type due to the presence of the PK fibers that, in accordance with DMA results, inhibit the $sPSO_2$ segmental motion. The congruence of the division between the conductivity regions and the DMA β transition signifies that charge transfer migration in the studied materials is directly correlated to the dynamics of the polymer host, which is significantly affected by the mechanical relaxation events of the membranes. Furthermore, in B-type membranes the pseudoactivation

dx.doi.org/10.1021/cm2014797 |Chem. Mater. 2011, 23, 4452–4458

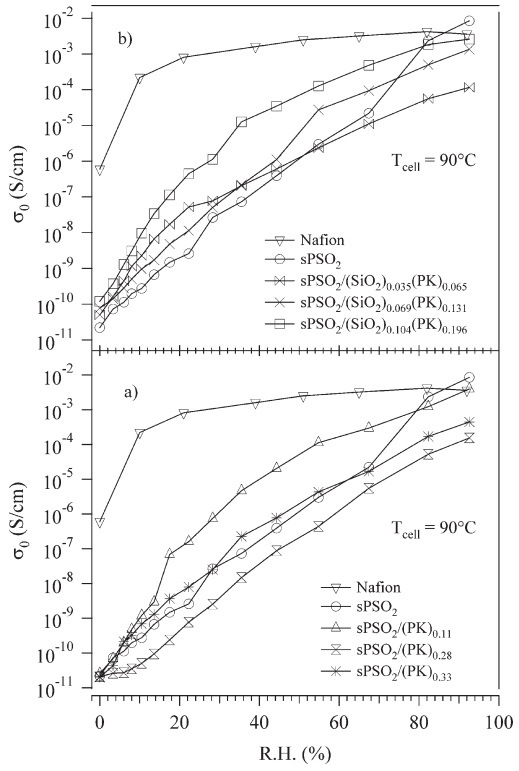

Figure 5. Plot of the bulk conductivity vs relative humidity (R.H.) at 90 °C: a) $sPSO_2$ and A-type membranes and b) $sPSO_2$ and B-type membranes. σ_0 was extrapolated from the plateau of the conductivity spectra.

energies (Table 1) are influenced only slightly by the filler-$sPSO_2$ interactions. Finally, a remarkable phenomenon occurs above 100 °C, where the conductivities of $sPSO_2$, $[sPSO_2/(SiO_2)_{0.035}(PK)_{0.065}]$, and $[sPSO_2/(SiO_2)_{0.104}(PK)_{0.196}]$ membranes are overlapped suggesting that B-type membranes are interesting materials for application in PEMFCs.

The dependence of the bulk conductivity σ_0 at 90 °C as function of the relative humidity (R.H.%) is reported in Figure 5 for the A- (part a) and B-type membranes (part b) and compared to the $sPSO_2$ reference membrane. For all samples the conductivity increases monotonically with the relative humidity toward a plateau at R.H. ≈ 100%. The effect of the hybrid nanofiller on the membranes' proton conductivity is evident for low values of relative humidity, i.e. less than 60%. In this condition, the proton conductivity of all B-type membranes is higher than that of pristine $sPSO_2$, while for A-type membranes this only occurs for the sample containing 11 wt % of PK. The hybrid nanofiller reduces the water content necessary for the long-range migration of the proton due to the formation of percolation pathways at the interfaces between the hydrophobic and hydrophilic domains present inside the material. These percolation pathways allow the B-type membranes to maintain good proton conductivity even at low water content. Furthermore, in agreement with the conductivity values measured when the materials are immersed in water (Figure 4), the highest conductivity value is obtained in the materials that exhibit the lowest β mechanical transition temperature, suggesting that the long-range conductivity in these materials occurs due to a facilitated side group relaxation, coupled with the segmental motion of the $sPSO_2$ backbone chains.

In summary, the experimental results reveal that in B-type materials the hybrid $[SiO_2/(PK)_{0.38}]$ nanofiller increases the

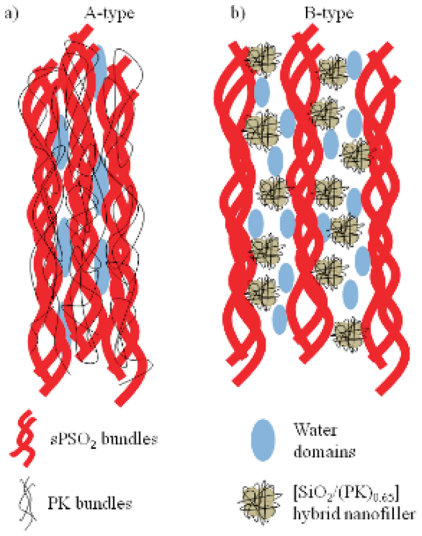

Figure 6. Schematic representation of membrane structure: a) A-type membranes and b) B-type membranes.

proton conductivity as compared to the $[sPSO_2/(PK)_x]$ membranes by maintaining strong dipolar interactions and the segmental motion of $sPSO_2$ backbone.

Recently Titvinidze et al. synthesized and studied a series of sulfonated poly(phenylene sulfone) membranes containing triphenylphosphine oxide moieties as constitutional units in the backbone, with IEC values (between 1.72 and 2.32 mequiv·g^{-1}) similar to those of the composite membranes presented here.[22] The authors reported water uptake values at 100% R.H. and room temperature between 40 and 50%, with values of λ between 19 and 28.[22] In the investigated composite membranes, despite similar values of IEC, the presence of the PK nanofibers reduces membrane swelling and water uptake due to a different membrane microstructure microstructure induced by the presence of PK nanofibers and the $[SiO_2/(PK)_{0.38}]$ nanofiller. Therefore, it is possible to hypothesize membrane structures for the A- and B-type nanocomposite membranes as reported in parts a) and b) of Figure 6, respectively.

In A-type membranes, the PK fibers, coiled around the $sPSO_2$ chains, not only reduce membrane swelling and water uptake but also reduce the proton conductivity, as compared to $sPSO_2$, by diluting the sulfonic acid groups and inhibiting the segmental motion of the $sPSO_2$ polymer chains. In B-type membranes, the hybrid nanofiller, consisting of silica nanoparticles wrapped with PK fibers, located at the interface between the hydrophobic and hydrophilic domains of $sPSO_2$ allows the material to maintain good mechanical properties and high proton conductivity values due to the formation of dipolar interactions between water, the hybrid nanofiller and the acids groups of $sPSO_2$ and due to the creation of percolation pathways at interface between the nanofiller and $sPSO_2$.

4. CONCLUSION

In this work, two series (A and B) of nanocomposite proton exchange membranes, which are based on poly(1-oxotrimethylene) (PK) and poly(*p*-phenylenesulfone) ($sPSO_2$), were prepared. A-type membranes, labeled $[sPSO_2/(PK)_x]$, consist of a blend of $sPSO_2$ containing 11, 28, and 33 wt % of PK. B-type materials consist of nanoparticles of silica covered with PK, which are

dx.doi.org/10.1021/cm2014797 |*Chem. Mater.* 2011, 23, 4452–4458

embedded in bulk poly(*p*-phenylenesulfone) material. The water uptake values of the A- and B-type membranes were half of that of pristine $sPSO_2$ and are higher for the membranes containing the hybrid nanofiller than for the $[sPSO_2/(PK)_x]$ materials. Swelling tests reveal that the presence of PK and the $[SiO_2/(PK)_{0.65}]$ nanofiller improve the mechanical stability of the composite membranes in a polar environment as compared to pristine $sPSO_2$.

Temperature dependent DMA studies conducted on dry samples showed that a) the mechanical properties, in terms of the Storage Modulus E′, of B-type materials are better than those of A-type membranes due to the presence of the hybrid nanofiller that increases the strength of the dipolar interactions between acid groups; and b) above 100 °C the E′ values for $[sPSO_2/(SiO_2)_{0.035}(PK)_{0.065}]$ and $[sPSO_2/(SiO_2)_{0.069}(PK)_{0.131}]$ are similar to those found for pristine $sPSO_2$. Furthermore, three mechanical transitions, α, β, and γ, associated with segmental motion, side group relaxation, and local fluctuation of $sPSO_2$ polymer chains were revealed, respectively, for all of the investigated materials.

Electric spectroscopy measurements performed on the fully hydrated materials and at different relative humidities reveal that the nanocomposite hybrid membranes show higher conductivity values than those of the $[sPSO_2/(PK)_x]$ membranes. Furthermore, at 90 °C and low R.H. all the membranes containing the hybrid nanofiller present conductivity values higher than those of pristine $sPSO_2$. This phenomenon is due to the presence of the inorganic nanofiller located at the interface between the hydrophobic and hydrophilic domains of the material that facilitates the charge transfer between the acid groups of $sPSO_2$ and enhances the long-range charge transfer between the $sPSO_2$ acid groups due to the formation of proton percolation pathways with high "free volumes".

Taken together, all these characteristics make B-type materials promising candidates for application in PEMFCs operating at temperatures higher than 100 °C and low humidification conditions.

AUTHOR INFORMATION

Corresponding Author

*Phone/Fax: +39 049 8275229. E-mail: vito.dinoto@unipd.it.

ACKNOWLEDGMENT

The authors thank Klaus-Dieter Kreuer for his invaluable contribution to this paper. This research was funded by the Italian Murst project PRIN2007 and NUME of FISR2003, "Sviluppo di membrane protoniche composite e di configurazioni elettrodiche innovative per celle a combustibile con elettolita polimerico".

REFERENCES

(1) Gasteiger, H. A. *Electrochemistry* **2007**, *75*, 103.
(2) Kreuer, K. D. *ChemPhysChem* **2002**, *3*, 771.
(3) Kreuer, K. D. *J. Membr. Sci.* **2001**, *185*, 29.
(4) Mauritz, K. A.; Moore, R. B. *Chem. Rev.* **2004**, *104*, 4535.
(5) Mathias, M. F.; Makharia, R.; Gasteiger, H. A.; Conley, J. J.; Fuller, T. J.; Gittleman, C. J.; Kocha, S. S.; Miller, D. P.; Mittelsteadt, C. K.; Xie, T.; Yan, S. G.; Yu, P. T. *Electrochem. Soc. Interface* **2005**, *14* (3), 24.
(6) Alberti, G.; Narducci, R.; Sganappa, M. *J. Power Sources* **2008**, *178*, 575.
(7) Harrison, W. L.; Hickner, M. A.; Kim, Y. S.; McGrath, J. E. *Fuel Cells* **2005**, *5*, 201.
(8) Alberti, G.; Casciola, M.; Massinelli, L.; Bauer, B. *J. Membr. Sci.* **2001**, *185*, 73.
(9) Kreuer, K. D. In *Handbook of Fuel Cells - Fundamentals, Technology and Applications*; Vielstich, W., Lamm, A., Gasteiger, H. A., Eds.; Wiley: Chichester, 2003; Vol. 3, p 420.
(10) Hickner, M. A.; Ghassemi, H.; Kim, Y. S.; Einsla, B. R.; McGrath, J. E. *Chem. Rev.* **2004**, *104*, 4587.
(11) de Araujo, C. C.; Kreuer, K. D.; Schuster, M.; Portale, G.; Mendil-Jakani, H.; Gebel, G.; Maier, J. *Phys. Chem. Chem. Phys.* **2009**, *11*, 3305.
(12) Schuster, M.; Kreuer, K. D.; Andersen, H. T.; Maier, J. *Macromolecules* **2007**, *40*, 598.
(13) Schuster, M.; de Araujo, C. C.; Atanasov, V.; Andersen, H. T.; Kreuer, K. D.; Maier, J. *Macromolecules* **2009**, *42*, 3129.
(14) Drent, E.; van Broekhoven, J. A. M.; Doyle, M. J. *J. Organomet. Chem.* **1991**, *417*, 235.
(15) Cavinato, G.; Toniolo, L.; Vavasori, A. *Top. Organomet. Chem.* **2006**, *18*, 125.
(16) Benetollo, F.; Bertani, R.; Bombieri, G.; Toniolo, L. *Inorg. Chim. Acta* **1995**, *233*, 5.
(17) Vittadello, M.; Negro, E.; Lavina, S.; Pace, G.; Safari, A.; Di Noto, V. *J. Phys. Chem. B* **2008**, *112*, 16590.
(18) Di Noto, V.; Piga, M.; Piga, L.; Polizzi, S.; Negro, E. *J. Power Sources* **2008**, *178*, 561.
(19) Di Noto, V.; Piga, M.; Lavina, S.; Negro, E.; Yoshida, K.; Ito, R.; Furukawa, T. *Electrochim. Acta* **2010**, *55*, 1431.
(20) Di Noto, V. *J. Phys. Chem. B* **2002**, *106*, 11139.
(21) Di Noto, V.; Lavina, S.; Wintersgill, M. C.; Fontanella, J. J. *Phys. Chem. Chem. Phys.* **2010**, *12*, 5993.
(22) Titvinidze, G.; Kaltbeitzel, A.; Manhart, A.; Meyer, W. H. *Fuel Cells* **2010**, *10* (3), 390.
(23) Di Noto, V.; Gliubizzi, R.; Negro, E.; Pace, G. *J. Phys. Chem. B* **2006**, *110*, 24972.
(24) Di Noto, V.; Gliubizzi, R.; Negro, E.; Vittadello, M.; Pace, G. *Electrochim. Acta* **2007**, *53*, 1618.
(25) Vittadello, M.; Suarez, S.; Chung, S. H.; Fujimoto, K.; Di Noto, V.; Greenbaum, S. G.; Furukawa, T. *Electrochim. Acta* **2003**, *48*, 2227.

THE JOURNAL OF PHYSICAL CHEMISTRY C

ARTICLE

pubs.acs.org/JPCC

Influence of Anions on Proton-Conducting Membranes Based on Neutralized Nafion 117, Triethylammonium Methanesulfonate, and Triethylammonium Perfluorobutanesulfonate. 1. Synthesis and Properties

Vito Di Noto,*[,†] Matteo Piga,[†] Guinevere A. Giffin,[†] Sandra Lavina,[†] Eugene S. Smotkin,[‡] Jean-Yves Sanchez,[§] and Cristina Iojoiu[§]

[†]Dipartimento di Scienze Chimiche, Università di Padova, Via Marzolo 1, I-35131 Padova (Pd), Italy

[‡]Northeastern University, Department of Chemistry and Chemical Biology, 360 Huntington Avenue, Boston, Massachusetts 02115, United States

[§]Laboratoire d'Electrochimie et de Physico-chimie des Matériaux et des interfaces, UMR 5631 CNRS-INPG, 1139 Rue de la Piscine, associée à l'UJF, ENSEEG B.P. 75 38402 Saint-Martin-d'Heres, Cedex, France

ABSTRACT: The effect of the anion structure of proton-conducting ionic liquid dopants on the properties of a Nafion 117 membrane, neutralized by triethylammonium, is described. The synthesis and the properties of proton-conducting membranes doped with triethylammonium methanesulfonate (TMS) or triethylammonium perfluorobutanesulfonate (TPFBu) ionic liquids are described. The properties of the doped membranes were investigated by thermogravimetric analysis, differential scanning calorimetry, and dynamic-mechanical analysis. The key findings are that the uptake of the ionic liquid is ca. 25 and 40 wt % for TMS and TPFBu, respectively, and these ionic liquid dopants extend the membranes thermal stability to 140 °C. Information concerning the structure and the interactions between the membrane components was obtained by Fourier transform infrared spectroscopy.

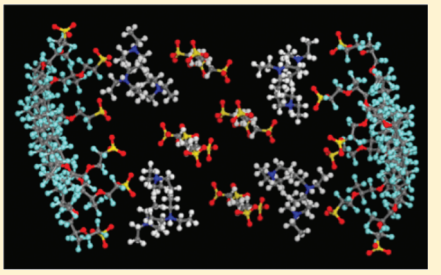

1. INTRODUCTION

Electrochemical devices for the conversion of chemical energy into electrical power, such as proton exchange membrane (PEM) fuel cells are of intense interest to industry and the scientific community because of their high energy conversion efficiency, low environmental impact, and the possibility for use in a wide variety of applications from portable electronic devices to light-duty electric vehicles.[1] At the core of the fuel cell is a PEM that allows the transport of hydrogen ions, evolved at the anode, to the cathode where oxygen is reduced to water. The prevalent PEMs today feature perfluorinated main chains functionalized with perfluoroether side chains terminated with acid $-SO_3H$ groups. These materials (Dupont Nafion, Asashi Aciplex, Dow, and Flemion), in general, are characterized by a high chemical, thermal, and mechanical stability; they also exhibit good proton conductivity at high levels of hydration. The hydration requirements limit widespread commercial use of conventional PEMs, which have inadequate proton conductivity at temperatures >90 °C and at low values of relative humidity.[2] Fuel cells capable of operating above 120 °C at low levels of hydration would: (a) obviate the need of bulky and expensive water management modules; (b) simplify thermal management; and (c) reduce the impact of catalyst poisons such as carbon monoxide.[3,4] Current DOE targets require that a membranes must be mechanically durable (cycles with <10 standard cubic centimeter per minute of crossover of the reactant gases at operating conditions of 120 °C and 40−80 kPa partial pressure of water) for greater than 20 000 cycles and chemically durable for 500 h. The permeability of oxygen is about half of that of hydrogen based on molecular size. Membranes must show conductivities >0.9 $S \cdot cm^{-1}$ at the maximum operating temperature and 40−80 kPa water, 0.9 $S \cdot cm^{-1}$ at 80 °C and 25−40 kPa water, 0.6 $S \cdot cm^{-1}$ at 30 °C and up to 4 kPa water, and 0.09 $S \cdot cm^{-1}$ at −20 °C.[5] The current reference membrane is still Nafion, which has good mechanical properties (460 and 131 MPa under dehydrated and fully hydrated conditions, respectively, at 25 °C for Nafion 117)[6] in fuel cells. New membranes must improve the conductivity at high temperatures and low relative humidities but also have mechanical properties comparable to that of Nafion 117.

In an effort to overcome the limitations of conventional PEMs, innovative PEMs based on polymeric membranes doped with proton-conducting ionic liquids (PCILs) have been developed.[7−9] PCILs are a category of ionic liquids (ILs) and are synthesized by directly reacting a Bronsted acid with a Bronsted base.[10] The distinguishing feature of PCILs, versus ILs, is the transfer of protons between proton-donor and proton-acceptor sites, which can

Received: May 6, 2011
Revised: December 6, 2011

ACS Publications © XXXX American Chemical Society

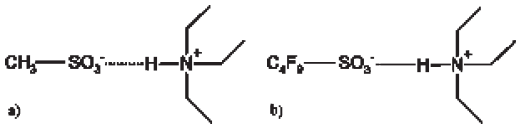

Figure 1. Chemical structure of PCILs: (a) triethylammonium methanesulfonate (TMS) and (b) triethylammonium perfluorobutanesulfonate (TPFBu).

subsequently be used in the formation of hydrogen bonds.[10] PCILs have highly mobile protons and are thus ideal candidates for fuel cell electrolyte components that can function at medium temperatures, between 100 and 150 °C, and possibly under anhydrous conditions.[11,12] Recently, Di Noto et al. reported that PEMs based on Dupont Nafion 117 neutralized with triethylamine (TEA) and doped with the PCIL triethylammonium trifluoromethanesulfonate (TEA-TF) are characterized by an increased stability range of conductivity and show higher conductivity values (7.3×10^{-3} S·cm^{-1}) at 145 °C versus the standard Nafion 117.[13] Therefore, PCIL-doped membranes are ideal electrolytes for medium-temperature fuel cells. This Article extends that work with the preparation and the study of two new membranes based on Nafion 117 neutralized with TEA and doped with either of two PCILs (i.e., triethylammonium methanesulfonate (TMS) or triethylammonium perfluorobutanesulfonate (TPFBu)). This work elucidates the effect of the PCIL anion structure on the properties of the hybrid nanocomposite membranes. The properties of these materials are studied by thermogravimetric (TG) analyses, differential scanning calorimetry, and dynamic-mechanical analysis, whereas the structure and the interactions between the membrane components are investigated by Fourier transform infrared spectroscopy.

2. EXPERIMENTAL SECTION

2.1. Synthesis of TMS and TPFBu Proton-Conducting Ionic Liquids. Methanesulfonic (MS) and perfluorobutanesulfonic (PFBu) acids (Aldrich) were used as received. TEA and the other organic solvents used in the synthesis of the ILs were distilled before use. The ILs were synthesized by the reaction of the organic acid with TEA as previously reported.[14] Briefly, a solution of the organic acid (10 mL of organic acid/100 mL of water) was cooled in an ice-bath, stirred for 10 min, and then neutralized with TEA to a pH 8. The excess water and TEA were removed by evaporation under vacuum and by freeze-drying, respectively, yielding the ILs TMS and TPFBu. The purification of TMS was carried out by dissolving the IL in methanol, filtering the solution through an active carbon column and finally evaporating the excess methanol. The purification of TPFBu was obtained by the recrystallization of the IL in a 50/50 (v/v) solution of acetonitrile and diethyl ether. The ILs were dried (48 h) at 130 °C under vacuum. The chemical structures of TMS and TPFBu are shown in Figure 1.

2.2. Membrane Preparation. Membranes were prepared by the procedure of Martinez et al.[14] Nafion 117 (N117) was immersed in 2 M HNO_3 and refluxed for 2 h. The membrane was subsequently neutralized by immersion in a 50/50 (v/v) solution of ethanol and 4 M $TEA_{(aq)}$ for 48 h at ambient temperature, yielding the neutralized Nafion (nN117). The nN117 was finally washed with distilled water, dried at 130 °C for 48 h under vacuum, and moved into a drybox. All further preparation and manipulation of the samples and the ILs were carried out within the drybox. The membrane was doped with the IL by immersion into either TMS or TPFBu, for 48 h at 80 °C to yield NTMS and NTPFBu, respectively. The NTMS and NTPFBu were stored for 1 week inside a drybox in argon. The uptake of IL (%PCIL) was calculated using eq 1

$$\%\mathrm{PCIL} = [(w_f - w_i)/w_f]*100 \quad (1)$$

where w_i and w_f are the membrane mass before and after the absorption of IL, respectively. The uptake of TMS by NTMS is 25 wt %, whereas that of TPFBu by NTPFBu is 40 wt %.

2.3. Instruments and Methods. TG analyses were carried out using a high-resolution thermobalance TGA 2950 (TA Instruments) under nitrogen (100 sccm). The instrument sensitivity ranges from 0.1 to 2%·min^{-1}, and the resolution is 1 μg. TG profiles were collected from 20 to 800 °C. Approximately 5 mg of sample was loaded onto an open platinum pan. The heating rate was varied from 50 to 0.001 °C·min^{-1}, depending on the first derivative of the weight loss. Differential scanning calorimetry (DSC) analyses were carried out using a mDSC 2920 (TA Instruments) equipped with a liquid nitrogen cooling system using a heating rate of 5 °C·min^{-1} from −100 to 350 °C. The measurements were carried out by loading 5 mg of sample inside a hermetically sealed aluminum pan. Dynamic-mechanical analyses (DMA) were obtained with a TA Instruments DMA Q800 equipped with a clamp specifically designed to test films or fibers in tension mode. The spectra were collected every 5 °C from −100 to 200 °C by applying a sinusoidal deformation of amplitude 4 μm at 1 Hz. A rectangular sample ($30 \times 7 \times 0.2$ mm^3) was subjected to a preloading force of 0.05 N. The viscoelastic behavior of the samples was quantified in terms of elastic modulus (E'), loss modulus (E''), and loss factor ($\tan \delta = E''/E'$). FT-IR spectra were obtained by signal averaging 500 scans acquired on a Nicolet FT-IR Nexus spectrometer at a resolution of 4 cm^{-1}. Transmission spectra of the pristine ILs were obtained between KBr pellets. Spectra of the doped membranes were obtained in attenuated total reflectance (ATR) mode with a Perkin-Elmer frustrated multiple internal reflections 186-0174 accessory.

3. RESULTS AND DISCUSSION

3.1. Thermogravimetric Analysis. TG profiles are recorded from room temperature to 800 °C for the ILs, TMS and TPFBu, and for the PCIL-doped membranes, NTMS and NTPFBu, for two reasons: (1) to explore the temperature region where the materials are thermally stable and (2) to explore the effect of the IL-nN117 and the IL-IL interactions on the thermal degradation of the doped membranes. It is possible that these interactions could lead to reduced thermal stability of the membranes. The TG profiles are shown in Figure 2 along with the TG results of nN117 obtained from the literature.[13] The insets I, II, and III of Figure 2 show the derivative $dw\%/dT$ from 25 to 160, from 150 to 350, and from 350 to 600 °C, respectively. Three different thermal degradation processes, divided into regions I, II, and III, were identified. The elimination of traces of water occurs in region I between 20 and 150 °C. It is expected that the level of hydration of the doped membranes is negligible as compared with pristine Nafion because the hydrophilic domains are filled with the ILs. Therefore, the water content of the membranes depends on the water uptake of the ILs. The weight loss due to water at 150 °C is about 2.3, 2, 1, and 0.5 wt % for samples TMS, NTMS, TPFBu, and NTPFBu, respectively. These data suggest that: (a) the IL TPFBu includes about half as much water as TMS

dx.doi.org/10.1021/jp204241y |J. Phys. Chem. C XXXX, XXX, 000–000

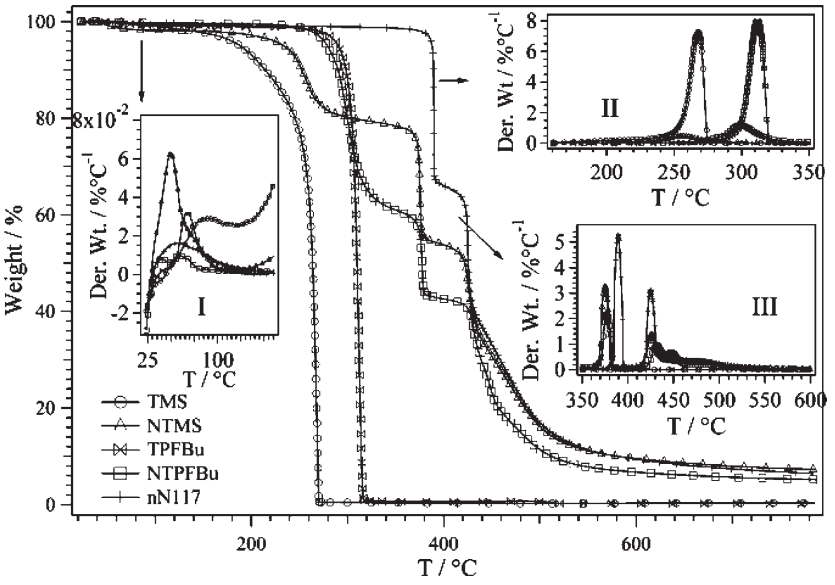

Figure 2. TG profiles of TMS, TPFBu, NTMS, NTPFBu, and nN117. The insets show the derivative dw%/dT in the temperature range: (I) 30−160 °C, (II) 150−350 °C, (III) 350−600 °C. The TG curve of nN117 is taken from the literature.[13]

due to its higher hydrophobicity, which arises from the presence of the C_4F_9 group and (b) the water content of the NTMS and NTPFBu membranes is less than their respective ILs and follows the behavior of their respective pristine PCIL; that is, the water content of NTPFBu (0.5%) is lower than that of NTMS (1%). Overall, the doped membranes are more hydrophobic because of the presence of the ILs.

The association of the weight reductions detected in region II, between 170 and 350 °C (Figure 2 (II)), with thermal degradation of the IL is supported by the following: (1) the TG profiles of pristine MST and TPFBu reveal a weight loss of ∼100% in this temperature range and (2) the absence of a mass reduction event in this temperature range for nN117. The IL content of the NTMS and NTPFBu membranes can be estimated using the weight change from 170 to 350 °C. The uptake of IL is determined to be 20 and 39 wt % for NTMS and NTPFBu, respectively. These values are in agreement with the results determined during the synthesis of the doped membranes, as reported in the Experimental Section, which are equal to 25 and 40 wt % for NTMS and NTPFBu, respectively. Using the uptake values, the IL MWs of 198 and 402 $g \cdot mol^{-1}$ for TMS and TPFBu, respectively, and a nN117 side group concentration of 0.83 × 10^{-3} $mol \cdot g^{-1}$, the ratio (φ) between the moles of PCIL and the moles of sulfonate groups in the polymeric matrix can be determined. The values of φ for NTMS and NTPFBu are 2.02 and 2.00, respectively, suggesting that the uptake of IL per moles of sulfonate group of nN117 is the same.

Using the derivative dw%/dT shown in inset II of Figure 2, the initial thermal degradation or onset, $T_{d,ons}$, and the maximum thermal degradation temperature, $T_{d,max}$, are determined as shown in Figure 3. The values of $T_{d,ons}$ and $T_{d,max}$ (Table 1) show that the TMS decomposition temperature is lower than that of TPFBu, even when the ILs are embedded in bulk polymer membranes. The increased $T_{d,ons}$ and $T_{d,max}$ for TPFBu are explained by the increased acid dissociation constants of pristine organic acids (PFBuH), pK_a= −13.2 and methanesulfonic acid (MSH), pK_a = −2 used in the preparation of the ILs.[14] These results are in agreement with Martinez et al.[14]

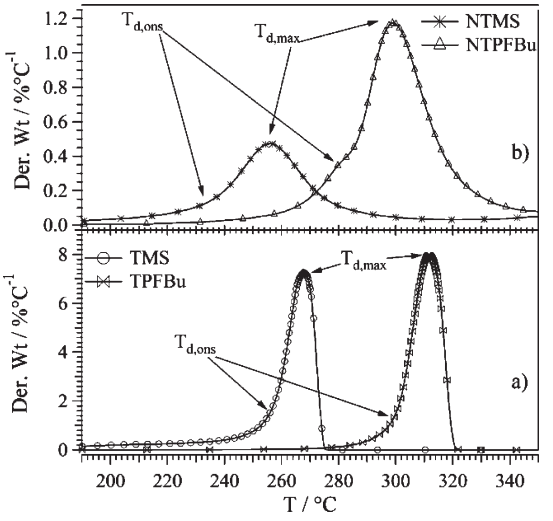

Figure 3. Behavior of dw%/dT in the thermal range 190−350 °C for: (a) TMS and TPFBu and (b) NTMS and NTPFBu.

Table 1. Values of Onset, $T_{d,ons}$, and Thermal Degradation Temperatures, $T_{d,max}$

	TMS	NTMS	$\Delta T_{TMS/NTMS}$	TPFBu	NTPFBu	$\Delta T_{TPFBu/NTPFBu}$
$T_{d,ons}$/°C	256	233	23	300	281	19
$T_{d,max}$/°C	268	256	12	312	299	13

The increased thermal stability under measurement conditions of TPFBu versus TMS indicates that the anion (conjugated base) of PFBuH is a weaker base than the anion of MSH. Therefore, the anion−cation interaction should be more important in TMS than in TPFBu. However, because PFBuH is more acidic than MSH acid, the equilibrium AH + TEA ⇌ A^- + $TEAH^+$ should be shifted further to the right with PFBuH than with MSH, resulting in a delay of the weight loss to higher temperature.

dx.doi.org/10.1021/jp204241y |J. Phys. Chem. C XXXX, XXX, 000–000

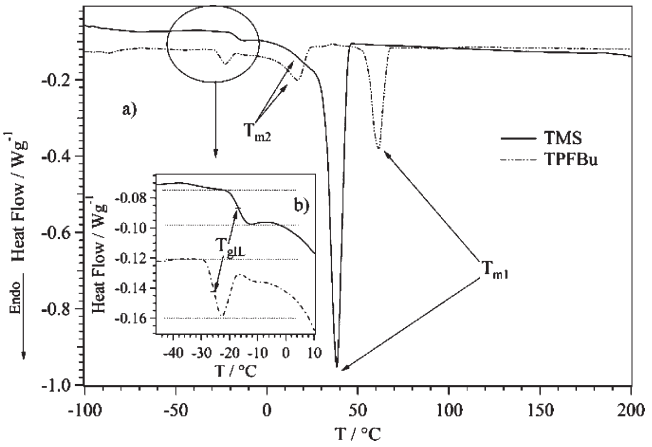

Figure 4. (a) DSC curves of TMS and TPFBu collected in the temperature range from −100 to 200 °C. (b) Expansion of the DSC curves at the glass transition temperature, $T_{gIL} \approx -20$ °C.

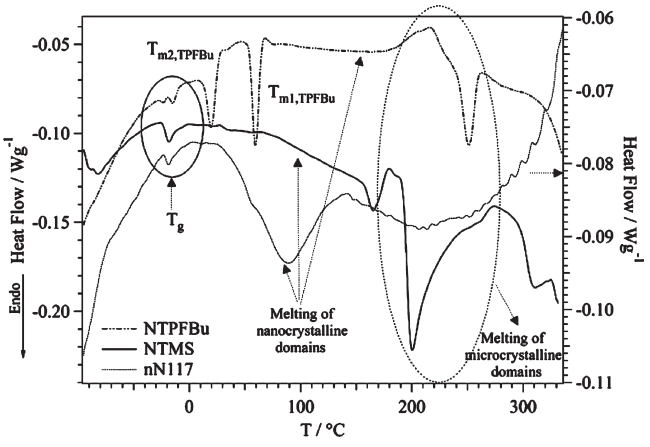

Figure 5. DSC curves of NTMS, NTPFBu, and nN117 collected in the temperature range from −100 to 350 °C. The DSC curve of nN117 are shown for the sake of comparison and are taken from the literature.[13]

The $T_{d,ons}$ of the ILs is reduced by ∼20 °C when they are incorporated into the nN117 membrane (ΔT of Table 1). The reduction of the thermal stability under measurement conditions of the ILs incorporated into the membrane is explained by the diminished strength of the interactions between the ions as compared to the pristine ILs, probably due to the formation of electrostatically interacting confined nanodomains within the bulk nN117. The presence of the IL in very small domains results in a large surface area that is available for interaction with the membrane. As a result, there are significant IL-membrane interactions that lead to a decrease in the ion−ion interactions in the PCILs. Consistent with prior studies[15−17] and with the TG profile of nN117,[13] the weight reductions corresponding to region III, between 350 and 600 °C, are assigned to polymer matrix decomposition. The peaks between 350 and 400 °C correspond to the decomposition of the polyether side chain, whereas the peaks between 400 and 550 °C are associated with the degradation of the main fluorocarbon backbone chain. The decomposition of the polyether side chains in the doped membranes occurs ∼13 °C lower than in nN117. This reduction in temperature is attributed to the plasticizing effect of the IL in the NTMS and NTPFBu membranes. The IL causes a weakening of the electrostatic interactions within the neutralized side groups of nN117, resulting in a reduction of thermal stability. It could be hypothesized that the weakening of electrostatic interactions is due to the aggregation of IL cations and anions that creates larger charged clusters than in the pristine ILs. These aggregates interact with the neutralized side groups of the host matrix. The phenomenon acts to weaken the $SO_3^- \cdots TEAH^+$ interactions as compared to the pristine nN117 by the formation of $SO_3^- \cdots TEAH^+ \cdots$[aggregate] moieties via an extended hydrogen bonding network. This behavior is expected given the stabilizing effect of the neutralization of the sulfonate group in pristine nN117. This stabilization results in an increased thermal stability of the sulfonate group as compared with the sulfonic group of pristine N117. The thermal decompositions attributed to the degradation of the main fluorocarbon backbone chain, shown in the inset III of Figure 2, appear to be independent of the IL used. In summary, TG measurements show that the polymeric membranes NTMS and NTPFBu: (a) are thermally stable under measurement conditions up to temperatures of ∼220 °C; (b) include 20 and 39 wt % of TMS and TPFBu, respectively; (c) show three distinct thermal degradation processes; and (d) are characterized by a lower thermal stability than the ILs they contain (Table 1).

3.2. DSC Analysis. DSC analysis elucidates thermal transitions in the PCIL-doped membranes. The DSC profiles of the pristine ILs (Figure 4) exhibit a glass transition, T_{gIL}, between −30 and −15 °C. By considering T_{gIL} as the midpoint between the onset and the end point temperatures of the glass transition, values of −17 and −23 °C are obtained for TMS and TPFBu, respectively. Endothermic peaks present at $T_{m1,TMS}$ = 38.4 °C and $T_{m1,TPFBu}$ = 61.3 °C are due to the melting of the ordered aggregates of ILs.[14] The melting temperature, T_{m1}, depends on the properties of the pristine organic acids used in the synthesis and increases with IL hydrophobicity.[14] The DSC results of both ILs show the presence of a second endothermic peak, T_{m2}, which is less intense and shifted to lower temperatures with respect to T_{m1}. For TMS, the second endothermic peak $T_{m2,TMS}$ is observed at ∼20 °C, as a shoulder on the $T_{m1,TMS}$ peak, whereas for TPFBu, the peak $T_{m2,TPFBu}$ is well-resolved and centered at 17 °C. The presence of T_{m2} suggests that at low temperatures the IL nanostructure consists of two distributions of ordered aggregates with different sizes, which on average melt at T_{m1} and T_{m2}. The DSC curve of the NTMS and NTPFBu samples, together with that of nN117,[13] is reported in Figure 5.

All examined samples show a thermal transition in the range from −30 to −10 °C. In the case of nN117, this thermal event is associated with a conformational transition involving the polyether side groups of nN117.[8] In the PCIL-doped membranes, the thermal events between −30 and −10 °C are attributed to the superposition of two different phenomena: (1) the glass transition of the pristine IL as seen in Figure 4 and (2) the conformational transition of the polyether side groups in the nN117 polymeric matrix.

By comparing the DSC curves in Figures 4 and 5, it is observed that the first melting peak of the pristine IL in the NTMS membranes, $T_{m1,TMS}$, has vanished. In the NTPFBu membrane, both TPFBu melting peaks remain and can be located at $T_{m1,TPFBu}$ = 19.4 °C and $T_{m2,TPFBu}$ = 59.3 °C. The absence of the DSC melting peak $T_{m1,TMS}$ of NTMS suggests that even at low temperatures the IL TMS embedded inside the membrane is well-dispersed and forms nanodomains with very small sizes. The highly dispersed state of TMS likely results from interactions between TMS and the polymer matrix. These interactions significantly

dx.doi.org/10.1021/jp204241y |J. Phys. Chem. C XXXX, XXX, 000–000

Table 2. Enthalpy of Fusion $\Delta H_{f,i}$ for TMS, NTMS, TPFBu, and NTPFBu

$\Delta H_{f,i}/Jg^{-1}$	TMS	NTMS	TPFBu	NTPFBu
$\Delta H_{f,Tm1}$	70.5		23.2	4.9
$\Delta H_{f,Tm2}$	22.1		12.7	3.9

reduce the size of the IL nanoaggregates that are confined inside the polar domains of nN117, efficiently solvating the surface of its hydrophobic domains. The presence of partially ordered TPFBu nanodomains inside the NTPFBu membrane suggests that TPFBu···$TEAH^+$···N117 interactions are weaker than TMS···$TEAH^+$···N117 interactions and, as a consequence, the size of nanodomains of TPFBu inside the membranes is larger than that of TMS.

The enthalpy of fusion values ΔH_{f1} and ΔH_{f2} associated with the first and second melting peaks are shown in Table 2. The total enthalpy of fusion, $\Delta H_{f,tot} = \Delta H_{f,Tm1} + \Delta H_{f,Tm2}$, of the pristine ILs are 92.6 (18.3 kJ·mol^{-1}) and 35.9 J·g^{-1} (14.4 kJ·mol^{-1}) for TMS and TPFBu, respectively. These values suggest that the exchange of the methanesulfonate anion in TMS with the perfluorobutylsulfonate anion in TPFBu reduces the lattice energy by ∼20%. The total enthalpy of fusion for the PCIL inside NTPFBu is 8.8 J·g^{-1}. Given that according to TG measurements NTPFBu includes 39 wt % of TPFBu, the total enthalpy of fusion, $\Delta H_{f,tot}$, for TPFBu inside nN117 can be estimated to be $\Delta H_{f,tot}$ = 8.8 J·g^{-1}/39 wt % = 22.5 J·g^{-1}. This is 37% lower than the enthalpy of fusion of the pristine IL.

The DSC analyses suggest that the confinement of the IL inside the polymer matrix yields effects that depend on the interactions between the two system components and on the nanostructuring of PCILs in bulk materials. For the NTMS membrane, confinement results in the presence of a completely dispersed TMS IL that is confined in very small amorphous nanoaggregates. For the NTPFBu membranes, the outcome of the confinement involves a reduction in crystallinity by ∼37%, with respect to that of the pristine IL.

The broad endothermic peaks between 100 and 180 °C in the DSC curves of NTMS and NTPFBu (Figure 5) are due to the melting of the hydrophobic nanocrystalline domains of nN117 that consist of fluorocarbon chains.[16] In the case of the nN117 membrane, the melting of the nanocrystalline hydrophobic domains is identified by a large peak that spans from 30 to 150 °C[13] and occurs about 50 to 60 °C lower than in the NTMS and NTPFBu membranes. Finally, at temperatures higher than 160 °C, the endothermic peaks present in each of the DSC profiles of NTMS, NTPFBu, and nN117 are due to the melting of microcrystalline hydrophobic domains of the nN117 membrane formed by fluorocarbon chains.[13,15−17] The enthalpies of fusion for the microcrystalline hydrophobic domains, ΔH_{mc}, are 31.5, 46.7, and 15.1 J·g^{-1} for nN117,[13] NTMS, and NTPFBu, respectively. These values indicate that nN117 has a degree of microcrystallinity in the hydrophobic domains between that of NTPFBu and NTMS and that the degree of crystallinity of the NTPFBu polymeric matrix is 67% smaller than that of NTMS.

The trend in the crystallinity degree of the hydrophobic perfluorinated microdomains of doped membranes is the opposite of that of the ILs present within nN117. NTMS shows a higher degree of crystallinity than NTPFBu, whereas TMS is completely dispersed in the bulk material and TPFBu is partially crystallized. This behavior can be explained by considering the fact that the

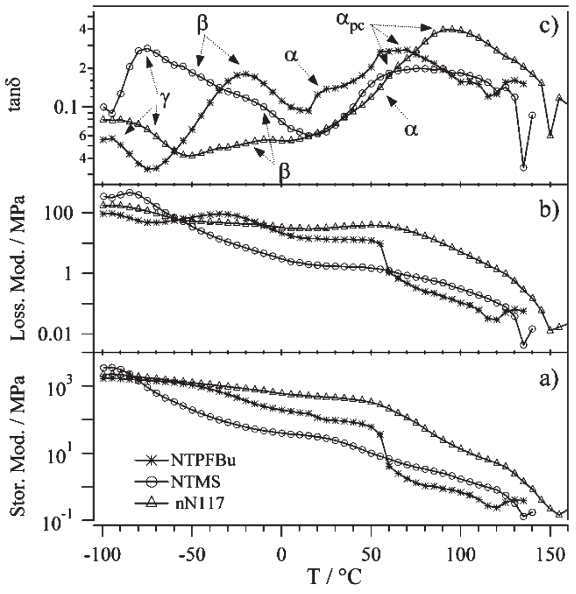

Figure 6. DMA profiles of NTMS, NTPFBu, and nN117. The graphs show the behavior of: (a) the elastic modulus (E'); (b) the loss modulus (E''); and (c) tan δ with respect to the temperature. α-Type transitions occur due to conformational relaxation modes of the fluorocarbon backbone chains of PTFE domains. The β-mechanical transition corresponds to the fluctuations of the dipole moments associated with the polyether side chain groups of nN117. The γ transition results from the local fluctuations of dipole moments of CF_2 moieties of the main fluorocarbon chains of the PTFE hydrophobic domains of nN117. The α_{pc} transition is attributed to the long-range movement of the fluorocarbon domains and side chains due to weakening of electrostatic interactions within the polar aggregates and involves the dynamics of both the hydrophobic and hydrophilic domains of nN117.

presence of a highly dispersed IL (e.g., TMS) inside the polar domains of the nN117 matrix allows the IL with a low steric hindrance and thus with small nanoaggregates sizes to more efficiently plasticize the nN117 side chains, which allows increased motion of host fluorocarbon polymeric matrix. As a result of these two effects, TMS acts as a very efficient plasticizing agent. In contrast, the presence of partially ordered IL domains with larger sizes like those detected in pristine TPFBu inside nN117 hampers the possibility for long-range ordering of the fluorocarbon chains and limits the total degree of crystallinity of the host polymer because of its rigidity and formation of ordered nanostructures in the hydrophilic domains of the membranes. DSC measurements elucidate thermal transitions in these materials, which reveal that a stronger PCIL-nN117 interaction (plasticization phenomenon) stimulates the organization of the nN117 fluorocarbons chains into a microcrystalline structure. Specifically, the DSC results show that: (a) the glass-transition temperature of ILs is about −20 °C, and both pristine ILs undergo two melting processes, which occur at the temperatures of 20 and 38.4 °C for TMS and 17 and 61.3 °C for TPFBu, respectively; (b) the confinement of the ILs inside the doped membrane reduces their degree of crystallinity (by 37% for TPFBu and by 100% for TMS); and (c) the degree of microcrystallinity of the NTPFBu fluorocarbon chains is ∼67% smaller than that of NTMS.

3.3. Dynamic Mechanical Studies. The effect of the PCIL-nN117 interactions on the mechanical properties and the structural relaxations of the doped membranes was investigated by measuring the temperature dependent spectra of the elastic

dx.doi.org/10.1021/jp204241y |J. Phys. Chem. C XXXX, XXX, 000–000

Table 3. Elastic Modulus (E') of nN117, NTMS, and NTPFBu Measured at $T = -50$, 50, and 100°C

	E'/MPa		
	T/−50 °C	T/50 °C	T/100 °C
nN117	1248	326	13
NTPFBu	1061	60	0.7
NTMS	191	10	1.7

modulus (E'), loss modulus (E''), and tan δ. These studies were performed using a dynamic oscillatory method with small sinusoidal mechanical elongations (4 μm) at a frequency of 1 Hz. (Refer to the Experimental Section.) DMA measurements are of crucial importance to determine the mechanical properties of the doped membranes in terms of the elastic modulus and mechanical relaxations as compared to the standard reference material N117. The state-of-the-art N117 materials have an elastic modulus of approximately 460 and 131 MPa in dehydrated and fully hydrated conditions, respectively, at 25 °C and a mechanical relaxation at ∼100 °C.[6] E', E'', and tan δ are shown in Figure 6a−c, respectively. These profiles show a loss of mechanical properties in the doped membranes at temperatures >140 °C, whereas this does not occur until temperatures >150 °C for nN117 (Figure 6a). Above −80 °C, the elastic modulus of the membranes containing the ILs is clearly inferior to that of nN117. Values of E' for all three systems are reported for −50, 50, and 100 °C in Table 3. The reduction of the mechanical stability range of the doped membranes, in terms of the elastic modulus, is due to the plasticizing effect of the ILs. This effect is enhanced with temperature due to the progressive increase in the fluidity and the solvation effect of the IL domains within the polymeric matrix. In the case of NTPFBu, the profiles of E' and E'' show an abrupt decrease at ∼60 °C, which corresponds to the melting temperature of TPFBu revealed by the DSC measurements. The E' and E'' profiles of NTMS do not show a sharp decrease near the TMS melting temperature but instead a monotonic decrease starting at approximately −80 °C. This trend is consistent with the DSC data for NTMS, which showed the absence of the TMS melting peak at ∼38 °C. These results confirm that TMS is completely dispersed at the interfaces between the hydrophobic and hydrophilic nanodomains of the doped membranes because of the formation of an efficient plasticizing solvation shell on the surface of hydrophobic and hydrophilic domains of nN117 host material.

By comparing the elastic modulus of the doped membranes both in Figure 6a and Table 3, it is observed that from −80 to 60 °C NTPFBu shows higher values of E' than NTMS. This difference in E' values is attributed to: (a) the difference in the dimensions of the nanodomains of the PCILs, which is a result of the molecular dimensions of the constituent anions (both PCILs include triethylammonium as the cation) and their interactions with the polymeric matrix, and (b) the difference in structural organization of the PCILs when they are present inside the interfaces between the hydrophobic−hydrophilic nanodomains of polymeric membranes. TPFBu nanoclusters are larger because they contain the perfluorobutanesulfonate anion, which has an extended perfluorinated chain unlike the much smaller methyl group in the methanesulfonate anion of TMS. Below 20 °C, when both PCILs contained inside the polar domains of the polymer membrane are expected to be in the solid state, the steric hindrance of the nanodomains of TPFBu is greater than that of TMS, resulting in an increased elastic modulus for NTPFBu. Below the PCILs melting point, TPFBu in NTPFBu is partially organized in an ordered nanostructure, whereas TMS is highly dispersed within the NTMS membranes. Consequently, the difference in the structural organization of the PCILs at the interfaces between hydrophobic and hydrophilic domains of the nN117 host material results in a reduction of the mechanical properties of NTMS as compared to NTPFBu.

Figure 6c shows the tan δ profiles of the PCIL-doped membranes and nN117. In the tan δ spectrum of nN117, the α_{pc} transition is present at ∼100 °C and is attributed to the long-range movement of the fluorocarbon domains and side chains due to weakening of electrostatic interactions within the polar aggregates.[13,16,18,19] The "pc" subscript of α_{pc} indicates that this mechanical mode, unlike the α-mechanical relaxation associated with the segmental motion of the perfluorinated backbone, involves the dynamics of both the hydrophobic and hydrophilic domains of nN117. When comparing the doped membranes to nN117, the α_{pc} peak shows a reduction in intensity and a shift to slightly lower temperatures with a maximum at ∼70 °C. This behavior has been reported in the literature for similar systems.[13,14] The trend in the α_{pc} peak suggests that the energy dissipated in the long-range motion of both the nN117 primary and secondary structure during the α_{pc} transition is higher in nN117. This is due to the steric hindrance and weak van der Waals interactions within the polar domains between the different $TEAH^+$-neutralized anionic side groups. In the doped membranes, the energy dissipated is very small because the polar side groups, which are neutralized by the $TEAH^+$ cation, are solvated and plasticized by the IL resulting in the reduction of the dipolar interactions within the hydrophilic domains of the membrane. The α_{pc} peak of the doped membranes is broader than in nN117 because of the superposition of PCIL melting in this temperature range.

The analysis of tan δ profiles for the temperatures from 0 to 50 °C also reveals the presence of α−type relaxations associated with the mechanical energy dissipated by the segmental motion of the fluorocarbon backbone chain of nN117.[6,16,18] As seen above with the α_{pc} transition, in the doped membranes the α-type mechanical relaxation occurs at temperatures lower than that observed for nN117, which shows transitions at ca. $T_\alpha = 40$ °C and $T_{\alpha'} = 60$ °C. α-Type transitions occur due to conformational relaxation modes of the fluorocarbon backbone chains of PTFE domains, specifically a $13_6 \rightarrow 15_7$ conformational transition for α and an order−disorder conformational transition for α'.[16,18] In the PCIL-doped membranes, the α transition is found at ca. $T_\alpha =$ 30 °C. The reduction of T_α for the NTMS and NTPFBu membranes, as compared with nN117, is attributable to the IL that solvates and plasticizes the $TEAH^+$-neutralized side group of nN117. The presence of the PCIL reduces the dipolar interactions inside the polar domains of host polymer, resulting in a consequent mobility increase in the main fluorocarbon backbone chains. Between −50 and 0 °C, the tan δ profiles show a β-secondary mechanical transition that is attributed to the conformational relaxation mode of the polyether side groups. These modes correspond to the fluctuations of the dipole moments associated with the polyether side chain groups of nN117. The intensity of the β-transition peaks of NTMS and NTPFBu appears to be significantly larger than that of nN117. The presence of PCILs inside the nN117 polymer matrix causes a reduction in the dipolar interaction cross-links between the polyether side groups and consequently increases the number density of

dx.doi.org/10.1021/jp204241y |J. Phys. Chem. C XXXX, XXX, 000–000

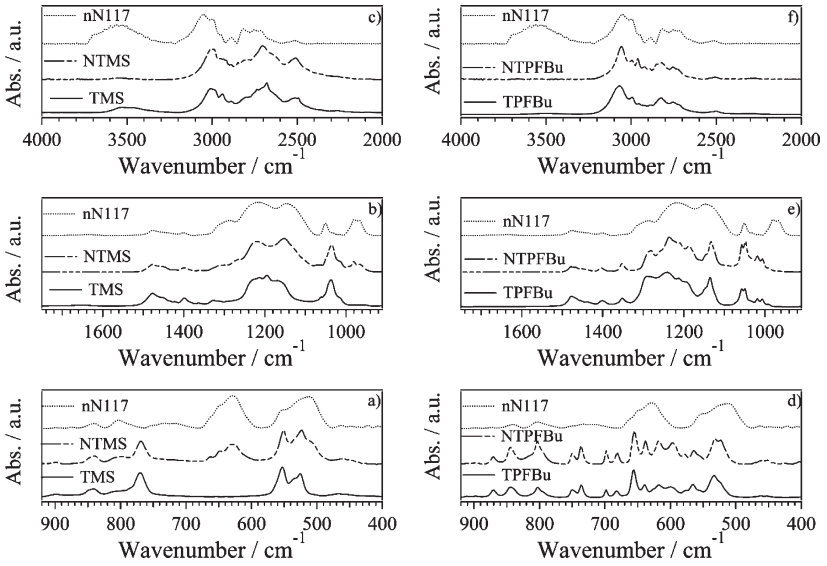

Figure 7. Infrared spectra of TMS, TPFBu, NTMS, NTPFBu, and nN117. (a,d) Spectral region from 900 to 400 cm^{-1}. (b,e) Spectral region from 1700 to 900 cm^{-1}. (c,f) Spectral region from 4000 to 2000 cm^{-1}. The spectrum of nN117 is taken from the literature.[13]

nN117 side chains involved in the β-mechanical relaxations. Finally in the tan δ curve shown in Figure 6c for nN117, there is a mechanical relaxation present at approximately −80 °C associated with a γ transition resulting from the relaxation mode associated with the local fluctuations of dipole moments of CF_2 moieties. These CF_2 moieties belong to the main fluorocarbon chains of the PTFE hydrophobic domains of nN117.[20,21] The intensity and temperature maximum of the γ peak decrease according to the degree of microcrystallinity of the nN117 matrix in the order NTMS > nN117 > NTPFBu. This result indicates that increasing the degree of order in the fluorocarbon hydrophobic domains increases the density of CF_2 groups involved in the γ transition. DMA measurements reveal: (a) the membranes doped with PCILs present a thermal mechanical stability of ∼140 °C and inferior mechanical properties than nN117, in terms of the elastic modulus, E'; (b) the elastic modulus of the doped membranes at lower temperatures depends on the degree of crystallinity and the dimension of embedded PCIL nanoaggregates; and (c) there are four mechanical relaxations α_{pc}, α, β, and γ. The α_{pc} and α relaxations in the doped membranes shift to lower temperatures as compared to nN117. This shift occurs due to the plasticizing effect of the PCIL contained within the membranes. Finally, the γ transition depends on the microcrystallinity degree in hydrophobic domains of the polymeric matrix of nN117.

3.4. FT-IR Studies. The TMS and NTMS infrared spectra are reported in the Figure 7a−c, whereas those for TPFBu and NTPFBu are in Figure 7d−f. Parts a and d, b and e, and c and f show the IR spectra divided into three spectral regions, 400 to 900, 900 to 1700, and 2000 to 4000 cm^{-1}, respectively. These spectra are compared with the IR spectra of nN117 found in the literature.[13] Evidence of water is visible in the FT-IR spectra of Figure 7c,f, consistent with TG results. The broad peak between 3700 and 3200 cm^{-1} is due to vibrational modes arising from water OH stretching motions. The breadth of this very weak peak indicates the presence of water molecules with varying hydrogen-bond strengths that are likely present in a range of hydrogen-bonding environments. The intensity of the ν(OH) stretching peaks confirms TG measurements, indicating that traces of water are present in investigated materials. The CH_3 and CH_2

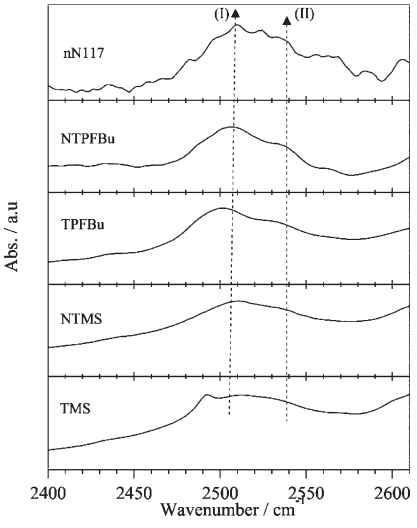

Figure 8. Infrared spectra in the spectral region from 2400 to 2610 cm^{-1}. The spectrum of nN117 is taken from the literature.[13]

antisymmetric and symmetric stretching modes are found between 3000 and 2600 cm^{-1}. The CH stretching modes cover a larger frequency range, in accordance with the spectra of compounds where the CH-containing moieties are located next to a nitrogen atom,[22,23] particularly when the nitrogen atom is protonated. All of the examined samples, including the nN117 membrane, have a band at ∼2500 cm^{-1}. This band is seen in the expanded spectra shown in Figure 8 and is associated with the $N-H^+$ stretching mode of the $TEAH^+$ cation.[24,25] Here the $N-H^+$ stretching band contains two spectral features, one at higher frequencies, labeled I at ca. 2530 cm^{-1}, and another at lower frequencies, labeled II ranging between 2512 and 2501 cm^{-1}. There is an additional feature present in the TMS spectrum at 2491 cm^{-1}. The presence of two or three features in the $N-H^+$ stretching band indicates that the $TEAH^+$ cations are involved in hydrogen-bonding networks of varying strengths. I and II remain when the PCILs are incorporated into the doped membranes,

dx.doi.org/10.1021/jp204241y |J. Phys. Chem. C XXXX, XXX, 000–000

but the peak at 2491 cm^{-1} in TMS is no longer visible in the spectrum. The population of $TEAH^+$ cations responsible for this peak experiences the strongest hydrogen bonds. It is possible that the loss of this cation population may be correlated to the loss of crystallinity when TMS is embedded in the nN117 membranes. Finally, there is a slight shift of feature I in the $N-H^+$ stretching band to higher frequency when the PCILs are present in the polymeric membrane. This phenomenon is consistent with a weakening of the hydrogen-bond strength and a reduced interaction between anions and cations of the PCIL in the doped membrane.

The spectral region shown between 1380 and 1080 cm^{-1} (Figure 7b,e) primarily contains modes associated with the CF_2 moieties of the nN117 membrane.[16,26] These modes are sensitive to the backbone conformation and contain contributions from CF_2 internal coordinates of both the 15_7 and 10_3 helices typical of Nafion.[13,16] Significant differences in the modes can be seen when comparing the bands of NTMS and NTPFBu. In NTMS, whereas there is evidence of the TMS peaks in the spectrum, the CF_2 band shape remains largely unchanged and still strongly resembles the spectrum of nN117. In contrast, the NTPFBu spectrum more strongly resembles the spectrum of TPFBu, and only small contributions from the nN117 matrix can be seen. The IR data in this spectral region suggest that the presence of TPFBu in the nN117 membrane slightly influences the morphology of the hydrophobic domains of the membrane, maintaining primarily the features of both the pristine PCIL and the nN117 phases, whereas TMS has a strong effect on the overall structure of the matrix. The main spectral features of TMS disappear, and the profiles of CF regions of nN117 are significantly modified. These results are in agreement with the previously discussed DSC results. This trend also is revealed throughout the entire lower frequency region of the spectra. In general, whereas the NTMS spectrum can be described as a result of interactions between nN117 and the TMS component, the NTPFBu spectrum is clearly dominated by peaks associated with TPFBu. This trend can be seen also in the C−O−C stretching modes of the polyether side chain visible in the spectrum of nN117 at 980 and 967 cm^{-1}.[13,16] These ether modes are clearly present in both the nN117 and the NTMS spectra but are not visible in the spectrum of NTPFBu. Results indicate that in CF region of: (a) NTPFBu, TPFBu forms PCIL nanodomains of larger size, which are segregated in the bulk membranes, and (b) NTMS, TMS is completely dispersed in bulk material and forms a uniform solvation shell on the hydrophobic and hydrophilic domains of the host nN117 polymer owing to the strong nN117···TMS interactions. As a result of these latter interactions, in the NTMS membrane there is no predominance of the TMS spectral features in the CF region. This phenomenon is easily explained by considering that the spectral features of fluorocarbon backbone hydrophobic domains, which are weaker in intensity in nN117 as compared to the bands of the pristine PCILs, are diagnostic vibrational modes of the nN117···TMS interactions.

4. CONCLUSIONS

This Article reports the synthesis and the study of two new PEMs based on nN117 doped with two ILs, TMS and TPFBu. The membranes are obtained by a three-step protocol: (1) synthesis of the PCILs; (2) neutralization of N117 by TEA, yielding nN117; and (3) preparation of the PCIL-doped membranes by soaking nN117 in the PCILs. The materials are characterized with TG, DSC, and FT-IR spectroscopy, whereas the mechanical properties of the NTMS and NTPFBu are analyzed by DMA. The studies reveal that the anionic substitution of perfluorobutanesulfonate for methanesulfonate is reflected in varying thermal and structural properties of both the pristine ILs and the doped membranes due to increased steric hindrance, acidity, and hydrophobicity of the perfluorobutanesulfonate anion. The anion is responsible for different interactions between the PCIL and nN117. A stronger PCIL−nN117 interaction stimulates the organization of the fluorocarbon domains of the host nN117 in a microcrystalline structure and reduces the degree of crystallinity of the PCILs inside the membranes. The FT-IR studies provide evidence of the effect that ILs have on the structure of nN117 membrane components and confirm the significant difference between PCILs in their interactions with the host nN117 polymer. The presence of bands between 2450 and 2560 cm^{-1} associated with the $N-H^+$ stretching modes indicates different hydrogen-bonding environments for the $TEAH^+$ cations. Shifts in this band are seen upon incorporation of the PCILs in the nN117 matrix signifying a change in the interaction between the anions and cations. NTMS shows vibrational bands typical of perfluorinated chains contained inside the nN117 hydrophobic domains, whereas the NTPFBu spectrum is dominated by bands of the IL. The difference in the spectra in the CF_2 stretching region supports the DSC analysis that indicates a higher degree of crystallinity for NTMS. Structural differences between NTMS and NTPFBu also are reflected in the mechanical properties. Differences in storage modulus values are due to the dimensions of the nanodomains and the structural organization of the PCILs when they are present inside the polymeric membranes. Both doped membranes present a thermomechanical stability up to 140 °C and the presence of four mechanical transitions. These transitions shift to lower temperatures in the doped membranes due to the plasticizing effect of the IL contained within. The IL solvates and plasticizes the nN117 side group reducing the cross-linking dipolar interactions inside the polar domains resulting in a mobility increase in the main fluorocarbon backbone chains. This phenomenon increases in the order NTPFBu < NTMS. This work aims to characterize PEMs that can function in fuel cells operating under anhydrous conditions by focusing on the structural differences between TMS and TPFBu and the effect of the PCIL structure on the membrane properties. To fully evaluate these membranes for application in fuel technologies, there must be a clear understanding of the electrical properties, particularly the proton conduction mechanism. The electrical properties and the mechanism of conduction will be discussed in detail in a second publication on these PEMs.

AUTHOR INFORMATION

Corresponding Author
*E-mail: vito.dinoto@unipd.it.

ACKNOWLEDGMENT

This research was funded by the Italian MURST project PRIN2008, entitled "Direct Polymer Electrolyte Membrane Fuel Cells: Synthesis and Study in Prototype Cells of Hybrid Inorganic−organic Membranes and Electrode Materials".

REFERENCES

(1) O'Hayre, R.; Cha, S. W.; Prinz, F. B. *Fuel Cell Fundamentals*; Wiley: Hoboken, NJ, 2006.

(2) Vielstich, W.; Lamm, A.; Gasteiger, H. A. *Handbook of Fuel Cells: Fundamentals Technology and Applications*; Wiley: Chichester, England, 2003; Vol. 3.

(3) Wainright, J. S.; Litt, M. H.; Savinell, R. F. High-temperature Membranes. In *Handbook of Fuel Cells*; Vielstich, W., Lamm, A., Gasteiger, H. A., Eds.; Wiley: Chichester, England, 2003; Vol. 3, pp 436−446.

(4) Li, Q.; He, R.; Jensen, J. O.; Bjerrum, N. J. *Chem. Mater.* **2003**, *15*, 4896–4915.

(5) Satyapal, S. In *Hydrogen and Fuel Cell Activities*, 5th International Conference on Polymer Batteries & Fuel Cells, Argonne, Illinois, U.S. Department of Energy: Energy Efficiency & Renewable Energy: Argonne, IL, 2011.

(6) Di Noto, V.; Piga, M.; Pace, G.; Negro, E.; Lavina, S. *ECS Trans.* **2008**, *16*, 1183–1193.

(7) Lee, S. Y.; Ogawa, A.; Kanno, M.; Nakamoto, H.; Yasuda, T.; Watanabe, M. *J. Am. Chem. Soc.* **2010**, *132*, 9764–9773.

(8) Lin, B.; Cheng, S.; Qiu, L.; Yan, F.; Shang, S.; Lu, J. *Chem. Mater.* **2010**, *22*, 1807–1813.

(9) Yan, F.; Yu, S.; Zhang, X.; Qiu, L.; Chu, F.; You, J.; Lu, J. *Chem. Mater.* **2009**, *21*, 1480–1484.

(10) Greaves, T. L.; Drummond, C. J. *Chem. Rev.* **2008**, *108*, 206–237.

(11) Martinelli, A.; Matic, A.; Jacobsson, P.; Borjesson, L.; Fernicola, A.; Panero, S.; Scrosati, B.; Ohno, H. *J. Phys. Chem. B* **2007**, *111*, 12462–12467.

(12) Noda, A.; Susan, A. B.; Kudo, K.; Mitsushima, S.; Hayamizu, K.; Watanabe, M. *J. Phys. Chem. B* **2003**, *107*, 4024–4033.

(13) Di Noto, V.; Negro, E.; Sanchez, J. Y.; Iojoiu, C. *J. Am. Chem. Soc.* **2010**, *132*, 2183–2195.

(14) Martinez, M.; Molmeret, Y.; Cointeaux, L.; Iojoiu, C.; Lepretre, J. C.; El Kissi, N.; Judeinstein, P.; Sanchez, J. Y. *J. Power Sources* **2010**, *195*, 5829–5839.

(15) Di Noto, V.; Gliubizzi, R.; Negro, E.; Vittadello, M.; Pace, G. *Electrochim. Acta* **2007**, *53*, 1618–1627.

(16) Di Noto, V.; Piga, M.; Lavina, S.; Negro, E.; Yoshida, K.; Ito, R.; Furukawa, T. *Electrochim. Acta* **2010**, *55*, 1431–1444.

(17) Di Noto, V.; Piga, M.; Piga, L.; Polizzi, S.; Negro, E. *J. Power Sources* **2008**, *178*, 561–574.

(18) Di Noto, V.; Gliubizzi, R.; Negro, E.; Pace, G. *J. Phys. Chem. B* **2006**, *110*, 24972–24986.

(19) Page, K. A.; Cable, K. M.; Moore, R. B. *Macromolecules* **2005**, *38*, 6472–6484.

(20) Hodge, I. M.; Eisenberg, A. *Macromolecules* **1978**, *11*, 289–293.

(21) Yeo, S. C.; Eisenberg, A. *J. Appl. Polym. Sci.* **1977**, *21*, 875–898.

(22) Lin-Vien, D.; Colthup, N. B.; Fateley, W. G.; Grasselli, J. G. *The Handbook of Infrared and Raman Characteristic Frequencies of Organic Molecules*; Academic Press, Inc.: New York, 1991.

(23) Socrates, G., *Infrared and Raman Characteristic Group Frequencies*, 3rd ed.; John Wiley & Sons: New York, 2001.

(24) DeTar, D. F.; Novak, R. W. *J. Am. Chem. Soc.* **1970**, *92*, 1361–1365.

(25) Giffin, G. A.; Boesch, S.; Bopege, D. N.; Powell, D. R.; Wheeler, R. A.; Frech, R. *J. Phys. Chem. B* **2009**, *113*, 15914–15920.

(26) Gruger, A.; Regis, A.; Schmatko, T.; Colomban, P. *Vib. Spectrosc.* **2001**, *26*, 215–225.

THE JOURNAL OF PHYSICAL CHEMISTRY C

ARTICLE

pubs.acs.org/JPCC

Influence of Anions on Proton-Conducting Membranes Based on Neutralized Nafion 117, Triethylammonium Methanesulfonate, and Triethylammonium Perfluorobutanesulfonate. 2. Electrical Properties

Vito Di Noto,*[,†,‡] Matteo Piga,[†] Guinevere A. Giffin,[†] Sandra Lavina,[†] Eugene S. Smotkin,[§] Jean-Yves Sanchez,[∥] and Cristina Iojoiu[∥]

[†]Dipartimento di Scienze Chimiche, Università di Padova, Via Marzolo 1, I-35131 Padova (Pd), Italy

[‡]Istituto di Scienze e Tecnologie Molecolari, ISTM-CNR and INSTM, Dipartimento di Scienze Chimiche, Via Marzolo 1, I-35131 Padova (Pd), Italy

[§]Northeastern University, Department of Chemistry and Chemical Biology, 360 Huntington Avenue, Boston, Massachusetts 02115, United States

[∥]Laboratoire d'Electrochimie et de Physico-chimie des Matériaux et des interfaces, UMR 5631 CNRS-INPG, 1139 Rue de la Piscine, associée à l'UJF, ENSEEG B.P. 75 38402 Saint-Martin-d'Heres, Cedex, France

Supporting Information

ABSTRACT: The electrical properties of a Nafion proton exchange membrane change dramatically when neutralized and then doped with a proton-conducting ionic liquid (PCIL). Broadband electric spectroscopy elucidates the molecular relaxation and polarization phenomena of neutralized Nafion (nN117) doped with triethylammonium methanesulfonate (TMS) and triethylammonium perfluorobutanesulfonate (TPFBu) ionic liquids. These data, coupled with those of part 1 suggest proton conduction mechanisms for both the pure PCILs and in PCIL-doped nN117. At 130 °C, the PCILs have conductivities of $\sigma_{TMS} = 1.4 \times 10^{-2}$ S/cm and $\sigma_{TPFBu} = 9 \times 10^{-3}$ S/cm, while correspondingly doped nN117 have conductivities of $\sigma_{NTMS} = 6.1 \times 10^{-3}$ S/cm and $\sigma_{NTPFBu} = 1.8 \times 10^{-3}$ S/cm. The pure PCILs show three interfacial polarizations associated with proton transfer mechanisms above the melting point. PCIL-doped nN117 also has three interfacial polarizations that depend on the nanostructure characteristics of the PCIL sorbed within the nN117 polar domains. Below the PCIL melting point, doped nN117 has two dielectric relaxations, α and β, associated with dipolar relaxations involving both the sorbed PCILs and the ionomer matrix. The data indicate a long-range charge transfer process that occurs through proton exchange between cationic clusters. Segmental motion of the polymer chains and the molecular dimensions of the ionic liquid nanoaggregates mediate this charge transfer.

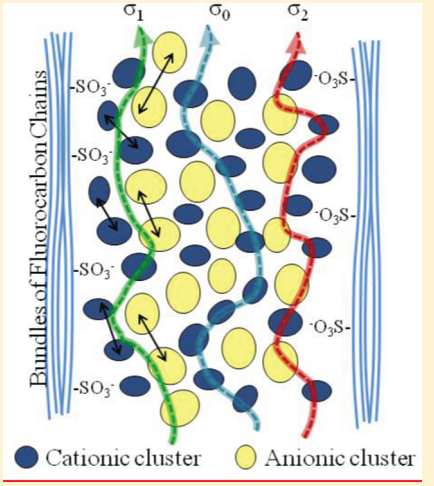

1. INTRODUCTION

Proton exchange membranes are extensively used as fuel cell electrolytes.[1] Of particular interest are membranes that operate above 120 °C without the need for humidification. These conditions are advantageous because thermal management is easier; platinum-based catalysts have higher activities; and the higher temperatures render catalysts less susceptible to carbon monoxide poisoning.[1,2] Recently, membranes based on Dupont Nafion 117[3] neutralized with the triethylammonium ion and doped with proton-conducting ionic liquids (PCILs) have shown improved thermal and mechanical properties and an increased range of operating temperatures compared to Nafion 117.[4] In this series of publications, triethylammonium neutralized Nafion impregnated with triethylammonium methanesulfonate (TMS) and triethylammonium perfluorobutanesulfonate (TPFBu) PCILs were studied to evaluate the effect of the PCIL anion on the properties of PCIL-doped neutralized Nafion. In part 1,[5] the thermal and mechanical properties of these two novel membrane systems were characterized, and the structures and interactions between system components were correlated. In this part 2, the electrical properties and the proton conduction mechanism are investigated using broadband electric spectroscopy (BES).

BES is ideal for the correlation of composite electrolyte structures to physical properties, particularly when paired with other techniques such as nuclear magnetic resonance or dynamic mechanical analysis. Charge transfer and dielectric relaxation data obtained by BES are connected to the material structure to determine charge conduction mechanisms. BES has been extensively used to study a

Received: May 6, 2011
Revised: December 6, 2011

 © XXXX American Chemical Society dx.doi.org/10.1021/jp204242q | J. Phys. Chem. C XXXX, XXX, 000–000

wide variety of systems,[6] including more recent studies focused on the electrical properties of ionic liquids.[7−9]

Ionic liquids are a class of salts characterized by relatively low melting points; i.e., they can exist in a liquid state at or close to room temperature. Ionic liquids are of intense interest for a variety of applications, including synthesis, green chemistry, biotechnology, electrochemistry, and energy conversion devices.[10−16] It is important to understand both the morphology and the types of motion and relaxation that exist within these materials. Recent studies have shown that ionic liquids self-assemble into nanoscale aggregates, both as pristine ionic liquids and in solution.[7,17−19] The presence of nanoscale aggregates can result in multiple dielectric relaxation phenomena. There is an abundance of literature discussing relaxation phenomena in imidazolium-type ionic liquids.[17−19] For example, Nakamura and Shikata[7] reveal the presence of three dielectric relaxation phenomena in 1-alkyl-3-methylimidazolium ionic liquids. The slower relaxation events are dependent on several factors including the volume, viscosity, and dipole of the ions that are present and are attributed to rotational modes of the ions.[7] The faster relaxation events are attributed to interionic motion.[7] For electrochemical and energy conversion applications, understanding ion-conduction phenomena is key to improving performance. The presence of aggregates in ionic liquids can also result in multiple conduction phenomena with varying relaxation times. These phenomena are attributed to the presence of electrode polarizations resulting from long-range charge motion or interfacial polarizations arising from the build-up of charge at the variety of domain boundaries within the material.[4,6]

For ionic liquids at room temperature, molecular relaxations are typically found in the giga and terahertz frequencies.[8] Identifying relaxation modes occurring at lower frequencies has been difficult because such responses are "swamped" by conduction phenomena. This work shows that PCIL molecular relaxations can be probed at lower frequencies (i.e., millihertz to megahertz) by conducting the measurements at significantly reduced temperature. This innovation enables the characterization of the electric properties of both the pristine PCILs and the PCIL-impregnated membranes above and below the PCIL melting points (T_m). These studies reveal the presence of molecular relaxations below the T_m and several conduction phenomena above T_m. The results elucidate charge conduction mechanisms for both the pristine ionic liquids and the doped membranes.

2. EXPERIMENTAL SECTION

2.1. Ionic Liquid Syntheses and Membrane Preparation. The PCILs TMS and TPFBu and the doped membranes were prepared as previously reported.[5] The triethylammonium neutralized Nafion 117 (nN117) treated with TMS and TPFBu are referred to as NTMS and NTPFBu, respectively. The NTMS membrane contains 25 wt % of TMS, while the NTPFBu membrane contains 40 wt % of TPFBu.

2.3. Instruments and Methods. BES measurements were collected over the frequency range from 10^{-2} to 10^{7} Hz using a Novocontrol Alpha analyzer from −100 to 150 °C in 10 °C intervals with accuracy better than ±0.1 °C. The temperature was controlled with a homemade cryostat equipped with a gaseous nitrogen heating−cooling system. Samples were placed between two gold disk electrodes with a 20 mm diameter and a 1 mm thickness. To avoid exposure of the samples to ambient humidity, the samples and electrodes were loaded into a homemade Teflon cell inside a drybox.

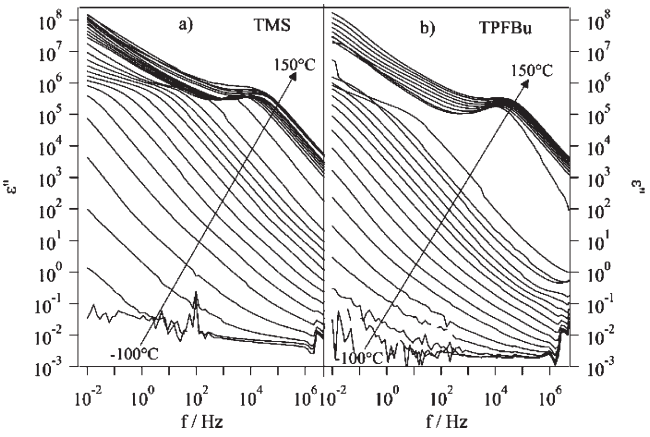

Figure 1. Profiles of ε'' as a function of frequency at temperatures between −100 and 150 °C for PCILs: (a) TMS and (b) TPFBu.

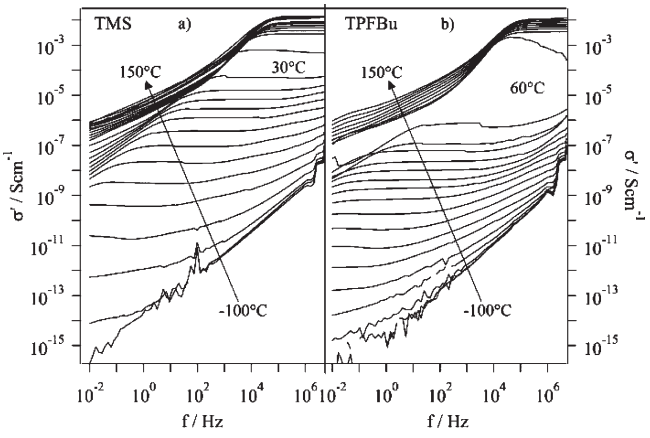

Figure 2. Profiles of σ' as a function of frequency at temperatures between −100 and 150 °C in steps of 10 °C for TMS (a) and TPFBu (b).

3. RESULTS AND DISCUSSION

BES measurements are utilized to examine conductivity and dielectric relaxations and to investigate the mechanism of charge conduction. For pure TMS and TPFBu, the imaginary component of the permittivity (ε'') and the real component of the conductivity (σ') versus frequency over a 250 °C temperature range are shown in Figures 1 and 2, respectively. Several trends are evident in Figure 1. Melting of the ionic liquid increases ε'' above 30 °C for TMS and above 60 °C for TPFBu. These data are consistent with DSC measurements.[5] With increasing temperature, a peak with values of ε'' ranging from 10^5 to 10^6 appears and moves toward higher frequencies. This peak exhibits a large shift to higher frequency at the T_m of the ionic liquid. At temperatures below 0 °C and frequencies above 100 Hz the presence of a dielectric relaxation for both TMS and TPFBu is identified by an inflection point in ε''. Finally, for lower frequencies and temperatures near and above the PCIL melting point, ε'' increases with decreasing frequency.

The σ' spectra (Figure 2) undergo a step increase of 2−3 orders of magnitude in conductivity that corresponds to the ionic liquid T_m. This trend is more evident for TPFBu than TMS. The profiles of σ' show an inflection point, marking the beginning of a plateau that is correlated with the appearance of the intense peaks

dx.doi.org/10.1021/jp204242q | J. Phys. Chem. C XXXX, XXX, 000–000

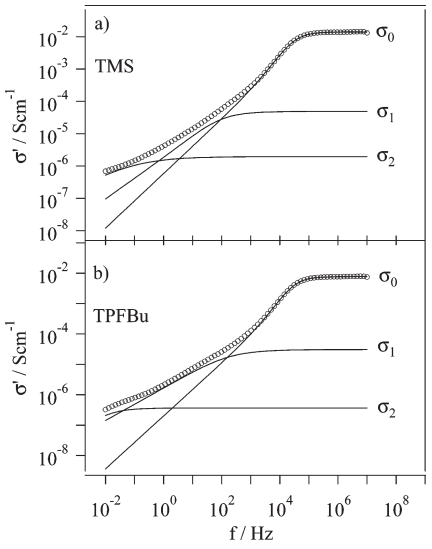

Figure 3. Spectra of σ' as a function of frequency measured at 120 °C for TMS (a) and TPFBu (b). σ_0, σ_1, and σ_2 are the conductivities associated with polarization phenomena.

in the spectra of ε''. This plateau indicates the "bulk" conductivity, σ_{dc}, of the ionic liquid.[20,21] The presence of the intense peak in ε'' and the corresponding decline in σ' indicates that this behavior corresponds to an electrode polarization event, caused by the measurement electrodes, that blocks the charge carriers of the PCILs at the interface of the electrode and the electrolyte.[6,22] Profiles of σ', similar to those reported in Figure 2, were recently obtained for "imidazolium-based" ionic liquids and resulted from the combination of the bulk conductivity and the electrode polarization.[23,24] Comparing the profiles for the permittivity and the conductivity reported in Figures 1 and 2 show: (a) the increase of σ' below T_m and above 100 Hz due to the presence of a dielectric relaxation, and (b) for low frequency and temperatures close to or higher than T_m, the increase in ε'' suggests the presence of polarization phenomena other than the electrode polarization.

Polarization phenomena occur where a density of charge accumulates in ionically conducting materials due to the presence of suitable morphologies and interactions within the material. The charges which form the accumulated density cannot simply move through the bulk material but are associated with interfaces present within the matrix. The electrode polarization phenomenon results from the accumulation of charge at the electrode−material interfaces when blocking electrodes are used. Interfacial polarization occurs in heterogeneous materials due to the accumulation of charge densities at the interfaces between two nanodomains with different dielectric constants and conductivities.

All polarization events can be described as a number of resistance and complex capacitance elements connected in series. The conductance accounts for the exchange of charge between different domains of accumulated charge, while the capacitance describes the accumulation of charge at interfaces. It can be hypothesized that: (a) the accumulation of charge at the electrode−material interface (electrode polarization) occurs when blocking electrodes are used and when a high density of charge at the electrode−material interfaces results from very fast microscopic exchange processes in bulk materials due to the direct current conductivity (σ_{DC}); (b) a local accumulation of charge is produced in bulk materials (interfacial polarization) due to the presence of domains with different permittivities. The interfacial conductivity is associated with charge exchange between different local accumulations of charge at the interfaces between domains with different permittivities.

The electric response of the pure ionic liquids above the T_m is characterized by the presence of three distinct polarization phenomena associated with σ_0, σ_1, and σ_2. These conductivity components, determined from eqs 1 and 2 shown below, can be seen in the spectra of σ' at 120 °C for TMS and TPFBu (Figure 3).

$$\sigma^*(\omega) = i\omega\varepsilon_0\varepsilon^*(\omega) \quad (1)$$

In eq 1, $\sigma^*(\omega) = \sigma'(\omega) + i\sigma''(\omega)$ and $\varepsilon^*(\omega) = \varepsilon'(\omega) - i\varepsilon''(\omega)$ are the complex electric conductivity and permittivity, respectively; ε_o is the dielectric permittivity in vacuum; and ω is the radial frequency in rad/s.

At high temperatures, the presence of polarizations occurring at different frequencies is typically observed in ionic conductors consisting of two or more phases with different dielectric constants.[6] For TMS and TPFBu, this scenario could occur assuming the partial formation of nanoaggregates in a variety of morphologies induced by van der Waals interactions between the alkyl chains in both the cationic and the anionic components of the PCILs. This hypothesis is consistent with the work of Di Noto et al. that suggests the ionic liquid triethylammonium trifluoromethanesulfonate (TEATF) confined in the nN117 membrane has a nanostructure in which the triflate anions organize into aggregates.[4] Martinez et al. have shown that the presence of the perfluorinated butane chain in TPFBu results in a reduction of the degree of dissociation, as compared to TEATF and TMS, and the possible formation of micellar-like structures.[25] The possibility of aggregation in "dialkyl-imidazolium-based" room temperature ionic liquids (RTILs) was reported by Turton et al.[19] They found that data from both optical Kerr effect spectroscopy and BES suggested the formation of clusters due to interactions between the imidazolium rings or due to the coupling of the cation alkyl tails. Triolo et al. used X-ray diffraction to investigate alkylimidazolium-based RTILs to demonstrate the existence of nanosegregation induced by the presence of the alkyl chains.[18,26] Dyson et al. detected the formation of aggregates between 30 and 100 °C with a predominance of cationic and anionic complexes such as C_2A^+, $C_3A_2^+$, CA_2^-, and $C_2A_3^-$ for *N*-butylpyridinium tetrafluoroborate using Electrospray Ionization Mass Spectrometry (ESI-MS).[17]

The presence of aggregates in PCILs was discovered 30 years ago by Kholer et al.[27,28] during a study of the thermodynamic and physicochemical properties of a mixture of acetic acid and triethylamine. They suggested that the formation of a A_3B complex (A = acetic acid, B = triethylamine) occurred due to the attractive interactions between the polar molecule AB and an acetic acid dimer.[27,28] Conductometric measurements by Hojo et al.[29] showed the formation of aggregates containing ions of the type M_2X^+ (MX_2^-) and M_2X_2 for trialkylammonium salts in the presence of aprotic organic solvents.[29] Using ESI-MS, Kennedy et al. found the following for PCILs based on dialkylammonium nitrates: (a) ethyl, propyl, and butylammonium nitrates formed stable $C_8A_7^+$ nanoaggregates (C = cation, A = anion) where the abundance and stability of these aggregates is independent of the

dx.doi.org/10.1021/jp204242q |*J. Phys. Chem. C* XXXX, XXX, 000–000

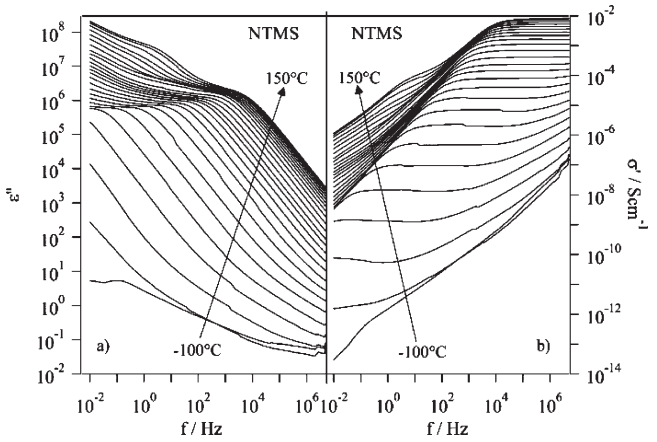

Figure 4. Profiles of (a) ε'' and (b) σ' as a function of temperature for NTMS.

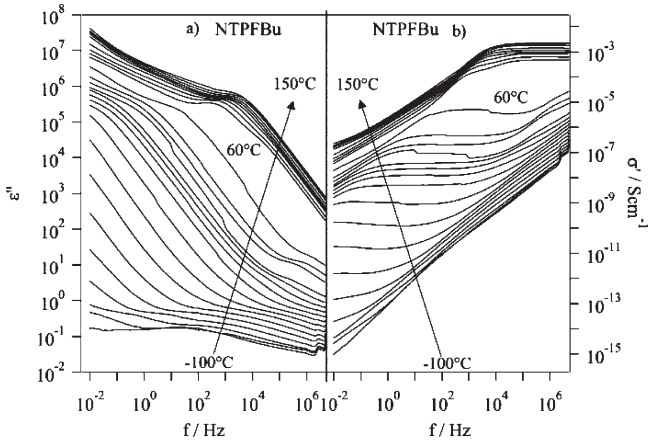

Figure 5. Profiles of (a) ε'' and (b) σ' as a function of temperature for NTPFBu.

length of the cation alkyl chain; (b) anionic aggregates are equally dispersed in clusters of different dimensions; (c) the dimensions of the cationic clusters are reduced with increasing order of the amine cations, i.e., from primary, secondary, and tertiary amines, due to increased steric hindrance and fewer hydrogens available for the formation of hydrogen bonds; (d) the formation of nanoaggregates increases in the presence of anions with higher charge densities, such as the nitrate ion, and decreases with increasing anionic dimension.[30] The literature consistently points out that the PCILs containing primary, secondary, and tertiary alkylammonium cations form both ionic and neutral aggregates.

The spectra of ε'' and σ' measured for NTMS and NTPFBu shown in Figures 4 and 5 are very similar to those of their respective PCILs, suggesting that the electric properties of the doped membranes are strongly influenced by the PCIL. The profiles of ε'' and σ' of the polymeric membranes reveal: (a) the presence of an intense peak due to electrode polarization with values of ε'' of the order of 10^6; this peak moves to higher frequency with increasing temperature and corresponds to the beginning of a plateau in σ' associated with the "bulk" conductivity σ_0 of the material; (b) the absence of a sharp increase in ε'' and σ' for NTMS at the melting point $T_{m2,TMS}$= 38.4 °C; (c) an increase in the values of ε'' and σ' for NTPFBu at $T_{m2,TPFBu}$= 61.3 °C;

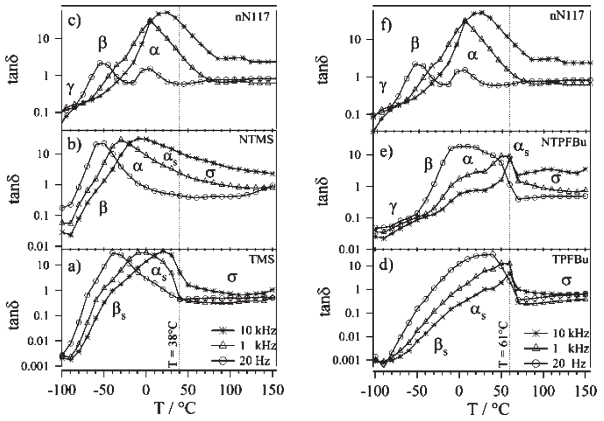

Figure 6. Profiles of tan δ as a function of temperature measured at 20 Hz, 1 kHz, and 10 kHz for: (a) TMS, (b) NTMS, (d) TPFBu, and (e) NTPFBu. For the sake of comparison, parts (c) and (f) report the profiles of tan δ for nN117 presented by Di Noto et al.[4]

(d) the presence of a dielectric relaxation at temperatures below the PCIL melting point and frequencies higher than 100 Hz; and (e) an increase of ε'' and a decrease of σ' with decreasing frequency for frequencies less than 1000 Hz and temperatures higher than 50 °C that suggest the presence of different polarization phenomena. In the polymer membranes, the presence of multiple polarizations is due to the accumulation of charge at interfaces between domains with different dielectric constants.[4] Free charge carriers migrating through the bulk membranes under the influence of an applied field may become trapped due to charge amassed at a barrier such as the hydrophobic moiety of low permittivity domains. This phenomenon results in the creation of a localized accumulation of charge that will induce mirrored charges on the skin of hydrophobic domains producing a macroscopic dipole moment and constitute a mechanism of polarization in the bulk membranes (interfacial polarization). The doped membranes are characterized by the coexistence of hydrophobic domains with lower permittivity (≈2.2) consisting of the fluorocarbon chains of nN117 and hydrophilic polar domains with slightly higher permittivities consisting of the anionic groups of the nN117 side chains and the ionic liquids.[31,32] Rollet et al. report that hydrated Nafion 117 membranes neutralized with $N(CH_3)_4^+$ have segregated hydrophilic and hydrophobic nanodomains, where the interfaces consist of the negatively charged sulfonate groups and the $N(CH_3)_4^+$ cations.[33] These data suggest the existence of increased interfacial polarization phenomena.[4,34]

In the ε'' profiles of the PCILs and the doped membranes, dielectric relaxations can be seen at temperatures below the melting point of the PCILs. These dielectric relaxations can be easily observed by plotting the values of tan $\delta = \varepsilon''/\varepsilon'$ as a function of temperature at three reference frequencies: 20 Hz, 1 kHz, and 10 kHz. These plots are shown in Figure 6 for the pure PCILs (parts a and d), the doped membranes (parts b and e), and the nN117 matrix (parts c and f).[4] Below the melting point, the PCILs exhibit the presence of α_s and β_s relaxations that are associated with a solid state order−disorder transition linked to the glass transition temperature (T_g) and the local "bulk" relaxation modes of the PCILs, respectively.[4] The spectra of nN117 reveal typical α and β relaxations associated with a conformational transition involving the main fluorocarbon chains (α) and the polyether side groups (β) of the nN117 matrix and γ relaxations related to the local fluctuations of the

dx.doi.org/10.1021/jp204242q | J. Phys. Chem. C XXXX, XXX, 000–000

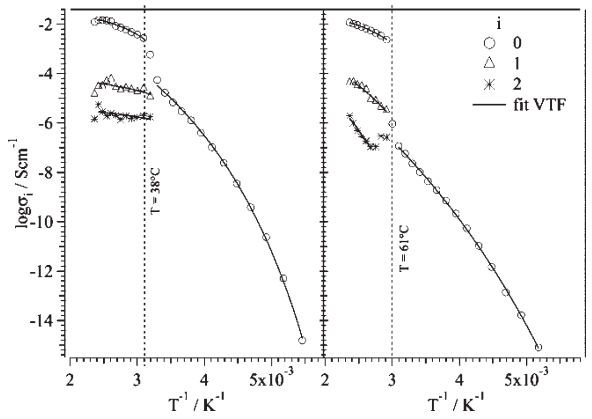

Figure 7. Log plot of conductivities σ_0, σ_1, and σ_2 as a function of reciprocal temperature for the PCILs: (a) TMS and (b) TPFBu. The dashed vertical line shows the melting point of the ionic liquid.

CF_2 groups on the main fluorocarbon chain.[4] α_s and β_s are relaxations that are completely different from the α, β, and γ relaxations that occur in membranes. For NTMS and NTPFBu, the profiles of tan δ show the presence of transitions associated with both the polymeric matrix and the PCILs. Below the PCIL melting points, in agreement with the DSC profiles,[5] there are peaks connected to β modes (T less than 0 °C) and α modes (T between 0 °C and the melting point). These peaks are associated with the relaxation of the nN117 matrix interacting with the ionic liquid. In agreement with the profiles of tan δ obtained from the DMA analysis,[5] the tan δ spectra of the membranes (Figure 6) show the appearance of the electric α_{pc} transition at temperatures above approximately 70 °C. The α_{pc} transition, which is associated with the presence of polarization phenomena, is derived from the long-range movement of the fluorocarbon chains and the side groups due to reduced electrostatic interactions between the dipolar domains. In addition, for NTPFBu at temperatures below −50 °C, there is a γ transition related to the short-range molecular fluctuations of the CF_2 groups belonging to the main nN117 fluorocarbon chain.

For all of the investigated materials, to determine the conductivity values and to investigate the relaxation times associated with the polarization phenomena and the dielectric relaxations, the experimental profiles of $\varepsilon^*(\omega) = \varepsilon'(\omega) - i\varepsilon''(\omega)$ are fit with eq 2.[4,34,35]

$$\varepsilon^*(\omega) = -i\left(\frac{\sigma(T)}{\varepsilon_0\omega}\right)^{N(T)} + \sum_{k=0}^{2}\frac{\sigma_k(i\omega\tau_k)^{\gamma_k}}{i\omega[1 + (i\omega\tau_k)^{\gamma_k}]} + \sum_{j=1}^{2}\frac{\Delta\varepsilon_j(T)}{[1 + (i\omega\tau_j(T))^{\mu_j(T)}]} + \varepsilon_\infty \quad (2)$$

The first term describes the conductivity of the material at frequencies lower than those experimentally measured. The second term accounts for the electrode ($k = 0$) and interfacial ($k = 1,2$) polarization phenomena. The variables σ_k and τ_k are the conductivity and relaxation time associated with the kth polarization event, while γ_k is a shape parameter that describes the broadness and asymmetry of the kth peak. The third term expresses the dielectric relaxation through a Cole−Cole type equation.[36] Specifically, $\omega = 2\pi f$ is the angular frequency of the electric field; τ_j is the relaxation time of the jth event of intensity $\Delta\varepsilon_j$; and μ_j is a shape parameter bound to the distribution of the relaxation times associated with the jth event. Two different indices, k and j, are used in the terms of eq 2 to represent relaxation events that have different physical meanings. Equation 2 is used to fit simultaneously the experimental spectra of tan δ, ε', ε'', σ', and σ'' which were determined from the permittivity spectra from eq 1. The experimental data are fit using: (a) one conductivity σ_0 and two dielectric relaxations, α and β, at temperatures less than the melting point of the ILs and (b) three conductivity terms σ_0, σ_1, and σ_2 at temperatures higher than the melting point. The values of the conductivities σ_0, σ_1, and σ_2 are reported as a function of reciprocal temperature for TMS and TPFBu in Figure 7. The values of σ_0 determined by the fit correspond to those read directly from the high-frequency plateau of the σ' spectra.[20,21] In the solid PCILs, proton conduction must occur via proton hopping between acid and base sites. The logarithm of σ_0 as a function of reciprocal temperature has a Vogel−Tammann−Fulcher (VTF) form.[36] At temperatures below the PCIL melting points, the σ_{0TMS} values are about 3 orders of magnitude higher than those of σ_{0TPFBu}. The higher values of σ_{0TMS} are attributed to the smaller size of the constituent PCIL anion: TPFBu forms larger nanoaggregates because the perfluorobutane group of TPFBu is larger than the TMS methyl group. This nanometric TPFBu morphology increases the median distance between the proton hopping sites and thus reduces the overall conductivity. The activation energy and the temperature T_0 obtained from the fit parameters are 16 ± 1 kJ/mol and 124 K for TMS and 21 ± 1 kJ/mol and 112 K for TPFBu.

Above the PCIL melting points, the $\log(\sigma_0)$ vs reciprocal temperature follows VTF-like behavior and yields activation energies of 2.3 ± 0.1 kJ/mol and 3.2 ± 0.1 kJ/mol for TMS and TPFBu, respectively. These values are in agreement with PCIL activation energies between 3.4 and 5.3 kJ/mol and values of T_0 between −100 and −60 °C reported by Iojoiu et al.[37] For TEATF, Di Noto et al. determined an activation energy for conduction of the "bulk" material of 1.37 ± 0.04 kJ/mol above the melting point.[4] For TMS and TPFBu, the values of T_0 obtained from the VTF fit are 245 and 241 K, respectively. These values are in agreement with the T_g values of these PCILs determined by DSC measurements.[5] Above the T_m, σ_{0TMS} is larger than σ_{0TPFBu} because of the higher viscosity of the fluorinated ionic liquid.[25] At 120 °C, σ_{0TMS} and σ_{0TPFBu} are 0.0137 and 0.0076 S cm^{-1}, respectively. The σ_0 values enable calculation of diffusion coefficients for ions involved in the long-range conduction through the Nernst−Einstein equation.[38]

$$D^{ch} = \frac{\sigma_0 RT}{F^2 c} \quad (3)$$

In eq 3, F is Faraday's constant; c is the molar concentration of the ionic liquid; T is in degrees Kelvin; and R is the universal gas constant. The diffusion coefficients from 100 to 150 °C are found to be between 5×10^{-7} and 1×10^{-6} cm^2 s^{-1} for TMS and between 5.3×10^{-7} and 1.3×10^{-6} cm^2 s^{-1} for TPFBu.

Judeinstein et al. measured diffusion coefficients of several PCILs containing the $TEAH^+$ cation using pulse field gradient nuclear magnetic resonance (PFG-NMR); they obtained similar diffusion coefficient values for protons (D^+), anions (D^-), and triethylamine (D^{TEA}).[39] Martinez et al. reported diffusion coefficients determined with PFG-NMR at 120 °C of $D^+ = 2.71 \times 10^{-6}$ cm^2 s^{-1}, $D^{TEA} = 2.67 \times 10^{-6}$ cm^2 s^{-1}, and $D^- = 2.38 \times 10^{-6}$ cm^2 s^{-1} for TMS and for TPFBu values of $D^+ = 1.14 \times 10^{-6}$ cm^2 s^{-1}, $D^{TEA} = 1.13 \times 10^{-6}$ cm^2 s^{-1}, and $D^- = 8.43 \times 10^{-7}$ cm^2 s^{-1}.[25] Almost identical

dx.doi.org/10.1021/jp204242q | J. Phys. Chem. C XXXX, XXX, 000–000

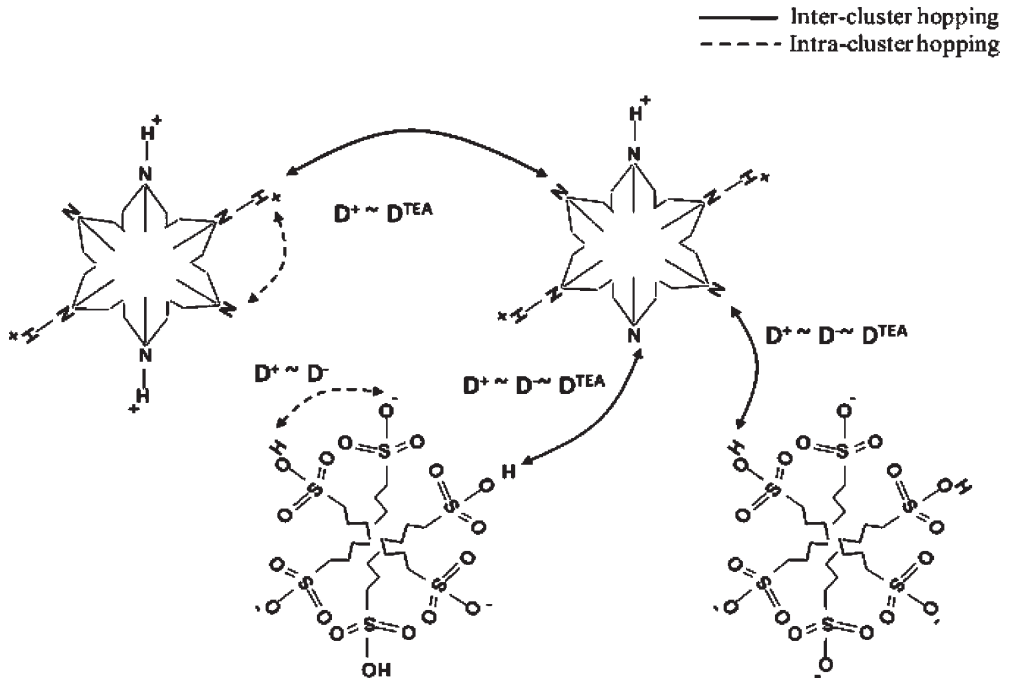

Figure 8. Scheme of the short-range mechanism of charge transfer due to proton hopping between the proton-donor and proton-acceptor sites of the ionic and neutral nanoaggregates present in the PCILs.

values were found for all species in diethylmethylammonium trifluoromethanesulfonate $\approx 4 \times 10^{-6}$ cm^2 s^{-1} at 120 °C by Lee et al.[40] The diffusion coefficients determined at 120 °C with eq 3 are $D^{ch} = 9.1 \times 10^{-7}$ cm^2 s^{-1} for TMS and $D^{ch} = 7.9 \times 10^{-7}$ cm^2 s^{-1} for TPFBu and are of the same order of magnitude as the D^+, D^-, and D^{TEA} values reported by Martinez et al.[25] It is noteworthy that diffusion coefficients estimated from conductivity measurements are generally lower than those obtained from PFG-NMR because PFG-NMR examines local dynamics, while conductivity measures long-range migration.[25,39] In contrast, the self-diffusion coefficients of cations derived from conductivity measurements and PFG-NMR are very similar for an aqueous electrolyte solution containing the TEA cation.[41] In solid membranes like those presented here, the mesoscopic structure which is based on the hydrophilic and hydrophobic domains of the Nafion host results in a differentiation between the long-range charge migration and the local charge migration. The local charge migration detected by NMR is associated with the exchange of protons between different neighboring Lewis base sites, while the long-range charge migration in bulk membranes is directly related to the charge migration between aggregates and therefore depends on the mesoscopic morphology of the materials. Similar values for the diffusion coefficients obtained from BES measurements and PFG-NMR[25] indicate that the mobility of protons, anions, and cations in the PCILs is comparable and that all three species participate in the mechanism of charge conduction. This suggests that proton conduction occurs through a vehicular-type mechanism where the proton is transported by the TEA cation ($D^+ \approx D^{TEA}$). However, this mechanism does not explain a diffusion coefficient for the anion that is almost the same as that for the proton and TEA, particularly in the case of TPFBu considering the difference in the molecular mass of the TEA cation (101 g mol^{-1}) and the perfluorobutanesulfonate anion (300 g mol^{-1}).

Martinez et al. have shown that TMS and TPFBu are partially dissociated by comparing the experimental conductivity (σ_{exp}) with those calculated from the diffusion coefficients D^+ and D^- (σ_{calc}). These authors estimate degrees of dissociation of 35% and 22% at 120 °C for TMS and TPFBu,[25] respectively, and ascribe the lower degree of dissociation for TPFBu to the partial formation of ionic micellar-like aggregates. The literature results and the appearance of phenomena attributed to interfacial polarization in the electric spectra (Figure 3) suggest that ionic liquids exist as nanoaggregates composed of both ionic and neutral species. The presence of these nanoaggregates is due to the formation of hydrogen bonds between the polar heads of the PCIL constituent ions and van der Waals interactions between the nonpolar groups of the PCIL cations and the anions. These nanoaggregates contain proton-acceptor ($-SO_3^-$, TEA) and proton-donor sites ($-SO_3H$, $TEAH^+$) that participate cooperatively and simultaneously in the mechanism of proton transport via short-range inter- and intracluster transfer according to the scheme reported in Figure 8. On a local scale, the mechanism of charge transfer shown in Figure 8 is the result of proton hopping between the donor and acceptor sites of ionic and neutral nanoaggregates present inside the PCILs indicating a Grotthuss-like process. The transfer of protons involves a constant exchange of the ionic species ($-SO_3^-$, $TEAH^+$) and their respective neutral forms ($-SO_3H$, TEA), which is limited by the rate of proton exchange resulting in $D^+ \approx D^- \approx D^{TEA}$ in accordance with the results of Martinez et al.[25]

BES measurements reveal three different PCIL conductivities, σ_0, σ_1, and σ_2, that could contribute to the long-range mechanism of charge conduction. Consideration of the PCIL nanomorphologies described above suggests the existence of three contributions to the long-range mechanism of proton transfer:

(1) *Cationic−Cationic "Homosite" Hopping (CCHH):* This processes describes proton transfer through cationic clusters.

(2) *Cooperative Cationic−Cationic Anionic−Anionic "Homosite" Hopping (CoCC&AA):* This relaxation event describes a proton transfer process that occurs through a concerted

dx.doi.org/10.1021/jp204242q | J. Phys. Chem. C XXXX, XXX, 000–000

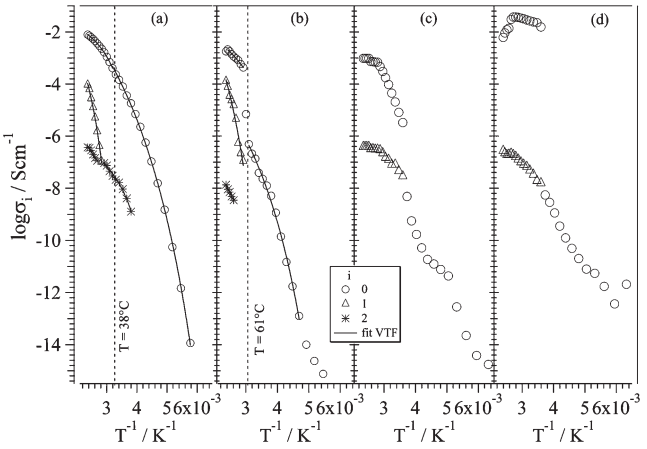

Figure 9. Log plot of conductivities σ_0, σ_1, and σ_2 as a function of reciprocal temperature for the doped membranes: (a) NTMS and (b) NTPFBu. The dashed vertical line shows the melting point of the ionic liquid. Parts (c) and (d) show the conductivities of nN117 and N117, respectively, as a reference.

mechanism between the cationic clusters and between anionic clusters.

(3) *Cationic—Anionic "Heterosite" Hopping (CAEH):* In this case the relaxation phenomenon takes into account a proton transfer process that occurs directly between cationic and anionic clusters.

A detailed explanation of the hypothesized mechanism of long-range charge transport can be found in the Supporting Information.

In this scenario, a mechanism for charge transfer can be derived from the BES measured conductivities and relaxation times. The conductivity σ_0 and the corresponding relaxation time τ_0 are associated with the CCHH mechanism, where the protons are transferred by a hopping mechanism between cationic clusters. These events involve the highest values of conductivity and are associated to the smallest relaxation time indicating the highest proton mobility. The conductivity σ_1 (associated with τ_1) is associated with the CoCC&AA mechanism and involves proton exchange between cationic clusters, which must correspond to a simultaneous exchange of protons between cationic and anionic clusters. It is clear that this event occurs at a longer relaxation time and is less frequent than the CCHH process. Finally, the CAEH mechanism is ascribed to the lowest conductivity values σ_2 and the longest relaxation times because of the low probability associated with the mutual transfer of protons between cationic and anionic clusters.

From the profiles reported in Figure 7, conductivities σ_1 and σ_2 are between 10^{-7} and 10^{-4} S/cm and show VTF behavior as a logarithmic function of reciprocal temperature. Activation energies for these conductivities are $E_{\sigma 1} = 2.0 \pm 0.5$ kJ/mol and $E_{\sigma 2} = 0.7 \pm 0.3$ kJ/mol for TMS and $E_{\sigma 1} = 7.9 \pm 0.5$ kJ/mol and $E_{\sigma 2} = 15 \pm 1$ kJ/mol for TPFBu. The activation energies associated with the conductivities σ_1 and σ_2 for TMS are not substantially different and are lower than those associated with TPFBu. This implies that the energy difference between the cationic and anionic clusters of TMS is smaller than the same difference in TPFBu. Thus, exchange between these clusters is thermodynamically favorable for TMS. For TPFBu, $E_{\sigma 2}$ is equal to approximately $2E_{\sigma 1}$. The activation energy $E_{\sigma 2}$ associated with the CAEH mechanism is much higher than the other activation energies because it involves protonation by a weak acid, TEAH+, to form a superacid, PFBuH.

Table 1. Values of the Activation Energy $E_{\sigma o}$ and E_{fo} for TMS, TPFBu, NTMS, and NTPFBu

	LT ($T < T_m$)		HT ($T > T_m$)	
	$E_{\sigma 0}$ (kJ mol^{-1})^a	E_{f0} (kJ mol^{-1})^b	$E_{\sigma 0}$ (kJ mol^{-1})^a	E_{f0} (kJ mol^{-1})^b
TMS	16 ± 1	17 ± 1	2.3 ± 0.1	2.2 ± 0.5
NTMS	15 ± 1	13 ± 1	3.9 ± 0.1	3.8 ± 0.1
TPFBu	21 ± 1	18 ± 1	3.2 ± 0.1	1.9 ± 0.1
NTPFBu	15 ± 1	12 ± 1	2.6 ± 0.5	1.7 ± 0.3

^{a} Values determined by fitting data of Figures 7 and 10 with the VTF equation:[36] $\sigma = A_\sigma T^{-1/2} e^{((-E_\sigma)/R(T-T_0))}$. ^{b} Values determined by fitting data (not shown) with the VTF equation:[36] $f_0 = f_{f_0} T^{-1/2} e^{((-E_{f0})/R(T-T_0))}$.

In summary, pure TMS and TPFBu above the T_m consist primarily of cationic and anionic nanoaggregates. The mechanism of proton conduction involves proton transport between these nanoclusters. The σ_0 conductivity can be described as proton hopping between the cationic nanoclusters, while conductivities σ_1 and σ_2 are associated with conduction involving both the cationic and anionic nanoaggregates.

Conductivities σ_0, σ_1, and σ_2 for NTMS and NTPFBu obtained by fitting the experimental data with eq 2 are plotted versus reciprocal temperature in Figure 9. NTPFBu shows a jump in conductivity σ_0 at the T_m of TPFBu (61 °C) while presenting VTF behavior above and below the T_m. In contrast, there is no discontinuity at the TMS melting point (38 °C) in the σ_0 conductivities of NTMS, and the data exhibit a VTF-type trend that is divisible into two regions, one above and one below the TMS T_m, and is consistent with the DSC and DMA results.[5] Between 70 and 150 °C, where both ionic liquids are expected to be present in liquid nanodomains inside the polymeric membrane, the conductivity σ_0 of NTMS is larger than that of NTPFBu. At 120 °C, $\sigma_{0,NTMS} = 0.0053$ S cm^{-1} and $\sigma_{0,NTPFBu} = 0.0014$ S cm^{-1}. Conductivity depends on the concentration and mobility of free charge carriers. The membranes contain a similar number of moles of the PCILs per sulfonic acid group, as shown in the TG measurements,[5] so the reduction of the NTPFBu conductivity as compared to NTMS is due to a lower mobility of the free charge carriers in the membrane. This reduced mobility results from: (1) the higher viscosity of TPFBu[25] and (2) the presence of TPFBu nanoaggregates in the polymer membrane that are larger in dimension than those of TMS, probably due to perfluorobutane chains that tend to organize in a micellar-like structure.[4] The activation energies $E_{\sigma 0}$ are obtained by fitting the values of σ_0 with the VTF equation at temperatures above and below the PCIL T_m. These $E_{\sigma 0}$ are reported for the membranes and their respective pure ionic liquids in Table 1. Also shown in Table 1 are the activation energies, E_{f0}, obtained from fitting the frequency values f_0 with a VTF equation[21] (data not shown) above and below the PCIL T_m, where $f_0 = 1/(2\pi\tau_0)$ and τ_0 is the relaxation time associated with the conductivity σ_0. The activation energies associated with the conductivity and the relaxation times τ_0 obtained for the doped membrane are similar to those obtained for the pure PCILs. This similarity indicates that: (1) the mechanism of long-range charge transfer in the doped mechanism is dependent on the dynamics of the polymer membrane and of the PCILs contained within;[4] and (2) in both

dx.doi.org/10.1021/jp204242q | J. Phys. Chem. C XXXX, XXX, 000–000

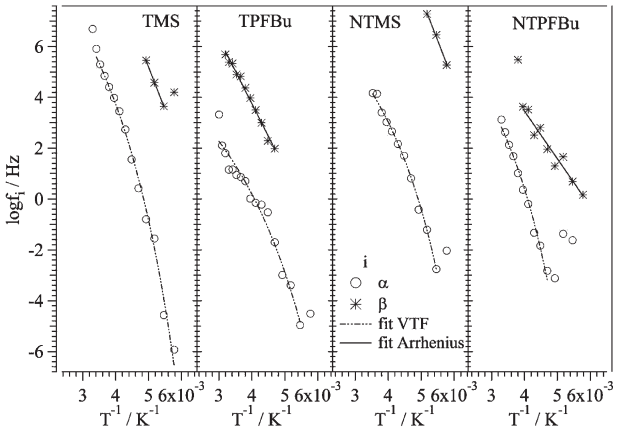

Figure 10. Profiles of log f_α and log f_β as a function of reciprocal temperature for TMS, TPFBu, NTMS, and NTPFBu.

membranes, as in the pure PCILs, long-range conduction is due to the transfer of protons between PCIL cationic clusters present inside the polar domains of nN117. In the doped membrane, the sulfonate group is neutralized with TEA. Therefore, the chemical species involved in charge conduction are the same as for the pure PCILs (TEA, $TEAH^+$, $-SO_3H$, $-SO_3^-$). It is important to distinguish between two types of sulfonates: one belonging to the PCIL anion and one bound to the fluorocarbon chain of nN117. As the charged species are the same, the mechanisms of charge conduction described above (CCHH, CoCC&AA, and CAEH) for the pure PCILs can also explain conduction in the doped membrane. Conductivities σ_0, σ_1, and σ_2 can be associated, respectively, with mechanisms similar to CCHH, CoCC&AA, and CAEH as described for the pure PCILs.

The interfacial conductivities σ_1 and σ_2 appear at temperatures higher than 60 °C. The values of σ_1 and σ_2 expressed as a function of reciprocal temperature are fit with the VTF equation (Figure 9). From the fitting equation, activation energies are obtained for both membranes: $E_{\sigma 1} = 15.2 \pm 0.2$ kJ/mol and $E_{\sigma 2} = 6.7 \pm 0.5$ kJ/mol for NTMS and $E_{\sigma 1} = 19.6 \pm 1.2$ kJ/mol and $E_{\sigma 2} = 9.5 \pm 0.5$ kJ/mol for NTPFBu. Considering the activation energies for σ_1 and σ_2, $E_{\sigma 1}$ is approximately equal to $2E_{\sigma 2}$. The activation energies indicate a lower energy barrier for the CAEH mechanism signifying that this conduction process is facilitated by the host matrix more than the CoCC&AA mechanism. While the activation energies for σ_0 remain almost the same when the PCIL is embedded within the composite membrane, the activation energies $E_{\sigma 1}$ and $E_{\sigma 2}$ (TMS only) exhibit an increase with $E_{\sigma 2} > E_{\sigma 1}$. This behavior is the opposite of that detected in the pristine PCILs. This indicates that the distribution of the PCILs inside the nN117 host material is controlled by interactions with the matrix, which therefore reduces the ability of the PCIL anions to substantially participate in the conduction process. Furthermore, the difference between the $E_{\sigma 1}$ values for TMS is significantly larger than the same difference in TPFBu, which supports a stronger interaction with the nN117 matrix for the unfluorinated PCIL. The activation energy $E_{\sigma 2}$ for NTPFBu is lower than $E_{\sigma 2}$ for pristine TPFBu, suggesting that the CAEH is enhanced by the dynamics of the nN117 host matrix. The presence of VTF-like behavior for conductivities is consistent with the DMA tan δ results.[5] At temperatures above 60 °C both samples exhibit a mechanical transition α_{pc} associated with a decrease in the long-range electrostatic interactions involving the entire nN117

Table 2. Values of the Activation Energy E_β and E_α and of T_0 for TMS, TPFBu, NTMS, and NTPFBu

	E_β or $E_{\beta s}$ (kJ mol^{-1})[a]	E_α or $E_{\alpha s}$ (kJ mol^{-1})[b]	T_0 (K)[b]
TMS	64 ± 1	20 ± 1	115 ± 10
NTMS	64 ± 5	14 ± 4	118 ± 13
TPFBu	49 ± 2	16 ± 2	106 ± 10
NTPFBu	36 ± 3	18 ± 3	131 ± 9

[a] Values determined by fitting data with the Arrhenius equation:[36] $f_\beta = f_{0,\beta} e^{(-E_\beta)/(R(T-T_0))}$. [b] Values determined by fitting data with the VTF equation.[36]

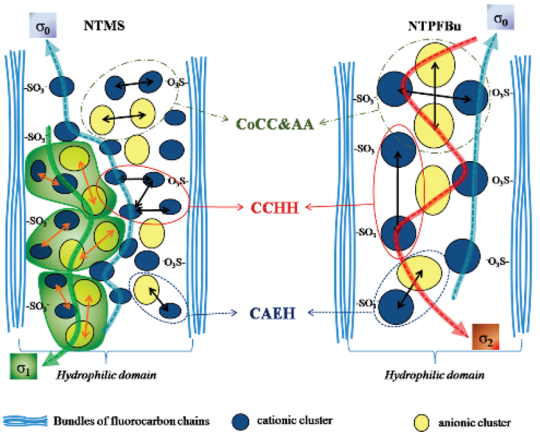

Figure 11. Mechanisms of proton conduction CCHH, CoCC&AA, and CAEH for the doped membranes NTMS and NTPFBu.

structure (primary and secondary structure).[4,42−44] In this context, it is plausible that the electric properties of the membrane, particularly the interfacial polarizations, are dependent on the system morphology and result in the transition at mid to high temperatures (60−150 °C).

From the molecular relaxations observed below the PCIL T_m, the values of the relaxation time associated with the α and β transitions for the membranes and α_s and β_s for the PCILs at different temperatures can be determined by fitting the ε'' spectra with the third term of eq 2. The frequency data $(f_m = (2\pi\tau_i)^{-1}$ with $m = \alpha, \beta, \alpha_s$, or $\beta_s)$ as a function of reciprocal temperature are shown in Figure 10. For the PCILs and the doped membranes, fitting with Arrhenius and VTF equations for the log f_m yields the activation energies, E_m, and T_0 as reported in Table 2. $E_{\alpha s}$ and T_0 are 20 kJ/mol and 115 K for TMS and 16 kJ/mol and 106 K for TPFBu. These values are similar to the E_σ and T_0 values determined from the VTF plots of conductivities at low temperature, which indicates that the mechanism of long-range conduction occurs via the CCHH proton exchange process, which in the membrane is mediated by the segmental motion of the nN117 chains and by the molecular dimensions of the ionic liquid moieties at lower temperatures.

A comparison of the activation energies, E_β, of the β transitions in the doped membranes sheds light on the interaction of the ionic liquid with the polymer matrix. Recall from Paper I[5] that a stronger interaction exists between TMS and the polyether side chain of the nN117 matrix than between TPFBu and the matrix. As discussed above, the β transition represents the relaxation of the polyether side chain interacting with the PCIL. The activation energy E_β for NTMS is almost double that of NTPFBu.

dx.doi.org/10.1021/jp204242q | J. Phys. Chem. C XXXX, XXX, 000–000

A higher activation energy indicates that more energy is required for the relaxation event to occur and therefore a stronger interaction. The implication of this interaction, as also discussed in paper I,[5] is a reduction in the size of the nanodomains of the ionic liquid TMS within the doped membrane NTMS as compared to TPFBu within NTPFBu.

Given that TG results[5] revealed that the membranes contain similar amounts of PCIL per sulfonic group, domains of smaller size would necessarily imply that there is a larger number of PCIL clusters in NTMS and the distance between these clusters is smaller, as shown in Figure 11. More nanodomains closer together would facilitate interaction with the host matrix and increase the density of the proton hopping processes between the domains, resulting in an increase in conductivity inside the hydrophilic domains. The greater conductivity in the NTMS membrane as compared to NTPFBu supports this interpretation. However, the total number of clusters and the ease of proton hopping in the polar local environment alone would not necessarily lead to increased long-range conductivity. The overall morphology of the polymer matrix also must be conducive to the long-range transport of protons: The effect of the PCIL on the overall polymer matrix is important. A stronger interaction of the PCIL with the nN117 side chain stimulates the organization of the nN117 fluorocarbon backbones into the microcrystalline domains.[5] DSC results in Paper I[5] showed that the NTMS matrix had a 67% higher degree of microcrystallinity than the NTPFBu matrix. The higher crystallinity would increase the size of the ordered hydrophobic domains, which could result in a decreased interface between the hydrophobic and hydrophilic domains.

A smaller interface between the hydrophobic and hydrophilic domains increases the connectivity between ionic clusters within the hydrophilic domains and reduces the tortuosity of the channel-like structure of the nN117 host matrix.[45,46] These phenomena promote the conduction process, which would result in an higher conductivity in NTMS when compared to NTPFBu, where the same degree of microcrystalline order is not present.

The overall conduction process would have contributions from all three mechanisms, and the total conductivity, σ_{total}, as shown in eq 8 could be considered the sum of the three conductivities found in Figure 9.

$$\sigma_{total} = \sum_{i=0}^{2} \sigma_i = \sigma_0 + \sigma_1 + \sigma_2 \quad (8)$$

For both NTMS and NTPFBu, σ_0 is at least 2 orders of magnitude higher than either σ_1 or σ_2, meaning that these two conductivities have a negligible contribution to the overall conductivity. Therefore, eq 8 could be simplified to $\sigma_{total} = \sigma_0$, indicating that the long-range conduction process would be primarily due to the CCHH process. In Figure 11, all three conduction processes are shown for both membranes. However, given the simplification of eq 8, the long-range proton transfer largely would follow a path similar to that represented by the blue arrow and would occur via proton exchange between cationic clusters that is mediated by the segmental motion which is associated with the dynamics of the fluorocarbon polymer host matrix.

The work presented here is a fundamental study of the structural modulation of Nafion due to the incorporation of an IL dopant into the host matrix and the effect of the structural reorganization on the properties of the system, specifically the conductivity. This work leads to the conclusion that the conductivity of the system can be improved when the dopant stimulates the matrix to organize into percolation pathways for the migration of charge. In the NTMS and NTPFBu membranes, the PCILs present in the hydrophilic domains of the membrane create percolation pathways for the movement of protons. These percolation pathways provide "shortcuts" for the movement of protons through the membrane as compared to pristine N117 or nN117. Therefore, new membranes that incorporate dopants which induce the formation of well-established pathways for proton conduction will likely lead to the greatest improvement in the conductivity. Furthermore, the mechanical properties of NTMS and NTPFBu, which were reduced by the plasticizing effect of the PCILs, must be improved for the implementation of these membranes as PEMs in a medium-temperature fuel cell. One possible solution in the design of new N117 membranes doped with PCILs may be the use of a hybrid membrane based on N117 doped with a suitable filler that can interact with both the ionic liquid and the polymer matrix as the host matrix because the filler increases the thermo-mechanical stability of the membrane.[43]

4. CONCLUSION

BES measurements of the electric properties of TMS, TPFBu, and doped nN117 membranes elucidate the mechanism of charge conduction and the dielectric relaxations. For the pure PCILs above the T_m, the BES measurements show the presence of three interfacial polarizations associated with mechanisms of proton transfer that are dependent on the nanostructuring of the ionic liquids as molecular aggregates. For the doped membranes, the electric measurements show that the mechanism of long-range charge transfer is mediated by the dynamics of the fluorocarbon polymeric matrix and the nanostructure of the ionic liquids embedded inside the host nN117. BES measurements of the doped membranes also show the presence of three interfacial polarizations, which are dependent on the nanostructuring of the ionic liquid embedded within the polar domains of NTMS and NTPFBu membranes. This interpretation is in accordance with the structure of the doped membrane, which consists of amorphous, microcrystalline, and nanocrystalline domains of the fluorocarbon chains of nN117 and of the polar clusters containing the ionic liquids. These polar clusters are responsible for the ionic conductivity of the material. For temperatures below the PCIL melting points, the BES measurements reveal the presence of two dielectric relaxations α and β that are associated with the dipolar relaxations involving the ionic liquids and the nN117 matrix. The increased activation energy of the β transition for NTMS indicates a stronger interaction between the side chain and the PCIL than in NTPFBu. This suggests a composite membrane structure where the ionic liquids present within the nN117 hydrophilic channels are organized in cationic and anionic nanoaggregates. The size of these aggregates depends on the interaction between the PCIL and the nN117 matrix, resulting in smaller aggregates for TMS than TPFBu. In the composite membrane, the difference in composition is solely due to the selected PCIL anions, so the change in interaction is due to the anion. Stronger interactions lead to an increase in the nN117 matrix microcrystallinity. Together, these two effects result in higher conductivity in NTMS than NTPFBu. The conductivities measured at 130 °C yield $\sigma_{TMS} = 1.4 \times 10^{-2}$ S/cm, $\sigma_{TPFBu} = 9 \times 10^{-3}$ S/cm, $\sigma_{NTMS} = 6.1 \times 10^{-3}$ S/cm, and $\sigma_{NTPFBu} = 1.8 \times 10^{-3}$ S/cm. In the membranes, the mechanism

dx.doi.org/10.1021/jp204242q | J. Phys. Chem. C XXXX, XXX, 000–000

of long-range charge transfer occurs via a proton exchange process between cationic clusters, which is mediated by the segmental motion of the nN117 chains and the molecular dimensions of the ionic liquid aggregates.

Despite a necessity for improved mechanical properties, which are reduced by the plasticizing effect of the ionic liquids, the conductivities measured at temperatures above 100 °C and the good thermal stability[5] make NTMS and NTPFBu promising materials for PEMFCs operating at 120 °C.

■ ASSOCIATED CONTENT

Supporting Information. Additional experimental details. This material is available free of charge via the Internet at http://pubs.acs.org.

■ AUTHOR INFORMATION

Corresponding Author
*E-mail: vito.dinoto@unipd.it.

■ ACKNOWLEDGMENT

This research was funded by the Italian MURST project PRIN2008, entitled "Direct polymer electrolyte membrane fuel cells: synthesis and study in prototype cells of hybrid inorganic–organic membranes and electrode materials".

■ REFERENCES

(1) Wainright, J. S.; Litt, M. H.; Savinell, R. F. High-temperature Membranes. In *Handbook of Fuel Cells: Fundamentals Technology and Applications*; Vielstich, W., Lamm, A., Gasteiger, H. A., Eds.; Wiley: West Sussex, 2003; Vol. 3, pp 436–446.

(2) Li, Q.; He, R.; Jensen, J. O.; Bjerrum, N. J. *Chem. Mater.* **2003**, *15* (26), 4896–4915.

(3) "The DuPont Oval Logo, DuPont, and The miracles of science are trademarks or registered trademarks of DuPont or its affiliates."

(4) Di Noto, V.; Negro, E.; Sanchez, J. Y.; Iojoiu, C. *J. Am. Chem. Soc.* **2010**, *132* (7), 2183–2195.

(5) Di Noto, V.; Piga, M.; Giffin, G. A.; Lavina, S.; Smotkin, E. S.; Sanchez, J. Y.; Iojoiu, C. *J. Phys. Chem. C* **2011**, DOI: 10.1021/jp204241y.

(6) Schonhals, A.; Kremer, F. *Broadband Dielectric Spectroscopy*; Springer: Berlin, 2003.

(7) Nakamura, K.; Shikata, T. *ChemPhysChem* **2010**, *11* (1), 285–294.

(8) Weingartner, H.; Sasisanker, P.; Daguenet, C.; Dyson, P. J.; Krossing, I.; Slattery, J. M.; Schubert, T. *J. Phys. Chem. B* **2007**, *111* (18), 4775–4780.

(9) Wulf, A.; Ludwig, R.; Sasisanker, P.; Weingartner, H. *Chem. Phys. Lett.* **2007**, *439* (4–6), 323–326.

(10) Galinski, M.; Lewandowski, A.; Stepniak, I. *Electrochim. Acta* **2006**, *51* (26), 5567–5580.

(11) Malhotra, S. V. *Ionic Liquid Applications: Pharmaceuticals, Therapeutics, and Biotechnology*; American Chemical Society: Washington DC, 2010; Vol. 1038.

(12) Plechkova, N. V.; Rogers, R. D.; Seddon, K. R. *Ionic Liquids: From Knowledge to Application*; American Chemical Society: Washington DC, 2009; Vol. 1030.

(13) Rogers, R. D.; Seddon, K. R. *Ionic Liquids: Industrial Applications for Green Chemistry*. American Chemical Society: Washington DC, 2002; Vol. 818.

(14) Onho, H. *Electrochemical Aspects of Ionic Liquids*; Wiley: Hoboken, 2005.

(15) Lin, B.; Cheng, S.; Qiu, L.; Yan, F.; Shang, S.; Lu, J. *Chem. Mater.* **2010**, *22* (5), 1807–1813.

(16) Yan, F.; Yu, S.; Zhang, X.; Qiu, L.; Chu, F.; You, J.; Lu, J. *Chem. Mater.* **2009**, *21* (8), 1480–1484.

(17) Dyson, P. J.; Khalaila, I.; Luettgen, S.; McIndoe, J. S.; Zhao, D. B. *Chem. Commun.* **2004**, No. 19, 2204–2205.

(18) Triolo, A.; Russina, O.; Bleif, H. J.; Di Cola, E. *J. Phys. Chem. B* **2007**, *111* (18), 4641–4644.

(19) Turton, D. A.; Hunger, J.; Stoppa, A.; Hefter, G.; Thoman, A.; Walther, M.; Buchner, R.; Wynne, K. *J. Am. Chem. Soc.* **2009**, *131* (31), 11140–11146.

(20) Di Noto, V. *J. Phys. Chem. B* **2002**, *106* (43), 11139–11154.

(21) Di Noto, V.; Vittadello, M.; Lavina, S.; Fauri, M.; Biscazzo, S. *J. Phys. Chem. B* **2001**, *105* (20), 4584–4595.

(22) Klein, R. J.; Zhang, S. H.; Dou, S.; Jones, B. H.; Colby, R. H.; Runt, J. *J. Chem. Phys.* **2006**, *124*, 14.

(23) Krause, C.; Sangoro, J. R.; Iacob, C.; Kremer, F. *J. Phys. Chem. B* **2010**, *114* (1), 382–386.

(24) Serghei, A.; Tress, M.; Sangoro, J. R.; Kremer, F. *Phys. Rev. B: Condens. Matter* **2009**, *80*, 18.

(25) Martinez, M.; Molmeret, Y.; Cointeaux, L.; Iojoiu, C.; Lepretre, J. C.; El Kissi, N.; Judeinstein, P.; Sanchez, J. Y. *J. Power Sources* **2010**, *195* (18), 5829–5839.

(26) Xiao, D.; Hines, L. G.; Li, S. F.; Bartsch, R. A.; Quitevis, E. L.; Russina, O.; Triolo, A. *J. Phys. Chem. B* **2009**, *113* (18), 6426–6433.

(27) Kohler, F.; Atrops, H.; Kalali, H.; Liebermann, E.; Wilhelm, E.; Ratkovics, F.; Salamon, T. *J. Phys. Chem.* **1981**, *85* (17), 2520–2524.

(28) Kohler, F.; Liebermann, E.; Miksch, G.; Kainz, C. *J. Phys. Chem.* **1972**, *76* (19), 2764–2768.

(29) Hojo, M.; Miyauchi, Y.; Imai, Y. *Bull. Chem. Soc. Jpn.* **1990**, *63* (11), 3288–3295.

(30) Kennedy, D. F.; Drummond, C. J. *J. Phys. Chem. B* **2009**, *113* (17), 5690–5693.

(31) Dura, J. A.; Murthi, V. S.; Hartman, M.; Satija, S. K.; Majkrzak, C. F. *Macromolecules* **2009**, *42* (13), 4769–4774.

(32) Rubatat, L.; Rollet, A. L.; Gebel, G.; Diat, O. *Macromolecules* **2002**, *35* (10), 4050–4055.

(33) Rollet, A.-L.; Diat, O.; Gebel, G. *J. Phys. Chem. B* **2002**, *106* (12), 3033–3036.

(34) Di Noto, V.; Lavina, S.; Negro, E.; Vittadello, M.; Conti, F.; Piga, M.; Pace, G. *J. Power Sources* **2009**, *187* (1), 57–66.

(35) Di Noto, V.; Vittadello, M.; Greenbaum, S. G.; Suarez, S.; Kano, K.; Furukawa, T. *J. Phys. Chem. B* **2004**, *108* (49), 18832–18844.

(36) Vittadello, M.; Suarez, S.; Chung, S. H.; Fujimoto, K.; Di Noto, V.; Greenbaum, S. G.; Furukawa, T. *Electrochim. Acta* **2003**, *48* (14–16), 2227–2237.

(37) Iojoiu, C.; Judeinstein, P.; Sanchez, J. Y. *Electrochim. Acta* **2007**, *53* (4), 1395–1403.

(38) Atkins, P.; de Paula, J. *Physical Chemistry*. 8th ed.; Oxford University Press: Oxford, 2006.

(39) Judeinstein, P.; Iojoiu, C.; Sanchez, J. Y.; Ancian, B. *J. Phys. Chem. B* **2008**, *112* (12), 3680–3683.

(40) Lee, S. Y.; Ogawa, A.; Kanno, M.; Nakamoto, H.; Yasuda, T.; Watanabe, M. *J. Am. Chem. Soc.* **2010**, *132* (28), 9764–9773.

(41) Hertz, H. G.; Lindman, B.; Siepe, V. *Ber. Bunsenges. Phys. Chem.* **1969**, *73* (6), 542–9.

(42) Di Noto, V.; Gliubizzi, R.; Negro, E.; Pace, G. *J. Phys. Chem. B* **2006**, *110* (49), 24972–24986.

(43) Di Noto, V.; Piga, M.; Lavina, S.; Negro, E.; Yoshida, K.; Ito, R.; Furukawa, T. *Electrochim. Acta* **2010**, *55* (4), 1431–1444.

(44) Page, K. A.; Cable, K. M.; Moore, R. B. *Macromolecules* **2005**, *38* (15), 6472–6484.

(45) Kreuer, K. D. *J. Membr. Sci.* **2001**, *185* (1), 29–39.

(46) Wu, D.; Paddison, S. J.; Elliott, J. A. *Energy Environ. Sci.* **2008**, *1* (2), 284–293.